

THE ARCHAEOMETRICAL INVESTIGATIONS OF SOME IRON
COMPONENTS FROM THE OTTOMAN PERIOD STRUCTURES

A THESIS SUBMITTED TO
THE GRADUATE SCHOOL OF NATURAL AND APPLIED SCIENCES
OF
MIDDLE EAST TECHNICAL UNIVERSITY

BY

NURDAN YUCEL

IN PARTIAL FULFILLMENT OF THE REQUIREMENTS
FOR
THE DEGREE OF DOCTOR OF PHILOSOPHY
IN
ARCHAEOMETRY

SEPTEMBER 2022

Approval of the thesis:

**THE ARCHAEOMETRICAL INVESTIGATIONS OF SOME IRON
COMPONENTS FROM THE OTTOMAN PERIOD STRUCTURES**

submitted by NURDAN YUCEL in partial fulfillment of the requirements for the degree of **Doctor of Philosophy** in **Archeometry**, **Middle East Technical University** by,

Prof. Dr. Halil Kalıpçılar
Dean, **Graduate School of Natural and Applied Sciences** _____

Prof. Dr. Gülay Ertaş
Head of the Department, **Archeometry** _____

Prof. Dr. Emine N. Caner-Saltık
Supervisor, **Archeometry, METU** _____

Prof. Dr. Ali Kalkanlı
Co-Supervisor, **Metallurgical and Materials Eng., METU** _____

Examining Committee Members:

Prof. Dr. Ömür Bakırer
Archeometry, METU _____

Prof. Dr. Emine N. Caner Saltık
Archeometry, METU _____

Prof. Dr. Ali İhsan Arol
Mining Engineering, METU _____

Prof Dr. Özgül Keleş
Metallurgical and Materials Eng., İ.T.Ü. _____

Prof. Dr. Meriç Bakiler
Kültür Varlıklarını Koruma ve Onarım Böl., M.S.G.Ü _____

Date: 02.09.2022

I hereby declare that all information in this document has been obtained and presented in accordance with academic rules and ethical conduct. I also declare that, as required by these rules and conduct, I have fully cited and referenced all material and results that are not original to this work.

Name Surname: Nurdan Yücel

Signature:

ABSTRACT

THE ARCHAEOMETRICAL INVESTIGATIONS OF SOME IRON COMPONENTS FROM THE OTTOMAN PERIOD STRUCTURES

Yücel, Nurdan
Doctor of Philosophy, Archeometry
Supervisor: Prof. Dr. Emine N. Caner Saltık
Co-Supervisor: Prof. Dr. Ali Kalkanlı

September 2022, 347 pages

Characterization of corrosion layers on iron artifacts and their iron oxide phases are important for long term prediction of complex iron corrosion mechanisms in different atmospheric conditions for improvements in corrosion resistance of iron products as well as maintenance and conservation treatments of iron artifacts.

Exposed iron components in the Ottoman period historical buildings visually seem to be in quite a good state of preservation, in spite of their longterm exposure to atmospheric conditions. The purpose of this study was to investigate metallurgical and corrosion properties of iron components used in some Ottoman period historical buildings to derive information on their technological and corrosion characteristics.

In this study, some iron components taken from the hammam buildings (Gazi Mihal Hammam constructed around 1450 and Kılıç Ali Paşa Hammam around 1580) representing the the Classical Period and other iron components from some historical dwellings in Foça, Izmir and in Tekkekoy, Samsun representing late Ottoman period (19th cc) were examined.

The metalurgical properties of the artifacts were investigated in terms of their Brinell hardness measurements, elemental composition by spark emission spectrometry and the microstructure of the main metal bodies by using a metallographic microscope and digital microscope. The corrosion layers were examined on polished and etched cross-sections using μ -Raman spectrometer and SEM-EDX. Powdered samples scraped from the corrosion layers were studied by XRD and FTIR.

All iron objects examined have corrosion layers on their surface where the corrosion products are mainly goethite and rarely hematite formed in open air environments namely urban, rural (interior, exterior) and burial environment. The goethite formation on the iron objects is favorable in open air atmospheric conditions during repeated wet-dry cycles at around pH 7-8. The corrosion layers of the objects are further classified as perfect, medium and imperfect corrosion layers depending on their thickness and compactness. They are mostly composed of nano-sized goethite particles with good crystallinity and are free of impurities. The perfect corrosion layers have finer nano-sized particles with good crystallinity that is thought to be an indication of good stability for goethite in comparison to its amorphous state. The protective ability of the corrosion layer is closely related with fine size of goethite particles and its compactness. Nano-sized goethite particles appear to have the super-paramagnetic property affecting the compactness of corrosion layer on the iron object.

The microstructural properties of the historical objects seem to have some influence on perfect corrosion layer formation. Objects having perfect corrosion layers have finer ferrite grain size. Some elements in the composition of the objects such as manganese, carbon, silicon, phosphorous, sulfur, chromium and nickel were further discussed for their influence in the formation of protective corrosion layer.

Keywords: Historical Steel, Corrosion Products, Goethite Formation, Microstructure, μ -Raman Spectroscopy.

ÖZ

**OSMANLI DÖNEMİ YAPILARINDA KULLANILAN BAZI DEMİR
ELEMANLARIN ARKEOMETRİK YÖNDEN İNCELENMESİ**

Yücel, Nurdan
Doktora, Arkeometri
Tez Yöneticisi: Prof. Dr. Emine N. Caner Saltık
Ortak Tez Yöneticisi: Prof. Dr. Ali Kalkanlı

Eylül 2022, 347 sayfa

Demir objeler üzerinde atmosferik koşullarda oluşan korozyon tabakalarının ve bu tabakaların içeriğindeki demir oksit fazlarının tanımlanma arařtırmaları, demir ürünlerinin korozyon direncinin uzun bir zaman dilimi için sağlanmasında ve ayrıca demir eserlerin bakım ve koruma işlemlerine yönelik ilerlemeler konusundaki çalışmalarda önem taşımaktadır.

Osmanlı dönemi tarihi yapılarında bulunan demir aksamaların, uzun süreli atmosferik koşullara maruz kalmalarına rağmen görsel olarak oldukça iyi durumda oldukları izlenmektedir. Bu çalışmanın amacı, bazı Osmanlı dönemi tarihi yapılarında kullanılan demir aksamaların metalürjik ve korozyon özelliklerini arařtırmak, teknolojik ve korozyon özellikleri hakkında bilgi edinmektir.

Bu çalışmada, Klasik Dönemi temsil eden hamam yapılarından (~1450 yılında yapılan Gazi Mihal Hamamı ve ~1580 yılında yapılan Kılıç Ali Paşa Hamamı) alınan bazı demir objeler ile geç Osmanlı dönemini (19. yy) temsil eden, Foça, İzmir ve Samsun, Tekkeköy'deki bazı tarihi konutlarda kullanılmış olan çeşitli demir parçalar incelenmiştir.

Eserlerin metalurjik özellikleri, Brinell sertlik değerleri, emisyon spektrometrisi ile belirlenen elementel bileşimleri, metalografik mikroskop ve dijital mikroskop kullanılarak ana metal gövdelerinin mikro yapı tespit çalışmaları ile araştırılmıştır. Korozyon tabakaları, parlatılmış ve dağlanmış kesitlerde μ -Raman spektrometresi ve SEM-EDX kullanılarak incelenmiştir. Korozyon tabakalarından kazınan toz numuneler ise XRD ve FTIR analizleri ile incelenmiştir.

Açık hava ortamlarında bulunan tüm demir objelerin yüzeylerindeki korozyon tabakasının hemen her zaman götit ve nadiren hematit bileşiminde olduğu görülmüştür. Demir objelerin üzerinde götit oluşumu için gereken şartlar, tekrarlanan ıslak-kuru döngüler ile açık hava atmosferik koşullarında ve pH 7-8 civarında sağlanabilmektedir. Demir objelerin üzerindeki korozyon tabakaları ayrıca kalınlık ve doluluk durumuna göre mükemmel, orta ve bozuk götit tabakaları olarak sınıflandırılmıştır. Mükemmel götit tabakaları çoğunlukla iyi kristal yapıya sahip olup, nano boyutlu götit parçacıklarından oluşmakta ve safsızlık içermemektedir. Amorf götit parçacıkları ile karşılaştırıldığında mükemmel götit tabakalarının içeriği daha dengelidir. Götit tabakasının koruyucu özelliği, götit parçacıklarının ince boyutu ve doluluk durumu ile yakından ilişkilidir. Ayrıca, nano boyutlu götit parçacıklarının, süper paramanyetik özelliğe sahip olmaları, demir obje üzerindeki götit tabakasının doluluk durumunu destekleyen diğer bir parametredir.

Demir objelerin mikroyapısal özelliklerinin, mükemmel götit tabakası oluşumu üzerinde de etkisi olduğu görülmektedir. Mükemmel götit katmanlarına sahip objelerin daha küçük boyutta ferrit tanelerinden oluştuğu görülmektedir. Çalışmada ayrıca, objelerin bileşiminde bulunan mangan, karbon, silikon fosfor, kükürt, krom ve nikel gibi bazı elementlerin koruyucu götit tabakasının oluşumundaki etkileri de tartışılmıştır.

Anahtar Kelimeler: Tarihi Demir, Korozyon Ürünleri, Götit Oluşumu, Mikroyapı, μ -Raman spektroskopisi.

*I would like to dedicate this work to
my mother Nejla Yücel and my father Hasan Şevki Yücel...*

ACKNOWLEDGEMENTS

I would like to express my deepest gratitude and thanks to my supervisor, Prof. Dr. Emine N. Caner-Saltık and co-supervisor, Prof. Dr. Ali Kalkanlı for their guidance, patience, advice, criticism, encouragements and insight throughout the research.

I would also like to thank Prof. Dr. Ömür Bakırer and Prof. Dr. Ali İhsan Arol for their suggestions and comments. I also could not have undertaken this journey without my defense committee, who generously provided knowledge and expertise.

I am thankful to the staff and technicians at METU Research Laboratory for the Conservation of Historical Monuments and at METU Metallurgical and Materials Engineering department, who have helped me during my research. I would also like to thank to my class-mates for their kind helps during my studies.

I am also very grateful to Prof. Dr. Nevin Ozkan Speelman and Dr. Fulya Karahan Dag who have assisted me and given me advice during my programs.

Technical assistance of material's laboratory and machining shop team of Samsun Makina Sanayi and Layne Bowler Pompa Sanayi A.Ş. are gratefully acknowledged.

Very special thanks to Kutlu Karavelioğlu who has been an ideal teacher, mentor, and role model, offering advice and encouragement throughout my professional and academic life that have been very important to me.

Looking back over the past years, I can think of many people who deserve credit for their contributions to my studies. I would like to express my deepest gratitude to my uncles Mehmet Aydın, Turgut Aydın, Turhan Aydın and Mehmet Nuri Yücel, my aunt Emine Erişen, my brother Y. Adnan Yücel, my sisters Berrin Yücel-İnce, Zerrin Demirkaya and Handan Yücel-Yıldırım for encouraging and supporting me throughout my studies. Last, but not least, I would like to thank to my family, my cousins, my nieces and nephews, and close friends for supporting me throughout this process.

TABLE OF CONTENTS

ABSTRACT.....	v
ÖZ vii	
ACKNOWLEDGEMENTS.....	x
LIST OF TABLES.....	xiv
LIST OF FIGURES.....	xix
LIST OF ABBREVIATIONS.....	xxxviii
CHAPTERS	
INTRODUCTION.....	1
1.1 Argument.....	2
1.2 Aims and Objectives.....	4
1.3 Disposition.....	5
LITERATURE REVIEW.....	9
2.1 Use of Iron and Steel as Construction Components in Historical Structures of the Ottoman Period.....	10
2.2 Ottoman Period Iron Metallurgy.....	11
2.2.1 Iron production centers and trade activities during the 15th, 16th and 19th centuries.....	11
2.3 Iron Ore Deposits in Anatolia at Present.....	17
2.4 Studies on Iron Goods and Production Processes in Ottoman Land.....	21
2.5 Iron Oxides and Their Properties.....	28
2.6 Formation and Transformation Mechanisms of Iron Oxides.....	38
2.7 Precursors for Goethite and Hematite Formation.....	42
EXPERIMENTAL METHODS.....	49

3.1 Monuments, Sampling and Nomenclature	50
3.2 Methods of Analyses	60
3.2.1 Visual, Dimensional and Weight Analysis of Iron Samples:	61
3.2.2 Preparation of Samples to be Used for Analyses:	61
3.2.3 Metallographic analysis by Metallographic Microscopes:	62
3.2.4 SEM-EDX Analysis:	64
3.2.5 Hardness Test:	64
3.2.6 Analysis by Spark Emission Spectrometry:	64
3.2.7 Mineralogical Analysis:	65
3.2.8 PAI Calculations	68
EXPERIMENTAL RESULTS	71
4.1 Basic Visual and Dimensional Characteristics	72
4.2 Results of Elemental Compositions by Using Spark Emission Spectrometer and SEM-EDX	78
4.2.1. Results of Elemental Compositions by Using Spark Emission Spectrometer	78
4.2.2. Results of Elemental Compositions by Using SEM-EDX	85
4.3 Results of Microscopical Investigations on Metal Body and Corrosion Layer	100
4.3.1 Metallographic characteristics of metal bodies	101
4.3.2 Morphological and Compositional Characteristics of the Corrosion Layers	117
4.4. FTIR Spectroscopy Analyses: Compositional Characteristics of the Corrosion Layers in Powder Form	147

4.5 Examination of morphological and compositional characteristics of the corrosion layers by using μ -Raman Spectroscopy	176
4.5.1 Raman Analyses of the 15 th Century Samples	176
4.5.2 Raman Analyses of the 16 th Century Samples	187
4.5.3 Raman Analyses of the 19 th Century Samples	216
4.5.4 Protective Ability Index (PAI) of the Corrosion Layer	254
4.6 Compositional characteristics of the corrosion layers in powder form by using X-ray powder diffraction (XRD) spectroscopy	261
DISCUSSIONS	285
5.1. Types and Properties of Protective Corrosion Layers on Historical Iron Objects	285
5.1.1 Classification of protective corrosion layers based on their thickness and morphological characteristics	286
5.1.2 Protective ability of corrosion layers for the 15 th , 16 th and 19 th century objects in terms of their PAI Values, Rate of Corrosion, Average Particle Size of Goethite and Its Crystallinity	293
5.2 Description of metallurgical properties of historical iron	300
5.2.1 Characteristics of Goethite Layer and Elemental Composition of Metal Body:	300
5.2.2 Cross examination of Data Multiple Factors Effecting Formation of Goethite Layer	312
CONCLUSION	317
6.1 Future Studies	321
REFERENCES	323
CURRICULUM VITAE	347

LIST OF TABLES

TABLES

Table 2. 1 Some Regions in Anatolia and the Balkans and their iron ore reserves.	19
Table 2. 2 The main physical properties of some iron oxides, hydroxides and oxyhydroxides found in nature (BD: Bulk density; MP: Melting Point).	35
Table 2. 3 Some important thermodynamic characteristics of iron ore minerals.	37
Table 3. 1 The iron objects, their coding and description.	52
Table 3. 2 List of samples from Gazi Mihal Hammam, Edirne and their description (15th cc):	53
Table 3. 3 List of studied samples from Kılıç Ali Paşa Hammam, Tophane, Istanbul and their description (16th cc):	55
Table 3. 4 List of studied samples from Foça dwellings, Izmir and their description (19th cc):	57
Table 3. 5 List of studied samples from Tekkekoy Dwelling, Samsun and their description (19th cc).	59
Table 3. 6 Summary of the different phases theoretically calculated in percentage by using the C content of the samples:	63
Table 4. 1 Visual and dimensional characteristics of iron samples from Gazi Mihal Hamamı, Edirne (15th cc):	72
Table 4. 2 Visual and Dimensional characteristics of iron samples from Kılıç Ali Paşa Hammam, Istanbul (16th cc):	73
Table 4. 3 Visual and Dimensional characteristics of iron samples from Foça Dwellings, Foça – Izmir, (19th cc).	75
Table 4. 4 Visual and dimensional characteristics of iron samples from Tekkekoy Dwellings, Tekkekoy – Samsun, (19th cc):	77
Table 4. 5 Weight percentages of some important elements in the composition of the sample (GMH-Me-02) from the 15th century and the samples from the 16th century analyzed by spark emission spectrometer.	79

Table 4. 6 Weight percentages of some important elements in the composition of the samples from 19th century analyzed by spark emission spectrometer.	80
Table 4. 7 Weight percent of important elements in the composition of the nail sample body (MSH-KAP-01) (16th century) by the EDX analysis.	87
Table 4. 8 EDX analysis of a pit (point 1) from the main body of an iron sample (MSH-KAP-03) (16th cc): Weight percentage of some important elements in the pit's composition.....	95
Table 4. 9 EDX analysis of the main body in the nail sample head (MSH-KAP-12) (16th cc): Weight percentage of the elements in its composition.	97
Table 4. 10 EDX analysis of the main body in an iron sample (MSH-KAP-12) (16th cc): Weight percentage of elements in its composition.....	98
Table 4. 11 EDX analysis of the shark (sword) shaped formation in the main body of the iron sample (MSH-KAP-12) (16th cc): Weight percentage of elements in its composition.....	99
Table 4. 12 EDX analysis of a pitting location in the main body of an iron sample (MSH-KAP-12) (16th cc): Weight percentage of elements in its composition.....	99
Table 4. 13 The theoretically calculated FeC (cementite) phase percentages of the samples from 15th, 16th and 19th centuries.	102
Table 4. 14 Microstructural analyses and Brinell hardness results of the samples from 15th century.....	104
Table 4. 15 Microstructural analyses and Brinell hardness results of iron samples from the 16th century.....	109
Table 4. 16 Microstructural analyses and Brinell hardness results of iron samples from 19th century.....	115
Table 4. 17 Morphological characteristics and thickness of corrosion layers for the samples from 15th century.....	121
Table 4. 18 Weight percentage of elements in the composition of RF (MSH-KAP-02) analyzed by EDX (16th cc).	131
Table 4. 19 Weight percentage of the elements in the composition of the crack location (MSH-KAP-02) analyzed by EDX (16th cc).	133

Table 4. 20 Weight percentage of elements in the composition from ICL of a nail (MSH-KAP-12) analyzed by EDX (16th cc).	135
Table 4. 21 Morphological characteristics and thickness of corrosion layers for iron samples from 16th century.	136
Table 4. 22 Morphological characteristics and thickness of corrosion layers for iron samples from 19th century.	146
Table 4. 23 Interpretation of the degree of crystallinity of goethite and lepidocrocite by FTIR Analysis.	149
Table 4. 24 Iron oxides layering in the corrosion of the samples used for 15th century Gazi Mihal Hammam in Edirne by FTIR Analysis.	152
Table 4. 25 Iron oxides layering in the corrosion of the samples used for 16th century Kılıç Ali Paşa Hammam by FTIR Analysis.	157
Table 4. 26 Iron oxides layering in the corrosion of the objects from the 19th century dwellings in Foça, İzmir and Tekkekoy, Samsun under different atmospheric conditions observed by FTIR Analysis.	173
Table 4. 27 Iron oxides found by FTIR in the corrosion layer of the samples from 15th, 16th and 19th century objects.	175
Table 4. 28 Iron oxides followed by μ -Raman analyses in the corrosion layer of a door lock piece (GMH-Me-02) (15th cc).	181
Table 4. 29 Iron oxides found by μ -Raman analyses in the corrosion layer of a plaster nail (GMH-Me-04) (15th cc).	187
Table 4. 30 Iron oxides followed by μ -Raman analyses in the corrosion layer of a nail (MSH-KAP-01) (16th cc).	191
Table 4. 31 Iron oxides followed by μ -Raman analyses in the corrosion layer of an iron object (MSH-KAP-02) (16th cc).	196
Table 4. 32 Iron oxides followed by μ -Raman analyses in the corrosion layer of a nail (MSH-KAP-03) (16th cc).	204
Table 4. 33 Iron oxides followed by μ -Raman analyses in the corrosion layer of a nail (MSH-KAP-09) (16th cc).	211

Table 4. 34 Iron oxides followed by μ -Raman analyses in the corrosion layer of a nail (MSH-KAP-12) (16th cc).	214
Table 4. 35 Iron oxides followed by μ -Raman analyses in the corrosion layers of the objects from Kiliç Ali Pasha Hammam building (16th cc).	215
Table 4. 36 Iron oxides followed by μ -Raman analyses in the corrosion layer of the nail (FKM-02) (19th cc).	218
Table 4. 37 Iron oxides followed by μ -Raman analyses in the corrosion layer of a door lock piece (FKM-03) (19th cc).	220
Table 4. 38 Iron oxides followed by μ -Raman analyses in the corrosion layer of a hinge piece (FKM-04) (19th cc).	223
Table 4. 39 Iron oxides followed by μ -Raman analyses in the corrosion layer of a female hinge piece (FKM-05) (19th cc).	225
Table 4. 40 Iron oxides followed by μ -Raman analyses in the corrosion layer of a buried nail (FKM-07) (19th cc).	227
Table 4. 41 Iron oxides followed by μ -Raman analyses in the corrosion layer of an L-shaped iron object (FKM-08) (19th cc).	233
Table 4. 42 Iron oxides followed by μ -Raman analyses in the corrosion layer of an iron nail (FKM-10) (19th cc).	237
Table 4. 43 Iron oxides followed by μ -Raman analyses in the corrosion layer of an iron nail (FKM-11) (19th cc).	246
Table 4. 44 Iron oxides followed by μ -Raman analyses in the corrosion layer of a door lock piece (T-D-01) (19th cc).	248
Table 4. 45 Iron oxides followed by μ -Raman analyses in the corrosion layer of a door lock piece (T-N-04) (19th cc).	252
Table 4. 46 Iron oxides followed by μ -Raman analyses in the corrosion layers of the objects in dwellings of Foça – İzmir and Tekkekoy - Samsun together with the samples from Ottoman layer excavations in Foça - İzmir (19th cc).	253
Table 4. 47 Corrosion layer thicknesses and PAI values of the 15th century objects.	254

Table 4. 48 Corrosion layer thicknesses and PAI values of the 16th century objects.	256
Table 4. 49 Corrosion layer thicknesses and PAI values of the 19th century objects.	259
Table 4. 50 The relationship with the crystallite size and the full width at half maximum derived from XRD analyses (Speakman, 2007).....	262
Table 4. 51 XRD peaks at 2θ data for most common iron oxides and common minerals observed.....	263
Table 4. 52 Iron oxides layering in the corrosion of the samples from the 15th, 16th and 19th centuries examined by XRD Analysis.....	283
Table 5. 1 Summary of the analytical results on the properties of inner corrosion layers belonging to the iron objects from different historical periods.....	291

LIST OF FIGURES

FIGURES

Figure 2. 1 The most important iron ore deposits and production centers in Rumelia in the Ottoman period.	13
Figure 2. 2 The important iron ore deposits and production centers in Anatolia in the Ottoman period	13
Figure 2. 3 Important iron ore deposits in Turkey	20
Figure 2. 4 Four main stages of production process for iron goods	22
Figure 2. 5 Solubilities of goethite, hematite and lepidocrocite as a function of pH	32
Figure 3. 1 Gazi Mihal Hammam, Edirne (Photo taken by Nurdan Yucel, 2012)	53
Figure 3. 2 Kılıç Ali Paşa Hammam, Tophane, Istanbul: a) Exterior of the Hammam b) Interior of the Hammam after restoration	54
Figure 3. 3 Dwellings from Foça, Izmir: a) A dwelling currently under restoration, b) An uninhabited dwelling.. ..	56
Figure 3. 4 Dwelling from Tekkeköy, Samsun: a) North and east view, b) South view from main entrance.	58
Figure 4. 1 a) SEM image of a door locking iron piece (GMH-Me-02) from 15th century: elemental analysis area starting from metal body to TM Layer. b) EDX analysis results: Fe, O, Ca, Si, Mg, Al, K and Cl.	85
Figure 4. 2 a) SEM image of a nail (GMH-Me-04) from 15th century: elemental analysis area starting from metal body to TM Layer. b) EDX analysis results: Fe, O, Ca, Si, Mn, Al, Cr and S.	86
Figure 4. 3 SEM image (550x) of a nail head (MSH-KAP-01): Shark (sword) shaped images containing manganese sulfide (MnS) and pitting corrosion locations having Fe, Si, Mn and O.	87

Figure 4. 4 EDX spectrum of a nail head (MSH-KAP-01) at a shark (sword) shaped location: Mn and S.....	88
Figure 4. 5 EDX spectrum of a grain from a nail head (MSH-KAP-01): Fe as the main element.	88
Figure 4. 6 EDX spectrum of a grain boundary from a nail head (MSH-KAP-01) with no segregation.....	89
Figure 4. 7 EDX spectrum of a pitting corrosion location in the nail head (MSH-KAP-01): Fe, Si, O, Mn and S.....	89
Figure 4. 8 EDX spectrum of a pitting corrosion location in the nail head (MSH-KAP-01): Fe, Si, O and Mn.....	90
Figure 4. 9 SEM image of the main metal body in an iron sample head (MSH-KAP-02). Numbers indicate the locations of EDX analyses.	91
Figure 4. 10 EDX spectrum representing the points 4, 5 and 6 in the main body of the iron sample head (MSH-KAP-02): Fe as the main element.	91
Figure 4. 11 EDX spectrum representing the points 1, 2 and 7 in the main body of the iron sample head (MSH-KAP-02): Fe, Si, Mn, P, S, Al, Ca, Mg and O.....	92
Figure 4. 12 EDX spectrum of the point 3 in the main body of the iron sample head (MSH-KAP-02): Fe, Mn, O, Si, Al, P and Ca.....	92
Figure 4. 13 EDX spectrum of the point 8 in the main body of an iron sample head (MSH-KAP-02): Fe, Si, Na, Cl, S and K.	93
Figure 4. 14 SEM image (1000X) of the main body: An iron nail head from the dome (MSH-KAP-03).	94
Figure 4. 15 EDX analysis at the main body of the iron sample (MSH-KAP-03): Fe is the main element.	94
Figure 4. 16 EDX analysis at the main body of the iron sample (MSH-KAP-03): Fe, O, Si, Ca, S, P, Cl and Al.	95
Figure 4. 17 a) SEM view from the main body of the sample head (MSH-KAP-12), b) EDX analysis of the main body: Fe, O, Si, Ca and Al.	96
Figure 4. 18 a) SEM view of the main body in the nail sample head (MSH-KAP-12). b) EDX analysis of the main body: Fe, O, Si, Ca, Al and S.....	97

Figure 4. 19 a) SEM view of a sword shaped impurity in the main body of the iron sample (MSH-KAP-12), b) EDX spectrum of the sword shaped impurity: Mn and S.	98
Figure 4. 20 a) SEM image of the pitting locations in the main body of an iron nail (MSH-KAP-12); b) EDX analysis of a pitting location: Fe, Na, Cl, and K.	99
Figure 4. 21 a) SEM image and EDX analysis of the main body in an iron nail (FKM-02): Fe and Si. b) SEM image and EDX analysis of the main body in an iron nail (FKM-11): Fe and Si.	100
Figure 4. 22 Microstructural images of samples taken by Huvitz digital microscope after etching with nitric acid in alcohol (a, b, c).	103
Figure 4. 23 Microstructural images of the samples taken by Nikon metallographic microscope (a, c and d) and microstructural image of the sample by Huvitz digital microscope (b) after etching with nitric acid in alcohol (16th cc).	106
Figure 4. 24 Microstructural images of samples taken by Nikon metallographic microscope (e, h) and microstructural images of samples taken by Huvitz digital microscope (f, g) after etching with nitric acid in alcohol (16th cc).	107
Figure 4. 25 Microstructural image of the sample taken by Nikon metallographic microscope (i) and Microstructural images of the samples taken by Huvitz digital microscope (j, k) after etching with nitric acid in alcohol (16th cc).	108
Figure 4. 26 Microstructural images of iron samples by Nikon metallographic microscope (a, c) and Huvitz digital microscope (b, d) after etching with nitric acid in alcohol (19th cc).	111
Figure 4. 27 Microstructural images of iron samples by Nikon metallographic microscope (g) and Huvitz digital microscope (e, f, h) after etching with nitric acid in alcohol (19th cc).	112
Figure 4. 28 Microstructural image of iron samples by Nikon metallographic microscope (i) and Huvitz digital microscope (j) after etching with nitric acid in alcohol (19th cc).	113

Figure 4. 29 Microstructural images of iron samples by Nikon metallographic microscope (l, n) and Huvitz digital microscope (k, m) after etching with nitric acid in alcohol (19th cc).....	114
Figure 4. 30 Digital microscopy images (a, c) and SEM images (b, d) of iron samples after etching with nitric acid in alcohol (15th cc).....	119
Figure 4. 31 a) SEM image of a door locking iron piece (GMH-Me-02): elemental analysis area starting from metal body to the TM layer. b) EDX analysis results: Fe, Si, Ca, Al, K, Mg and Cl.	120
Figure 4. 32 a) SEM image of a plaster nail (GMH-Me-04): elemental analysis area starting from metal body to TM Layer. b) EDX analysis: Fe, Si, Mn, Cr, Al and S.	120
Figure 4. 33 Digital microscopy image (a) and SEM image (b) of iron nail after etching with nitric acid in alcohol (16th cc).....	122
Figure 4. 34 Digital microscope image (a) and SEM image (b) of an iron object after etching with nitric acid in alcohol (16th cc).....	123
Figure 4. 35 Digital microscopy image (a) and scanning electron microscopy (SEM) image (b) of a nail sample after etching with nitric acid in alcohol (16th cc).....	123
Figure 4. 36 Digital microscopy image of an iron object embedded in mortar (MSH-KAP-06) at the interior of the hammam after etching with nitric acid in alcohol (500x) (16th cc),.....	124
Figure 4. 37 Digital microscopy image of a nail embedded in the mortar of stone masonry (MSH-KAP-07) after etching with nitric acid in alcohol (500x), (16th cc).	125
Figure 4. 38 SEM image (a) and digital microscopy image (b) of a nail at the interior of the hammam building, after etching with nitric acid in alcohol (16th cc).	125
Figure 4. 39 SEM image of a nail head (MSH-KAP-01) showing three main layers: Metal, ICL including RF and TM Layers. Numbers indicate the EDX analysis locations. Red arrow presents the area where line-scan was performed.	126
Figure 4. 40 EDX spectrum of an iron nail (MSH-KAP-01) at point 1 in reaction front: Fe, Ca, Si and Mn (16th cc).....	127

Figure 4. 41 EDX spectrum of an iron nail (MSH-KAP-01) at point 5 in reaction front: Fe, Ca, Si and Mn (16th cc).	127
Figure 4. 42 EDX spectrum of an iron nail (MSH-KAP-01) at points 3 and 4 in inner corrosion layer (ICL): Fe and O (16th cc).	128
Figure 4. 43 EDX line scan spectrum of an iron nail (MSH-KAP-01) starting from transformed media (TM) to the main metal body (16th cc).....	128
Figure 4. 44 SEM image of total corrosion layer next to the metal body of an iron sample (MSH-KAP-02) (60x). Red arrow represents the area where line scan is performed.....	129
Figure 4. 45 SEM image of reaction front (RF) next to the metal body in the iron object (MSH-KAP-02) (150x).	130
Figure 4. 46 EDX analysis of the reaction front (RF) next to the metal body (MSH-KAP-02): Ca, Fe, Mg, Na, O and S.	130
Figure 4. 47 EDX line scan spectrum of an iron object (MSH-KAP-02) starting from transformed media (TM) to main metal body: calcium is the most abundant impurity in the corrosion layer.	131
Figure 4. 48 SEM image of a deep crack inside the inner corrosion layer of an iron object (MSH-KAP-02) (600x).	132
Figure 4. 49 EDX analysis at the crack (MSH-KAP-02): Fe, Ca, O and Al.	132
Figure 4. 50 EDX spectrum of the reaction front (RF) in an iron nail (MSH-KAP-03): Fe, Si, Ca, P and Cl (16th cc).	133
Figure 4. 51. EDX spectrum of a nail (MSH-KAP-03) at a point in the inner corrosion layer (ICL): Fe, Si, Ca, P and Cl.....	134
Figure 4. 52 SEM image and EDX line scan spectrum of the nail(MSH-KAP-03): starting from transformed media (TM) to main body: calcium is the most abundant impurity in the corrosion layer.....	134
Figure 4. 53 (a) SEM image of the inner corrosion layer (ICL) in the iron nail (MSH-KAP-12) (16th cc). (b) EDX analysis at the ICL: Fe, O, Si, Ca, Al and Mn.	135
Figure 4. 54 Digital microscopy image (a) and SEM images (b, c) of iron samples (FKM-02 and FKM-05) after etching with nitric acid in ethanol (19th cc).....	137

Figure 4. 55 Digital microscopy images (a, c) and SEM images (b, d) of iron samples (FKM-07 and FKM-11) after etching with nitric acid in ethanol. FKM-07 is in burial conditions and FKM-11 is partially exposed to atmospheric conditions (19th cc).	138
Figure 4. 56 Digital microscopy images (a, b, c) and SEM image (d) of iron samples (T-W-01, T-D-01 and T-N-04) after etching with nitric acid in ethanol (19th cc).	139
Figure 4. 57 EDX analysis at the RF of iron sample (FKM-02): Fe, Si, Al, Ca, P and Mn.....	140
Figure 4. 58 EDX analysis at the ICL of the iron sample (FKM-02): Fe, Si, Al, Ca, P, Ti and K.....	141
Figure 4. 59 EDX analysis at the ICL of the iron sample (FKM-02): Fe, Si, Cl, Na, K and S.	141
Figure 4. 60 EDX analysis at the ICL of the iron sample (FKM-02): Fe, Si, P, Al, Ca and K.	142
Figure 4. 61 SEM image of an iron nail head (FKM-07) (a) and EDX line scan spectrum starting from transformed media (TM) to main body (b).	143
Figure 4. 62 SEM image of an iron nail head (FKM-07) (a) and EDX analysis at the crack point in ICL (b): Fe, Si, Ca, Al, S, K and Cl.	143
Figure 4. 63 SEM images of an iron nail (FKM-11) at the ICL (a, b), and EDX analysis (c): Fe, Si, Al, Cl, P and Na.	144
Figure 4. 64 SEM image of a nail (T-N-04) starting from transformed media (TM) to main body (a) and its EDX line scan spectrum (b): Fe, N, Al, S, Si, Cl, K, Ca and Mg.....	145
Figure 4. 65 FTIR spectrum of the mixture including inner corrosion layer and TM layer belonging to a 15th century door lock piece (GMH-Me-02): Goethite (α -FeOOH), lepidocrocite (γ -FeOOH) and magnetite (Fe ₃ O ₄).....	151
Figure 4. 66 FTIR spectrum of the mixture including inner corrosion layer and TM layer belonging to a 15th century plaster nail (GMH-Me-03): Goethite (α -FeOOH) and lepidocrocite (γ -FeOOH).	151

Figure 4. 67 FTIR spectrum of corrosion layer including ICL and TM of the nail (MSH-KAP-01) from the dome representing outdoor atmospheric condition: Goethite (α -FeOOH), lepidocrocite (γ -FeOOH) and hematite (α -Fe ₂ O ₃).	155
Figure 4. 68 FTIR spectrum of corrosion layer including ICL and TM of the nail (MSH-KAP-03) from the dome representing outdoor atmospheric condition: Goethite (α -FeOOH), and lepidocrocite (γ -FeOOH).	155
Figure 4. 69 FTIR spectrum of corrosion layer including ICL and TM of the iron piece convenient to anchoring (MSH-KAP-02) at the wall representing indoor atmospheric condition: Goethite (α -FeOOH), and lepidocrocite (γ -FeOOH).	156
Figure 4. 70 FTIR spectrum of corrosion layer including ICL and TM of the window guard iron piece (FKM-01) at the dwelling in Foça representing partially open outdoor atmospheric conditions: Goethite (α -FeOOH), lepidocrocite (γ -FeOOH) and quartz.	159
Figure 4. 71 FTIR spectrum of corrosion layer including ICL and TM of the timber jointing nail (FKM-02) at the dwelling in Foça representing partially open outdoor atmospheric conditions: Mainly goethite (α -FeOOH).	160
Figure 4. 72 FTIR spectrum of corrosion layer including ICL and TM of the door lock piece (FKM-03) at the dwelling in Foça representing partially open outdoor atmospheric conditions: Goethite (α -FeOOH) and lepidocrocite (β -FeOOH).	161
Figure 4. 73 FTIR spectrum of corrosion layer including ICL and TM of the door's male hinge (FKM-04) at the dwelling in Foça representing partially open outdoor atmospheric conditions: Goethite (α -FeOOH), lepidocrocite (β -FeOOH) and quartz.	162
Figure 4. 74 FTIR spectrum of corrosion layer including ICL and TM of the door's female hinge (FKM-05) at the dwelling in Foça representing partially open outdoor atmospheric conditions: Goethite (α -FeOOH) and lepidocrocite (β -FeOOH).	164
Figure 4. 75 FTIR spectrum of corrosion layer including ICL and TM of the nail (FKM-11) from a dwelling in Foça representing partially open atmospheric conditions: Goethite (α -FeOOH).	164

Figure 4. 76 FTIR spectrum of corrosion layer including ICL and TM of the nail (FKM-07) from the Ottoman layer excavations in Foça showing buried conditions: Lepidocrocite (β -FeOOH).	166
Figure 4. 77 FTIR spectrum of corrosion layer including ICL and TM of the iron piece (FKM-08) from the Ottoman layer excavations in Foça showing buried conditions: Goethite (α -FeOOH) and lepidocrocite (β -FeOOH).	166
Figure 4. 78 FTIR spectrum of corrosion layer including ICL and TM of the iron piece (FKM-09) from the Ottoman layer excavations in Foça showing buried conditions: Quartz, goethite (α -FeOOH), lepidocrocite (γ -FeOOH) and hematite (α -Fe ₂ O ₃).	168
Figure 4. 79 FTIR spectrum of corrosion layer including ICL and TM of the nail (FKM-10) from the Ottoman layer excavations in Foça showing buried conditions: Goethite (α -FeOOH) and lepidocrocite (β -FeOOH).	168
Figure 4. 80 FTIR spectrum of a corrosion layer including ICL and TM of the nail (T-N-05) from a timber column of a dwelling in Tekkekoy representing exterior conditions: goethite (α -FeOOH) and lepidocrocite (β -FeOOH).	170
Figure 4. 81 FTIR spectrum of a corrosion layer including ICL and TM of a hinge pin from the entrance hall's window (T-W-01) of a dwelling in Tekkekoy representing an iron object partially open to atmospheric conditions: goethite (α -FeOOH) and lepidocrocite (β -FeOOH).	171
Figure 4. 82 FTIR spectrum of a corrosion layer including ICL and TM of the crossbar of the main entrance door locking (T-D-01) from a dwelling in Tekkekoy representing an iron object partially open to atmospheric conditions: goethite (α -FeOOH), lepidocrocite (β -FeOOH) and quartz.	172
Figure 4. 83 SEM image of a door lock piece (GMH-Me-02) after etching with nitric acid in alcohol (a) and the first five points located around RF of the same sample (b) (15th cc).	177
Figure 4. 84 Raman spectra of the first five points located around RF in the corrosion layer of a door lock piece (GMH-Me-02): goethite is the most abundant phase	

together with hydrated iron (III) oxide or oxyhydroxide, hematite and akaganeite.	177
Figure 4. 85 Raman spectra of the second five points located in the ICL after RF in the corrosion layer of a door lock piece (GMH-Me-02): hydrated iron (III) oxide or oxyhydroxide and goethite are the most abundant phases with some hematite. ..	178
Figure 4. 86 Raman spectra of the third region with four points located in the ICL of a door lock piece (GMH-Me-02): Hydrated iron (III) oxide or oxyhydroxide, hematite, goethite and magnetite are the iron oxides observed.	179
Figure 4. 87 Raman spectra of the fourth region with three points located in the ICL of a door lock piece (GMH-Me-02): magnetite.	180
Figure 4. 88 Raman spectra of the fifth region with two points located close to the TM of a door lock piece (GMH-Me-02): goethite is the most abundantly observed iron oxide together with hydrated iron (III) oxide or oxyhydroxide.	181
Figure 4. 89 SEM image of a plaster nail (GMH-Me-04) after etching with nitric acid in alcohol (a) and μ -Raman microscopic image of first five points located around RF of the same sample (b) (15th cc).	182
Figure 4. 90 μ -Raman spectra of the first five points located around RF in the corrosion layer of a plaster nail from interior (GMH-Me-04) (a, b, c, d, e): goethite is the most abundant phase from p1 to p4 (a, b, c, e); presence of hydrated iron (III) oxide or oxyhydroxide together with some goethite (d).	183
Figure 4. 91 μ -Raman spectra of the second 5 points located in the ICL after RF in the corrosion layer of a plaster nail from interior (GMH-Me-04): Goethite is the most abundant phase.	184
Figure 4. 92 Raman spectra of the second 5 points located in the ICL after RF in the corrosion layer of a plaster nail from interior (GMH-Me-04) (a, b): Lepidocrocite is observed at p9 (a), Goethite together with lepidocrocite is observed at p10 (b). .	185
Figure 4. 93 μ -Raman spectra of the third area where 6 points are located in the ICL of a plaster nail from interior (GMH-Me-04) (a, b): Goethite is the phase observed.	185

Figure 4. 94 μ -Raman spectra of the fourth area where 3 points are located close to the TM in the corrosion layer (a, c, d, e) and the fifth area where 1 point is located in the TM (b, f) of a plaster nail from interior (GMH-Me-04): Lepidocrocite (c), hydrated iron (III) oxide or oxyhydroxide (d, e) and goethite (f) are the phases observed.....	186
Figure 4. 95 A digital microscopy image (a) and SEM image (b) of the corrosion layer belonging to a nail (MSH-KAP-01) (16th cc): Sub-layers are identified as RF: Metal-ICL interface; ICL: inner corrosion layer (~50 μ m); OSL: original surface limit; TM: transformed media. ICL-TM interface includes OSL.....	188
Figure 4. 96 μ -Raman spectra of the nail (MSH-KAP-01) at the RF and the transition zones: points of measurement (a); reaction-front (p2) having magnetite (M) (b); RF-ICL transition zone (p3) showing magnetite (M), maghemite (Mh) and hematite (c); ICL-TM transition zone (p1) showing hematite (H) (d).	189
Figure 4. 97 μ -Raman spectra of a nail (MSH-KAP-01) at ICL: measurement points (a); presence of goethite in ICL (b).	190
Figure 4. 98 μ -Raman spectra of a nail (MSH-KAP-01) at TM: measurement points (a); presence of goethite, magnetite + maghemite, lepidocrocite (b); presence of goethite, magnetite + maghemite (c); and presence of goethite (d).	191
Figure 4. 99 SEM image of the corrosion layer at an iron object (MSH-KAP-02) (a) (16th cc); measurement point at RF (b); and μ -Raman spectrum indicating presence of goethite (c).	192
Figure 4. 100 μ -Raman spectra of an iron object (MSH-KAP-02) at RF towards ICL: measurement points (a); and presence of hydrated iron (III) oxide or oxyhydroxide at P1 to P4 (b, c, d).	193
Figure 4. 101 μ -Raman spectrum of an iron object (MSH-KAP-02) at ICL: measurement points (a); and presence of hydrated iron (III) oxide or oxyhydroxide from P1 to P4 (b, c, d).	194
Figure 4. 102 μ -Raman spectrum of an iron object (MSH-KAP-02) at ICL towards TM: measurement points (a); and presence of goethite at p1 and p2 (b, c).	195

Figure 4. 103 SEM image (a) and digital microscopic image (b) of a dome nail (MSH-KAP-03) after etching with nitric acid in alcohol (16th cc).	197
Figure 4. 104 μ -Raman spectra of the 2 points located in RF viewed by SEM and digital microscope (MSH-KAP-03): measurement points (a), magnetite at point 1 (b) and hydrated iron (III) oxide or oxyhydroxide at point 2 (c).	197
Figure 4. 105 μ -Raman spectra of the 2 points located in the ICL after RF (MSH-KAP-03): measurement points (a); magnetite with some goethite at p3 (b); and goethite is the main phase observed at p4 (c).	198
Figure 4. 106 μ -Raman spectra of the successive area where 2 points are located in the ICL (MSH-KAP-03): measurement points (a); hydrated iron (III) oxide or oxyhydroxide at p5 (b); and goethite at p6 (c).	199
Figure 4. 107 μ -Raman spectra of the successive step where 2 points are located in the ICL (MSH-KAP-03): measurement points (a); hydrated iron (III) oxide or oxyhydroxide, goethite and lepidocrocite at p7 (b); and goethite and lepidocrocite at p8 (c).	200
Figure 4. 108 μ -Raman spectra of the successive area where 2 points are located in the ICL (MSH-KAP-03): measurement points (a); hydrated iron (III) oxide or oxyhydroxide at point 9 (b); and maghemite, magnetite, goethite and lepidocrocite are the phases observed at point 10 (c).	201
Figure 4. 109 μ -Raman spectra of the successive area where 2 points are located in the ICL close to TM border of a nail (MSH-KAP-03): measurement points (a); goethite and lepidocrocite at point 11 (b); and goethite at point 12 (c).	202
Figure 4. 110 μ -Raman spectra of the successive areas where 2 points are located in the TM of a nail (MSH-KAP-03): measurement points (a, c); goethite at point 13 (b); and lepidocrocite at point 14 (d).	203
Figure 4. 111 SEM image (a) and digital microscopic image (b) of a nail (MSH-KAP-09) after etching with nitric acid in alcohol (16th cc).	205
Figure 4. 112 μ -Raman spectra of the two points located in RF towards ICL of a nail (MSH-KAP-09): measurement points (a); goethite at point 1 (b); hydrated iron (III)	

oxide or oxyhydroxide and goethite at point 2 (c); magnetite at point 3 and 4 (d), maghemite, magnetite, goethite at point 5 (e); and goethite at point 6 (f).	206
Figure 4. 113 μ -Raman spectra of the successive four points located in the ICL after RF in the corrosion layer of a nail (MSH-KAP-09): measurement points (a); hydrated iron (III) oxide or oxyhydroxide with some goethite at p1 and p4 (b); and goethite is the main phase observed at p2 and p3 (c, d).....	207
Figure 4. 114 μ -Raman spectra of the successive area where 4 points have been located in the ICL of a nail (MSH-KAP-09): measurement points (a); lepidocrocite at p1 (b); magnetite at p2 and p3 (c); and goethite at p4 (d).	208
Figure 4. 115 μ -Raman spectra of the successive area where 5 points are located in the ICL of a nail (MSH-KAP-09): measurement points (a); maghemite at point 1 (b); hydrated iron (III) oxide or oxyhydroxide together with goethite at point 2 to 5 (c).	209
Figure 4. 116 μ -Raman spectra of the successive area where 5 points are located in the ICL close to TM of a nail (MSH-KAP-09): measurement points (a); goethite with hydrated iron (III) oxide or oxyhydroxide at all points (b).	210
Figure 4. 117 Digital microscopic (a) and Raman microscopic (b) images of a timber jointing nail (MSH-KAP-12) after etching with nitric acid in alcohol (16th cc)..	211
Figure 4. 118 μ -Raman spectra of the 1st area where 4 points are located in the RF towards ICL of a nail (MSH-KAP-12): measurement points (a, b); magnetite at p1 to p3 (c), and hematite at p4 (d).	212
Figure 4. 119 μ -Raman spectra of the successive area where 4 points are located in the ICL of a nail (MSH-KAP-12): measurement points (a); wustite at p1 (b); wustite at p1 to p4 (c).....	213
Figure 4. 120 μ -Raman spectra of the successive area where 2 points are located in the ICL towards TM of a nail (MSH-KAP-12): measurement points (a); hematite at p1 to p2 (b, c).....	214
Figure 4. 121 Digital microscopic (a) and SEM (b) images of a nail (FKM-02) at load bearing timber beam after etching with nitric acid in alcohol (19th cc). μ -Raman	

spectra of the 6 points located in the RF towards ICL: hematite at p1 to p3 (c, d); and hydrated iron (III) oxide or oxyhydroxide at p4 to p6 (e, f).	217
Figure 4. 122 Stereo microscopic (a) and Raman microscopic (b) images of a door lock piece (FKM-03) after etching with nitric acid in alcohol (19th cc).	219
Figure 4. 123 μ -Raman spectra of the 4 points located in the RF towards ICL of a door lock piece (FKM-03) (19th cc): measurement points (a); hydrated iron (III) oxide or oxyhydroxide at p1 and p2 (b, c); goethite with hydrated iron (III) oxide or oxyhydroxide at p3 (d); goethite with magnetite+magnetite at p4 (e).....	219
Figure 4. 124 μ -Raman spectra of the 3 points located in the ICL towards TM of a door lock piece (FKM-03): measurement points (a); goethite at p6 and p7 (b, c); and hydrated iron (III) oxide or oxyhydroxide at p8 (d).....	220
Figure 4. 125 Stereo microscopic (a) and Raman microscopic (b) images of a male hinge (FKM-04) (19th century) after etching with nitric acid in alcohol.	221
Figure 4. 126 μ -Raman spectra of the 4 points located in the RF towards TM of a hinge piece (FKM-04) (19th century): measurement points (a, b); goethite with hydrated iron (III) oxide or oxyhydroxide at p2, p3, and p5 (c, d, f); hydrated iron (III) oxide or oxyhydroxide at p4 (e).	222
Figure 4. 127 Stereo microscopic (a) and SEM (b) images of a female hinge (FKM-05) after etching with nitric acid in alcohol (19th cc).	224
Figure 4. 128. μ -Raman spectra of the 3 points located in the RF towards TM of a female hinge piece (FKM-05) (19th cc): measurement points (a); hydrated iron (III) oxide or oxyhydroxide with some goethite at p1, p2 and p3 (b, c, d).....	224
Figure 4. 129 Digital microscopic (a) and SEM (b) images of a buried nail (FKM-07) after etching with nitric acid in alcohol (19th cc). μ -Raman spectra of the 2 points located in the ICL: Measurement points (c, d); goethite at p1 and p2 (e, f).	226
Figure 4. 130 μ -Raman microscopy image of powder samples collected by a magnet on the surface of the iron object (FKM-08) (a); μ -Raman spectrum of goethite together with magnetite (b).	228
Figure 4. 131 Raman microscopic image of an L-shaped iron object (FKM-08) from the Ottoman layer excavation (19th cc) (a); μ -Raman spectra taken at the 4 points	

located in the RF towards ICL: measurement points (b); goethite at p1 and p2 (c); goethite at p3 and p4 (d); μ -Raman spectra taken at a marble located in ICL: measurement point (e); hydrated iron (III) oxide or oxyhydroxide at p5 (f).	229
Figure 4. 132 μ -Raman spectrum taken in the ICL of an iron object (FKM-08): measurement point (a); goethite at p6 (b).....	230
Figure 4. 133 μ - Raman spectra taken at 3 points located in the ICL of an iron object (FKM-08): measurement points (a); goethite at p9 and hematite with some lepidocrocite as well as magnetite at p7 and p8 (b).....	230
Figure 4. 134 μ -Raman spectra taken at 2 points located in the ICL of an iron object (FKM-08): measurement points (a, c); goethite at p10 (b); goethite (G) and magnetite (M) at p11 (d).	231
Figure 4. 135 μ -Raman spectra taken at 5 points located in the ICL near TM of an iron object (FKM-08): measurement points (a, c); goethite at p12 and p13 (b); goethite and magnetite / maghemite at p16 and hydrated iron (III) oxides or oxyhydroxides at p14 and p15 (d).	232
Figure 4. 136 μ -Raman microscopy image at the 1st location of the powder sample collected by a magnet on the surface of the iron nail (FKM-10): measurement points (a); goethite at p1 and p2 (b).	233
Figure 4. 137 μ -Raman microscopy image at the 2nd location of the powder sample of an iron nail (FKM-10): measurement points (a); goethite at p4 and p5 (b); goethite together with magnetite at p6 and p7 (b, c).	234
Figure 4. 138Figure 4.138 μ -Raman microscopy image at the 3rd location of the powder sample of an iron nail (FKM-10): measurement points (a); magnetite with some goethite at p8 to p10 (b); goethite at p11 and p12 (c).	235
Figure 4. 139 μ -Raman microscopy image at the 4th location of the powder sample of an iron nail (FKM-10): measurement points (a); goethite at p13; goethite with maghemite (Mh) / magnetite (M) at p15 and goethite with lepidocrocite (L) at p16 (b).	236

Figure 4. 140 μ -Raman microscopy image at the 5th location of the powder sample of an iron nail (FKM-10): measurement points (a); goethite at p17, goethite with hydrated iron (III) oxides or oxyhydroxides at p18 and lepidocrocite at p19 (b).	237
Figure 4. 141 SEM image (a) of a nail (FKM-11) from a dwelling in Foça (19th cc). μ -Raman spectra taken at 4 points located in the RF towards ICL: measurement points (b); maghemite (Mh) and lepidocrocite (L) at p1 and p4 (c); goethite at p2 and p3 (d).	239
Figure 4. 142 μ -Raman spectra at the successive 4 points in the ICL next to RF: measurement points (a); goethite at p1 (b); goethite at p1 and p2, goethite with maghemite and magnetite at p3 (c); goethite with maghemite and magnetite at p3 and p4 (d).	240
Figure 4. 143 μ -Raman spectra at the successive 4 points located in the ICL: measurement points (a); goethite at p1 (b); goethite, maghemite / magnetite at p2 and p3 (c); goethite at p4 (d).	241
Figure 4. 144 μ -Raman spectra taken at the successive 5 points located in the ICL: measurement points (a); goethite at p1 to p5 (b, c, d).	242
Figure 4. 145 μ -Raman spectra taken at successive 5 points located in the ICL near TM: measurement points (a); goethite at p1 (b); hydrated iron (III) oxides or oxyhydroxides at p2 to p5 (c, d).	243
Figure 4. 146 μ -Raman spectra taken at successive 5 points located in TM: measurement points (a); maghemite and akageneite at p1 and p2 (b).	244
Figure 4. 147Figure 4.147 μ -Raman spectra taken at successive 8 points located in TM of FKM-11: measurement points (a, c) ; akageneite and maghemite at p1 and 2 (b); akageneite and maghemite at p7 to p12 (d, e); comparison of the first point at RF and last point at TM.	245
Figure 4. 148 The digital microscopic image (a) of the door lock piece (T-D-01) after etching with nitric acid in alcohol (19th cc). μ -Raman spectra taken at 4 points located in RF towards TM: measurement points (b, c); magnetite and maghemite at p1 and p2 (d); hematite at p3 and p4 (e).	247

Figure 4. 149 Digital microscopic (a) image of the nail (T-N-04) from the door frame of a dwelling in Tekkekoy, Samsun after etching with nitric acid in alcohol (19th cc). μ -Raman spectra taken at 6 points located in RF towards ICL: measurement points (b, d); hydrated iron (III) oxides or oxyhydroxides at p1 to p3 in RF (c); goethite at p4 to p6 in RF - ICL border (e).	249
Figure 4. 150 μ -Raman spectra taken at the successive 4 points located in ICL: measurement points (a, c); goethite at p7 and p8 (b); goethite at p9 and lepidocrocite with goethite at p10 (d).....	250
Figure 4. 151 μ -Raman spectra taken at the successive 4 points located in ICL towards TM: measurement points (a, c); lepidocrocite at p11 and goethite at p12 (b); lepidocrocite with goethite at p13 and goethite at p14 (d).	251
Figure 4. 152 XRD spectra of the corrosion layer powder including ICL and TM of the plaster nail (GMH-Me-03) (15th cc): maghemite (Mh), magnetite (M), hematite (H), goethite (G) and lepidocrocite (L) are identified.	266
Figure 4. 153 XRD spectra of the corrosion layer powder including ICL and TM of the nail (MSH-KAP-01) (16th cc): goethite (G), maghemite (Mh), magnetite (M), hematite (H), lepidocrocite (L) and calcite (C).	269
Figure 4. 154 XRD spectra of the corrosion layer powder including ICL and TM of the nail (MSH-KAP-03) (16th cc): maghemite (Mh), magnetite (M), hematite (H), goethite (G), lepidocrocite (L), ferrihydrite (Fh), wustite (W), quartz (Q) and calcite (C) are identified.....	270
Figure 4. 155 XRD spectra of the corrosion layer powder including ICL and TM of the iron jointing piece (MSH-KAP-02) (16th cc): maghemite (Mh), magnetite (M), hematite (H), goethite (G), lepidocrocite (L), ferrihydrite (Fh), wustite (W), quartz (Q) and calcite (C)	271
Figure 4. 156 XRD spectra of the corrosion layer powder including ICL and TM of the iron nail (FKM-02) (19th cc): goethite (G), maghemite (Mh), magnetite (M), hematite (H), ferrihydrite (Fh), wustite (W), siderite (S), quartz (Q) and calcite (C).	274

Figure 4. 157 XRD spectra of the corrosion layer powder including ICL and TM of the of the main entrance door hinge (FKM-04) (19th cc): goethite (G), akaganeite (A), maghemite (Mh), magnetite (M), hematite (H), lepidocrorite (L), ferrihydrite (Fh), feroxhyte (Fx).	275
Figure 4. 158 XRD spectra of the corrosion layer powder including ICL and TM of the of the nail (FKM-11) (19th cc): goethite (G), akaganeite (A), maghemite (Mh), magnetite (M), lepidocrorite (L), quartz (Q).	276
Figure 4. 159 XRD spectra of the corrosion layer powder including ICL and TM of the of the nail (FKM-06) (19th cc): goethite (G), akaganeite (A), maghemite (Mh), magnetite (M), hematite (H) lepidocrorite (L), ferrihydrite (Fh), calcite (C).	278
Figure 4. 160 XRD spectra of the corrosion layer powder including ICL and TM of the of the nail (FKM-11) (19th cc): goethite (G), hematite (H), maghemite (Mh), magnetite (M), lepidocrorite (L), ferrihydrite (Fh).	279
Figure 4. 161 XRD spectra of the corrosion layer powder including ICL and TM of the of the iron piece (FKM-09) (19th cc): goethite (G), hematite (H), maghemite (Mh), magnetite (M), lepidocrorite (L), wustite (W), quartz (Q).	281
Figure 4. 162 XRD spectra of the corrosion layer powder including ICL and TM of the of the iron piece (FKM-10) (19th cc): goethite (G), hematite (H), maghemite (Mh), magnetite (M), lepidocrorite (L), ferrihydrite (fh), calcite (C), quartz (Q).	282
Figure 5. 1 Average thickness of corrosion layers on the 23 iron objects and their classification: as perfect (<200 μm), medium perfect (201-500 μm and imperfect (>500 μm).	287
Figure 5. 2: Relationship between ICL thickness, silicon (Si) and carbon (C) contents of the objects from the 15th, 16th and 19th centuries. “*” indicates the objects with medium perfect corrosion layer. “**” indicates the objects with imperfect corrosion layer.	301
Figure 5. 3 Relationship between ICL thickness and phosphorous (P) content of the objects from the 15th, 16th and 19th centuries. “*” indicates the objects with medium	

perfect corrosion layer. “***” indicates the objects with imperfect corrosion layer.
..... 302

Figure 5. 4 Relationship between ICL thickness and sulfur content of the objects from the 15th, 16th and 19th centuries. “*” indicates the objects with medium perfect corrosion layer. “***” indicates the objects with imperfect corrosion layer. 304

Figure 5. 5 Relationship between ICL thickness and manganese (Mn) content of the objects from the 15th, 16th and 19th centuries. “*” indicates the objects with medium perfect corrosion layer. “***” indicates the objects with imperfect corrosion layer.
..... 305

Figure 5. 6 Relationship between manganese (Mn) content and hardness of the objects from the 15th, 16th and 19th centuries. “*” indicates the objects with medium perfect corrosion layer. “***” indicates the objects with imperfect corrosion layer.
..... 306

Figure 5. 7 Relationship between ICL thickness and magnesium (Mg) content of the objects from the 15th, 16th and 19th centuries. “*” indicates the objects with medium perfect corrosion layer. “***” indicates the objects with imperfect corrosion layer.
..... 307

Figure 5. 8 Relationship between ICL thickness and aluminum (Al) content for objects from the 15th, 16th and 19th centuries. “*” indicates the objects with medium perfect corrosion layer. “***” indicates the objects with imperfect corrosion layer.
..... 308

Figure 5. 9 Relationship between ICL, chromium (Cr) and nickel (Ni) contents of the objects from the 15th, 16th and 19th centuries. “*” indicates the objects with medium perfect corrosion layer. “***” indicates the objects with imperfect corrosion layer. 309

Figure 5. 10 The average hardness classification of the 26 objects from the 15th, 16th and 19th centuries: thin as soft (up to 150 HB), medium hard (151-250 HB) and hard (>251 HB)..... 313

Figure 5. 11 Comparison of hardness and corrosion layer thickness of the objects.
..... 314

Figure 5. 12 Comparison between hardness and microstructure (in terms of total ferrite and fraction of pearlite contents) of the objects from the 15th, 16th and 19th centuries to investigate the effect on the formation of perfect corrosion layer. ... 314

LIST OF ABBREVIATIONS

ABBREVIATIONS

RF: Reaction Front where metal -ICL interface is observed as a thin layer

ICL: Inner Corrosion Layer including reaction front up to TM

OSL: Original Surface Limit that is observed in between ICL – TM interface

TM: Transformed Media that is the outer surface of the corrosion layer consisting the impurities from the surrounding environment such as impurities from mortar, air pollutants, etc.

PAI: Protective Ability Index

Eq.: Equation

CHAPTER 1

INTRODUCTION

In a world filled with finite resources, the industry must adapt and embrace sustainable practices that benefit our planet. All processes starting from the design to reusing / recycling have to be covered not only for the present uses but for the future. Learning from the history through the well preserved, successful materials is important to improve contemporary materials' performance and find solutions for their maintenance. Due to high demand on the iron / steel use as building materials and goods, their corrosion problems become an important subject to be studied. Those studies and their findings have contributions on the intelligent use of natural resources and environmental protection issues that are the current topics of growing importance. Since the production stages of iron / steel components consume huge amount of energy and produce carbon emissions to the atmosphere that contributes the global warming, the long-term use of iron products is of economic and ecological importance.

Learning from the past experiences is an important approach that can be used to improve the performance of today's materials. The study on the historical materials that are in good state of preservation and survival conditions gives an opportunity to discover the reasons of success related to those materials. In this study, some iron components taken from the hammam buildings (Gazi Mihal Hammam constructed around 1450 and Kılıç Ali Paşa Hammam around 1580) representing the the Classical Period and other iron components from some historical dwellings in Foça, Izmir and in Tekkekoy, Samsun representing late Ottoman period (being 18th – 19th centuries) were examined. In addition to those objects that were kept in open atmospheric conditions, some iron objects from the excavations in Foça, Izmir

belong to the layer indicates the 19th century Ottoman period were also studied. The list of the samples and their descriptions are given at the third chapter of this thesis.

In Ottoman architecture, iron metal components as construction and structural elements such as tie beams, clamps, nails and architectural elements such as door and roof framings and window railings were widely used. The objects mostly analyzed were the nails together with some door / window related components.

Conservation of old buildings is an important mission not only for their historical value but also for helping the continuation of the materials and structures with durable and compatible characteristics that has enabled their survival to our time. In literature, many studies focused on the brick, mortar and stone materials used in the construction of historical monuments can be found. However, studies on the metallic materials, such as iron (steel) products used in the Ottoman period constructions are rather rare.

This study deals with the examination of the corrosion layers formed on the ancient well-preserved iron / steel materials. The argument and main objectives of the research are explained under the respective subheadings.

The term “iron” used in the text refers both to the low alloy carbon steel having low or medium carbon content in its composition. In the thesis, iron components refer to the materials used in the historical buildings or the objects collected from excavations.

1.1 Argument

Iron components are used in a wide range in buildings either structural or non-structural elements. They bring both durability and aesthetic features to a monument. However, they are mostly ignored by the conservation architects. Conservation of cultural heritage is very important, not only because the better understanding the properties of materials leads to the better protection of them but also brings benefits from the experiences of the past.

Control of corrosion for iron and steel is an important problem of industry. Corrosion mechanisms are very complex, especially the prediction of their evolution in the long term. Laboratory simulations and site exposure aging studies highlight the corrosion mechanisms in relatively short periods of time (e.g. around couple of 10 years).as detailed in the literature review (Ahlström et al, 2018, Aramendia et al, 2014, Morcillo et al, 2013 and 2014, Oh et al, 1999, Wang et al, 2013, Xu et al, 2021, Yamashita et al, 1994 and 2007, Zhang et al, 2021). While the ancient monuments withstand in well preserved condition, the modern steel elements are sometimes observed seriously deteriorated in a few decades whereas some historical steel artefacts prove to be resistant to atmospheric corrosion without serious degradations (Balasubramaniam, 2000; Bellot-Gurlet et al 2009; Monnier et al 2010; Waseda and Suzuki 2005). Although there have been many valuable studies on iron corrosion in different aspects, the number of studies with extensive examination of the phenomenon is few. There is need to study in more detail the corrosion layer formation for the long-term.

Considered as the classical period of the Ottoman architecture, in 16th and 17th centuries iron production activities increased, important iron production centers were known to exist in Anatolia and Rumelia (Nerantzis 2009, Eruz 2004). Bibliographical surveys have shown that although the Ottoman iron production centers (Tanyeli, 1990) and some of the components' production technology (Tanyeli and Geçkinli, 1991) is mentioned, there are not many studies focusing on the material properties, deterioration conditions and provenance of iron components in Ottoman Period. The scientific studies on where and what kind of productions have been practiced are rarely done. For the important structures, such as mosques (Süleymaniye Cami ve İmaretı) (Çelik, 2009), the constructions have been well documented and material purchase information such as purpose, place, amount, and date can be obtained. Those documents can help us to discover the raw material sources and production sites to produce the related components for those buildings.

In spite of their long-term exposure to atmospheric conditions, quite a number of iron artefacts in Ottoman period historical buildings seem to be in rather good state

of preservation. For this reason, it is thought that studies on some the Ottoman period iron objects may give important clues on the formation of protective corrosion layer. Some investigations on medieval historical iron objects have been performed not only in terms of interactions between metal and its environment, but also the materials and technological properties (Bellot-Gurlet et al 2009; Monnier et al 2011; Balasubramaniam and Kumar 2000).

Within the analysis techniques, μ -Raman studies have a special importance due to the technique proved to be a very powerful analytical method to identify and localize iron corrosion phases, and transformation mechanisms at a micrometric scale starting from the surface of the metal towards the exterior part of the corrosion layer (Colomban 2011, Dillman et al 2007; Feron et al 2004). Therefore, μ -Raman is included along with the other analytical tools of this study.

1.2 Aims and Objectives

The main aim of the study is to investigate metallurgical and corrosion properties of iron components used in some of the Ottoman period historical buildings in relation to their environmental conditions. Their corrosion layers are studied in more detail.

Exposed iron components in Ottoman period historical buildings visually seem to be in quite a good state of preservation in spite of their exposure to the atmospheric conditions for centuries. In this context, it appears to be important to better evaluate and focus on the state of preservation of those iron materials by the examination of their corrosion layers and corrosion products as well as their metallurgical properties in terms of their composition and microstructure. It is thought that the knowledge on ancient iron technology and corrosion characteristics will be useful for the conservation of historical iron objects and for today's iron (steel) industry.

Throughout the study, the following are the goals and objectives that support the main aim:

- to identify the individual corrosion products, their relative abundance, and distribution in the corrosion layers in order to explain the long-term iron corrosion formation mechanisms,
- to classify the corrosion layers in terms of thickness and compactness properties of inner corrosion layers formed on the surface of the iron objects,
- to investigate the degree of protective ability of the inner corrosion layer formed on the main body of the objects,
- to develop a method for calculation the protective ability index (PAI) value for different environments,
- to explain the formation and importance of nano-sized goethite particles as protective layer,
- to find out the contribution of composition and metallographic properties of the low alloy carbon steels on the formation of protective layer,
- to examine the relationship of corrosion layer with the authenticity of iron object belonging to the different periods of time,
- to make a contribution to the long-term corrosion control of today's iron and steel industry by examining the corrosion layer formation on the historical iron objects.

1.3 Disposition

This thesis is composed of six chapters, including Introduction, Literature Survey, Experimental Methods, Results, Discussion, and Conclusion.

In the first chapter, following a brief introduction of the thesis, the argument section prepared and included the importance of the iron corrosion studies and the contribution of the studies conducted on understanding the perfect protective layer formation. Aims and objectives were presented very briefly. Finally, the content of the thesis was described in the disposition part.

In the second chapter, a literature survey was presented, including the studies, reviews, and book chapters about the subjects included in the context of this thesis. The literature review was based on some previous studies in literature done on the use of iron and steel materials as well as the corrosion mechanisms and the protective ability of oxide layers on iron and steel in terms of following topics: the use of iron and steel as construction components in Ottoman period structures, iron metallurgy, production centers and production activities during the 15th, 16th and 19th centuries, current iron ore deposits and ore types in Anatolia as well as Balkan regions. The review was followed with the iron oxides, their formation and transformation characteristics in nature as well as their occurrence on the iron artefacts in terms of their main physical properties, solubility and thermodynamic characteristics, contribution of environment and minor elements in corrosion control, assessment of iron corrosion products for their protective ability; goethite as main protective coating.

The third chapter of the thesis was titled as Experimental Methods. That chapter covers two main sections: i) information about the monuments, their collected samples and nomenclatures ii) description of the analytical procedures given in detail. The description of major analytical equipment, the methods used for dimensional, weight and color identification, metallographic analyses in terms of chemical analysis with spark emission spectroscopy, hardness and main body morphology with metallography microscopes as well as digital microscope and morphological and mineralogical analysis of corrosion layers, by using XRD, FTIR, SEM-EDX and μ -Raman spectroscopy were done.

The fourth chapter was titled as Experimental Results that present the results of the above-mentioned experiments and analyses together with relevant stereomicroscope, metallography microscope, digital microscope and SEM images, as well as spark emission analyses, SEM-EDX analyses, μ -Raman spectroscopy analyses with location images, PAI calculations, XRD diagrams and FTIR spectra.

In the fifth chapter, a brief discussion was made on the comparative and combined results of the analyses performed on the historical iron constructional elements from 15th, 16th and 19th century historical structures to describe their metallurgical properties and corrosion performance as well as the properties of protective corrosion layers, their related environmental conditions together with related literature in the second chapter.

Finally, the summary of the study, possible environment for the formation of protective layer on iron objects, recommendations, and further studies were presented in the conclusion chapter.

CHAPTER 2

LITERATURE REVIEW

Control of corrosion for iron and steel is an important problem of industry not only from the economical point of view but also for the sustainability issues due to the yearly increased amount of material loss observed in steel structures and components are concerned. Corrosion process is a complex phenomenon. Since its control depends on better understanding the process, it is the subject of a great number of research studies. Quite a number of those research studies concentrate on the corrosion behavior of steel in a relatively short period of time (e.g., approximately of 10 years) (Ahlström et al, 2018, Aramendia et al, 2014, Morcillo et al, 2013 and 2014, Oh et al, 1999, Wang et al, 2013, Xu et al, 2021, Yamashita et al, 1994 and 2004, Zhang et al, 2021) while long-term corrosion behavior is still a question to be clarified. Modern steel elements that are exposed to atmospheric conditions are often seriously deteriorated in a few decades whereas some historical steel artefacts are found to be resistant to atmospheric corrosion without serious degradation (Balasubramaniam, 2000 and 2004, Bellot-Gurlet et al, 2009, Monnier et al, 2010, Nieuwmeijer, 2005, Waseda and Suzuki, 2005). In Ottoman architecture, there is a very wide usage of iron and steel elements in the buildings either as structural or non-structural components such as nails, tie rods, clamps and architectural elements such as window, door and roof framings. Quite a number of iron elements in those buildings seem to be in rather good state of preservation (Aydüz, 2006, Bilgi, 2004, Çelik, 2009, Eruz, 2004, Tanyeli 1990, Tanyeli et al, 1990, Uluengin, 2005).

In this study, some iron objects belonging to historical structures of the Ottoman period were selected to be examined for the characteristics of their corrosion behavior. Although there exist some studies on the production techniques and the

use of iron elements in those historical buildings, detailed laboratory investigations on their metallurgical and corrosion characteristics are rather rare (Aydüz, 2006, Bilgi, 2004, Çelik, 2009, Eruz, 2004, Tanyeli 1990, Tanyeli et al, 1990).

In this chapter, some previous studies in literature done on the use of iron and steel materials as well as the corrosion mechanisms and the protective ability of oxide layers on iron and steel have been reviewed under the following topics:

- Use of iron and steel as construction components in Ottoman period structures,
- Iron metallurgy, production centers and production activities during the 15th, 16th and 19th centuries,
- Current iron ore deposits and ore types in Anatolia,
- Common iron oxides, their main physical properties, solubility and thermodynamic characteristics,
- Iron corrosion mechanisms related to the characteristics of corrosion layer oxides; contribution of environment as outdoor and indoor conditions, contribution of minor elements in corrosion control,
- Assessment of iron corrosion products for their protective ability; goethite as main protective coating,
- Importance of μ -Raman spectroscopic analysis in corrosion studies in combination with other analytical methods such as FTIR, XRD, SEM-EDX and digital microscopy.

2.1 Use of Iron and Steel as Construction Components in Historical Structures of the Ottoman Period

Iron use as a building material in the Ottoman architecture can be divided into two main groups (Tanyeli 1990, Tanyeli and Tanyeli, 1993):

- Non-structural iron elements
- Structural iron elements

Non-structural iron elements are window railings with/without balls (*lokmalı / lokmasız*), iron components of timber window frames and doors, iron pipelines (the oldest example being a fountain made/built for Nakşidil Sultan), stairs, balusters (*railings*), oil lamp hangers, iron doors, iron sheets nailed on the wooden doors, window and door hinges, window and door hooks, window and door shutters, garden railings, iron accessories mounted on the walls (e.g., rings for hanging purpose), balcony railings, door lock parts, nails, chains, etc. (Tanyeli 1990, Tanyeli and Tanyeli 1993, Uluengin 2005, Serpil 2009, Batur 2009).

Structural iron elements are identified as nails, clamps (*kened*), dowels (*zıvana*), tie-rods (*gergiler*), auxiliary beams (*yardımcı kirişler*), transition elements (*geçiş ögeleri*), jointing elements (*bağlantı ögeleri*), load bearing columns (*taşıyıcı kolonlar*), buttresses (*payanda*) for roofing, balconies and cantilevers (*çıkma*), supporting systems (simple support, column supports, iron rings/grommet supports (*simitli mesnetleme*), sword supports (*kılıçlı mesnetleme*)), tension swords, iron frameworks in domes, infrastructure collar beams (*altyapı kuşaklamaları*) and roofing collar beams (*örtü kuşaklamaları*) (Tanyeli 1990, Tanyeli and Tanyeli 1993, Uluengin 2005, Çelik 2009, Batur 2009).

2.2 Ottoman Period Iron Metallurgy

In this sub-chapter iron production centers, trade activities and studies on iron goods and production processes in Ottoman land during the 15th, 16th and 19th centuries as well as current iron ore deposits and ore types in Anatolia have been briefly reviewed.

2.2.1 Iron production centers and trade activities during the 15th, 16th and 19th centuries

By the middle of the 1300s the Ottomans were able to control Asia Minor where they had crossed the Dardanelles and started to expand towards Europe (Danışman 2007).

Both Seljuk and Ottoman Turks are thought to contribute to the transfer of iron production technology between Far East and the Western world, particularly between China and Europe (Danışman 2007).

During Mehmed II's reign, the Ottoman conquests in the Balkans and Anatolia led to an increase in mineral reserves and in their diversity along with military and political achievements. After the conquest of the Balkan area, especially in the Bulgarian and Serbian territories, the Ottomans gained the iron ore mines and became rich due to iron production (Ayduz, 2006). Most of the Balkan mines were conquered by the Ottomans through the second half of the 15th century and first decades of the 16th century. The iron production and metallurgy achieved its highest level in 1540's and 1550's in comparison to Europe and other parts of the world (Eruz 2004). The Balkans and Rumelia were the main suppliers for Istanbul and its environs. Iron technology and its trade started to slow down in the years between 1580-1640 and its decline became sharper thereafter (Stoianovich, 1994).

There were many production centers in Anatolia even though the state did not interfere or pay much attention. Important iron production centers in Anatolia were within the Erzincan province, Sivas, Bilecik, the Marmara region near Kırklareli and Sakarya. However, Rumelia - Bulgaria, Bosnia (Dobnice, Kostendil, Sofia, Etrebolu, Samakov, Filibe and Tatarpazarı), Yugoslavia (Eğri Palanga and Kratova) and Kırklareli (Demirköy) - always had a major role in the iron production industry because of their accessibility to Istanbul (Eruz 2004). Maps (Figures 2.1 and 2.2) are given to show the most important iron ore deposits and production centers in the Ottoman period (Tanyeli 1990).



Figure 2. 1 The most important iron ore deposits and production centers in Rumelia in the Ottoman period (Tanyeli 1990).



Figure 2. 2 The important iron ore deposits and production centers in Anatolia in the Ottoman period (http://www.maden.org.tr/resimler/ekler/bd987257ff0eddc_ek.pdf)

There exist some important documents related to the Anatolian iron production centers. The oldest text mentioning iron reinforcement elements in the 1700's is "Tarih-i Cami-i Şerif-i Nur-i Osmani" written by Ahmed Efendi (Çelik, 2009). In his study, he mentions the iron collar beams. The construction notebooks of "Süleymaniye Cami ve İmaret-i İnşaatı" (Suleymaniye Mosque and its Complexes) from the historical archives have been extensively studied by several authors such as Ö. L. Barkan (1972-1979) and S. Çelik (2009). In addition, M. Erdoğan (1953, 1955) has studied the Ottoman period architecture regarding various buildings. Those sources give important information on iron elements used in Ottoman period buildings.

In the 16th century the most important production centers in Anatolia were Kiği in Erzincan province and Bilecik in Marmara Region. The other main centers were Geregan (Kockıran) in Van province and Divriği (Sivas) where most nails were produced (Tanyeli 1990, Eruz 2004). However, there is no precise information about the production of constructional iron elements in those locations although the records show that iron materials were sent to Istanbul, Baghdad and Romania from Kiği in the 16th and 17th centuries (Tanyeli, 1990, Tanyeli and Tanyeli 1993).

In the 16th century, there were 67 iron bloomeries (demir ergitme ocağı) in Bilecik, used for the production of cannon balls. There is no information whether those iron products were sent to Istanbul or not. Iron materials were quite probably sent to middle and western Anatolia to be used in building constructions because of the ease of transportation. However, after the 17th century, the production stopped in Bilecik whereas the centers of Samakov in Rumelia and Niş state in Western Anatolia were still active.

Rumelia was a predominantly important region for the iron production industry. The three key reasons were: ore deposits, charcoal and constant flow of water supply all year round. Besides, Istanbul, being close to Rumelia, was the main consumption center.

The other important production centers were without any doubt Eğripalanga and Kratova in Yugoslavia and the south part of Bulgaria. The Ottomans captured Kratova mines just after the Kosovo Battle (1389) and those regions are considered be active starting from the 15th century.

For the Süleymaniye Mosque, iron materials were brought from Samakov and Kuziçe in Bulgaria. Some of those materials were ahen (iron-demir), ahen-i ham (raw iron-ham demir), ahen-i çubuk (bar iron-çubuk demir), pareha-i ahen (iron pieces-demir parça), çelik-i sızdırma (drain steel-akıtma çeliği), çelik-i frengi (European steel-Avrupa çeliği), kiriş-i kubbe (dome beam- kubbe kirişi), kiriş-i büzürk (big roof tile-büyük kiremit), kened-i büzürk (big clamp-büyük kened), kened-i frengi (European clamp- Avrupa kenedi), mismar-ı sağış (small nails-küçük çivi), mismar-ı çibuk (timber nails-ahşap çivisi), etc. (Tanyeli 1990, Çelik 2009). The nails were ordered from Kuziçe whereas the other iron materials were provided by Samakov. Çelik's research indicates that the material order was initially made about one month prior to the start of the construction (Çelik 2009).

In the Ottoman period, iron trade with Western Europe dates back to the 14th century. Starting from the 1370's the iron ingot trade including all other strategic materials that are essential for weapons and war were banned by the Christian Rulers to Ottoman Turks and Muslims (Inalcık, 1957, Parry 1970). However, the trade of those materials continued from the West mainly by Genoese and Venetian merchants throughout centuries. The Ottoman authorities encouraged those trades by giving some privileges to the above-mentioned merchants. Bartolomeo de Giano who lived in Istanbul in 1438 wrote letters to Venetian authorities mentioning that he had seen Venetian, Genoese, other Italian (Latin) and Western merchants shipping iron and steel in abundance to Gallipoli, Adrianople and Pera. The excuse of those merchants was that they did not sell the goods to Turks, but to Jews and Greeks (Ayduz, 2006).

The archive documents related to the accounting books are valuable sources for the trade activities related to iron either as raw or finished material. Foundries in Dubrovnik which produced cannons and firearms were main suppliers to the Balkans

and Venice. For example, the Ottoman army used cannons supplied by Dubrovnik in the Kosovo battle in 1389 against Christians (Ayduz, 2006). During the reigns of Selim the 1st and Suleiman the 1st, Frankish steel was bought to cast the cannons as written in the Tophane-i Amire accounting books. An accounting book dated 1500 A.D. indicates that cannons were casted in Volona (Avlonya) and Preveza for the Ottoman Navy. It is also indicated that the Ottomans bought iron wires for cannons to be casted in place. Those iron materials were kept in imperial foundry warehouses and stores. Another accounting book indicates that during the reign of Selim the 2nd in the year 1597, a request was made to the Venetians to send 1000 kantar (54000 kg) iron (steel) to Egypt (Ayduz, 2006).

During the classical period, Ottoman mines were run by state monopoly due to their military and financial precedence. Hungarian and German cannon masters worked for Sultan Mehmed the 2nd (Ayduz, 2006). Mainly non-Muslim experts (foundrymen) worked in the foundries. In fact, the French ambassador to Istanbul of the period 1547-48 reports that besides Jewish masters, German, French, Spanish, Venetian, Genoese and Sicilian experts worked at Tophane-i Amire or at the Imperial Cannon Foundry (Ayduz, 2006).

In the 16th century, iron use increased for building constructions; in the Balkans, especially Samakov became the main production centers where not only long iron rods were produced by forging (ordered as per the project length) but also small items as clamp, dowels, nails, etc (Tanyeli and Tanyeli 1993).

For the Ottomans an important iron mining and iron material production center was Samakocuk (Demirköy) which is in present Kırklareli. A document dated 1696 regarding Demirköy mentions that the state built some workshops in the village. The state continued to produce iron ingot and iron goods starting from the end of the 17th century until the last quarter of the 19th century (Danişman et al, 2012). Evidences on iron production in the 17th century were found in the excavations in Demirköy where findings such as shaft (bloomery) furnaces, water canals, water wheels, bellows, heavy hammer and anvil, heap of slag, nails were obtained (Danişman,

2007, Danişman, et. al. 2006, Danişman et al, 2012). After the 17th century, it seems that the state did not operate any iron production centers in those regions and that those centers have been operated by private companies (Danişman, et. al. 2006).

In the 18th century, iron products for Istanbul and its environs were mainly obtained from South-west Bulgaria and Yugoslavia. It seems that the Ottomans were not satisfied with the quality of iron products from Rumelia. In consequence, they made some efforts to encourage the improvement of iron technology in production centers in Anatolia. However, those productions were not sufficient and the iron trade was intensified with Western Europe (Danişman, et. al. 2006, Eruz 2004).

2.3 Iron Ore Deposits in Anatolia at Present

Turkey has iron ore deposits in Anatolia having a capacity of around 83 million tons. Those deposits are active mainly in the following regions – Divriği, Bingöl (Avnik Mines), Erzincan, Malatya, Kayseri, Kesikköprü, Balıkesir and Adapazarı (Figure 2.3 and Table 2.1). The iron ore deposits are classified in terms of their capacity as below (DPT Report, 2001):

- 1) Sivas Divriği - Malatya - Erzincan Region: The largest iron ore region of Turkey due to its content and high-grade. It is also expected to be the iron mining center of Turkey in the future.
- 2) Kayseri - Adana Region: The second important iron ore region of Turkey having high-grade ore and meeting a significant part of the needs of iron and steel factories in the country.
- 3) Ankara - Kesikköprü Region: The main iron ore source for the Karabük Iron - Steel Facilities since many years.
- 4) Western Anatolia Region: Although the iron deposits are generally of high grade, they contain considerable impurities to be eliminated.

5) Other regions: Spread over different parts of Turkey such as Bingöl - Genç - Avnik; Sakarya - Karasu - Çamdağ; Payas; İçel; Bitlis - Meşesürü - Öküzyatağı; Adıyaman - Çelikhan - Bulam; Kahraman Maraş - Beritdağı and Yozgat - Sarıkaya, etc. The mentioned deposits mostly require enrichment processes to eliminate the impurities they contain.

Divriği (Sivas) is the largest iron production center in the country. Both hematite and magnetite ores are processed there. Divriği iron ore deposits contain some tourmaline and skarn minerals. The main iron ore minerals in the reserves of Anatolia are given in Table 2.1. Iron ores in nature are magnetite (Fe_3O_4), hematite (Fe_2O_3), limonite ($\alpha\text{-FeOOH}\cdot 2\text{H}_2\text{O}$), goethite ($\alpha\text{-FeOOH}$), siderite (FeCO_3) and pyrite (FeS_2) minerals. MTA (Turkish General Directorate of Mineral Research and Exploration) reports that the main iron ore reserves in Turkey have a rich iron content of 55% Fe on the average. Due to low levels of iron ore processing, iron and steel industry in Turkey relies on imports of ingots, mainly from Brazil, Russia, Sweden and Ukraine.

However, Turkey is Europe's first-ranked and world's seventh-ranked crude steel producer with 40.4 million tons in 2021 as indicated in the statistics of the World Steel Association. Crude steel is the first usable form of steel as ingots, semi-finished products (billets, blooms, slabs), and liquid steel for castings. As a matter of fact, iron and steel industry is the largest and the most dynamic industry in the world. Currently, the world's most important engineering and construction materials are iron and steel. The importance of the iron and steel industry is not only due to its economic aspect but also to relevant issues on technological development, environmental protection and social sustainability. Since Turkey has been an important country in steel industry throughout history, an additional concern is the importance of conservation of iron objects in historical structures. The survival of iron objects in many historical structures in Turkey up to present day prove their durability properties and the importance of production technologies used in the past. At that point, detailed research on the corrosion characteristics and technological properties of historical steel objects seems to be an important field of study.

Table 2. 1 Some Regions in Anatolia and the Balkans and their iron ore reserves.

Location	Fe Ore Type
Sivas Divriği - Malatya Region	Mainly: hematite and magnetite ¹
Kayseri - Adana Region	Mainly: hematite, goethite and siderite with some siderite, pyrite, limonite ²
Ankara - Kırşehir Region	Mainly: magnetite and pyrite with hematite, goethite, chalcopyrite and marcasite ³
İçel Region	Mainly: hematite with limonite and siderite ⁴
Payas Kilis Region	Mainly: hematite, goethite, maghemite with quartz, berthierine and diasphorite ⁵
Giresun Region	Mainly: magnetite with pyrite and chalcopyrite ⁶
Sakarya - Çamdağ Region	Mainly: hematite, chamosite, siderite ⁷ ,
Çanakkale - Balıkesir Region	Mainly: hematite ^{8,9} , magnetite, pyrite and chalcopyrite ⁹
Kütahya Region	Mainly: magnetite, hematite, pyrite, marcasite, ilmenite, limonite ¹⁰
Aydın - İzmir Region	Mainly: hematite, magnetite with limonite and pyrite ¹¹
Kırklareli Demirköy Region	Mainly: hematite and magnetite together with goethite-limonite ¹²

Sources: ¹Yıldız, 2010, ²Tiringa, et al, 2009, ³Koç, et al, 2008, ⁴Arıkan, 1969, ⁵Koç, et al 1991, ⁶Kurt, 2014, ⁷MTA Report 1980, ⁸Ertin, 2001, ⁹Çağlan, et al, 2016, ¹⁰Cengiz, 2018, ¹¹Öztunalı, 1965, ¹²Tiringa, et al, 2019.

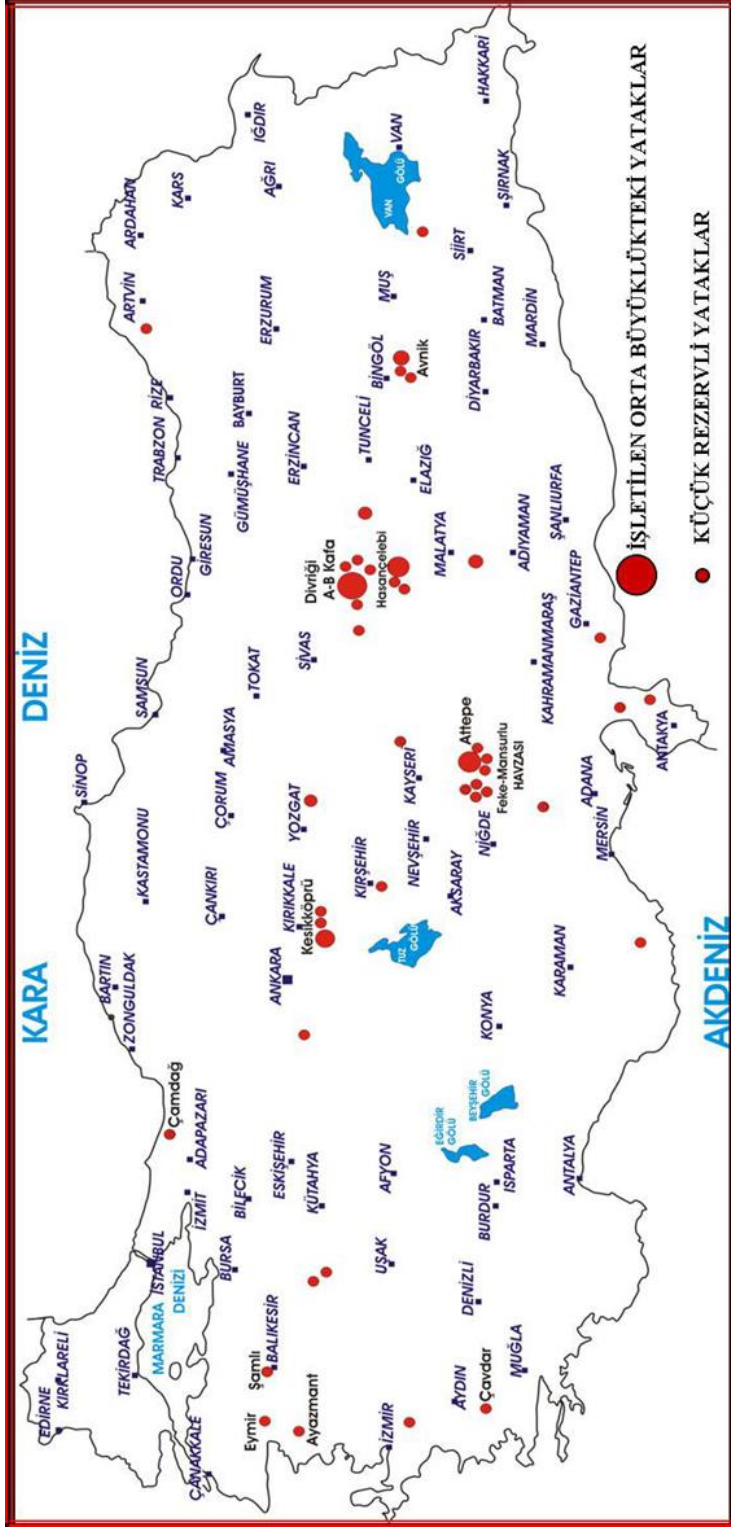


Figure 2. 3 Important iron ore deposits in Turkey
 (Source: <http://www.haritaburada.com/turkiye-demir-madeni-yataklari-haritasi/>)

2.4 Studies on Iron Goods and Production Processes in Ottoman Land

In the Ottoman period, iron production and trade of iron and steel goods were of high importance. However, limited information is available on the specific sources of iron supply and production centers through the 16th and 18th centuries across the wide geography under the Ottoman rule (Eruz, 2004). The Ottoman central administration took the control in hand and supervised the use of resources even for local needs. Rumelia always had a major role in iron production industry because of its ores, charcoal, constant water power and climate (Eruz 2004) as well as its importance in supplying goods to Istanbul.

The production techniques of those objects were either forging or casting. During the mentioned periods, most of the constructional iron/steel objects such as beams, clamps, nails, etc. were produced by forging, but window railing balls (lokma) and cannons were casted (Tanyeli 1990, Eruz 2004). Those forged objects were produced at either local production centers (small workshops) for small objects or large workshops especially for long structural beams made of one piece (e.g., 17 m) such as the ones in Selimiye Mosque. However, it is difficult to determine the distance of the production to the raw material supply location. The forging methods such as hot, cold or repeated forging and the impurities in the raw materials are known to influence the performance properties of iron and steel goods at production state (Tanyeli et al, 1990).

Producing an iron object needs skilled masters starting from the treatment of raw materials, followed by melting and shaping processes (Figure 2.4). The ore is extracted to metallic iron by smelting after roasting it in a fire to remove unwanted material. Hence, during the ancient periods, it was important for the mines to be close to the sources such as fuel (charcoal) and water power.

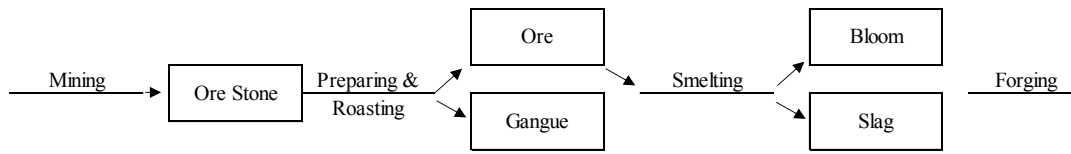


Figure 2. 4 Four main stages of production process for iron goods (Hodges 1964).

In Anatolia, during the late Hittite and Iron age, the earliest smelting method was bloomery smelting. The process continued with shaping the iron by forging or casting at the smithy (Tylecote, 1976, Yalçın, 2008). A bloomery furnace was made of earth or clay with a chimney and the pipes close to the bottom to allow air to come in by an opening at the bottom. It was used for smelting the iron ore from its oxides and to produce a porous mass of iron called a bloom and slag. The porous mass of iron, also termed as sponge iron, was then shaped. The bloomery smelting method continued into the post-medieval period but began to be superseded by blast furnace smelting around late 15th century (Tylecote 1976). By the 1500's, two types of smelting furnaces continued to be used: bloomery furnaces for wrought iron and blast furnaces (yüksek fırın) for producing pig iron (Tylecote 1976). Pig iron is produced by using fuel (coke), iron ore and a flux, generally limestone (CaCO_3), in a blast furnace with continuous air supply by a series of pipes at the lower section of the furnace. As a result, pig iron as molten metal and slag phases are collected from the bottom of the furnace (Schmult, 2016). The quality of steel depends on the slag remnants which are obtained during the smelting process done by either a bloomery furnace or a blast furnace. The bloom then needs to be purified with repeated heating and hammering, the process being called forging.

The ancient metallurgy and metalwork in Anatolia dates back to very early ages – from the 9th millennium B.C., towards the 2nd millennium B.C. - as described by Yalçın (2008, 2012) and Biber, et al (2008). Phrygians and Urartians were the most important nations during the Iron Age (Bilgi 2004, Biber, et al 2008). Iron metallurgy predominantly started after the 2nd millennium B.C. and the products were mainly weapons, tools, sculptures (figurines) and jewelry (Yalçın, 2008, Bilgi, 2004). Both

hammering and casting processes were used for shaping (Bilgi 2004, Biber, et al 2008). The first metallurgists obtained steel in bloomery furnaces. Mostly figurines, arrowheads and fibulas were casted. Other iron products were usually produced by hammering at the smithy (Bilgi, 2004, Yalçın, 2008, Biber, et al 2008).

Another process used for iron production is known as the crucible process. It involves the heating of either blister steel fragments or short lengths of wrought iron bars mixed with charcoal inside fire clay crucibles. The resulting molten steel is allowed to run through iron molds. The steel obtained is called cast iron. Cast steel is hard and homogenous.

The ancient artifacts that were mainly observed as low carbon steels were either produced directly by the bloomery process or the cementation process. Cementation process is a method to introduce carbon as powder to the steel by heat treatment around 700°C and the carbon amount in the composition is usually around 0.75% to 1.5%. The conditions slowly diffuse carbon into iron and cause the carbon to become dissolved in the iron, raising the carbon percentage. In antiquity, cementation was done on the anvil during forging to allow bloom to absorb carbon from charcoal, but this process was very slow at room temperature (Hodges, 1964).

As the final shaping phase of steel, forging is known as the main process during the historical periods. For iron and steel forging, the iron is brought to red heat and forged generally with a hammer on a flat surfaced anvil while it is hot. If necessary, the process continues by repeated heating and hammering to remove impurities from inside the steel body as newly formed oxides (Hodges 1964). However, this process needs good mastership in order not to create further problems such as increase in brittleness in the iron material while forging. Brittleness problem occurs if the steel is over-heated (hot shortness) in presence of high sulfur content or less-heated (cold shortness) in presence of high phosphorous content coming from the ores. As a result, those materials need to be re-melted. Thinning (drawing) and bending processes continue on anvil by hammering. When needed, the final shape is given by hammering the soft iron to pass through a hole in order to obtain the desired shape.

As mentioned before, this study is focused on the Ottoman Period iron production with an emphasis on the objects used in Ottoman buildings starting from the 15th century onwards. Since Rumelia had important iron production centers in the Ottoman period, findings from recent excavations in Kırklareli - Demirköy foundries and workshops are of special interest (Danışman et al, 2006, 2007, Ozbal et al, 2008, Ozbal 2010, Danışman and Ozbal, 2010). The excavations in Demirköy (Samakocuk), where production continued until the beginning of the 20th century, show that foundries (workshops) were built near the bed of rivers enabling the continuous energy supply necessary for foundry processes (Danışman et al, 2006, Danışman and Ozbal 2010). Small foundries and workshops rented from the state were operated by private sectors as sub-contractors. However, the blast-furnaces were operated by the state. The initial archaeometric studies done on the findings collected during the excavations in Demirköy (Samakocuk) exhibit the concurrent use of blast furnaces and bloomery furnaces for iron production (Danışman et al, 2006, Danışman and Ozbal 2010).

Some iron materials such as slag, nail, cannon ball, iron hammer, iron clamp of a wooden water wheel, iron blower, iron ingots of blast furnaces and spongy-like ingots (bloom) from the bloomery furnaces were found during the 2002 - 2008 excavation seasons in Demirköy (Danışman et al, 2007, Ozbal et al, 2008, Ozbal 2010, Danışman and Ozbal 2010). Rectangular nails were abundantly found during the excavations. In addition, documents from the Ottoman archives indicate supply of nails for the construction of some buildings nearby Saray township (Danışman et al 2007). The microstructural investigations performed on the bloom samples revealed some coal and slag composed of wüstite (50-60% FeO), fayalite and anorthite containing regions (Ozbal et al, 2008, Danışman and Ozbal 2010). The blooms containing 0.23% carbon and some undefined iron materials containing 0.6% carbon were classified as low carbon steels with ferrite grains and inclusions (Ozbal et al, 2008). The nail artefacts with a square-shaped body having ferritic structure showed the signs of hammering and were produced from the blooms with similar methods used in the Ottoman period (Ozbal et al, 2008, Ozbal 2010). Such nails were

produced from rectangular iron profiles and the head of the nail was shaped by placing it into a hole suitable for its section and hammered to get the shape (Ozbal 2010). The microscopic analyses performed on the cast iron ingots with approximately 3% carbon showed that they were gray cast iron and cementite rods, densely dispersed into the pearlite grains (Danışman et al, 2007, Ozbal 2010). Archive documents indicate that those cast iron ingots were sent to Istanbul for casting nests (yuvalak) or humbaras (Danışman et al, 2007, Ozbal et al, 2008). Some slags from the 2005-2006 excavation seasons were classified in two groups: one being “dense, gray slag” composed of wüstite with some fayalite, the other as “iron-rich slag” having higher iron oxide content with high magnetic property (Danışman et al, 2007, Ozbal 2010). The findings from the excavations in 2008 were dated to the 19th and to the beginning of the 20th century (Ozbal 2010). Some slag analyses show that the body was covered with iron oxide as wüstite.

Another important Archaeometrical analyses study was performed on seven constructional iron components composed of a clamp (kenet), a portico tightener (revak gergisi), a dowel (zıvana), a repair bracing (onarım kuşaklaması) and window railing balls (pencere parmaklık topu) collected from the 15th to the 18th century buildings to obtain knowledge on the Ottoman Period metallurgy (Tanyeli et al, 1990). Objects analyzed had a ferritic structure with heterogenous grain size and carbon, phosphorous and potassium rich slag regions. The high percentage of phosphorus level increased hot workability of iron and decreased the smelting temperature (Tanyeli et al. 1990). All objects, except the window railing balls which were casted, were hot forged and forging was repeated after folding several times to remove the slags inside the metal body and increase its strength. Silicon ratios of iron objects were found to be very low which may indicate that no fluxing agent (SiO_2 ve CaCO_3) was used during the smelting process and the smelting process was done by mixing iron ore and charcoal in bloomery type furnaces (Tanyeli et al, 1990). The lack of sulfur content and the presence of potassium in those iron objects may indicate the use of charcoal in furnaces (Tanyeli et al, 1990). In the production techniques of iron products between 15th - 18th century, no significant difference

has been observed. The technology was well developed and not inferior to the one used in Western Europe, on the contrary, it was probably beyond it: During the construction of Bayezid Mosque in Istanbul, beams having the weight of 1.2 tones were used, whereas, until the 18th century, similar long beams have not been observed in Western Europe (Tanyeli et al, 1990).

Besides those Anatolian archeometallurgical analyzes performed on the iron/steel objects dating back to the Ottoman period, some relevant studies were done on cannon humbaras and weapons manufactured in the Kiği mine (Erzurum) between the 17th and the 19th centuries (Baş, 2011). Iron weapons, nests and humbaras were produced for the needs of Erzurum and its environs. However, they were also sent to other locations, even to the western parts of Anatolia, either as raw material or as finished products when the need occurred.

Batur (2009) states that the initial architectural use of iron was as jointing elements for stone such as clamps and dowels because simple melting furnaces carved into the ground and charcoal were sufficient for their production. With the use of hydraulic energy, the iron/steel production increased. Hence, the use of steel/iron as constructional component such as beams increased in buildings. However, the main improvement in technology took place in the 18th century with the use of fossil coal “coke” enabling to reach higher temperatures and as a result molten iron was obtained. The ease of production increased the use of steel, like beams in construction, in the 18th century. In the 19th century, steel beams with bricks were used for floors and the use of steel reinforced cement started in the middle of the 19th century. That method increased the resistance of steel against loads and corrosion. As a result, it became indispensable for constructions and was not only used in Western Europe but also in the Ottoman Empire contemporarily. By that industrial progress, the steel beam floors and T-profiles started to be used in the multistorey structures. The above-mentioned developments needed important financial power and the urban morphology of the big cities such as Istanbul, Thessaloniki and Izmir started to change (Batur 2009). The earliest examples of

reinforced concrete were the lecture halls of Seririyat Hospital of the Mekteb-i Tıbbiye in Haydarpaşa (Istanbul), and the hypocaust flooring of the Hammam in the Mekteb-i Tıbbiye. The construction of the mentioned building was completed in 1900. The flooring elements were brought from Belgium, and the large metal windows were brought from Austria, as indicated in the records.

Significant developments have taken place in Ottoman industry during the Tanzimat Era as an influence of the developments led by the Industrial Revolution in Europe (Seyitdanlıoğlu 2009). Tanzimat supporters made considerable efforts for some major investments in the first half of the 19th century particularly in Istanbul, but problems related to planning, qualified personnel, cost, marketing and transportation did not consent the developments to be long-lived (Seyitdanlıoğlu 2009). To solve the problem of qualified personnel for blacksmithing, foundry, machinery, architecture and the carpentry needs of the industry, an industrial school in Istanbul was founded in 1868. The early form of “industrial zone” was first established in Zeytinburnu (Istanbul) where a wide variety of items were produced in good quality, similar to the ones in Western Europe. Among those items were iron pipes, steel rails, tools for agriculture, spearheads, swords, locks, keys, knives, razors, cannon balls, weapons, helmets, armors, etc. (Seyitdanlıoğlu 2009). The second “industrial zone” was built in Bakırköy (Istanbul) where an iron workshop with two furnaces was constructed. In 1844, additional iron foundries were opened in Beşiktaş (Istanbul) and in Samakov (nowadays in Bulgaria) for casting cannonballs. Another iron casting workshop was opened in Baghdad between 1842-1847. During the same period, there were also a number of iron factories and workshops affiliated to Tophane (Istanbul) and a foundry in Samakocuk (Kırklareli). However, in later periods, those production centers had some operational problems due to their dependency on foreign resources in terms of machinery, spare parts and qualified personnel.

From the above-mentioned studies, some information on production methods of iron and steel goods such as forging or casting, production location, hardness,

microstructure and chemical composition can be gathered. However, there are not many studies on the state of deterioration of iron/steel components used in the construction of the Ottoman period buildings, their performance properties and corrosion characteristics.

In order to assess the corrosion characteristics of iron objects and the factors affecting them, it is necessary to look at the subject in a wider perspective and include the roles of production techniques, impurities in the composition, and the environmental conditions that they are exposed to.

2.5 Iron Oxides and Their Properties

Iron at its pure metallic form is rarely found in nature. However, iron minerals are quite common and found as oxides, hydroxides, oxy-hydroxides, carbonates, sulfides, sulphates and others depending on the geological history of their location (Yıldız, 2010, Schwertmann and Taylor, 1989). The common iron ores used for the production of iron objects are known as magnetite (Fe_3O_4), hematite ($\alpha\text{-Fe}_2\text{O}_3$), limonite ($\alpha\text{-FeOOH}\cdot 2\text{H}_2\text{O}$), goethite ($\alpha\text{-FeOOH}$), siderite (FeCO_3) and pyrite (FeS_2) minerals.

A corrosion layer develops on the surfaces of iron materials as one or more types of compounds, similar to the ones found in nature, in the forms of oxides, hydroxides, oxy-hydroxides depending on the environment they are exposed to, their compositional and microstructural properties. Iron in the corrosion layers can exist as Fe^{3+} or Fe^{2+} valences or their co-presence. In most cases, it is in trivalent state (Fe^{3+}) such as hematite ($\alpha\text{-Fe}_2\text{O}_3$), goethite ($\alpha\text{-FeOOH}$), lepidocrocite ($\gamma\text{-FeOOH}$), maghemite ($\gamma\text{-Fe}_2\text{O}_3$) as well as in combination of two (Fe^{2+}) and three valent (Fe^{3+}) states as in magnetite (Fe_3O_4) and less commonly in two valent state as wüstite (FeO) and iron hydroxide ($\text{Fe}(\text{OH})_2$).

In iron oxides, Fe^{3+} and Fe^{2+} interact with other negatively charged ions such as O^{2-} / OH^- in an environment that may change the energy states of iron. The characteristics

of iron oxide minerals are affected by the 3d electrons in Fe where Fe^{3+} has five unpaired and Fe^{2+} has four unpaired electrons in its orbital at the ground state with lowest energy. 3d orbitals can be filled in different ways and affect the crystal field stabilization energy of the compound. Those 3d electrons influence the magnetic, electrical, optical and spectroscopic behavior of iron oxides and their thermodynamic properties. The migration of free charge carriers in iron - either electrons in the empty conduction band (n-type) or vacancies in the full valance band (p-type) - cause electrical conductivity which is an important characteristic of the related iron oxide (Cornell and Schwertmann, 2003). Depending on the vacancies and the distribution of electrons in the 3d orbital, iron oxides act as n or p type semiconductors as well as including both types and performing different levels of conductivity.

At room temperature, magnetite, hematite, wustite and maghemite are semiconductors. However, among them, magnetite differs in the type and level of conductivity. Magnetite having metallic properties as slightly metal deficient is an n and p type semiconductor; it has a very low band gap as 0.1 eV between valance band formed of full 3d electrons and conduction band with empty d-orbitals. Hematite and maghemite have n-type semi-conductivity with an approximately 2.2 eV and 2.03 eV band gap respectively (Zhang et al, 1993). When the band gap is small, mobile electrons easily promoted with the external effects become conductive i.e., having less resistivity towards electrical currents and can easily transform to other oxides. Magnetite is the most conductive iron oxide with 10^2 - $10^3 \Omega^{-1} \text{cm}^{-1}$ value (Quinn et al, 1976). The interaction is an important parameter for the level of energy of the band gaps: the lower the flat band potential the greater the efficiency of semiconductor and the easier the transformation. For this reason, magnetite having the lowest flat band potential within the iron oxide products can easily transform, while hematite is relatively stable.

At room temperature, FeOOH polymorphs such as goethite, lepidocrocite, akaganeite and feroxyhyte have very low conductivity (ca. $10^{-9} \Omega^{-1} \text{cm}^{-1}$) and their conductivity increase with the heating to ca. 140°C which causes dehydration and produce Fe^{2+} on the surface, initiating some electron changes between Fe^{2+} and

Fe³⁺ (Kaneko and Inouye, 1974). Goethite, lepidocrocite and akaganeite have the band gaps 2.10, 2.06 and 2.12 eV respectively (Cornell and Schwertmann, 2003). In goethite, the band gap decreases as the particle size increase, that may partially explain size-dependent chemical and photochemical reactivity of goethite (Zhang et al, 2011). Goethite having particle size between 9-38 nm, appears to show direct band gap (3.1-2.5 eV) behavior (Zhang et al, 2011). Similar conclusions are noted in other nano sized iron oxyhydroxides and iron oxides such as the decrease of band gap of hematite from 2.95 to 2.18 eV with increasing nanoparticle size from 7 nm to 120 nm (Chernyshova, 2010). Those results indicate that nano sized particles of goethite have relatively higher band gaps than the hematite of approximately the same size of nano particles.

During the contact with water solution or water film, a positive charge occurs on the surface of an n type semiconductor as a result of electronic charge redistribution with the solution. In the contact with a polar medium (water), the majority of mineral particles show a definite surface charge as the consequence of ionization, ionic adsorption and ionic dissolution (Salopek et al, 1992). At the surface in contact with water or a water film where electrical forces are acting, a solid/liquid interface occurs and that interface is called “a double layer”. The electrical double layer is a physical model in which oppositely charged ions are adsorbed in a single layer on the surface. The double layer gives very important information about the behavior of colloidal particles in contact with the solution. Within this diffused surface there appears a boundary called “the slip surface”. The charged particle and the part of the ions around it, up to the slip surface boundary, move as a single piece.

The potential at this slip surface is called “the zeta potential”, used in colloid chemistry for observing the behavior of dispersive systems in liquids. It is affected by both the surface structure of the grain and the content of the liquid it is in (Salopek et al, 1992). The most important reason for determining the zeta potential value, relevant in flotation and flocculation processes, is to determine the size of the diffused double layer around the particle (Ocepek, 1989). The zeta potential is related to the surface charge density and the double layer thickness. The surface charge

density depends on the concentration of the potential determining ions. In many systems, the zeta potential is pH dependent, since the H⁺ ion is the potential determining ion (Salopek et al, 1992).

For magnetite, zeta-potential is positive in acid media up to pH 4 and it is negative in poor acid or alkaline media (Salopek et al, 1992). The stability of the suspension is the lowest when the zeta potential is zero and stability increases due to the increase in the electronegativity of the particle.

Iron oxides are generally low or sparingly soluble except at extreme pH values, they maintain very low total iron in solution. In the pH range 4 to 10 and in the absence of complexing or reducing agents, total iron concentration (Fe_T) is < 10⁻⁶ (Cornell and Schwertmann, 2003). Goethite is the least soluble iron oxide, followed by hematite and lepidocrocite near neutral pH being 7.8. Its formation is the most favorable at that pH (Figure 2.5) (Cornell and Schwertmann, 2003). It is also expected that less ordered, amorphous phases precipitate first. However, it was found that well crystalline phases form first. The formation of feroxyhyte demonstrate that the enthalpy of formation (ΔH°) for poorly crystalline feroxyhyte is higher in comparison to samples with better crystallinity indicating that well crystalline phases may form more easily (Majzlan et al, 2008).

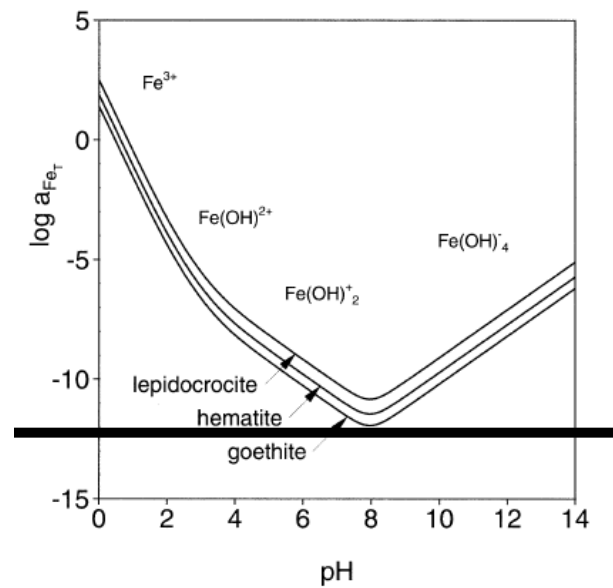


Figure 2. 5 Solubilities of goethite, hematite and lepidocrocite as a function of pH (Cornell and Schwertmann, 2003).

Iron oxide minerals and their important characteristics such as magnetic properties, bulk density, color, melting point and their important thermodynamic parameters such as enthalpy of formation (ΔH°), Gibb's energy of formation (ΔG°), standard molar entropy (S°) and molar heat capacity (C_p) at 298.15 are compiled in Table 2.2 and Table 2.3. K dissociation constant is not indicated in the tables, because of its extensive variation with the pH values and other environmental parameters.

The primary differentiating characteristics of iron oxide phases are their distinct magnetic behavior which results from the vacancies and valance states of iron in sublattices (Shokrollahi, 2017). Magnetic property is directly related to Fe-O-Fe bond angle (Coey, 1988). In $Fe^{3+} - Fe^{3+}$ ion pair with 90° bond angle, those phases have weak anti-ferromagnetic properties while at $120-180^\circ$ bond angle they have strong antiferromagnetic properties similarly to Fe^{2+} ion pairs. The types of magnetism of the substances are classified as diamagnetic and paramagnetic. All iron oxides are paramagnetic, being attracted towards a magnetic field and their magnetic susceptibility, influenced by temperature, is positive and small (0-0.01). They are further classified as ferromagnetic, ferrimagnetic, antiferromagnetic, spero-magnetic

and super-paramagnetic. Both ferri- and ferro- magnetic substances are strongly attracted by a magnetic field. While for ferromagnetic substances the alignment of electron spins is parallel with positive susceptibility ($0.01-10^6$), for ferrimagnetic substances, the electron spins are of equal magnetic moment and aligned in an antiparallel manner with unequal moment that results in a net magnetic moment. Antiferromagnetic substances are also aligned in antiparallel manner. That results in a zero overall magnetic moment of electron spins and a small positive magnetic susceptibility (0-0.1). Super-paramagnetic substances, affected by the particle size at room temperature, occur as a result of magnetic anisotropy and appear being easily magnetized along the 111 directions. The spero-magnetic iron oxides having amorphous and poorly ordered structure contain Fe-O-Fe bonds and the iron carrying a magnetic moment supports super-exchange reactions (Coey and Readman, 1973).

Magnetite (Fe_3O_4), being the most magnetic and naturally occurring mineral on earth, is ferrimagnetic when attracted to a magnet and can be used a permanent magnet itself. Maghemite ($\gamma\text{-Fe}_2\text{O}_3$) is also a ferrimagnetic material with strong magnetization properties like magnetite. Although hematite is the polymorph of maghemite, it has antiferromagnetic properties. All oxy-hydroxide polymorphs - goethite, lepidocrocite and akaganeite - are antiferromagnetic with weak paramagnetic properties at room temperature (Cornell and Schwertmann, 2003). Among the iron oxyhydroxides, feroxyhyte ($\delta\text{-FeOOH}$) presents ferromagnetic ordering while the other FeOOH polymorphs with antiferromagnetic (Majzlan et al, 2008). Magnetic properties of iron oxides have been described above as they are found in nature, but there are some studies reporting the change in the magnetic properties of iron oxides in relation to particle size. For the iron oxides smaller than 10 nm in size, paramagnetic properties arise (Cornell and Schwertmann, 2003). Hematite, having a particle size smaller than 23 μm decreases performance of magnetic separation and becomes super-paramagnetic (Shao et al 1996, Hirt et al 2002, Grau-Crespo et al, 2010, Jin et al, 2022). Particles of goethite smaller than 15-20 nm are super-paramagnetic at room temperature (Janot et al, 1973). The studies also mention that magnetic susceptibility of an iron oxide mineral could be affected

by temperature as well as by particle size. At elevated temperatures, iron content and the magnetic susceptibility of iron oxide minerals increase gradually. Iron ores containing limonite (goethite) and hematite transform to magnetite at 480°C at which phase ferrimagnetic properties occur (Jin et al 2022).

Bulk density (BD) in a mass is the weight of the material including the intergranular air space in unit volume considering both the solids and the pore space, typically expressed as g/cm³. Magnetite, hematite, maghemite and wüstite have higher bulk density ranging between 5.1 - 5.70 g/cm³ in comparison to FeOOH polymorphs with different structures which have lower bulk density in the range of 2.7 - 4.4 g/cm³. Magnetite, hematite and maghemite have hardness values (Mohs Hardness grade) between 5.5 - 6.5 HM while wustite, goethite and the other oxyhydroxide polymorphs have hardness values between 4.0 - 5.5 MH. Polymorphs of oxyhydroxides and wüstite are softer than magnetite, hematite and maghemite. Oxides are found in a wide range of colors which cannot be used as a significant identification parameter by visual and microscopic analyses. The most commonly observed colors of oxides are brown, reddish brown, blackish gray and black. Heating effects the color of the iron oxides as well as their particle size and composition.

Table 2. 2 The main physical properties of some iron oxides, hydroxides and oxyhydroxides found in nature (BD: Bulk density; MP: Melting Point).

Mineral	Chemical Formula and % Fe	BD g/cm ³	MP °C	Hardness (HM)	Color	Magnetic Properties
Magnetite	¹ Fe ₃ O ₄ 72%	¹ 5.1- 5.2	⁷ 1583- 1597	¹ 5.5-6.0	¹ Grayish black, iron black	⁸ Naturally strong magnetic Ferrimag netic
Hematite	² α-Fe ₂ O ₃ 70%	² 5.2	² 1565 ⁷ 1350	² 5.5-6.5	^{1, 2, 3} Reddish gray, blackish red, brown to cherry red, black	⁸ Antiferro- magnetic
Maghemite	¹ γ-Fe ₂ O ₃ 70%	¹ 5.2	1539 - 1565	^{1,4} 6.0	^{1,4} Dark brown, ⁴ reddish- brown, ¹⁴ blueish- black	⁸ Strongly magnetic, Ferrimag netic
Goethite	¹ α-FeOOH 60-63%	¹ 4.1 ¹² 4.3	⁵ 350	¹ 5.0-5.5	¹ Brown, reddish brown, brownish yellow, ocher yellow	^{7,9} Antiferro -magnetic
Lepidocrocite	¹ γ-FeOOH 62.85%	¹ 3.9 ⁴ 4.5- 4.1		⁴ 5.0	¹ Red, yellowish brown, blackish brown	^{7,9} Antiferro -magnetic
Ferrihydrite	¹ Fe ₂ O ₃ •0.5H ₂ O %66.21 ⁴ Fe ₁₀ O ₁₄ (OH) ₂	¹ 3.8 ⁴ 4.0			^{1,4} Yellow brown, dark brown	⁷ Superpara -magnetic
Feroxyhyte	¹ δ-FeOOH 62.85%	^{1,4} 4.2			^{1,4} Brown, ⁴ yellow-brown	^{7,9} Ferro- magnetic

Sources: ¹www.webmineral.com - ²<https://pubchem.ncbi.nlm.nih.gov/> - ³Hirt et al (2002) ⁴<https://www.mindat.org> - ⁵www.chemicalbook.com - ⁶Shao et al (1996) - ⁷Cornell and Schwertmann, 2003, ⁸Shokrollahi (2017) - ⁹www.sciencedirect.com/topics/earth-and-planetary-sciences/limonite - ¹⁰Dekkers et al (2017) - ¹¹Waters et al (2008) - ¹²<https://geology.com/minerals/> - ¹³<https://www.minerals.net/> - ¹⁴<https://rruff.info/> - ¹⁵<https://www.cs.mcgill.ca/~rwest/wikispeedia/wpcd/wp/p/Pyrite.htm>

Table 2.2 The main physical properties of some iron oxides, hydroxides and oxyhydroxides found in nature (BD: Bulk density; MP: Melting Point). (continued)

Mineral	Chemical Formula and % Fe	BD g/cm ³	MP °C	Hardness (HM)	Color	Magnetic Properties
Limonite	¹ FeOOH.nH ₂ O 48%	⁴ 2.7- 4.3		¹³ 4.0-5.5	¹³ Brown, red-brown, ocher yellow, yellowish brown, brownish yellow,	⁵ Weakly paramagnetic
Akaganeite	¹ β-FeOOH.Cl 55.75%	⁴ 3.52- ¹³ 3.64			^{1,4} Yellowish brown, rusty brown	⁷ Antiferromagnetic
Wüstite	¹ FeO 77.73%	¹⁵ 7.0	⁷ 1377	⁴ 5.0-5.5	¹ Gray, ⁴ black	⁷ Antiferromagnetic
Siderite	¹ FeCO ₃ 48%	^{1,4} 3.96 -3.93		⁴ 3.75-4.25 ¹³ 3.5-4	^{4,13} Yellowish brown, brown, yellowish gray, gray, greenish gray, white	¹⁰ Antiferromagnetic

Sources: ¹www.webmineral.com - ²<https://pubchem.ncbi.nlm.nih.gov/> - ³Hirt et al (2002) ⁴<https://www.mindat.org> - ⁵www.chemicalbook.com - ⁶Shao et al (1996) - ⁷Cornell and Schwertmann, 2003, ⁸Shokrollahi (2017) - ⁹www.sciencedirect.com/topics/earth-and-planetary-sciences/limonite - ¹⁰Dekkers et al (2017) - ¹¹Waters et al (2008) - ¹²<https://geology.com/minerals/> - ¹³<https://www.minerals.net/> - ¹⁴<https://rruff.info/> - ¹⁵<https://www.cs.mcgill.ca/~rwest/wikispeedia/wpcd/wp/p/Pyrite.htm>

The important thermodynamic parameters of iron oxides found in nature are given in Table 2.3 indicating enthalpy of formation (ΔH°), Gibb's energy of formation (ΔG°), standard molar entropy (S°) and molar heat capacity (C_p) at 298.15 K. Magnetite is the most stable compound of iron oxides having the lowest enthalpy of formation (ΔH°) -1115.7 kJ/mol and Gibb's energy of formation (ΔG°) -1012.6 kJ/mol followed by hematite, maghemite, akaganeite and goethite (Cornell and Schwertmann, 2003). Goethite has ΔH° value of -559.3 kJ/mol and ΔG° value of -488.6 kJ/mol that are similar to the values of lepidocrocite and feroxyhyte. In natural atmospheric conditions, goethite and hematite are found as the most stable iron oxides in Fe³⁺ form.

Table 2. 3 Some important thermodynamic characteristics of iron ore minerals.

Mineral	Chemical Formula	$\Delta_f H^\circ$ kJ/mol	$\Delta_f G^\circ$ kJ/mol	S° kJ/mol K	C_p kJ/mol K
Magnetite	Fe ₃ O ₄	¹ -1115.7	¹ -1012.6	¹ 146.1	¹ 150.3
Hematite	α -Fe ₂ O ₃	¹ -824.2	¹ -742.7	¹ 87.4	¹ 103.9
Maghemite	γ -Fe ₂ O ₃	¹ -805.8	¹ -725.1	¹ 91.4	¹ 104.0
Goethite	α -FeOOH	¹ -559.3	¹ -488.6	¹ 60.5	¹ 74.3
Akaganeite	β -FeOOH	¹ -557.6	¹ -752.7	³ 81.8	¹ 50.0
Lepidocrocite	γ -FeOOH	¹ -556.4	¹ -486.3	¹ 62.5	¹ 76.2
Ferrihydrite	⁵ Fe ₂ O ₃ •0.5H ₂ O ⁷ Fe ₁₀ O ₁₄ (OH) ₂	⁸ -830.3	¹ -699.0	⁸ 122.2	⁹ 71.7
Feroxyhyte	δ -FeOOH	⁴ -552.6	⁴ -478.1	⁴ 65.0	-
Wüstite	FeO	¹ -266.3	¹ -244.6	¹ 54.3	¹ 50.0
Fayalite	Fe ₂ SiO ₄	⁶ -1478.2	⁶ -1379.0	⁶ 151.0	⁶ 131.9

Source: ¹Cornell and Schwertmann (2003) – ²<https://pubchem.ncbi.nlm.nih.gov/> - ³Snow et al (2011) – ⁴Majzlan et al (2008) – ⁵www.webmineral.com - ⁶Robbie et al (1982) - ⁷<https://www.mindat.org> – ⁸Majzlan et al (2004)- ⁹Snow et al (2013).

The solubility of iron oxides is very low, K_{so} ranging from 10^{-42} to 10^{-44} . K_{so} values suggest that hematite is less soluble than goethite and the order of solubility is akaganeite, ferrihydrite, lepidocrocite, maghemite, goethite and hematite in decreasing order (Berner 1969). However, it may also be that hematite has greater solubility than goethite in alkaline media (Cornell and Giovanoli, 1990). The Fe(II) oxides are more soluble than Fe(III) oxides with magnetite being more soluble than Fe(OH)₂ (Cornell and Schwertmann, 2003).

The particle size of an iron oxide crystal has an influence on the solubility of the iron oxide compound. Several studies show that surface energy provides a significant contribution to the overall energy of nanomaterials and this contribution may be sufficient to invert the thermodynamic stability of phases, making phases metastable in the bulk and stable at the nanoscale (McHale et al., 1997; Pitcher et al., 2005; Mazeina and Navrotsky, 2007). Goethite precipitates from the hydrolysis of Fe³⁺

solutions in aqueous media or by oxidation /hydrolysis of Fe²⁺ in alkaline media (Cornell and Schwertmann, 2003). In general solubility of the iron oxide crystals increase when particle size decreases e.g., K_{so} increases by two orders of magnitude when particle size decreases from 1 μm to 10 nm for both hematite and goethite particles commonly found in nature. Goethite is more stable than hematite down to a particle size of ca. 0.15 μm (150 nm) up to 40°C and this situation often occurs in natural systems (Cornell and Schwertmann, 2003, p 199). Surface free energy for goethite is greater than hematite based on the calculation solubility product that indicates that coarse-grained goethite is more stable than hematite (Diakonov et al, 1994).

The particle size exerts major control over the relative stability and formation of iron oxides and oxyhydroxides. In atmospheric conditions and cyclic changes of water and water films, goethite becomes thermodynamically stable relative to hematite and water at surface areas greater than about 15 $\text{m}^2 \text{g}^{-1}$ (particle size 60 nm, assuming spherical particles) (Navrotsky et al, 2008). Under wet conditions prevalent on Earth surface condition, goethite and other oxyhydroxides are competitive at nanoscale. As a conclusion, the size-driven thermodynamic differences among iron oxide phases that are closely balanced in overall thermodynamic properties must be taken into account to understand and predict the formation, stability, and transformation of these complex materials in atmospheric conditions (Navrotsky et al, 2008).

2.6 Formation and Transformation Mechanisms of Iron Oxides

In the light of all the above-mentioned properties of iron oxides, their formation and transformation characteristics can be investigated. All iron oxides have a potential to convert to more stable phases where those transformations occur by two main mechanisms, either reconstructive or topotactic. A topotactic transformation occurs in solid phase at elevated temperatures with the movement of certain atoms and a correspondence in three dimensions between the initial and final structure is needed. A reconstructive transformation arises by the dissolution of the initial phase and the

precipitation from the solution of the new phase depending on the solubility and dissolution rate of the precursor at ambient temperature. A reconstructive transformation involves chemical changes as dehydration, de-hydroxylation and oxidation/reduction as well as further dissolution and precipitation phenomena closely related to the thermodynamic properties and environmental factors. As a result, no structural relationship is required between the precursor and the transformation product. (Pedersen, 2006). Although thermodynamic data give main information about the relative stability of the compounds, the stability of the oxides are also affected by the environmental factors such as temperature, pH, redox potential (Eh), partial pressure of oxygen, partial pressure of carbon dioxide, pollutants, availability of water or water film and the duration of wetting and drying conditions as well as the grain size and crystallinity of the products formed (Cornell and Schwertmann, 2003).

Crystals of iron oxides are generally found from a size of a few microns to a size of nanometers, enabling a higher surface area to volume ratio where smaller size indicates a larger ratio of surface area to volume. As the particle size decreases, the surface free energies come into play and the dissolution and crystallization of those compounds will take place accordingly. The size of nanoparticles and crystallinity seem to affect the free energy formation of iron oxides. In nanomaterials surface energy characteristics play important role and that may affect the thermodynamic stability of the phases such as metastable phases in the bulk may be stable at the nanoscale (Majzlan et al, 2008).

Goethite and hematite are found to be the most stable phases in open atmospheric conditions in nature and under oxic conditions, they are the end member of many transformation pathways (Cornell and Schwertmann, 2003). Goethite and hematite are also the most observed corrosion products found on the corrosion layers of the iron artifacts while magnetite is seen as the first iron oxide phase at the reaction front next to the iron body (Yamashita et al, 1998; Oh et al, 1999; Cook et al, 1999; Balasubramaniam and Kumar 2000; Asami and Kikuchi, 2003; Antunes et al, 2003; Balasubramaniam, 2004; Feron et al, 2004; Neff et al, 2004; Neff et al, 2006;

Dillmann et al 2007; Bellot-Gurlet et al, 2009; Monnier *et al* 2010; Monnier *et al* 2011; de la Fuente *et al*, 2011; Morcillo *et al*, 2013; Aramendia *et al*, 2013 and Aramendia *et al*, 2014). The studies show the transformations of iron oxides from less stable phases to more stable ones generally as goethite or hematite phases of different particle size and crystallinity depending on the transformation reactions in certain environmental conditions.

At 298 K and 1 bar water pressure, goethite and hematite appear to be in equilibrium (Majzlan et al, 2003-2) and with the increase in pressure goethite becomes more stable up to 400 K in comparison to hematite being at stable phase at elevated temperatures in oxidizing conditions. At decreasing redox potential, the iron oxides become thermodynamically unstable with respect to various ferrous containing solid phases of which magnetite, siderite and iron sulfides are the most stable (Zachara et al., 2002).

Formation of the stable phases goethite and hematite do not occur directly, but depend on the formation and transformation mechanisms of the precursors, mainly magnetite and ferrihydrite. Under normal atmospheric conditions, both ferrihydrite and magnetite are the unstable phases that transform to more stable phases in relation to the environmental conditions. The transformation of ferrihydrite and lepidocrocite to hematite is topotactic whereas the transformation of ferrihydrite to lepidocrocite and goethite is a reconstructive process as well as that of lepidocrocite to goethite. The processes that lead to formation of goethite and hematite are competitive. Conditions promoting goethite formation are therefore unfavorable for hematite formation and vice versa (Schwertmann and Murad, 1983).

The rate of transformation process changes with temperature as well as with the abundance of Fe^{2+}/Fe^{3+} in the solution. The time of conversion of ferrihydrite to goethite at room temperature takes months in the absence of Fe^{2+} (Cornell and Schwertmann, 2003) but only days when Fe^{2+} is present (Jang *et al.*, 2003; Pedersen *et al.*, 2005). The high pH and a high Fe^{2+}/Fe^{3+} ratio seem to favor the formation of magnetite (Mann *et al.*, 1989; Jolivet *et al.*, 1992; Pedersen *et al.*, 2005). The

transformation of ferrihydrite into goethite occurs at room temperature, at pH 8 with a low Fe^{2+} concentration whereas with a higher Fe^{2+} concentration magnetite formation is favored (Tronc *et al.*, 1992 and Jolivet *et al.*, 1992). Goethite and hematite have been found to remain unchanged at pH 6-8, under microbially mediated reductive conditions whereas ferrihydrite transforms into magnetite (Zachara *et al.*, 2002).

Transformation of goethite ($\alpha\text{-FeOOH}$) to hematite and lepidocrocite ($\gamma\text{-FeOOH}$) to maghemite are simple de-hydroxylation processes of the iron oxyhydroxides dependent on the starting materials and their particle size as well as temperature and annealing time (Bagin 1967; Hedley 1968; Sakash and Solntseva 1971; McClelland and Goss 1993; Özdemir and Dunlop 1993; Gehring and Hofmeister 1994; Gendler *et al.* 1999, Gendler *et al.*, 2005). Although goethite ($\alpha\text{-FeOOH}$) transforms to hematite directly by de-hydroxylation, lepidocrocite transforms to hematite in three steps via maghemite: i) desorption of molecular water, ii) de-hydroxylation of lepidocrocite to maghemite ($\gamma\text{-Fe}_2\text{O}_3$) and iii) transition of maghemite ($\gamma\text{-Fe}_2\text{O}_3$) to hematite ($\alpha\text{-Fe}_2\text{O}_3$) (Gendler *et al.*, 2005). The removal of OH groups (de-hydroxylation) in lepidocrocite begins at 142–155°C (Gehring and Hofmeister 1994) and the maghemite starts to form above 150–200°C in the laboratory environment (De Bakker *et al.*, 1991) and while it would require thousands of years at ambient temperatures (Gendler *et al.*, 2005). The process follows the formation of poorly crystalline maghemite grains at about 570°C. Maghemite having a size around 5 nm is thermodynamically metastable with respect to hematite. Hematite appears at high-temperatures above >450°C and maghemite undergoes complete transformation into hematite at about 625°C (Özdemir and Dunlop 1993). Further annealing may cause those grains to recrystallize into larger grains being 35–72 nm at the final stage of the reaction (Gendler *et al.* 2005). Finally, the resultant hematite formed from lepidocrocite via maghemite has higher degree of crystallinity and has larger particle size in comparison to maghemite.

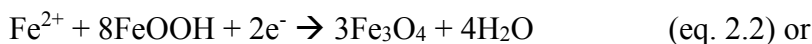
Synthesis of hematite pigments from surface oxide layers of weathered iron bars in atmospheric conditions were also done by heat treatments (Colpas-Ruiz *et al.* 2020).

The surface oxide layers of weathered iron bars consisted of various types of iron oxides, i.e., magnetite, maghemite, wustite, lepidocrocite, hematite and goethite. The highest hematite yield was achieved at 850 °C during one hour heating of weathered iron bars (Colpas-Ruiz et al 2020).

2.7 Precursors for Goethite and Hematite Formation

Iron oxides (goethite, magnetite or maghemite) that are found in variable conditions in nature can be obtained in the laboratory by the mixing of alkali to an Fe(II)/Fe(III) salt solutions and keeping the precipitated solids in suspension for aging at different conditions (Guyodo et al., 2003; Jaiswal et al., 2013).

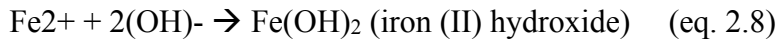
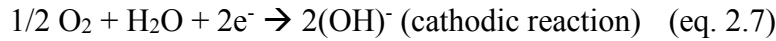
Iron and steel readily oxidize at atmospheric conditions, where a magnetite formation seems to be the most likely phase that appears first (Nasrazadani, 1990). The magnetite can be found at the rust-metal interface underneath the FeOOH polymorphs (Misawa, *et al*, 1971; Misawa, *et al*, 1974 and Singh, *et al.*, 1985). Possible formation routes of magnetite (Fe₃O₄) can be either precipitation from a mixture of Fe(II)/Fe(III) in alkaline aqueous solution or oxidation of Fe(II) via green rust (Fe(OH)₂) or interaction of Fe(II) with ferrihydrite or with high temperature reduction of Fe(III) oxides (Cornell and Schwertmann, 2003). In alkaline aqueous environments, magnetite predominates the layers in reducing conditions and hematite is stable at oxidizing conditions (Cornell and Schwertmann, 2003). Magnetite formation can be expressed under atmospheric and wet conditions when access to oxygen is limited, with the following equations (eq. 2.1, 2.2 and eq. 2.3) (Evans, 1965 and Evans *et al*, 1972):



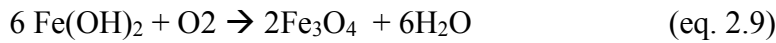
As the rust dries and is permeated by oxygen, magnetite is re-oxidized to the ferric forms (eq. 2.4 and eq. 2.5):



Misawa et al (1971) propose the following reactions for the formation of magnetite in atmospheric conditions (eq. 2.6, 2.7 and eq. 2.8):



Under slightly basic conditions magnetite (Fe_3O_4) readily forms (Misawa et al, 1971) (eq. 2.9):



Misawa, et al. (1974) concluded in their later studies that, based on FeOOH being a good electrical conductor, it is also unnecessary to consider that the cathodic reduction on atmospheric rusting is not the reduction of oxygen dissolved in water film on rust, but the reduction of ferric rust to magnetite. Misawa, et al. (1971) also mentioned that when the aqueous solution on the metal surface is neutral or slightly acidic, $\text{Fe}(\text{OH})_2$ cannot be formed, but various Fe^{2+} hydroxy complexes may be formed depending on the existing anions in aqueous solution. Nastrazadani (1990) concludes that in atmospheric conditions the corrosion product of steel structures are mainly oxyhydroxides of iron and magnetite and is the only product seen to form at the metal-rust interface below the air exposed oxyhydroxides. Literature data indicate limited access of oxygen to the steel substrate as an essential requirement for the formation of magnetite. However, Nastrazadani's experimental work proves to the contrary. Steel coupons at room temperature in the fog (humidity) chamber, where large amount of oxygen was present, showed magnetite as the main constituent of rust even on the air contact surface of the rust layer. Continuous fogging and cyclic wetting and drying conditions produced magnetite as the major constituent. Therefore, the presence of oxygen at room temperature is more tolerable under wet conditions once the magnetite is formed under fast oxidative conditions.

It appeared that so long as the rate of oxidation of iron at the anodic sites where ferrous ions are produced exceeds the reduction rate of ferrous ions to ferric ions, magnetite could form and stay stable (Nasrazadani, 1990). Formation of α -FeOOH on Fe₃O₄ was reported in highly basic environments with a chloride presence (Nasrazadani, 1997; Albani *et al*, 1990).

Magnetite and maghemite, being both ferromagnetic in nature, their nanosized particles used in the biomedical applications due to their high magnetic moments, they are efficient, economic and nontoxic synthesis (Muzquiz-Ramos *et al*, 2015). Their magnetic property is beneficial for the use in cancer treatments. Magnetite is obtained from the mixture of FeCl₃.6H₂O and FeCl₂.4H₂O dissolved in distilled water and by prompt addition of NH₄OH at 70°C with continuous stirring. Maghemite is obtained via magnetite nanoparticles by heating in air at 200, 250 and 300°C for 3, 5 and 8 hours. Stirring velocity, heating temperature and time effects the crystallite size and degree of magnetization. Increase in heating temperature decreases the particle size. The nano particles of maghemite having 10.1-12.5 nm size show superparamagnetic behavior and can be heated successfully under a low magnetic field (Muzquiz-Ramos *et al*, 2015). Higher temperature for magnetite nanoparticles at the interface of corrosion layer and metal can be provided by the weak magnetic field of iron metal having 10.2 kA/m and 362 kHz.

Studies on magnetite transformations to goethite being more pronounced under increasing alkaline conditions has also been performed in order to clarify whether goethite was transformed from magnetite or formed separately as an Fe corrosion product (He and Traina 2007). Their aim was to examine the corrosion characteristics and contamination risks of leakages from waste storage tanks under high-level radioactive conditions. In their experimental work, He and Triana (2007) examined the formation of goethite from synthetic magnetite by addition of 0, 0.1, 0.5, 1 and 2 mol/l NaOH reacted at 50°C in an incubator. The reaction was monitored at intervals of 1, 4, 16 and 32 days. Solid phases were separated through centrifugation and dried under Ar (g) before collecting data. Formation of goethite was suggested to be through reconstructive dissolution/crystallization reactions of

two possible pathways: (a) directly from dissolution of magnetite leading to the precipitation of goethite; or (b) through dissolution of a newly formed maghemite intermediate, followed by precipitation of goethite. Those reactions (eq. 2.10, 2.11, 2.12 and 2.13) can be written as:



They have concluded that the transformation of magnetite to goethite decreased the risks of radioactive contamination by elimination of the role of magnetite in the reduction of soluble oxidants such as Cr(VI) and by introduction of the adsorptive role of goethite (He and Traiana (2007)).

Ferrihydrite is another possible precursor that may be important in the transformation into goethite. It is omnipresent in nature and can bind ions in large quantities, regulating bioavailability and ion mobility. Its structural models as nano particles (2 to 9 nm) have been studied and discussed as a precursor leading to the other prevalent Fe(III) oxide minerals, such as goethite and hematite (Hiemstra, 2013, Schwertmann *et al.*, 2004; Cudennec and Lecerf, 2006). Ferrihydrite was synthesized in the laboratory either from $\text{FeCl}_3 \cdot 6\text{H}_2\text{O}$ or $\text{Fe}(\text{NO}_3)_3 \cdot 9\text{H}_2\text{O}$ mixing with NaOH bringing pH to 6.5 and until the pH reaching 7.5 (Schwertmann and Cornell, 2007; Li *et al.*, 2011). Its synthesis process was performed at around pH 8 under different conditions to obtain the compound in variable specific surface areas (SSA) by aging the precipitate at 60°C at different durations. Longer aging resulted in higher SSA. In the synthesis of goethite from Fe(III) salts, addition speed of NaOH is another important parameter in the hydrolysis of aqueous Fe(III) and the resulting particle size. When the rate of addition decreases, SSA increases for goethite formation (Villacís-García *et al*, 2015). A typical transformation to goethite from the initial ferrihydrite precipitate occurs at 60 °C after 24 h. Goethite precipitates were repeatedly washed, shaken, and centrifuged (Villacís-García *et al*, 2015). In other

studies, goethite has also been obtained from ferrihydrite in alkaline solution at 373 K (100 °C) after 5 days and lepidocrocite has also been obtained from oxidation of Fe⁺² at pH 6 at room temperature in laboratory environment (Majzlan *et al* 2003 -1, Cornell and Schwertmann, 2003). Goethite with different SSA starting from 40, 60, 80 and 100 m²/g were prepared from the hydration of Fe(III) salt solutions by the controlled addition of NaOH and aging of the precipitate (Guyodo *et al.*, 2003). Several studies showed that the surface reactivity of iron oxides is highly dependent on crystal sizes. In the synthesis of goethite, the crystal size of goethite decreased as the temperature fell from 70 to 4°C that resulted in an increase in the SSA (Schwertmann *et al.*, 1985; Montes-Hernandez *et al.*, 2011). Villacís-García *et al*, 2015 have found that when the SSA decreases, in other words, the particle size increases, the surface reactivity of the bigger goethite particles increases. Goethite being an abundant constituent of terrestrial soils, its particles generally show high SSA in nature with strong affinities for surface binding of oxyanions and heavy metals (Fendorf *et al.*, 1997; Villalobos and Leckie, 2001; Antelo *et al.*, 2005; Granados-Correa *et al.*, 2011; Perelomov *et al.*, 2011). Nevertheless, the adsorptive power of goethite in relation to their particle size needs to be confirmed through other adsorption measurements (Villacís-García *et al*, 2015).

Ferrihydrite transforms to hematite by decomposition of magnetite via maghemite at neutral pH at temperature close to 100°C through an internal dehydration and rearrangement within the ferrihydrite aggregates (Schwertmann, 1959; Schwertmann and Fischer, 1966; Fischer and Schwertmann, 1975; Cornell and Schwertmann, 2003). Goethite crystals form in solution from dissolved Fe(III) ions produced by the dissolution of ferrihydrite. In the dry state magnetite is readily oxidized to maghemite by air even at room temperature over years (Murad and Schwertmann, 1993). Maghemite transforms to hematite at >300°C in the dry state.

Schwertmann and Murad (1983) studied transformation of ferrihydrite in aqueous suspensions to goethite and hematite at 24°C in the pH range 2.5 to 12 for as long as three years. Maximum hematite was formed between pH 7 and 8, and maximum

goethite at pH 4 and at pH 12. The conditions favorable for the formation of goethite are unfavorable for the formation of hematite and vice versa.

Diakonov et al (1994) reviewed that hematite and goethite synthesis in aqueous solutions at different pH from strongly acid to slightly basic conditions (Wefers, 1966a, Schwertmann *et al.*, 1985; Schwertmann and Cornell, 1991). Hematite has been synthesized in aqueous solutions of different pH (from strongly acid to slightly basic) and usually at higher temperatures than goethite (>70°C). Goethite was synthesized in basic solutions (pH > 12), and below 125°C. The duration of synthesis is at least of several days. Hematite has also been synthesized via the thermal decomposition of goethite and iron hydroxide (Ferrier, 1966; Schwertmann and Cornell, 1991).

Goethite can transform to hematite directly by heating without any intermediate phase. The transformation temperature depends on the degree of crystallinity and Al-substitution (Cornell and Schwertmann, 2003). Increasing crystallinity of goethite shifts the heating temperature from 260°C to 320°C (Cornell and Schwertmann, 2003). If Al-substitution exists, higher temperatures are needed for dehydroxylation. Replacement of one Fe in the structure with other cations such as Al can affect the stability of goethite which increases parallel to the increase of the Al/Fe mol ratio (Cornell and Schwertmann, 2003).

As a product of long-term corrosion, goethite phase is observed most abundantly in the historical steel objects. On the historical steel objects, while goethite is present as a stable protective layer, it is concluded that lepidocrocite is generally formed at early stages and its gradual transformation to goethite happens in time under atmospheric conditions (Aramendia *et al*, 2012; Aramendia *et al*, 2014; Yamashita *et al*, 1998).

CHAPTER 3

EXPERIMENTAL METHODS

In this study, material characteristics and long-term corrosion characteristics of some constructional iron components from the 15th, 16th and 19th century Ottoman period stone and brick masonry structures at coastal town atmosphere have been examined. The 15th century represents the early Ottoman period, where iron use in construction was less, while the 16th century is the classical period known to have high iron production capacity. The 19th century is the collapsing period of the Ottoman Empire where iron production capacity has dramatically decreased opposite to the “trendy” use in European countries.

In natural environments, iron oxide minerals are represented by a variety of minerals that range from well to poor crystalline state. While examining the corrosion layers of iron samples, magnetite and goethite were found to be of prime importance.

Iron components taken from historical structures were analyzed to determine their chemical and mineralogical compositions together with their physical and mechanical properties. In this chapter, information about the monuments and their collected samples as well as description of the analytical procedures are given in detail under the following subtitles:

- Monuments, Sampling and Nomenclature
- Methods of Analyses

It is important to note that samples from historical buildings bear some restrictions; representative samples were selected and all analytical procedures were adapted according to the sample size.

3.1 Monuments, Sampling and Nomenclature

In this study, nail and beam samples from the Ottoman period historical structures at coastal town atmosphere have been collected. The samples are chosen from west and north regions of Turkey (Marmara, Aegean and Black Sea Regions) to make a comparison of those iron elements in terms of their technological and deterioration properties. A group of samples represents the early Ottoman period (Gazi Mihal Hammam), the second group the classical period iron elements (Kılıç Ali Paşa Hammam) and the last group represents the late Ottoman period (Tekkeköy dwellings, Foça dwellings and some excavated material from Foça). The list of the samples collected and to be analyzed is given in Tables 3.2, 3.3, 3.4, 3.5 and 3.6.

An iron bar and a nail from Gazi Mihal Hammam (Figure 3.1) were collected during a field trip to Edirne. Gazi Mihal Hammam was constructed by Gazi Mihal Bey around 1450 as çift Hammam, and is on the Edirne – Kapıkule highway, next to the Gazi Mihal Mosque. Stone and brick were used as main building materials for the square-planned Hammam. The samples were found partly embedded in the pozzolanic lime mortar of the brick masonry abbreviated as GMH (Gazi Mihal Hammam).

Nails and indoor iron elements from Kılıç Ali Paşa Hammam (Figure 3.2) were provided by the restorers during the restoration work performed at the Hammam. Kılıç Ali Paşa Hammam was built between 1580-1587 by Mimar Sinan and is located in Tophane, Istanbul as a part of a Külliye Complex – a mosque, a hammam, a türbe, a medrese and a fountain, following the order of Grand Admiral (Kapdan-ı Derya) Kılıç Ali Paşa. The mentioned Paşa had wanted the construction of a monument from Sinan to show his endurance against “sea and time”. The building is known as one of Sinan’s most impressive monuments with its 14-meter-wide and 17-meter-high dome. The samples were found partly embedded in the pozzolanic lime mortar of the brick masonry abbreviated as MSH-KAP (Mimar Sinan’s Kılıç Ali Paşa Hammam).

When the two above-mentioned hammam constructions are compared, Edirne Gazi Mihal Hammam was built 130 years prior to the Istanbul Kılıç Ali Paşa Hammam (built around 1450). It is observed that lesser number of iron components was used in the earlier Hammam building. Gazi Mihal Hammam continued to function until the Russian invasion in 1829, after which it was closed (Aşut, 2012). Although it was restored by Mualla Eyüboğlu Anhegger, a restoration architect, between 1961-1971 (Çokuğraş and Gençer, 2018), the Hammam has been observed to be in a very deteriorated condition (Aşut, 2012, Figure 3.1) whereas Kılıç Ali Paşa Hammam has been recently restored and restarted to operate as a Hammam.

As to the dwellings in Foça – İzmir (Figure 3.3) and Tekkekoy – Samsun (Figure 3.4), they have been constructed almost in the same period (~1830-1850) and the information gathered from the analyses of the samples from the dwellings have been used as a good example for the comparison of their technological properties. The 19th century dwellings from Foça - İzmir and Tekkeköy - Samsun, were used as family residential houses until recently. A few beam and nail samples were collected from the 19th century stone masonry dwellings from both towns and a few others were provided by the Foça archaeological excavation team. Excavation materials were taken from the Ottoman level and were grouped as “material at burial conditions” for analyses. Beams and nails from the 19th century stone dwellings represent iron components exposed to atmospheric environment, whereas excavated material from Foça show Ottoman iron kept in burial conditions, approximately 150 years old.

The studied samples are coded with the letters indicating either the name of the building or their location and use of purpose. The samples are numbered sequentially (Table 3.1). As seen in the lists below (Table 3.2, 3.3, 3.4 and 3.5) samples found successively have been added to the examined objects. The location of the sample as either indoor or outdoor is described in the detailed definition of the sample.

Table 3. 1 The iron objects, their coding and description.

No	Building	Code	Code Description
1	Gazi Mihal Hammam	GMH-Me-01	GMH stands for Gazi Mihal Hammam – Me Metal – 01 Sample’s sequence number
2	Kılıç Ali Paşa Hammam	MSH-KAP-001	MSH indicating Mimar (Architect) Sinan who was the architect of the Hammam – KAP indicating Kılıç Ali Paşa, the name of the Hammam – 001 Sample’s sequence number.
3	Foça Dwellings	FKM-001	FKM represents Foça Dwelling (Konut) Metal – 001 Sample’s sequence number.
4	Tekkeköy dwellings	T-N-001	T-N signifies Tekkeköy Dwelling’s Nail – 001 Sample’s sequence number
5	Tekkeköy dwellings	T-W-001	T-W symbolize Tekkeköy Dwelling’s window metal – 001 Sample’s sequence number
6	Tekkeköy dwellings	T-D-001	T-D means Tekkeköy Dwelling’s door metal – 001 Sample’s sequence number



Figure 3. 1 Gazi Mihal Hammam, Edirne (Photo taken by Nurdan Yucel, 2012)

Table 3. 2 List of samples from Gazi Mihal Hammam, Edirne and their description (15th cc):

No	Sample Code	Description
1	GMH-Me-01	Pipe piece collected from the basin of the bath
2	GMH-Me-02	Door/window locking rest iron piece, Indoor
3	GMH-Me-03	Plaster nail (1) from wall, indoor
4	GMH-Me-04	Plaster nail (2) from wall, indoor





(a)



(b)

Figure 3. 2 Kılıç Ali Paşa Hammam, Tophane, Istanbul: a) Exterior of the Hammam (Photo: Nurdan Yucel, 2013), b) Interior of the Hammam after restoration (https://media-cdn.t4.com.tr/media/stories/2018/04/raw_mimar-sinanin-ustalik-donemi-eserlerinden-kilic-ali-pasa-hamamina-restorasyon-odulu_200100738.jpg)

Table 3. 3 List of studied samples from Kılıç Ali Paşa Hammam, Tophane, Istanbul and their description (16th cc):

No	Sample Code	Description
5	MSH-KAP-01	Nail used for stone building, collected from dome, square shape (1), outdoor
6	MSH-KAP-02	Iron piece, used for jointing of other metals (chains or hooks) to the wall, indoor.
7	MSH-KAP-03	Nail used for stone building, collected from dome, square shape (2), outdoor
8	MSH-KAP-04	Nail used for timber jointing, square shape, indoor
9	MSH-KAP-05	Iron hinge, from main entrance timber door, partially open to atmosphere
10	MSH-KAP-06	Iron element for towel hanging, indoor
11	MSH-KAP-07	Nail used for stone building, indoor
12	MSH-KAP-08	Nail used for lead covering of dome, outdoor
13	MSH-KAP-09	Nail used for stone building, square shape, indoor
14	MSH-KAP-10	Nail used for stone building, square shape, indoor
15	MSH-KAP-11	Nail used for stone building, square shape, indoor
16	MSH-KAP-12	Nail used for timber jointing, square shape, indoor
17	MSH-KAP-13	Nail used for timber jointing, square shape, indoor





(a)



(b)

Figure 3. 3 Dwellings from Foça, Izmir: a) A dwelling currently under restoration, b) An uninhabited dwelling. (Photos: Nurdan Yucel, 2015).

Table 3. 4 List of studied samples from Foça dwellings, Izmir and their description (19th cc).

No	Sample Code	Description
18	FKM-01	Window guard iron piece from a stone dwelling, outdoor
19	FKM-02	Nail for jointing load bearing, main timber beams, indoor
20	FKM-03	Door lock piece from main entrance, indoor
21	FKM-04	Male hinge for main entrance door, partially open to atmosphere
22	FKM-05	Female hinge for main entrance door, indoor
23	FKM-06	Nail, Ottoman layer, burial condition
24	FKM-07	Nail, Ottoman layer, burial condition
25	FKM-08	L shaped iron piece, Ottoman layer, burial condition
26	FKM-09	Iron piece, Ottoman layer, burial condition
27	FKM-10	Nail, Ottoman layer, burial condition
28	FKM-11	Nail, dwellings embedded in building stone tuff, partially open to atmosphere
29	FKM-12	Nail, Ottoman layer, burial condition
30	FKM-13	Nail, Ottoman layer, burial condition
31	FKM-14	Nail, Ottoman layer, burial condition
32	FKM-15	Nail, Ottoman layer, burial condition
33	FKM-16	Door & wall jointing iron bar with diamond shaped head, partially open to atmosphere





(a)



(b)

Figure 3. 4 Dwelling from Tekkeköy, Samsun: a) North and east view, b) South view from main entrance. (Photos: Nurdan Yucel, 2015)

Table 3. 5 List of studied samples from Tekkekoy Dwelling, Samsun and their description (19th cc).

No	Sample Code	Description
34	T – N – 01	Iron nail from timber column, outdoor
35	T – N – 02	Iron nail from main entrance door frame, indoor
36	T – N – 03	Iron nail from lath & plaster, outdoor
37	T – N – 04	Iron nail from door frame, indoor
38	T – N – 05	Iron nail from timber column, outdoor
39	T – N – 06	Iron nail from lath & plaster, outdoor
40	T – W – 01	Iron hinge pin from entrance hall's left window, partially open to atmosphere
41	T – D – 01	Iron crossbar for main entrance door locking, partially open to atmosphere



3.2 Methods of Analyses

In the study, the samples have been examined initially using non-destructive methods such as visual analysis and other investigation techniques in the METU Material Conservation Laboratory, METU Central Laboratory, METU Metallurgical Engineering Laboratory and Material's Laboratory of Samsun Makina Sanayi A.Ş. Foundry. Besides, some destructive analysis methods have been applied due to the nature of the analysis itself, like cutting, burning, abrasion and polishing. The laboratory analyses of the samples covered the determination of chemical and mineralogical compositions as well as the physical and mechanical properties of the iron samples. The selected examination methods in this study are:

- i. Dimensional and weight identification,
- ii. Color identification, to give some clue about the composition of corrosion products,
- iii. Hardness, to understand what treatment the object has undergone and to give information about the material's performance on abrasion resistance,
- iv. Metallography and phase calculations, to obtain a picture of the composition, grain distribution and structure of the sample,
- v. Chemical analysis, to gather information about the chemical composition of the material, qualitatively and quantitatively,
- vi. Morphological and mineralogical analysis of the corrosion layers, by using XRD, FTIR, SEM-EDX and μ -RAMAN spectroscopy to identify and prove the morphological and mineralogical characteristics of the corrosion layers.

The first step was about forming an inventory of the materials and giving a detailed description of their color, dimension and weight. The materials have been studied in terms of their metallurgical, chemical and physical properties. The preparation of the samples and detailed test procedures have been described in the following sections.

3.2.1 Visual, Dimensional and Weight Analysis of Iron Samples:

Iron samples collected were first recorded by the visual observations of their color and deterioration condition. General and macro view of the samples were photographed by a Leica model microscope (Model 1: DFC 425).

Their dimensional measurement, shape and corrosion thickness measurements were done - where applicable - at the material conservation laboratory. The dimensions of the iron elements were measured with the Mitutoyo brand digital calipers with 0.01 mm precision. The weights of the samples were determined by the CHYO JL-200 brand and 0.0001 g sensitivity analytical balance.

3.2.2 Preparation of Samples to be Used for Analyses:

Due to restricted amounts of samples taken from the monuments, cross-sections through the metal body and corrosion layer as well as powdered samples representing the corrosion layer were prepared for each iron component. Cross-sections were used for metallographic examinations, hardness, spark emission spectroscopy analyses, SEM and μ -Raman analyses. Powdered samples from corrosion layers were used for FTIR and XRD analyses.

Metal Cross-sections:

Longitudinal and transverse cuts of the nail heads and bodies together with their corrosion layers were obtained by cutting the nails in the mentioned directions and polishing the cut surfaces. The cut surfaces were polished by abrading with silicon carbide papers having 80, 120, 240 and 600 grits successively on a Metkon (Forcipol) polishing instrument. The surface was further polished with felt having alumina polishing suspension on it. This process continued until a fully polished surface was obtained. The polished cross-sections were used to carry out several analyses such as the measurement of thickness of the corrosion layer, hardness tests and spectrometric analyses by spark emission spectroscopy.

The surfaces were then etched with nital solution (2.5 wt% HNO₃ in ethanol) and polished with felt by hand. The analyses continued on polished and etched surfaces with metallographic examinations, hardness, spark emission spectroscopy analyses, SEM and micro-Raman analysis.

Powdered samples:

Full depth of the iron corrosion layers from the samples were scraped until reaching the metal body. They were reduced to fine powder in an agate mortar. Those powders were analysed by using XRD and FTIR spectroscopy.

3.2.3 Metallographic analysis by Metallographic Microscopes:

Metallographic characteristics such as microstructure at different phases of the main metal bodies are studied by using a metallographic microscope. The etched surface of the main metal body is examined using two types of microscopes: a Nikon IMM901 brand metallurgical microscope having 50x-200x magnification with “MSQ 6.2.1 2003” analyses software and a Huvitz HDS 5800 brand digital microscope from 50x to 5800x magnification. All functions for observation, recording, measurement and reporting have been integrated into a single unit in a Huvitz HDS 5800 brand digital microscope. It has been noted that while working with the digital microscope, quick observation without additional work on samples is possible. The brand creates fully-focused field images of high depth, even at high magnification while the optical technology and precise z-axis control provides image acquisition from different focal depths.

In addition to the visual identification of different phases by metallographic microscopes, the percent amount of the different phases is theoretically calculated by using the C content of the samples. As a result, two different methods are used for the identification of the phases in the metal body. They are described in this section and summarized in table 3.6 (Callister and Rethwisch, 1997).

Table 3. 6 Summary of the different phases theoretically calculated in percentage by using the C content of the samples:

Century of the Structure	Sample's Code	Carbon (C) Content (w/w%)	Fraction of pearlite	Total ferrite	Cementite	Fraction of proeutectoid alpha	Eutectoid ferrite
14 th century	GMH-Me-02	0,121	0,134	0,985	0,015	0,866	0,119
16 th Century	MSH-KAP-01	0,155	0,180	0,980	0,020	0,820	0,160
	MSH-KAP-02	0,002	-0,027	1,003	-0,003	1,027	-0,024
	MSH-KAP-03	0,003	-0,026	1,003	-0,003	1,026	-0,023
	MSH-KAP-05	0,016	-0,008	1,001	-0,001	1,008	-0,007
	MSH-KAP-07	0,420	0,539	0,940	0,060	0,461	0,480
	MSH-KAP-08	0,042	0,027	0,997	0,003	0,973	0,024
	MSH-KAP-09	0,118	0,130	0,986	0,014	0,870	0,116
	MSH-KAP-12	0,148	0,171	0,981	0,019	0,829	0,152
	MSH-KAP-13	0,124	0,138	0,985	0,015	0,862	0,123
19 th century	FKM-01	1,500	0,875		0,125		
	FKM-02	0,002	-0,027	1,003	-0,003	1,027	-0,024
	FKM-03	0,025	0,004	1,000	0,000	0,996	0,004
	FKM-04	1,500	0,875		0,125		
	FKM-05	0,002	-0,027	1,003	-0,003	1,027	-0,024
	FKM-07	0,002	-0,027	1,003	-0,003	1,027	-0,024
	FKM-08	0,002	-0,027	1,003	-0,003	1,027	-0,024
	FKM-09	0,056	0,046	0,995	0,005	0,954	0,041
	FKM-11	0,002	-0,027	1,003	-0,003	1,027	-0,024
	T-D-01	0,289	0,362	0,960	0,040	0,638	0,322
	T-N-01	0,132	0,149	0,984	0,016	0,851	0,133

3.2.4 SEM-EDX Analysis:

Cross-sections were further examined by a Scanning Electron Microscope coupled with EDX analysis unit (SEM-EDX) (Manufacturer: Tescon, Model: Vega II) for metallographic characteristics, corrosion layer thickness and its morphology. Since the samples were conductive, there was no need to coat the samples with either carbon or gold. The etched surface of the samples was placed under the microscope where the main body and the corrosion layers were analyzed. Elemental analyses were performed by EDX unit on the cross-section views of corrosion layers and metal body as spot and area analyses.

3.2.5 Hardness Test:

The Brinell hardness test is preferred for iron materials' hardness measurement as the method is considered to be non-destructive. Hardness measurements have been performed to all samples before etching the surfaces. A Heckert WMPA brand test instrument with a HBW2.5/187.5B measurement range was used for hardness measurements. The instrument's ruler capacity was between 0-1.5 mm and its scale was 0.01 mm. The Brinell hardness of the samples was processed by using "MSQ 6.2.1 2003" software.

3.2.6 Analysis by Spark Emission Spectrometry:

Elemental analyses were done by using an argon supply spark emission spectrometer (Manufacturer: OBSL, model GS 1000). The tests have been performed on polished surfaces after the hardness test.

The sample to be analyzed has been placed on a spectrometer air-tightly where the ignition process has been performed. During the analysis, OBLF WiN analysis software was used by selecting the material type as "gray-spheroidal". At the end of the ignition process, the software evaluates the elemental composition of the sample.

For the same sample, the ignition process and the software analysis were repeated three times and their average was taken to determine the final result.

Chemical analysis of some samples could not be performed due to the small sample diameter which needed to be at least 1.2 cm to fully cover the cell of the instrument. In addition, some of the samples had too deep cracks obstaculating the instrument to make readings from the surface.

3.2.7 Mineralogical Analysis:

Mineralogical analysis from the corrosion layer and the body itself have been conducted by using μ -Raman spectrometry (Manufacturer: Bruker, Model: MultiRAM), FTIR spectrometry (Manufacturer: Bruker, Model: Alpha P) and X-Ray Diffractometer (XRD) instrument (Manufacturer: Bruker, Model: D8 Advance Diffractometer with SolX detector).

μ -Raman Spectroscopy:

Examination of cross-sections including the corrosion layer and the metal body itself have been conducted by using μ -Raman spectrometry (Manufacturer: Bruker Senterra II, Model: MultiRAM). It is important to note that Raman microscopy is extensively used by material scientists. The SENTERRA II supports the researcher with utmost precision and offers up to 3 excitation lasers as well as an optional coupling to FT-Raman for minimized fluorescence.

The SENTERRA II is a method widely used in the conservation and restoration of historical buildings, paintings and artwork materials. Raman microscopy provides precise information about the chemical identity and origin of unknown substances resulting from the examination due to the high spatial resolution down to the nanometer range.

μ -Raman spectroscopic analyses were conducted directly on the etched and polished cross-sections (see section sample preparation). The corrosion layers and the body

itself were thoroughly investigated by analysis of selected areas at random points. Analysis of corrosion layers was done starting from the metal body along with defined lines crossing the corrosion layer at several parts of the sample.

μ -Raman analyses were carried out using a Bruker Senterra dispersive Raman Microscope Spectrometer with Opus 7.2 analysis software operating at 532 nm, using a laser power of 0.2mW. Backscattered Raman signals were collected with a cooled CCD detector. The instrument operated mostly at integration times of 150 and 200 s with 2 spectra accumulations. The samples were put under the microscope, focused with a Leica 20X lens and then viewed with a 100X objective lens. The above settings have proved to be at optimum level as a result of a great number of tests performed at intervals. The interpretations of Raman spectra have been performed by comparisons with literature (Oh *et al*, 1999; Aramendia *et al*, 2014; Monnier *et al*, 2010; Colomban, 2011, Das *et al*, 2011; Hanesch, 2009; Neff *et al*, 2006 and 2004).

FTIR Spectroscopy:

The powdered corrosion products were also analyzed by a FTIR spectrometer (Bruker, Model: Alpha P) with an ATR module on it.

As well known, FTIR and Raman spectroscopy are complimentary techniques that both are based on molecular vibrations. However, Raman focuses on scattering of light, along with the change in polarizability of a molecule while FTIR uses absorption of light, and depends on a change in dipole moment. Both methods are universally applicable and permit the selective analysis of individual particles even having a size of a few micrometers. As a complementary method, Raman microscopy is used for the analysis of samples enabling a contactless measurement. Typically, a CCD sensor is used as a detector with laser wavelengths of 532 and 785 nm. When compared to the IR-microscopy, the lateral resolution of the Raman microscope is higher and particles with a size in the lower micron range can be identified. In the case of inorganic samples, the Raman technique also offers a better differentiation. A disadvantage of the technique, however, is that many samples show fluorescence.

The typically broad and intense fluorescence signal can even completely cover the signal of the sample. This can be circumvented very often by the choice of a larger laser wavelength. Accordingly, the optimal sample wavelength can be selected for any sample (Seeba, 2022).

During the FTIR analyses, the powdered corrosion products were directly measured by the use of the ATR unit. For each spectrum, 32 scans were run between 400–4000 cm^{-1} . Interpretations of FTIR spectra have been performed using the Bruker library of the instrument together with literature (Gadsden 1975 and Nakamoto 1997).

Standard samples, either prepared in the laboratory or ready (commercial) samples such as akaganeite and hematite have been used for calibration purposes and to verify the spectrum.

XRD Spectroscopy:

Powdered samples of the corrosion layers were studied by using X-Ray Powder Diffraction (XRD) (Bruker, Model: D8 Advance Diffractometer with a SolX detector) and Fourier Transform Infrared Spectroscopy (FTIR). The corrosion layers were scraped from the surface of the sample and reduced to powder in agate mortar.

The analyses have been performed by XRD using CuK α radiation, adjusted to 40kV, 40mA. The XRD traces were recorded at 2Θ values from 2° - 70° and the instrument was set to a scan speed of 2 seconds at 0.02° intervals.

As mentioned before, in natural environments, iron oxide minerals are represented by a variety of minerals that range from well to poor crystalline state. While examining the corrosion layers of iron samples, magnetite and goethite were found to be of prime importance. As an experimental work to study the long-term transformation characteristics of magnetite which is a well-crystallized iron oxide, it was expected to undergo some changes in aqueous media where the transformation products are closely related to the pH of the environment. The transformation of "magnetite" to "goethite" together with the common phase "maghemite" ($\gamma\text{-Fe}_2\text{O}_3$) was found to be favorable in a high alkaline environment (Colomban 2011).

3.2.8 PAI Calculations

Assessment of corrosion layer characteristics in reducing the corrosion rate and its protective ability to prevent the metal from further corrosion is of great interest (Yamashita et al 1998, Feron et al 2004, Kamimura et al, 2006, Dillmann et al, 2007, Aramendia et al, 2014, Waseda and Suzuki 2005). In this study, the Protective Ability Index (PAI) of the corrosion layers were roughly estimated and expressed as the ratio of the isotropic goethite band thickness to the total thickness of other oxides and oxyhydroxides namely magnetite, maghemite, hematite, lepidocrocite in the corrosion layer, distinguished by μ -Raman which is a unique method for phase identification. The objects were analyzed starting from RF towards TM step by step during μ -Raman analysis. The step thicknesses were identified by dividing the number of steps to the total thickness. The composition of minerals at each thickness were identified by μ -Raman. If the mentioned thickness would include more than one mineral, the individual thickness of each mineral was found by dividing that step thickness to the number of total corrosion minerals found in that step. Hence, the goethite in the total thickness is calculated by adding the thickness found in each step. The same calculation was adapted for the other corrosion fractions found in the total thickness. Those thickness were used to estimate the mass fraction of corrosion products. The following formula was used to identify the PAI values for each object (Aramendia *et al*, 2014):

for seaside – rural environment (equation 1);

$$\alpha/\gamma PAI = \frac{\text{mass fraction } \alpha - FeOOH}{\text{mass fraction } (\gamma - FeOOH + \beta - FeOOH + Fe_3O_4)}$$

for urban – industrial environment (equation 2);

$$\alpha/\gamma PA = \frac{\text{mass fraction } \alpha - FeOOH}{\text{mass fraction } (\gamma - FeOOH + \beta - FeOOH + Fe_3O_4 + \alpha - Fe_2O_3)}$$

However, for iron artifacts in burial condition, Dillmann et al. (2004) proposes a modification of the protective ability ratio for ancient corrosion layers, calling it α^*/γ^* . Although magnetite exhibits some conductivity, it can be considered to be protective because of its high stability. The following formula was used to identify the PAI values for each iron object in burial condition (Aramendia *et al*, 2014) (equation 3):

$$\alpha^*/\gamma^* PAI = \frac{\text{mass fraction } (\alpha - FeOOH + Fe_3O_4)}{\text{mass fraction } (\gamma - FeOOH + \beta - FeOOH + \alpha - Fe_2O_3)}$$

In this research, for iron nails embedded in timber, which generates an organic atmosphere, a new modification of the protective ability ratio for ancient corrosion layers, named as α''/γ'' , is proposed. The iron objects embedded in timber did not reveal any goethite during the analysis but showed wüstite and/or hematite. Wüstite which is commonly observed iron oxide, has an unusual prolonged stability at nanoscale (Yin *et al*, 2007). Wüstite and magnetite are less noble but more effective as cathodic surfaces than hematite. (Ahlström *et al*, 2018). The following formula was used to identify the PAI values for each iron object embedded in timber (equation 4):

$$\alpha''/\gamma'' PAI = \frac{\text{mass fraction } (Fe_3O_4 + FeO)}{\text{mass fraction } (\gamma - FeOOH + \beta - FeOOH + \alpha - Fe_2O_3)}$$

FTIR results were also used as an alternative data to semi-quantify the main corrosion phases of iron artefacts for the calculation of PAI with the above equations (Veneranda *et al*, 2018). The ratio of the total amount of goethite and magnetite with respect to unstable phases obtained from FTIR spectroscopic analysis of powdered samples can be used to calculate the PAI values. However, it is important to keep in mind that powdered samples used for FTIR results consist of impurities from transformed media mixed with the corrosion products. Therefore, the PAI ratio does

not represent only the inner corrosion layer. On the other hand, while working with the Raman spectroscopic analysis results, the layers are well observed and it is easy to define the thickness of each sub-layers.

PAI was calculated with the first equation for the objects at seaside – rural environment and with the second one for the urban – industrial environment. For burial iron objects, Dillmann's equation was used (equation 3). For iron objects embedded in timber, PAI calculations were done by using equation 4. PAI results bigger than 2 were accepted to show the good state of stability of the corrosion layer (Yamashita *et al*, 1998). PAI values were used to evaluate the objects' protective capabilities and the achievement of a stable corrosion layer.

CHAPTER 4

EXPERIMENTAL RESULTS

In this chapter, the results of the analyses that were performed to explore production technology, compositional properties and the corrosion performance of historical iron constructional elements are presented. Firstly, results of visual and dimensional analyses that describe the initial condition of the samples are given as well as basic metallographic characteristics of the metal bodies in terms of microstructural constituents, hardness and elemental composition. Afterwards, analyses of corrosion layers and their results are given in detail relating the thickness, sub-layering, compactness and mineralogical composition starting from main body towards exterior.

Overall composition of each corrosion layer is studied by the analyses of the powdered samples using XRD and FTIR whereas microstructure and the sub-layers of the corrosion on the samples are studied in-situ by μ -Raman & SEM-EDX in order to define mineral and amorphous phases that were formed during the corrosion process and the distribution of those phases.

The experimental results are given in the sub-sections named below:

- i) Basic visual and dimensional characteristics,
- ii) Results of metal body's elemental composition by spark emission spectrometer and EDX,
- iii) Results of microscopical investigations of metal body and corrosion layers,
- iv) Results of hardness measurements on metal body,
- v) Results of corrosion layer analyses by using XRD, FTIR, μ -Raman Spectroscopy and SEM-EDX,
- vi) Protective Ability Index (PAI) calculations: Combined results of corrosion layer thickness and goethite layer thickness.

4.1 Basic Visual and Dimensional Characteristics

The visual characteristics such as colour and dimensional measurements of the samples are shown in Tables 4.1, 4.2, 4.3 and 4.4. They describe the initial condition of the corroded iron samples collected from historical buildings constructed at different periods in history: namely a 15th century monument “Gazi Mihal Hamamı”, a 16th century monument, “Kılıç Ali Paşa Hamamı” and some 19th century dwellings in Foça - İzmir and Tekkekoy - Samsun.

Table 4. 1 Visual and dimensional characteristics of iron samples from Gazi Mihal Hamamı, Edirne (15th cc):

L: Length, D: Diameter at mid-point; T: max. thickness; W: Width

Sample Code and Description	Location	Surface Color	Dimensions in cm	Weight in grams
GMH-Me-02 iron lock piece from door / window	partially open to atmosphere	Variable: from reddish-brown to yellow	L= 12.0 T= 0.3 W= 1.1	33.94
GMH-Me-03 iron nail (1) Embedded in mortar/ plaster	Interior	Reddish-brown	L= 6.5; D= 0.45	8.11
GMH-Me-04 Iron nail (2) Embedded in mortar/ plaster	Interior	Variable: from black to reddish-brown	L= 4.2; D= 0.37	2.04

Table 4. 2 Visual and Dimensional characteristics of iron samples from Kılıç Ali Paşa Hammam, Istanbul (16th cc).

L: Length, D: Diameter at mid-point; T: max. Thickness; W: Width.

Sample Code and Description	Location	Surface Color	Dimensions in cm	Weight in grams
MSH-KAP-01 Iron nail, (1) body with square cross-section, collected from dome	Exterior	Variable: from reddish-brown, orange to yellow	L= 6.95 D _(body) = 1.10 D _(head) = 1.85	42.6
MSH-KAP-02 Iron jointing element for future connections	Interior	Variable: from reddish-brown to orange	L= 14.3 W= 1.0 D _(ring) = 1.3 D _(ring ext.) = 2.7	90.9
MSH-KAP-03 Iron nail, (2) body with square cross-section, collected from dome	Exterior	Variable: from reddish-brown, to dark brown-black	L= 9.3 D _(body) = 1.3 D _(head) = 2.3 -2.5	107.8
MSH-KAP-04 Iron nail, used for timber jointing, body with square cross-section,	Interior	Variable: from reddish-brown, to dark brown-black	L= 20 D= 1	68.6
MSH-KAP-05 Iron hinge; main entrance timber door jointing element	Interior	Dark brown-black	L= 18 x 3.2 T= 1.1 W= 3.1	426
MSH-KAP-06 Iron ring piece for towel hanging with wall anchoring section	Interior	Variable: from reddish-brown, to dark brown - black	L= 14.8 T= 1.3 D _(ring ext x int.) = 10.4 x 7.6	402.2

Table 4.2. Visual and Dimensional characteristics of iron samples from Kılıç Ali Paşa Hammam, Istanbul (16th cc) (continued).

L: Length, D: Diameter at mid-point; T: max. Thickness; W: Width.

Sample Code and Description	Location	Surface Color	Dimensions in cm	Weight in grams
MSH-KAP-07 Iron nail, body with quadrangle cross-section	Interior	Variable: from reddish-brown, to dark brown-black	L= 13.1 T= 10.6 W= 21.9 D _(head) = 2.4-1.85	45.0
MSH-KAP-08 Iron nail used for lead sheets of dome	Exterior	Dark brown-black	L= 6.76 D _(body) = 0.46 D _(body) = 0.98 D _(head) = 3.65	45.0
MSH-KAP-09 Iron nail, body with square cross-section, triangle head	Interior	Dark brown-black	L= 12.6 T= 1.3-0.95 W _(head) = 3.5	106.9
MSH-KAP-12 Nail, body with square cross-section	Interior	Variable: from reddish-brown, to dark brown-black	L= 12.4 T _(max) = 1.1 W= 0.5 D _(head) = 2.8-2.2	81.5
MSH-KAP-13 Nail, body with square cross-section, used for timber jointing	Interior	Variable: from reddish-brown to dark brown	L= 14.3 D _(max.) = 1.2	81.7

Table 4. 3 Visual and Dimensional characteristics of iron samples from Foça Dwellings, Foça – Izmir, (19th cc).

L: Length, D: Diameter ad mid-point; T: max. Thickness; W: Width.

Sample Code and Description	Location	Surface Color	Dimensions in cm	Weight in grams
FKM-01 Iron bar, two pieces, for window guard	Exterior	Variable: from reddish-brown to dark brown	L _(total) = 25.0 D _(max) = 1.95 (1 st piece); D _(max) = 1.7 (2 nd piece)	333.6
FKM-02 Iron nail, for jointing the main timber beams, body with square cross-section	Interior	Variable: from reddish-brown to dark brown-black	L= 14.0 T _(body) = 0.84 D _(head) = 1.5	58.9
FKM-03 Iron door lock piece, from main entrance	Interior	Variable: from reddish-brown, orange to yellow	L= 15.6 W= 3.3 T= 0.7 D _(ring) = 3.0	601.4
FKM-04 Iron hinge piece, for main entrance door, L-shaped, body with rectangular cross-section	Interior	Variable: from reddish-brown to dark brown-black	L _(total) = 30.0 T= 1 W= 3.8 L _(L-shape) = 7	1100
FKM-05 Iron hinge piece, for main entrance door	Interior	Variable: from reddish-brown to dark brown-black	L= 15.5 T= 0.7 W= 3.2	2013.2
FKM-06 Iron nail body, anchoring two stones, square cross-section	Interior	Variable: from reddish-brown to dark brown-black	L= 5.2 D= 1.2	42.6
FKM-07 Iron nail, body with square cross-section excavated from Ottoman layer	Buried	Variable: from reddish-brown to orange	L= 8.5 T _(body) = 1.2 D _(head) = 2.0	53.2

Table 4.3. Visual and Dimensional characteristics of iron samples from Foça Dwellings, Foça – Izmir (19th cc) (Continued)

L: Length, D: Diameter at mid-point; T: max. thickness; W: Width.

Sample Code and Description	Location	Surface Color	Dimensions in cm	Weight in grams
FKM-08 Iron piece, L-shaped excavated from Ottoman layer	Buried	Variable: from reddish-brown, dark brown, orange to yellow	L= 3.9 x 8.3 D _(body) = 1.5	57.4
FKM-09 Iron piece, one side flat, one side round, excavated from Ottoman layer	Buried	Variable: from reddish-brown, dark brown to orange	L= 17 W _(max) = 2.2	72.4
FKM-10 Iron nail, body with square section, excavated from Ottoman layer	Buried	Variable: from reddish-brown, dark brown to orange	L= 9.9 T= 0.9 D _(head) = 2	50.8
FKM-11 Iron nail piece, body with square cross-section; situated between two stones of a stone house's façade	Partially open to atmosphere	Variable: from reddish-brown, dark brown-black to orange	L= 6.3 T _(body) = 1.2	20.4
FKM-12 Iron nail, body with square cross-section, excavated from Ottoman layer	Buried	Variable: from reddish-brown to dark brown	L= 9.6 T= 1 D _(head) = 2.6	39.1
FKM-13 Iron nail, body with square cross-section, excavated from Ottoman layer	Buried	Variable: from reddish-brown, dark brown to orange	L= 16 T= 1.3 D _(head) = 2.3	140.3

Table 4. 4 Visual and dimensional characteristics of iron samples from Tekkekoy Dwellings, Tekkekoy – Samsun, (19th cc).

L: Length, D: Diameter at mid-point; T: max. thickness; w: Width; W: Weight.

Sample Code and Description	Location	Surface Color	Dimensions in cm	Weight in grams
T-N-01 Iron nail from timber column	Exterior	Variable: from thin black to reddish-brown	L=8.3 D _(body) =0.7 D _(head) = 1.2	24.3
T-N-02 Iron nail from main entrance, timber door frame	Interior	Reddish-brown	L= 7.6 D _(body) = 0.4 D _(head) = 1.0	10.2
T-N-03: Iron nail from timber lath and plaster	Exterior	Variable: from black, dark brown to reddish brown	L=3.4 D _(body) = 0.2 D _(head) = 0.5	1.0
T-N-04 Iron nail from door frame	Interior	Variable: from thin reddish brown to dark brown	L=7.8; D _(body) =0.5 D _(head) = 1.0	9.4
T-N-05 Iron nail from timber column	Exterior	Variable: from thin reddish brown to dark brown	L=9 D _(body) =0.5 D _(head) = 0.9	11.1
T-N-06 Iron nail from timber lath and plaster	Exterior	Variable: from black, dark brown to reddish brown	L=3.7 D _(body) =0.2 D _(head) =0.6	0.7
T-W-01 Iron hinge pin from a window in the main entrance	Partially open to atmosphere	Variable: from thin reddish brown to dark brown	L=14.0 D _(body) = 0.5 D _(head) = 0.7	20.4
T-D-01 Iron crossbar of the entrance door lock	Interior	Variable: from dark brown to reddish brown	L= 20.3 T= 0.8 H= 2.8 W= 2.5	183.2

4.2 Results of Elemental Compositions by Using Spark Emission Spectrometer and SEM-EDX

Compositional properties have an important role in their corrosion resistance. Hence, investigation of the elements in the composition gives a significant clue about their contributions on higher resistivity performances against corrosion. These elemental analyses were done by using an argon supply spark emission spectrometer and energy-dispersive X-ray spectroscopy (EDX) on the SEM views of the samples. EDX analyses were executed on the main bodies in addition to spark emission spectrometric analysis to detect the existing elements in the composition.

4.2.1. Results of Elemental Compositions by Using Spark Emission Spectrometer

Elemental analyses were done to obtain information about the chemical composition of the iron objects by using an argon supply spark emission spectrometer. Chemical analysis of some samples such as GMH-Me-03, GMH-Me-04, MSH-KAP-04 and FKM-10 could not be achieved due to their small sizes or several / deep cracks on their surfaces. Weight percentages of important elements such as carbon (C), silicon (Si), phosphorous (P), sulfur (S), manganese (Mn), aluminum (Al), nickel (Ni) and chromium (Cr) of the main bodies for the samples from the 15th, 16th and 19th centuries were given in Tables 4.5 and 4.6 respectively. From the 15th century only one sample was tested and its results were included in the same table of the samples belonging to the 16th century.

The weight percentages of carbon were also utilized for the calculation of the theoretical FeC (cementite) phase in the metallographic characteristics of metal bodies.

Morphology of the etched surface of the nail heads was revealed by using scanning electron microscopy (SEM) and chemical characterization of the samples was performed by energy-dispersive X-ray spectroscopy (EDX). Both metal bodies and

grain boundaries (Figures 4.1 - 4.21) were analyzed and following results were gathered:

Table 4. 5 Weight percentages of some important elements in the composition of the sample (GMH-Me-02) from the 15th century and the samples from the 16th century analyzed by spark emission spectrometer.

Element	15 th Century Sample	16 th Century Samples (MSH-KAP-)									% Standard Deviation (±)
		-01	-02	-03	-05	-07	-08	-09	-12	-13	
C	0.121	0.155	0.002	0.003	0.016	0.420	0.042	0.118	0.148	0.124	1,041
Si	0.003	0.023	0.161	0.165	0.523	0.571	0.136	0.056	0.018	0.038	2,403
Mn	0.001	0.511	0.097	0.022	0.058	0.916	0.274	0.418	0.359	0.039	0,940
P	0,007	0.052	0.280	0.231	0.219	0.092	0.043	0.007	0.009	0.113	1,524
S	0,009	0.047	0.075	0.023	0.137	0.052	0.016	0.027	0.020	0.034	4,066
Mg	0,006	0.000	0.0136	0.0021	0.0111	0.0007	0.0012	0.006	<0.0001	0.008	5,431
Cr	0,001	<0.001	0.049	<0.001	0.604	0.038	<0.001	0.309	<0.001	0.428	1,286
Ni	0,015	0.024	<0.001	0.016	<0.001	0.068	0.014	0.129	0.150	<0.001	1,176
Mo	0.002	0.004	<0.001	<0.001	<0.001	<0.001	<0.001	<0.001	<0.001	<0.001	1,360
Cu	0.101	0.062	0.046	<0.001	0.079	0.199	0.061	0.115	0.050	0.057	1,928
Al	0.004	<0.001	0.008	0.036	0.115	<0.001	<0.001	0.024	<0.001	0.034	2,047
Ti	0.001	0.0007	0.0021	0.0040	0.0115	0.0010	0.0010	0.0009	0.0004	0.0252	0,000
V	0.001	0.009	0.012	0.001	0.028	0.029	0.005	0.016	<0.001	0.023	0,820
W	0.003	0.005	<0.003	<0.003	<0.003	0.007	<0.003	<0.003	0.004	<0.003	1,307
Sn	0.002	0.012	<0.001	0.001	<0.001	0.007	0.008	0.003	0.003	<0.001	1,667
Pb	0.001	<0.001	0.016	<0.001	0.166	0.002	<0.001	0.068	<0.001	0.114	1,111
Zn	0.001	<0.001	0.001	<0.001	0.023	0.001	<0.001	0.017	<0.001	0.025	1,667

Table 4. 6 Weight percentages of some important elements in the composition of the samples from 19th century analyzed by spark emission spectrometer.

Element	19 th Century Samples					% Standard Deviation (±)
	FKM-01	FKM-02	FKM-03	FKM-04	FKM-05	
C	<1.50	<0.002	0.025	<1.50	<0.002	1,041
Si	0.20	0.226	0.182	0.190	0.032	2,403
Mn	0.087	0.039	0.028	0.027	0.170	0,940
P	0.269	0.241	~0.351	0.121	0.126	1,524
S	0.010	0.077	0.030	0.030	0.018	4,066
Mg	0.008	0.0042	0.002	0.002	0.002	5,431
Cr	0.028	0.129	<0.007	<0.004	<0.001	1,286
Ni	0.013	<0.001	0.071	0.010	0.051	1,176
Mo	<0.001	<0.001	<0.001	<0.001	<0.001	1,360
Cu	0.018	0.038	0.147	0.043	0.059	1,928
Al	0.013	0.034	0.009	0.018	<0.001	2,047
Ti	0.007	0.0053	0.0090	0.004	0.001	0,000
V	0.005	0.013	0.014	0.006	0.003	0,820
W	<0.005	<0.003	<0.003	<0.005	<0.003	1,307
Sn	<0.001	<0.001	0.006	<0.001	<0.001	1,667
Pb	0.009	0.039	0.005	<0.002	<0.001	1,111
Zn	<0.001	0.003	<0.001	<0.001	<0.001	1,667

Table 4.6. Weight percentages of some important elements in the composition of the samples from 19th century analyzed by spark emission spectrometer (continued).

Element	19 th Century Samples						% Standard Deviation (±)*
	FKM-07	FKM-08	FKM-09	FKM-11	T-N-01	T-D-01	
C	<0.002	<0.002	0.056	<0.002	0.132	0.289	1,041
Si	0.155	0.113	0.101	0.233	0.009	0.094	2,403
Mn	0.036	0.016	0.148	0.115	0.483	0.019	0,940
P	0.282	0.262	0.066	0.243	0.027	0.090	1,524
S	0.060	0.203	0.010	0.099	0.025	0.004	4,066
Mg	0.0075	0.0019	0.0006	0.0345	0.001	0.0113	5,431
Cr	0.148	0.104	<0.001	0.187	0.135	<0.001	1,286
Ni	0.012	0.006	0.019	<0.001	0.085	0.039	1,176
Mo	<0.001	<0.001	0.001	<0.001	0.012	<0.001	1,360
Cu	0.046	0.036	0.170	0.058	0.214	0.019	1,928
Al	0.015	0.049	<0.001	0.023	0.030	0.006	2,047
Ti	0.0064	0.0028	0.0034	0.0033	0.001	0.0017	0,000
V	0.022	0.009	<0.001	0.012	0.002	<0.001	0,820
W	<0.003	<0.003	0.005	<0.003	0.003	<0.003	1,307
Sn	<0.001	<0.001	0.009	<0.001	0.004	<0.001	1,667
Pb	0.031	0.023	<0.001	0.036	0.006	<0.001	1,111
Zn	<0.001	0.002	<0.001	<0.001	0.003	<0.001	1,667

* Standard deviation for each element obtained from the recalibration standard sample after 10 readings. All values are in w%.

Carbon content of all samples belonging to 15, 16 and 19th centuries are in the range of 0.002% (FKM-02) to 1.5% (FKM-01). They fall in the definition of “plain carbon steel” having three further groups as low, medium and high carbon content within the range of 0.001 to ~1.5% (Singh, 2016). Except the nail (MSH-KAP-07) that has 0.42% carbon content being in the medium carbon range and iron bar (FKM-01) and iron door hinge piece (FKM-04) from 19th century being in high carbon content range with 1.5% carbon, all the other objects are classified as the low carbon steels. Low carbon content steel can be shaped by hot and cold forging, drawing or pressing (Aktakka, 2006, Yavuz 2010).

Silicon content of the samples are also very low: the lowest one was 0.003% from the 15th century sample, the door lock piece (GMH-Me-02) and the highest one was 0.571% from the 16th century sample the nail (MSH-KAP-07) from interior.

When phosphorous contents of the samples are compared, all samples have phosphorous content higher than good quality steel ranging from 0.007% to 0.351%. The lowest amount, 0.007%, belongs to door lock piece (GMH-Me-02) and nail (MSH-KAP-09) and the highest amount, 0.351%, belongs to a door lock piece from 19th century (FKM-03). In good quality steel, the phosphorus content should be not more than 0.005%. In normal quality steel, phosphorous is not more than 0.05%. Most of the iron objects in this study have a phosphorous content in the normal steel quality range which is not more than 0.05%. Phosphorous may cause brittleness but may increase its workability (Yıldız, 2010). Phosphorous distribution in the metal may change with time.

Sulfur content is an important parameter for the deterioration performance of the iron samples. High sulfur content causes brittleness in steel (Yıldız, 2010). The sulfur content of the objects is in the range of 0.004% - 0.203%. The door lock piece from 19th century (T-D-01) has the lowest amount and the L-shaped iron piece from 19th century from Ottoman layer excavation (FKM-08) has the highest amount of sulfur.

Sulfur content in good quality steel should be between 0.02 % and 0.035 %. Thirteen samples have low sulfur content (0.004%-0.034%) as specified for good quality

steel. Those samples belong to the periods 15th, 16th and 19th centuries (GMH-Me-02 from the 15th century; MSH-KAP-03, -08, -09, -12, -13 from the 16th century and FKM-01, -03, -04, -05, -09, T-N-01, T-D-01 from the 19th century).

Eight samples have higher sulfur content than 0.035% (MSH-KAP-01, -02, -05, -07, FKM-02, -07, -08, -09). Among those objects, the three samples having the highest sulfur amounts are an L-shaped iron piece from 19th century Ottoman layer excavation (FKM-08) being 0.203%; an iron nail from a stone dwelling in Foça (FKM-11) being 0.099% and an iron hinge from a main entrance timber door (MSH-KAP-05) being 0.137%. The high content of sulfur in the composition might come from ore and the ore might contain pyrite (FeS_2). Although four of the samples (FKM-02, FKM-08, FKM-11 and MSH-KAP-01) have sulfur content above 0.035% in their composition, their hardness values are in the soft range.

Manganese content in the composition of steels above 1% makes the steel considerably harder (Yildiz 2010; Radovic et al, 2010; Singh 2016). When compared with that amount, all iron objects examined have less than 1% manganese in their composition. The manganese content of the analyzed samples shows its relationship with hardness. The sample having the lowest manganese content being 0.001%, which is a door lock piece from the 15th century (GMH-Me-02) has the hardness in the soft grade (91 HB). The sample having the highest manganese content being 0,916%, which is a nail from 16th century (MSH-KAP-07), has the highest hardness grade (281 HB). All other samples have a low manganese content and a “soft” hardness grade.

Nickel and chromium contents are known to contribute to the corrosion resistance in steel (Xu et al, 2021; Cheng et al, 2017; Smola et al, 2019; Singh 2016). Nickel contents in the composition of the samples vary between 0.001% - 0,150%. Three nails from 16th century (MSH-KAP-02, -05, -11) and two nails from the 19th century (FKM-02, -11) have the lowest nickel amount. A nail from the 16th century (MSH-KAP-12) has the highest nickel amount being 0,150%. Chromium contents in the composition of the samples vary between 0.001% - 0,604%. The lowest chromium

content samples are a 15th century door lock piece, four nails from 16th century (MSH-KAP-01, -03, -08, -11) and three different samples from the 19th century (FKM-09, -05; T-D-01). The highest chromium amount 0,604% is observed in a nail from 16th century (MSH-KAP-05).

Aluminum content in the composition of steels especially being 1% improves considerably the corrosion resistance of the steel and decreases the corrosion rate of the passivation film (Zhang et al, 2021). All iron objects have low aluminum content in their composition ranging between 0.001 to 0.115% being less than 1%. The sample having the highest aluminum content being 0.115% is a nail from the dome of Kılıç Ali Paşa Mosque from 16th century (MSH-KAP-03). The samples having the lowest aluminum content being 0,001% are MSH-KAP-01, -07, -08, -12 from the 16th century, FKM-05 and FKM-09 from the 19th century. The oxidation rate of Fe–Al–Si alloys is three to four orders lower than that of Fe–Al and Fe–Si alloys due to the presence of a dense aluminum oxide layer and a layer of iron silicides below it, which acts as a secondary oxidation protection (Novak et al, 2019).

When magnesium contents of the samples are compared, all samples have magnesium content ranging from 0.000% to 0.0345%. 16 out of 21 tested samples have magnesium less than 0.01%. The lowest amount, 0.000%, belongs to a nail from a dome (MSH-KAP-01) and the highest amount, 0.0345%, belongs to a nail from 19th century (FKM-11).

All objects have minor element composition including carbon are in the following range: 0.279% (for 15th century object (GMH-Me-02)) to 2.4057% (for 16th century object (MSH-KAP-07)). They are classified as low alloy steel.

4.2.2. Results of Elemental Compositions by Using SEM-EDX

By using spark emission spectrometer, some restricted elements such as calcium (Ca) and sodium (Na) cannot be detected, whereas analyses of restricted elements can be added by EDX. Although the obtained results from EDX are semi-quantitative, they are in parallel with spark emission spectrometer.

Two samples (GMH-Me-02 and 04) from the 15th century's iron components were analyzed by using SEM-EDX (Figure 4.1 & 4.2). The main body of the door lock piece (GMH-Me-02), contains the elements Fe, O, Ca, Si, Mg, Al, K and Cl (Figure 4.1) in its composition. A nail embedded in the interior wall plaster (GMH-Me-04) contains Fe, O, Ca, Si, Mn, Al, Cr and S elements (Figure 4.2). Those results were obtained from the main body in the figure 4.15 and not from the corrosion layer.

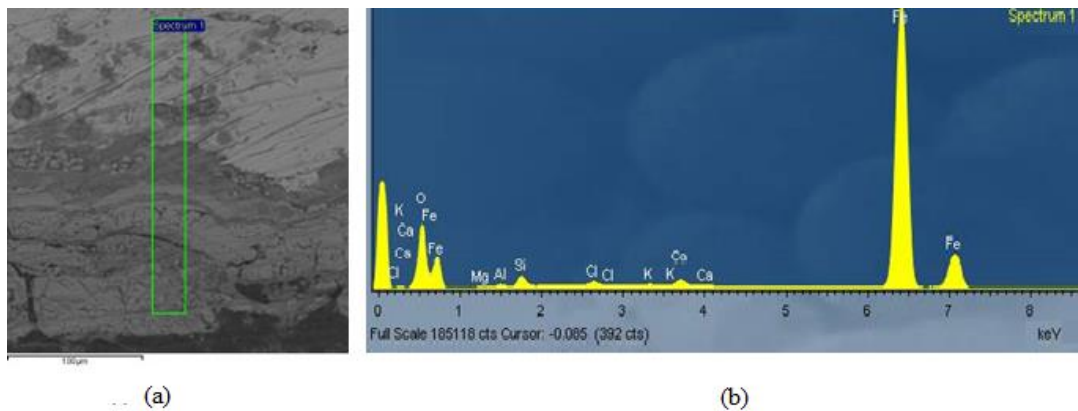


Figure 4. 1 a) SEM image of a door locking iron piece (GMH-Me-02) from 15th century: elemental analysis area starting from metal body to TM Layer. b) EDX analysis results: Fe, O, Ca, Si, Mg, Al, K and Cl.

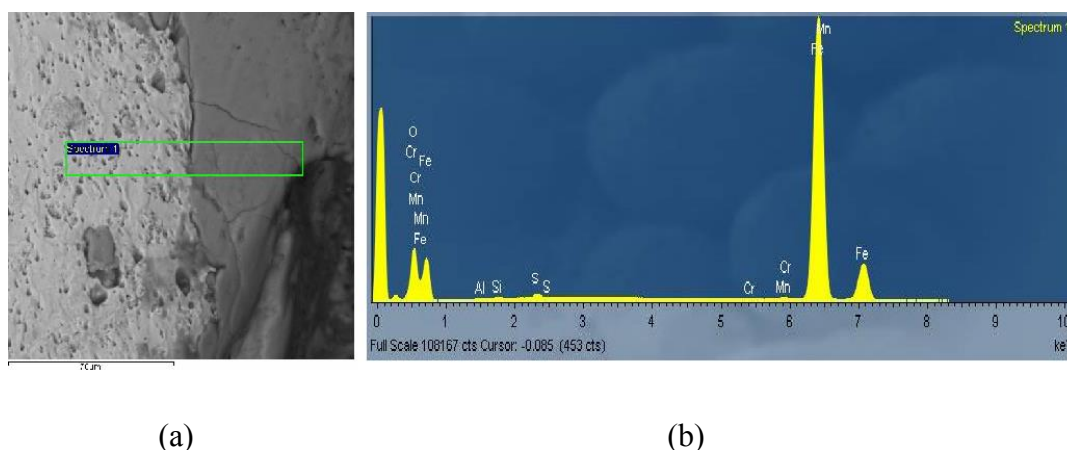


Figure 4. 2 a) SEM image of a nail (GMH-Me-04) from 15th century: elemental analysis area starting from metal body to TM Layer. b) EDX analysis results: Fe, O, Ca, Si, Mn, Al, Cr and S.

Four samples of 16th century iron objects were analyzed and the EDX results are presented together with the SEM images of the related sample. The nail from the dome of the hammam building (MSH-KAP-01) has iron, silicon and manganese as main elements in the metal body (Figure 4.3 and Table 4.7). Shark (sword) like shapes is considered as the locations in the body with the composition of manganese sulfide (MnS) (Figure 4.4). The elemental analysis confirms the presence of main elements as manganese and sulfur (Figure 4.4) in their composition. The EDX analyses performed at grain and grain boundaries show only the presence of iron without any segregation at grain boundaries (Figure 4.5 and 4.6). The EDX analyses of four different pitting corrosion locations reveal the presence of iron, silicon, manganese and oxygen (Figure 4.7 and 4.8). Those pitting corrosion locations are thought to have the composition of manganese oxide (MnO). In some locations, manganese, sulfur and oxygen are also observed together with iron element.

Table 4. 7 Weight percent of important elements in the composition of the nail sample body (MSH-KAP-01) (16th century) by the EDX analysis.

Element	Weight Conc. %	Atom Conc. %
Si	0.37	0.73
Mn	0.70	0.71
Fe	98.93	98.56

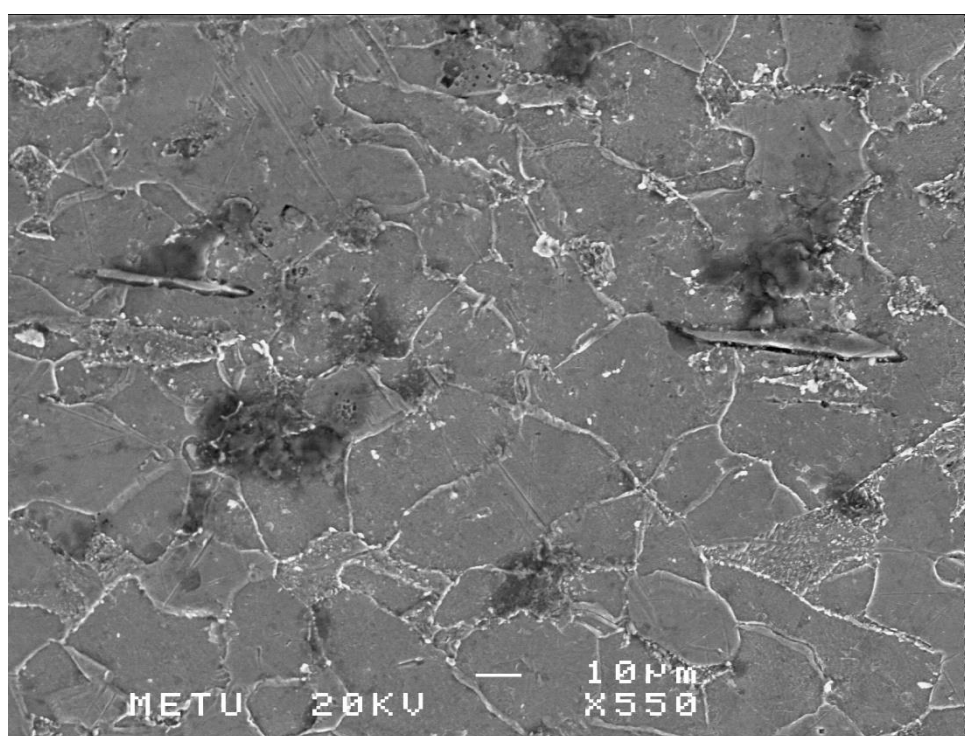


Figure 4. 3 SEM image (550x) of a nail head (MSH-KAP-01): Shark (sword) shaped images containing manganese sulfide (MnS) and pitting corrosion locations having Fe, Si, Mn and O.

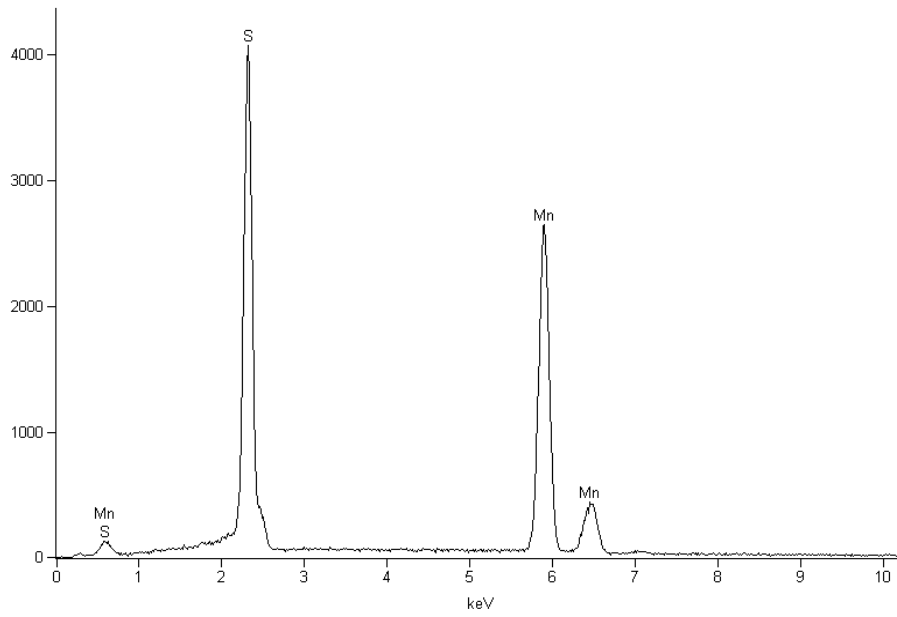


Figure 4. 4 EDX spectrum of a nail head (MSH-KAP-01) at a shark (sword) shaped location: Mn and S.

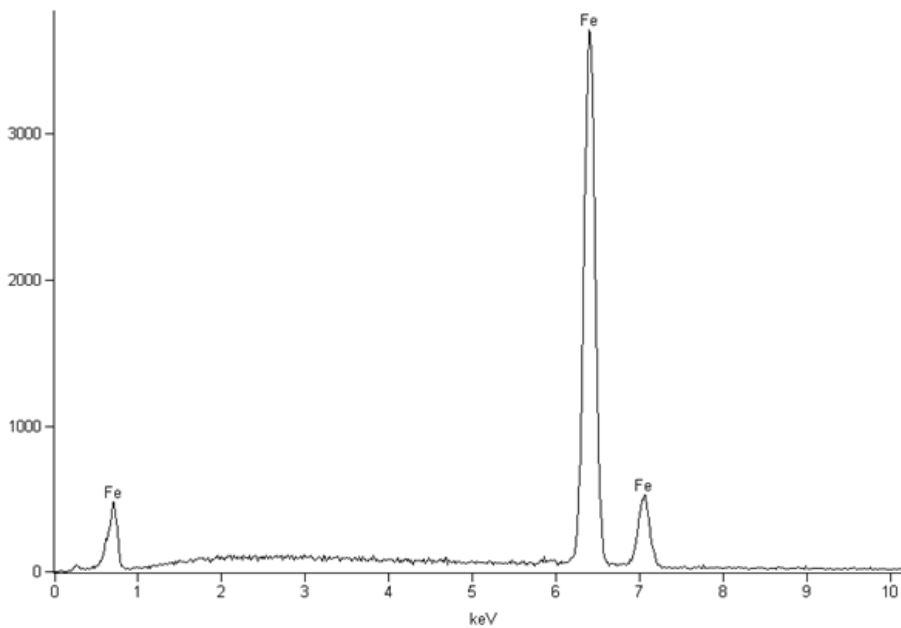


Figure 4. 5 EDX spectrum of a grain from a nail head (MSH-KAP-01): Fe as the main element.

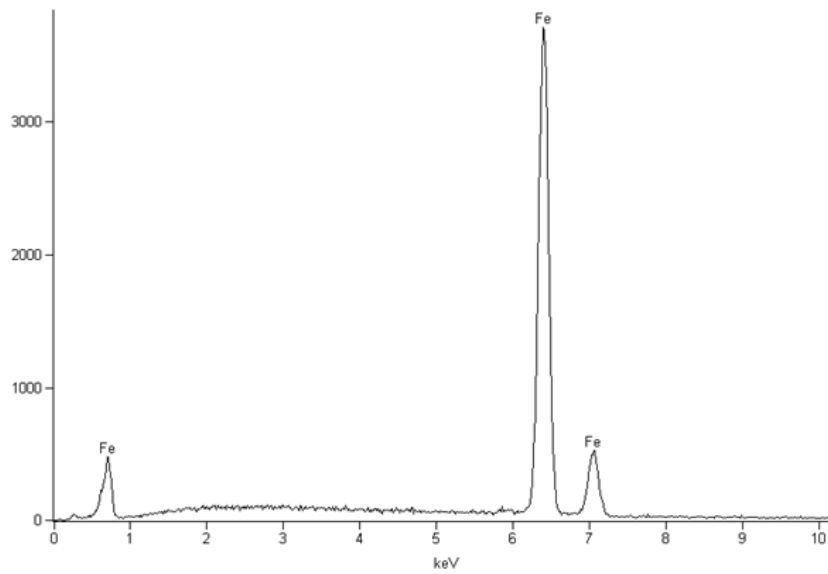


Figure 4. 6 EDX spectrum of a grain boundary from a nail head (MSH-KAP-01) with no segregation.

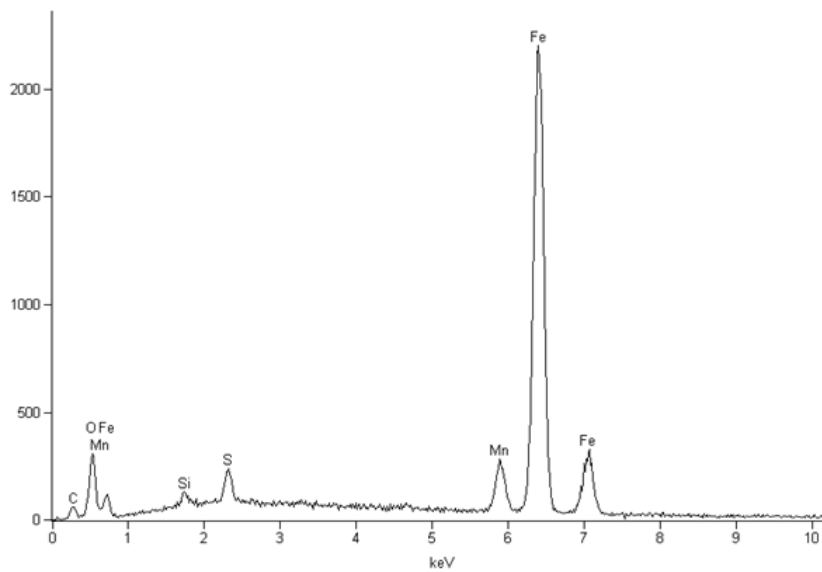


Figure 4. 7 EDX spectrum of a pitting corrosion location in the nail head (MSH-KAP-01): Fe, Si, O, Mn and S.

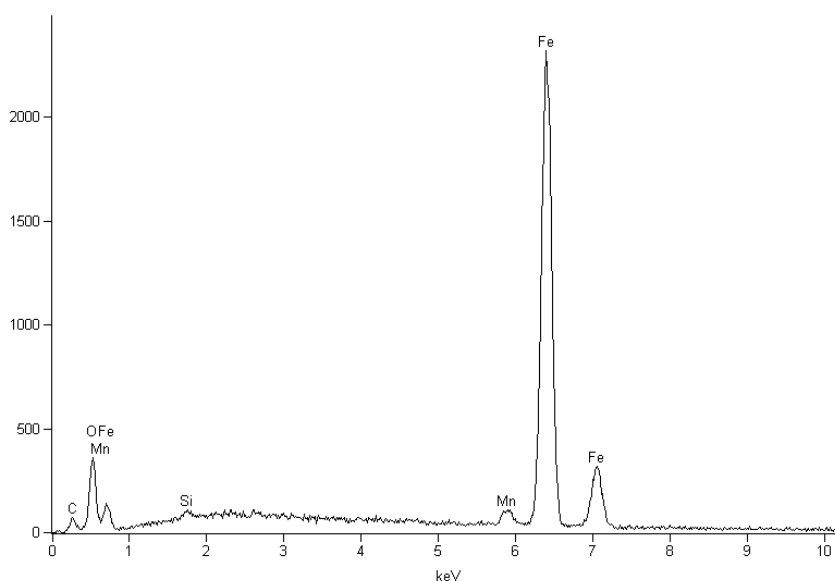


Figure 4. 8 EDX spectrum of a pitting corrosion location in the nail head (MSH-KAP-01): Fe, Si, O and Mn.

The sample from 16th century belonging to an object used for further anchoring purposes from inside the hammam building (MSH-KAP-02) has iron as main element at points 4, 5 and 6 in the metal body (Figure 4.10). Several locations in the main body (Figure 4.9) were examined. Iron, silicon, manganese, phosphorous, sulfur, aluminum, calcium, magnesium and oxygen are observed in regions 1, 2 and 7 (Figure 4.11). Region 3 contains the same element with 1, 2 and 7 with the exception of magnesium and sulfur (Figure 4.12). The elemental analysis performed at location 8 which is a dark colored pitting corrosion location, shows the presence of iron, silicon, sodium, chlorine, sulfur and potassium which are probably the alkaline salts moved into the body through capillaries (Figure 4.13).

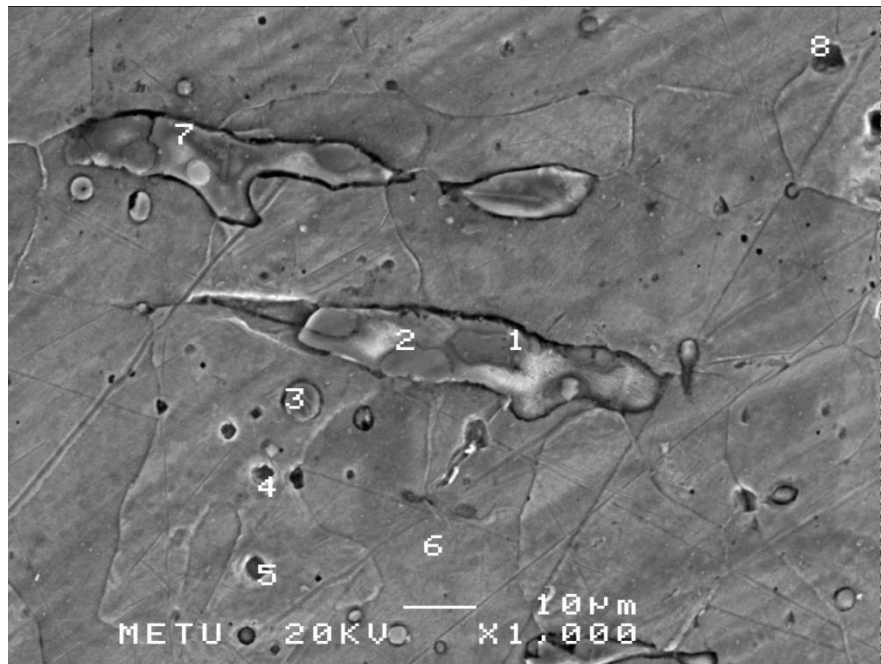


Figure 4. 9 SEM image of the main metal body in an iron sample head (MSH-KAP-02). Numbers indicate the locations of EDX analyses.

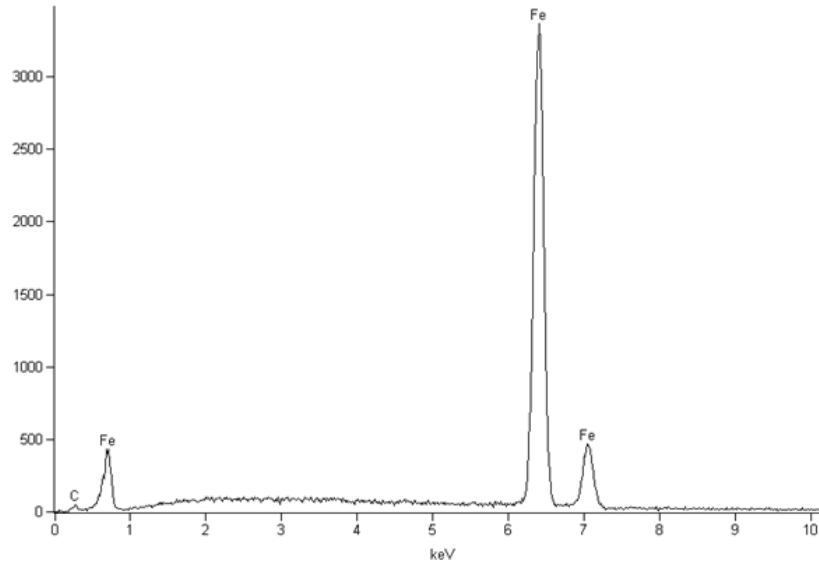


Figure 4. 10 EDX spectrum representing the points 4, 5 and 6 in the main body of the iron sample head (MSH-KAP-02): Fe as the main element.

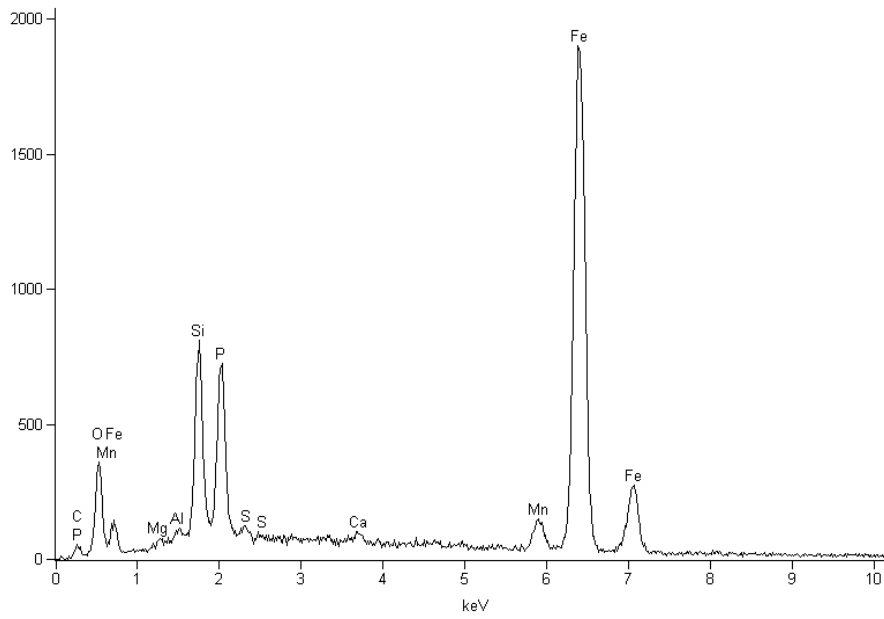


Figure 4. 11 EDX spectrum representing the points 1, 2 and 7 in the main body of the iron sample head (MSH-KAP-02): Fe, Si, Mn, P, S, Al, Ca, Mg and O.

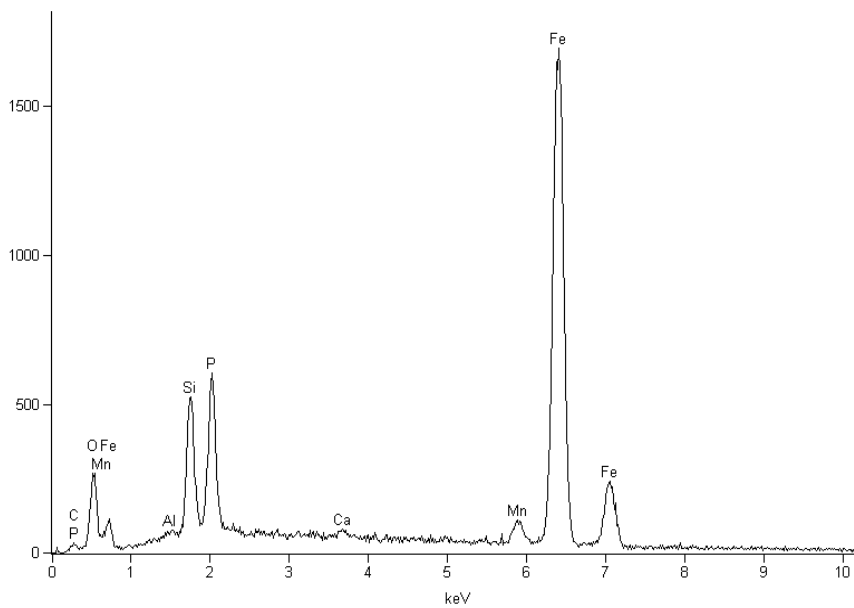


Figure 4. 12 EDX spectrum of the point 3 in the main body of the iron sample head (MSH-KAP-02): Fe, Mn, O, Si, Al, P and Ca.

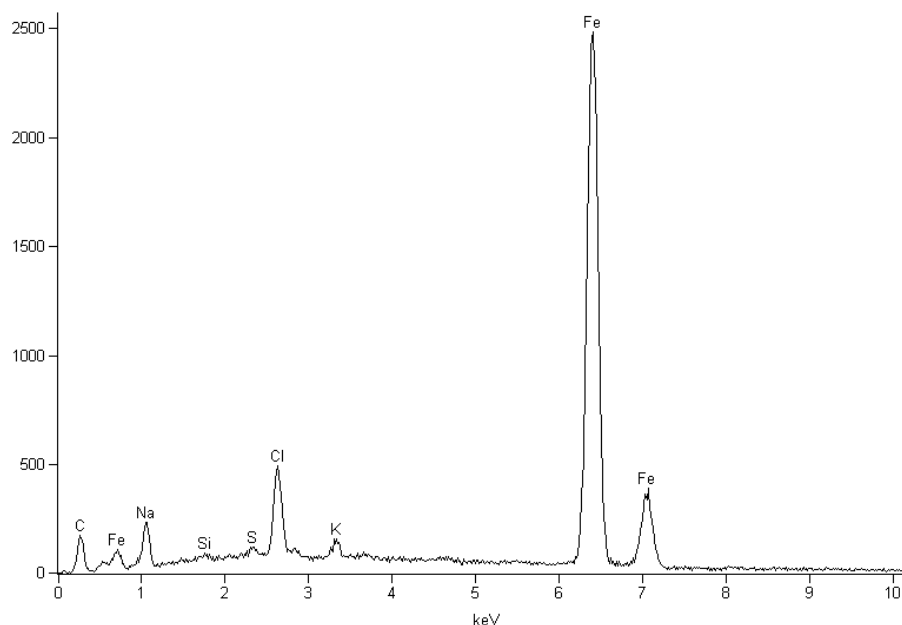


Figure 4. 13 EDX spectrum of the point 8 in the main body of an iron sample head (MSH-KAP-02): Fe, Si, Na, Cl, S and K.

The sample representing a nail from the dome of the 16th century hammam building (MSH-KAP-03) was analyzed in the body and its pitting locations (Figure 4.14). The body's EDX analysis reveals iron as the main element (Figure 4.15). In the pitting location, iron, silicon, calcium, phosphorous, chlorine, sulfur, aluminum and oxygen are the main elements observed (Figure 4.16). The weight percentages of the elements in the pitting locations show that the amount of aluminum is the second important element after iron in the composition (Table 4.8).

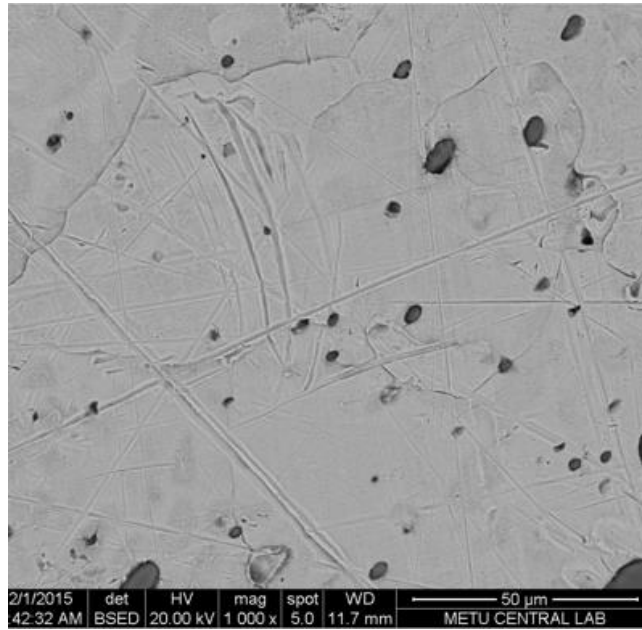


Figure 4. 14 SEM image (1000X) of the main body: An iron nail head from the dome (MSH-KAP-03).

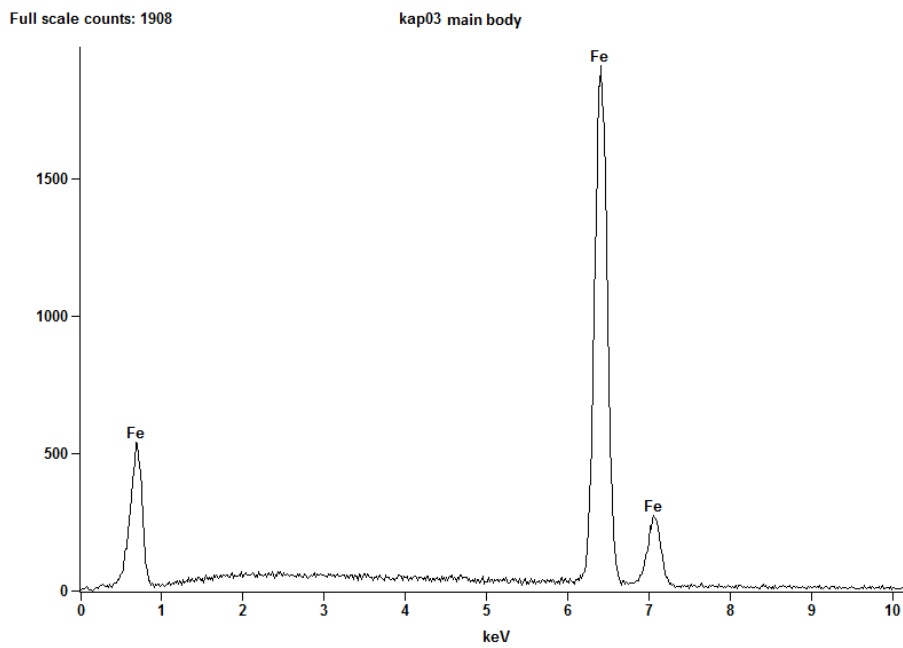


Figure 4. 15 EDX analysis at the main body of the iron sample (MSH-KAP-03): Fe is the main element.

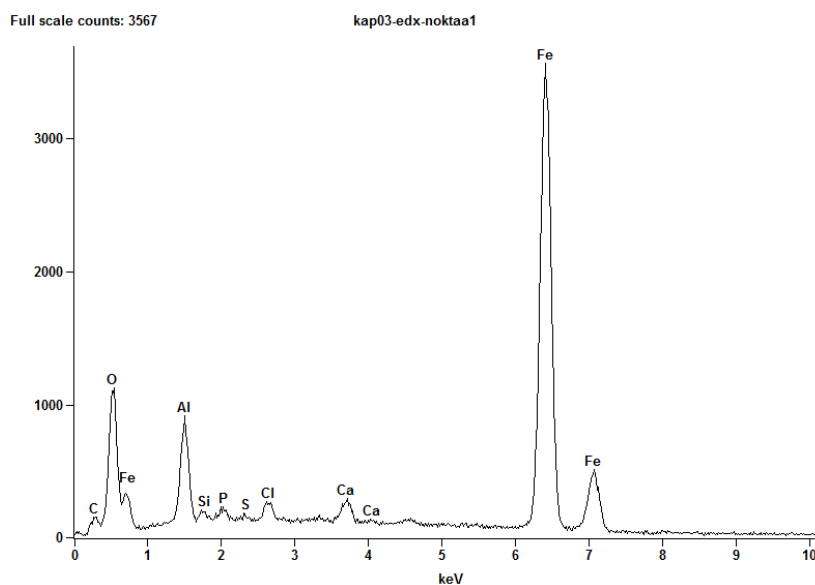


Figure 4. 16 EDX analysis at the main body of the iron sample (MSH-KAP-03): Fe, O, Si, Ca, S, P, Cl and Al.

Table 4. 8 EDX analysis of a pit (point 1) from the main body of an iron sample (MSH-KAP-03) (16th cc): Weight percentage of some important elements in the pit's composition.

Element	Weight Conc %	Atom Conc %	Compnd Conc %	Formula
O	32.50	59.78	0.00	
Al	3.35	6.93	12.00	Al ₂ O ₃
Si	0.40	0.42	0.86	SiO ₂
P	0.56	0.54	1.29	P ₂ O ₅
S	0.21	0.19	0.53	SO ₃
Cl	0.88	0.73	0.88	Cl
Ca	1.38	1.02	1.94	CaO
Fe	57.71	30.41	82.51	Fe ₂ O ₃

Analysis of another nail object from the interior of the above-mentioned 16th century hammam building (MSH-KAP-12) was performed in four locations of the body of the sample. In the first location, EDX analysis reveals the presence of iron, silicon,

calcium, aluminum and oxygen (Figures 17 a and b). In the second location, sulfur is identified in addition to the elements in the first location (Figures 18 a and b). In the weight percentages of the elements, calcium is the second important element revealed next to iron (Tables 9 and 10). A sword shape on the body was analyzed. Iron, manganese and sulfur are also observed in its composition (Figures 19 a and b; Table 11). The mentioned sword shape is considered as a manganese sulfide (MnS) location. Lastly, the 4th location, which is a pitting location, shows the presence of iron, sodium, chlorine and potassium elements in the body's pitting corrosion location: Fe, Na, K and Cl (Figures 20 a and b). The weight percentages of the elements in the composition were characterized as impurities with very low concentration levels, much lower than iron (Table 12).

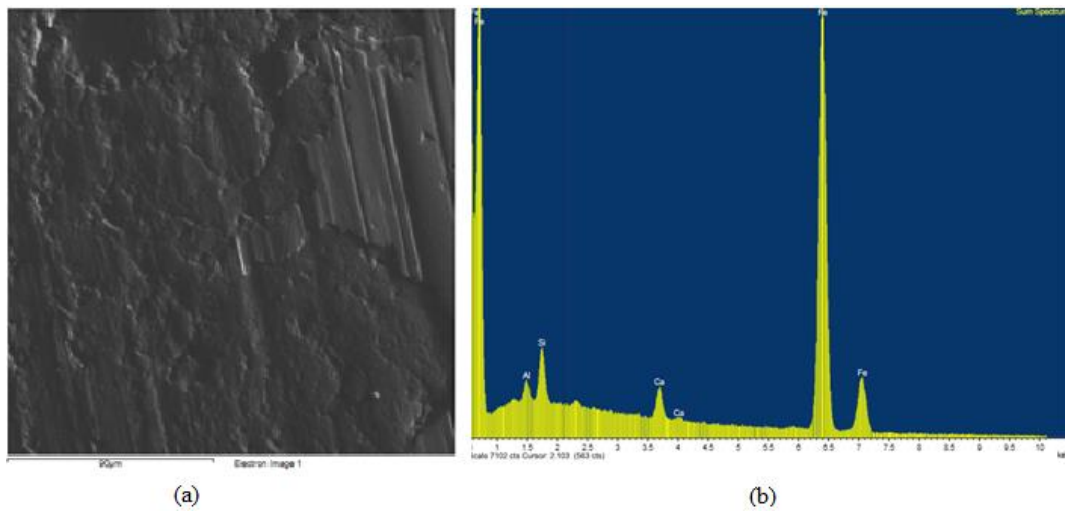


Figure 4. 17 a) SEM view from the main body of the sample head (MSH-KAP-12), b) EDX analysis of the main body: Fe, O, Si, Ca and Al.

Table 4. 9 EDX analysis of the main body in the nail sample head (MSH-KAP-12) (16th cc): Weight percentage of the elements in its composition.

Element	Weight Conc. %	Atom Conc. %
O	33.50	56.03
Al	0.45	0.45
Si	1.17	1.12
Ca	1.18	0.79
Fe	57.35	27.48

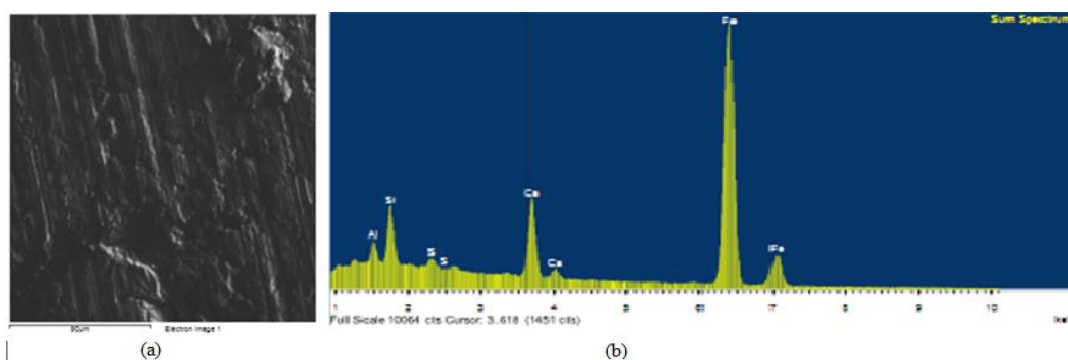


Figure 4. 18 a) SEM view of the main body in the nail sample head (MSH-KAP-12). b) EDX analysis of the main body: Fe, O, Si, Ca, Al and S.

Table 4. 10 EDX analysis of the main body in an iron sample (MSH-KAP-12) (16th cc): Weight percentage of elements in its composition.

Element	Weight Conc. %	Atom Conc. %
<i>O</i>	39.87	68.26
<i>Al</i>	0.74	0.75
<i>Si</i>	1.82	1.77
<i>S</i>	0.41	0.35
<i>Ca</i>	4.35	2.98
<i>Fe</i>	52.81	25.90

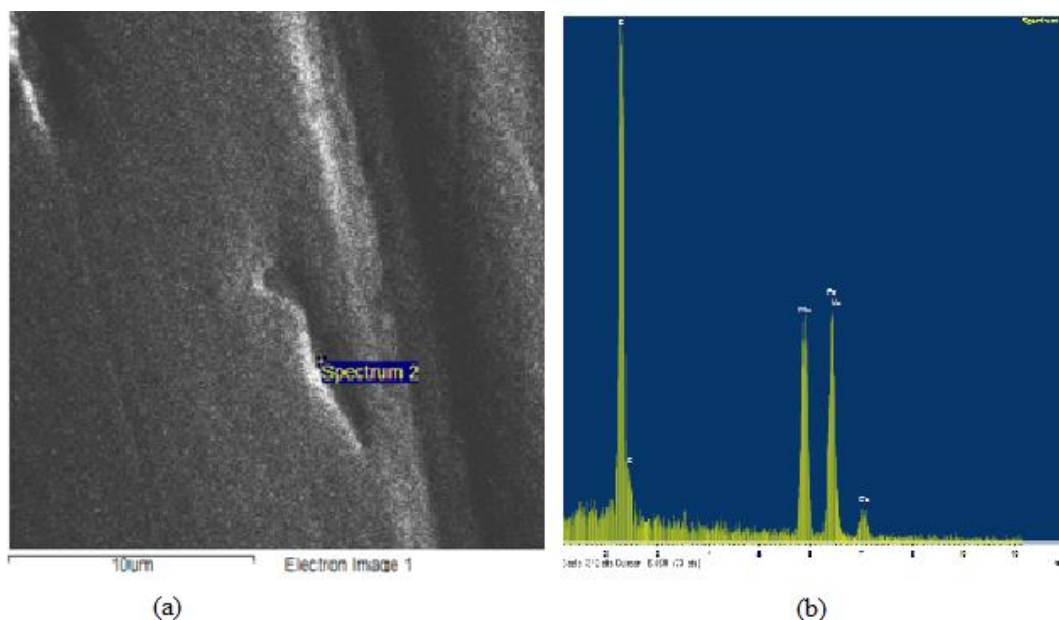


Figure 4. 19 a) SEM view of a sword shaped impurity in the main body of the iron sample (MSH-KAP-12), b) EDX spectrum of the sword shaped impurity: Mn and S.

Table 4. 11 EDX analysis of the shark (sword) shaped formation in the main body of the iron sample (MSH-KAP-12) (16th cc): Weight percentage of elements in its composition.

<i>Element</i>	<i>Weight Conc. %</i>	<i>Atom Conc. %</i>
S	18.08	22.55
Mn	32.73	23.82
Fe	42.13	30.16

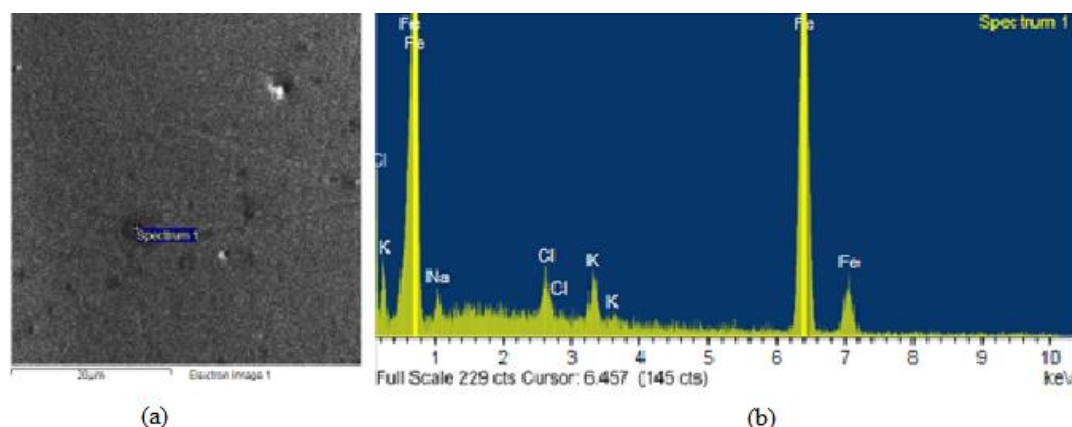
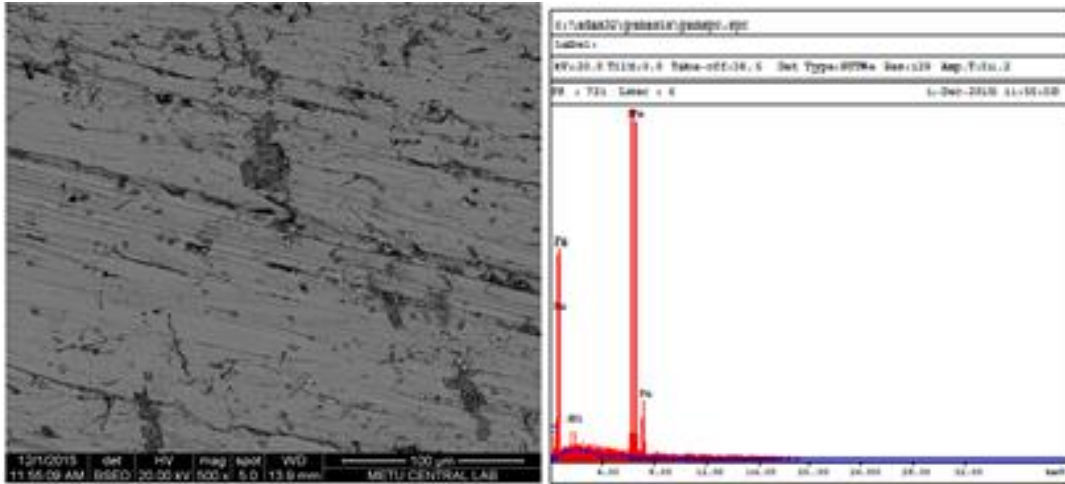


Figure 4. 20 a) SEM image of the pitting locations in the main body of an iron nail (MSH-KAP-12); b) EDX analysis of a pitting location: Fe, Na, Cl, and K.

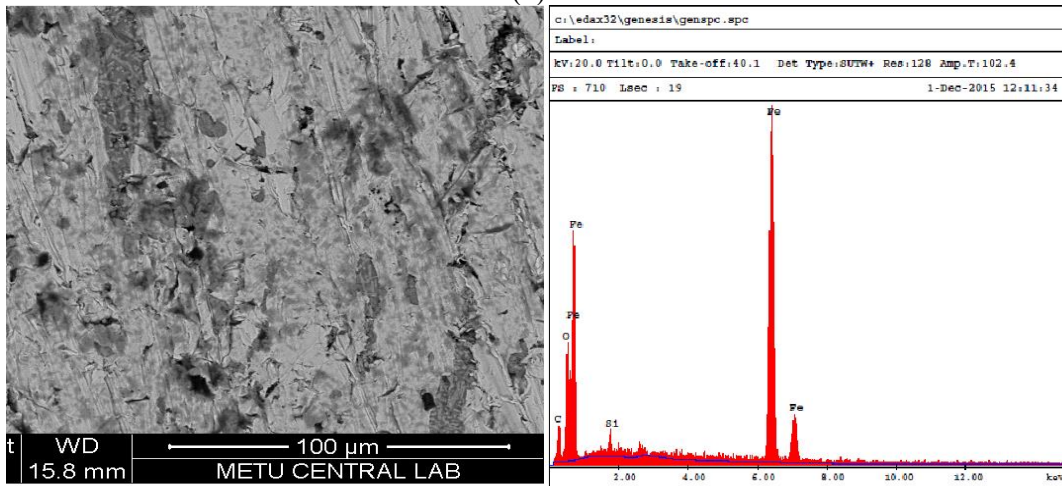
Table 4. 12 EDX analysis of a pitting location in the main body of an iron sample (MSH-KAP-12) (16th cc): Weight percentage of elements in its composition.

<i>Element</i>	<i>Weight Conc. %</i>	<i>Atom Conc. %</i>
<i>Na</i>	1.95	4.49
<i>Cl</i>	2.20	3.29
<i>K</i>	3.07	4.16
<i>Fe</i>	92.78	88.06

Two objects from 19th century were analyzed and the EDX results are presented together with the SEM images of the related samples. The nail embedded in timber from the dwelling in Foça (FKM-02) and the nail (FKM-11) embedded in building stone from another dwelling in Foça have iron and silicon as main elements in the metal body (Figure 4.21).



(a)



(b)

Figure 4. 21 a) SEM image and EDX analysis of the main body in an iron nail (FKM-02): Fe and Si. b) SEM image and EDX analysis of the main body in an iron nail (FKM-11): Fe and Si.

4.3 Results of Microscopical Investigations on Metal Body and Corrosion Layer

Microscopical examination of the samples on main metal bodies and their corrosion layers were done on the polished surfaces by using metallographic microscope

(Nikon IMM901), digital microscope (Huvitz HDS 5800) and scanning electron microscope (Tescan VegaII). Observations are given in the following sections:

4.3.1 Metallographic characteristics of metal bodies

Metallographic characteristics were investigated by microscopic observations of the cross-sections, Brinell hardness measurements and theoretical FeC (cementite) phase calculations. Microstructural constituents of the metal bodies from 15th century, 16th century and 19th century samples are described by using microscopical observations of the cross-sections (Figures 4.22 - 4.29). The microscopical observations and Brinell hardness measurements are summarized in Table 4.14 - 4.16. In addition, the theoretical FeC (cementite) phase calculation results are documented in Table 4.13.

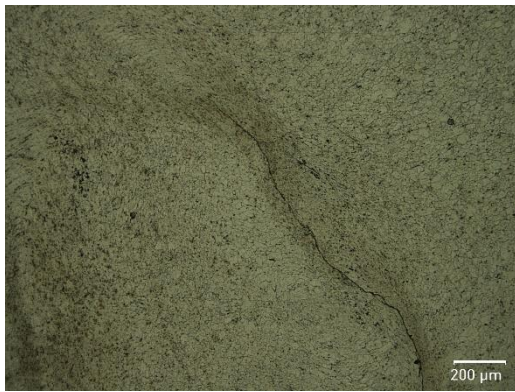
Microscopical observation results and phase calculation results based on carbon content of samples determined by spark emission spectroscopy are combined together to explain the metallographic characteristics of the individual samples. Carbon content of the samples is taken into consideration to calculate the amount of pearlite-ferrite to better interpret microscopic views of the samples. Those results are summarized in tables 4.14-4.15-4.16 in terms of metallographic characteristics versus hardness characteristics of individual samples belonging to three main historical periods (15th, 16th and 19th centuries).

Table 4. 13 The theoretically calculated FeC (cementite) phase percentages of the samples from 15th, 16th and 19th centuries.

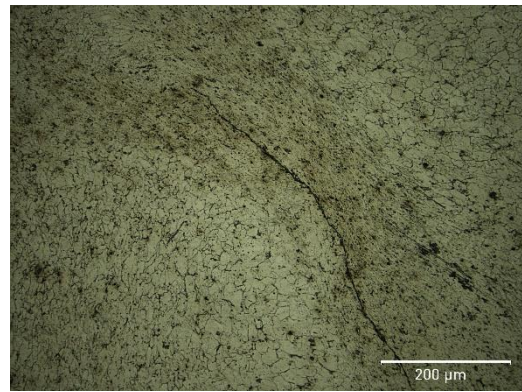
Century of the structure	Sample's code	Carbon (C) content w/w%	Fraction of pearlite	Total ferrite	Cementite	Fraction of proeutectoid alpha	Eutectoid ferrite
15th century	GMH-Me-02	0.121	0.134	0.985	0.015	0.866	0.119
16th Century	MSH-KAP-01	0.155	0.180	0.980	0.020	0.820	0.160
	MSH-KAP-02	0.002	-0.027	1.003	-0.003	1.027	-0.024
	MSH-KAP-03	0.003	-0.026	1.003	-0.003	1.026	-0.023
	MSH-KAP-05	0.016	-0.008	1.001	-0.001	1.008	-0.007
	MSH-KAP-07	0.420	0.539	0.940	0.060	0.461	0.480
	MSH-KAP-08	0.042	0.027	0.997	0.003	0.973	0.024
	MSH-KAP-09	0.118	0.130	0.986	0.014	0.870	0.116
	MSH-KAP-12	0.148	0.171	0.981	0.019	0.829	0.152
	MSH-KAP-13	0.124	0.138	0.985	0.015	0.862	0.123
19th century	T-D-01	0.289	0.362	0.960	0.040	0.638	0.322
	T-N-01	0.132	0.149	0.984	0.016	0.851	0.133
	FKM-01	1.500	0.875		0.125		
	FKM-02	0.002	-0.027	1.003	-0.003	1.027	-0.024
	FKM-03	0.025	0.004	1.000	0.000	0.996	0.004
	FKM-04	1.500	0.875		0.125		
	FKM-05	0.002	-0.027	1.003	-0.003	1.027	-0.024
	FKM-07	0.002	-0.027	1.003	-0.003	1.027	-0.024
	FKM-08	0.002	-0.027	1.003	-0.003	1.027	-0.024
	FKM-09	0.056	0.046	0.995	0.005	0.954	0.041
	FKM-11	0.002	-0.027	1.003	-0.003	1.027	-0.024

Samples collected from the interior of Gazi Mihal Hammam built in 15th century have similar microstructures with each other (Figure 4.22). An iron door lock piece (GMH-Me-02) having 0.12% carbon has mostly ferritic structure (98.5% total ferrite) with little amount of pearlite fraction (13%), cementite (1.5%) and eutectoid ferrite phase (1.1%) (Table 4.13). Nail samples (GMH-Me-03 and GMH-Me-04) from the same building have ferritic structure with fine grains (Figure 3.1.b-c) similar to the iron door lock piece which has 0.12% C in it. Cracks and inclusions are

observed on the polished surfaces of all mentioned samples. The hardness measurement of only one of the samples from 15th century could be taken due to the fact that the other samples had insufficient surface areas for such measurements. The hardness value of the door lock piece (GMH-Me-02) from Gazi Mihal Hammam is 90.9 HB being in very soft range. This result reveals an expected hardness value for a ferritic structure.



(a) GMH-Me-02 (200x), interior



(b) GMH-Me-03 (200x), interior



(c) GMH-Me-04 (200x), interior

Figure 4. 22 Microstructural images of samples taken by Huvitz digital microscope after etching with nitric acid in alcohol (a, b, c).

Table 4. 14 Microstructural analyses and Brinell hardness results of the samples from 15th century.

Sample Code	Microstructure	Average Brinell Hardness (HBS)
GMH-Me-02 Door lock piece, interior	<ul style="list-style-type: none"> • Ferritic structure. Ferrite grains are ~30 μm • Corrosion / slag fragments. Corroded regions • Deep cracks on the surface 	91 – very soft
GMH-Me-03 Nail, interior	<ul style="list-style-type: none"> • Ferritic structure • Corrosion / slag fragments. Corroded regions • Deep cracks on the surface 	ND*
GMH-Me-04 Nail, interior	<ul style="list-style-type: none"> • No regular ferrite- pearlite structure • More stressed structure • Corrosion / slag fragments 	ND*

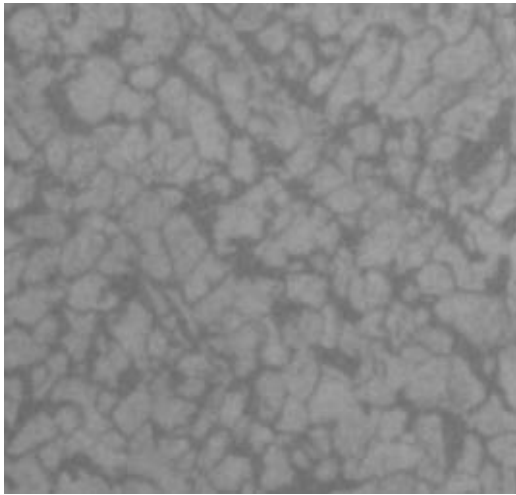
* ND: Not detected due to small size of the sample.

Four samples from 16th century have mainly ferritic structure (Table 4.14) with visible ferrite grain boundaries and some pearlite. The three samples (MSH-KAP-02, 03 and 05) are composed of ferritic structure only. The other samples (MSH-KAP-01, 09, 12 and 13) have around 98% ferrite and 13-18% pearlite in the structure. Interior wall nail (MSH-KAP-07) has the least total ferrite (94%) with the highest amount of pearlite (53.9%). Ferrite grains in the samples differ in morphology. Due to bending, some ferrite grains are low elongated and some are still in equiaxial form.

SEM-EDX analyses have also been involved for metallographic investigations of samples from 16th century. Varying amounts of slag fragments are observable in the images of all samples with some characteristic forms as sword shape. Sword shaped streaks of impurities are distributed in the views of the cross-sections. The major elements in their composition are manganese and sulfur detected by SEM-EDX. The three samples (MSH-KAP-01, 02, and 04) show mostly elongated slag streaks while the nail from the dome (MSH-KAP-03) shows some slag inclusions in dot form. The

samples from the interior of the hammam (MSH-KAP-05 and 06) have large slag fragments. The nail from the dome (MSH-KAP-08) having nearly 100% ferritic structure has little amount of dot-formed slag fragments. The three samples from the interior of the hammam building (MSH-KAP-9, 12 and 13) have ~98% ferritic structure with little amount of corrosion / slag fragments on the surface. Nail samples MSH-KAP-09 and MSH-KAP-13 are observed together with deep cracks on the surface probably due to forging.

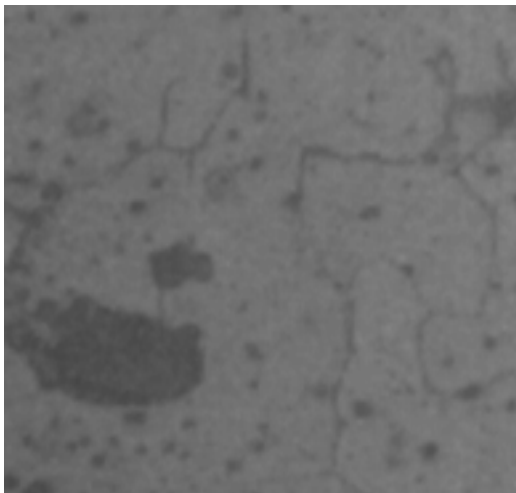
Hardness measurements of eleven iron elements from a 16th century hammam building in Istanbul have been effectuated. Hardness degrees of eleven samples are in the range of soft to hard (125 HB to 281 HB). Eight of the samples are nails. The hardness of three nails are in the soft range: a dome nail (MSH-KAP-01) with 125 HB; two nails from interior (MSH-KAP-09 and MSH-KAP-13) with 129 HB and 133 HB. Four nails are in the medium hardness range: two nails from the dome with ferritic structure (MSH-KAP-03 and MSH-KAP-08) have hardness value 166 HB and 177 HB respectively; a timber jointing nail (MSH-KAP-04) from interior having ferritic structure with some pearlite (20%) has hardness value 162 HB; a nail (MSH-KAP-12) from interior with ferritic structure has hardness value 181 HB. Only one nail (MSH-KAP-07) having pearlitic structure has hardness in the high range (281 HB). An iron hanger sample (MSH-KAP-06) having pearlitic-ferritic structure at the interior of the hammam has hardness in the soft range (138 HB), while a jointing element (MSH-KAP-02) with ferritic structure from the interior and a door hinge (MSH-KAP-05) with ferritic-pearlitic structure have hardness in medium range (160 HB and 180.2 HB successively). The hardness degrees of samples MSH-KAP-05 and 08 are quite similar, having 180 and 177 HB medium hardness respectively. MSH-KAP-05 has ferritic + pearlitic structure while MSH-KAP-08 has almost 100% ferritic structure.



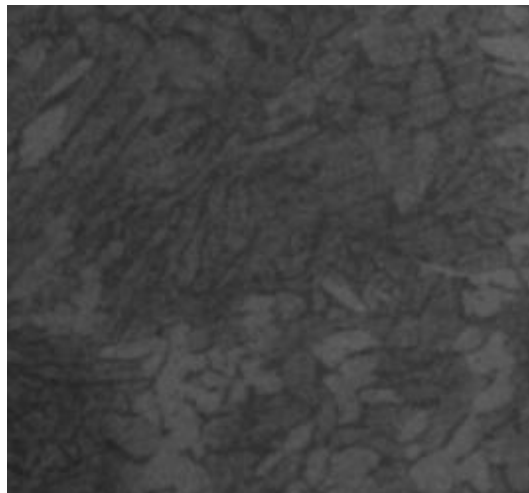
(a) MSH-KAP-01 (100x), exterior



(b)MSH-KAP-02 (200x), interior

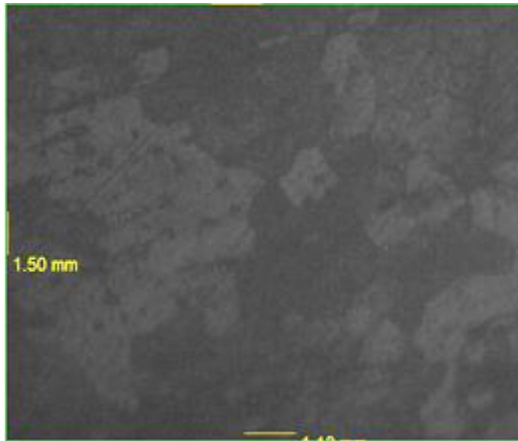


(c) MSH-KAP-03 (100x), exterior

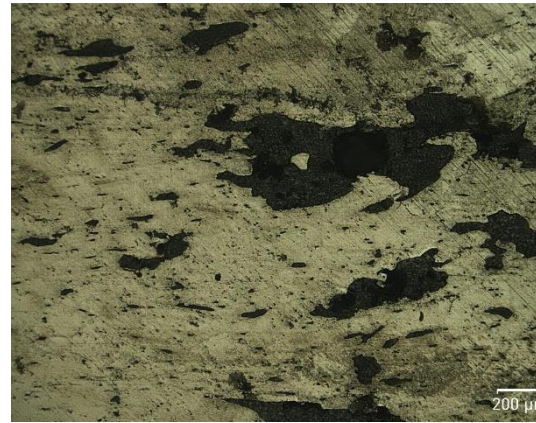


(d) MSH-KAP-04 (100x), interior

Figure 4. 23 Microstructural images of the samples taken by Nikon metallographic microscope (a, c and d) and microstructural image of the sample by Huvitz digital microscope (b) after etching with nitric acid in alcohol (16th cc).



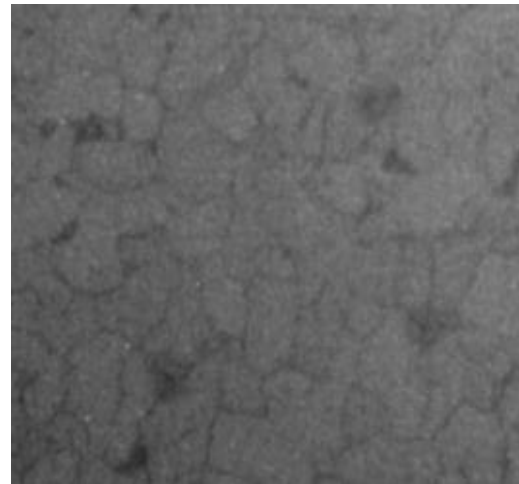
(e) MSH-KAP-05 (100x), interior



(f) MSH-KAP-06 (200x), interior

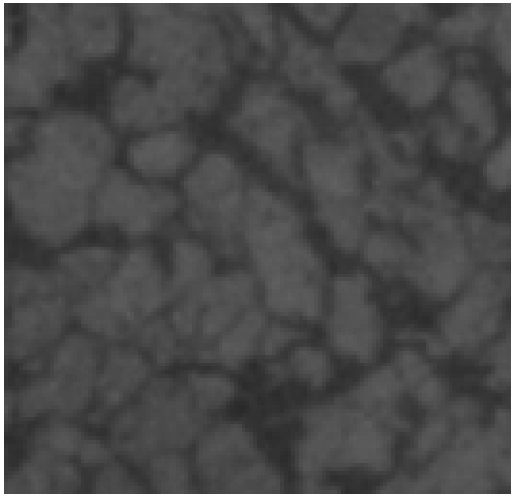


(g) MSH-KAP-07 (500x), interior



(h) MSH-KAP-08 (100x), exterior

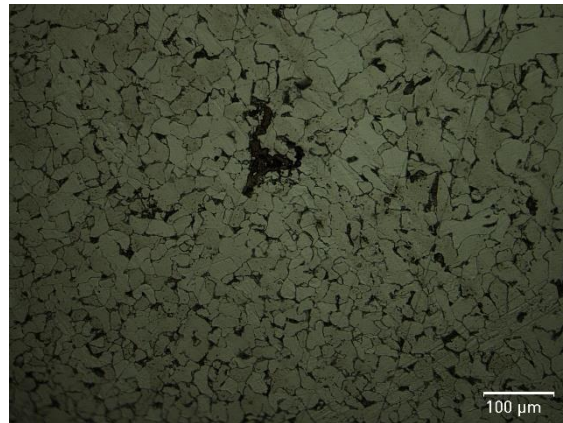
Figure 4. 24 Microstructural images of samples taken by Nikon metallographic microscope (e, h) and microstructural images of samples taken by Huvitz digital microscope (f, g) after etching with nitric acid in alcohol (16th cc).



(i) MSH-KAP-09 (200x), interior



(j) MSH-KAP-12 (500x), interior



(k) MSK-KAP-13 (500x), interior

Figure 4. 25 Microstructural image of the sample taken by Nikon metallographic microscope (i) and Microstructural images of the samples taken by Huvitz digital microscope (j, k) after etching with nitric acid in alcohol (16th cc).

Table 4. 15 Microstructural analyses and Brinell hardness results of iron samples from the 16th century.

Sample Code	Microstructure	Average Brinell Hardness (HBS)
MSH-KAP- 01 Nail from dome, outdoor	<ul style="list-style-type: none"> • Mostly Ferritic structure (98%), %18 pearlitic structure • Equiaxial ferrite grain boundaries are visible but not elongated. Ferrite grains are ~10 to 40 μm. • Small amount of corrosion/ slag fragments 	125 – soft
MSH-KAP- 02 Iron piece anchoring purpose, interior	<ul style="list-style-type: none"> • 100% ferritic structure. Ferrite grains are ~100 μm. • Equiaxial ferrite grain boundaries are visible and its slag impurities are oriented. • Forged and re-heated. • Large amount of corrosion/ slag fragments 	160 – medium hard
MSH-KAP- 03 Nail from dome, outdoor	<ul style="list-style-type: none"> • 100% ferritic structure. Ferrite grains are ~20 μm. • Equiaxial ferrite grain boundaries are visible and its slag impurities are not oriented • Large amount of corrosion/ slag fragments 	166 – medium hard
MSH-KAP- 04 Nail used for timber jointing, interior	<ul style="list-style-type: none"> • Mostly ferritic structure with some pearlite • Ferrite grains are layered and elongated. • Forged but not reheated after last forging. • Large amount of corrosion/ slag fragments. Deep cracks on the surface 	162 – medium hard
MSH-KAP- 05 Iron hinge, interior	<ul style="list-style-type: none"> • 100% Ferritic structure • Ferrite grain boundaries are visible • Large amount of corrosion/ slag fragments 	180 – medium hard
MSH-KAP- 06 Iron element for towel hanging, interior	<ul style="list-style-type: none"> • %40 Ferritic - %60 Pearlitic structure • Heavily corroded and cracked surface • Equiaxial ferrite grain boundaries are visible, ~50μm and its slag impurities are oriented. • Forged and re-heated. • Large amount of corrosion/ slag fragments 	138 - soft
MSH-KAP- 07 Nail used for stone building, interior	<ul style="list-style-type: none"> • Total Ferrite 94% - 53.9% Pearlitic structure. Highest amount of pearlite within the 16th century samples • Finer ferrite grains (~10 μm). Oriented slags. • Forged and re-heated. • Possibly, repair material dating from recent times 	281 – very high hardness
MSH-KAP-08 Nail used for lead covering of dome	<ul style="list-style-type: none"> • Mostly ferritic structure (99.7%), 2.7% pearlitic structure. Ferrite grains are ~60 μm. • Corrosion/ slag fragments. Heavily corroded areas 	177 – medium hard
MSH-KAP-09 Nail used for stone building, interior	<ul style="list-style-type: none"> • Mostly Ferritic structure (98.6%), 13% pearlitic structure • Ferrite grain boundaries are visible. Ferrite grain size ~75μm. • No corrosion/ slag fragments 	129 – soft

Table 4.15 Microstructural analyses and Brinell hardness results of iron samples from the 16th century (continued)

Sample Code	Microstructure	Average Brinell Hardness (HBS)
MSH-KAP-12 Nail used for timber jointing, interior	<ul style="list-style-type: none"> • Mostly ferritic structure (98.1%), 17.1% pearlitic structure • Corrosion/ slag fragments. Corroded areas. No orientation noticed • Ferrite grains are larger than the others around 30 μm. 	181 – medium hard
MSH-KAP-13 Nail used for stone building, interior	<ul style="list-style-type: none"> • Mostly Ferritic structure (98.5%), 13.8% pearlitic structure • Cracks probably due to forging • Least amount of corrosion / slag fragments 	133 – soft

Iron samples collected from dwellings and excavations of an Ottoman Layer in Foça, Izmir from 19th century have mostly 100% total ferrite, while two samples an iron bar of a window guard (FKM-01) and an entrance door hinge (FKM-04) have pearlitic structure (87.5%) with 12.5% cementite. The ferrite grain boundaries of the samples are clearly observable and varying amounts of corrosion/ slag fragments are also viewed on the surface. Some corrosion fragments are found in dot forms in addition to elongated ones while examining a nail (FKM-11) from the same century.

Hardness degrees of ten 19th century samples collected from Foça are in the range of soft to medium-hard (<94 HB to 199 HB). Considering the microstructure and hardness values together, the door lock piece (FKM-03) having ferritic structure has hardness in the soft range (129 HB). The iron bar from the window guard (FKM-01) and the main entrance door hinge (FKM-04) have pearlitic structure and their hardness values are in medium hardness range (156 HB and 164 HB respectively). The hardness of the timber beam nail (FKM-02) is 133 HB and is in the soft range. The buried nail from the Ottoman layer (FKM-07) is the hardest of all Foça samples (198.5 HB) being in the medium range. Hardness values of the objects having ferritic

structure (FKM-08 and FKM-09) are in the softest range (115 HB and < 94 HB respectively). The main entrance door hinge with ferritic structure (FKM- 05) has a hardness of 160 HB in the medium range. Hardness values of the two nails from the Ottoman layer (FKM-10 and FKM-11) are in the soft range (101 HB and 117 HB respectively).

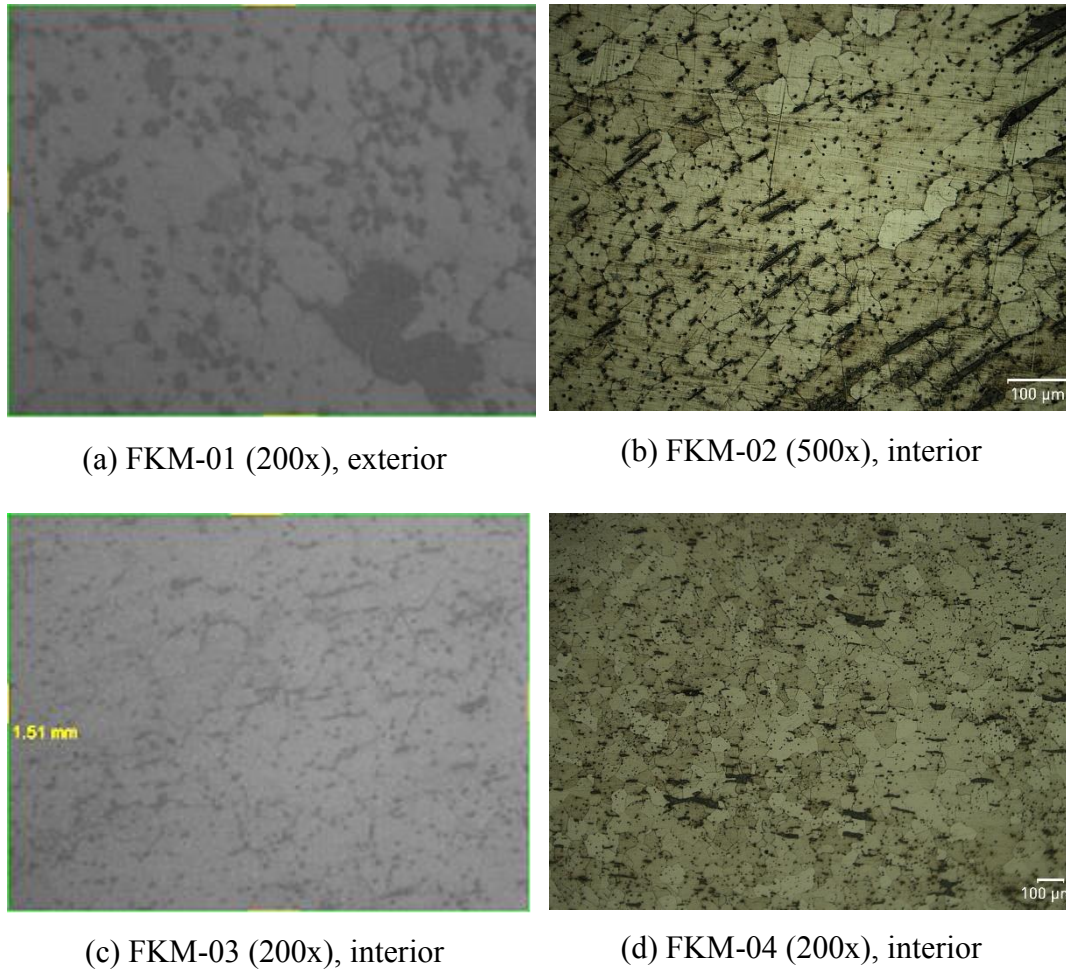
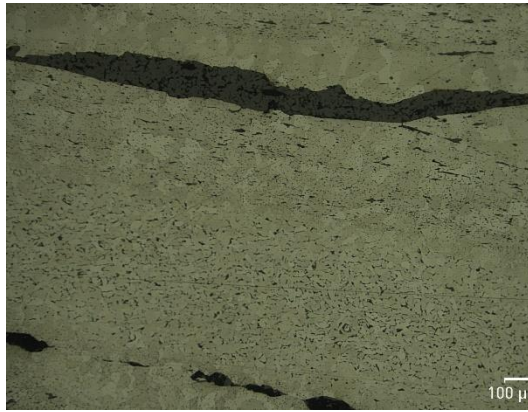
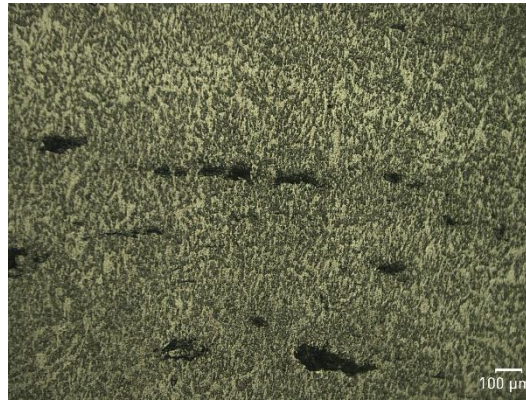


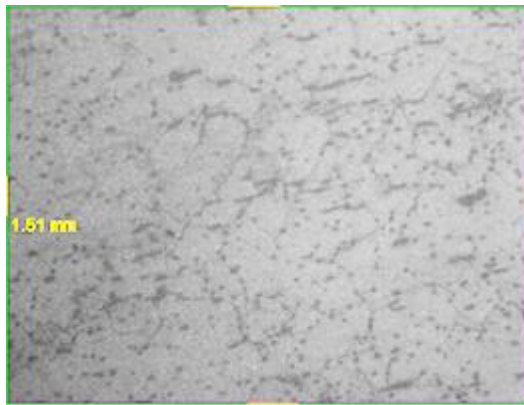
Figure 4. 26 Microstructural images of iron samples by Nikon metallographic microscope (a, c) and Huvitz digital microscope (b, d) after etching with nitric acid in alcohol (19th cc).



(e) FKM-05 (200x), interior



(f) FKM-07 (200x), buried



(g) FKM-08 (200x), buried



(h) FKM-09 (500x), buried

Figure 4. 27 Microstructural images of iron samples by Nikon metallographic microscope (g) and Huvitz digital microscope (e, f, h) after etching with nitric acid in alcohol (19th cc).

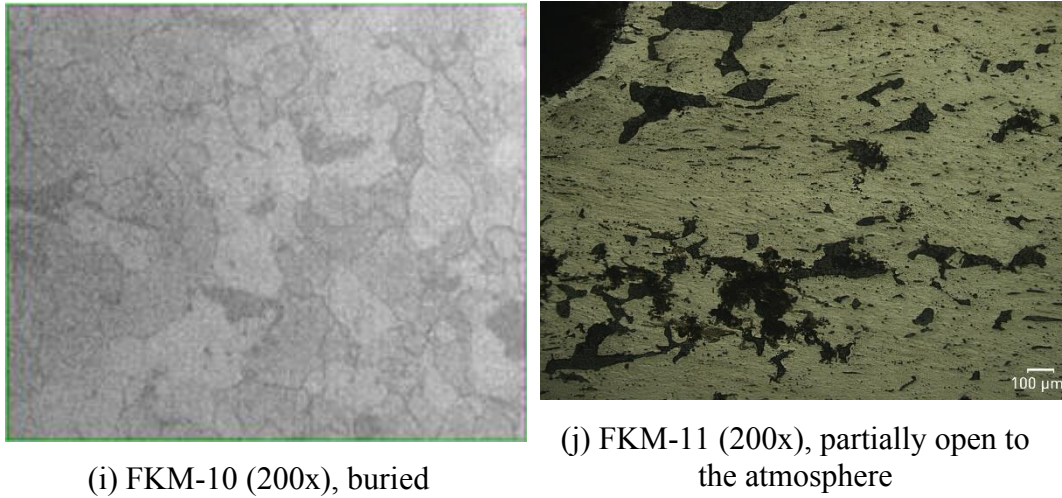


Figure 4. 28 Microstructural image of iron samples by Nikon metallographic microscope (i) and Huvitz digital microscope (j) after etching with nitric acid in alcohol (19th cc).

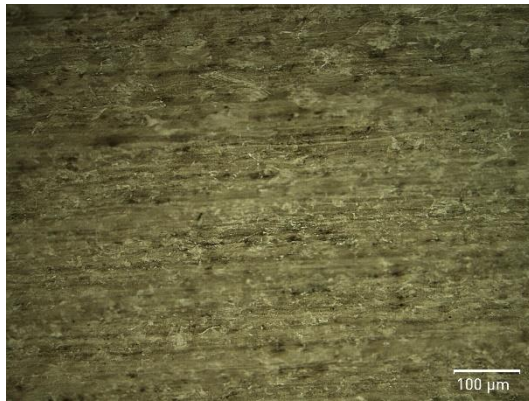
A nail and a door lock piece (T-N-01 and T-D-01 respectively) from the dwelling in Tekkekoy, Samsun, have 98.4% - 96% total ferrite and 14.9% - 36% pearlite respectively. The nail sample (T-N-05) has ferritic and pearlitic structure, but it has more ferritic grains than the door lock piece (T-D-01). The nail sample (T-N-05) has little amount of corrosion / slag fragments. A window hinge sample (T-W-01) has pearlitic structure, corrosion / slag fragments and locally deep corrosion fragments. The hardness values of Tekkekoy iron samples are in medium hard and very hard range (from 202 HB to 290 HB). The two nails (T-N-01 and T-N-05) have hardness values of 219 HB and 210 HB respectively. The door lock piece (T-D-01) from the same dwelling has a hardness value of 202 HB and a window hinge pin (T-W-01) has the hardness value of 290 HB, being in very hard range.



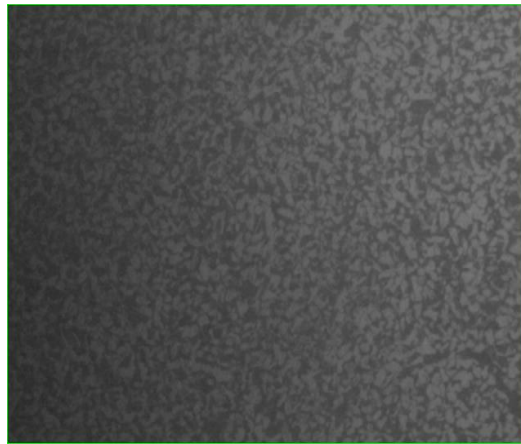
(k) T-N-01 (200x), exterior



(l) T-N-05 (100x), exterior



(m) T-W-01 (500x), interior



(n) T-D-01 (200x), interior

Figure 4. 29 Microstructural images of iron samples by Nikon metallographic microscope (l, n) and Huvitz digital microscope (k, m) after etching with nitric acid in alcohol (19th cc).

The nail from the 15th century Gazi Mihal Hammam has the lowest hardness (91 HB) and has ferritic microstructure. The three nails (MSH-KAP-01, -09 and -13) from the 16th century hammam have hardness values in the soft range. Their hardness values are in the range of 125 – 133 HB. They all have ferritic microstructure. 16th century nails (MSH-KAP-03, -04, -08, -12) have hardness values of 162 HB to 181 HB in the in the medium hardness range. The 19th century nails (FKM-02, FKM-10 and FKM-11) from Foça have the lowest hardness values in the soft range between 101

HB – 133 HB. They also have ferritic structure. The door lock piece (FKM-03) from Foça having a hardness value of 129 HB being in soft range has also ferritic structure. Some excavated iron components from the Ottoman layer of Foça have very low hardness (FKM-08 114 HB and FKM-09 95 HB) and they have ferritic structure. Thus, the results show that Brinell hardness values in the soft range are related with the ferritic structure.

Table 4. 16 Microstructural analyses and Brinell hardness results of iron samples from 19th century.

Sample Code	Microstructure	Average Brinell Hardness (HBS)
FKM-01 Iron bar of a window guard from a stone dwelling, exterior	<ul style="list-style-type: none"> • 87.5 % Pearlitic structure with 12.5% cementite • Ferrite grain boundaries are particular. Ferrite grains are ~150 μm • Corrosion fragments in dot forms • Corrosion fragments between ferrite grain boundries, probably due to rolling crack 	156 - medium hard
FKM-02 Nail for jointing load bearing, main timber beams, interior	<ul style="list-style-type: none"> • Mostly ferritic structure, ~10% pearlite • Ferrite grain boundaries elongated due to forging are observable. Ferrite grains are ~50 μm. • Corrosion/ slag fragments 	133 - soft
FKM-03 Door lock piece from main entrance, interior	<ul style="list-style-type: none"> • Ferritic structure. Ferrite grains are ~100 μm. • Ferrite grain boundaries oriented due to forming / forging method are observable • Ferrite grains without normal cell structure • Corrosion fragments in dot forms • Corrosion fragments between ferrite grain boundries 	129 - soft
FKM-04 Male hinge for main entrance door, interior	<ul style="list-style-type: none"> • 87.5 % Pearlitic structure with 12.5% cementite • Ferrite grain boundaries oriented due to forming / forging method are observable. Ferrite grains are ~70 μm. • Corrosion / slag fragments. Corrosion fragments in dot forms • Corrosion fragments between ferrite grain boundries, probably due to applied production technique 	164 – medium hard
FKM-05 Female hinge for main entrance door, interior	<ul style="list-style-type: none"> • Ferritic structure. Ferrite grains are ~25 μm. • Ferrite grain boundaries oriented due to forging are not easily observable • Corrosion / slag fragments 	160 - medium hard

Table 4.16. Microstructural analyses and Brinell hardness results of iron samples from 19th century (continued).

Sample Code	Microstructure	Average Brinell Hardness (HBS)
FKM-07 Nail, from Ottoman layer, buried	<ul style="list-style-type: none"> • Ferritic structure with around 10% pearlite • Ferrite grain boundaries are observable. Ferrite grains are ~120 μm • Some corrosion/ slag fragments • Less elongation of ferrite grains 	199 – medium hard
FKM-08 L shaped iron piece, buried	<ul style="list-style-type: none"> • Ferritic structure. Ferrite grains are ~130 μm • Ferrite grain boundaries oriented due to forging method are observable • Ferrite grains without normal grain structure • Corrosion / slag fragments 	115 - soft
FKM-09 Iron piece, from Ottoman layer, buried	<ul style="list-style-type: none"> • Ferritic structure • Ferrite grain boundaries oriented due to forming / forging method are observable • Corrosion / slag fragments with some deep local corrosion areas • Corrosion fragments in dot forms with some deep corrosion fragments between ferrite grain boundaries are observable 	< 94 -very soft
FKM-10 Nail, from Ottoman layer, buried	<ul style="list-style-type: none"> • Ferritic structure • Elongated ferrite grain boundaries are observable • Deep local corrosion fragments between ferrite grain boundaries at the sample's surface 	101 - soft
FKM-11 Nail, from a stone dwelling, partially open to atmosphere	<ul style="list-style-type: none"> • Ferritic structure. Ferrite grains are ~100 μm • Elongated ferrite grain boundaries are observable • Some dot-formed corrosion fragments 	117 - soft
T-N-01 Iron nail, from timber column, exterior	<ul style="list-style-type: none"> • 98.4% total ferrite with 14.9% pearlite. Ferrite grains are ~45 μm • Probably heat treated 	219 – medium hard
T-N-05 Iron nail, from timber column, exterior	<ul style="list-style-type: none"> • Mostly pearlitic structure • Stressed structure • Possibly repair material dating from recent times 	210 – medium hard
T-D-01 Iron crossbar of main entrance door locking, interior	<ul style="list-style-type: none"> • 96% total ferrite and 36% pearlite. Ferrite grains are ~30 μm • Ferrite grain boundaries are observable • Large corrosion / slag fragments 	202 – medium hard
T-W-01 Iron hinge pin, from entrance hall, interior	<ul style="list-style-type: none"> • %100 pearlitic structure • Corrosion / slag fragments • Deep local corrosion fragments • Possibly repair material dating from recent times 	290 – very high hardness

4.3.2 Morphological and Compositional Characteristics of the Corrosion Layers

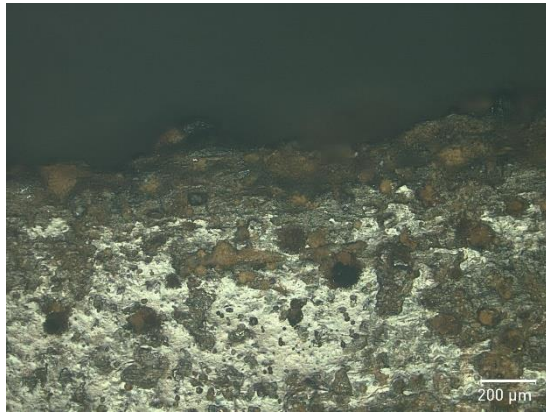
Morphological characteristics of corrosion body on the metal surface were investigated in terms of thickness, compactness, porosity and layering next to the metal body by using SEM and digital microscope views. Starting from the metal, corrosion layers identified are reaction front (RF) next to the metal body, inner corrosion layer (ICL) and transformed media (TM). The compositional characteristics of those layers were studied by μ -Raman spectroscopy, XRD and FTIR. The ratio between thickness of the protective corrosion layer which is considered as goethite rich layer and thickness of the total corrosion layer is used to identify Protective Ability Index (PAI) of the corrosion on the surface of the metal.

EDX analyses of the corrosion layers were effectuated to detect the presence of some important elements in the corrosion layer. All the observations and analyses are given in the following sections starting with morphological characteristics of the corrosion:

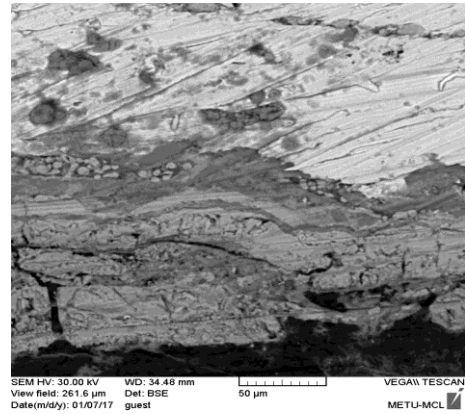
4.3.2.1 SEM-EDX and Digital Microscopic Views of Corrosion Layers

Etched cross-sections of the corroded iron objects were analyzed in the images of digital microscope and SEM complementing each other. The typical samples of iron objects from 15th, 16th and 19th centuries have been observed and compared regarding the morphological characteristics of corrosion layers. The results are summarized in Table 4.17, 4.21 and 4.22.

The corrosion characteristics of the 15th century iron objects were examined on the selected three objects. The digital microscopic image of the door lock piece (GMH-Me-02) from the 15th century hammam building shows a compact and distinct corrosion layer (Figure 4.30.a). The inner corrosion layer (ICL) thickness of the mentioned sample is between 100-200 μm . The back scattered SEM view supports the compact nature of ICL with a thickness of 100-200 μm . While the first half of the ICL next to the metal is observed free of cracks, the second half has some fine cracks in its compact structure (Figure 4.30.b). Two plaster nails from the interior of the hammam building were examined for the corrosion at their exposed heads. The digital microscopic view of the plaster nail (GMH-Me-03) presents a well observed ICL with a compact structure having a thickness of 200-250 μm (Figure 4.30.c). The first half of the ICL is almost free of cracks while the second half is observed to have some fine cracks and pores within the compact structure. A back scattered SEM image of another plaster nail from interior (GMH-Me-04) shows a lower ICL thickness of 50-100 μm (Figure 4.30.d) where its inner part is also more compact than the outer part. The inner part of the ICL of the 15th century iron objects is observed to be more compact in comparison to the outer part (Figure 4.30.a, b).



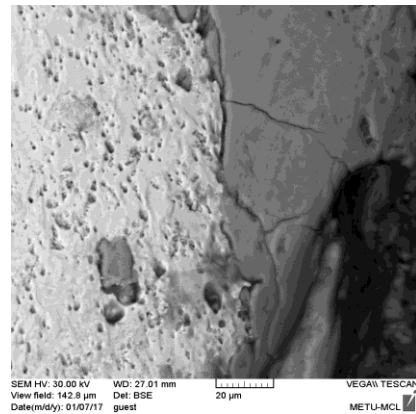
(a) GMH-Me-02 (200x), interior



(b) GMH-Me-02 (750x), interior



(c) GMH-Me-03 (500x), interior



(d) GMH-Me-04 (2000x), interior

Figure 4. 30 Digital microscopy images (a, c) and SEM images (b, d) of iron samples after etching with nitric acid in alcohol (15th cc).

Two samples (GMH-Me-02 and 04) of the 15th century's iron objects were analyzed by using SEM-EDX (Figure 4.31 & 4.32). The door lock piece (GMH-Me-02) has a considerably thick corrosion layer in comparison to the plaster nail (GMH-Me-04). Its EDX analysis starting from the metal body through the TM layer shows that iron, silicon, calcium, aluminum, potassium, magnesium, and chlorine are the main elements in the corrosion layer (Figure 4.31). The plaster nail from the interior wall (GMH-Me-04) has a quite low corrosion thickness compared to other iron objects of the same century. Its EDX analysis shows the presence of iron, silicon, manganese,

chromium, aluminum and sulfur elements in the corrosion layer (Figure 4.32). Both analyses were performed in a selected area starting from the metal body through the TM layer.

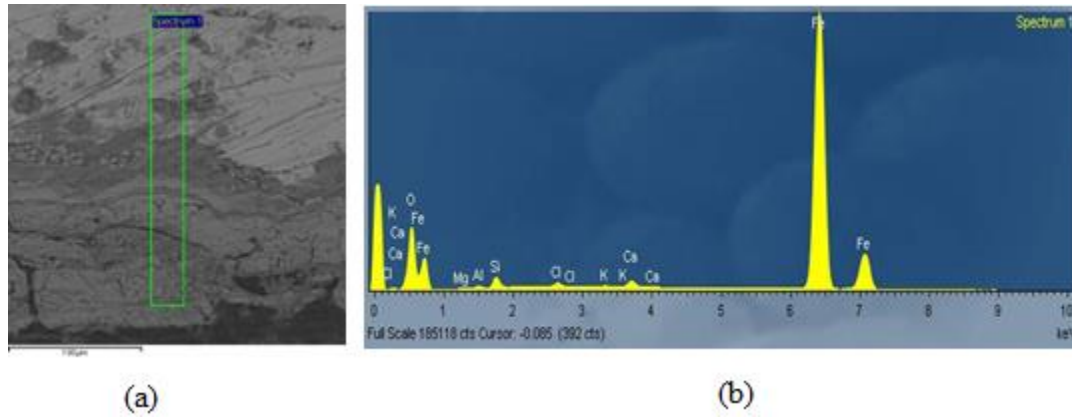


Figure 4. 31 a) SEM image of a door locking iron piece (GMH-Me-02): elemental analysis area starting from metal body to the TM layer. b) EDX analysis results: Fe, Si, Ca, Al, K, Mg and Cl.

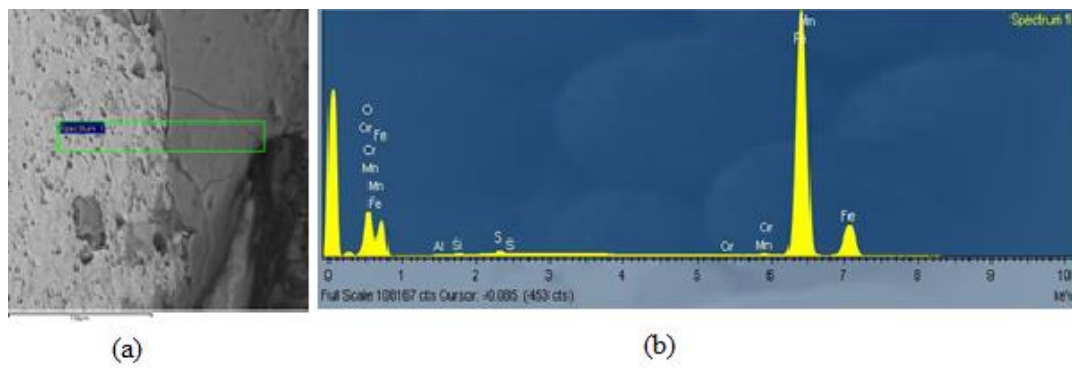
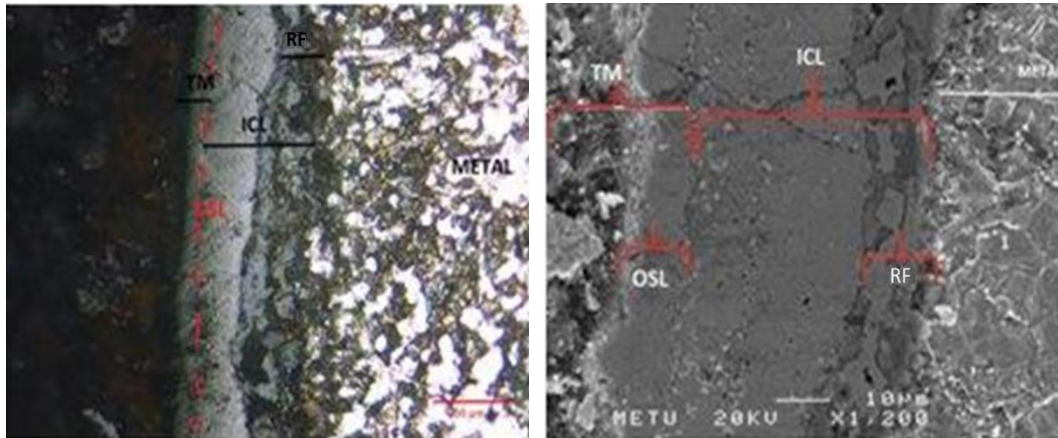


Figure 4. 32 a) SEM image of a plaster nail (GMH-Me-04): elemental analysis area starting from metal body to TM Layer. b) EDX analysis: Fe, Si, Mn, Cr, Al and S.

Table 4. 17 Morphological characteristics and thickness of corrosion layers for the samples from 15th century.

Sample Code	Corrosion Layer Characteristics	Inner Corrosion Layer (ICL) Thickness (μm)
GMH-Me-02 Door lock piece, interior	<ul style="list-style-type: none"> • Compact and distinct corrosion layer • The first half of the ICL free of cracks • The second half has some fine cracks • Fe, Si, Ca, Al, P, Mg and Cl are observed in the corrosion layer 	100-200
GMH-Me-03 Nail, interior	<ul style="list-style-type: none"> • Compact and distinct corrosion layer • The first half of the ICL almost free of cracks • The second half is observed to have some fine cracks and pores 	200-250
GMH-Me-04 Nail, interior	<ul style="list-style-type: none"> • Compact and distinct corrosion layer • The first half of the ICL free of cracks • The second half has some fine cracks in its compact structure • Fe, Si, Mn, Cr, Al and S elements in the corrosion layer 	50-100

Corrosion layers of six iron objects from the 16th century belonging to a hammam building were analyzed morphologically by using SEM and digital microscopy. Digital microscopic view of a nail sample used at the exterior of the dome at the hammam building (MSH-KAP-01) reveals a compact, very well observed corrosion layer having a light-colored isotropic band in it (Figure 4.33a). Several sub-layers in the compact corrosion layer are clearly identified in backscattered SEM images starting from the metal body as follows: a reaction front next to the metal (RF), inner corrosion layer (ICL), original surface layer (OSL) and transformed media (TM) (Figure 4.33b). The ICL thickness is around 50 μm including 10 μm thickness of RF.

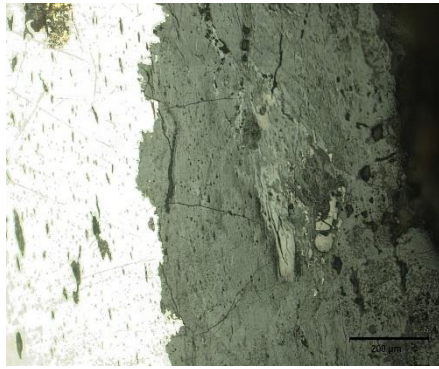


(a) MSH-KAP-01 (500x)

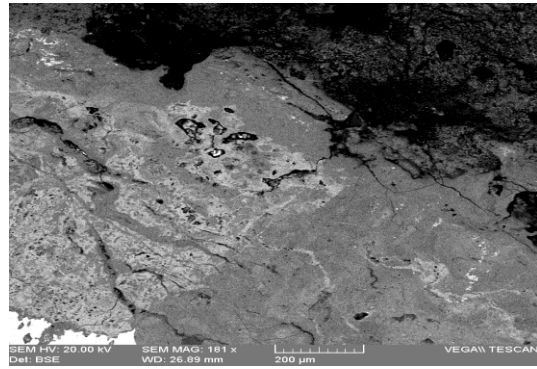
(b) MSH-KAP-01 (1200x)

Figure 4. 33 Digital microscopy image (a) and SEM image (b) of iron nail after etching with nitric acid in alcohol (16th cc).

An iron object (MSH-KAP-02) having a bent form used for jointing the other metals to the wall, situated at the interior has a compact corrosion layer with some cracks and pores detected by digital microscope and SEM backscattered views (Figure 4.34 a, b). The thickness of the corrosion layer is around 700-800 μm which is much thicker than the corrosion layer observed at the nail (MASH-KAP-01) from the exterior of the dome.



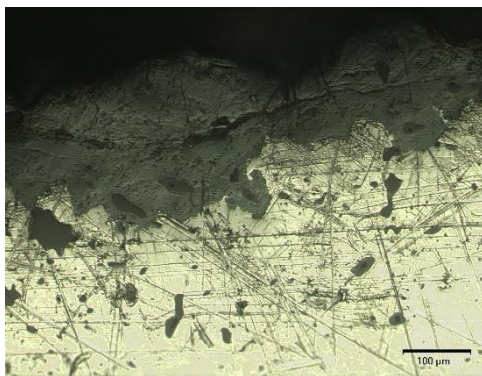
(a) MSH-KAP-02 (2360x)



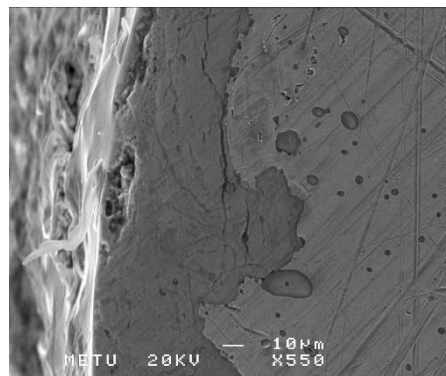
(b) MSH-KAP-02 (181x)

Figure 4. 34 Digital microscope image (a) and SEM image (b) of an iron object after etching with nitric acid in alcohol (16th cc)

Another nail sample collected from the exterior of the dome at the Kılıç Ali Paşa Hamamı (MSH-KAP-03) has a well identified and compact corrosion layer with ICL thickness around 50-150 μm (Figure 4.35 a, b). The sublayers are not well distinguished as in the other nail from the exterior of the dome (MSH-KAP-01). Its thickness and compactness are comparable to those of the exterior nail while the corrosion layer of the interior iron object is less compact with some cracks and pores.



(a) MSH-KAP-03 (560x)



(b) MSH-KAP-03 (550x)

Figure 4. 35 Digital microscopy image (a) and scanning electron microscopy (SEM) image (b) of a nail sample after etching with nitric acid in alcohol (16th cc).

Corrosion layer of an iron object embedded in mortar but used at the interior of the hammam (MSH-KAP-06) has a compact corrosion layer with some cracks and pores in it (Figure 4.36). Its ICL thickness is around 50-100 μm as seen at the digital microscopy images.

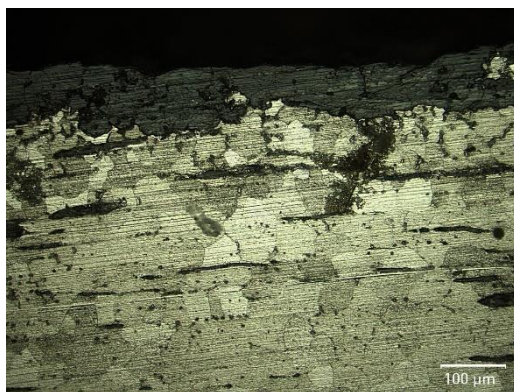


Figure 4. 36 Digital microscopy image of an iron object embedded in mortar (MSH-KAP-06) at the interior of the hammam after etching with nitric acid in alcohol (500x) (16th cc),

Corrosion layer of a nail embedded in the mortar of a stone masonry wall at the interior of the hammam (MSH-KAP-07) is observed to have a compact corrosion layer having the ICL thickness around 250 μm (Figure 4.37). The compact layer is almost free of crack and porous areas.

Another nail from the interior of the hammam building, (MSH-KAP-12) has also a compact corrosion layer with some cracks and porous areas in it (Figure 4.38 a, b). The ICL thickness is variable being around 100 μm - 300 μm , as observed with SEM and digital microscopic images.

Observations of the corrosion layers show that the iron samples from the exterior of the hammam exposed to atmospheric conditions have a compact corrosion layer where inner corrosion layer (ICL) and transported media (TM) are well observed. In addition, in one of the samples (MSH-KAP-01), reaction front (RF) and original surface layer (OSL) are also well distinguished. The corrosion layers of iron samples

from interiors, despite being compact, include some areas with cracks and pores. However, all interior iron samples have quite similar corrosion layer thicknesses with the exception of the bent iron object (MSH-KAP-02). It has much thicker corrosion layer than the others with cracks and porous regions in it.

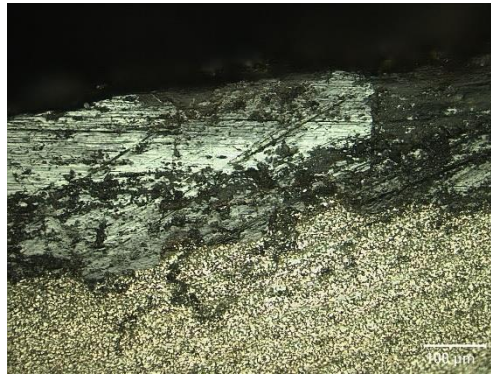
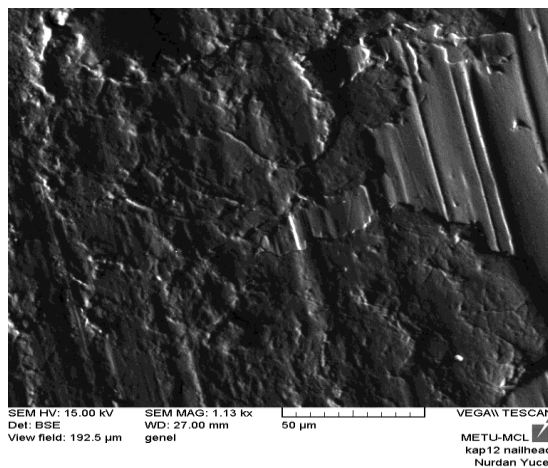
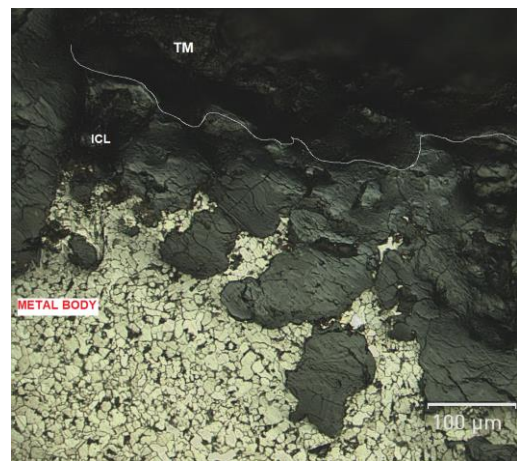


Figure 4. 37 Digital microscopy image of a nail embedded in the mortar of stone masonry (MSH-KAP-07) after etching with nitric acid in alcohol (500x), (16th cc).



(a) MSH-KAP-12 (1130x)



(b) MSH-KAP-12 (500x)

Figure 4. 38 SEM image (a) and digital microscopy image (b) of a nail at the interior of the hammam building, after etching with nitric acid in alcohol (16th cc).

Compositional characteristics of the corrosion layers were examined for four samples of the 16th century iron objects by SEM-EDX. Line scanning analysis performed from the transformed media (TM) to the interiors is not sensitive to the distance and gives semi-quantitative information about the elemental composition in the defined area. For the nail from the dome (MSH-KAP-01), starting from the metal body, following RF, ICL, OSL and TM, the elemental composition has undergone some changes. “Point 1” before the reaction front as well as “point 2 and 5” in reaction front (RF) have the presence of iron, calcium, silicon, magnesium and manganese” (Figure 4.39, 4.40 and 4.41). In the “points 3 and “4” situated in ICL (Figure 3.16) “iron” is the only element identified (Figure 4.42). In the transformed media, line scanning analysis shows the presence of iron, silicon, magnesium, manganese, phosphorous, sulfur and calcium elements (Figure 4.43) where the amounts of calcium and sulfur are noticeable.

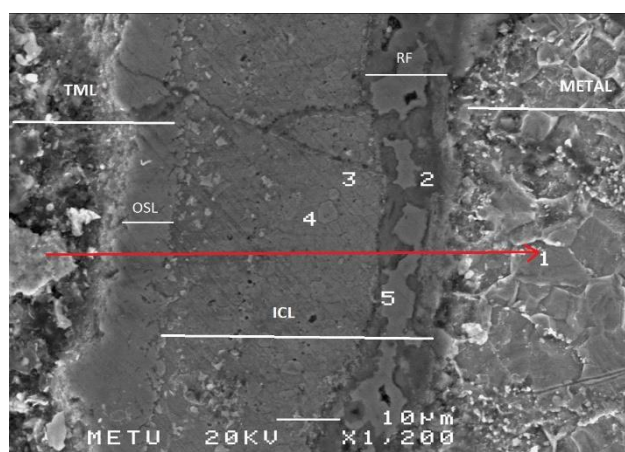


Figure 4. 39 SEM image of a nail head (MSH-KAP-01) showing three main layers: Metal, ICL including RF and TM Layers. Numbers indicate the EDX analysis locations. Red arrow presents the area where line-scan was performed.

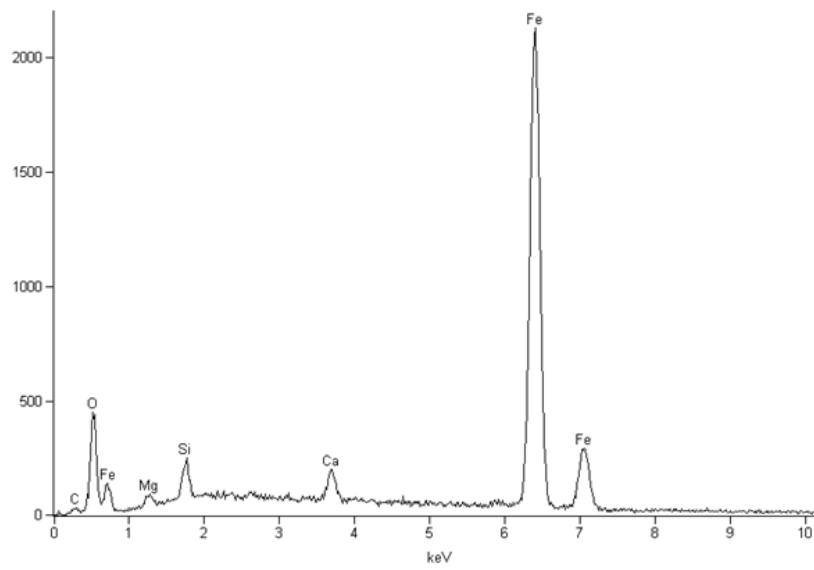


Figure 4. 40 EDX spectrum of an iron nail (MSH-KAP-01) at point 1 in reaction front: Fe, Ca, Si and Mn (16th cc).

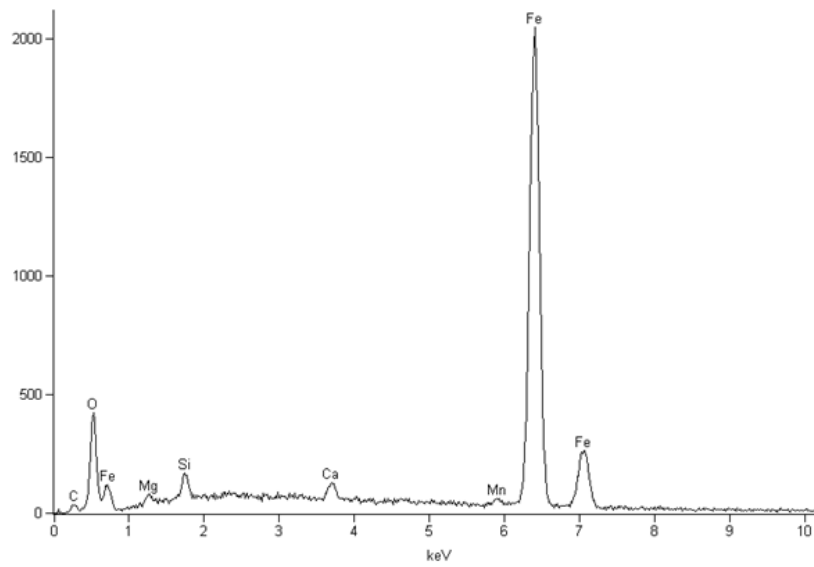


Figure 4. 41 EDX spectrum of an iron nail (MSH-KAP-01) at point 5 in reaction front: Fe, Ca, Si and Mn (16th cc).

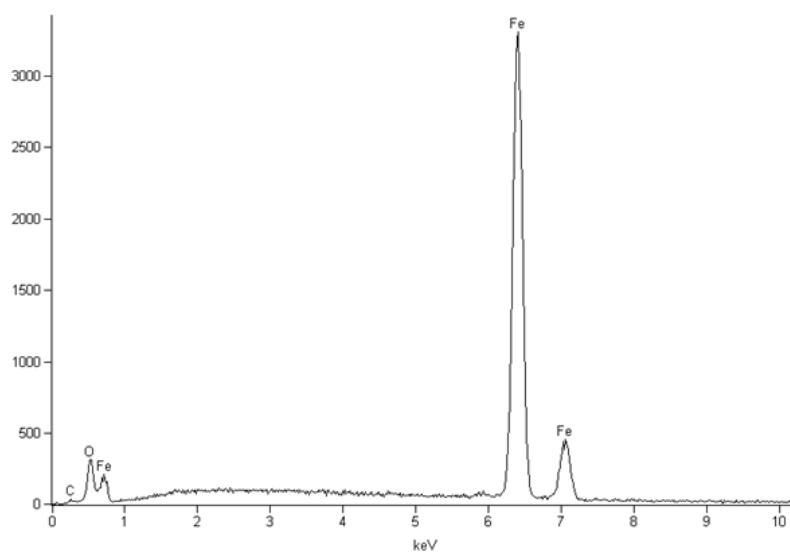


Figure 4. 42 EDX spectrum of an iron nail (MSH-KAP-01) at points 3 and 4 in inner corrosion layer (ICL): Fe and O (16th cc).

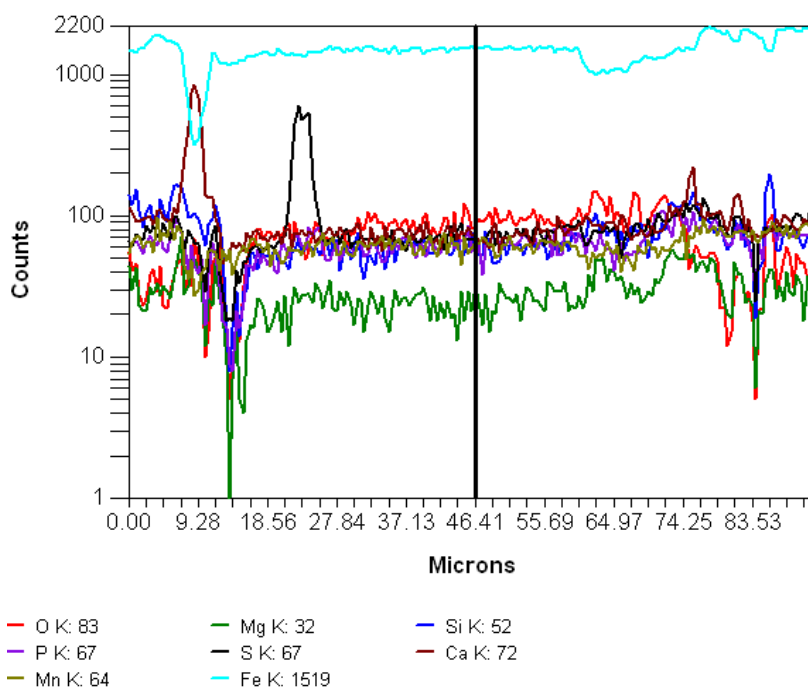


Figure 4. 43 EDX line scan spectrum of an iron nail (MSH-KAP-01) starting from transformed media (TM) to the main metal body (16th cc).

The total corrosion layer of the sample used for eventual anchoring purposes from inside the hammam building (MSH-KAP-02) having a thick corrosion layer being exposed to humidity continuously inside the hammam building was examined by EDX. The EDX analysis at corrosion layer next to the metal body RF was performed on the SEM imaged location (Figure 4.44) and iron, calcium, magnesium, sodium and sulfur are the main elements observed (Figure 4.45). Their weight percentages are identified in the composition where calcium oxide (CaO) is the main compound revealed after iron oxides (Table 18). Starting from the transformed media (TM) to body metal, line scanning was performed to witness the overall element change in the iron sample (Figure 4.46 and Figure 4.47). Calcium is the majority observed impurity in the corrosion layer where a deep crack is located. When focused on the crack point (Figure 4.48), EDX analysis revealed that iron, calcium, oxygen and aluminum were the main elements observed (Figure 4.49). Once again, calcium oxide (CaO) was the most abundantly identified impurity after iron oxides in the crack location (Table 19). It has been observed that other crack locations also contain a high amount of calcium whereas calcium is not present at the locations with no crack in ICL.

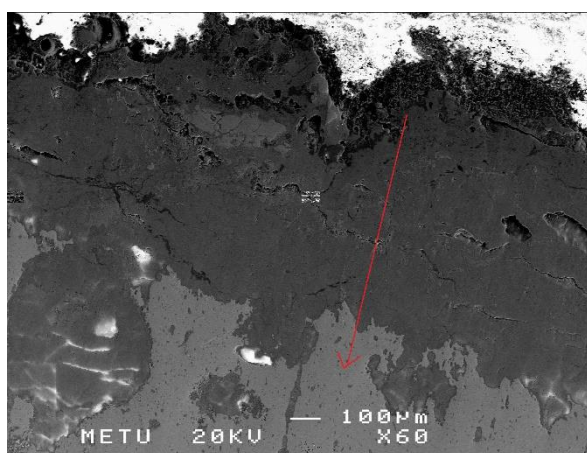


Figure 4. 44 SEM of image of total corrosion layer next to the metal body of an iron sample (MSH-KAP-02) (60x). Red arrow represents the area where line scan is performed.

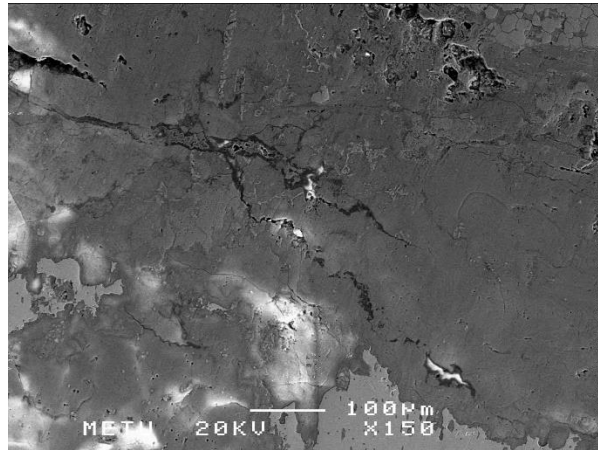


Figure 4. 45 SEM image of reaction front (RF) next to the metal body in the iron object (MSH-KAP-02) (150x).

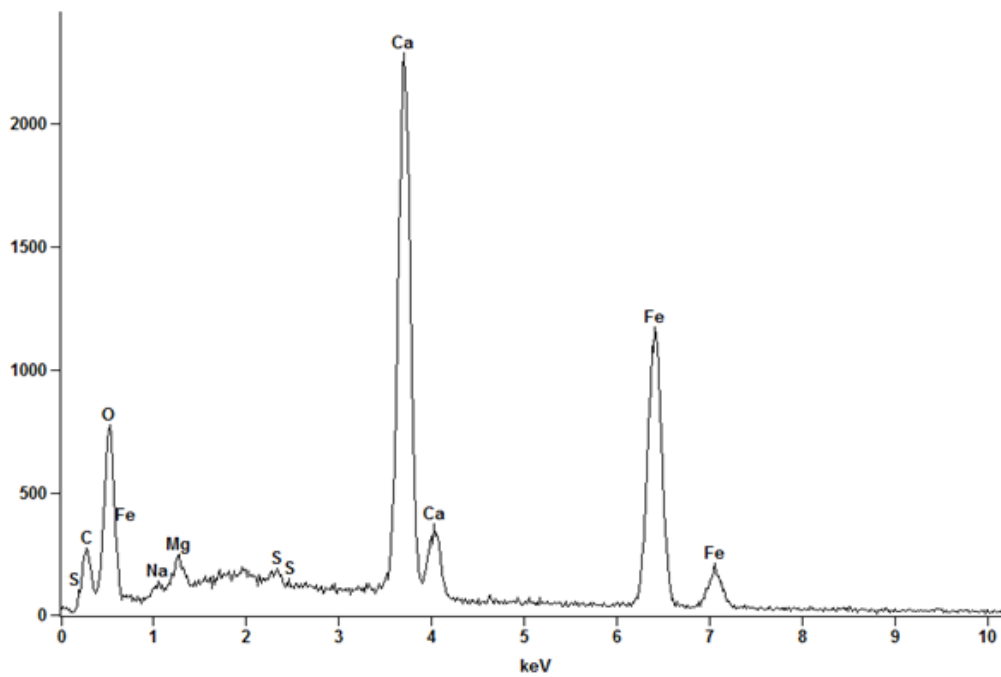


Figure 4. 46 EDX analysis of the reaction front (RF) next to the metal body (MSH-KAP-02): Ca, Fe, Mg, Na, O and S.

Table 4. 18 Weight percentage of elements in the composition of RF (MSH-KAP-02) analyzed by EDX (16th cc).

Element	Weight Conc. %	Atom Conc. %	Compound Conc. %	Formula
O	30.19	54.64	0.00	
Na	1.70	2.15	2.30	Na ₂ O
Mg	2.51	2.99	4.16	MgO
S	0.60	0.55	1.51	SO ₃
Ca	29.31	21.18	41.02	CaO
Fe	35.68	18.50	51.02	Fe ₂ O ₃

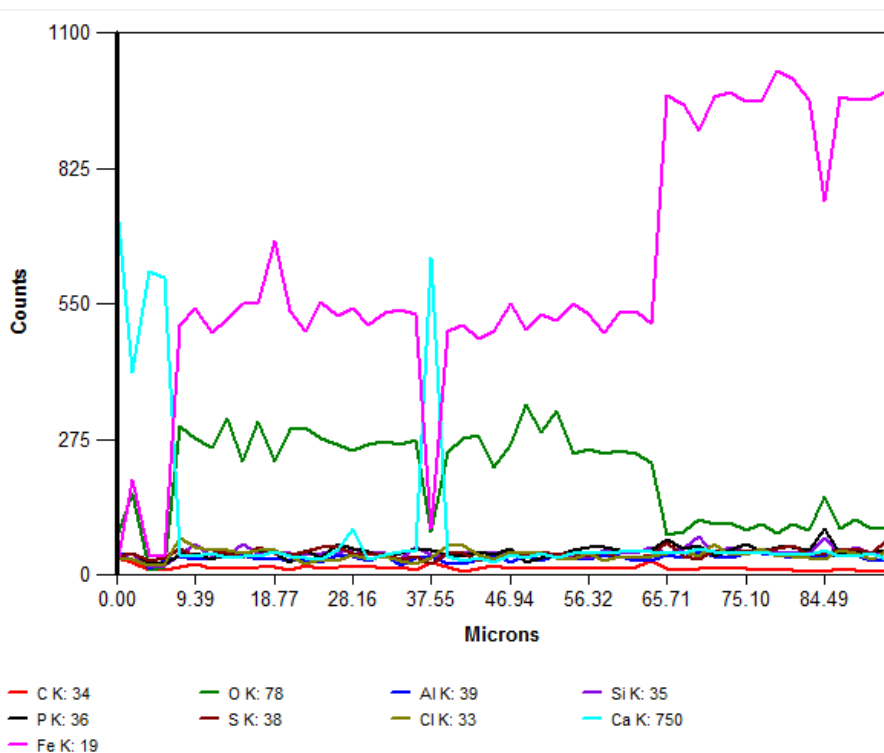


Figure 4. 47 EDX line scan spectrum of an iron object (MSH-KAP-02) starting from transformed media (TM) to main metal body: calcium is the most abundant impurity in the corrosion layer.

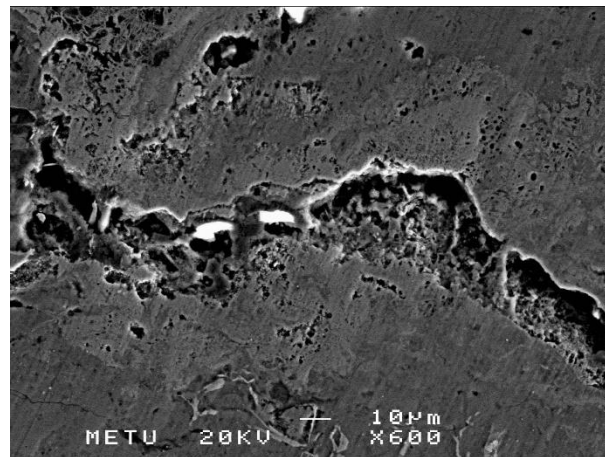


Figure 4. 48 SEM image of a deep crack inside the inner corrosion layer of an iron object (MSH-KAP-02) (600x).

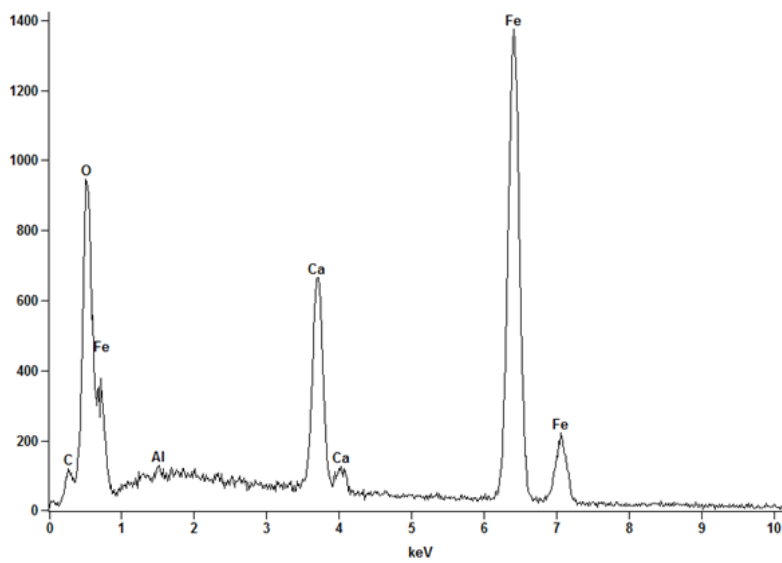


Figure 4. 49 EDX analysis at the crack (MSH-KAP-02): Fe, Ca, O and Al.

Table 4. 19 Weight percentage of the elements in the composition of the crack location (MSH-KAP-02) analyzed by EDX (16th cc).

<i>Element</i>	<i>Weight Conc. %</i>	<i>Atom Conc. %</i>	<i>Compound Conc. %</i>	<i>Formula</i>
<i>O</i>	29.93	58.25	0.00	
<i>Al</i>	0.34	0.40	0.65	Al ₂ O ₃
<i>Ca</i>	11.29	8.77	15.80	CaO
<i>Fe</i>	58.44	32.58	83.55	Fe ₂ O ₃

For another nail from the dome (MSH-KAP-03), starting from the metal body, following RF to TM, the elemental composition has undergone some changes. The reaction front has the presence of “iron, silicon, phosphorous, chlorine and calcium” (Figure 4.50). In the ICL “iron, silicon, aluminum, phosphorous, chlorine, sulfur and calcium” are the elements identified (Figure 4.51). Starting from the transformed media, line scanning analysis shows the presence of iron, silicon, calcium, sodium, phosphorous, aluminum, chlorine, magnesium and sulfur elements (Figure 4.52) where the amount of calcium is noticeable.

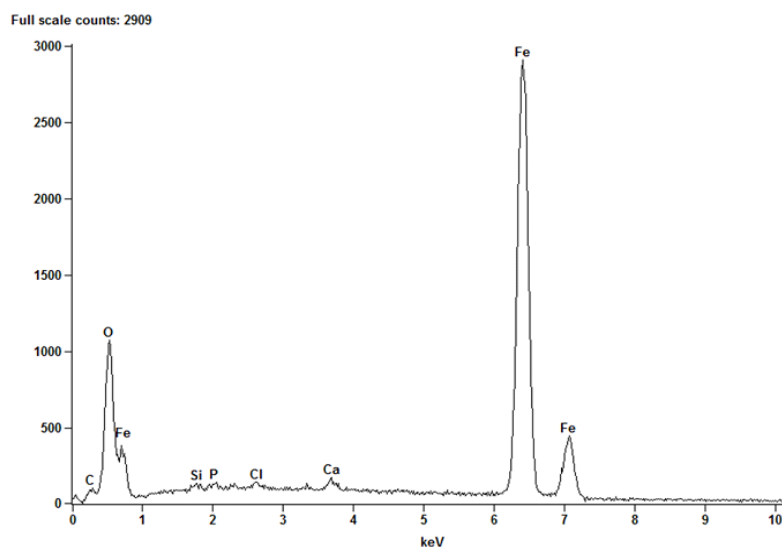


Figure 4. 50 EDX spectrum of the reaction front (RF) in an iron nail (MSH-KAP-03): Fe, Si, Ca, P and Cl (16th cc).

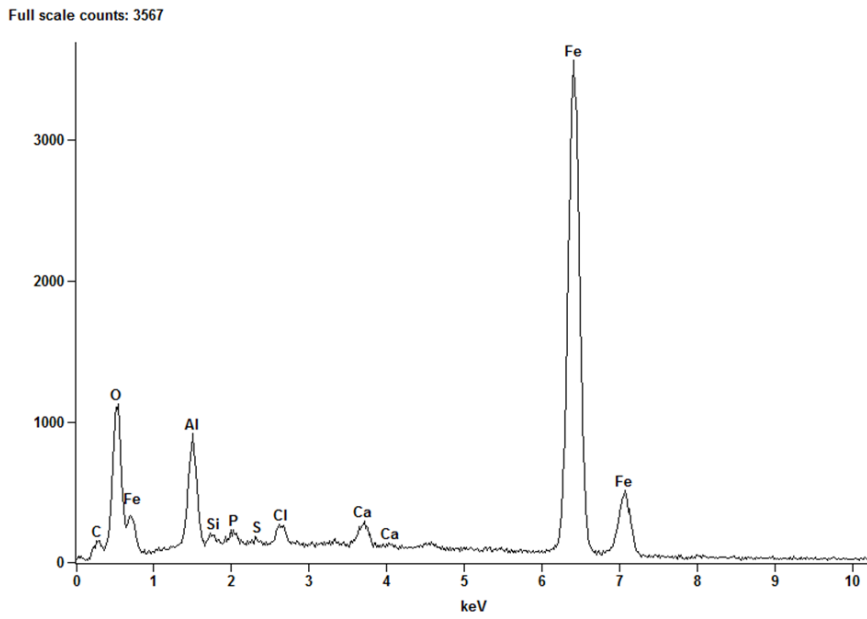


Figure 4. 51. EDX spectrum of a nail (MSH-KAP-03) at a point in the inner corrosion layer (ICL): Fe, Si, Ca, P and Cl.

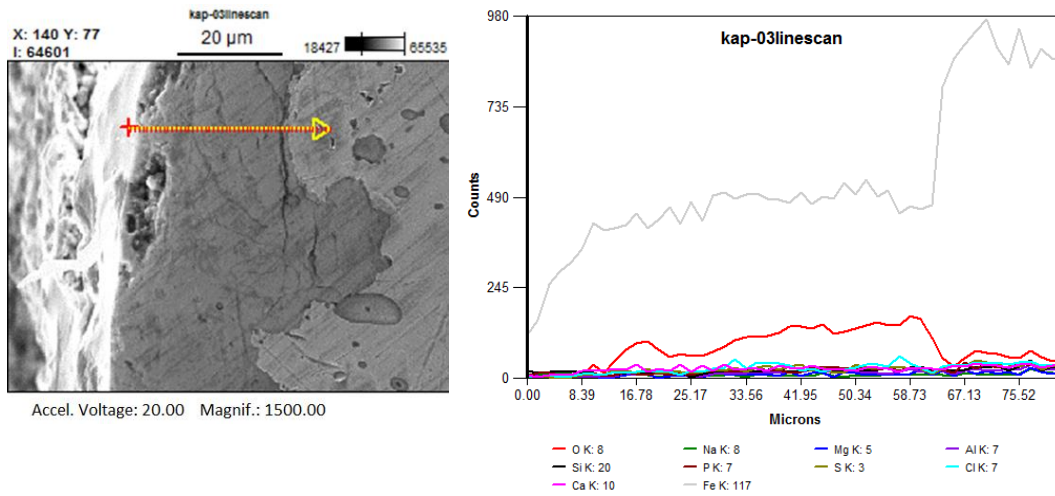


Figure 4. 52 SEM image and EDX line scan spectrum of the nail (MSH-KAP-03): starting from transformed media (TM) to main body: calcium is the most abundant impurity in the corrosion layer.

Another analysis of a nail (MSH-KAP-12) from inside the hammam building has been performed on a layer where ICL including RF in it were present. The inner Corrosion Layer (ICL) including Reaction front (RF) of the MSH-KAP-12 sample was studied and iron, oxygen, silicon, calcium, aluminum and manganese elements were examined in the ICL (Figure 4.53 a and b). The weight percentages of the elements were identified in the composition where calcium was the main compound revealed after iron (Table 4.20).

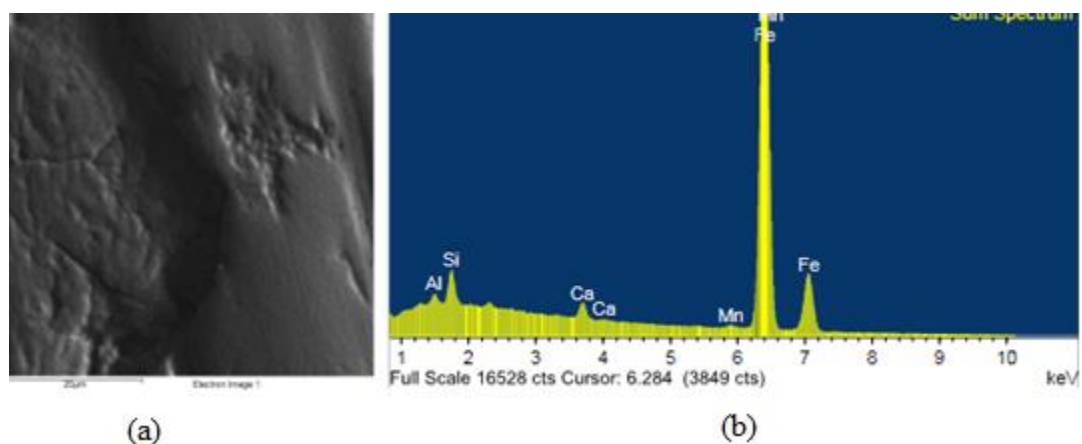


Figure 4. 53 (a) SEM image of the inner corrosion layer (ICL) in the iron nail (MSH-KAP-12) (16th cc). (b) EDX analysis at the ICL: Fe, O, Si, Ca, Al and Mn.

Table 4. 20 Weight percentage of elements in the composition from ICL of a nail (MSH-KAP-12) analyzed by EDX (16th cc).

Element	Weight Conc. %	Atom Conc. %
O	20.33	41.05
Al	0.27	0.32
Si	0.88	1.01
Ca	0.72	0.58
Mn	0.36	0.21
Fe	71.76	41.52

Table 4. 21 Morphological characteristics and thickness of corrosion layers for iron samples from 16th century.

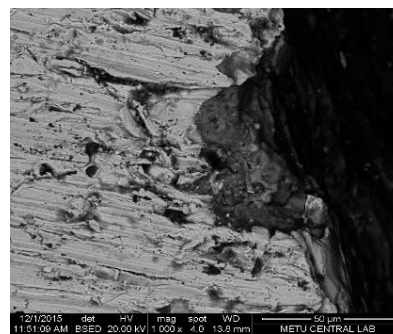
Sample Code	Corrosion Layer Characteristics	Inner Corrosion Layer Thickness (μm)
MSH-KAP- 01 Nail from the dome, exterior	<ul style="list-style-type: none"> • Compact, very well observed corrosion layer having a light-colored isotropic band in it • Several sub-layers in the compact corrosion layer are clearly identified • Fe, Si, Mg, Mn, P, S and Ca are elements observed in the corrosion layer • The amounts of calcium and sulfur are noticeable in the TM 	50
MSH-KAP- 02 Iron piece for an eventual anchoring, interior	<ul style="list-style-type: none"> • Compact corrosion layer • Some cracks and pores • Fe, Ca, Mg, Na and S are elements observed in the corrosion layer • Calcium is the majority observed impurity in the corrosion layer where a deep crack is located 	700-800
MSH-KAP- 03 Nail from the dome, exterior	<ul style="list-style-type: none"> • A well identified and compact corrosion layer • The sub-layers are not well distinguished as in the other nail from the exterior of the dome (MSH-KAP-01) • Less cracks than the iron objects from interior • Fe, Si, Ca, Na, P, Al, Cl, Mg and S are elements observed in the corrosion layer 	50-150
MSH-KAP- 06 Iron element for towel hanging, interior	<ul style="list-style-type: none"> • Compact corrosion layer • Some cracks and pores in it 	50-100
MSH-KAP- 07 Nail used in stone building, interior	<ul style="list-style-type: none"> • Compact corrosion layer • Almost free of crack and porous areas 	250
MSH-KAP-12 Nail used for timber jointing, interior	<ul style="list-style-type: none"> • Compact corrosion layer • Some cracks and porous areas in it • Fe, Si, Ca, Al and Mn are elements observed in the corrosion layer 	100-300

Corrosion layers of the 19th century iron objects consist of samples from Foça - İzmir dwellings and Tekkekoy - Samsun. Corrosion layer characteristics were examined in four objects of Foça samples being a load bearing nail for jointing main timber beams (FKM-02) (Figure 4.54 a, b); a female hinge for a main entrance door (FKM-05) (Figure 4.54 c); a nail piece (FKM-11) partially open to atmosphere from a stone house and a nail from an Ottoman layer excavation (FKM-07) (Figure 4.55

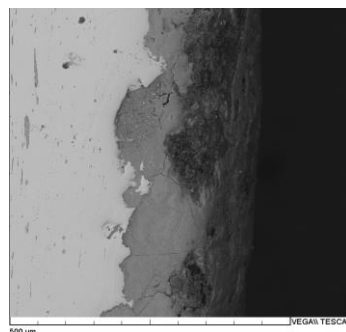
c, d and a, b). The nail used for jointing main timber (FKM-02) taken from the interior has a compact and well observed corrosion layer having ICL around 50-75 μ m thickness. The female hinge for the main entrance door (FKM-05) belonging to interiors has also a compact and well observed corrosion layer with an ICL around 100-125 μ m thickness. The nail sample (FKM-07) representing the burial condition and the nail (FKM-11) which was partially exposed to atmospheric conditions, both have thick corrosion layers with cracks and porous areas in it. The ICL of the nail sample (FKM-07) from a burial condition does not have a uniform compact layer and its thickness is variable between 350-600 μ m. The other nail sample (FKM-11) located in the lower part of the stone wall affected by dampness problems has the thickest ICL being around 1300 μ m with deep cracks.



(a) FKM-02 (1000x)



(b) FKM-02 (1000x)



(c) FKM-05 (353X)

Figure 4. 54 Digital microscopy image (a) and SEM images (b, c) of iron samples (FKM-02 and FKM-05) after etching with nitric acid in ethanol (19th cc).

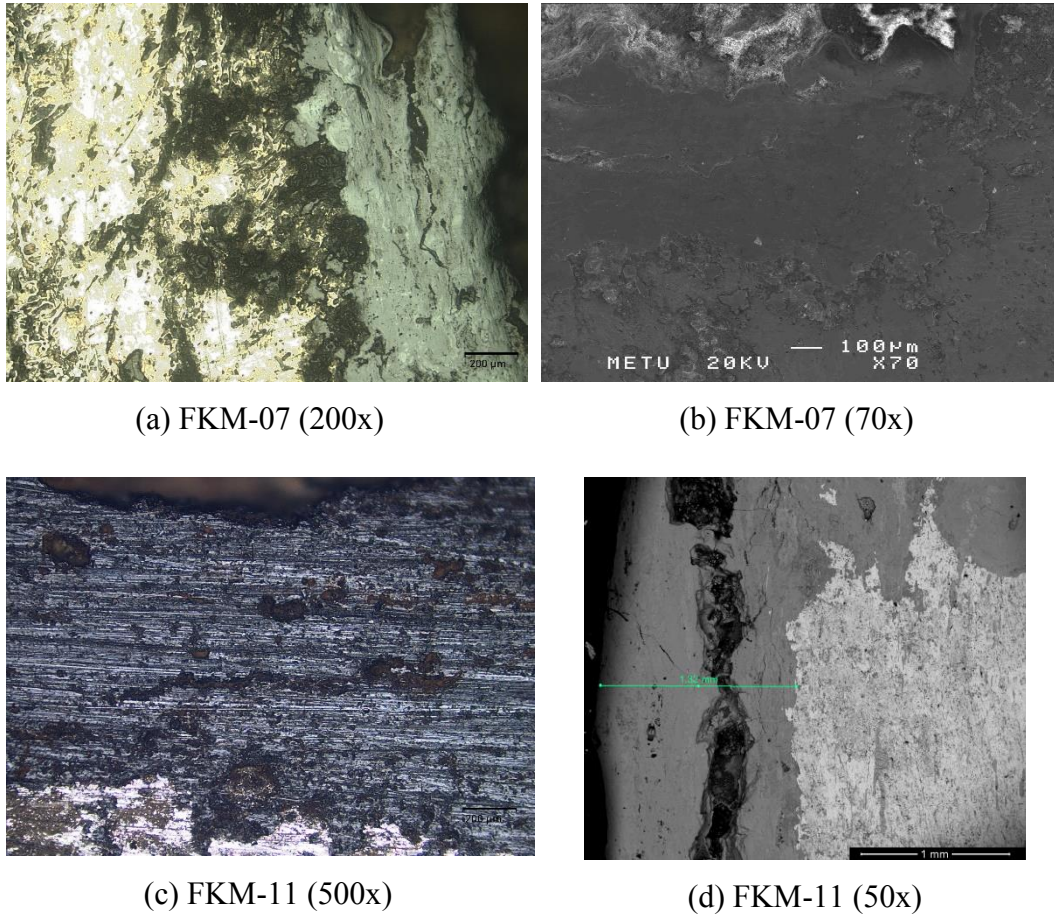


Figure 4.55 Digital microscopy images (a, c) and SEM images (b, d) of iron samples (FKM-07 and FKM-11) after etching with nitric acid in ethanol. FKM-07 is in burial conditions and FKM-11 is partially exposed to atmospheric conditions (19th cc).

Samples of 19th century collected from the interiors of a dwelling in Tekkekoy - Samsun consist of a window hinge pin (T-W-01) (Figure 4.56 a); an iron bar for door locking (T-D-01) (Figure 4.56 b) and a nail (T-N-04) (Figure 4.56 c, d). All three samples have compact, very well observed corrosion layers. While the door locking iron bar (T-D-01) has a uniform thickness of ICL being around 350 µm, the others have rather variable thicknesses. The ICL of the window hinge pin (T-W-01) has a thickness range of 150-300 µm and the nail sample (T-N-04) has a thickness range of 150-250 µm.

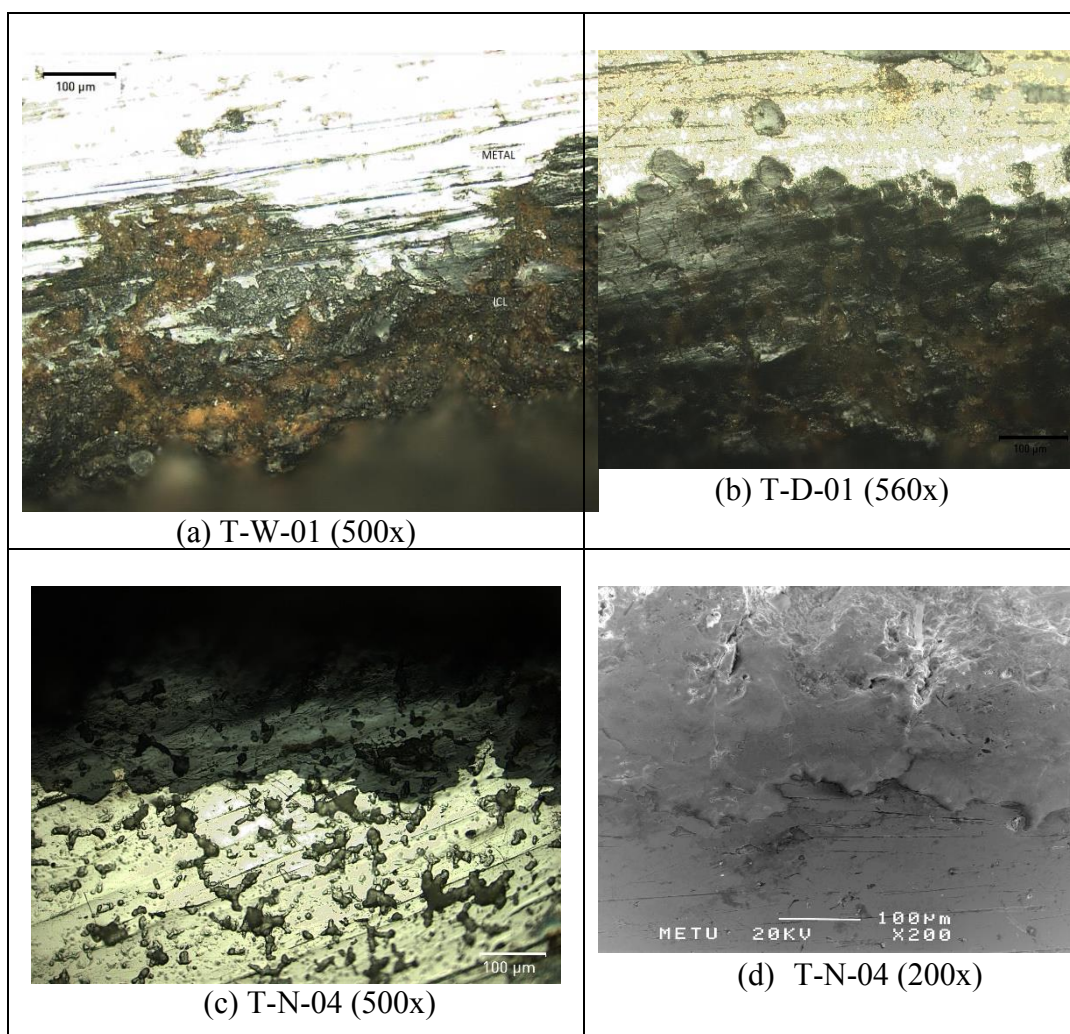


Figure 4. 56 Digital microscopy images (a, b, c) and SEM image (d) of iron samples (T-W-01, T-D-01 and T-N-04) after etching with nitric acid in ethanol (19th cc).

Compositional characteristics of the corrosion layers were examined of four samples from the 19th century iron objects by SEM-EDX to detect the existence of some major elements in the corrosion layer. The total corrosion layer of the nail from interior used for jointing the timber beam (FKM-02) has a variable composition starting from the reaction front (RF) towards ICL and TM (Figures 4.57-4.60). Reaction front showed the presence of iron, silicon, phosphorous, aluminum, calcium and manganese in decreasing order. In the ICL, iron, silicon, aluminum, calcium, phosphorous, titanium and potassium were observed. Towards the TM

layer, iron, silicon, chlorine, sodium, potassium and sulfur were observed while at another point close to TM iron, silicon, phosphorous, aluminum, calcium and potassium were identified.

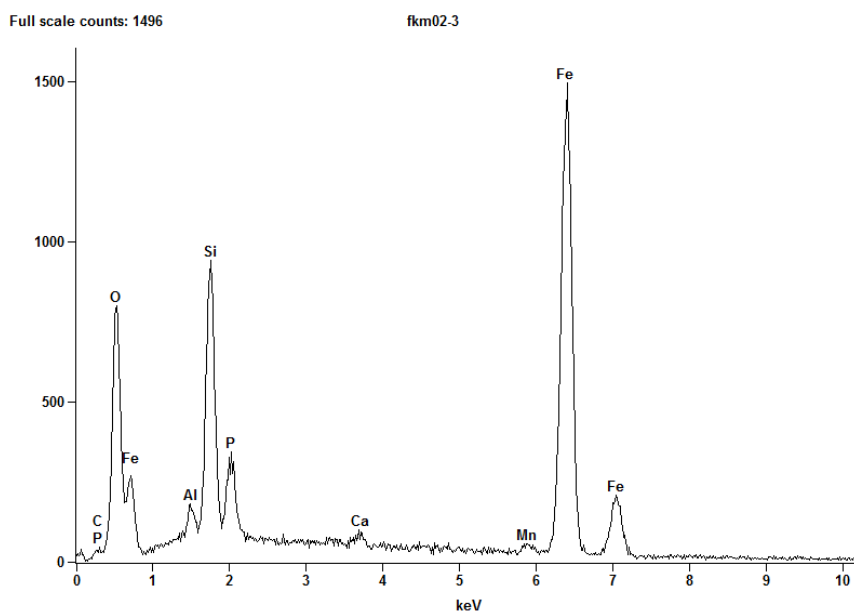


Figure 4. 57 EDX analysis at the RF of iron sample (FKM-02): Fe, Si, Al, Ca, P and Mn.

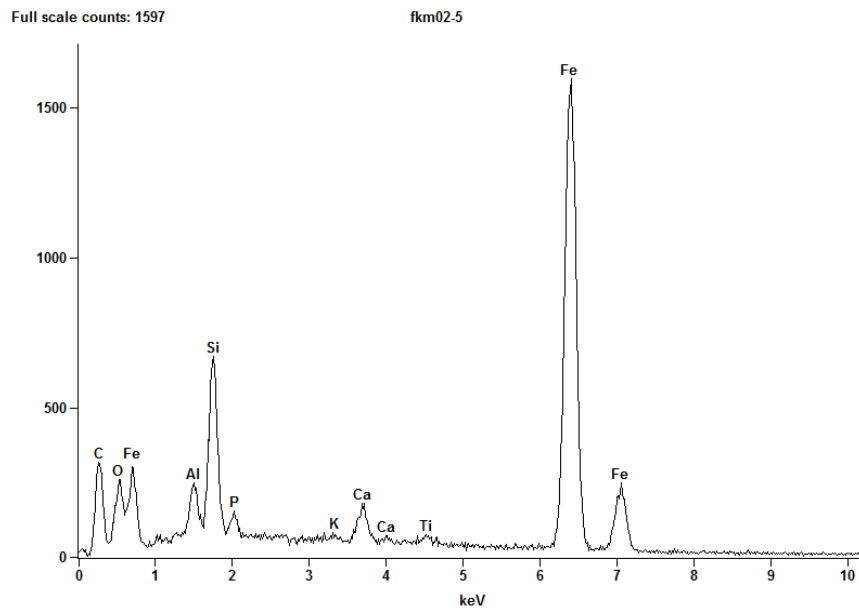


Figure 4. 58 EDX analysis at the ICL of the iron sample (FKM-02): Fe, Si, Al, Ca, P, Ti and K.

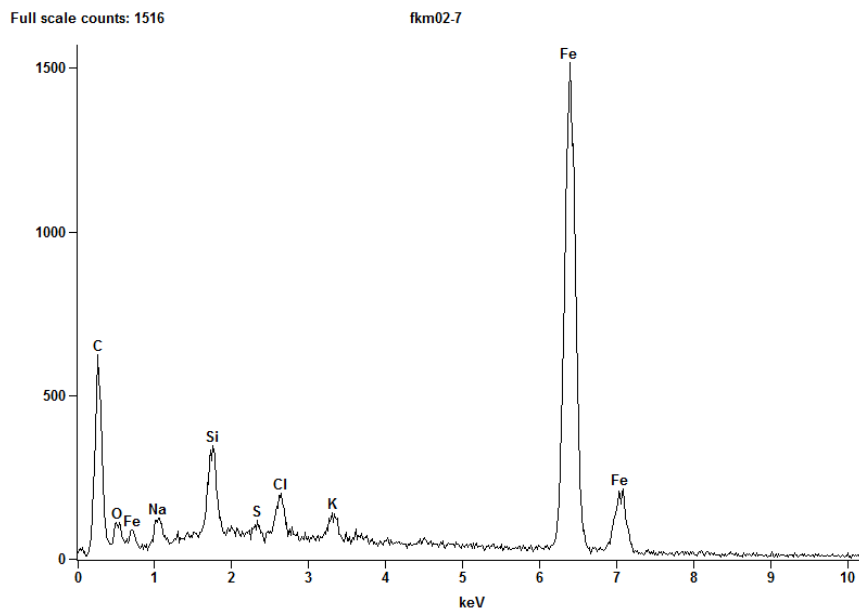


Figure 4. 59 EDX analysis at the ICL of the iron sample (FKM-02): Fe, Si, Cl, Na, K and S.

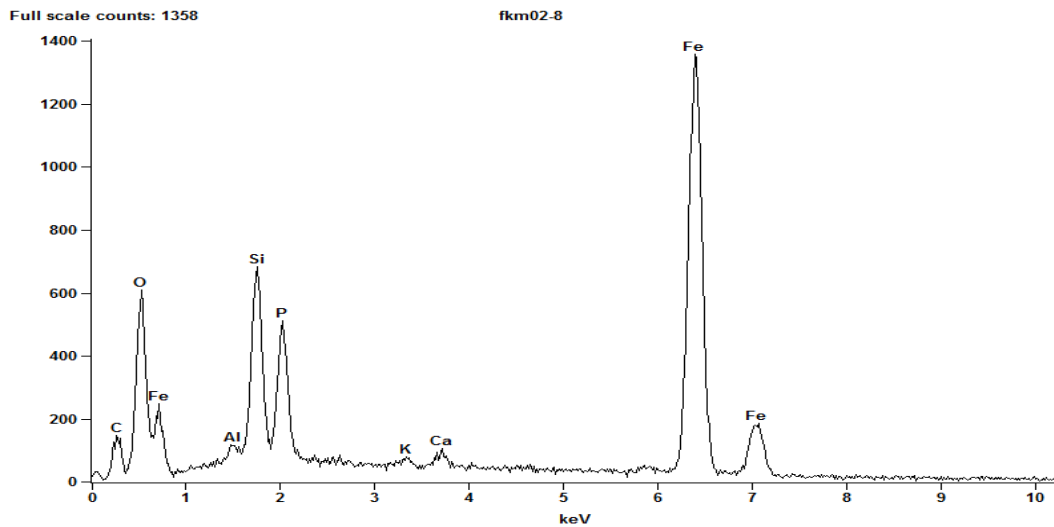
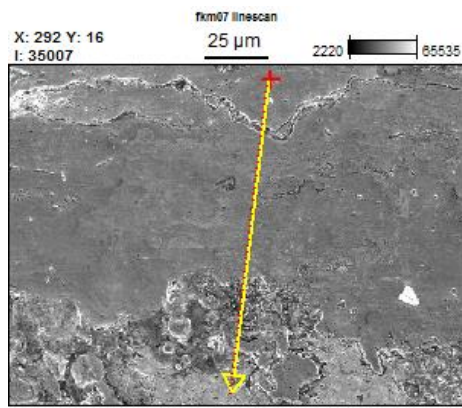


Figure 4. 60 EDX analysis at the ICL of the iron sample (FKM-02): Fe, Si, P, Al, Ca and K.

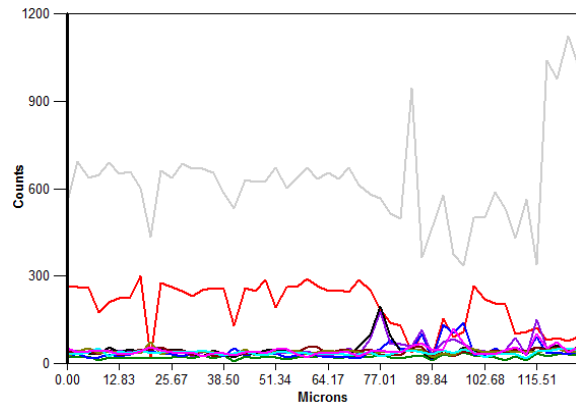
The total corrosion layer of a buried nail from an Ottoman layer excavation (FKM-07) with a thick corrosion layer was examined by EDX. Starting from the transformed media (TM) to body metal, line scanning was performed to witness the overall element change in the corrosion layer (Figure 4.61 a and b). Iron, calcium, silicon, sulfur, phosphorous, potassium, chlorine and aluminum are the main elements observed, starting from the most abundant one towards the least. When starting from the TM towards the RF, ICL has rather uniform presence of elements in the composition and close to the RF, the composition is more variable with added importance of silicon, aluminum, calcium and phosphorous.

The EDX analysis of the crack area close to TM in the corrosion layer shows the following elements in decreasing order: iron, silicon, calcium, aluminum, sulfur, potassium and chlorine (Figure 4.62).

The total corrosion layer of a nail sample (FKM-11) partially exposed to atmospheric conditions showing effects of dampness and having a thick corrosion layer was examined by EDX and sum spectrum results were obtained. Iron, silicon, aluminum, chlorine, phosphorous and sodium are the main elements observed (Figure 4.63).

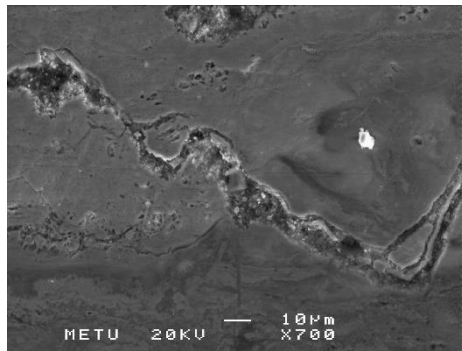


(a) Accel. Voltage: 20.00, Magnif.: 700X

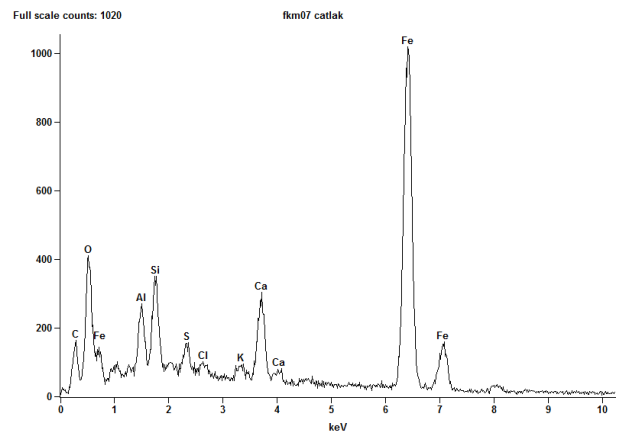


(b)

Figure 4. 61 SEM image of an iron nail head (FKM-07) (a) and EDX line scan spectrum starting from transformed media (TM) to main body (b).

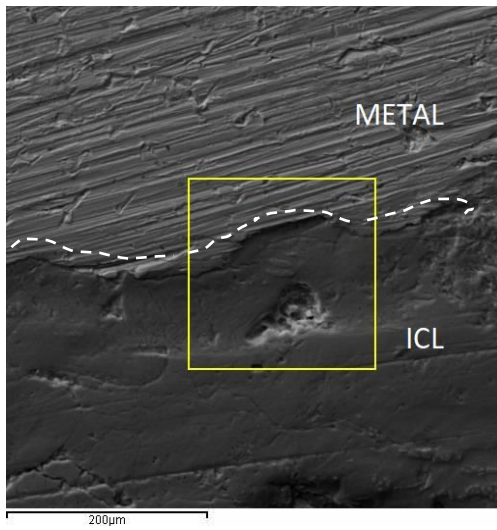


(a) FKM-07 (700x)

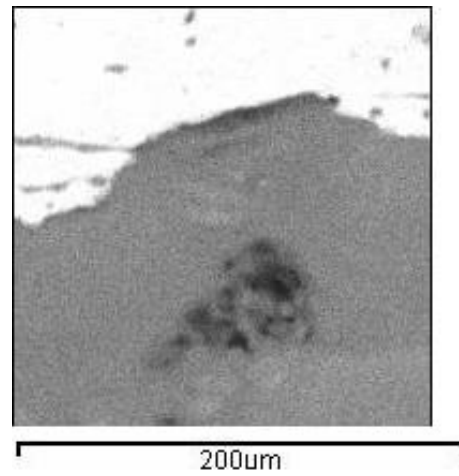


(b)

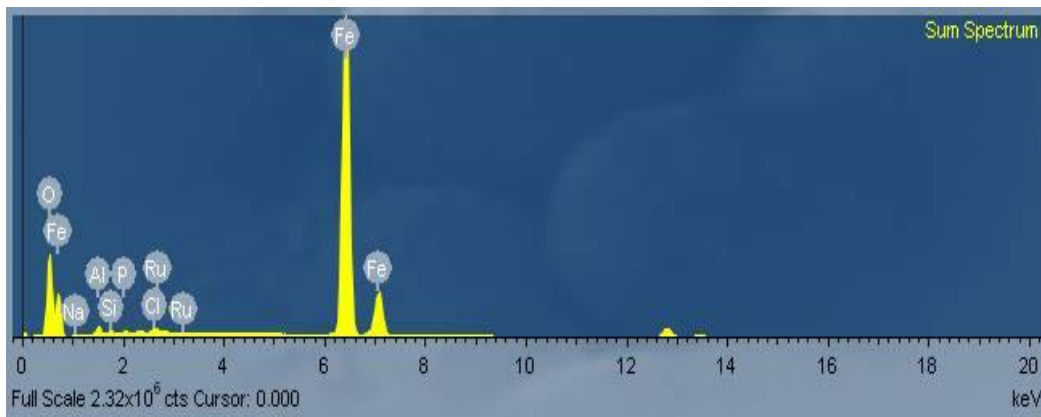
Figure 4. 62 SEM image of an iron nail head (FKM-07) (a) and EDX analysis at the crack point in ICL (b): Fe, Si, Ca, Al, S, K and Cl.



(a)



(b)

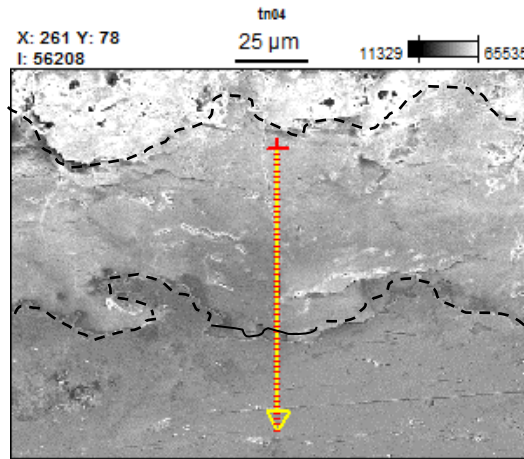


(c)

Figure 4. 63 SEM images of an iron nail (FKM-11) at the ICL (a, b), and EDX analysis (c): Fe, Si, Al, Cl, P and Na.

The total corrosion layer of a nail from the interior of a 19th century dwelling in Tekkekoy - Samsun (T-N-04) was examined by EDX. Starting from the transformed media (TM) to body metal, line scanning was performed to witness the overall element change in the corrosion layer (Figure 4.64 a). Iron, nitrogen, aluminum, sulfur, silicon, chlorine, potassium, calcium and magnesium are the main elements observed starting from the most abundant one towards the least. Line scanning

performed from TM towards RF shows that the composition of TM and ICL are rather variable with added importance of nitrogen, sulfur and chlorine elements (Figure 4.64 b).



(a) T-N-04 Magnif.: 700X

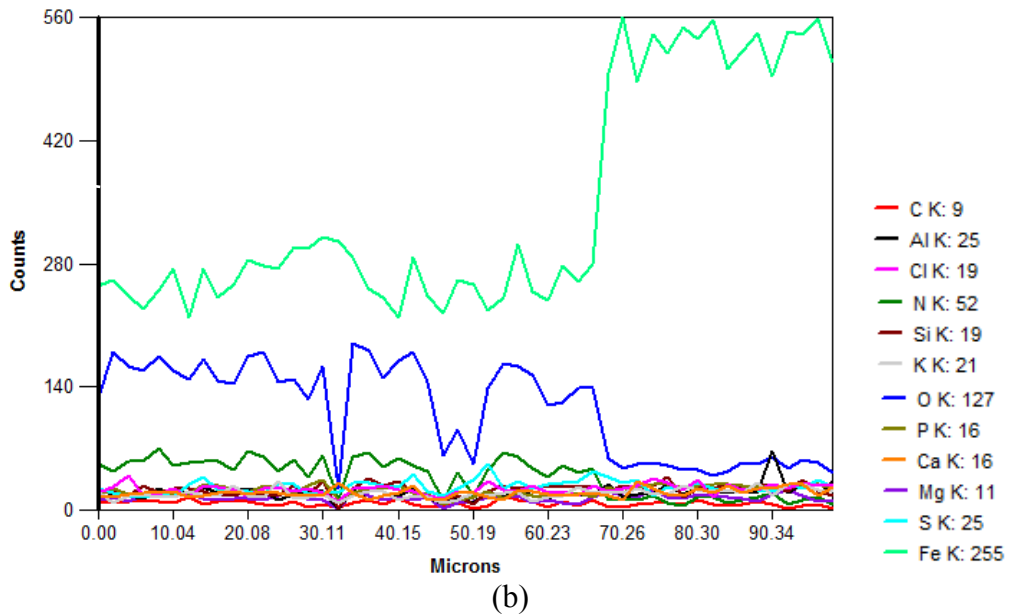


Figure 4. 64 SEM image of a nail (T-N-04) starting from transformed media (TM) to main body (a) and its EDX line scan spectrum (b): Fe, N, Al, S, Si, Cl, K, Ca and Mg.

Table 4. 22 Morphological characteristics and thickness of corrosion layers for iron samples from 19th century.

Sample Code	Corrosion Layer Characteristics	Inner Corrosion Layer (ICL) Thickness (μm)
FKM-02 Nail for jointing load bearing, main timber beams, interior	<ul style="list-style-type: none"> • Compact and well observed corrosion layer • Fe, Si, Al, P, Mn, Ca, K, Cl, Na, S and Ti are the elements observed in the corrosion layer 	50-75
FKM-05 Female hinge for main entrance door, interior	<ul style="list-style-type: none"> • Compact and well observed corrosion layer 	100-125
FKM-07 Nail, Ottoman layer, buried	<ul style="list-style-type: none"> • No uniform compact layer • Thick corrosion layers with cracks and porous areas in it • Fe, Si, Mg, P, Ca, S, Al, Cl and K are the elements observed in the corrosion layer 	350-600
FKM-11 Nail, from a stone dwelling, partially open to atmosphere	<ul style="list-style-type: none"> • No compact corrosion layer • Deep cracks and porous areas in the corrosion layer • Fe, Si, Al, Cl, P and Na are the elements observed in the corrosion layer 	1300
T-N-04 Iron nail from timber column, exterior	<ul style="list-style-type: none"> • Compact, very well observed corrosion layer • Fe, N, Al, S, Si, Cl, K, Ca and Mg are the elements observed in the corrosion layer 	150-250
T-D-01 Iron crossbar of main entrance door locking, interior	<ul style="list-style-type: none"> • Compact, very well observed corrosion layers 	350
T-W-01 Iron hinge pin, entrance hall's left window, interior	<ul style="list-style-type: none"> • Compact, very well observed corrosion layers 	150-350

4.4. FTIR Spectroscopy Analyses: Compositional Characteristics of the Corrosion Layers in Powder Form

During the FTIR analyses the powdered corrosion products were directly measured by the use of the ATR unit. FTIR and Raman spectroscopy are complimentary techniques, both based on molecular vibrations. The typical samples of iron objects from 15th, 16th and 19th centuries are observed and compared regarding their corrosion minerals as a mixture of corroded layers on the metal bodies.

The IR absorption bands at higher wavenumber region between 3000-3500 cm^{-1} (ν -OH) are due to OH stretching (Balasubramaniam et al, 2004). At lower wavenumbers between 400 -1200 cm^{-1} the OH bending and Fe-O stretching are observed. The peaks around 1500, 2920 and 2850 cm^{-1} arise from several impurities in the sample and atmosphere ((Balasubramaniam, 2002). The peaks at 786 – 791 cm^{-1} , and at 886 – 897 cm^{-1} are assigned to Fe-O-H bending vibrations (Schwertmann *et al*, 2003; Montes-Hernandez et al., 2011; Zamiri *et al.*, 2014). Goethite can be identified by its two standard-OH bending bands at ca. 892 cm^{-1} (δ -OH) and 795 cm^{-1} (γ -OH) (Cornell and Schwertmann, 2003; Gotic *et al*, 2007). The peaks found at 621 – 632 cm^{-1} are associated with the Fe-O stretching in FeO_6 octahedral lattice (Ruan *et al.*, 2001). There is a small peak around 1650 cm^{-1} that corresponds to bending modes of hydroxyl (Prasad et al., 2006). The broad peaks centered around 3101 – 3118 cm^{-1} correspond to the stretching of goethite hydroxyls and surface H_2O molecules (Prasad et al., 2006). In the goethite sample with the presence of leftover NO_3^- from incomplete washing, the wavenumber may be detected at around 1400 cm^{-1} . A close-up of the region between 1200 – 1700 cm^{-1} shows the presence of adsorbed water bending vibrations at 1651 – 1654 cm^{-1} , and of adsorbed carbonate with peaks of the asymmetric and symmetric O–C–O stretch vibrations at 1499 – 1509 cm^{-1} and 1307 – 1322 cm^{-1} , respectively (Villalobos and Leckie, 2001). Lepidocrocite (β - FeOOH) can be identified with its OH bending peaks at $1015 \pm 7 \text{ cm}^{-1}$ in FTIR traces (Pani *et al*, 2015).

There have been many studies done to investigate the relationship between crystallinity and IR properties of goethite. The crystallinity indicates the unit cell of the goethite molecule detected by the typical vibrational frequencies of Fe-OH and Fe-O bonds and their interactions with respect to unsubstituted goethite.

While the separation of two major OH bending bands namely δ -OH at 890 cm^{-1} and γ -OH at 790 cm^{-1} of goethite was correlated with the degree of crystallinity by Cornell and Schwertmann (2003); they are also affected by some substitutions such as Al in its molecular structure (Cornell and Schwertmann, 2003 and Salama et al, 2015). Variations with crystallinity do not allow the OH bending bands to exceed 900 or 800 cm^{-1} , unlike Al/Fe substitutions (Cambier 1986-2). Particle morphology and crystallinity influence the position of the symmetric Fe-O stretch at 630 cm^{-1} (Cornell and Schwertmann, 2003). In addition to goethite's major OH bending bands, the Fe-O band at $\sim 630\text{ cm}^{-1}$ has been recognized as a sensitive check for crystallinity (Sato *et al.*, 1969 and Cambier 1986, 1-2). The lattice band around 630 cm^{-1} is affected by particle shape and apparently has a transition moment parallel to "a" which is goethite's crystal dimension at direction "a" (Cambier 1986-1). Cambier (1986-1&2) also studied the effect of particle size on varying crystallinity. Although there is a relationship of the band separations at δ -OH at 890 cm^{-1} and γ -OH at 790 cm^{-1} with the mineral and particle size, the effects are not precise (Skulte et al, 2018) but it cannot be neglected. There is a high correlation of particle size with the half width of XRD principal peaks (Cambier 1986-2). XRD half peak width of goethite for 111-plane and IR bending band namely δ -OH at 890 cm^{-1} were found to be well correlated and can be used for observation of particle size properties of goethite (Cambier 1986-2).

In general, it can be summarized that decreasing crystallinity causes the bands to broaden, the frequencies of the OH bending bands to decrease and that of the OH stretch to increase (Cornell and Schwertmann, 2003). The OH bending bands also move closer together, with the separation decreasing from 97 cm^{-1} for well crystallized goethite to 94 cm^{-1} for poorly crystallized goethite (Schwertmann et al, 1985; Cambier 1986). 'Poor crystallinity' (interpreted as disorder) from effects due

to particle size, a second series with varying crystallinity and average particle size was added (Cambier 1986). Band width at δ -OH at 890 cm^{-1} can still be considered as an indication of particle size properties of goethite according to XRD-IR correlation studies of Cambier (1986) in relation to peak half widths. The criteria for the degree of crystallinity of goethite and lepidocrocite which are used for the interpretation of FTIR spectra of iron objects representing three different centuries is summarized in Table 4.23.

Table 4. 23 Interpretation of the degree of crystallinity of goethite and lepidocrocite by FTIR Analysis.

Crystallinity Scaling of Goethite:	Crystallinity Scaling of Lepidocrocite:
Sharp peak + separation $\geq 97\text{ cm}^{-1}$ = Good crystallinity	Sharp peak + peak at $1015 \pm 7\text{ cm}^{-1}$ = Good crystallinity
Sharp peak + separation $< 97\text{ cm}^{-1}$ = Variable crystallinity	Sharp peak + peak beyond $1015 \pm 7\text{ cm}^{-1}$ = Variable crystallinity
Broad peak + separation $\geq 97\text{ cm}^{-1}$ = Variable crystallinity	Broad peak + peak at $1015 \pm 7\text{ cm}^{-1}$ = Variable crystallinity
Broad peak + separation $< 97\text{ cm}^{-1}$ = Low crystallinity	Broad peak + peak beyond $1015 \pm 7\text{ cm}^{-1}$ = Low crystallinity

Individual interpretation of FTIR results will be given in the following paragraphs classified as groups of objects representing indoor and outdoor conditions, major corrosion products, indicating the frequencies of their OH bands, separation of bending bands, their relative intensities and crystallinity. They are summarized in Table 4.24 for 15th century; Table 4.25 for 16th century and Table 4.26 for 19th century iron objects.

Corrosion characteristics of the 15th century iron objects were examined on the selected two objects: a door lock piece (GMH-Me-02) and a plaster nail (GMH-Me-03) from interior wall. Goethite (α -FeOOH) as key absorption band at 873 cm^{-1} , lepidocrocite (γ -FeOOH) at 1021 cm^{-1} and magnetite (Fe_3O_4) at 575 cm^{-1} are identified in FTIR traces for the door lock piece (Figure 4.65). The separation of OH

bending bands of goethite for the door lock piece is $873-794 = 79 \text{ cm}^{-1}$. The lower frequencies of OH bending bands (δ -OH and γ -OH) and their lower separation may be taken as evidence for poorly crystallized goethite. Although their separation is low, the bending bands are sharp and have high intensity which can be the result of good crystallinity of goethite. Therefore, the corrosion layer most likely consists of goethite with variable crystallinity. Its γ -OH bending band at 794 cm^{-1} has lower intensity with δ -OH bending band at 873 cm^{-1} .

For the plaster nail (GMH-Me-03), goethite (α -FeOOH) at 876 cm^{-1} and lepidocrocite (γ -FeOOH) at 1017 cm^{-1} are observed (Figure 4.66) with the separation of OH bending bands being $876-791 = 85 \text{ cm}^{-1}$. The lower frequencies of OH bending bands (δ -OH and γ -OH) and their lower separation may be taken as evidence for poorly crystallized goethite. Although their separation is low, the bending bands are sharp and have high intensity which can be the result of good crystallinity of goethite. The corrosion layer may consist of goethite with variable crystallinity. Its γ -OH bending band at 794 cm^{-1} has lower intensity with δ -OH bending band at 873 cm^{-1} .

Lepidocrocite is observed in both objects. Their OH bending bands (δ -OH) are at 1021 cm^{-1} in the door lock piece with lower intensity and at 1017 cm^{-1} in the plaster nail with higher intensity. The bands are sharp and their sharpness is taken as evidence of good crystallinity of lepidocrocite in the corrosion layer. When the major peak intensities of goethite and lepidocrocite are compared with each other in the same sample, the presence of lepidocrocite is more pronounced than goethite in the plaster nail having medium perfect corrosion layer in comparison to the door lock piece having perfect corrosion layer.

Both objects have a broad band in the region $3000-3500 \text{ cm}^{-1}$. The door lock piece (GMH-Me-02) has OH stretching band at 3113 cm^{-1} while the plaster nail collected (GMH-Me-03) has OH stretching band at 3140 cm^{-1} with similar intensities.

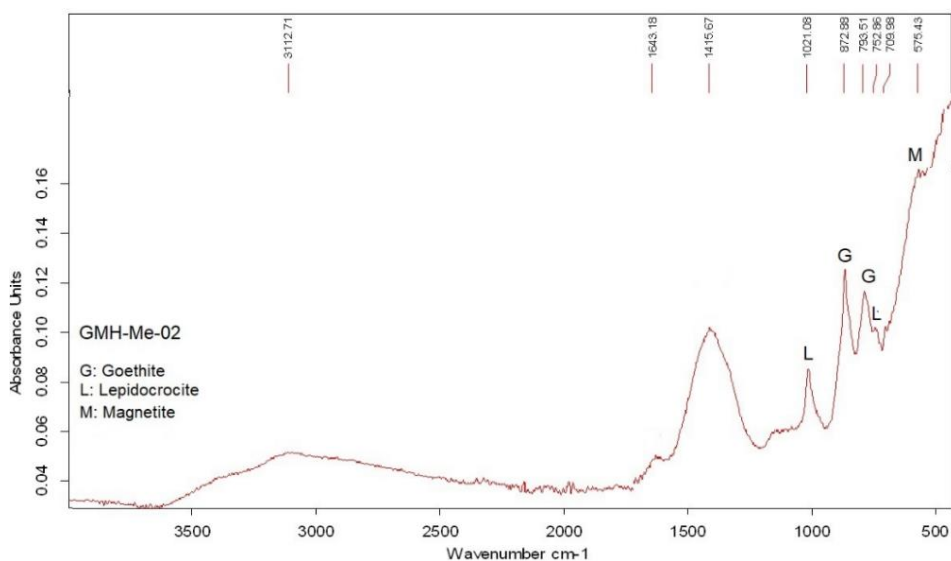


Figure 4. 65 FTIR spectrum of the mixture including inner corrosion layer and TM layer belonging to a 15th century door lock piece (GMH-Me-02): Goethite (α -FeOOH), lepidocrocite (γ -FeOOH) and magnetite (Fe_3O_4).

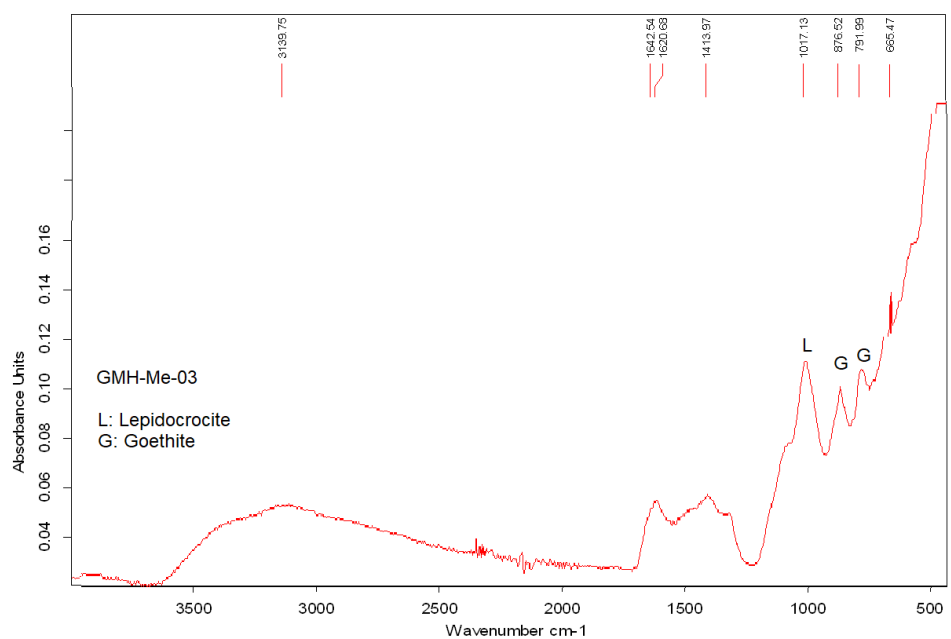


Figure 4. 66 FTIR spectrum of the mixture including inner corrosion layer and TM layer belonging to a 15th century plaster nail (GMH-Me-03): Goethite (α -FeOOH) and lepidocrocite (γ -FeOOH).

Table 4.24 Iron oxides layering in the corrosion of the samples used for 15th century Gazi Mihal Hammam in Edirne by FTIR Analysis.

Sample ID	Corrosion Minerals in Mixture of RF, ICL and TM	Goethite δ -OH and γ -OH frequencies, Band width and Peak intensity comparison (δ -OH vs γ -OH)	Separation	OH-stretching frequency and Peak intensity	Goethite Crystallinity	Lepidocrocite OH-bending frequency and Peak intensity in Comparison to Goethite δ -OH	Lepidocrocite Crystallinity
GMH-Me-02 Door lock piece, <i>Indoor</i>	Goethite Lepidocrocite Magnetite	873 cm^{-1} and 794 cm^{-1} High Sharp	79 cm^{-1} Low	3113 cm^{-1} Low	Variable	1021 cm^{-1} Low Sharp	Good
GMH-Me-03 Plaster nail, <i>indoor</i>	Goethite Lepidocrocite	877 cm^{-1} and 792 cm^{-1} Almost equal Less sharp	85 cm^{-1} Low	~3140 cm^{-1} Low	Variable	1021 cm^{-1} High Sharp	Good

Corrosion characteristics of the 16th century iron objects from Kılıç Ali Paşa Hammam were examined on the selected three objects of which two nails from its dome (MSH-KAP-01 and 03) representing outdoor atmospheric conditions and an iron piece used for jointing of other metals (chains or hooks) to the wall (MSH-KAP-02) showing the indoor conditions. The nail (MSH-KAP-01) from the dome reveals goethite (α -FeOOH) with key absorption band at 874 cm⁻¹, lepidocrocite (γ -FeOOH) at 1017 cm⁻¹ and hematite (α -Fe₂O₃) at 450 cm⁻¹ in FTIR traces (Figure 4.67). The separation of OH bending bands of goethite for the nail (MSH-KAP-01) is 874-796=78 cm⁻¹. The lower frequencies of OH bending bands (δ -OH and γ -OH) and their lower separation may be taken as evidence for poorly crystallized goethite. Although their separation is low, the bending bands are sharp and have high intensity which can be the result of good crystallinity of goethite. The corrosion layer may consist of goethite with variable crystallinity. Its γ -OH bending band at 796 cm⁻¹ has lower intensity with δ -OH bending band at 874 cm⁻¹.

Another nail from the dome (MSH-KAP-03) representing the outdoor atmospheric condition presents goethite (α -FeOOH) at 874 cm⁻¹ and lepidocrocite (γ -FeOOH) at 1019 cm⁻¹ in FTIR traces (Figure 4.68) with the separation of OH bending bands of goethite being 874-769=105 cm⁻¹. Their higher separation with sharp and high intensity may be taken as an evidence for good crystallized goethite seen in the corrosion layer. Its γ -OH bending band at 769 cm⁻¹ has lower intensity with δ -OH bending band at 874 cm⁻¹.

The iron piece for eventual anchoring (MSH-KAP-02) from the interior of the Hammam shows goethite (α -FeOOH) at 874 cm⁻¹ and lepidocrocite (γ -FeOOH) at 1020 cm⁻¹ (Figure 4.69) with the separation of OH bending bands being 874-794=80 cm⁻¹. The lower frequencies of OH bending bands (δ -OH) and their lower separation may be taken as evidence for poorly crystallized goethite. In addition, The OH bending bands (δ -OH and γ -OH) with sharp and high intensity may be taken as evidence for good crystallized goethite seen in the corrosion layer. The corrosion layer may consist of goethite with variable crystallinity. Its γ -OH bending band at 794 cm⁻¹ has lower intensity with δ -OH bending band at 874 cm⁻¹.

Lepidocrocite is observed in all three objects with similar intensities. The OH bending bands (δ -OH) of the nails from dome are at 1019 cm^{-1} and at 1020 cm^{-1} for the iron piece Iron piece used for jointing of other metals (MSH-KAP-02). Lepidocrocite in the corrosion layer of outdoor nails with a sharp band is taken as evidence of good crystallinity. The indoor iron piece (MSH-KAP-02) having a broader peak than the outdoor nails may be taken as evidence for the existence of lepidocrocite with lower crystallinity in the corrosion layer of MSH-KAP-02. When the major peak intensities of goethite and lepidocrocite are compared with each other in the same sample, presence of goethite is more pronounced than lepidocrocite in all samples of 16th century objects.

All three objects have a broad band in the region $3000\text{-}3500\text{ cm}^{-1}$. The nail from the dome (MSH-KAP-01) has a high intensity OH stretching band at 3118 cm^{-1} while the others display low and a slightly increased band in the mentioned region.

The nail having a higher separation of OH bending bands in FTIR has lower OH stretching peaks than the nail having a lower separation of OH bending bands. The nail having very sharp γ -OH bending at 873 cm^{-1} has also the highest OH stretching band at $\sim 3100\text{ cm}^{-1}$.

FTIR spectroscopy results of surface corrosion layers for the 16th century objects are summarized in Table 4.25.

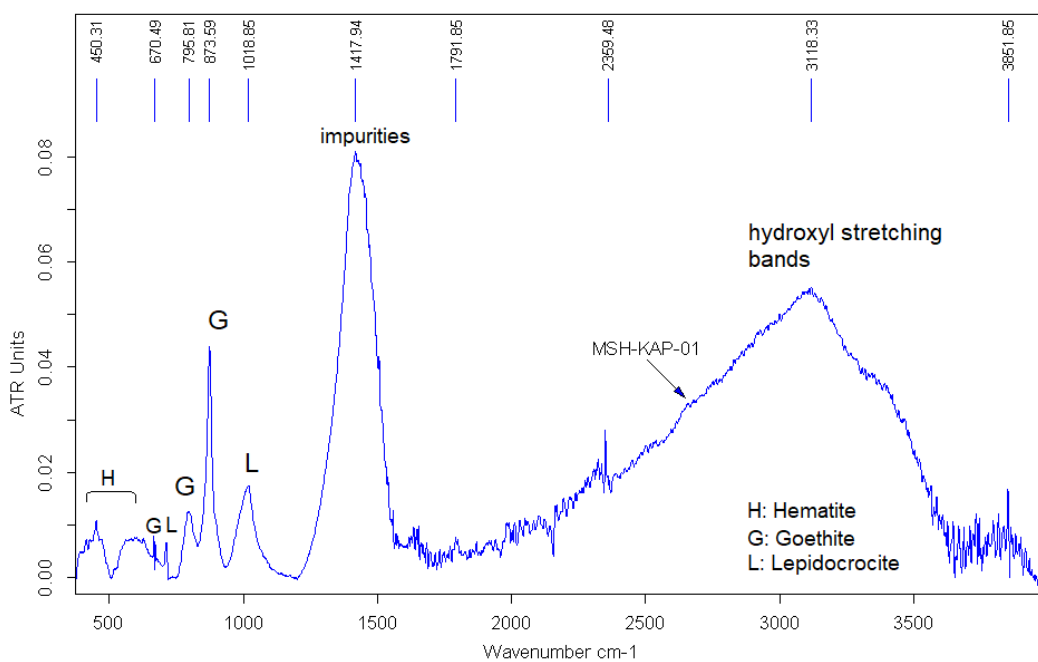


Figure 4. 67 FTIR spectrum of corrosion layer including ICL and TM of the nail (MSH-KAP-01) from the dome representing outdoor atmospheric condition: Goethite (α -FeOOH), lepidocrocite (γ -FeOOH) and hematite (α -Fe₂O₃).

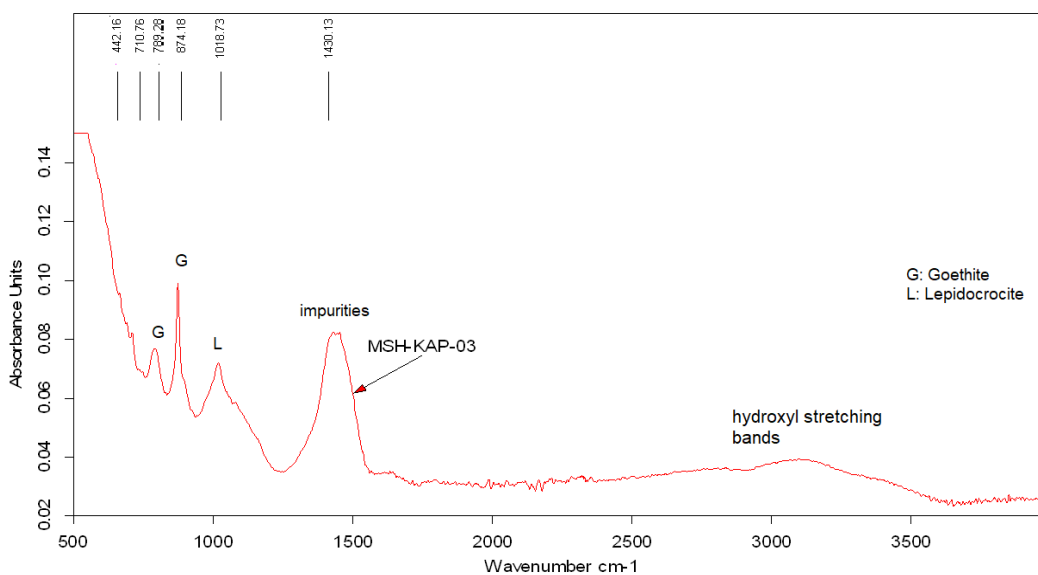


Figure 4. 68 FTIR spectrum of corrosion layer including ICL and TM of the nail (MSH-KAP-03) from the dome representing outdoor atmospheric condition: Goethite (α -FeOOH), and lepidocrocite (γ -FeOOH).

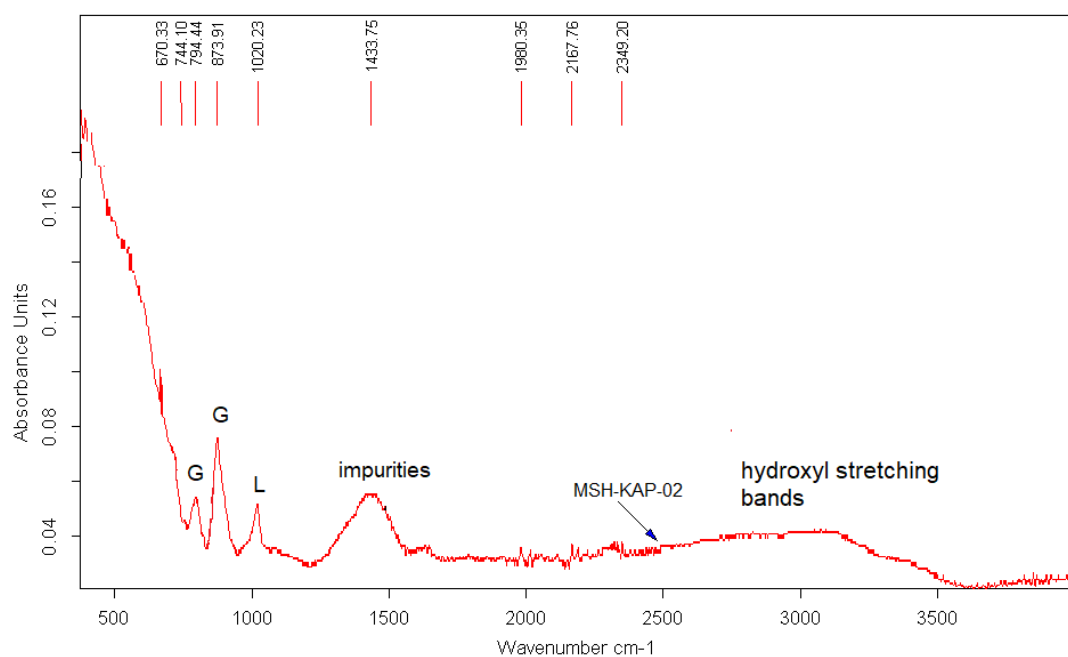


Figure 4. 69 FTIR spectrum of corrosion layer including ICL and TM of the iron piece convenient to anchoring (MSH-KAP-02) at the wall representing indoor atmospheric condition: Goethite (α -FeOOH), and lepidocrocite (γ -FeOOH).

Table 4.25 Iron oxides layering in the corrosion of the samples used for 16th century Kılıç Ali Paşa Hammam by FTIR Analysis.

Sample ID	Mixture of RF, ICL and TM	Goethite δ -OH and γ -OH frequencies, Band width and Peak intensity comparison (δ -OH vs γ -OH))	Separation	OH-stretching frequency and Peak intensity	Goethite Crystallinity	Lepidocrocite OH-bending frequency and Peak intensity in Comparison to Goethite δ -OH	Lepidocrocite Crystallinity
MSH-KAP-01 Nail from dome, <i>outdoor</i>	Goethite Lepidocrocite Hematite	874 cm^{-1} vs 796 cm^{-1} Sharp Very high	78 Low	3118 cm^{-1} Very High	Variable	1019 cm^{-1} Low Sharp	Good
MSH-KAP-03 Nail from dome, <i>outdoor</i>	Goethite Lepidocrocite	874 cm^{-1} vs 769 cm^{-1} Sharp Very high	105 high	~3100 cm^{-1} Low	Good	1019 cm^{-1} Low Broad	Variable
MSH-KAP-02 Iron piece from the wall, <i>indoor</i>	Goethite Lepidocrocite	874 cm^{-1} vs 794 cm^{-1} Sharp High	80 Low	~3100 cm^{-1} Low	Variable	1020 cm^{-1} Low Sharp	Good

Corrosion characteristics of the 19th century iron objects collected from Foça, İzmir and Tekkekoy, Samsun were examined by the FTIR traces on the selected thirteen objects. The six objects from the dwellings of Foça are partially open to outdoor atmospheric conditions: a window guard iron piece from a stone dwelling (FKM-01), a nail for jointing main timber beams (FKM-02), a door lock piece from main entrance (FKM-03), a male hinge for main entrance door (FKM-04), a female hinge for main entrance door (FKM-05) and a nail embedded in building stone tuff (FKM-11). Four objects from the Ottoman Layer excavations in Foça are representing buried conditions. Two of them are nails (FKM-07 and FKM-10) and the other two are iron pieces (FKM-08 and FKM-09). Three objects from a 19th century dwelling in Tekkekoy are a nail from a timber column at the façade of the dwelling (T-N-05), a hinge pin from the entrance hall's window (T-W-01) showing indoor atmospheric condition and a crossbar for the main entrance door locking piece (T-D-01) from the interior. These two samples are also partially open to outdoor atmospheric conditions due to their locations.

The window guard iron piece (FKM-01) from the dwelling of Foça reveals goethite (α -FeOOH) with its key absorption band at 909 cm^{-1} , lepidocrocite (γ -FeOOH) at 1019 cm^{-1} and quartz at 1088 cm^{-1} which may be due to its embedded position in stone masonry (Figure 4.70). The γ -OH and δ -OH bending bands of goethite have a separation of 129 cm^{-1} . The higher frequencies of OH bending bands (δ -OH and γ -OH) and their higher separation may be taken as evidence for well crystallized goethite. The sharp and high δ -OH bending band at 909 cm^{-1} of FKM-01 may be a good indicator for good crystallinity goethite. Its γ -OH bending band at 780 cm^{-1} has lower intensity with δ -OH bending band at 909 cm^{-1} .

The nail for jointing the main timber beams (FKM-02) of a dwelling in Foça shows mainly goethite (α -FeOOH) at 874 cm^{-1} with some impurities (Figure 4.71). Its OH bending bands of goethite are separated by 79 cm^{-1} . The lower frequencies of OH bending bands (δ -OH and γ -OH) and their lower separation may be taken as evidence for poorly crystallized goethite. The nail (FKM-02) has broader and medium intensity of the OH bending bands in comparison to the OH bending bands of FKM-

01. Its γ -OH bending band at 785 cm^{-1} has equal intensity with δ -OH bending band at 874 cm^{-1} .

Lepidocrocite is observed only in FKM-01 with the OH bending band (δ -OH) at 1019 cm^{-1} . The broad and low intensity of the OH bending band may be taken as evidence for low crystallinity of lepidocrocite in the corrosion layer of FKM-01.

Both objects have a broad band in the region $3000\text{-}3500\text{ cm}^{-1}$. The window guard iron piece (FKM-01) has a broad and lower intensity OH stretching band at 3326 cm^{-1} while the other object (FKM-02) displays a band at 3130 cm^{-1} with higher intensity.

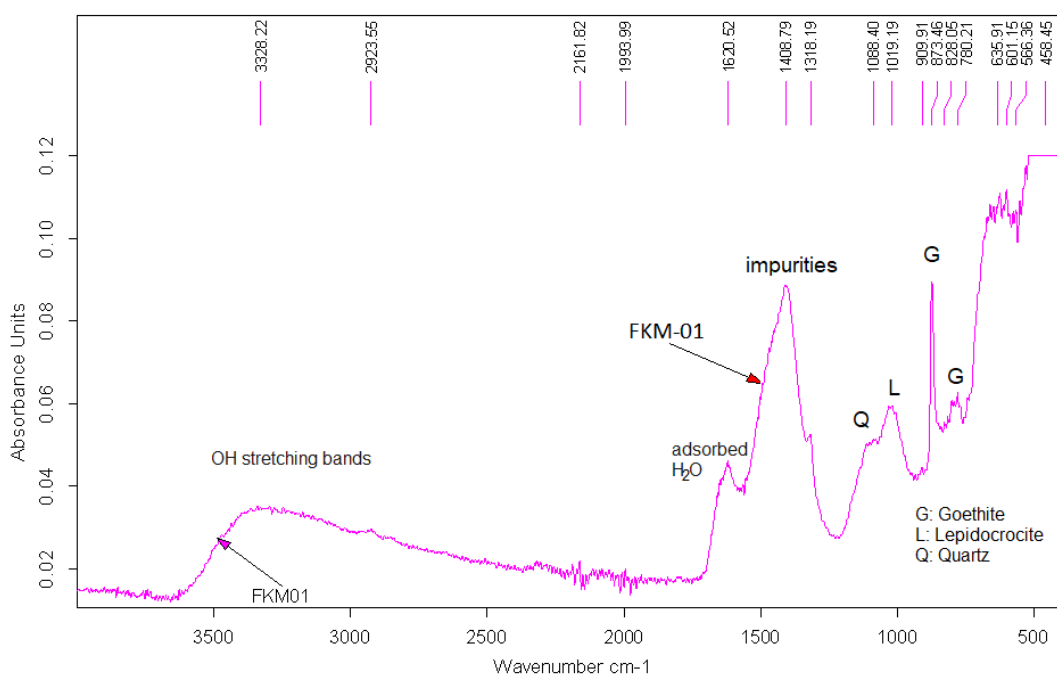


Figure 4. 70 FTIR spectrum of corrosion layer including ICL and TM of the window guard iron piece (FKM-01) at the dwelling in Foça representing partially open outdoor atmospheric conditions: Goethite (α -FeOOH), lepidocrocite (γ -FeOOH) and quartz.

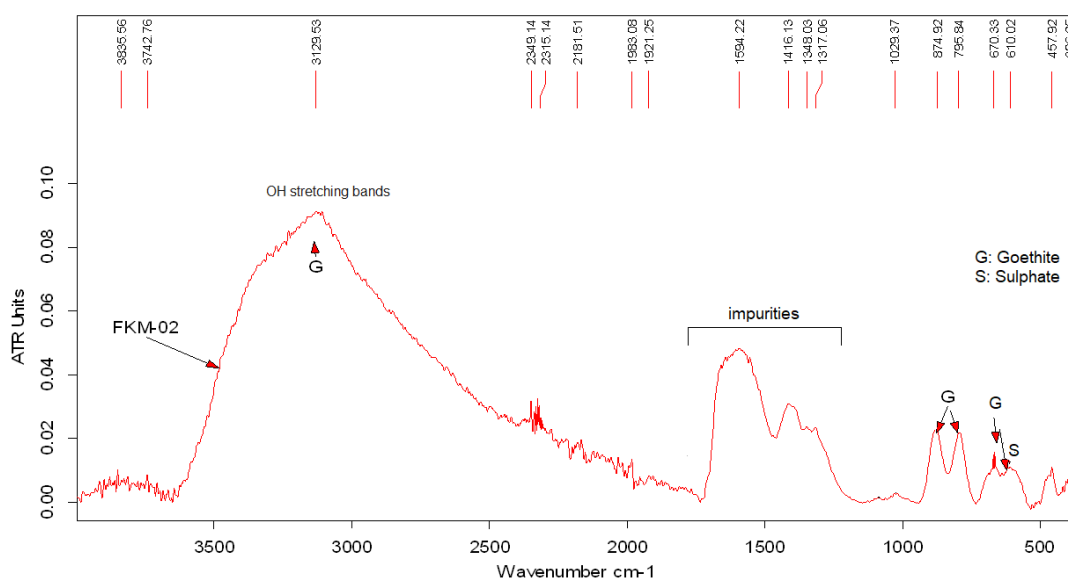


Figure 4. 71 FTIR spectrum of corrosion layer including ICL and TM of the timber jointing nail (FKM-02) at the dwelling in Foça representing partially open outdoor atmospheric conditions: Mainly goethite (α -FeOOH).

The door lock piece of the main entrance (FKM-03) from the dwelling in Foça shows mainly goethite (α -FeOOH) at 874 cm^{-1} and lepidocrocite (γ -FeOOH) at 1020 cm^{-1} in FTIR traces (Figure 4.72). Its OH bending bands of goethite are separated by 87 cm^{-1} . 2919 and 2850 cm^{-1} arise from C=O and O-H stretching which are present in the atmosphere. The lower frequencies of OH bending bands (δ -OH & γ -OH) and their low intensities with equal heights can be used as an indicator for its poor crystallinity.

The male hinge of the main entrance door (FKM-04) from a dwelling in Foça shows mainly goethite (α -FeOOH) at 875 cm^{-1} and lepidocrocite (γ -FeOOH) at 1020 cm^{-1} with some quartz around 1080 cm^{-1} (Figure 4.73). The OH bending bands of goethite are separated by 83 cm^{-1} . The lower frequencies of OH bending bands (δ -OH and γ -OH) and their lower separation may be taken as evidence for poorly crystallized goethite. Although their separation is low, the bending bands are sharp and have high intensity which can be the result of good crystallinity of goethite. The corrosion layer

may consist of goethite with variable crystallinity. Its γ -OH bending band at 792 cm^{-1} has lower intensity with δ -OH bending band at 874 cm^{-1} .

Lepidocrocite is observed in both objects. Their OH bending bands (δ -OH) are at 1020 cm^{-1} . The door lock piece (FKM-03) has a broader lepidocrocite band than the door hinge piece (FKM-04) and this may be taken as evidence for the existence of lepidocrocite with lower crystallinity in the corrosion layer of FKM-03 compared to FKM-04.

Both objects have a broad band in the region $3000\text{-}3500\text{ cm}^{-1}$. The door lock piece (FKM-03) has a lower intensity OH stretching band at 3249 cm^{-1} while the male hinge from the main entrance door (FKM-04) displays a band at 3118 cm^{-1} with very high intensity.

The iron object having higher separation of OH bending bands in FTIR has lower OH stretching peaks than the FKM-04 having lower separation of OH bending bands although their OH bending band heights at 875 and 790 cm^{-1} are equal.

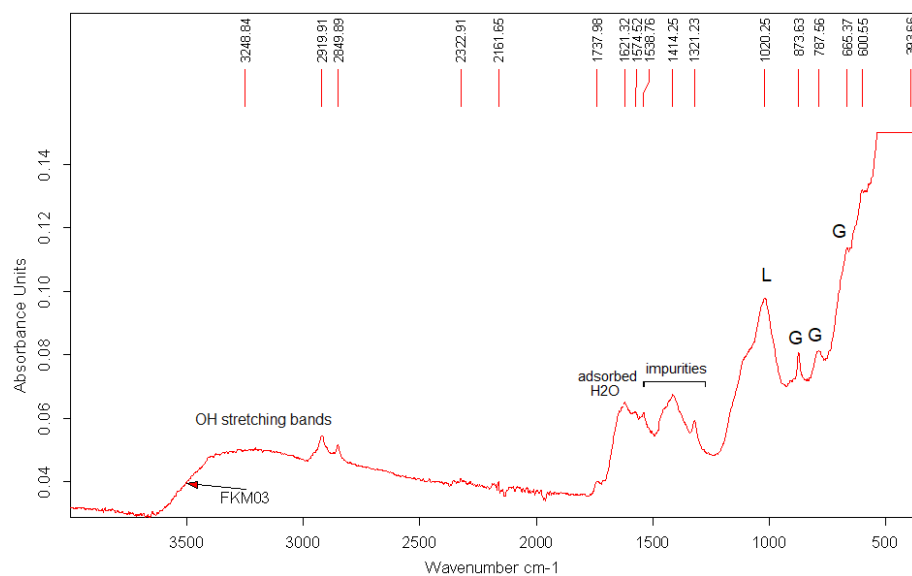


Figure 4. 72 FTIR spectrum of corrosion layer including ICL and TM of the door lock piece (FKM-03) at the dwelling in Foça representing partially open outdoor atmospheric conditions: Goethite (α -FeOOH) and lepidocrocite (β -FeOOH).

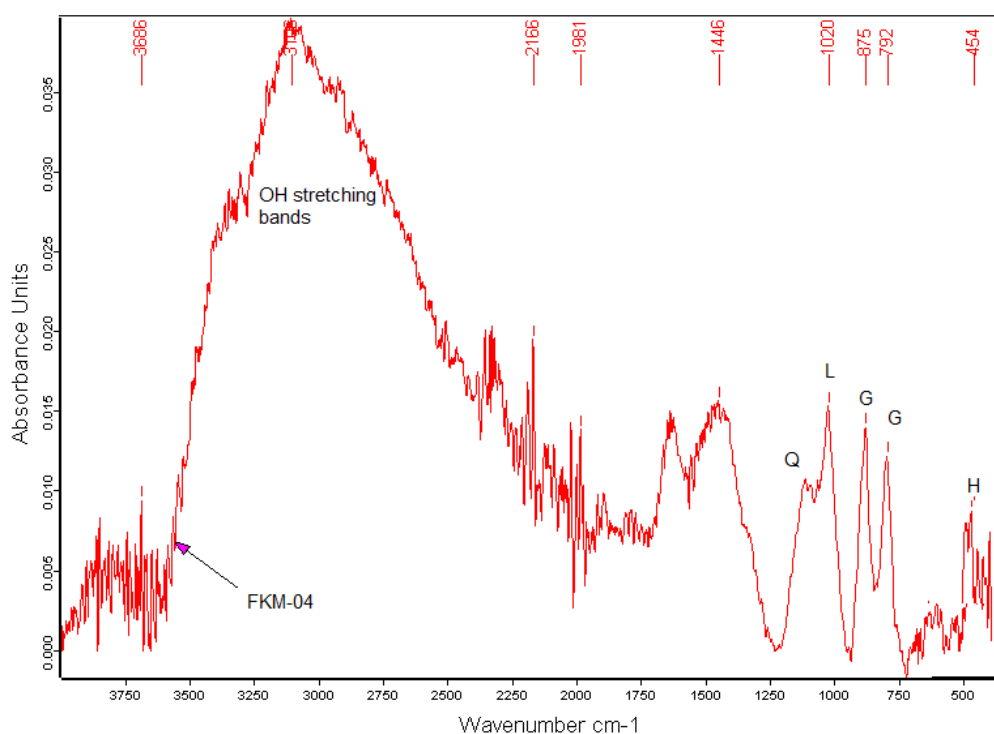


Figure 4. 73 FTIR spectrum of corrosion layer including ICL and TM of the door's male hinge (FKM-04) at the dwelling in Foça representing partially open outdoor atmospheric conditions: Goethite (α -FeOOH), lepidocrocite (β -FeOOH) and quartz.

The female hinge on the main entrance door (FKM-05) of the dwelling in Foça shows mainly lepidocrocite (γ -FeOOH) at 1019 cm^{-1} together with some goethite (α -FeOOH) at 873 cm^{-1} (Figure 4.74). The OH bending bands of goethite are separated by 93 cm^{-1} . 2919 cm^{-1} and 2850 cm^{-1} arise from C-O and O-H stretching which are present in the atmosphere. The lower frequencies of OH bending bands (δ -OH and γ -OH) and their lower separation can be taken as evidence for poorly crystallized goethite. In addition, the δ -OH bending band at 873 cm^{-1} of the object (FKM-05) having low intensity is an indicator for its poor crystallinity. The γ -OH bending band at 780 cm^{-1} has lower intensity than δ -OH bending band at 873 cm^{-1} .

The corrosion layer of the nail (FKM-11) from an Ottoman dwelling, embedded in building stone tuff, being partially open to atmosphere reveals goethite (α -FeOOH) with its OH bending peak at 867 cm^{-1} (Figure 4.75). The OH bending bands of

goethite are separated by 74 cm^{-1} . The lower frequencies of OH bending bands (δ -OH) and their lower separation can be taken as evidence for poorly crystallized goethite. The δ -OH bending band at 867 cm^{-1} of the object (FKM-11) having low and broad intensity is also a good indicator for its poor crystallinity. The γ -OH bending band at 793 cm^{-1} has higher intensity than δ -OH bending band at 867 cm^{-1} .

Corrosion layer of FKM-05 contains lepidocrocite while in FKM-11 it is not detected. The OH bending band (δ -OH) of lepidocrocite is at 1019 cm^{-1} . The broad band and its low intensity may be taken as evidence for poor crystallinity of lepidocrocite in the corrosion layer.

Both objects have broad bands in the region $3000\text{-}3500\text{ cm}^{-1}$ with some difference in peak frequency and intensity. The corrosion layer of the female hinge (FKM-05) has lower intensity OH stretching band at $\sim 3200\text{ cm}^{-1}$ than the nail (FKM-011) having a stretching band at 3313 cm^{-1} with higher intensity.

The iron object having a higher separation of OH bending bands in FTIR has lower OH stretching peaks than the FKM-11 having lower separation of OH bending bands although their OH bending band heights at 875 and 790 cm^{-1} are equal.

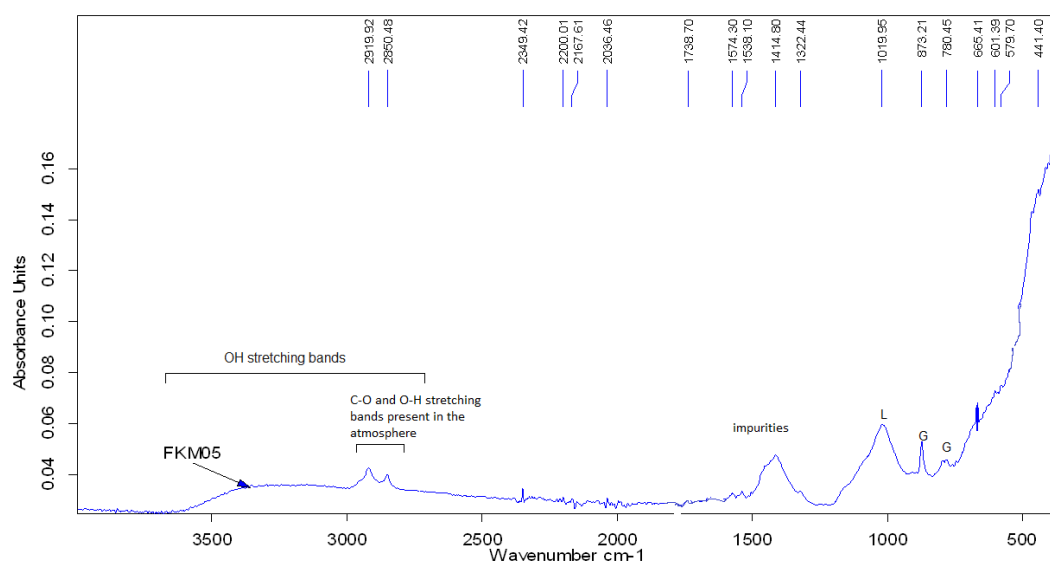


Figure 4. 74 FTIR spectrum of corrosion layer including ICL and TM of the door's female hinge (FKM-05) at the dwelling in Foça representing partially open outdoor atmospheric conditions: Goethite (α -FeOOH) and lepidocrocite (β -FeOOH).

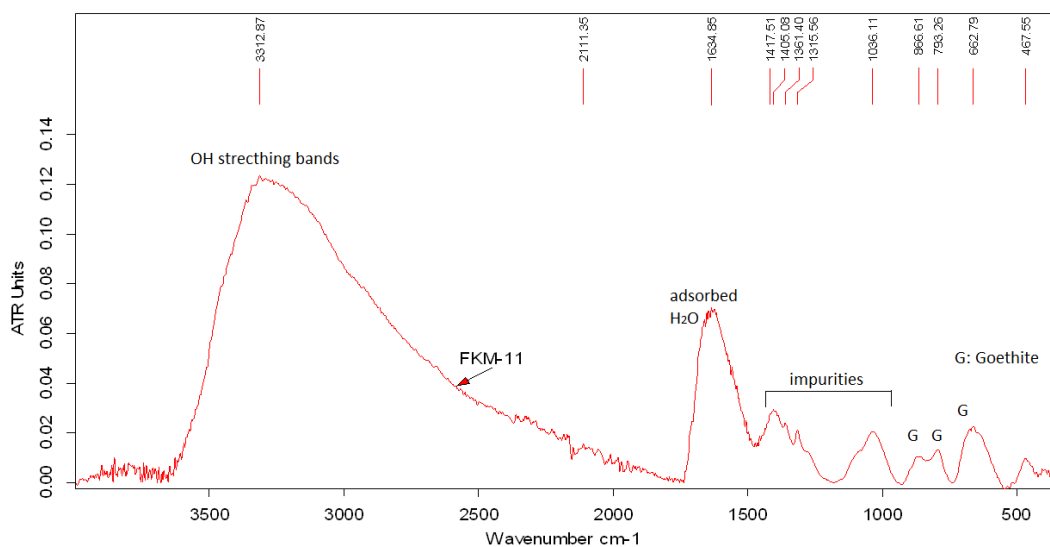


Figure 4. 75 FTIR spectrum of corrosion layer including ICL and TM of the nail (FKM-11) from a dwelling in Foça representing partially open atmospheric conditions: Goethite (α -FeOOH).

When the major peak intensities of goethite and lepidocrocite are compared with each other in the same sample for the 19th century objects, presence of goethite is

more pronounced than lepidocrocite in the window guard iron bar (FKM-01) showing corrosion at outdoor atmospheric conditions while lepidocrocite is more pronounced than goethite in the door lock piece (FKM-03) and the female hinge (FKM-05) showing the corrosion in objects partially open to outdoor atmospheric conditions. The presence of goethite and lepidocrocite is almost equal for the male hinge (FKM-04) showing the corrosion in objects partially open to outdoor atmospheric conditions.

The nail (FKM-07) in buried conditions from the Ottoman layer excavations shows mainly lepidocrocite (β -FeOOH) from its diagnostic OH bending band (δ -OH) at 1012 cm^{-1} ($1015 \pm 7\text{ cm}^{-1}$) (Figure 4.76). Its sharp band and high intensity may be taken as evidence of good crystallinity of lepidocrocite in the corrosion layer.

The L shaped iron piece (FKM-08) in buried conditions from the Ottoman layer excavations as coarse magnetic powder analysis sample reveals goethite (α -FeOOH) with its OH bending peak at 874 cm^{-1} and lepidocrocite (β -FeOOH) from its diagnostic OH bending peak at 1017 cm^{-1} ($1015 \pm 7\text{ cm}^{-1}$) in FTIR traces (Figure 4.77). The OH bending bands of goethite are separated by 82 cm^{-1} . Although their separation is low, the bending bands are sharp and have high intensity which can be the result of good crystallinity of goethite. The corrosion layer may consist of goethite with variable crystallinity. Its γ -OH bending band at 792 cm^{-1} has slightly lower intensity with δ -OH bending band at 874 cm^{-1} . Lepidocrocite in the corrosion layer of FKM-08 has a broad band with low intensity which may be taken as evidence for poor crystallinity of lepidocrocite in the corrosion layer.

Both objects have broad bands in the region $3000\text{-}3500\text{ cm}^{-1}$ with some difference in peak frequency and intensity. The corrosion layer of the nail (FKM-07) has a high intensity OH stretching band of lepidocrocite at $\sim 3202\text{ cm}^{-1}$. The L shaped iron piece (FKM-08) shows OH stretching band at 3104 cm^{-1} with low intensity.

The FKM-08 having respectively higher separation of OH bending bands in FTIR has lower OH stretching peaks than the FKM-07 in which there is no goethite observed.

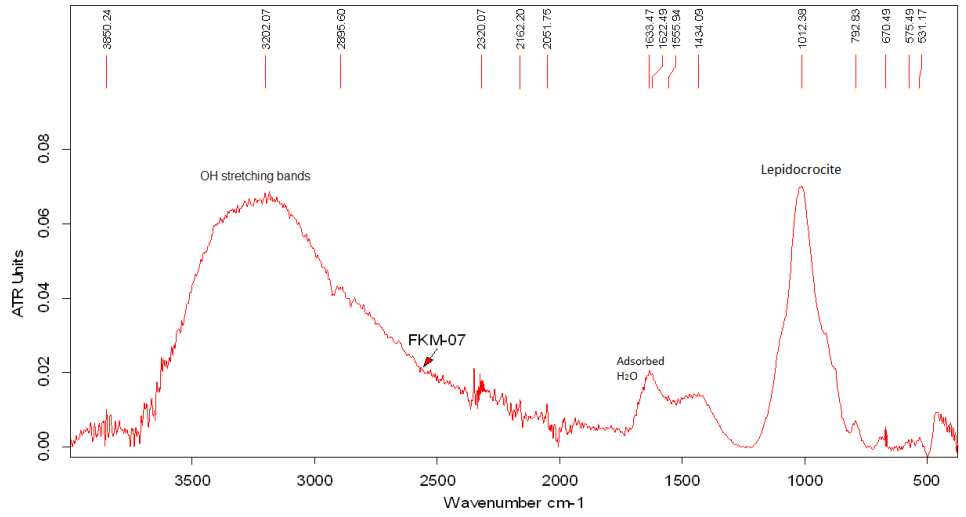


Figure 4. 76 FTIR spectrum of corrosion layer including ICL and TM of the nail (FKM-07) from the Ottoman layer excavations in Foça showing buried conditions: Lepidocrocite (β -FeOOH).

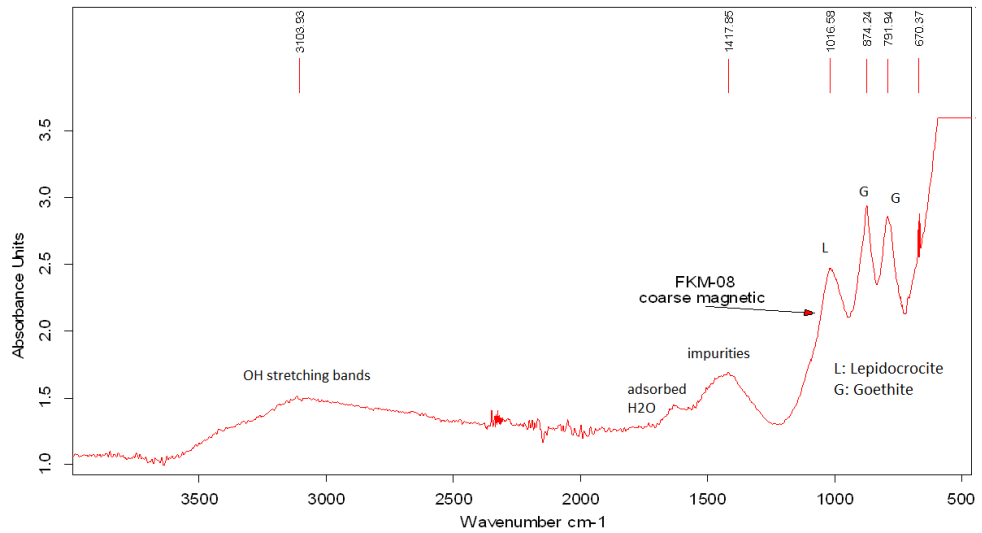


Figure 4. 77 FTIR spectrum of corrosion layer including ICL and TM of the iron piece (FKM-08) from the Ottoman layer excavations in Foça showing buried conditions: Goethite (α -FeOOH) and lepidocrocite (β -FeOOH).

Another iron piece (FKM-09) in buried conditions from the Ottoman layer excavations reveals main OH bending peak of lepidocrocite (γ -FeOOH) at 1005 cm^{-1} together with some goethite (α -FeOOH) having an OH bending peak at 874 cm^{-1} , hematite (α -Fe₂O₃) from its diagnostic Fe-O-Fe stretching peak at 524 cm^{-1} and quartz at 1082 cm^{-1} (Figure 4.78). The OH bending bands of goethite are separated by 78 cm^{-1} . The lower frequencies of OH bending bands (δ -OH and γ -OH) and their lower separation may be taken as evidence for poorly crystallized goethite. The δ -OH bending band at 874 cm^{-1} of the object (FKM-09) having very low and broad intensity is also a good indicator for its poor crystallinity. Its γ -OH bending band at 796 cm^{-1} has almost equal intensity with δ -OH bending band at 874 cm^{-1} .

The nail (FKM-10) in buried conditions from the Ottoman layer excavations as magnetic powder analysis sample reveals lepidocrocite (β -FeOOH) from its diagnostic OH bending peak at 1009 cm^{-1} ($1015 \pm 7\text{ cm}^{-1}$) and goethite (α -FeOOH) with its OH bending peak at 875 cm^{-1} (Figure 4.79). The OH bending bands of goethite are separated by 80 cm^{-1} . The lower frequencies of OH bending bands (δ -OH and γ -OH) and their lower separation may be taken as evidence for poorly crystallized goethite. The δ -OH bending band at 875 cm^{-1} of the nail (FKM-10) having very low and broad intensity may also be an indicator for its poor crystallinity. Its γ -OH bending band at 795 cm^{-1} has slightly higher intensity with δ -OH bending band at 875 cm^{-1} .

Lepidocrocite is observed in both samples. Their OH bending bands (δ -OH) are observed at 1005 cm^{-1} for FKM-09 and 1009 cm^{-1} for FKM-10. Their sharp and high intensity may be taken as evidence of good crystallinity of lepidocrocite in the corrosion layer.

Both objects have a broad band with high intensity in the region $3000\text{-}3500\text{ cm}^{-1}$. The iron piece (FKM-09) has an OH stretching band at $\sim 3218\text{-}3379\text{ cm}^{-1}$ and the nail (FKM-010) has an OH stretching band at $3150\text{-}3411\text{ cm}^{-1}$.

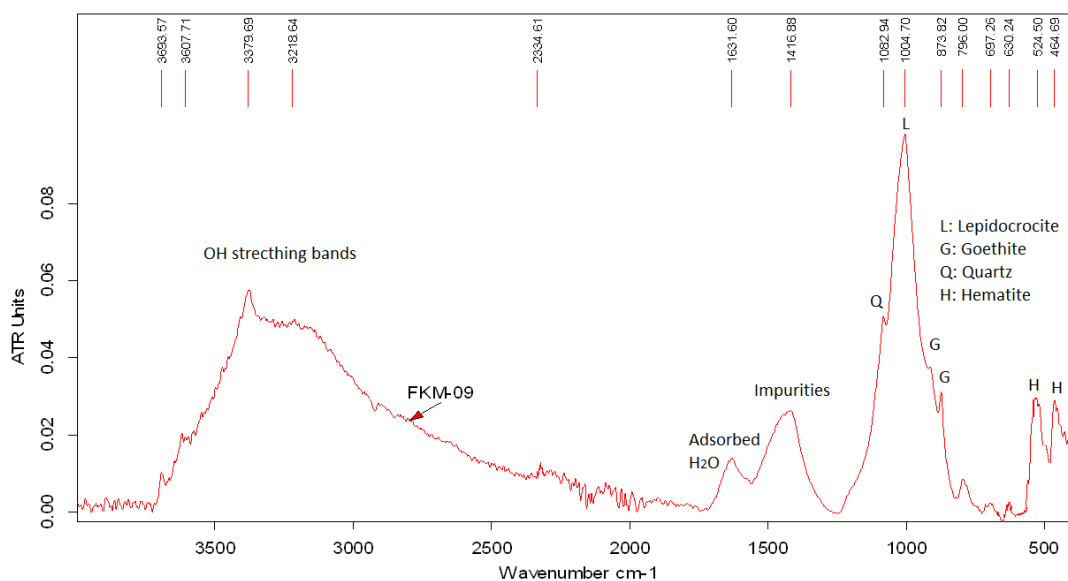


Figure 4. 78 FTIR spectrum of corrosion layer including ICL and TM of the iron piece (FKM-09) from the Ottoman layer excavations in Foça showing buried conditions: Quartz, goethite (α -FeOOH), lepidocrocite (γ -FeOOH) and hematite (α -Fe₂O₃).

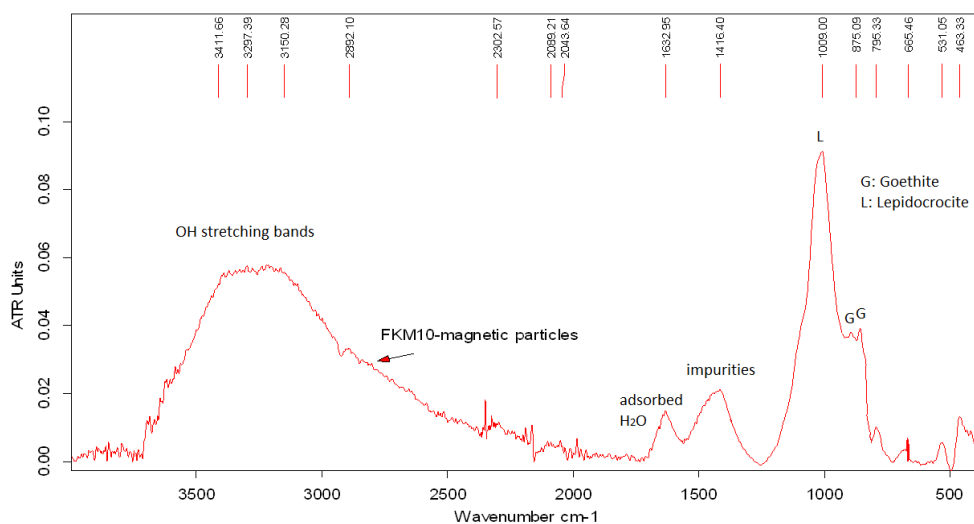


Figure 4. 79 FTIR spectrum of corrosion layer including ICL and TM of the nail (FKM-10) from the Ottoman layer excavations in Foça showing buried conditions: Goethite (α -FeOOH) and lepidocrocite (β -FeOOH).

When the major peak intensities of goethite and lepidocrocite are compared with each other in the same sample for the buried 19th century objects, there is only presence of lepidocrocite in the corrosion layer of the nail (FKM-07) and lepidocrocite is predominant in the iron piece (FKM-09). Magnetic particles collected from the corrosion powder of the nail (FKM-10) are mainly lepidocrocite with little amount of goethite while the other iron piece (FKM-08) has higher amount of goethite in comparison to lepidocrocite.

The other 19th century samples analyzed by FTIR are from a dwelling in Tekkekoy, Samsun. A nail (T-N-05) from a timber column at the façade of the dwelling representing outdoor atmospheric condition shows goethite (α -FeOOH) with its OH bending peak at 876 cm⁻¹ and lepidocrocite (β -FeOOH) with its characteristic OH bending peak at 1021 cm⁻¹ (Figure 4.80). The OH bending bands of goethite are separated by 82 cm⁻¹. The lower frequencies of OH bending bands (δ -OH and γ -OH) and their lower separation may be taken as evidence for poorly crystallized goethite. In addition, the δ -OH bending band at 876 cm⁻¹ of the nail (T-N-05) having broad and low intensity may be a sign for its poor crystallinity. Its γ -OH bending band at 794 cm⁻¹ has almost equal intensity with δ -OH bending band at 876 cm⁻¹. The broad and low intensity of δ -OH bending peak of lepidocrocite (β -FeOOH) may be taken as evidence of poor crystallinity of lepidocrocite in the corrosion layer. The nail (T-N-05) has a broad band with low intensity in the high wavenumber region 3000-3500 cm⁻¹ being OH stretching band at 3221 cm⁻¹.

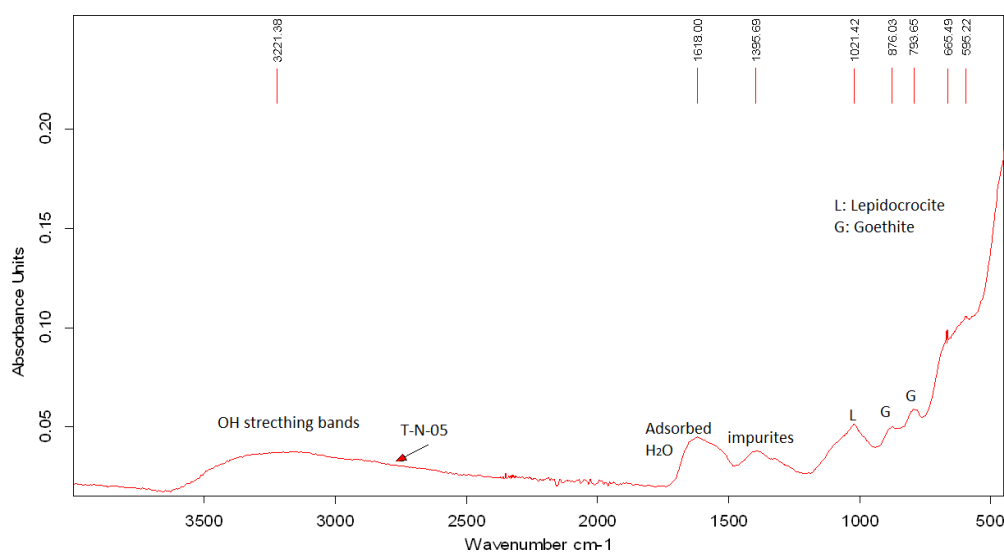


Figure 4. 80 FTIR spectrum of a corrosion layer including ICL and TM of the nail (T-N-05) from a timber column of a dwelling in Tekkekoy representing exterior conditions: goethite (α -FeOOH) and lepidocrocite (β -FeOOH).

The corrosion layer of a hinge pin from entrance hall's window (T-W-01) showing indoor atmospheric conditions which is also partially open to the outdoor atmosphere due to its location reveals goethite (α -FeOOH) with its OH bending peak at 872 cm^{-1} and lepidocrocite (β -FeOOH) with its characteristic OH bending peak at 1019 cm^{-1} (Figure 4.81). The OH bending bands of goethite are separated by 83 cm^{-1} . The lower frequencies of OH bending bands (δ -OH and γ -OH) and their lower separation may be taken as evidence for poorly crystallized goethite. The δ -OH bending band at 872 cm^{-1} having broad and low intensity may also be a sign of poorly crystallized goethite. The γ -OH bending band at 789 cm^{-1} has slightly higher intensity than δ -OH bending band at 872 cm^{-1} . The broad and low intensity of δ -OH bending peak of lepidocrocite (β -FeOOH) may be taken as evidence of its poor crystallinity in the same corrosion layer. The broad band with low intensity in the high wavenumber region $3000\text{-}3500\text{ cm}^{-1}$ has a peak at 3095 cm^{-1} .

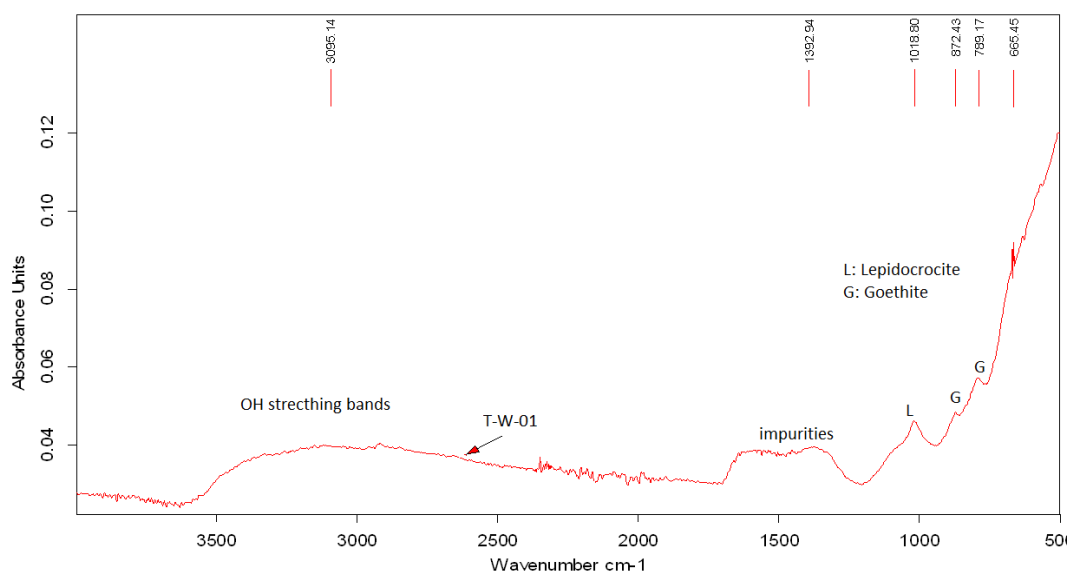


Figure 4. 81 FTIR spectrum of a corrosion layer including ICL and TM of a hinge pin from the entrance hall's window (T-W-01) of a dwelling in Tekkekoy representing an iron object partially open to atmospheric conditions: goethite (α -FeOOH) and lepidocrocite (β -FeOOH).

A crossbar of the main entrance door locking (T-D-01) from interior also partially open to outdoor atmosphere due to its location, displays goethite (α -FeOOH) with its OH bending peak at 873 cm^{-1} and lepidocrocite (β -FeOOH) with its OH bending peak at 1024 cm^{-1} (Figure 4.82). Quartz is also identified with its characteristic peak at 1088 cm^{-1} in its corrosion layer. The OH bending bands of goethite are separated by 90 cm^{-1} . The lower frequencies of OH bending bands (δ -OH and γ -OH) and their lower separation may be taken as evidence for poorly crystallized goethite. The δ -OH bending band at 873 cm^{-1} having broad and low intensity may also be a sign for its poor crystallinity. The γ -OH bending band at 789 cm^{-1} has slightly lower intensity than δ -OH bending band at 873 cm^{-1} . The broad and low intensity of δ -OH bending peak of lepidocrocite (β -FeOOH) may also indicate its poor crystallinity of lepidocrocite in the corrosion layer. The broad band with low intensity in the region $3000\text{-}3500\text{ cm}^{-1}$ has a peak at 3095 cm^{-1} .

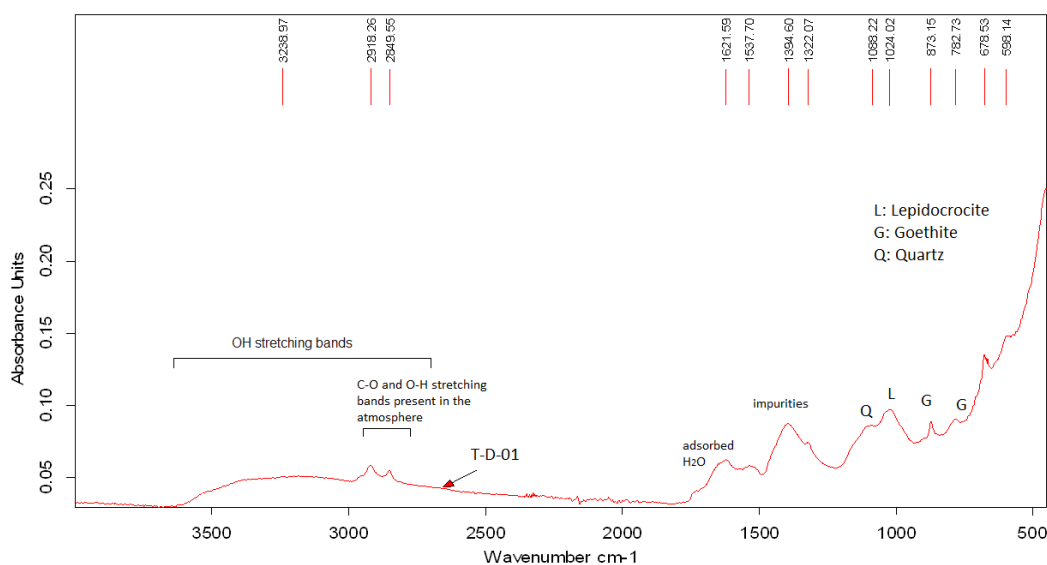


Figure 4. 82 FTIR spectrum of a corrosion layer including ICL and TM of the crossbar of the main entrance door locking (T-D-01) from a dwelling in Tekkekoy representing an iron object partially open to atmospheric conditions: goethite (α -FeOOH), lepidocrocite (β -FeOOH) and quartz.

Goethite together with lepidocrocite are the most important phases of surface corrosion layers in the 19th century iron objects. In the buried samples lepidocrocite has higher bending peak intensities than goethite. These results from FTIR analysis confirm μ -Raman results. FTIR spectroscopy results of surface corrosion layers for the 19th century objects are summarized in table 4.26.

When the major peak intensities of goethite and lepidocrocite are compared with each other in the same sample regarding the 19th century objects from Tekkekoy, the presence of lepidocrocite is more pronounced than goethite in all objects showing corrosion at both outdoor atmospheric conditions and partially open to outdoor atmospheric conditions. All objects have low crystallinity of both lepidocrocite and goethite in their corrosion layer.

Iron oxides found by FTIR in the corrosion layer of the samples from 15th, 16th and 19th century objects are summarized in table 27.

Table 4.2.6 Iron oxides layering in the corrosion of the objects from the 19th century dwellings in Foça, İzmir and Tekkeköy, Samsun under different atmospheric conditions observed by FTIR Analysis.

Sample ID	Mixture of RE, ICL and TM	Goethite δ -OH and γ -OH frequencies and peak intensity comparison (δ -OH vs γ -OH)	Separation	OH-stretching frequency and peak intensity	Goethite crystallinity	Lepidocrocite OH-bending frequency and peak intensity in comparison to Goethite δ -OH	Lepidocrocite crystallinity
FKM-01 - Window guard iron piece from a dwelling <i>Outdoor</i>	goethite lepidocrocite	910 cm^{-1} vs 713 cm^{-1} Very high Sharp	127 Very high	3328 cm^{-1} Low	Good	1019 cm^{-1} Low Broad	Variable
FKM-02 - Nail of a joining load bearing, main timbers eaves <i>Indoor</i>	goethite	875 cm^{-1} vs 796 cm^{-1} Almost equal Broad	79 Low	3330 cm^{-1} Very High	Low	-	-
FKM-03 - Door lock piece of the main entrance. <i>Partially open to atmosphere</i>	goethite lepidocrocite	874 cm^{-1} vs 718 cm^{-1} Almost equal Broad	56 Low	3249 cm^{-1} Low	Low	1020 cm^{-1} High Broad	Variable
FKM-04 - Male hinge of the main entrance door <i>Partially open to atmosphere</i>	goethite lepidocrocite quartz	875 cm^{-1} vs 792 cm^{-1} Almost equal Sharp	83 Low	3318 cm^{-1} Very high	Variable	1020 cm^{-1} Almost Equal Sharp	Good
FKM-05 - Female hinge of the main entrance door <i>Partially open to atmosphere</i>	goethite lepidocrocite	873 cm^{-1} vs 710 cm^{-1} High Broad	93 Low	Very Low	Low	1020 cm^{-1} High Broad	Variable
FKM-31 - Nail, embedded in building iron nail <i>Partially open to atmosphere</i>	goethite	847 cm^{-1} vs 793 cm^{-1} Almost equal Broad	76 Low	3313 cm^{-1} Very high	Low	-	-
<ul style="list-style-type: none"> • Crystallinity decrease \rightarrow Band width (Broaden) increase \rightarrow OH-bending bands frequency (cm^{-1}) decrease \rightarrow separation decreases \rightarrow OH-stretching bands (cm^{-1}) increase • Separation decrease \rightarrow Aluminum substitution decrease \rightarrow OH-stretching bands increase 							

Table 4.26 Iron oxides layering in the corrosion of the objects from the 19th century dwellings in Foça, İzmir and Tekkeköy, Samsun under different atmospheric conditions observed by FTIR Analysis (continued).

Sample ID	Mixture of RF, ICL and TM	Goethite δ -OH and γ -OH frequencies and Peak intensity comparison (δ -OH vs γ -OH)	Separation	OH-stretching frequency and Peak intensity	Goethite Crystallinity	Lepidocrocite δ OH-bending frequency, i) Peak intensity in Comparison to Goethite δ -OH, ii) its sharpness	Lepidocrocite Crystallinity
FKM-07 - Nail from the Ottoman layer, buried	lepidocrocite	-	-	3202 cm^{-1} Very high	-	i) 1014 cm^{-1} ii) Very High iii) Sharp	Good
FKM-08 - L shaped iron piece from the Ottoman layer, buried collected magnetic particles	goethite lepidocrocite	874 cm^{-1} vs 792 cm^{-1} Slightly high Sharp	82 Low	3104 cm^{-1} Low	Variable	i) 1017 cm^{-1} ii) Low iii) Broad	Low
FKM-09 - Iron piece, from the Ottoman layer buried	goethite lepidocrocite hematite quartz	874 cm^{-1} vs 795 cm^{-1} Almost equal Broad	79 Low	3379 cm^{-1} High	Low	i) 1005 cm^{-1} ii) Very High iii) Sharp	Variable
FKM-10 - Nail from the Ottoman layer buried collected magnetic particles	goethite lepidocrocite	875 cm^{-1} vs 795 cm^{-1} Low Broad	80 Low	3150-3411 3397 cm^{-1} High	Low	1009 cm^{-1} Very High Sharp	Variable
T-N-05 - Nail from the timber column, exterior	goethite lepidocrocite	876 cm^{-1} vs 794 cm^{-1} Almost equal	82 Low	3221 cm^{-1} Low	Low	1021 cm^{-1} Slightly high Broad	Low
T-W-01 - Iron hinge pin, from the entrance hall's window partially open to atmosphere	goethite lepidocrocite	872 cm^{-1} vs 789 cm^{-1} Low	83 Low	3095 cm^{-1} Low	Low	1019 cm^{-1} Slightly high Broad	Low
T-D-01 - Iron crossbar, for main entrance door locking partially open to atmosphere	goethite lepidocrocite quartz	873 cm^{-1} vs 783 cm^{-1} High	90 Low	3239 cm^{-1} Low	Low	1024 cm^{-1} High Broad	Low

Table 4. 27 Iron oxides found by FTIR in the corrosion layer of the samples from 15th, 16th and 19th century objects.

Sample ID and location	Minerals in the Powdered Mixture of Corrosion Layers				
	Goethite (α -FeOOH)	Lepidocrocite (β -FeOOH)	Hematite (α -Fe ₂ O ₃)	Magnetite (Fe ₃ O ₄)	Quartz
GMH-Me-02 - Door lock piece, Partially open to atmosphere	Goethite	Lepidocrocite		Magnetite	
GMH-Me-03 - Plaster nail, indoor	Goethite	Lepidocrocite			
MSH-KAP-01 - Nail from the dome, outdoor	Goethite	Lepidocrocite	Hematite		
MSH-KAP-03 - Nail from the dome, outdoor	Goethite	Lepidocrocite			
MSH-KAP-02 - Iron piece convenient to anchoring, indoor	Goethite	Lepidocrocite			
FKM-01 - Window guard iron piece from a dwelling, outdoor	Goethite	Lepidocrocite			
FKM-02 - Nail for a jointing load bearing, main timber beams, indoor	Goethite				
FKM-03 - Door lock piece from the main entrance, partially open to atmosphere	Goethite	Lepidocrocite			
FKM-04 - Male hinge from the main entrance door, partially open to atmosphere	Goethite	Lepidocrocite			Quartz
FKM-05 - Female hinge from the main entrance door, partially open to atmosphere	Goethite	Lepidocrocite			
FKM-11 - Nail embedded in building stone, partially open to atmosphere	Goethite				
FKM-07 - Nail from the Ottoman layer, buried		Lepidocrocite			
FKM-08 - L shaped iron piece from the Ottoman layer, buried (collected magnetic particles)	Goethite	Lepidocrocite			
FKM-09 - Iron piece from the Ottoman layer, buried	Goethite	Lepidocrocite	Hematite		Quartz
FKM-10 - Nail from the Ottoman layer, buried (collected magnetic particles)	Goethite	Lepidocrocite			
T-N-05 - Nail from a timber column, exterior	Goethite	Lepidocrocite			
T-W-01 - Iron hinge pin from the entrance hall's window, partially open to atmosphere	Goethite	Lepidocrocite			
T-D-01 - Iron crossbar from the main entrance door locking, partially open to atmosphere	Goethite	Lepidocrocite			Quartz

4.5 Examination of morphological and compositional characteristics of the corrosion layers by using μ -Raman Spectroscopy

Etched cross-sections of the corroded iron objects were analyzed in the images obtained by μ -Raman spectroscopy. The typical samples of iron objects from 15th, 16th and 19th centuries have been observed and compared for their corrosion minerals and the layering in the corrosion. Although mapping of the corrosion products determined by Raman spectroscopy has not been conducted, the analyses were performed on a line starting from metal towards TM by taking several Raman spectra of the locations.

4.5.1 Raman Analyses of the 15th Century Samples

Corrosion characteristics of the 15th century iron objects were examined on two selected objects. The SEM image of door lock piece (GMH-Me-02) from the 15th century hammam building shows a compact and distinct corrosion layer (Figure 4.83a and b). Starting from the metal body towards TM, 19 points were analyzed (Figures 4.84 a, b, c, d and e). The first 5 points were around the reaction front (RF). At point 1, akageneite (β -FeOOH) and goethite (α -FeOOH); at point 2, goethite (α -FeOOH) and at point 3, hydrated iron (III) oxide or oxyhydroxide have been observed. At point 4, goethite (α -FeOOH) has been very well identified and lastly, at point 5, the presence of abundant hydrated iron (III) oxide or oxyhydroxide together with some hematite (α -Fe₂O₃) have been observed (Figure 4.84 e). Goethite is the most abundant phase observed together with hydrated iron (III) oxide or oxyhydroxide, hematite and akaganeite in RF.

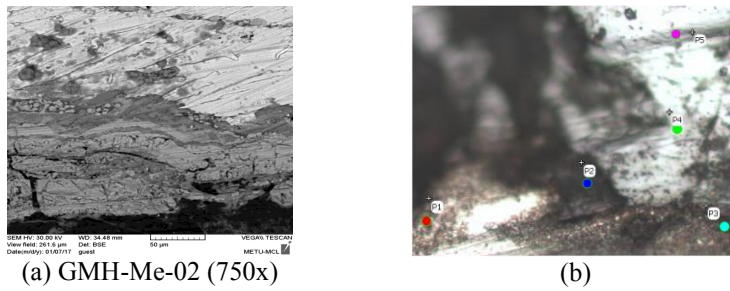


Figure 4. 83 SEM image of a door lock piece (GMH-Me-02) after etching with nitric acid in alcohol (a) and the first five points located around RF of the same sample (15th cc).

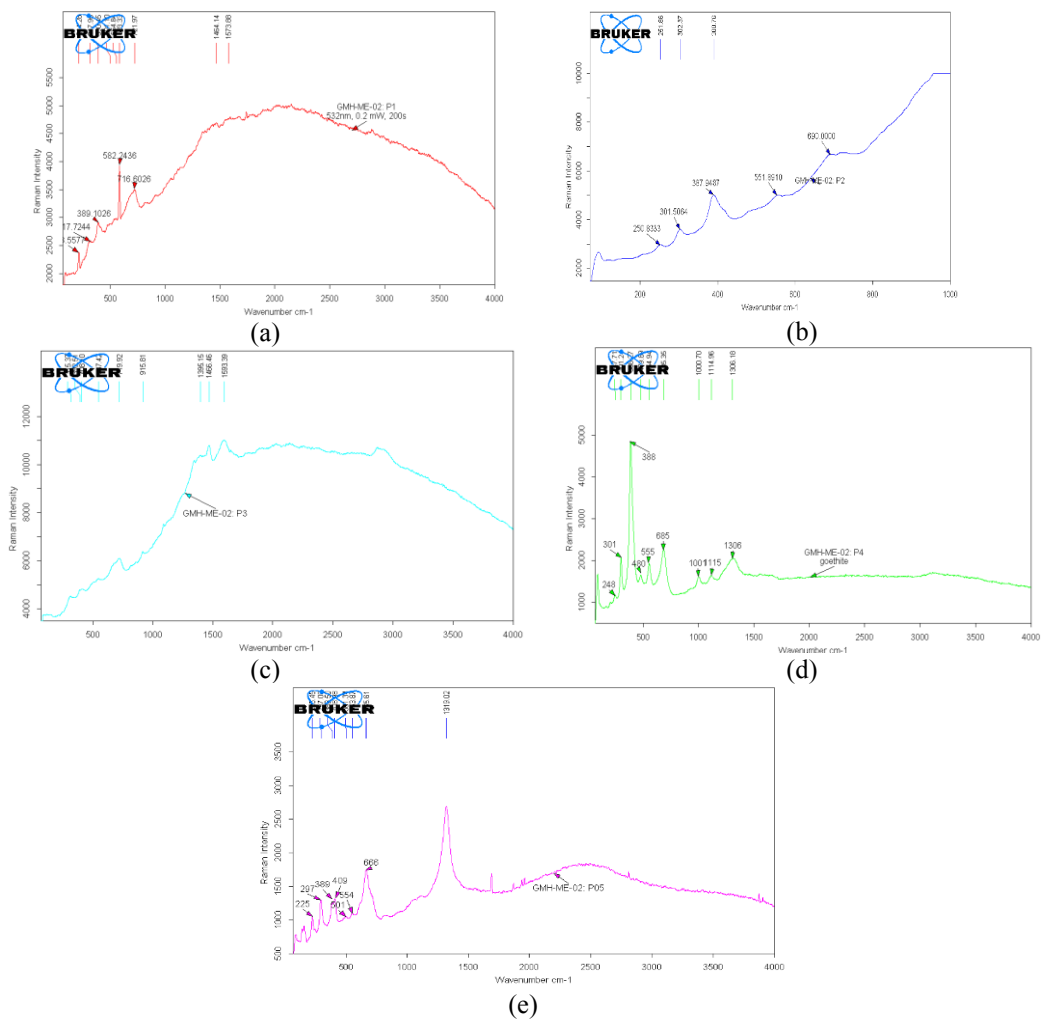


Figure 4. 84 Raman spectra of the first five points located around RF in the corrosion layer of a door lock piece (GMH-Me-02): goethite is the most abundant phase together with hydrated iron (III) oxide or oxyhydroxide, hematite and akaganeite.

The second 5 points were in the ICL after the RF (Figure 4.85 a). At points 6 to 8 hydrated iron (III) oxide or oxyhydroxide, together with some hematite ($\alpha\text{-Fe}_2\text{O}_3$), and at points 9 and 10 goethite ($\alpha\text{-FeOOH}$) have been identified (Figure 4.85 b, c, d and e). Hydrated iron (III) oxide or oxyhydroxide, goethite and hematite are the phases observed.

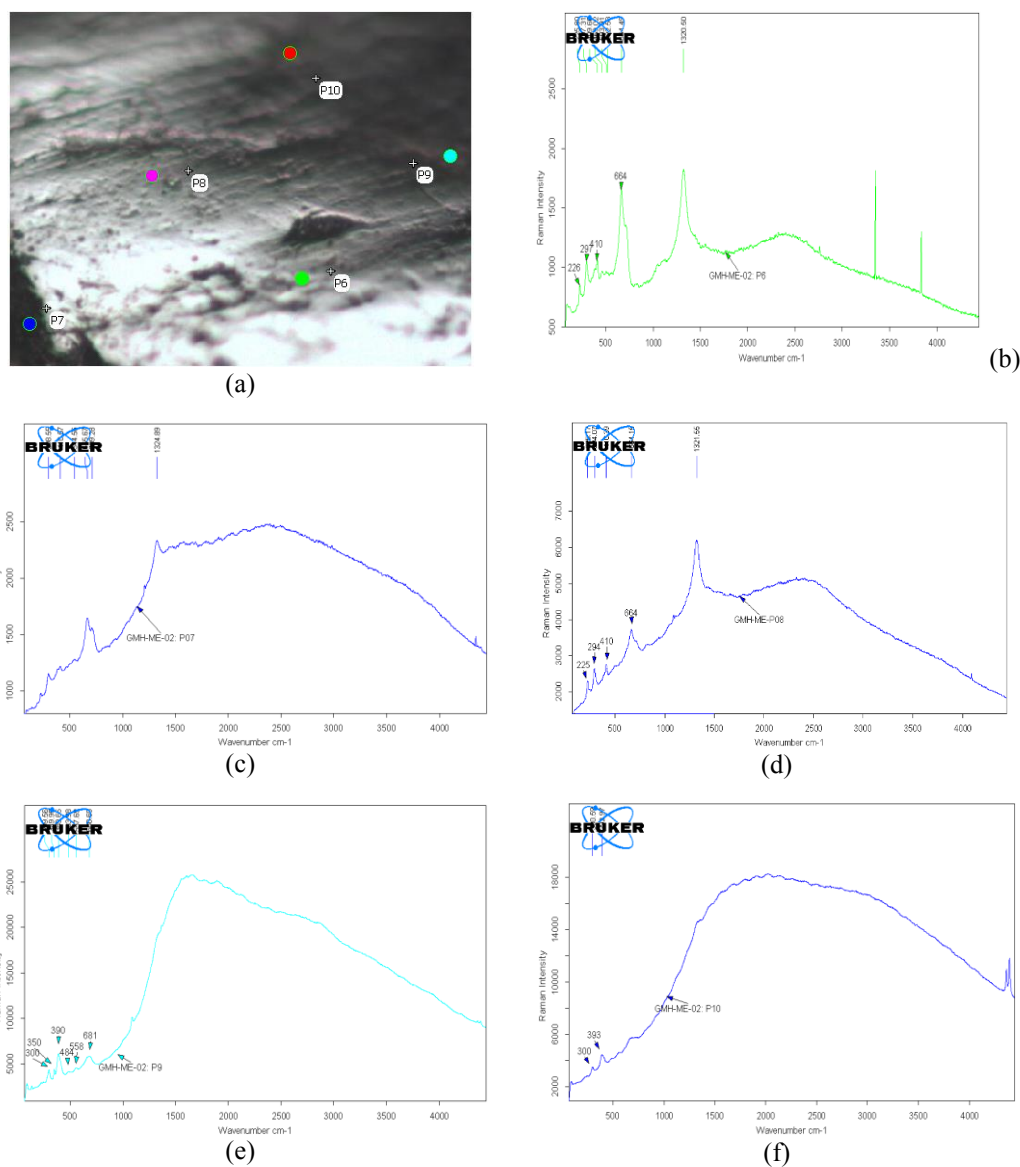


Figure 4. 85 Raman spectra of the second five points located in the ICL after RF in the corrosion layer of a door lock piece (GMH-Me-02): hydrated iron (III) oxide or oxyhydroxide and goethite are the most abundant phases with some hematite.

The following 4 points (P11-12-13 and 14) were in the ICL (Figure 4.86 a). At points 11 and 14 hydrated iron (III) oxide or oxyhydroxide together with some hematite (α -Fe₂O₃), at point 12 goethite (α -FeOOH) and at point 13 magnetite (Fe₃O₄) have been clearly detected (Figure 4.86 b, c, d, e). Hydrated iron (III) oxide or oxyhydroxide, hematite, goethite and magnetite are the iron oxides observed.

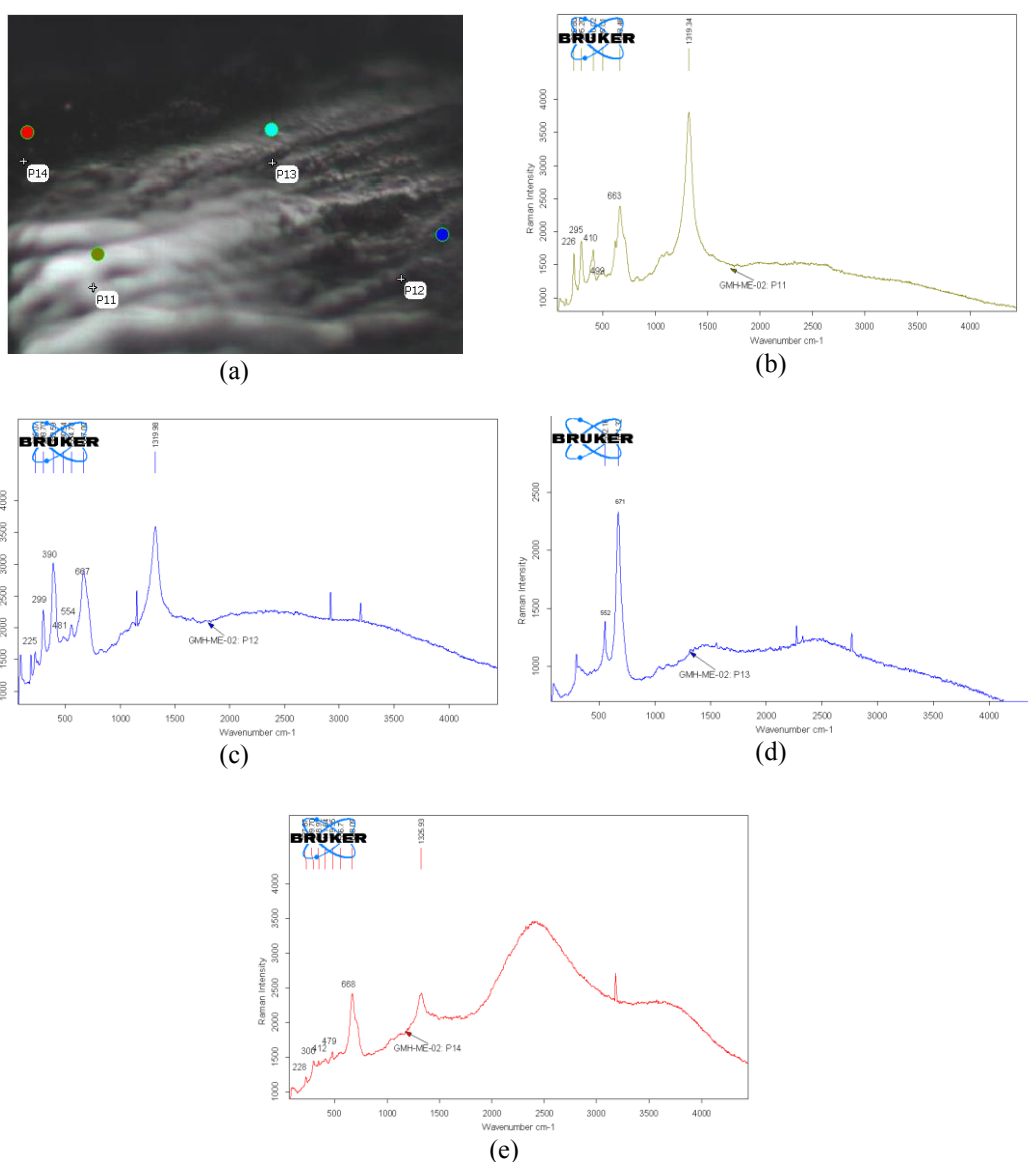


Figure 4. 86 Raman spectra of the third region with four points located in the ICL of a door lock piece (GMH-Me-02): Hydrated iron (III) oxide or oxyhydroxide, hematite, goethite and magnetite are the iron oxides observed.

The following 3 points (p15-16 and 17) were in the ICL (Figure 4.87 a). At points 15, 16 and 17 magnetite (Fe_3O_4) have been the iron oxides observed (Figure 4.87 b, c and d).

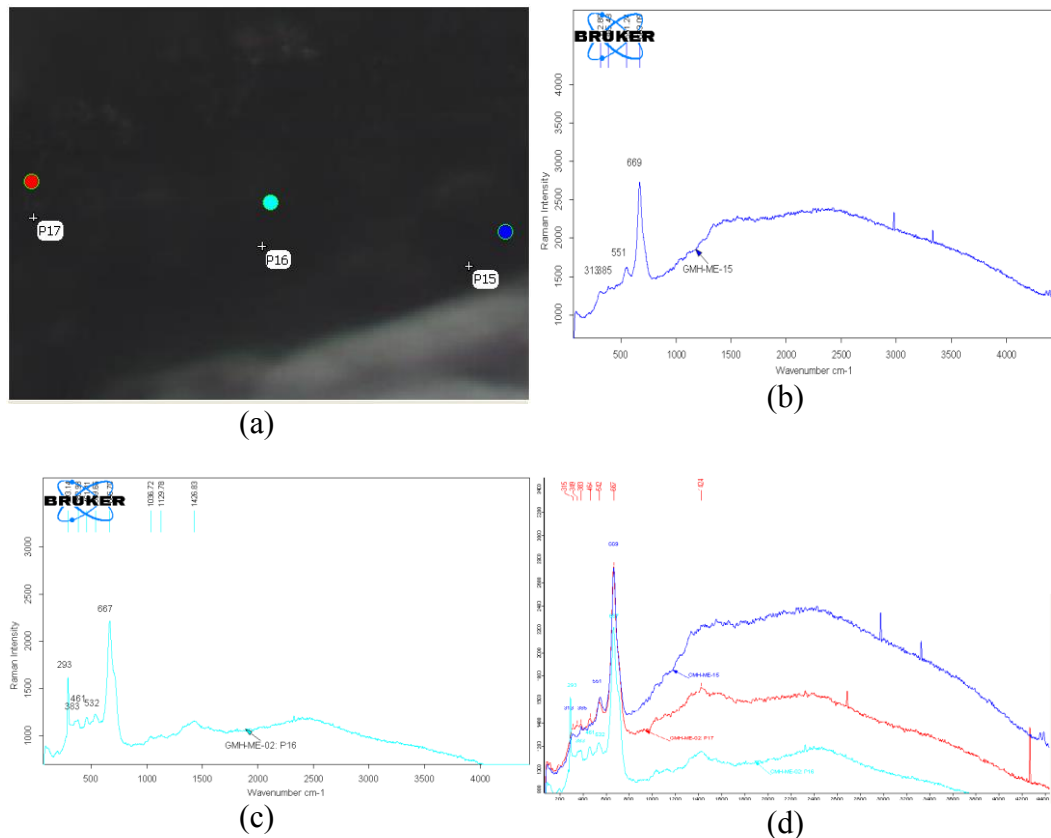


Figure 4. 87 Raman spectra of the fourth region with three points located in the ICL of a door lock piece (GMH-Me-02): magnetite.

The last 2 points (p18 and 19) of the door lock piece from the 15th century (GMH-Me-02) were close to the TM layer (Figure 4.88 a). At point 18, some hydrated iron (III) oxide or oxyhydroxide, while at point 19, goethite ($\alpha\text{-FeOOH}$) has been identified (Figure 4.88 b, c). The overall corrosion layers of the door lock piece (GMH-Me-02) and its layering are summarized in Table 4.28.

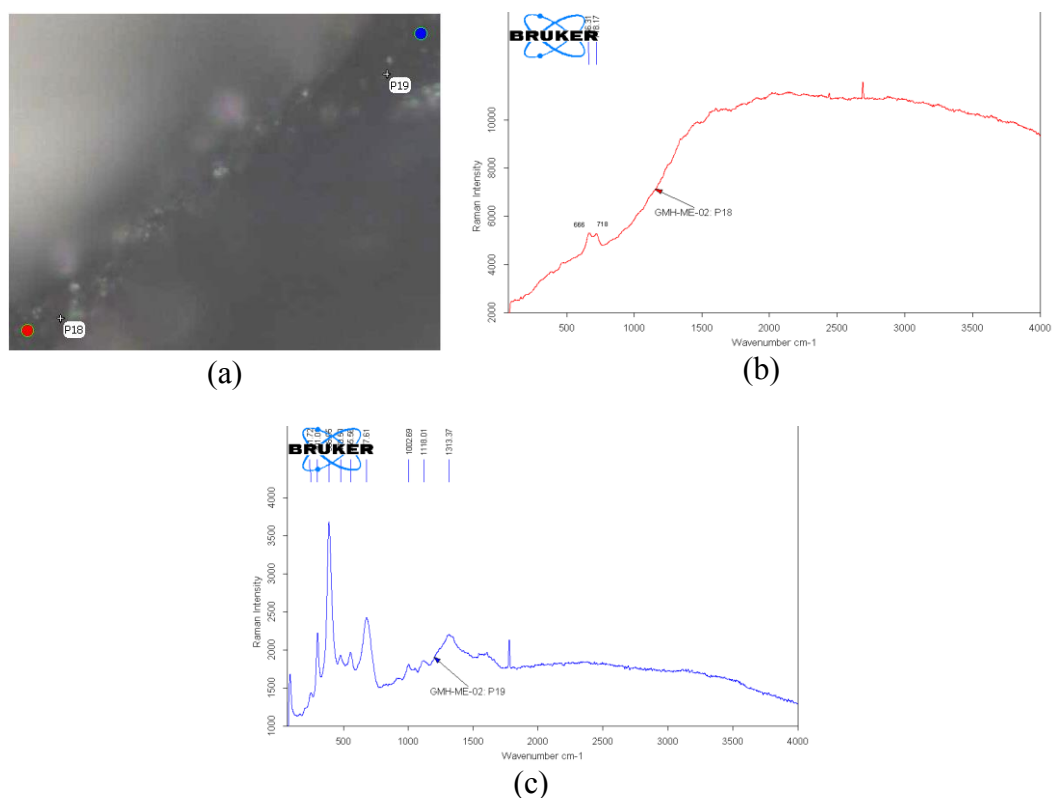
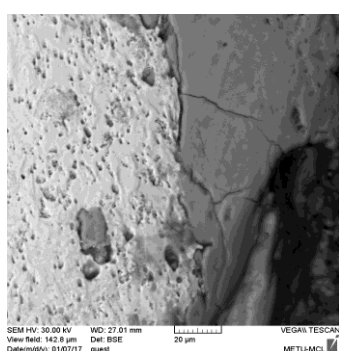


Figure 4. 88 Raman spectra of the fifth region with two points located close to the TM of a door lock piece (GMH-Me-02): goethite is the most abundantly observed iron oxide together with hydrated iron (III) oxide or oxyhydroxide.

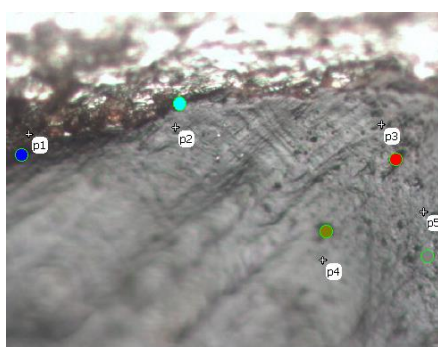
Table 4. 28 Iron oxides followed by μ -Raman analyses in the corrosion layer of a door lock piece (GMH-Me-02) (15th cc).

Location	Minerals Observed in the Corrosion Layer				
	Reaction Front RF \rightarrow ICL \rightarrow ICL-TM Border (OSL) \rightarrow TM				
Interior of the Hammam building – <i>partially open to atmospheric conditions</i>	Akageneite (β -FeOOH)	Hydrated iron (III) oxide or oxyhydroxide	Hydrated iron (III) oxide or oxyhydroxide	Magnetite (Fe_3O_4)	Hydrated iron (III) oxide or oxyhydroxide
	Goethite (α -FeOOH)	Hematite (α -Fe $2O_3$)	Hematite (α -Fe $2O_3$)		
	Hydrated iron (III) oxide or oxyhydroxide	Goethite (α -FeOOH)	Goethite (α -FeOOH)		Goethite (α -FeOOH)
	Hematite (α -Fe $2O_3$)		Magnetite (Fe_3O_4)		

The SEM image of the plaster nail from interior (GMH-Me-04) from the 15th century hammam building shows a compact and distinct corrosion layer with low corrosion thickness, $\sim 75 \mu\text{m}$ (Figure 4.89 a, b). Starting from the metal body towards TM, four steps with 20 total points have been analyzed (Figures 4.90, 4.91, 4.92, 4.93 and 4.94). The overall corrosion layers of the door lock piece (GMH-Me-04) and its layering are summarized in Table 4.29. The steps have been organized in such a way that each step follows the previous one. Each step covers a fixed area of almost equal dimensions. The first step covers the reaction front (RF) and includes μ -Raman analyses of 5 points. At point 1 up to point 4 goethite (α -FeOOH) is the main phase identified with its typical characteristic peaks at 390 cm^{-1} , 300 cm^{-1} , 680 cm^{-1} , 245 cm^{-1} and 1320 cm^{-1} in decreasing intensity (Figures 4.90 a, b, c and e). At point 5 (P5), presence of abundant hydrated iron (III) oxide or oxyhydroxide together with goethite (α -FeOOH) has been noticed (Figure 4.90 d) with a high intensity symmetrical peak observed at 702 cm^{-1} , together with typical peaks of goethite.



(a) GMH-Me-04 (2000x)



(b)

Figure 4. 89 SEM image of a plaster nail (GMH-Me-04) after etching with nitric acid in alcohol (a) and μ -Raman microscopic image of first five points located around RF of the same sample (b) (15th cc).

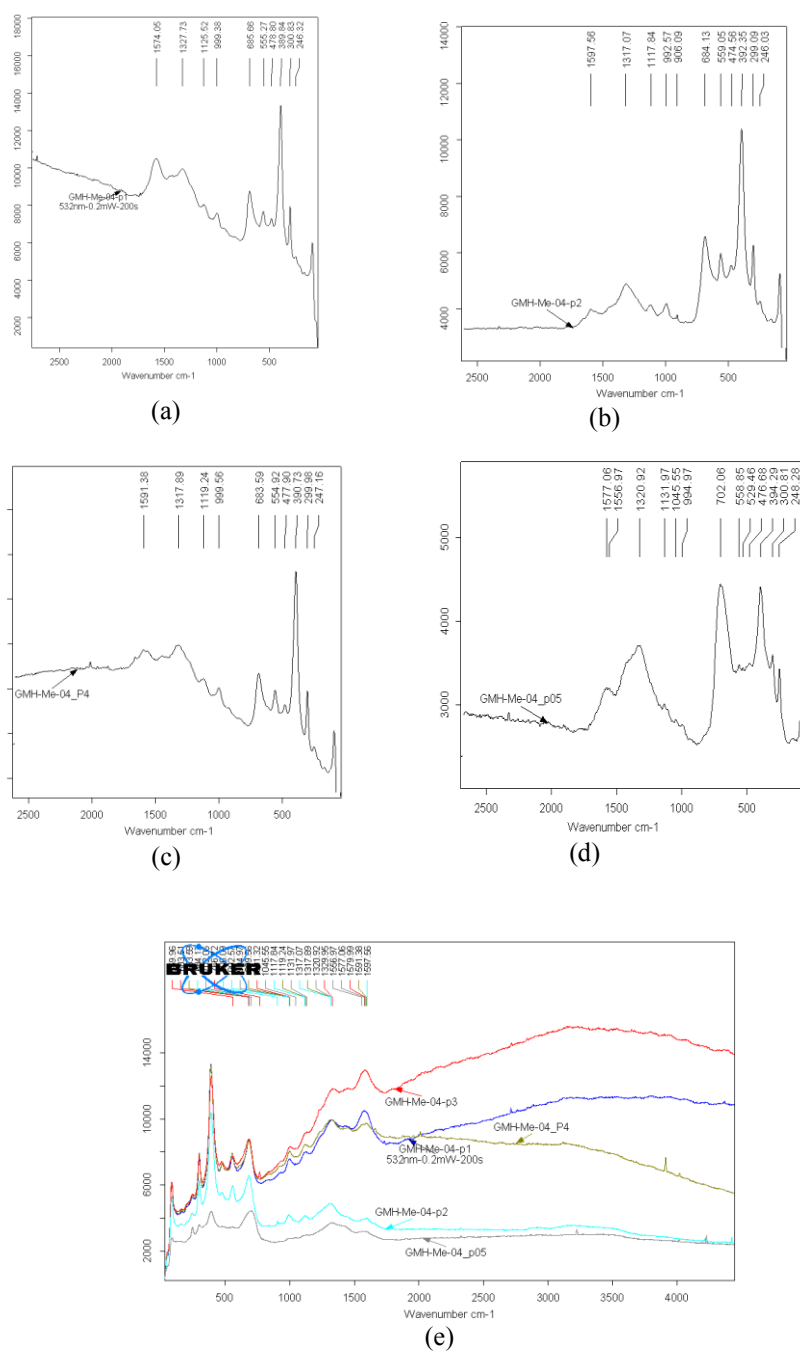


Figure 4. 90 μ -Raman spectra of the first five points located around RF in the corrosion layer of a plaster nail from interior (GMH-Me-04) (a, b, c, d, e): goethite is the most abundant phase from p1 to p4 (a, b, c, e); presence of hydrated iron (III) oxide or oxyhydroxide together with some goethite (d).

The second step involves 5 points in ICL after the RF (Figure 4.91 a). At points 6 to 8 goethite (α -FeOOH) is the main phase (Figure 4.91 b-d). At point 9 located next to a large pore, lepidocrocite (γ -FeOOH) is the main phase observed with its typical strong peak at 254 cm^{-1} (Figure 4.92 a). At P10 not very far from the P9, goethite (α -FeOOH) is observed (Figure 4.92 b). It can be concluded that at step 2, being in ICL next to the reaction phase, goethite is the main phase observed. However, presence of lepidocrocite is also seen.

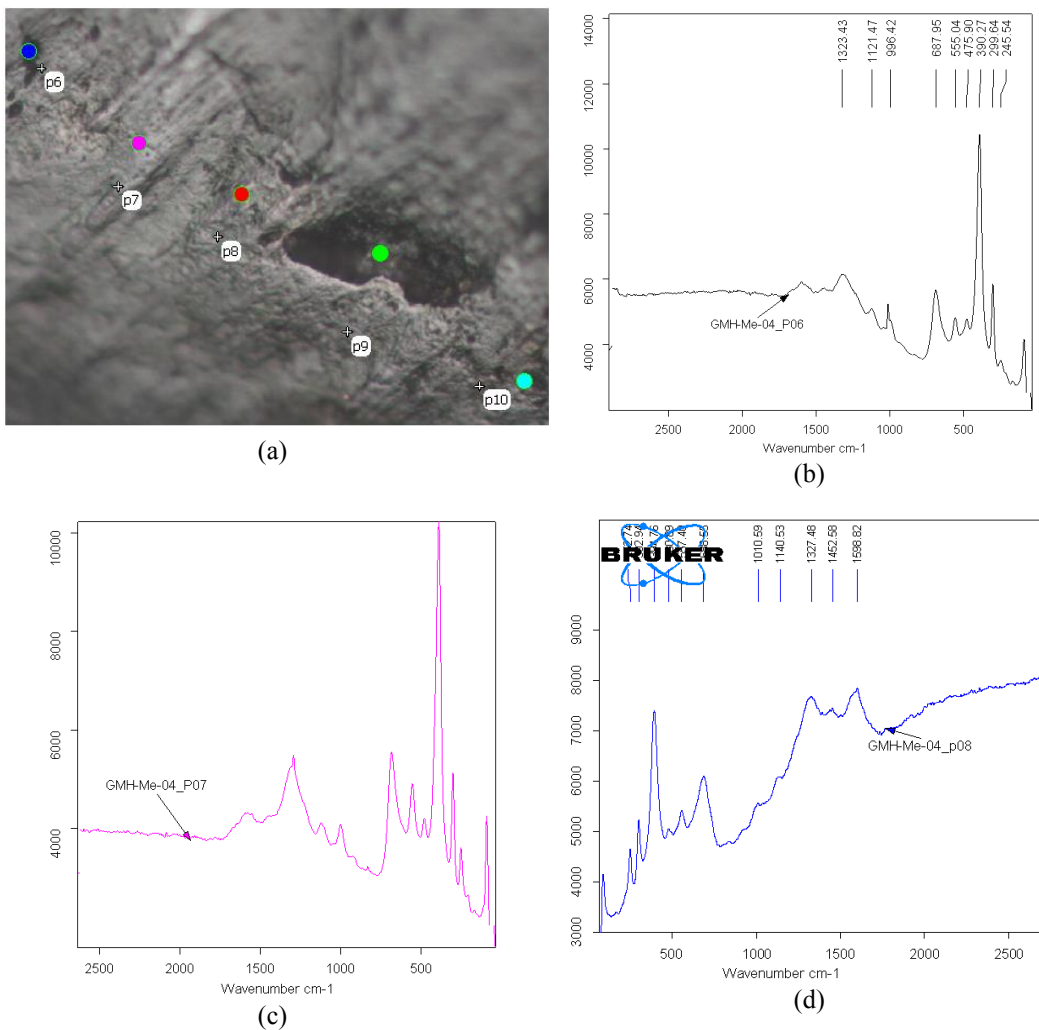


Figure 4. 91 μ -Raman spectra of the second 5 points located in the ICL after RF in the corrosion layer of a plaster nail from interior (GMH-Me-04): Goethite is the most abundant phase.

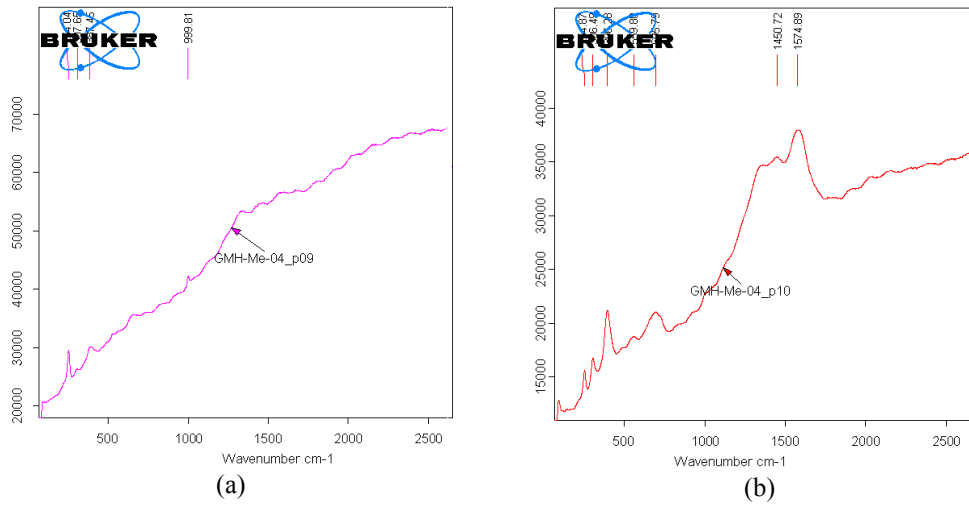


Figure 4.92 Raman spectra of the second 5 points located in the ICL after RF in the corrosion layer of a plaster nail from interior (GMH-Me-04) (a, b): Lepidocrocite is observed at p9 (a), Goethite together with lepidocrocite is observed at p10 (b).

The following 6 points (P11 to P16) in the ICL have been analyzed (Figure 4.93a). In all six points, goethite (α -FeOOH) is the only oxide phase identified (Figure 4.93b).

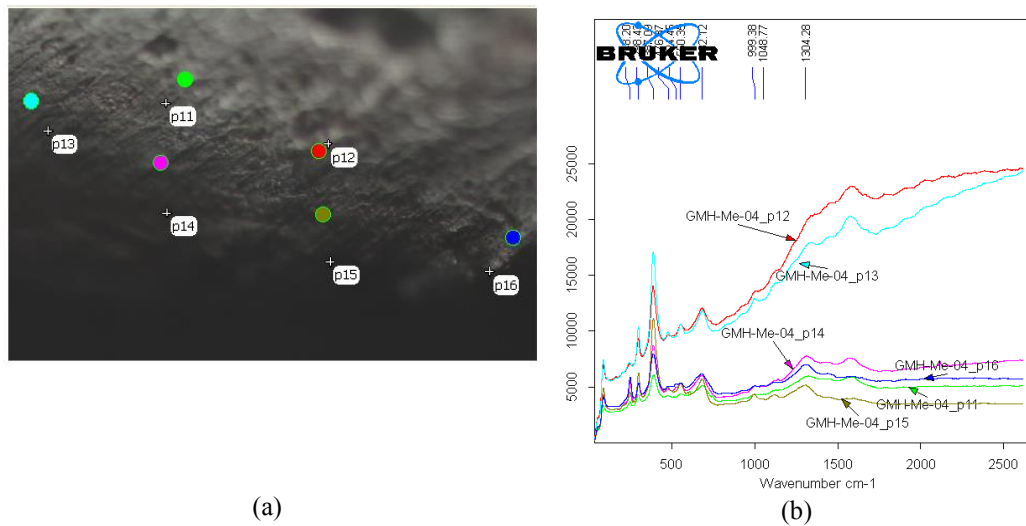


Figure 4.93 μ -Raman spectra of the third area where 6 points are located in the ICL of a plaster nail from interior (GMH-Me-04) (a, b): Goethite is the phase observed.

The fourth area consisting of 3 points (p17, p18 and p19) have been the points close to the TM (Figure 4.94 a, b). At point 17, lepidocrocite (γ -FeOOH) (Figure 4.94 c), at points 18 (p18) and 19 (p19) hydrated iron (III) oxide or oxyhydroxide have been identified (Figure 4.94 d, e). The following 1 point (P20) has been located in the TM (Figure 4.94 b). At the p20 goethite (γ -FeOOH) has been identified (Figure 4.94 f).

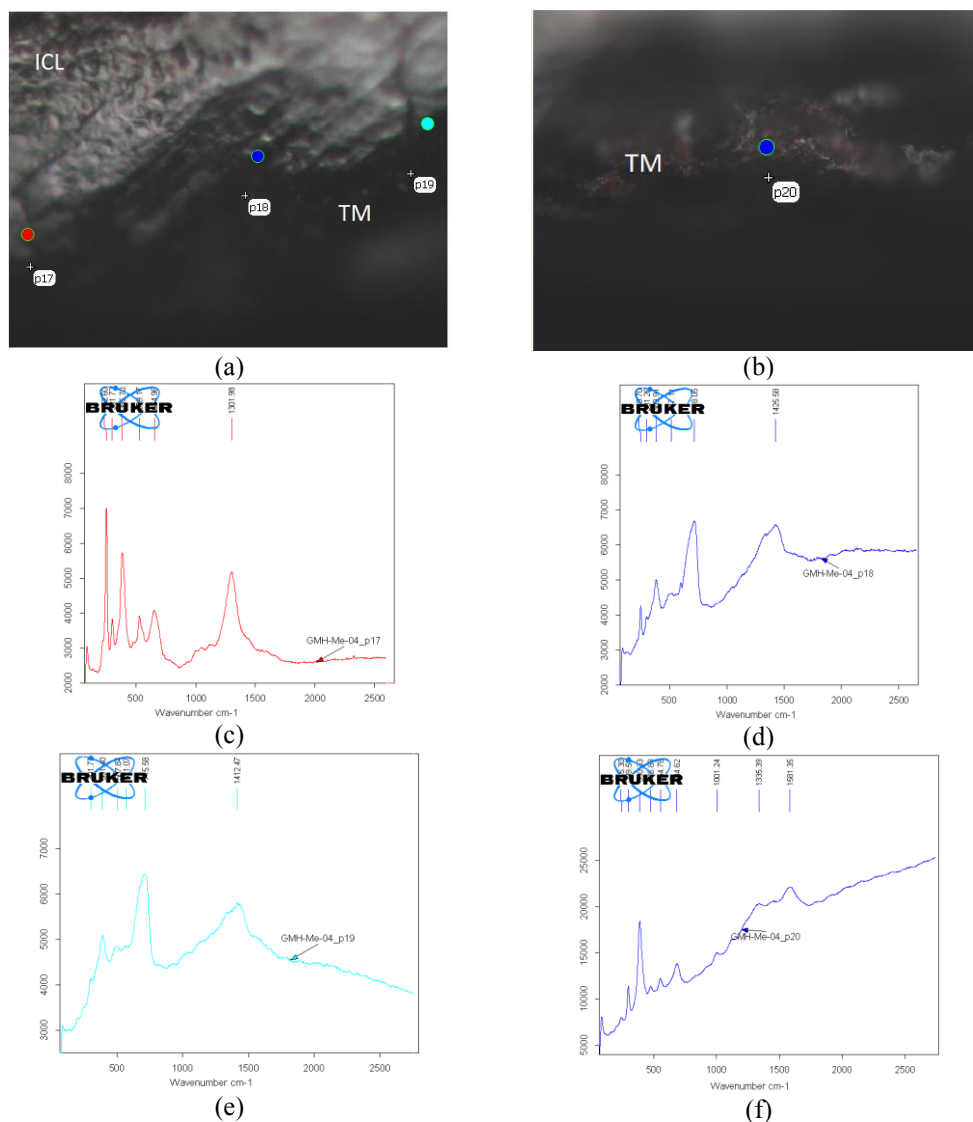


Figure 4. 94 μ -Raman spectra of the fourth area where 3 points are located close to the TM in the corrosion layer (a, c, d, e) and the fifth area where 1 point is located in the TM (b, f) of a plaster nail from interior (GMH-Me-04): Lepidocrocite (c), hydrated iron (III) oxide or oxyhydroxide (d, e) and goethite (f) are the phases observed.

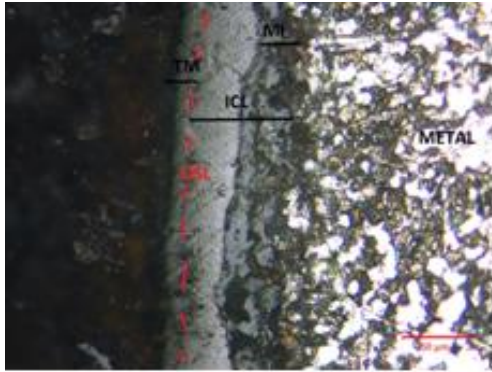
Table 4. 29 Iron oxides found by μ -Raman analyses in the corrosion layer of a plaster nail (GMH-Me-04) (15th cc).

Location	Observed Corrosion Minerals				
	Reaction Front RF \rightarrow ICL \rightarrow ICL-TM border (OSL) \rightarrow TM				
Interior of the Hammam building – <i>Indoor</i>	Goethite (α -FeOOH) Hydrated iron (III) oxide or oxyhydroxide	Goethite (α -FeOOH) Lepidocrocite (γ -FeOOH) Hydrated iron (III) oxide or oxyhydroxide	Goethite (α -FeOOH)	Lepidocrocite (γ -FeOOH) Hydrated iron (III) oxide or oxyhydroxide	Goethite (α -FeOOH)

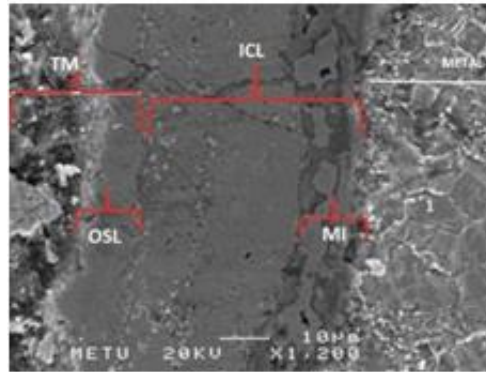
4.5.2 Raman Analyses of the 16th Century Samples

Corrosion characteristics of the 16th century iron objects have been examined on the following selected seven objects: Two nails from the dome (MSH-KAP-01 and -03), one iron piece convenient to anchoring (MSH-KAP-02) from interior of the hammam building and two nails – one for stone and one for timber jointing from interior (MSH-KAP-09 and -12). The SEM image of the nail from the dome of the Hammam (MSH-KAP-01) from the 16th century shows a compact and distinct corrosion layer (Figure 4.95 a, b). The inner corrosion layer is very well observed in the 16th century nails in optical microscopic images and characterized as a compact isotropic light-colored band of quite uniform thickness. Between the band and the metal there is a reaction-front of 10 μ m thickness (Figure 4.95 b). This sample with unique ribbon-like g corrosion layer has been first examined with its borderlines of the sublayers that form the distinct corrosion layers. They form the transition zones in the main corrosion layer. Later on, each sublayer has been examined in more detail. Compositional properties of each sublayer have been identified by μ -Raman

spectroscopy (Figure 4.95 a, b). Each sublayer has been examined in 3 or 4 points (Figures 4.96, 4.97 and 4.98).



(a) MSH-KAP-01 (2000x)



(b) MSH-KAP-01 (1200x)

Figure 4. 95 A digital microscopy image (a) and SEM image (b) of the corrosion layer belonging to a nail (MSH-KAP-01) (16th cc): Sub-layers are identified as RF: Metal-ICL interface; ICL: inner corrosion layer (~50 μm); OSL: original surface limit; TM: transformed media. ICL-TM interface includes OSL.

Reaction front (RF) appears as a thin, black colored layer of ~10- μm thickness next to the metal body which is rich in magnetite (Figure 4.96 b). At transition step RF to the ICL magnetite +maghemite and hematite rich areas have been observed (Figure 4.96 c). At the transition step of ICL to TM, hematite is the most abundant phase (Figure 4.96 d).

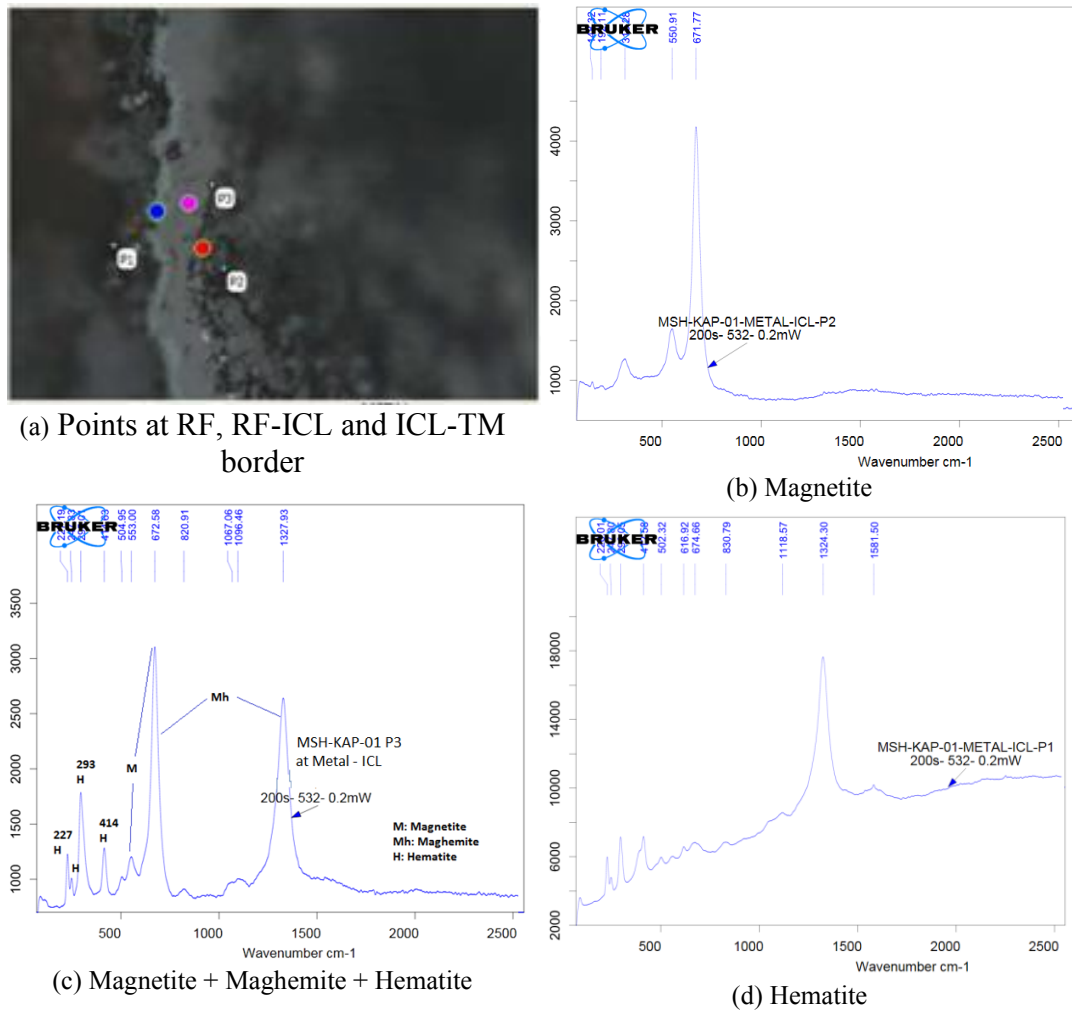
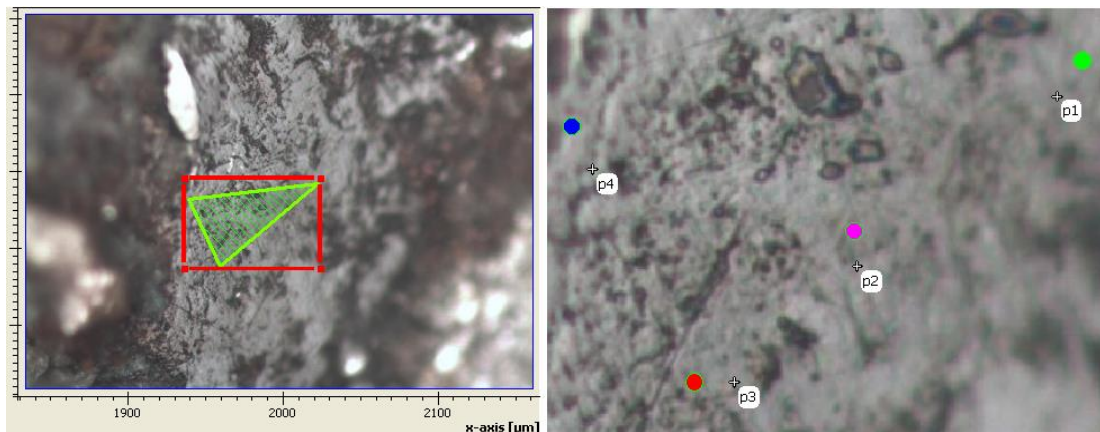
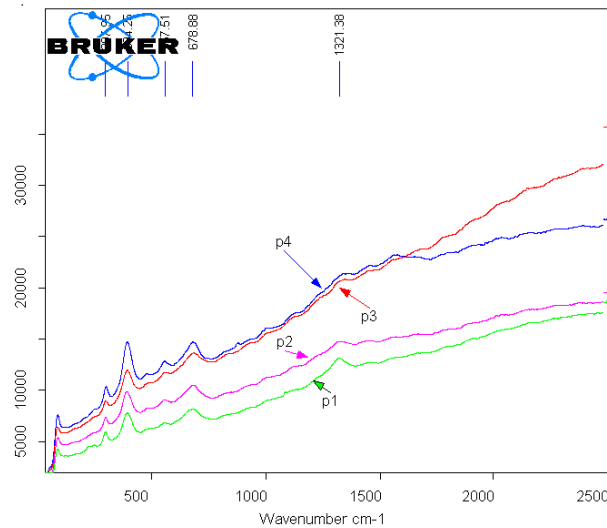


Figure 4. 96 μ -Raman spectra of the nail (MSH-KAP-01) at the RF and the transition zones: points of measurement (a); reaction-front (p2) having magnetite (M) (b); RF-ICL transition zone (p3) showing magnetite (M), maghemite (Mh) and hematite (c); ICL-TM transition zone (p1) showing hematite (H) (d).

ICL excluding RF appears to be an isotropic band of $\sim 40 \mu\text{m}$ composed of goethite ($\alpha\text{-FeOOH}$) in all steps and points analyzed (Figure 4.97 a, b).



(a) Points at ICL



(b)

Figure 4. 97 μ -Raman spectra of a nail (MSH-KAP-01) at ICL: measurement points (a); presence of goethite in ICL (b).

After passing the transition zone of ICL-TM rich in hematite, it has been observed that the transformed media has a variable composition with abundance of goethite together with magnetite +maghemite and lepidocrocite (Figure 4.98 a, b, c and d). Typical fingerprints of main corrosion products of each point on the nail from exterior (MSH-KAP-01) by using Raman Spectroscopic Analysis is given in Table 4.30.

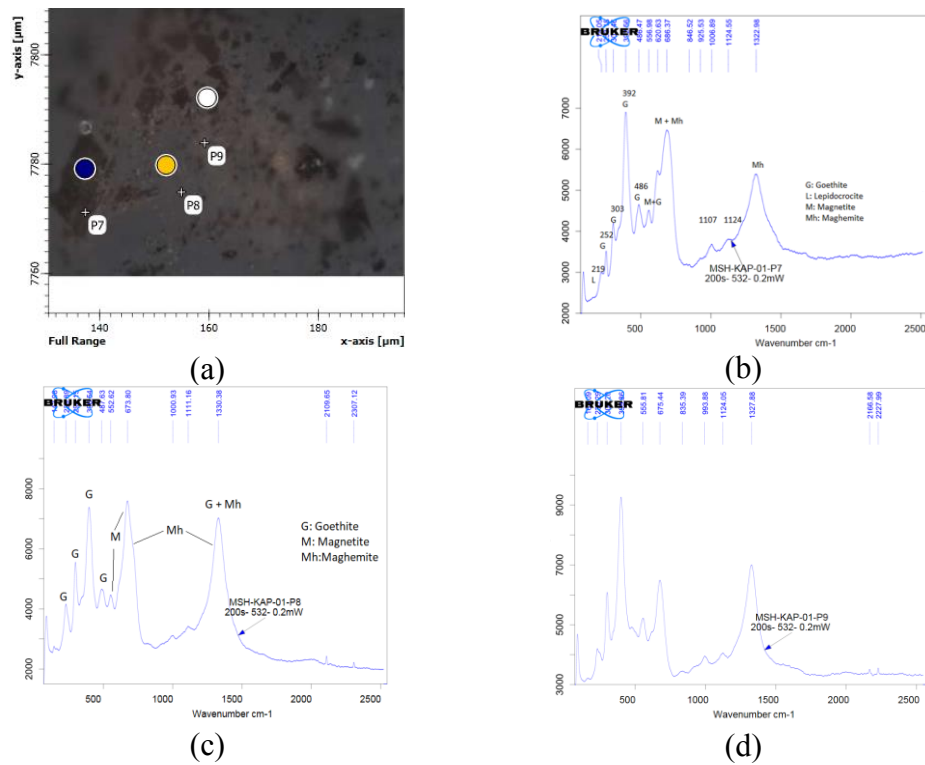


Figure 4. 98 μ -Raman spectra of a nail (MSH-KAP-01) at TM: measurement points (a); presence of goethite, magnetite + maghemite, lepidocrocite (b); presence of goethite, magnetite + maghemite (c); and presence of goethite (d).

Table 4. 30 Iron oxides followed by μ -Raman analyses in the corrosion layer of a nail (MSH-KAP-01) (16th cc).

Location	Observed Corrosion Minerals			
	RF	RF-ICL \rightarrow	ICL	ICL-TM \rightarrow TM (OSL)
Exterior of the Hammam building – <i>Outdoor</i>	Magnetite (Fe ₃ O ₄)	Magnetite (Fe ₃ O ₄) Maghemite (γ -Fe ₂ O ₃) Hematite (α -Fe ₂ O ₃)	Goethite (α -FeOOH)	Hematite (α -Fe ₂ O ₃) Goethite (α -FeOOH) Lepidocrocite (γ -FeOOH) Magnetite (Fe ₃ O ₄) Maghemite (γ -Fe ₂ O ₃)

The second object analyzed by μ -Raman was an iron piece convenient to anchoring, (MSH-KAP-02) from interior of the 16th century hammam building. The SEM image of the iron object shows a compact and distinct corrosion layer with high corrosion thickness, $\sim 750 \mu\text{m}$ (Figure 4.99 a). Starting from the metal body towards TM, four steps with 11 total points have been analyzed (Figures 4.99, 4.100, 4.101 and 4.102). The steps have been organized in such a way that each forward step followed the previous one. The first step covers one point at the reaction front (RF). At point 1 in the reaction front, goethite ($\alpha\text{-FeOOH}$) is the main phase identified with its typical characteristic peaks at 392 cm^{-1} , 301 cm^{-1} , 685 cm^{-1} , 556 cm^{-1} and 1300 cm^{-1} in decreasing intensity (Figure 4.99 b, c).

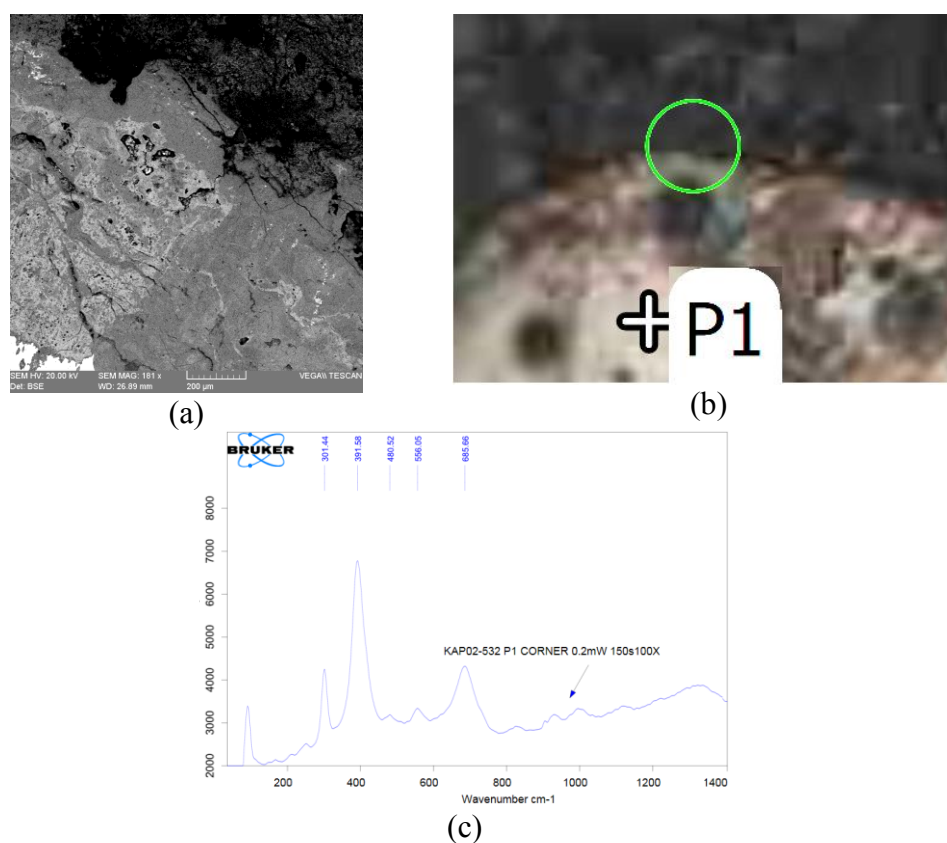


Figure 4. 99 SEM image of the corrosion layer at an iron object (MSH-KAP-02) (a) (16th cc); measurement point at RF (b); and μ -Raman spectrum indicating presence of goethite (c).

In the second step, starting from RF towards ICL, from point 1 (P1) to point 4 (P4), presence of hydrated iron (III) oxide or oxyhydroxide have been identified (Figure 4.100).

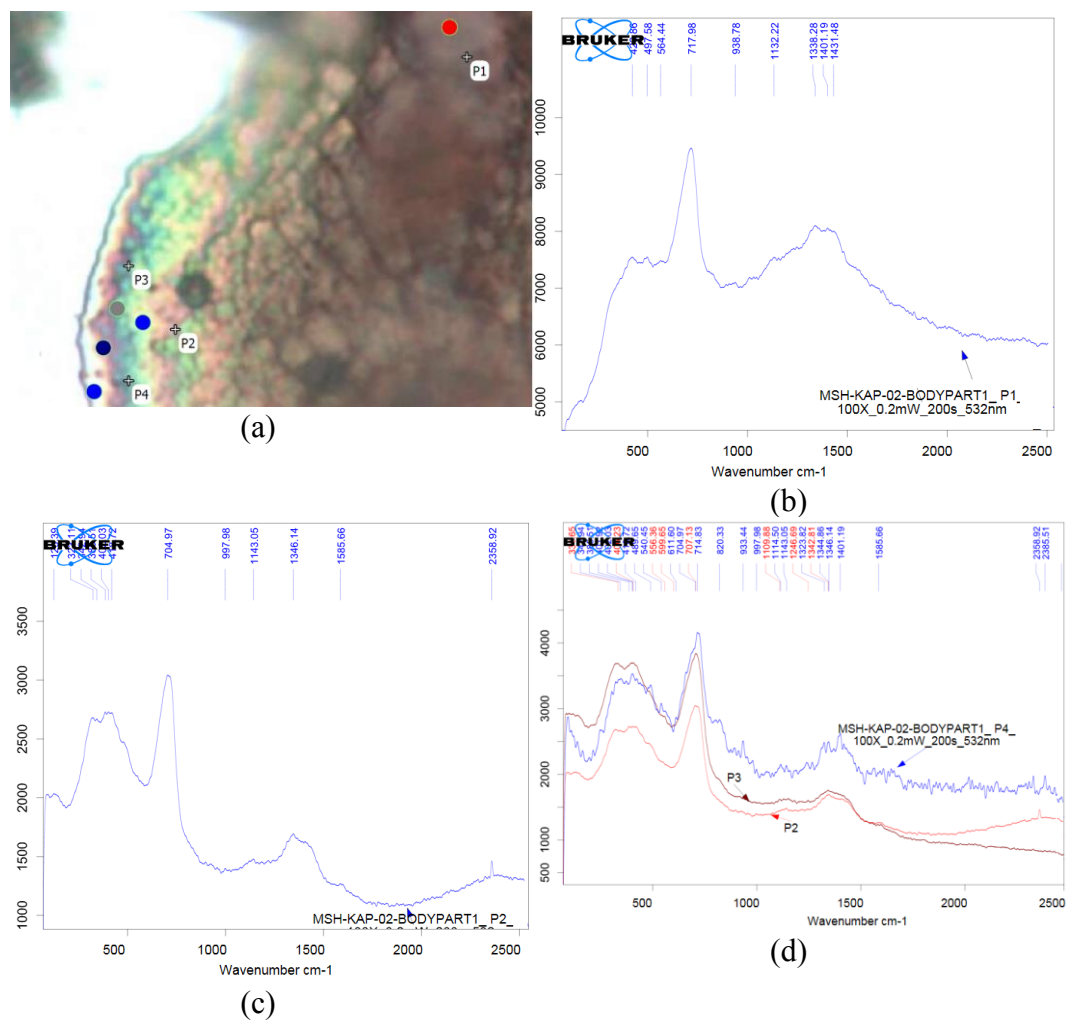


Figure 4. 100 μ -Raman spectra of an iron object (MSH-KAP-02) at RF towards ICL: measurement points (a); and presence of hydrated iron (III) oxide or oxyhydroxide at P1 to P4 (b, c, d).

In the third step, 4 points from ICL have been analyzed. From point 1 to point 4, the phase shows similar weak Raman spectra as in the previous step and, as a result, the phase can be called “hydrated iron (III) oxide or oxyhydroxide” (Figure 4.101).

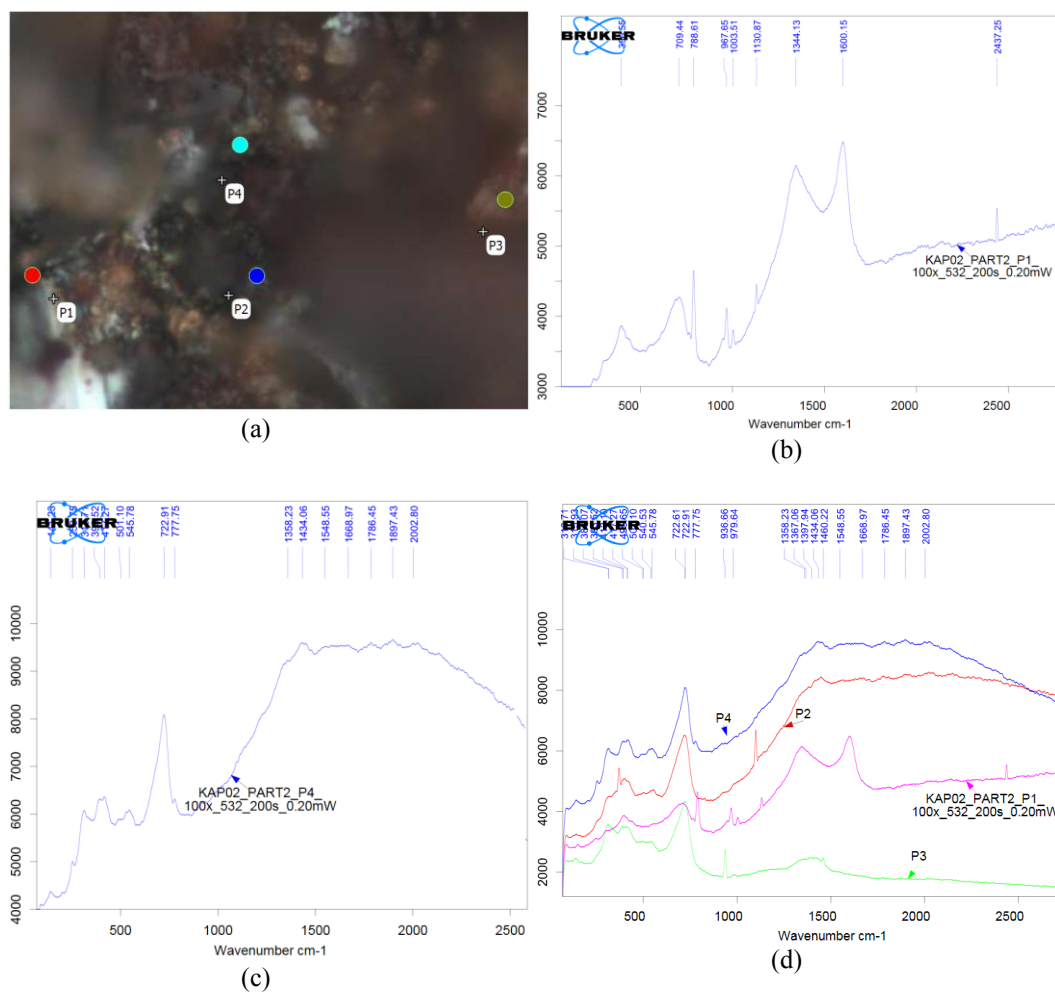


Figure 4. 101 μ -Raman spectrum of an iron object (MSH-KAP-02) at ICL: measurement points (a); and presence of hydrated iron (III) oxide or oxyhydroxide from P1 to P4 (b, c, d).

In the fourth step, 2 points from ICL towards TM have been analyzed. At point 1 and at point 2, presence of abundant goethite (α -FeOOH) is noticed (Figure 4.102) with a high intensity peak observed at 387, 299 cm^{-1} and 680 cm^{-1} .

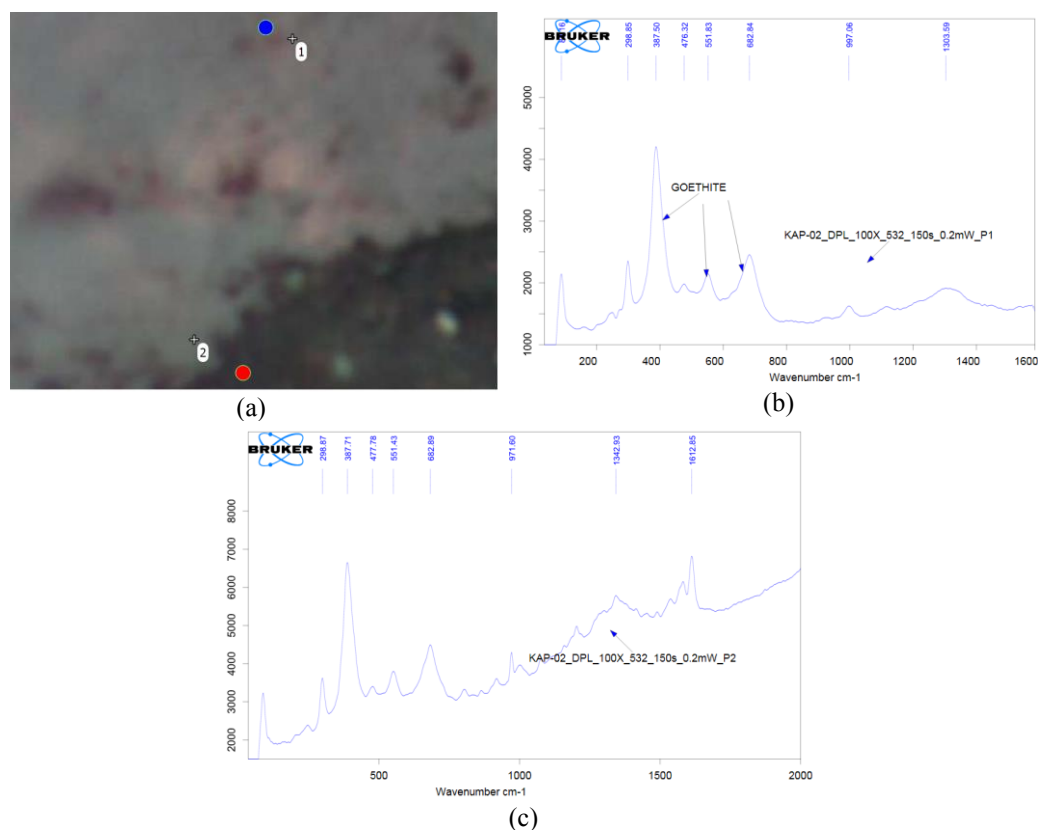


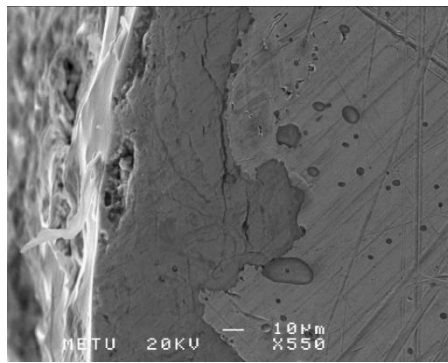
Figure 4. 102 μ -Raman spectrum of an iron object (MSH-KAP-02) at ICL towards TM: measurement points (a); and presence of goethite at p1 and p2 (b, c).

Typical fingerprints of main corrosion products of each point on iron object (MSH-KAP-02) from the interior of the hammam building by using Raman Spectroscopic Analysis is given in Tables 4.31.

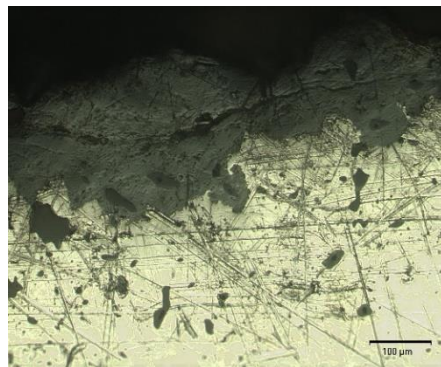
Table 4. 31 Iron oxides followed by μ -Raman analyses in the corrosion layer of an iron object (MSH-KAP-02) (16th cc).

Location	Observed Corrosion Minerals				
	RF	RF-ICL \rightarrow	ICL	ICL-TM \rightarrow (OSL)	TM
Interior of the hammam building – <i>Interior</i>	Goethite (α -FeOOH)	Iron (III) oxyhydr/ oxide	Iron (III) oxyhydr/oxide	Goethite (α -FeOOH)	-

The SEM and digital microscopic image of another dome nail from exterior (MSH-KAP-03) from the 16th century hammam building show a compact and distinct corrosion layer with an average thickness of $\sim 100 \mu\text{m}$ (Figure 4.103 a, b). Starting from the metal body towards TM, eight steps with 14 total points have been analyzed by μ -Raman (Figures 4.104, 4.105, 4.106, 4.107, 4.108, 4.109 and 4.110). The steps have been organized in such a way that each forward step followed the previous one. The first step covers the reaction front (RF) and include the analyses of 2 points (Figure 4.104 a). At point 1 magnetite (Fe_3O_4) and at point 2 hydrated iron (III) oxide or oxyhydroxide are the main phases identified. Magnetite is verified by its main peak at 675 cm^{-1} and its typical peak at 550 cm^{-1} (Figure 4.104 b). Presence of hydrated iron (III) oxide or oxyhydroxide has been noticed with a high intensity symmetrical peak observed at 673 cm^{-1} , 548 cm^{-1} , 388 cm^{-1} and 1315 cm^{-1} (Figure 4.104 c) (Hanesch, 2009; Bellot-Gurlet *et al*, 2009; Mazetti and Thistlethwaite 2002).



(a) MSH-KAP-03 (550X)



(b) MSH-KAP-03 (560X)

Figure 4. 103 SEM image (a) and digital microscopic image (b) of a dome nail (MSH-KAP-03) after etching with nitric acid in alcohol (16th cc).

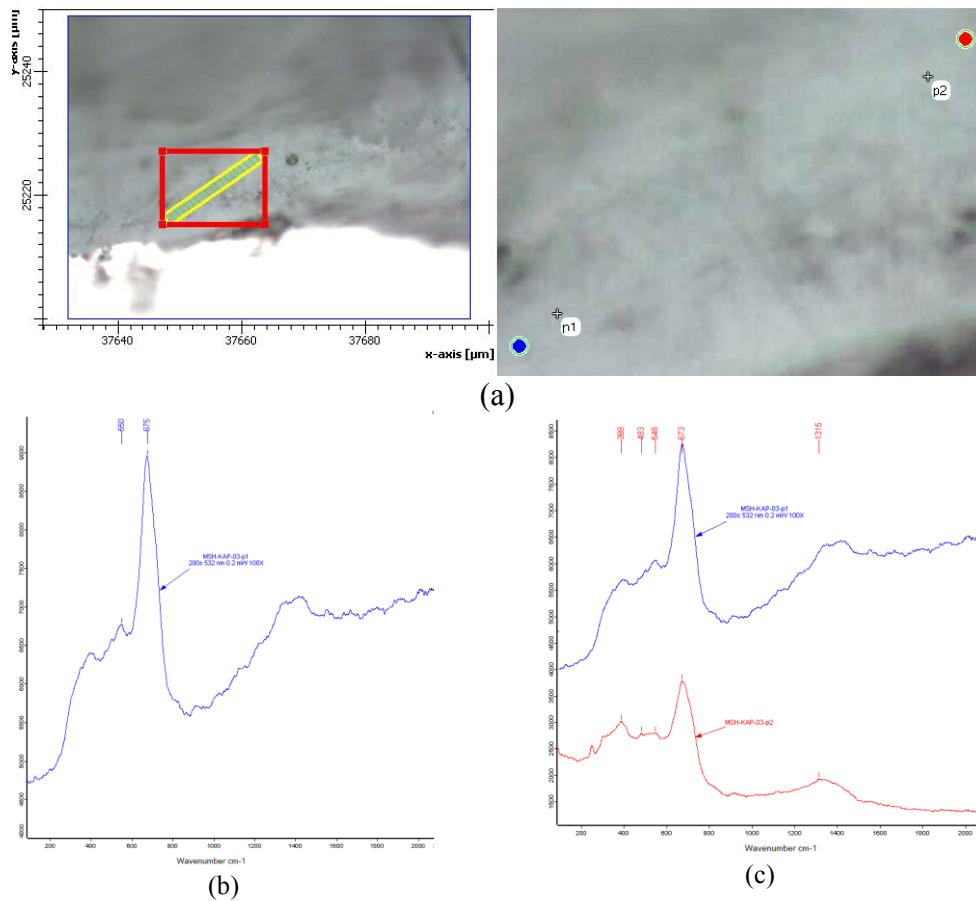


Figure 4. 104 μ -Raman spectra of the 2 points located in RF viewed by SEM and digital microscope (MSH-KAP-03): measurement points (a), magnetite at point 1 (b) and hydrated iron (III) oxide or oxyhydroxide at point 2 (c).

The second step involves 2 points in ICL after RF (Figure 4.105 a). At point 3, magnetite (Fe_3O_4) with some goethite ($\alpha\text{-FeOOH}$) are the main phases identified (Figure 4.105 b). Magnetite has been verified by its strong peak at 693 cm^{-1} together with its typical peak at 550 cm^{-1} . Goethite appears with its strong peak at 395 cm^{-1} and the existence of the peak at 1335 cm^{-1} . At point 4 goethite ($\alpha\text{-FeOOH}$) is the main phase (Figure 3.15 c) with its well-formed crystal structure, identified by the strongest peak at 395 cm^{-1} , and its other typical ones at 300 cm^{-1} and 683 cm^{-1} .

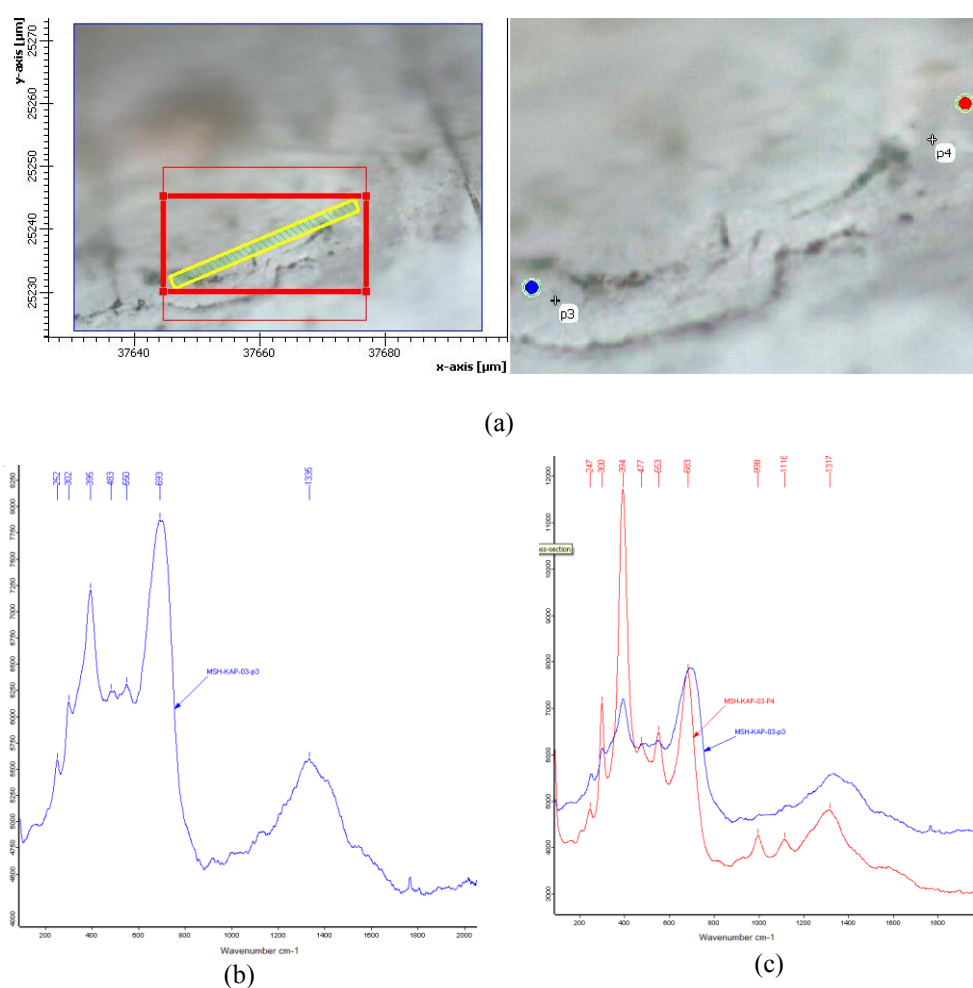


Figure 4. 105 μ -Raman spectra of the 2 points located in the ICL after RF (MSH-KAP-03): measurement points (a); magnetite with some goethite at p3 (b); and goethite is the main phase observed at p4 (c).

The following 2 points (p5 and p6) in the ICL have been analyzed (Figure 4.106 a). In point 5, hydrated iron (III) oxide or oxyhydroxide are the phases observed with the strong peaks at 703 cm^{-1} having a shoulder peak at 687 cm^{-1} , 535 cm^{-1} and 1325 cm^{-1} (Figure 4.106 b). In point 6, goethite ($\alpha\text{-FeOOH}$) with a well-formed crystal structure is identified with its strongest peak at 396 cm^{-1} and all of its typical peaks are sharp and visible (Figure 4.106 c).

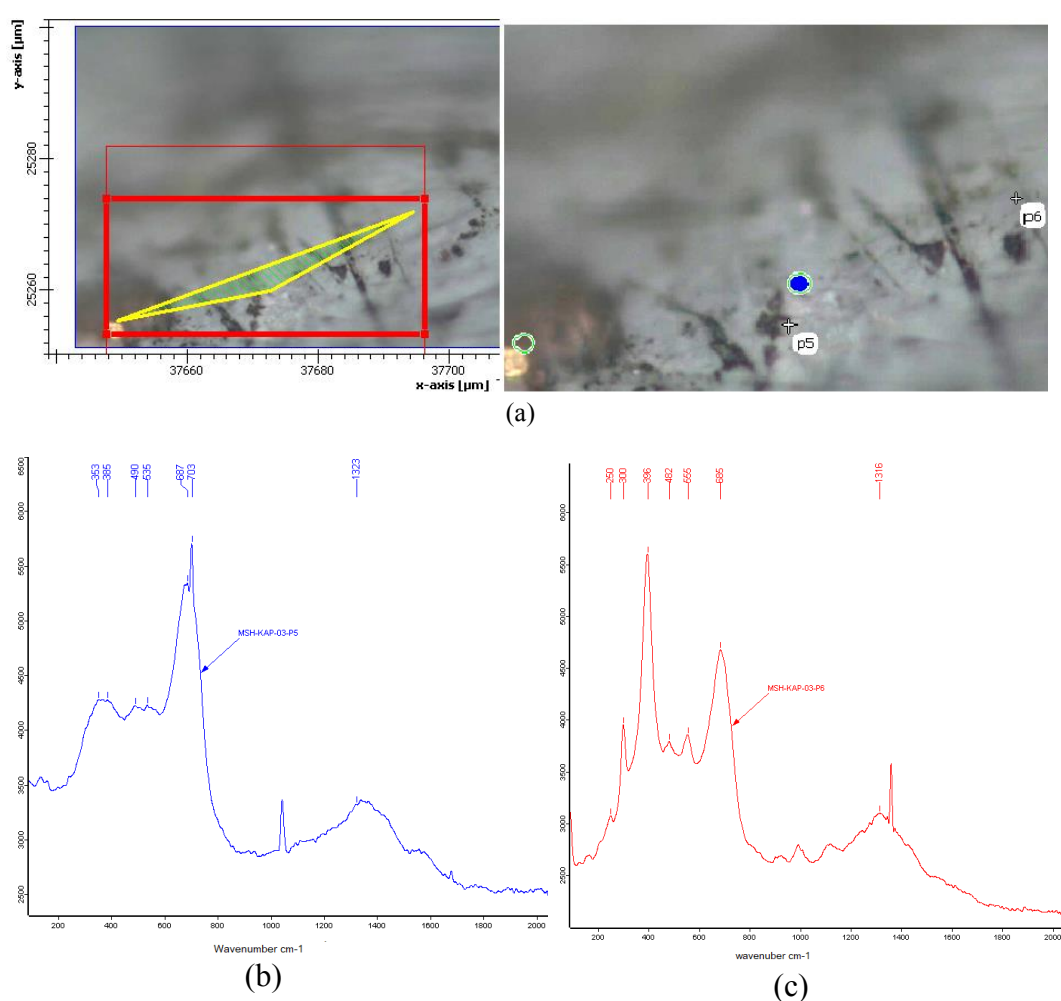


Figure 4. 106 μ -Raman spectra of the successive area where 2 points are located in the ICL (MSH-KAP-03): measurement points (a); hydrated iron (III) oxide or oxyhydroxide at p5 (b); and goethite at p6 (c).

The fourth step consists of 2 points (p7 and p8) in ICL (Figure 4.107 a). At point 7, hydrated iron (III) oxide or oxyhydroxide with its enlarged peak at 681 cm^{-1} , goethite ($\alpha\text{-FeOOH}$) with its strongest peak at 394 cm^{-1} , 1321 cm^{-1} and lepidocrocite ($\gamma\text{-FeOOH}$) with its strongest peak at 253 cm^{-1} have been identified. The location is observed as a low crystallinity / amorphous phase (Figure 4.107 b). At point 8, goethite ($\alpha\text{-FeOOH}$) and lepidocrocite ($\gamma\text{-FeOOH}$) with a well-formed crystal structure have been identified with their strongest peak at 396 cm^{-1} for goethite, 252 cm^{-1} for lepidocrocite and all of their typical peaks are sharp and visible (Figure 4.107 c).

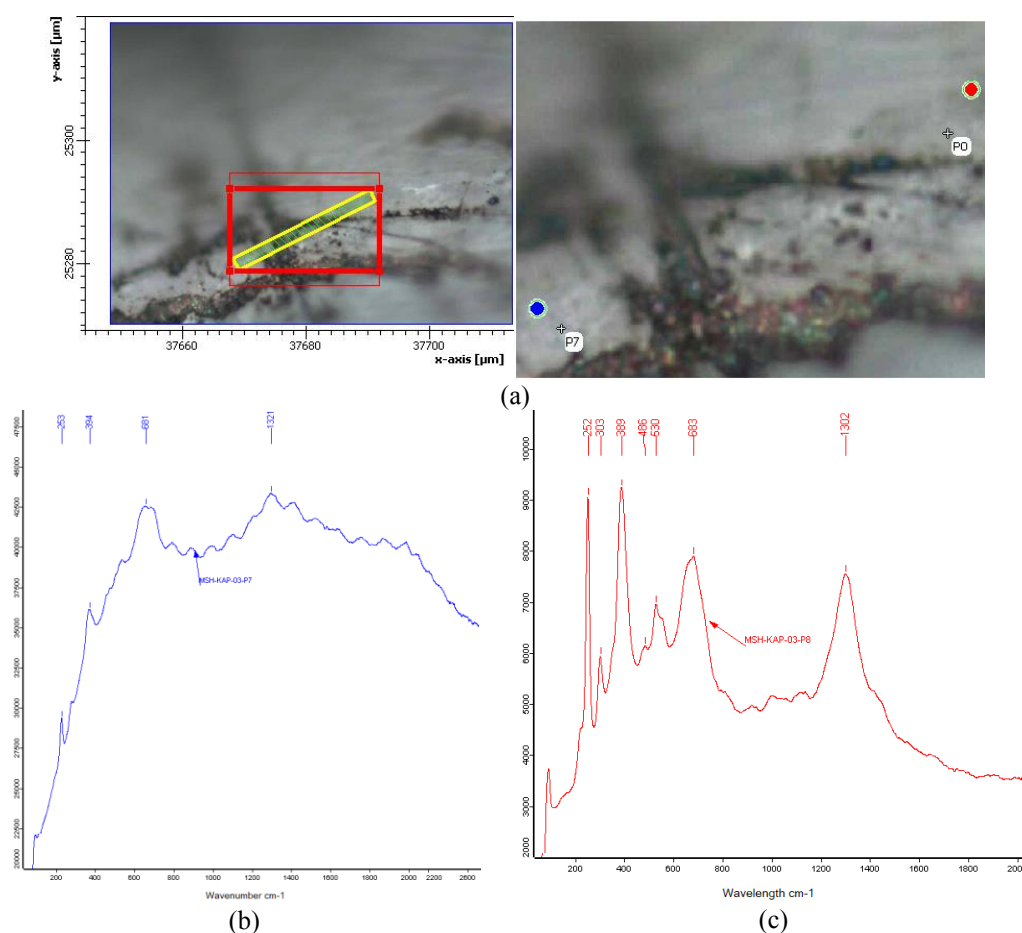


Figure 4. 107 μ -Raman spectra of the successive step where 2 points are located in the ICL (MSH-KAP-03): measurement points (a); hydrated iron (III) oxide or oxyhydroxide, goethite and lepidocrocite at p7 (b); and goethite and lepidocrocite at p8 (c).

The fifth step consists of 2 points (p9 and p10) in the ICL towards the TM (Figure 4.108 a). At point 9, hydrated iron (III) oxide or oxyhydroxide with its sharp peak at 686 cm^{-1} , 503 cm^{-1} , 388 cm^{-1} and 1350 cm^{-1} (Figure 4.108 b) (Hanesch 2009) and at point 10, maghemite ($\gamma\text{-Fe}_2\text{O}_3$) with some magnetite (Fe_3O_4) with its enlarged peak at 683 cm^{-1} , mixing of goethite ($\alpha\text{-FeOOH}$) with its strongest peak at 394 cm^{-1} and lepidocrocite ($\gamma\text{-FeOOH}$) with its strongest peak at 253 cm^{-1} have been identified (Figure 4.108 c) (Monnier *et al*, 2010). All of their typical peaks are also sharp and visible and the point has a well-formed crystal structure.

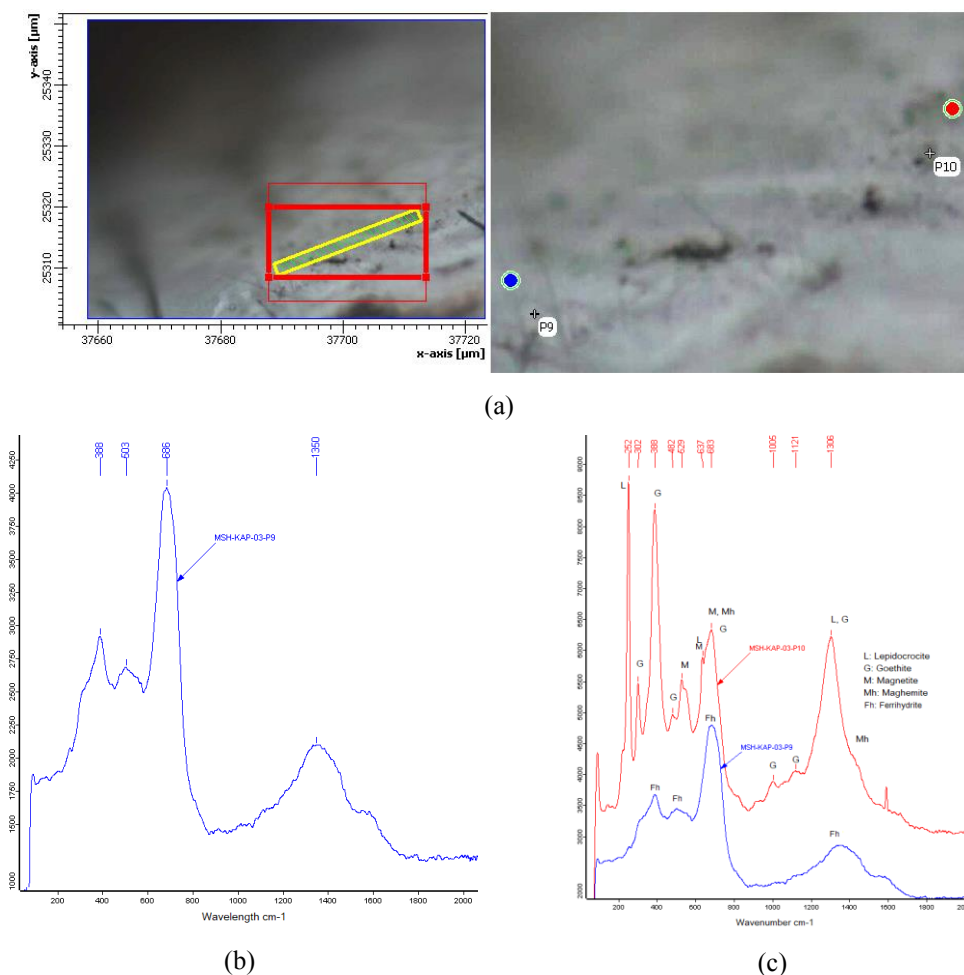


Figure 4. 108 μ -Raman spectra of the successive area where 2 points are located in the ICL (MSH-KAP-03): measurement points (a); hydrated iron (III) oxide or oxyhydroxide at point 9 (b); and maghemite, magnetite, goethite and lepidocrocite are the phases observed at point 10 (c).

The sixth step consists of 2 points (p11 and p12) close to the TM (Figure 4.109 a). At point 11 goethite (α -FeOOH) with its strongest peak at 388 cm^{-1} and lepidocrocite (γ -FeOOH) with its strongest peak at 251 cm^{-1} have been identified (Figure 4.109 b). At point 12 goethite (α -FeOOH) has been identified (Figure 4.109 c). All of its typical peaks are also sharp and visible and the point has a well-formed crystal structure.

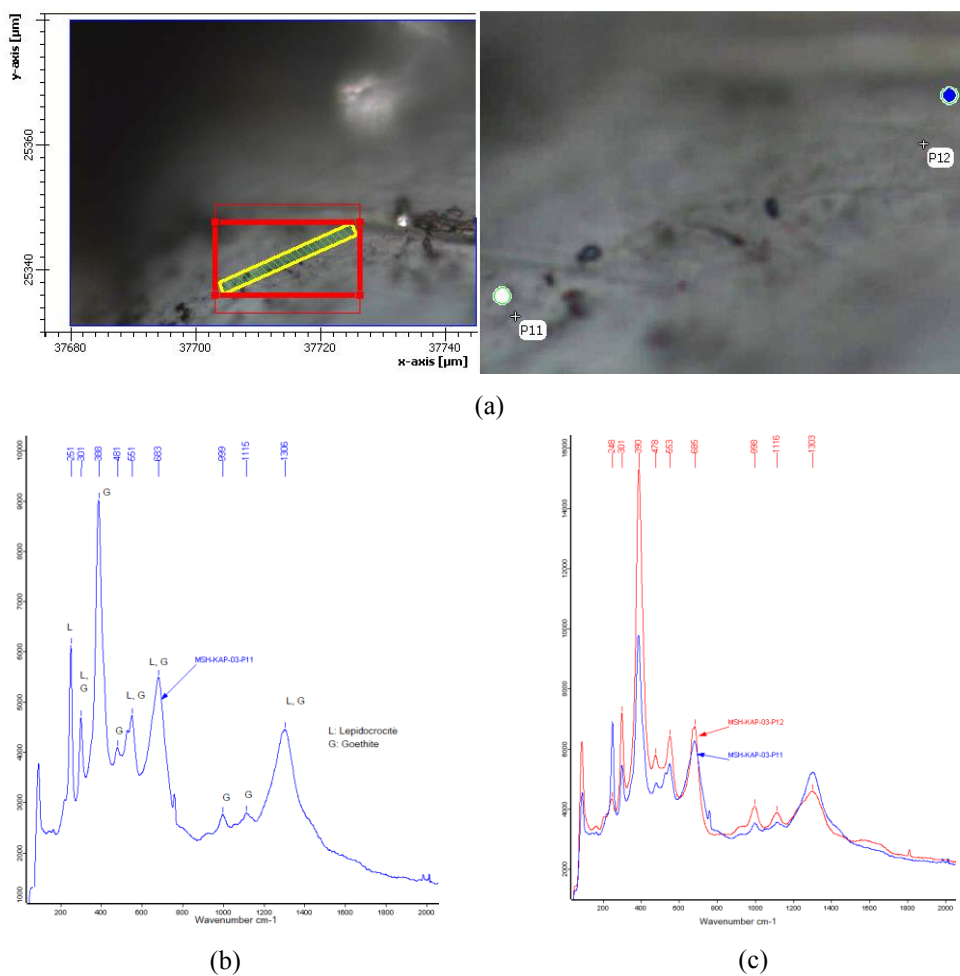


Figure 4. 109 μ -Raman spectra of the successive area where 2 points are located in the ICL close to TM border of a nail (MSH-KAP-03): measurement points (a); goethite and lepidocrocite at point 11 (b); and goethite at point 12 (c).

The seventh step consists of 1 point (p13) in the TM (Figure 4.110 a). At point 13 goethite (α -FeOOH) is identified (Figure 4.110 b) with its peaks at 390 cm^{-1} , 685 cm^{-1} , 301 cm^{-1} , 1305 cm^{-1} , 553 cm^{-1} , 1000 cm^{-1} , 1115 cm^{-1} , 479 cm^{-1} and 250 cm^{-1} . In the eighth step consisting of 1 point (p14) in the TM (Figure 4.110 c) lepidocrocite (γ -FeOOH) is identified with its strongest peak at 253 cm^{-1} , 308 cm^{-1} , 1306 cm^{-1} , 655 cm^{-1} and 529 cm^{-1} (Figure 3.110 d).

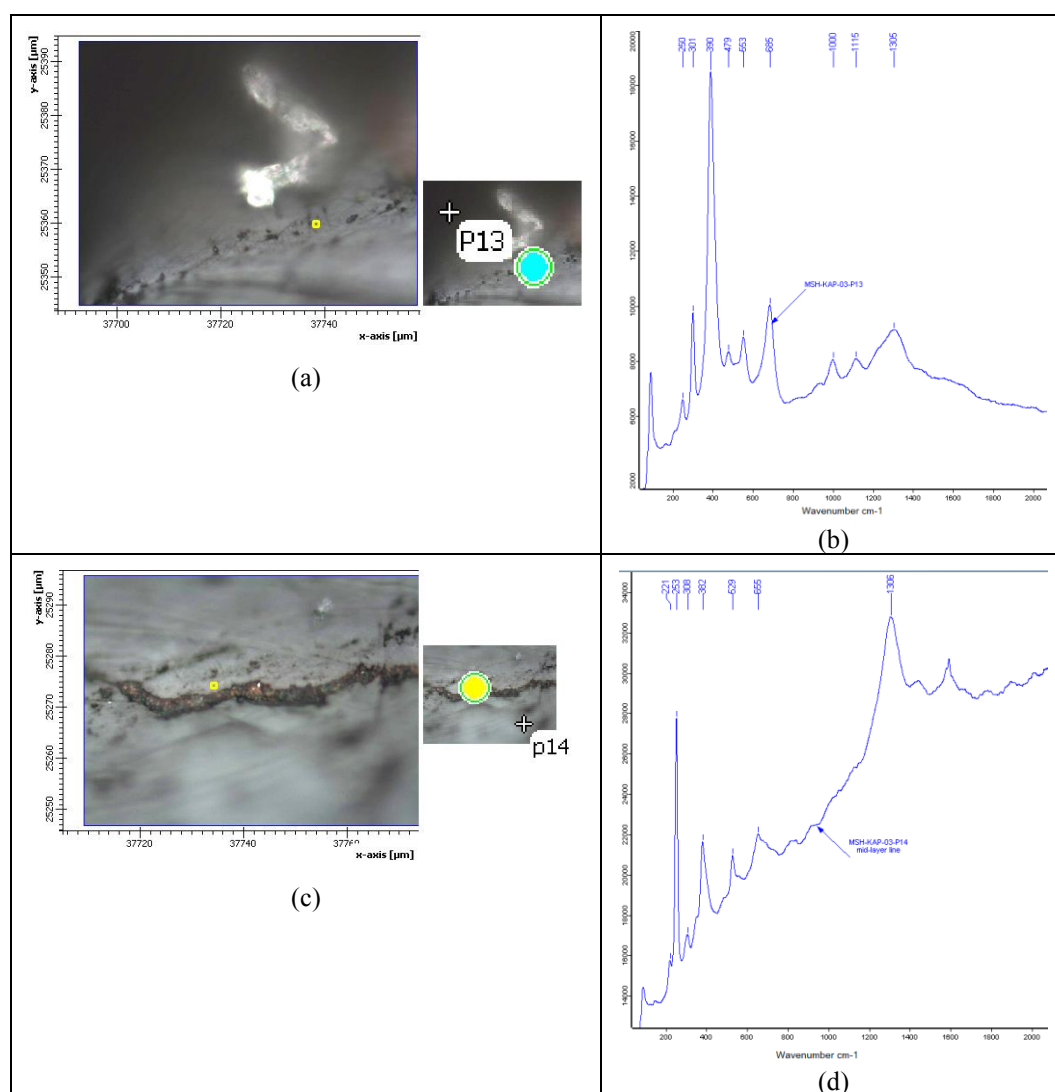


Figure 4. 110 μ -Raman spectra of the successive areas where 2 points are located in the TM of a nail (MSH-KAP-03): measurement points (a, c); goethite at point 13 (b); and lepidocrocite at point 14 (d).

The overall corrosion layers and typical fingerprints of main corrosion products of each point on the nail (MSH-KAP-03) from the exterior by using Raman Spectroscopic Analysis have been given in Table 4.32.

Table 4. 32 Iron oxides followed by μ -Raman analyses in the corrosion layer of a nail (MSH-KAP-03) (16th cc).

Location	Observed Corrosion Minerals						
	Reaction Front RF → ICL → ICL-TM border (OSL) → TM						
Exterior of the hammam building – <i>Outdoor</i>	Magnetite (Fe ₃ O ₄)	Magnetite (Fe ₃ O ₄)	Maghemite (γ-Fe ₂ O ₃)	Hydrated iron (III) oxyhydr/oxide	Goethite (α-FeOOH)	Goethite (α-FeOOH)	Goethite (α-FeOOH)
	Hydrated iron (III) oxyhydr/oxide	Goethite (α-FeOOH)	Magnetite (Fe ₃ O ₄)		Maghemite (γ-Fe ₂ O ₃)	Lepidocrocite (γ-FeOOH)	Lepidocrocite (γ-FeOOH)
			Goethite (α-FeOOH)		Lepidocrocite (γ-FeOOH)	Lepidocrocite (γ-FeOOH)	

The optical microscopic and Raman microscopic images of a nail (MSH-KAP-09) from the interior of a 16th century hammam building show a compact and distinct corrosion layer with an average thickness of 260 μm (Figure 4.111 a and b). Starting from the metal body towards TM, five steps with 24 total points have been analyzed by μ -Raman (Figures 4.112 – 4.116).

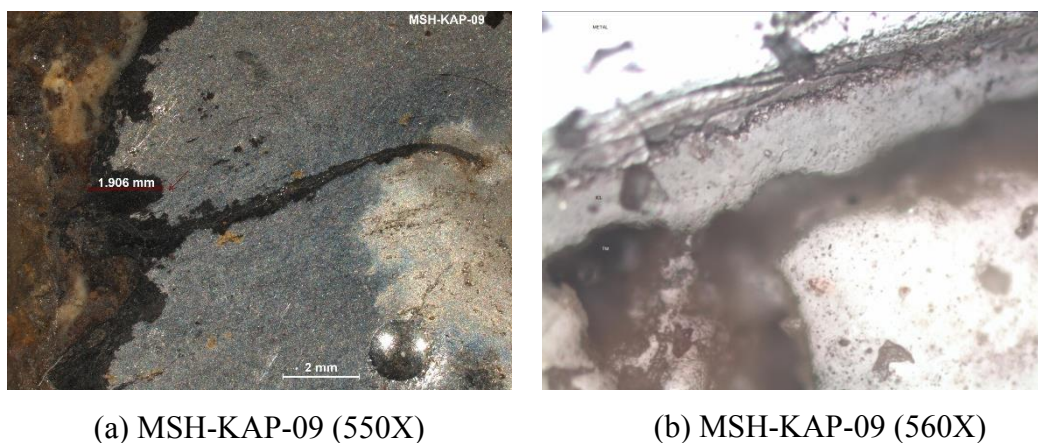


Figure 4. 111 SEM image (a) and digital microscopic image (b) of a nail (MSH-KAP-09) after etching with nitric acid in alcohol (16th cc).

The first step covers the reaction front (RF) towards ICL and include the analyses of 6 points (Figure 4.112 a). At point 1, goethite ($\alpha\text{-FeOOH}$) with its strongest peak at 388 cm^{-1} is observed (Figure 4.112 b). At point 2, hydrated iron (III) oxide or oxyhydroxide and goethite ($\alpha\text{-FeOOH}$) are the phases identified (Figure 4.112 c). The presence of hydrated iron (III) oxide or oxyhydroxide seems to be more probable with the broad peak at 692 cm^{-1} and a peak at 1328 cm^{-1} and goethite is confirmed with its strongest peak at 388 cm^{-1} . The point 2 is considered as a site having a poorly crystallized hydrated iron III oxide or oxyhydroxide transforming to a more stable phase goethite. Point 3 and 4 are the sites with reactive phase magnetite represented with its strongest peaks at 670 cm^{-1} and 550 cm^{-1} (Figure 4.112 d). At point 5, maghemite ($\gamma\text{-Fe}_2\text{O}_3$) with some magnetite (Fe_3O_4) and goethite ($\alpha\text{-FeOOH}$) are the phases identified (Figure 4.112 e). At point 6, goethite ($\alpha\text{-FeOOH}$) with its strongest peak at 388 cm^{-1} has been identified and it appears with a well-formed crystalline

structure (Figure 4.112 f). The reaction front (RF) is concluded to have abundance of reactive phases as magnetite, maghemite and a combination of poorly crystallized iron (III) oxide or oxyhydroxide phases and some stable oxyhydroxide phase goethite.

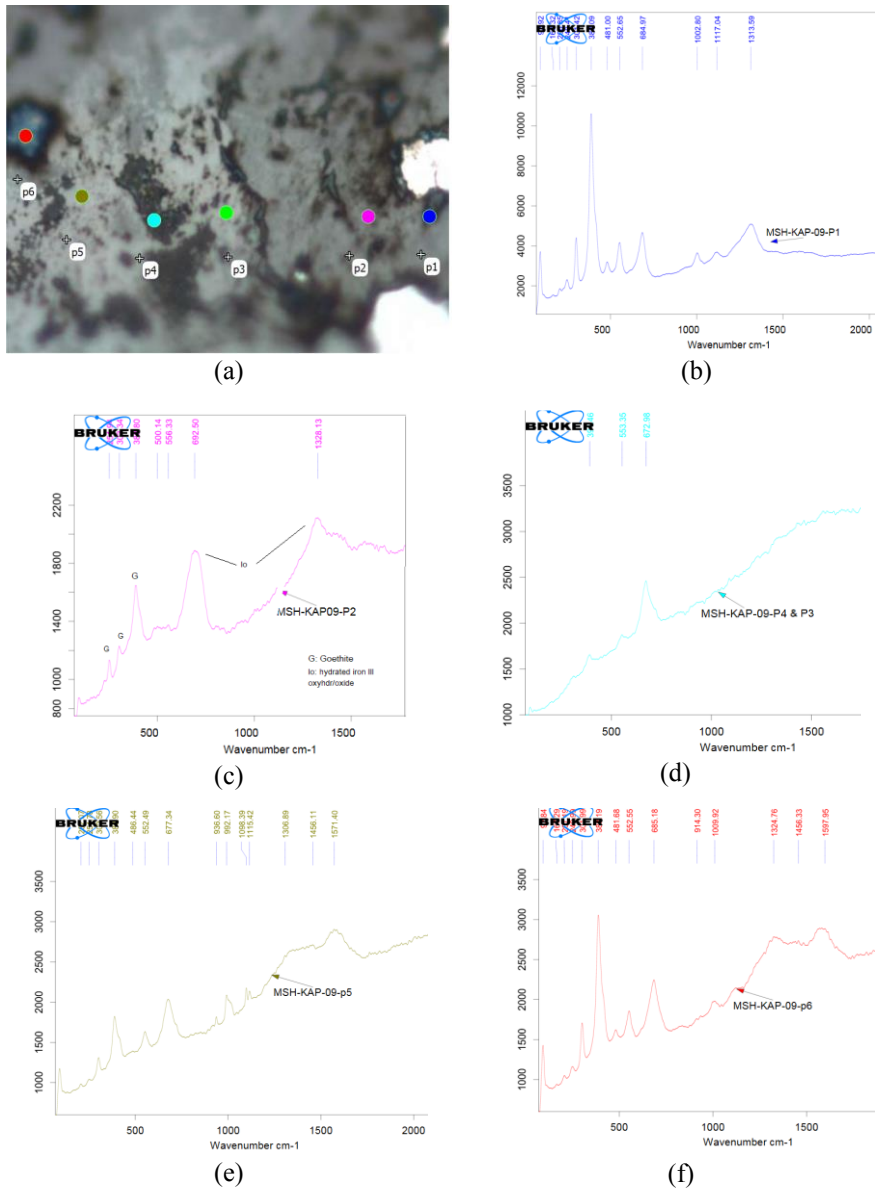


Figure 4. 112 μ -Raman spectra of the two points located in RF towards ICL of a nail (MSH-KAP-09): measurement points (a); goethite at point 1 (b); hydrated iron (III) oxide or oxyhydroxide and goethite at point 2 (c); magnetite at point 3 and 4 (d), maghemite, magnetite, goethite at point 5 (e); and goethite at point 6 (f).

The second step is analyzed at 4 points in ICL after RF (Figure 4.113 a). At point 1 and 4, hydrated iron (III) oxide or oxyhydroxide with some goethite (α -FeOOH) having its strong peak at 395 cm^{-1} are the main phases identified (Figure 4.113 b). Hydrated iron (III) oxide or oxyhydroxide is confirmed by enlargement of the peak at 670 cm^{-1} and the broad peak between $1380 - 1580\text{ cm}^{-1}$. The Raman signatures indicated show the probable combination of maghemite, ferrosityte and ferrihydrites. At point 2 and 3, goethite (α -FeOOH) is the main phase (Figure 4.113 c, d) with its well-formed crystal structure, identified by the strongest peak at 390 cm^{-1} , and its other typical peaks at 302 cm^{-1} and 685 cm^{-1} .

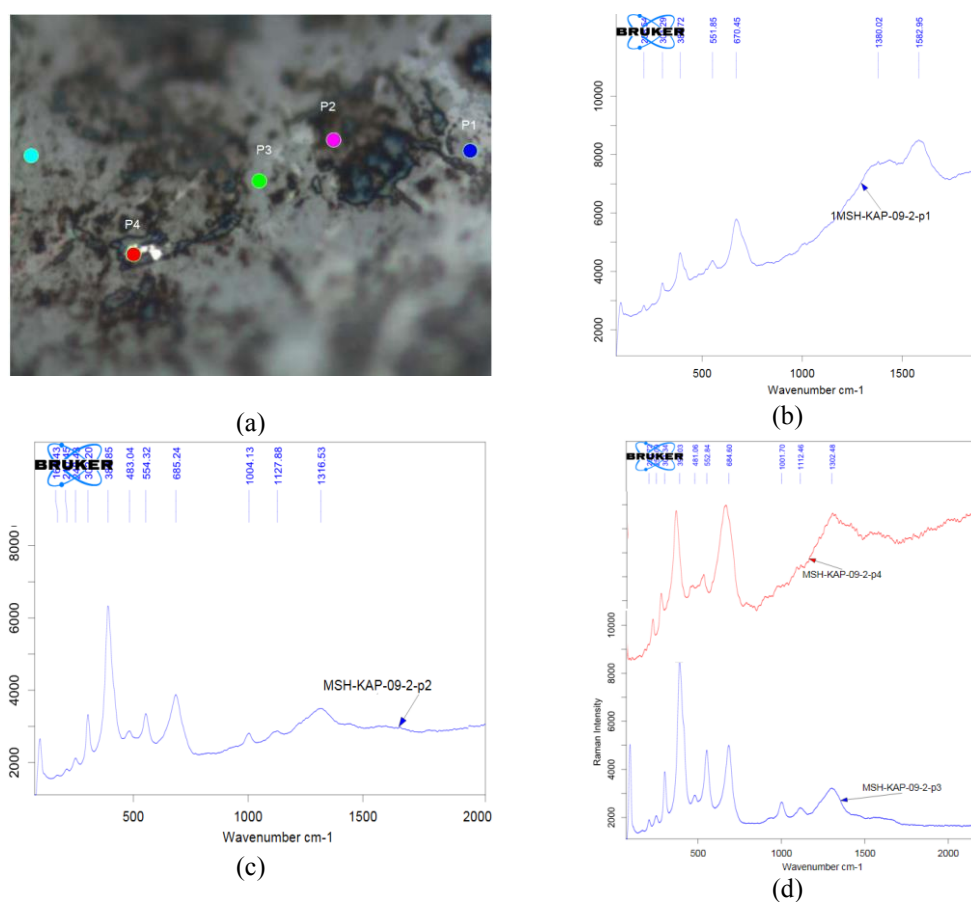


Figure 4. 113 μ -Raman spectra of the successive four points located in the ICL after RF in the corrosion layer of a nail (MSH-KAP-09): measurement points (a); hydrated iron (III) oxide or oxyhydroxide with some goethite at p1 and p4 (b); and goethite is the main phase observed at p2 and p3 (c, d).

The following 4 points (p1 to p4) in the ICL were analyzed (Figure 4.114 a): In p1, lepidocrocite (γ -FeOOH) with the strongest peaks at 251 cm^{-1} and all its sharp, typical peaks (Figure 4.114 b). In p2 and p3, magnetite (Fe_3O_4) with a well-formed crystal structure is identified with its strongest peak at 666 cm^{-1} ; all of its typical peaks are sharp and visible (Figure 4.114 c, e). Goethite (γ -FeOOH) with the strongest peak at 388 cm^{-1} is observed at point 4 (Figure 4.114 d).

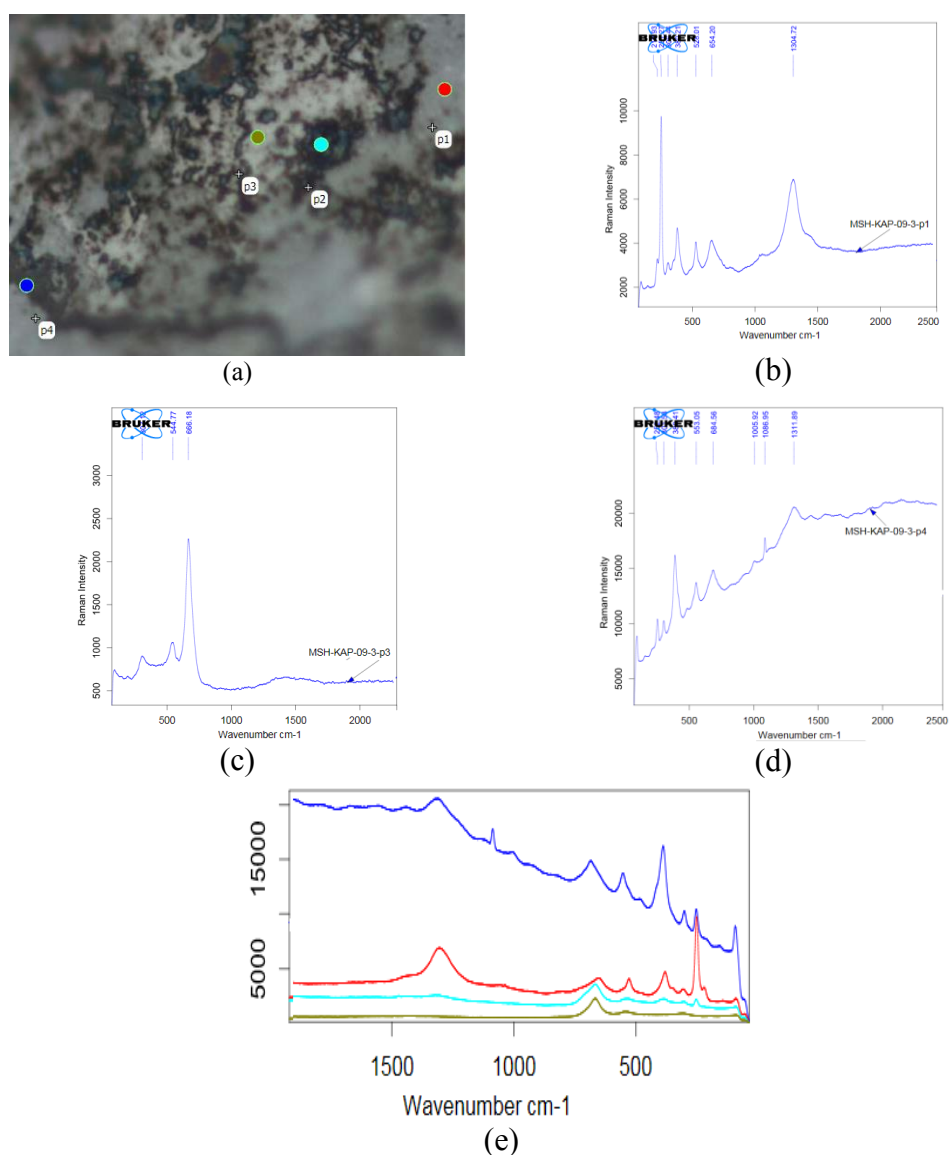


Figure 4. 114 μ -Raman spectra of the successive area where 4 points have been located in the ICL of a nail (MSH-KAP-09): measurement points (a); lepidocrocite at p1 (b); magnetite at p2 and p3 (c); and goethite at p4 (d).

The 4th step with 5 points (p1 to p5) in the ICL towards TM were analyzed (Figure 4.115 a): At point 1 maghemite ($\gamma\text{-Fe}_2\text{O}_3$) with the strongest peak at 714 cm^{-1} with its shoulder peak at 671 cm^{-1} (Figure 4.115 b) is identified. From point 2 to 5, hydrated iron (III) oxide or oxyhydroxide together with goethite ($\alpha\text{-FeOOH}$) is observed. Hydrated iron (III) oxide or oxyhydroxide is confirmed by enlargement of the peak at approximately $670\text{ cm}^{-1} - 720\text{ cm}^{-1}$ and the broad peak between $1340 - 1580\text{ cm}^{-1}$. (Figure 4.115 c). Goethite appears with its strongest peak at 388 cm^{-1} with its other typical peaks (Figure 4.115 c).

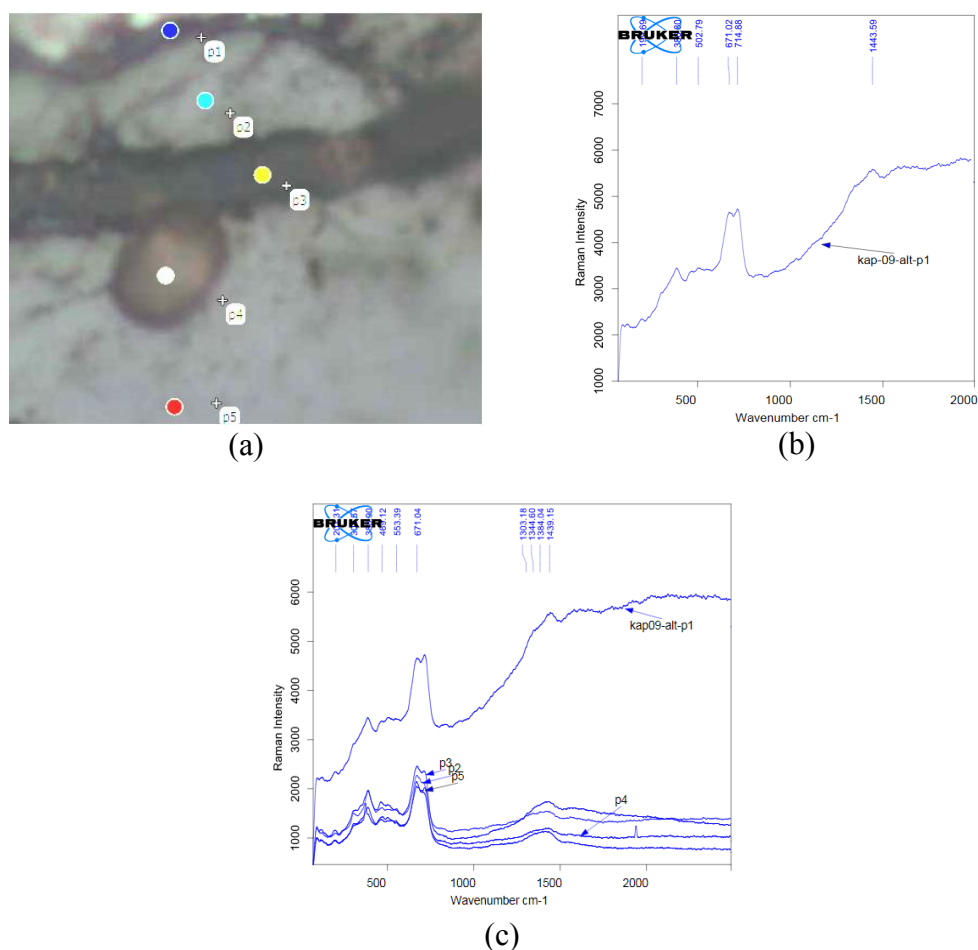


Figure 4. 115 μ -Raman spectra of the successive area where 5 points are located in the ICL of a nail (MSH-KAP-09): measurement points (a); maghemite at point 1 (b); hydrated iron (III) oxide or oxyhydroxide together with goethite at point 2 to 5 (c).

The 5th step with 5 points (p1 to p5) close to the TM were analyzed (Figure 4.116 a): From point 1 to 5, goethite (α -FeOOH) together with hydrated iron (III) oxide or oxyhydroxide is observed. Goethite appears with its strongest peak at 391 cm^{-1} and its other typical peaks. Hydrated iron (III) oxide or oxyhydroxide is confirmed by enlargement of peak at 670 cm^{-1} and the broad peak between 1340 - 1580 cm^{-1} (Figure 4.116 b). Typical layering of main corrosion products of each point on the nail (MSH-KAP-09) from the interior by using Raman Spectroscopic Analysis have been given in Tables 4.33.

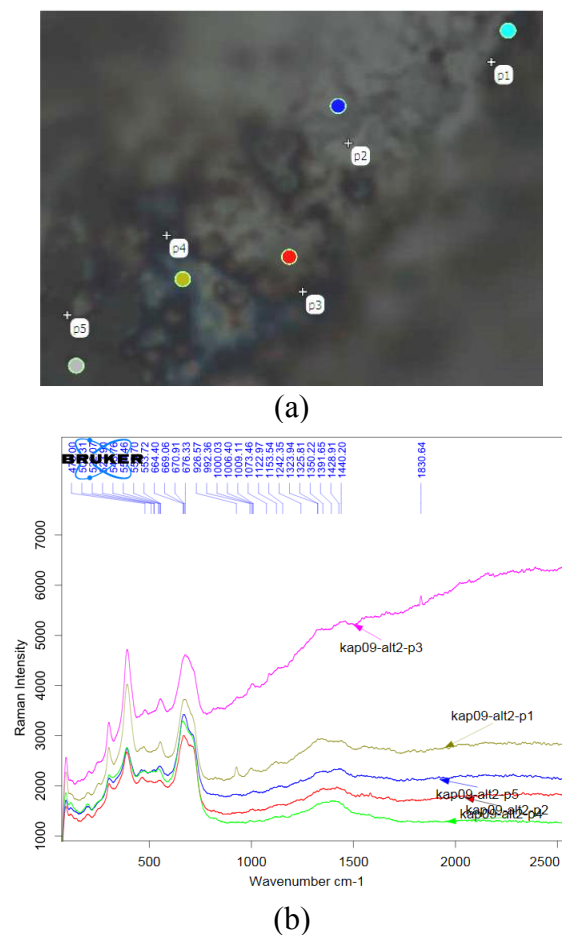
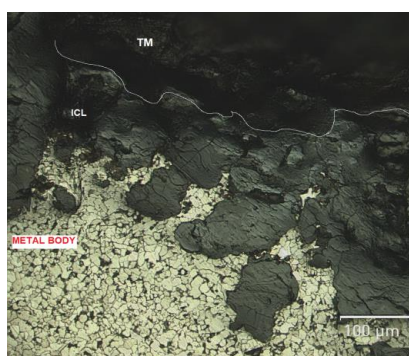


Figure 4. 116 μ -Raman spectra of the successive area where 5 points are located in the ICL close to TM of a nail (MSH-KAP-09): measurement points (a); goethite with hydrated iron (III) oxide or oxyhydroxide at all points (b).

Table 4. 33 Iron oxides followed by μ -Raman analyses in the corrosion layer of a nail (MSH-KAP-09) (16th cc).

Location	Observed Corrosion Minerals				
	Reaction Front RF \rightarrow ICL \rightarrow ICL-TM border (OSL) \rightarrow TM				
Interior of the Hammam building – <i>Indoor atmospheric condition</i>	Magnetite	Hydrated iron (III) oxide or oxyhydroxide	Lepidocrocite	Maghemite	Hydrated iron (III) oxide or oxyhydroxide
	Hydrated iron (III) oxide or oxyhydroxide	Goethite	Magnetite	Hydrated iron (III) oxide or oxyhydroxide	Goethite
	Maghemite		Goethite	Goethite	
	Goethite				

The digital microscopic and Raman microscopic images of a timber jointing nail (MSH-KAP-12) used for a stone building from interior of a 16th century hammam building show a compact and distinct corrosion layer having a thickness in the range of $\sim 200 \mu\text{m}$ (Figure 4.117). Starting from the metal body towards TM, 10 points in three steps were analyzed by μ -Raman (Figures 4.118 – 4.120). Typical layering of main corrosion products of each point on the nail (MSH-KAP-12) for timber jointing from the interior by using Raman Spectroscopic Analysis have been given in Table 4.34.



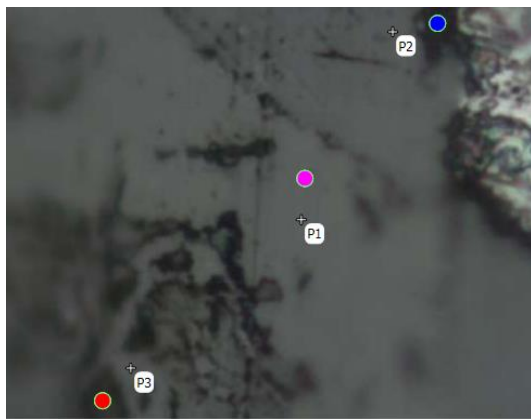
(a) MSH-KAP-12 (500X)



(b) MSH-KAP-12

Figure 4. 117 Digital microscopic (a) and Raman microscopic (b) images of a timber jointing nail (MSH-KAP-12) after etching with nitric acid in alcohol (16th cc).

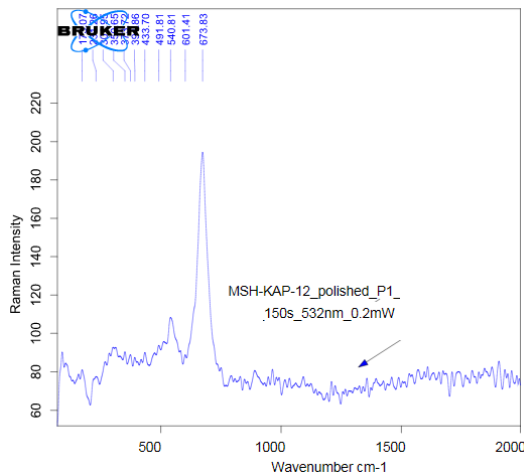
The 1st step covers the reaction front (RF) including ICL with the analyses of 3 points (Figure 4.118 a), besides those, 1 point (p4) following the p3 was analyzed (Figure 4.118 b). Magnetite (Fe₃O₄) with its strongest peak at 670 cm⁻¹ is observed in all 3 points. (Figure 4.118 c). In point 4, hematite is identified with its main peaks at 297 cm⁻¹, 413 cm⁻¹ and 1325 cm⁻¹.



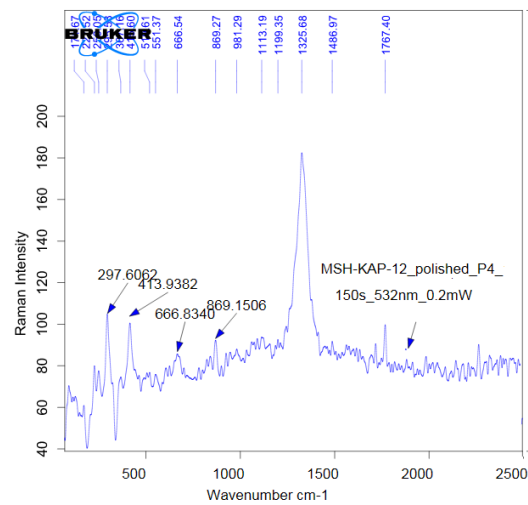
(a)



(b)



(c)



(d)

Figure 4. 118 μ -Raman spectra of the 1st area where 4 points are located in the RF towards ICL of a nail (MSH-KAP-12): measurement points (a, b); magnetite at p1 to p3 (c), and hematite at p4 (d).

At the following 2nd step in the ICL close to RF, wustite is observed at the analyzed 4 points with its peak at $\sim 650\text{ cm}^{-1}$ (Fig 4.119 a, b, c).

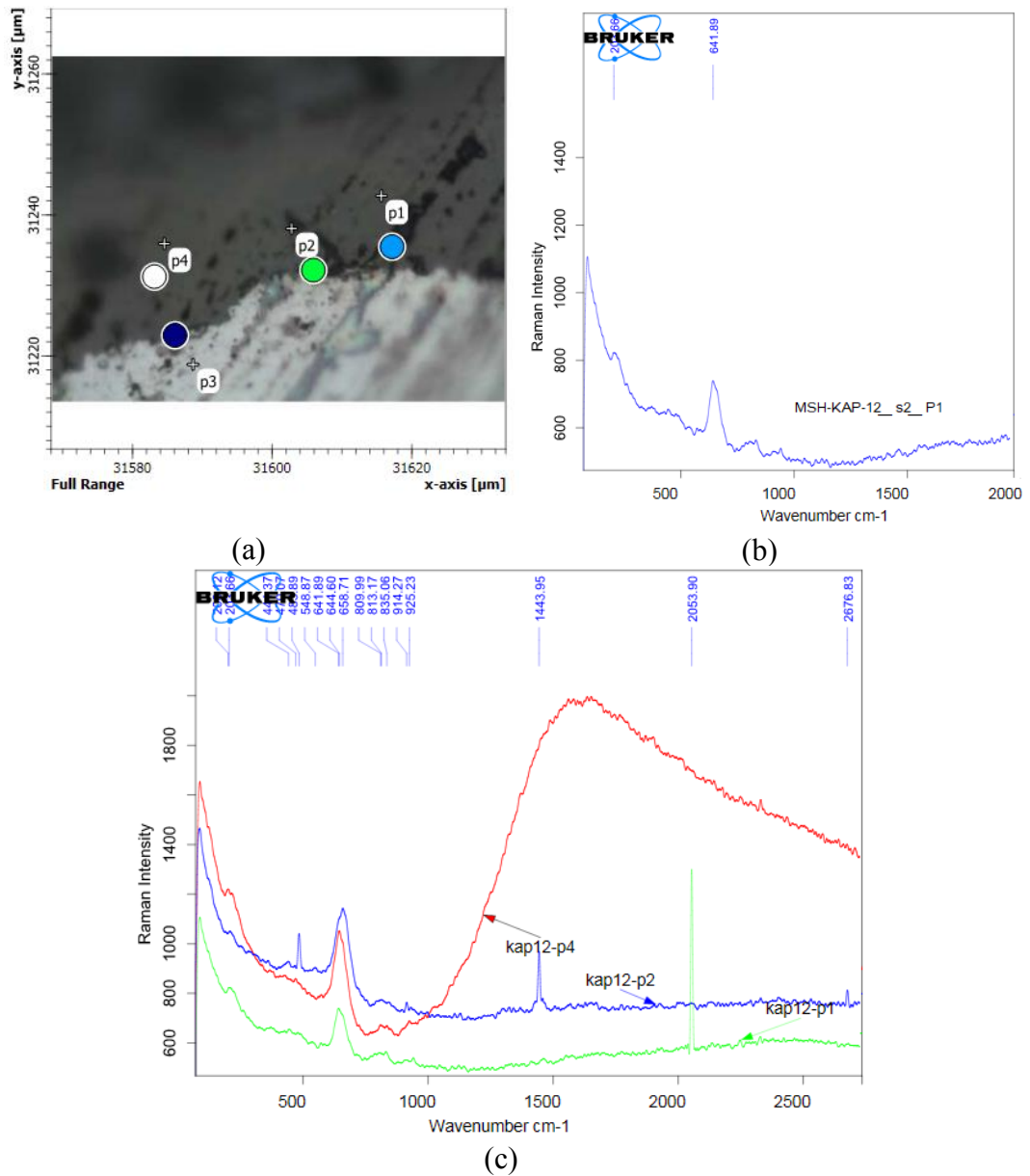


Figure 4. 119 μ -Raman spectra of the successive area where 4 points are located in the ICL of a nail (MSH-KAP-12): measurement points (a); wustite at p1 (b); wustite at p1 to p4 (c).

In the ICL towards TM, the other 2 points were analyzed: Hematite is observed at the analyzed 2 points with its peaks at $\sim 1324\text{ cm}^{-1}$, 297 cm^{-1} , 224 cm^{-1} and 410 cm^{-1} indicating a well crystallized phase (Fig 4.120 a, b, c).

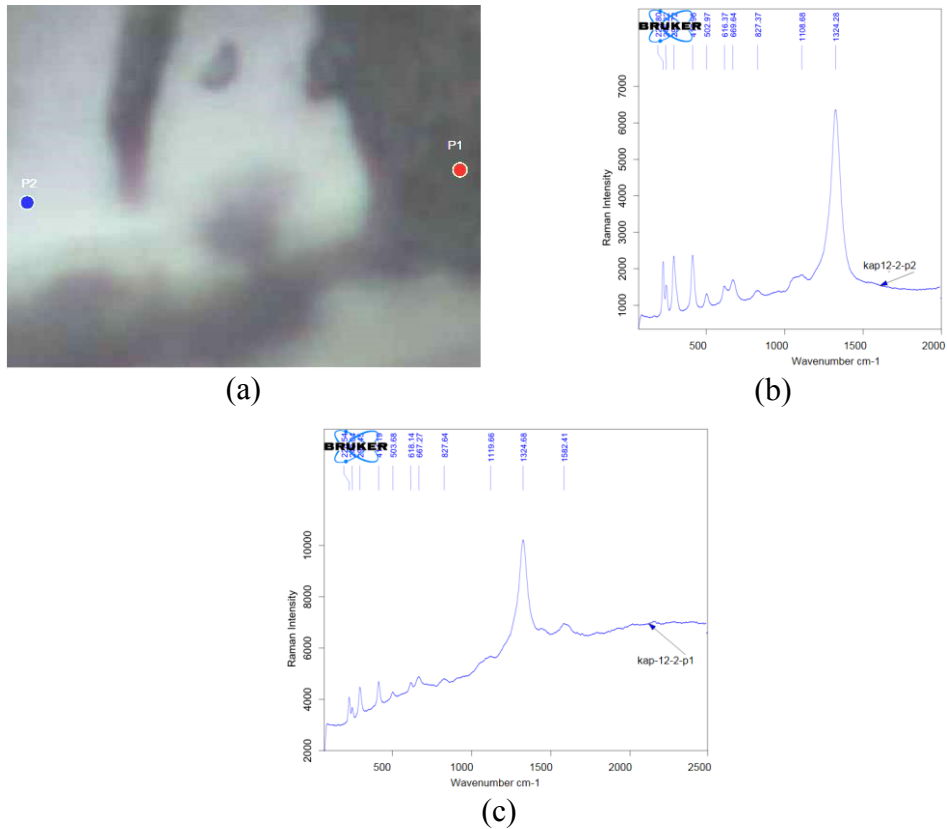


Figure 4. 120 μ -Raman spectra of the successive area where 2 points are located in the ICL towards TM of a nail (MSH-KAP-12): measurement points (a); hematite at p1 to p2 (b, c).

Table 4. 34 Iron oxides followed by μ -Raman analyses in the corrosion layer of a nail (MSH-KAP-12) (16th cc).

Location	Observed Corrosion Minerals			
	Reaction Front RF \rightarrow ICL \rightarrow ICL-TM border (OSL) \rightarrow TM			
Interior of the Hammam – <i>Indoor</i>	Wustite	Magnetite	Hematite	-

Iron oxides layering in the corrosion of the objects taken from Kiliç Ali Pasha Hammam Building constructed in the 16th century after Raman Spectroscopic Analysis documented together starting from RF towards TM (Table 4.35). In order to be clear and comprehensible, some abbreviations have been used in the following table.

Table 4. 35 Iron oxides followed by μ -Raman analyses in the corrosion layers of the objects from Kiliç Ali Pasha Hammam building (16th cc).

Location	Observed Corrosion Minerals						
	RF	RF-ICL →	ICL	ICL-TM →	TM (OSL)		
Exterior of the Hammam building – <i>Outdoor</i> <i>MSH-KAP-01</i>	Magnetite (Fe ₃ O ₄)	Magnetite (Fe ₃ O ₄) Maghemite (γ -Fe ₂ O ₃) and Hematite (α -Fe ₂ O ₃)	Goethite (α -FeOOH)	Hematite (α -Fe ₂ O ₃)	Goethite (α -FeOOH) Lepidocrocite (γ -FeOOH) Magnetite (Fe ₃ O ₄) Maghemite (γ -Fe ₂ O ₃)		
Interior of the Hammam building – <i>Interior</i> <i>MSH-KAP-02</i>	Goethite (α -FeOOH)	Iron (III) oxyhydr/oxide	Iron (III) oxyhydr/oxide	Goethite (α -FeOOH)	-		
Exterior of the Hammam building – <i>Outdoor</i> <i>MSH-KAP-03</i>	Magnetite (Fe ₃ O ₄) Hydrated iron (III) oxyhydr/oxide	Magnetite (Fe ₃ O ₄) Goethite (α -FeOOH)	Maghemite (γ -Fe ₂ O ₃) Magnetite (Fe ₃ O ₄) Goethite (α -FeOOH)	Hydrated iron (III) oxyhydr/oxide	Goethite (α -FeOOH) Magnetite (Fe ₃ O ₄) Maghemite (γ -Fe ₂ O ₃) Lepidocrocite (γ -FeOOH)	Goethite (α -FeOOH) Lepidocrocite (γ -FeOOH)	Goethite (α -FeOOH) Lepidocrocite (γ -FeOOH)
Interior of the Hammam building – <i>Indoor</i> <i>MSH-KAP-09</i>	Magnetite Hydrated iron (III) oxyhydr/oxide Maghemite Goethite	Hydrated iron (III) oxyhydr/oxide Goethite	Lepidocrocite Magnetite Goethite	Maghemite Hydrated iron (III) oxyhydr/oxide Goethite	Hydrated iron (III) oxyhydr/oxide Goethite		
Interior of the Hammam building – <i>Indoor</i> <i>MSH-KAP-12</i>	Magnetite Hematite	Wustite		Hematite	-		

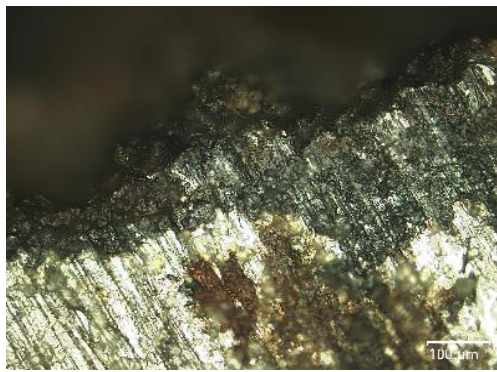
4.5.3 Raman Analyses of the 19th Century Samples

Corrosion characteristics of the 19th century iron objects were examined on the selected 10 samples. 8 of them were taken from the dwellings and excavations in Foça, Izmir and 2 from the dwelling of Tekkekoy, Samsun.

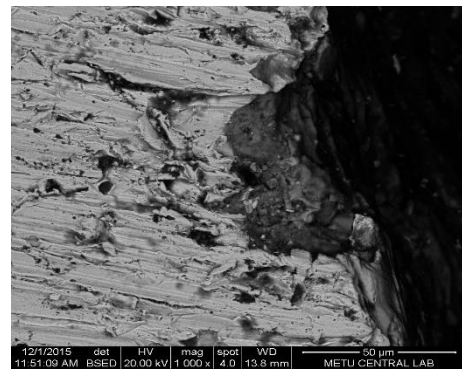
The selected samples from Foça were a nail (FKM-02) for jointing load bearing main timber beams; a door lock piece (FKM-03) from main entrance; a male hinge (FKM-04) and a female hinge (FKM-05) from the main entrance door; 3 nails (FKM-07, 10, 11) and an L shaped iron object (FKM-08) from the Ottoman excavation layer representing the buried conditions.

The samples from the dwelling in Tekkekoy were a nail (T-N-04) at the interior door frame and a crossbar (T-D-01) from the interior of the dwelling used for locking the main entrance door.

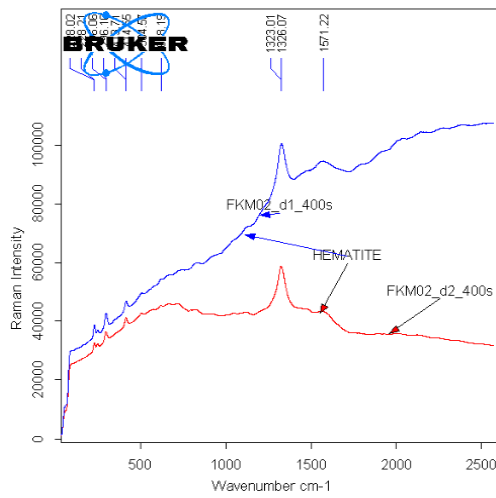
To begin with, regarding the dwelling in Foça, digital microscopic and SEM views of the nail (FKM-02) used for the jointing main load bearing timber beams show a compact corrosion layer having 67.5 μm thickness (Figures 4.121 a and b). Examination from the metal body towards TM was done at 6 points (Figures 4.121, c, d, e and f). At points 1, 2 and 3, hematite ($\alpha\text{-Fe}_2\text{O}_3$) is the main phase with its characteristic peaks at 296 cm^{-1} , 413 cm^{-1} , 228 cm^{-1} and 1323 cm^{-1} . At points 4 and 6, the weak Raman spectrum is dominated by a large band around 720 cm^{-1} and the broad peak between 1361 - 1516 cm^{-1} (Figure 3.18 b). The spectrum is difficult to decipher due to a poor crystallization state; as a result, the phases can be defined as hydrated iron (III) oxide or oxyhydroxides (Bellot-Gurlet, 2009). For this nail (FKM-02) embedded in the structural timber beam, hematite is the abundant phase observed with hydrated iron (III) oxide or oxyhydroxide marbling towards the exterior of the corrosion layer (Table 4.36).



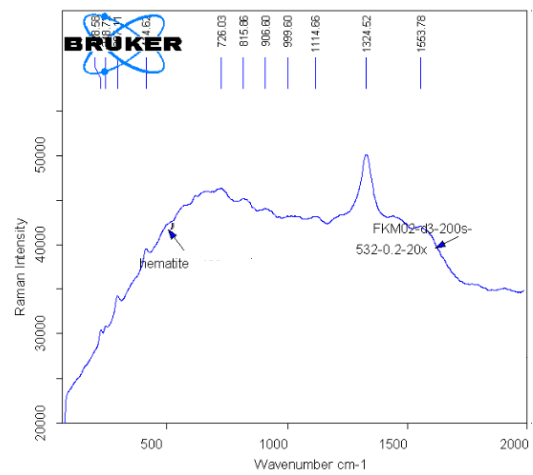
(a) FKM-02 (1000X)



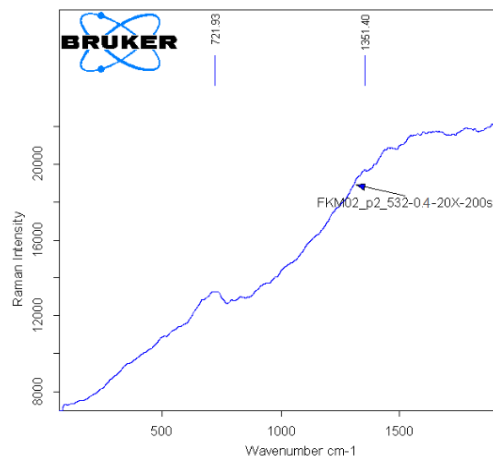
(b) FKM-02 (1000X)



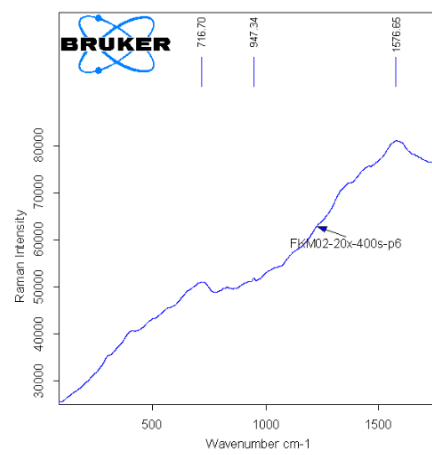
(c)



(d)



(e)



(f)

Figure 4. 121 Digital microscopic (a) and SEM (b) images of a nail (FKM-02) at load bearing timber beam after etching with nitric acid in alcohol (19th cc). μ -Raman spectra of the 6 points located in the RF towards ICL: hematite at p1 to p3 (c, d); and hydrated iron (III) oxide or oxyhydroxide at p4 to p6 (e, f).

Table 4. 36 Iron oxides followed by μ -Raman analyses in the corrosion layer of the nail (FKM-02) (19th cc).

Location	Observed Corrosion Minerals				
	RF	RF-ICL \rightarrow	ICL	ICL-TM \rightarrow (OSL)	TM
Interior of the dwelling – <i>Embedded in timber</i> <i>FKM-02</i>	Hematite (α -Fe ₂ O ₃)	Hematite (α -Fe ₂ O ₃)	Hematite (α -Fe ₂ O ₃)	Hydrated iron (III) oxide or oxyhydroxide	-

Another sample from Foça dwellings is a door lock piece (FKM-03) from the main entrance which shows a compact corrosion layer by stereo and Raman microscopic views (Figure 4.122). Starting from the metal body towards TM, 8 points in 2 steps were analyzed (Figures 4.123 and 4.124). At points 1 and 2 in the RF and at the transition phase towards ICL, hydrated iron (III) oxide or oxyhydroxide with its peaks by a large band around 710 cm⁻¹ and the broad peak at 1330-1350 cm⁻¹ is observed at a poorly crystallized phase (Figure 4.123 b, c). At point 3 in the ICL, a goethite phase with hydrated iron (III) oxide or oxyhydroxide is detected with its main peaks at 391 cm⁻¹, 300 cm⁻¹, 689 cm⁻¹ and 1314 cm⁻¹. At the following point in the ICL (p4), a well crystallized goethite with main peak at 388 cm⁻¹ and magnetite + maghemite rich areas are clearly identified (Figure 4.123 d, e). In the 2nd step, 3 points were analyzed. At 2 points (p6 and p7) in OSL and close to TM, a well crystallized corrosion layer is identified with its peaks at 399 cm⁻¹, 300 cm⁻¹, 686 cm⁻¹ and 1305 cm⁻¹ (Figures 4.124 b, c). At point 8 in TM, hydrated iron (III) oxide or oxyhydroxide with its peaks by a large band around 701 cm⁻¹ and the broad peak at 1330-1550 cm⁻¹ is observed at a poorly crystallized phase (Figure 4.124 d). The iron oxides layering in the corrosion of the door lock piece (FKM-03) by μ -Raman Analysis is summarized at Table 4.37. A noticeable goethite phase is observed between the reaction front and the transformed media composed of hydrated iron (III) oxide or oxyhydroxides.

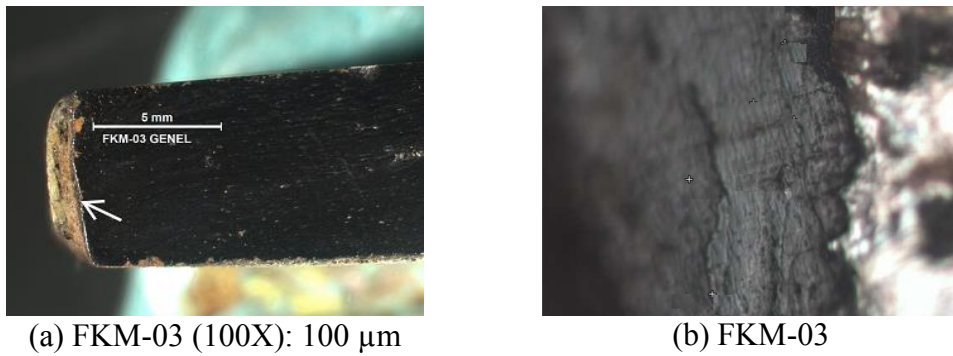


Figure 4.122 Stereo microscopic (a) and Raman microscopic (b) images of a door lock piece (FKM-03) after etching with nitric acid in alcohol (19th cc).

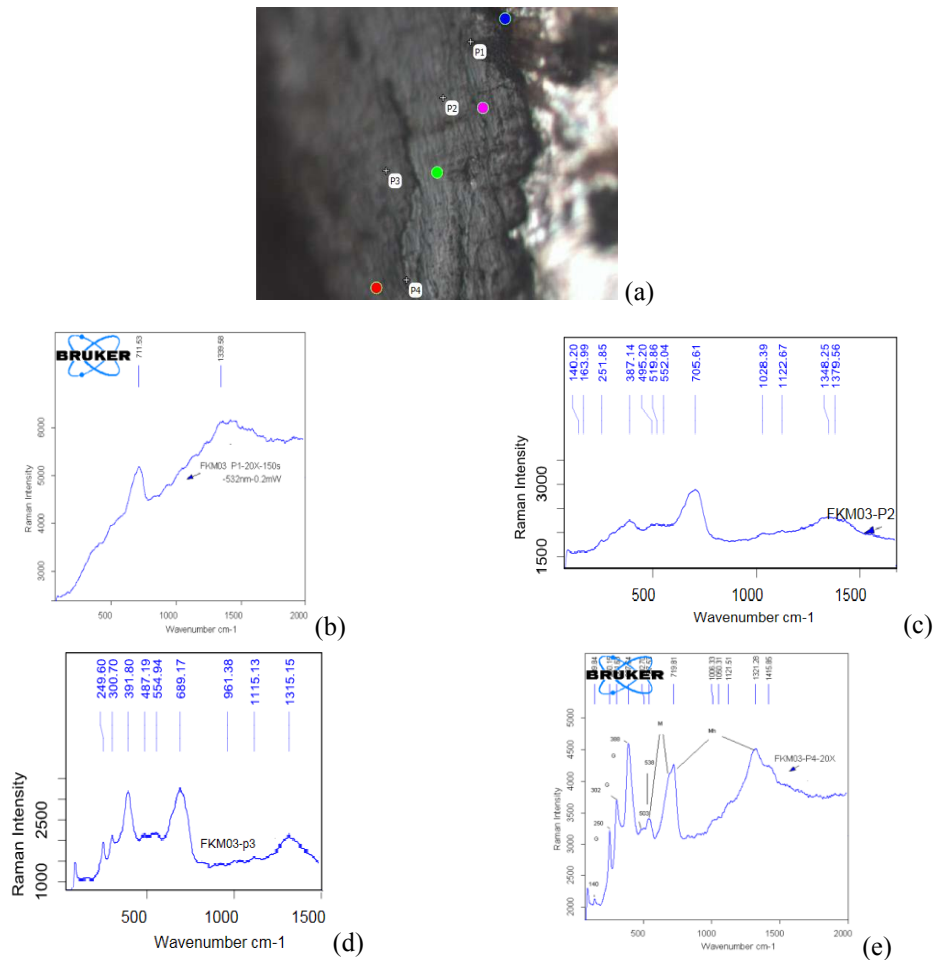


Figure 4.123 μ -Raman spectra of the 4 points located in the RF towards ICL of a door lock piece (FKM-03) (19th cc): measurement points (a); hydrated iron (III) oxide or oxyhydroxide at p1 and p2 (b, c); goethite with hydrated iron (III) oxide or oxyhydroxide at p3 (d); goethite with magnetite+magemhite at p4 (e).

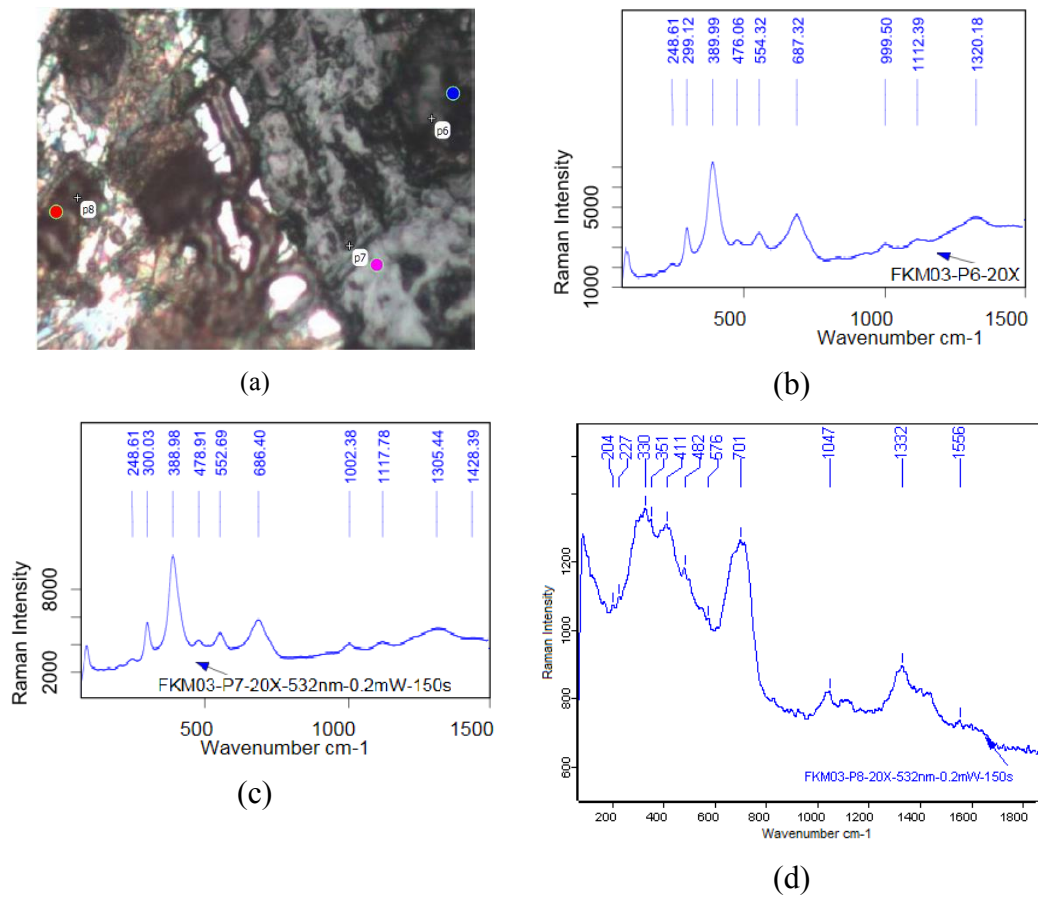


Figure 4. 124 μ -Raman spectra of the 3 points located in the ICL towards TM of a door lock piece (FKM-03): measurement points (a); goethite at p6 and p7 (b, c); and hydrated iron (III) oxide or oxyhydroxide at p8 (d).

Table 4. 37 Iron oxides followed by μ -Raman analyses in the corrosion layer of a door lock piece (FKM-03) (19th cc).

Location	Observed Corrosion Minerals				
	RF	RF-ICL \rightarrow	ICL	ICL-TM \rightarrow (OSL)	TM
Interior of the Dwelling – Door lock piece FKM-03	Hydrated iron (III) oxide or oxyhydroxide	Goethite (α -FeOOH) Hydrated iron (III) oxide or oxyhydroxide	Goethite (α -FeOOH) Magnetite (Fe_3O_4) Maghemite (α -Fe $_2\text{O}_3$)	Goethite (α -FeOOH)	Hydrated iron (III) oxide or oxyhydroxide

Another sample analyzed from the Foça dwellings is a male hinge (FKM-04) used in the main entrance door. It shows a compact corrosion layer observed by stereo and Raman microscopic views (Figure 4.125 a and b). Starting from the metal body towards TM, 4 points in 2 steps were analyzed (Figures 4.126 a and b). At points 2 and 3 in the RF and ICL, a goethite phase is detected with its main peaks at 391 cm^{-1} and 300 cm^{-1} together with hydrated iron (III) oxide or oxyhydroxide having a large band around 686 cm^{-1} and 1314 cm^{-1} (Figure 4.126 c and d). At point 5 being a point in OSL, a goethite phase with its main peaks at 390 cm^{-1} and 301 cm^{-1} is detected together with hydrated iron (III) oxide or oxyhydroxide by the presence of a large band around 701 cm^{-1} and 1321 cm^{-1} (Figure 4.126 f). At point 4 on TM, hydrated iron (III) oxide or oxyhydroxide with its peaks by a large band around 720 cm^{-1} and the broad peak at 1450 cm^{-1} is observed as a poorly crystallized phase (Figure 4.126 e). The μ -Raman results of FKM-04 are summarized in Table 4.38. Goethite is found to be the main phase surrounded by hydrated iron (III) oxide or oxyhydroxide in a diffused way.

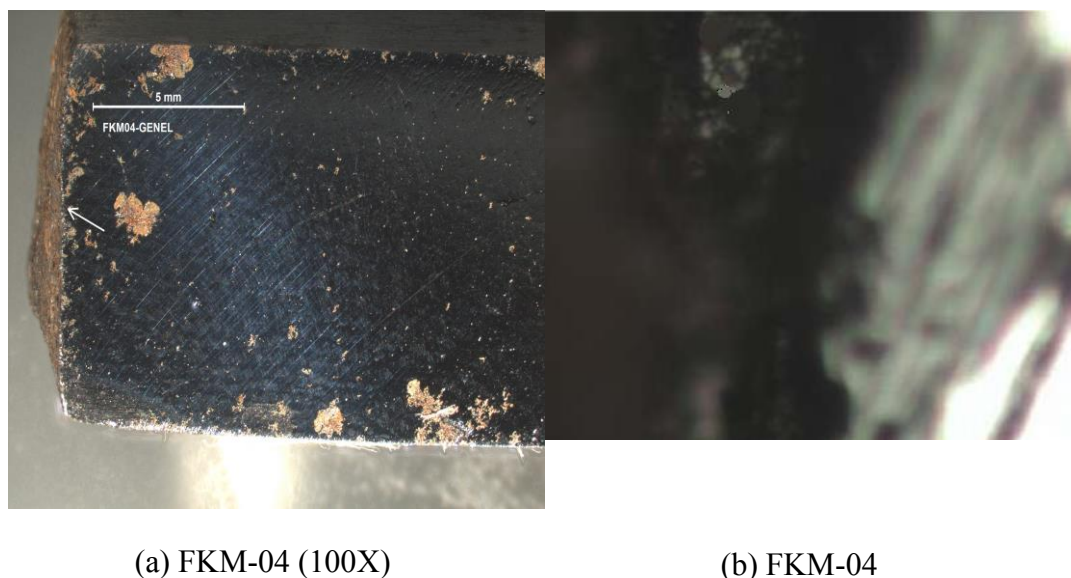
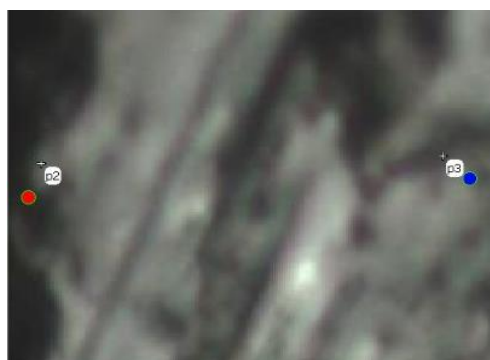
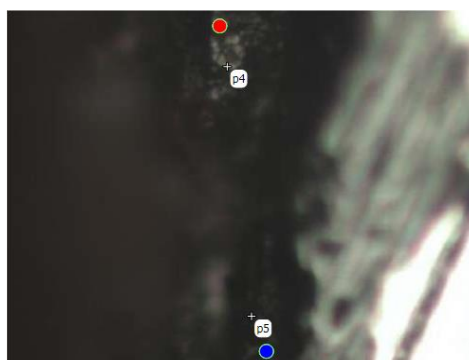


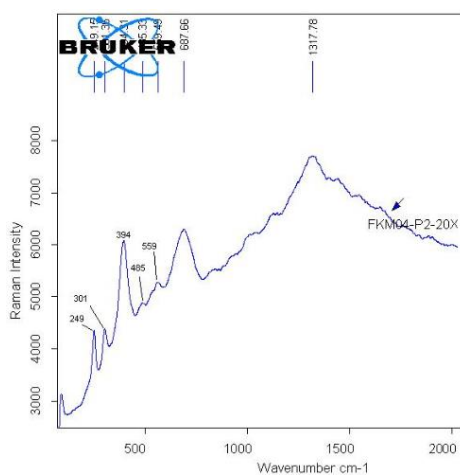
Figure 4. 125 Stereo microscopic (a) and Raman microscopic (b) images of a male hinge (FKM-04) (19th century) after etching with nitric acid in alcohol.



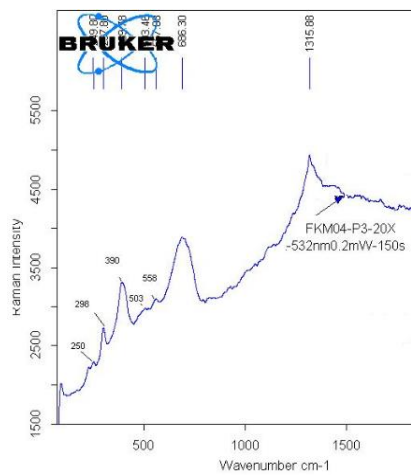
(a)



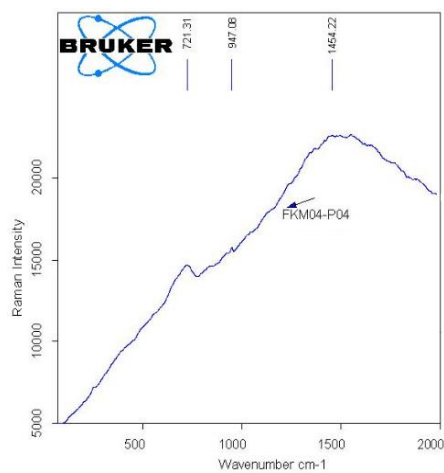
(b)



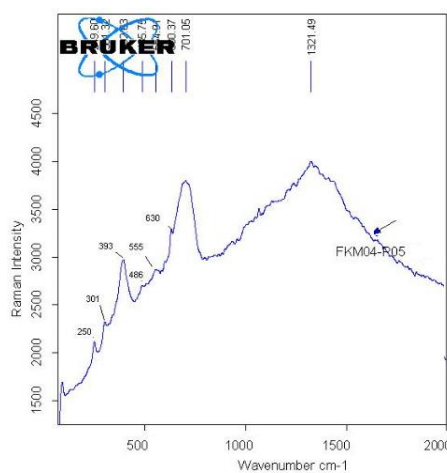
(c)



(d)



(e)



(f)

Figure 4. 126 μ -Raman spectra of the 4 points located in the RF towards TM of a hinge piece (FKM-04) (19th century): measurement points (a, b); goethite with hydrated iron (III) oxide or oxyhydroxide at p2, p3, and p5 (c, d, f); hydrated iron (III) oxide or oxyhydroxide at p4 (e).

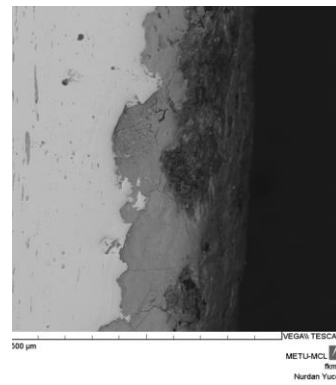
Table 4. 38 Iron oxides followed by μ -Raman analyses in the corrosion layer of a hinge piece (FKM-04) (19th cc).

Location	Observed Corrosion Minerals			
	RF	RF-ICL \rightarrow	ICL	ICL-TM \rightarrow (OSL)
Interior of the dwelling – Hinge from a main entrance door FKM-04	Goethite (α -FeOOH) Hydrated iron (III) oxide or oxyhydroxide	Goethite (α -FeOOH) Hydrated iron (III) oxide or oxyhydroxide	Hydrated iron (III) oxide or oxyhydroxide	Goethite (α -FeOOH) Hydrated iron (III) oxide or oxyhydroxide

The next object analyzed from the Foça dwellings is a female hinge (FKM-05) used in the main entrance door. It shows a compact corrosion layer by stereo microscopic and SEM views (Figure 4.127 a and b). Starting from the metal body towards TM, 3 points were analyzed (Figures 4.128 a). At point 1 in the RF, a goethite phase is detected with its weak main peaks at 396 cm^{-1} and 301 cm^{-1} together with hydrated iron (III) oxide or oxyhydroxide having a large band around 690 cm^{-1} and $\sim 1320\text{ cm}^{-1}$ (Figure 4.128 b). At point 2 in the ICL, hydrated iron (III) oxide or oxyhydroxide having a large band around 695 cm^{-1} and $\sim 1321\text{ cm}^{-1}$ is detected together with a poorly crystalized goethite phase having its weak main peaks at 386 cm^{-1} , 304 cm^{-1} and 250 cm^{-1} (Figure 3.18 c). At point 3 close to TM, hydrated iron (III) oxide or oxyhydroxide with a noticeable presence of maghemite (γ -Fe₂O₃) having a large asymmetric band around 720 cm^{-1} and broad bands $\sim 1314\text{ cm}^{-1}$ to 1558 cm^{-1} is detected together with a poorly crystalized goethite phase having its main peaks at 391 cm^{-1} , 304 cm^{-1} and 250 cm^{-1} (Figure 4.128 d). The iron oxides layering by μ -Raman Analysis in the corrosion of the iron hinge piece (FKM-05) is summarized in the Table 4.39.

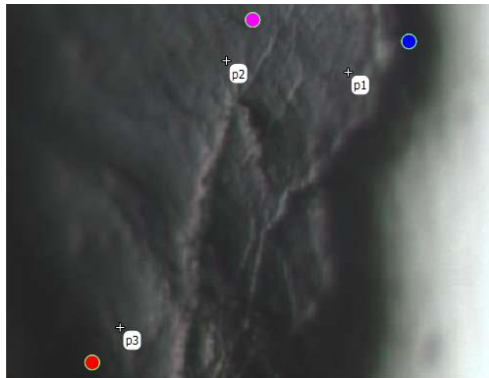


(a) FKM-05 (100X)

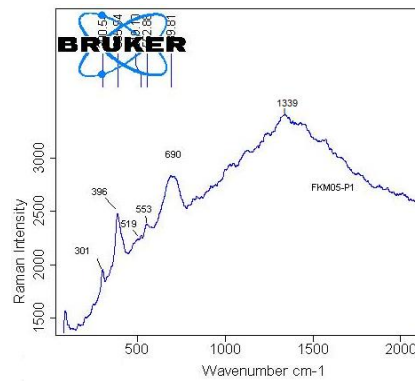


(b) FKM-05

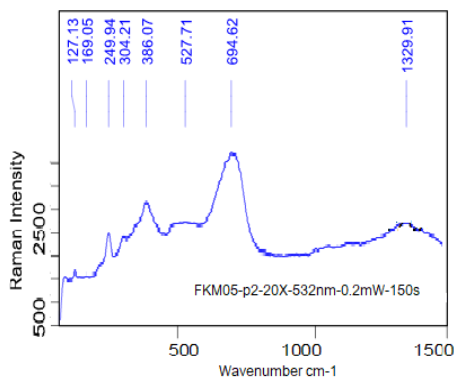
Figure 4. 127 Stereo microscopic (a) and SEM (b) images of a female hinge (FKM-05) after etching with nitric acid in alcohol (19th cc).



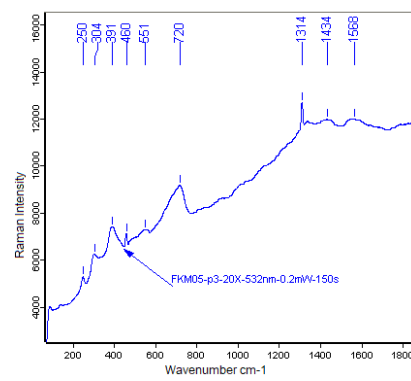
(a)



(b)



(c)



(d)

Figure 4. 128. μ -Raman spectra of the 3 points located in the RF towards TM of a female hinge piece (FKM-05) (19th cc): measurement points (a); hydrated iron (III) oxide or oxyhydroxide with some goethite at p1, p2 and p3 (b, c, d).

Table 4. 39 Iron oxides followed by μ -Raman analyses in the corrosion layer of a female hinge piece (FKM-05 (19th cc)).

Location	Observed Corrosion Minerals				
	RF	RF-ICL →	ICL	ICL-TM → (OSL)	TM
Interior of the Dwelling – Female hinge from a main entrance door FKM-05	Poorly crystalline goethite (α -FeOOH) Hydrated iron (III) oxide or oxyhydroxide	Poorly crystalline goethite (α -FeOOH) Hydrated iron (III) oxide or oxyhydroxide			Poorly crystalline goethite (α -FeOOH) Hydrated iron (III) oxide or oxyhydroxide

A nail (FKM-07) representing the object in a burial condition from excavations of an Ottoman layer shows a thick corrosion layer with a thickness between $\sim 475 \mu\text{m}$ having cracks and porous regions in it, as observed by digital microscopic and SEM views (Figure 4.129 a and b). A gray colored area covering 2 points in the ICL were analyzed (Figures 4.129 c and d). In this area, a well-formed goethite phase is detected with its main peaks at 392 cm^{-1} , 301 cm^{-1} , 685 cm^{-1} and 1320 cm^{-1} (Figure 4.129 e and f). Raman Analysis in the corrosion of the nail (FKM-07) is summarized in the Table 4.40.

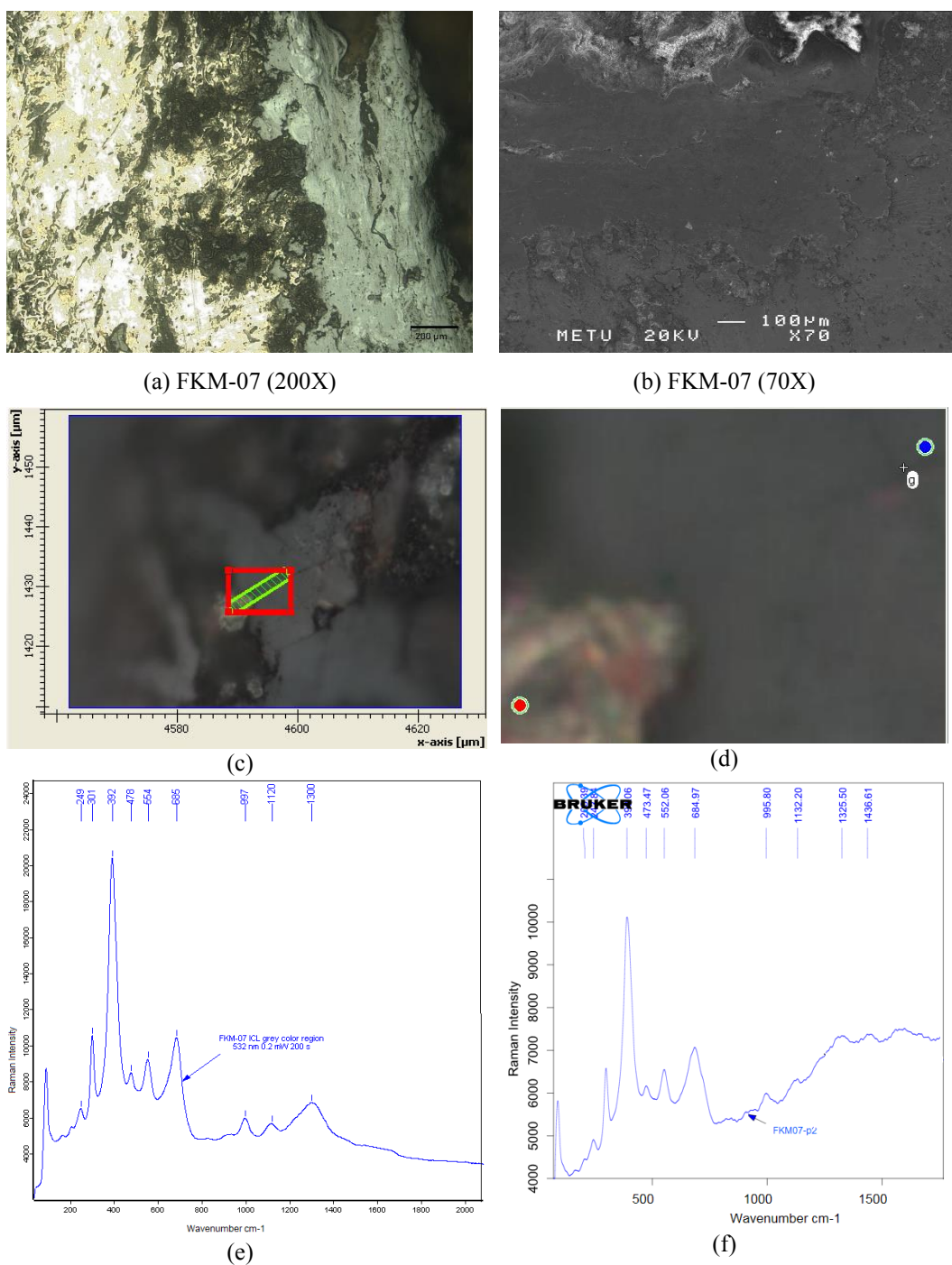


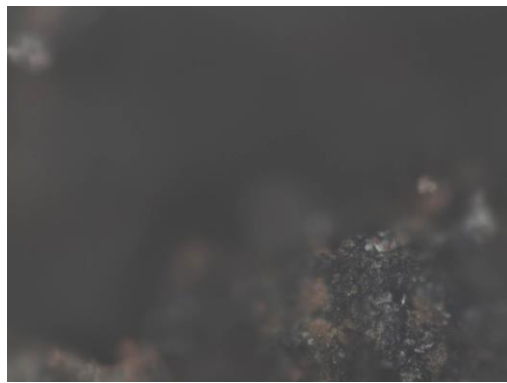
Figure 4. 129 Digital microscopic (a) and SEM (b) images of a buried nail (FKM-07) after etching with nitric acid in alcohol (19th cc). μ -Raman spectra of the 2 points located in the ICL: Measurement points (c, d); goethite at p1 and p2 (e, f).

Table 4. 40 Iron oxides followed by μ -Raman analyses in the corrosion layer of a buried nail (FKM-07) (19th cc).

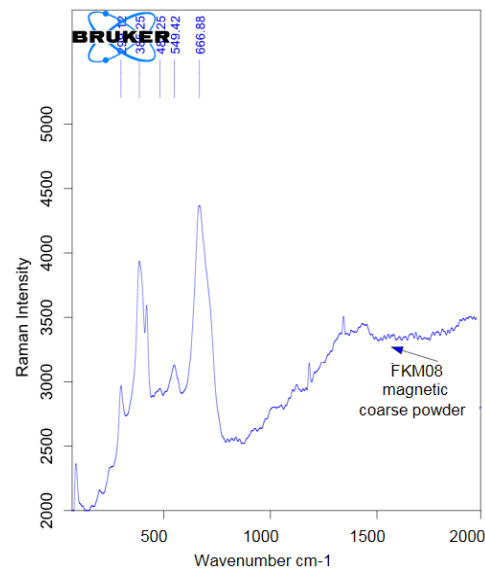
Location	Observed Corrosion Minerals					
	RF	RF-ICL →	ICL	ICL-TM → (OSL)	TM	
Ottoman layer excavation – A buried nail FKM-07			Goethite (α -FeOOH)			

Another sample analyzed from the Ottoman layer of the Foça excavations is an L shaped iron object (FKM-08). It shows a compact corrosion layer by Raman microscopic views (Figure 4.130 a). Starting from the metal body towards TM, 16 points were analyzed in 8 steps. Raman Analysis in the corrosion of the iron object (FKM-08) is summarized in the Table 4.41.

A fine grain powdered corrosion layer on the surface of the sample collected with a magnet was also analyzed. Powder samples are identified as goethite having its main peaks at 385 cm^{-1} and 299 cm^{-1} together with some magnetite having its peaks at 667 cm^{-1} and 549 cm^{-1} (Figure 4.130 a and b). Although the efficiency of magnetite signals in μ -Raman is quite low, the result shows the presence of magnetite as a major component in the corrosion layer together with goethite.



(a) FKM08-corrosion powder



(b)

Figure 4. 130 μ -Raman microscopy image of powder samples collected by a magnet on the surface of the iron object (FKM-08) (a); μ -Raman spectrum of goethite together with magnetite (b).

The 1st step covers 4 points in the RF (Figure 4.131 b). P1 and p2 are well crystallized goethite phase with its main peaks at 390 cm^{-1} , 300 cm^{-1} , 682 cm^{-1} and 1315 cm^{-1} (Figure 4.131 c). At p3 and p4 towards RF-ICL border, a well crystallized goethite phase is also observed with its main peaks at 393 cm^{-1} , 301 cm^{-1} , 685 cm^{-1} , and 1292 cm^{-1} (Figure 4.131 d). The reaction front is integrated with ICL. Next to the metal, there is a compact goethite layer in ICL that continues with some light gray marbling towards TM. At the 2nd step, those light gray marbles (p5) are characterized with a large band around 669 cm^{-1} and $\sim 1396 \text{ cm}^{-1}$ and identified in a general way as hydrated iron (III) oxides or oxyhydroxides indicating several phases at poor crystallization state (Figure 4.131 e and f) (Berlot-Gurlet, *et al*, 2009).

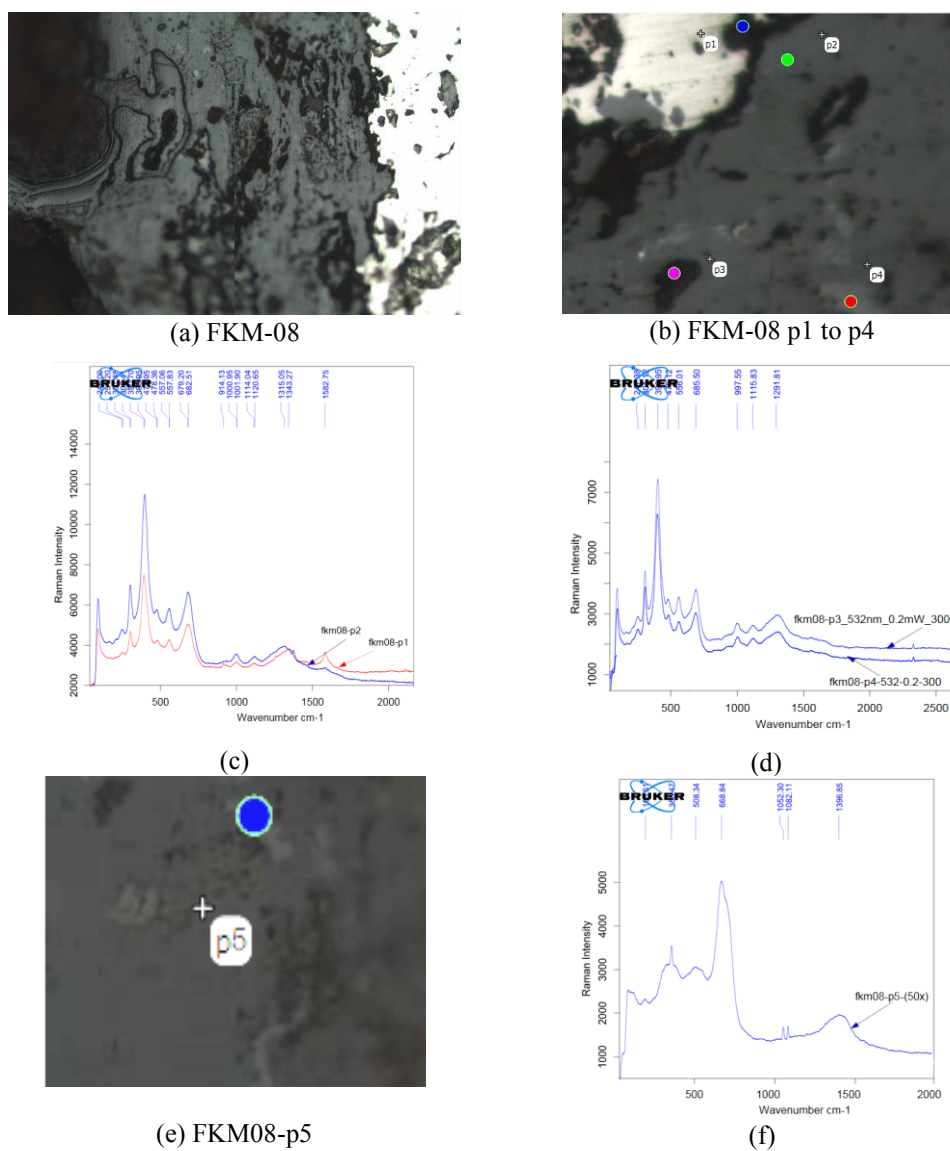
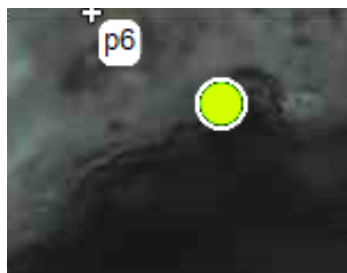


Figure 4. 131 Raman microscopic image of an L-shaped iron object (FKM-08) from the Ottoman layer excavation (19th cc) (a); μ -Raman spectra taken at the 4 points located in the RF towards ICL: measurement points (b); goethite at p1 and p2 (c); goethite at p3 and p4 (d); μ -Raman spectra taken at a marble located in ICL: measurement point (e); hydrated iron (III) oxide or oxyhydroxide at p5 (f).

The 3rd step is represented with 1 point, p6, in ICL (Figure 4.132 a). It also consists of a well crystallized goethite phase with its main peaks at 391 cm^{-1} , 301 cm^{-1} , 684 cm^{-1} , and 1300 cm^{-1} (Figure 4.132 b). The 4th step covers 3 points from p7 to p9 in ICL (Figure 4.133 a). P9 shows a well crystallized goethite phase. P7 and p8 have

the main peaks at 220 cm^{-1} , 291 cm^{-1} , 391 cm^{-1} , 496 cm^{-1} and 1316 cm^{-1} with relative intensities fitting to hematite. Those μ -Raman traces also include the major peak of lepidocrocite at 250 cm^{-1} (Figure 4.133 b). Therefore, p7 and p8 are identified as hematite with some lepidocrocite as well as magnetite with its specific peak at 662 cm^{-1} . The peak at 662 cm^{-1} is attributed to magnetite due to a considerable presence of magnetite in the powder sample belonging to the corrosion layer.



(a) FKM-08 p6

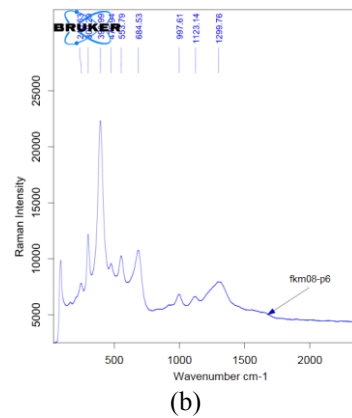
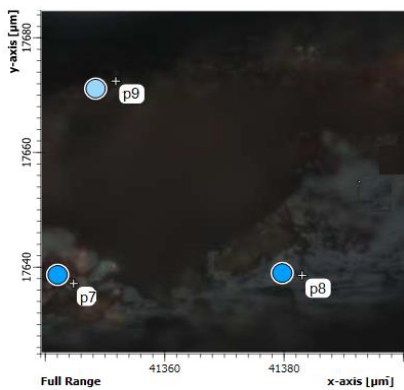


Figure 4. 132 μ -Raman spectrum taken in the ICL of an iron object (FKM-08): measurement point (a); goethite at p6 (b).



(a) FKM-08 p7 to p9

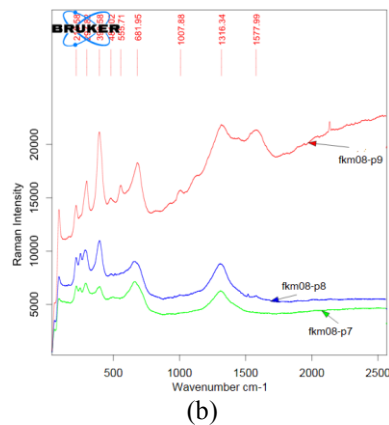
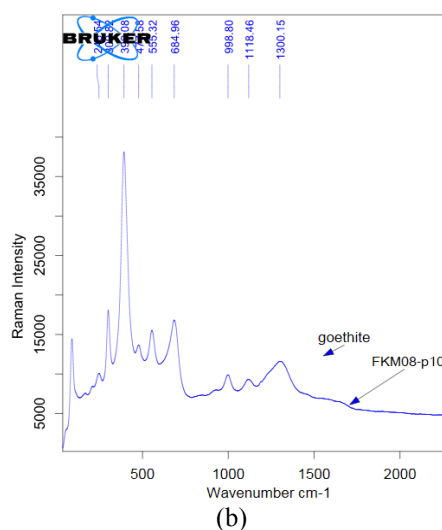


Figure 4. 133 μ - Raman spectra taken at 3 points located in the ICL of an iron object (FKM-08): measurement points (a); goethite at p9 and hematite with some lepidocrocite as well as magnetite at p7 and p8 (b).

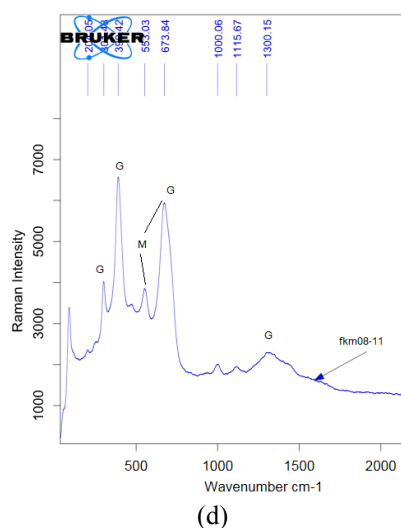
The 5th and 6th steps cover 2 points, p10 and p11, in ICL (Figure 4.134 a and b). P10 is a well crystallized goethite phase with its main peaks at 390 cm⁻¹, 301 cm⁻¹, 685 cm⁻¹ and 1300 cm⁻¹ (Figure 4.134 b). P11 represents a goethite phase with its main peaks at 390 cm⁻¹, 300 cm⁻¹, and 1300 cm⁻¹ together with a magnetite phase having its peaks at 674 cm⁻¹ and 553 cm⁻¹ (Figure 4.134 d).



(a) FKM-08, p10



(c) FKM-08, p11



(d)

Figure 4. 134 μ -Raman spectra taken at 2 points located in the ICL of an iron object (FKM-08): measurement points (a, c); goethite at p10 (b); goethite (G) and magnetite (M) at p11 (d).

The 7th step covers 2 points, p12 and p13, in ICL towards TM (Figure 4.135 a). At both points, a well crystallized goethite phase with its main peaks at 391 cm⁻¹, 300 cm⁻¹, 684 cm⁻¹ and 1302 cm⁻¹ is characterized (Figure 4.135 b). The 8th step includes 3 points, p14, p15 and p16, near TM (Figure 4.135 c). At p16, a goethite phase with its main peaks at 391 cm⁻¹ and 302 cm⁻¹ together with a magnetite / maghemite phase at 684 cm⁻¹, 546 cm⁻¹ and 1411 cm⁻¹ is observed (Figure 4.134 d).

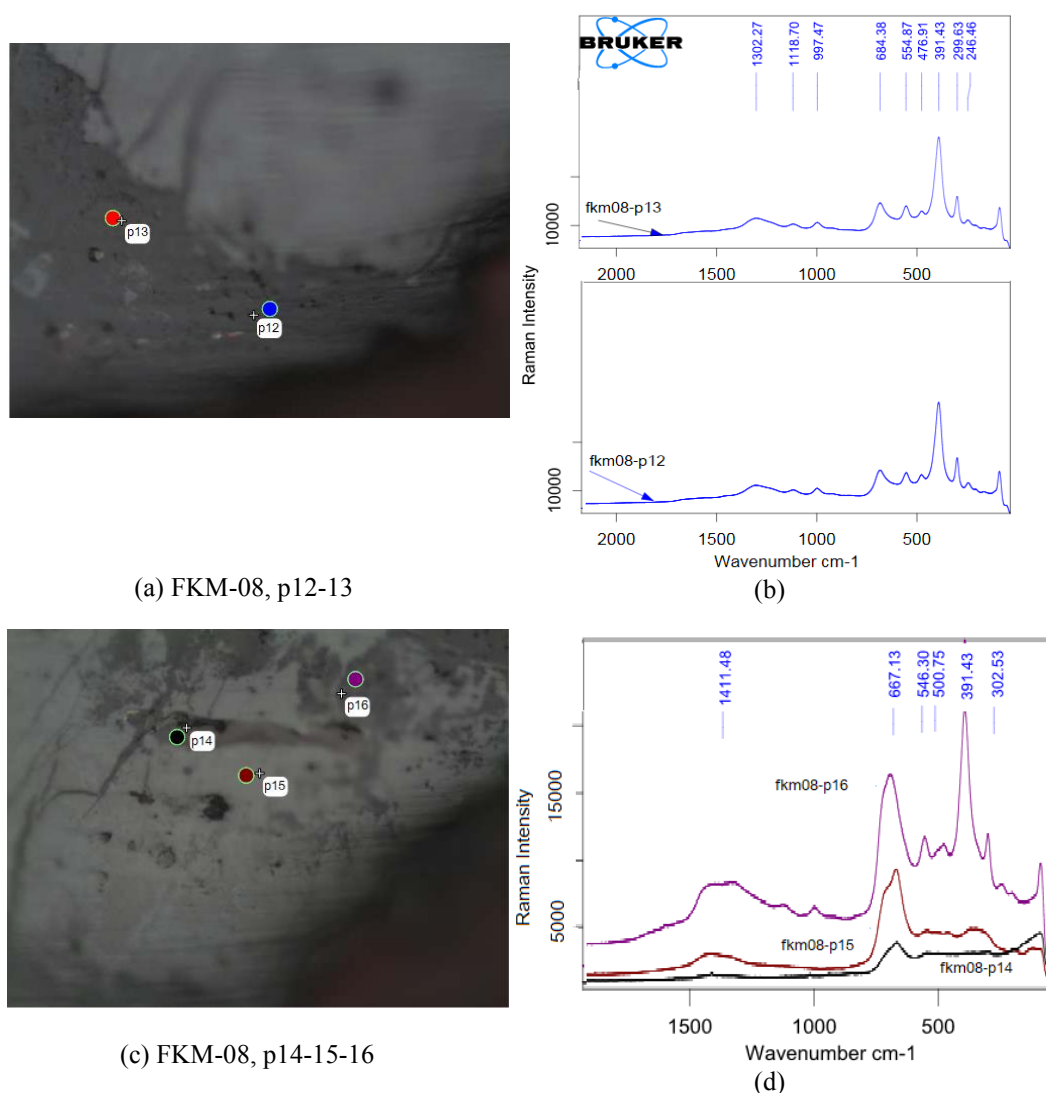
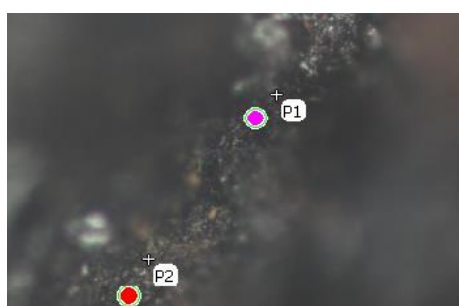


Figure 4. 135 μ -Raman spectra taken at 5 points located in the ICL near TM of an iron object (FKM-08): measurement points (a, c); goethite at p12 and p13 (b); goethite and magnetite / maghemite at p16 and hydrated iron (III) oxides or oxyhydroxides at p14 and p15 (d).

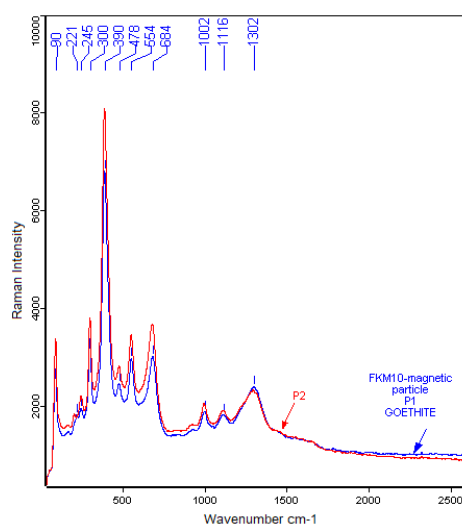
Table 4. 41 Iron oxides followed by μ -Raman analyses in the corrosion layer of an L-shaped iron object (FKM-08) (19th cc).

Location	Observed Corrosion Minerals						
	RF	RF-ICL	ICL	ICL-TM	TM	(OSL)	
Excavation – buried condition L-shaped iron object FKM-08	Goethite	Goethite Hydrated iron (III) oxide or oxyhydroxide	Goethite	Goethite Hematite Lepidocrocite Magnetite	Goethite Magnetite	Goethite	Goethite Magnetite / Maghemite Hydrated iron (III) oxide or oxyhydroxide

Another sample analyzed from the Ottoman layer of the Foça excavation is a nail (FKM-10) from burial condition. The corrosion layer on the iron object was scraped off and the mixture of the corrosion layer collected in powder form by a magnet. The collected sample was then analyzed in 5 locations consisting of 17 points in total. The 1st location of the powder sample covers 2 points (Figure 4.136a). P1 and p2 are a well crystallized goethite phase with its main pain peaks at 390 cm^{-1} , 300 cm^{-1} , 684 cm^{-1} and 1302 cm^{-1} (Figure 4.136b).



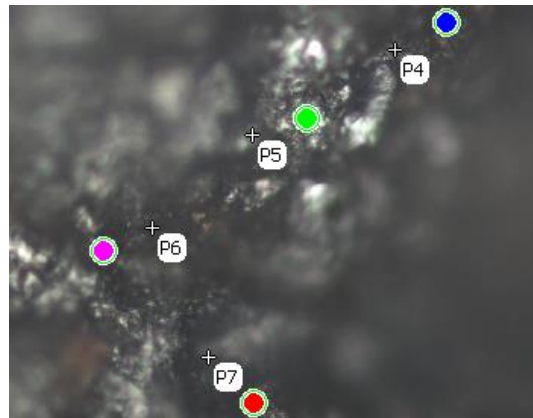
(a) FKM-10, step 1



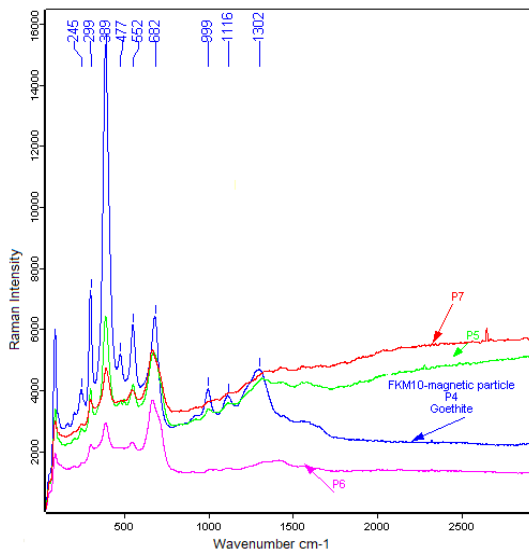
(b) FKM-10, p1 and p2

Figure 4. 136 μ -Raman microscopy image at the 1st location of the powder sample collected by a magnet on the surface of the iron nail (FKM-10): measurement points (a); goethite at p1 and p2 (b).

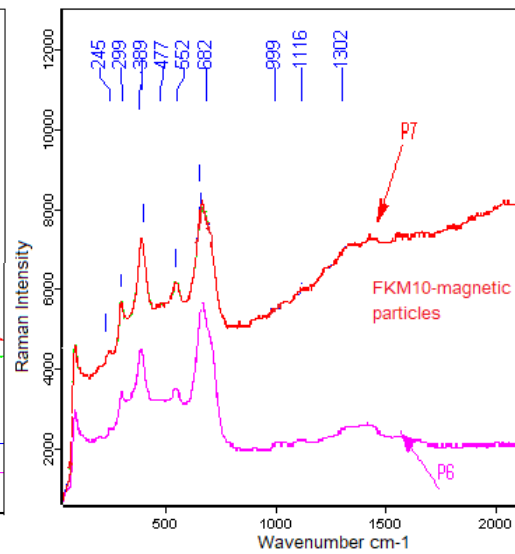
At the 2nd location, 4 points were analyzed from p4 to p7 (Figure 4.137 a). Well crystallized goethite phases are observed with main goethite peaks at 389 cm⁻¹, 299 cm⁻¹, 682 cm⁻¹ and 1302 cm⁻¹ in p4 and p5. P6 and p7 are identified as amorphous phases revealing goethite having its main peaks at 389 cm⁻¹ and 299 cm⁻¹ together with some magnetite. Magnetite is detected with its peaks at 682 cm⁻¹ and 552 cm⁻¹ (Figure 4.137b).



(c) FKM-10, step 2



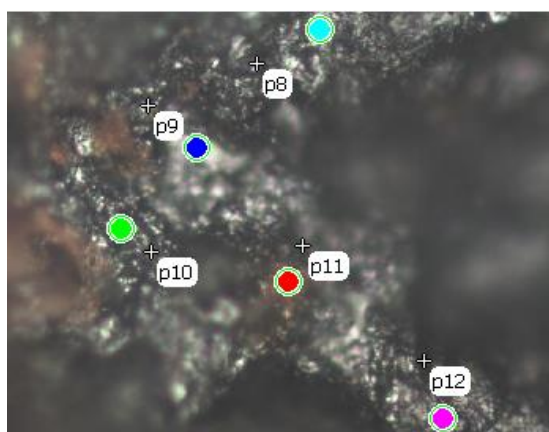
(b) FKM-10, p4 to p7



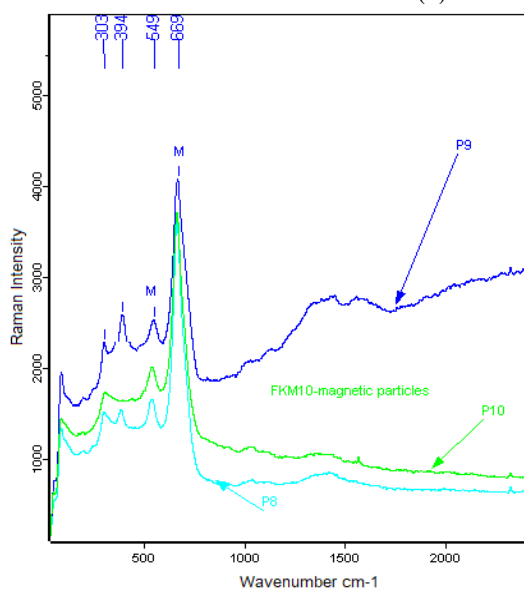
(c) FKM-10, p6 to p7

Figure 4. 137 μ -Raman microscopy image at the 2nd location of the powder sample of an iron nail (FKM-10): measurement points (a); goethite at p4 and p5 (b); goethite together with magnetite at p6 and p7 (b, c).

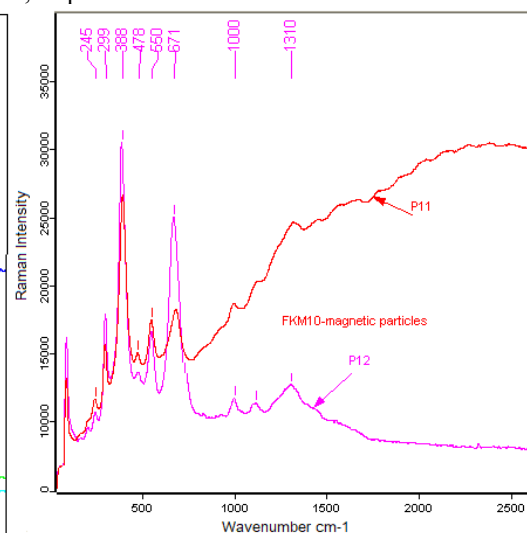
At the 3rd location, 5 points were analyzed from p8 to p12 (Figure 4.138 a). At p8 to p10, well-formed magnetite phases are seen with main magnetite peaks at 669 cm⁻¹ and 549 cm⁻¹ together with a poorly crystallized goethite phase having its main peaks at 394 cm⁻¹ and 303 cm⁻¹ (Figure 4.138 b). P11 and p12 reveal a well crystallized goethite phase with its main peaks at 388 cm⁻¹, 299 cm⁻¹, 671 cm⁻¹ and 1310 cm⁻¹ (Figure 4.138 c).



(a) FKM-10, step 3



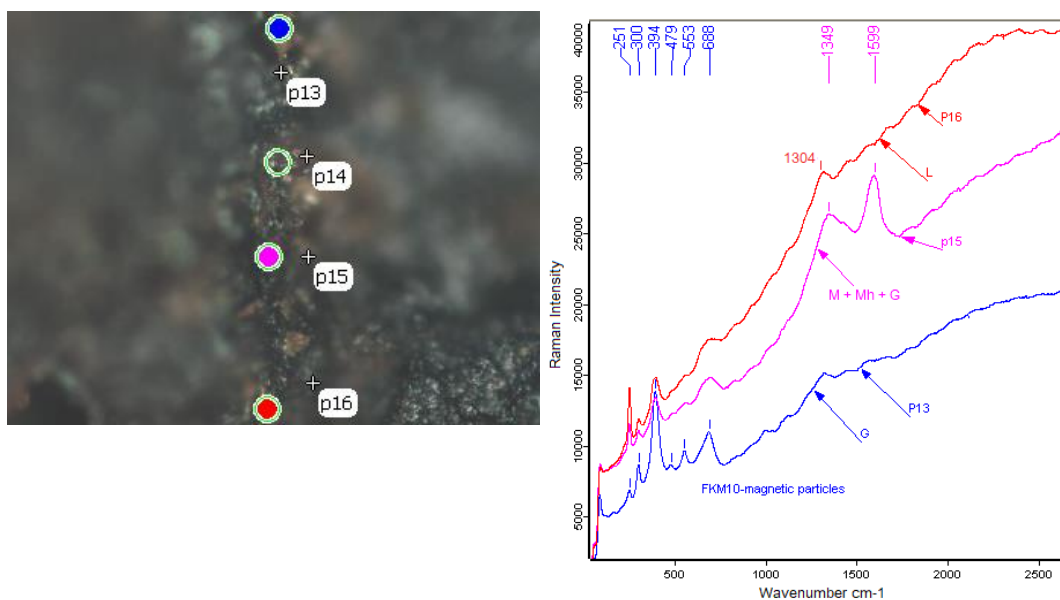
(b) FKM-10, p8 to p10



(c) FKM-10, p11 and p12

Figure 4. 138 Figure 4.138 μ -Raman microscopy image at the 3rd location of the powder sample of an iron nail (FKM-10): measurement points (a); magnetite with some goethite at p8 to p10 (b); goethite at p11 and p12 (c).

At the 4th location, 4 points were analyzed from p13 to p16 (Figure 4.139 a). At p13, a well-crystallized goethite phase is seen with its main peaks at 394 cm⁻¹, 300 cm⁻¹ and 668 cm⁻¹. A poorly crystallized phase of goethite, together with a hydrated iron (III) oxides or oxyhydroxides phase having peaks at 668 cm⁻¹ and 1599 cm⁻¹ is observed at p15. At p16, lepidocrocite is identified as an additional phase with its main peak at 251 cm⁻¹ together with some goethite having its peak at 394 cm⁻¹ and a common peak at 1304 cm⁻¹ (Figure 4.139 b).



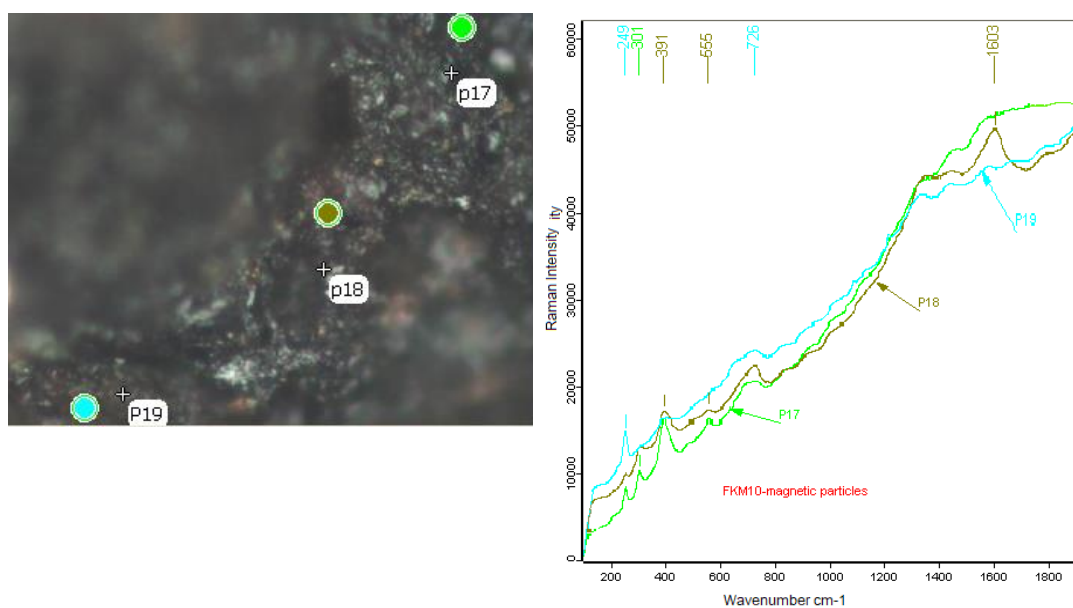
(a) FKM-10, step 4

(b) FKM-10, p13 to p16

Figure 4. 139 μ -Raman microscopy image at the 4th location of the powder sample of an iron nail (FKM-10): measurement points (a); goethite at p13; goethite with maghemite (Mh) / magnetite (M) at p15 and goethite with lepidocrocite (L) at p16 (b).

The last location analyzed in the corrosion powder of FKM-10 consists of 3 points from p17 to p19 (Figure 4.140 a). At p17, a goethite phase is observed with its main peaks at 391 cm⁻¹, 301 cm⁻¹ and around 680 cm⁻¹. A mixture of goethite, hydrated iron (III) oxides or oxyhydroxides phases with peaks at 726 cm⁻¹, 553 cm⁻¹ and an

additional peak at 1603 cm^{-1} are identified at p18. At p19, lepidocrocite is identified with its main peak at 251 cm^{-1} (Figure 4.140 b). Raman Analysis in the corrosion of the iron nail (FKM-10) is summarized in the Table 4.42.



(a) FKM-10, step 5

(b) FKM-10 p17 to p19

Figure 4. 140 μ -Raman microscopy image at the 5th location of the powder sample of an iron nail (FKM-10): measurement points (a); goethite at p17, goethite with hydrated iron (III) oxides or oxyhydroxides at p18 and lepidocrocite at p19 (b).

Table 4. 42 Iron oxides followed by μ -Raman analyses in the corrosion layer of an iron nail (FKM-10) (19th cc).

Location	Observed Corrosion Minerals in the mixed powder sample of RF, ICL and TM at its 5 locations				
Excavation - buried condition, iron nail <i>FKM-10</i>	Goethite	Goethite Magnetite	Goethite Magnetite	Goethite Magnetite / Maghemite Lepidocrocite	Goethite Magnetite / Maghemite Lepidocrocite

Another sample is a nail (FKM-11) partially open to atmospheric conditions and embedded in building stone tuff in Foça. The corrosion layer, ICL, is composed of a porous isotropic band of about 1300 microns without a clear reaction front next to the metal body (Figure 4.141a and b). During μ -Raman investigations, the corrosion layer of the nail (FKM-11) is divided into 7 steps from reaction front (RF) next to the metal towards outside (TM layer). The first 5 steps are in ICL and the last 2 steps are in TM. Each step is examined in 4 to 5 points, described as p1 to p4. μ -Raman data of the main corrosion products at those steps are shown in Figures 4.141 to 4.147, respectively. Raman Analysis in the corrosion of the iron nail (FKM-11) is summarized in the Table 4.43.

Following the metal body, maghemite and lepidocrocite are detected at p1 and p4 at the 1st step (Figure 4.141 c and d). Maghemite is observed with its main peaks at 693 cm^{-1} together with a shouldered peak at 670 cm^{-1} and 1556 cm^{-1} . Lepidocrocite is identified with its main peaks at 251 cm^{-1} and 1334 cm^{-1} . It is followed by mostly goethite rich regions in p2 and p3 with its main peaks at 393 cm^{-1} , 300 cm^{-1} and 686 cm^{-1} (Figure 4.141d).

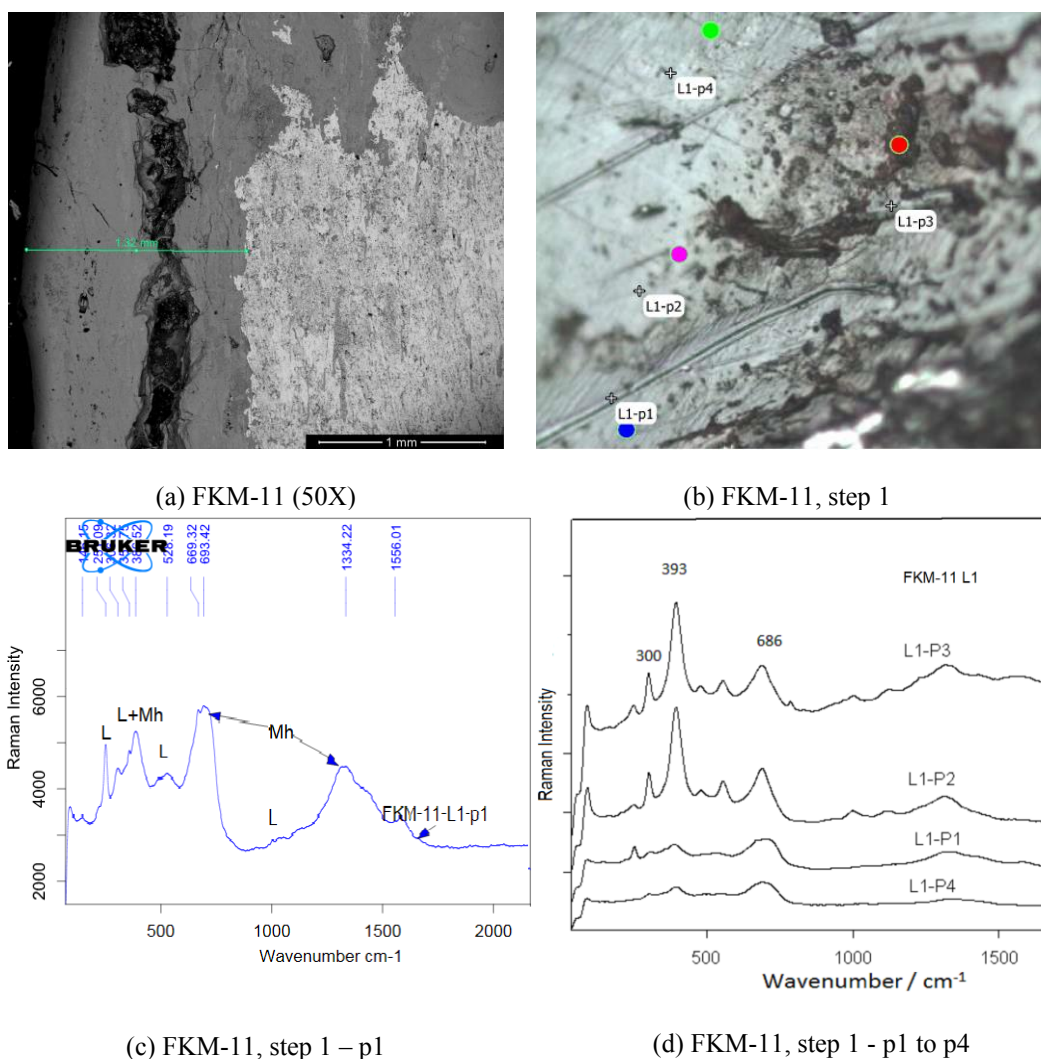


Figure 4. 141 SEM image (a) of a nail (FKM-11) from a dwelling in Foça (19th cc). μ -Raman spectra taken at 4 points located in the RF towards ICL: measurement points (b); maghemite (Mh) and lepidocrocite (L) at p1 and p4 (c); goethite at p2 and p3 (d).

The 2nd step consisting of 4 points described as p1 to p4 in ICL after RF (Figure 4.142a). In ICL next to RF, goethite is observed at p1 and p2 (Figure 4.142b and c). Goethite is detected with its main peaks at 390 cm^{-1} , 299 cm^{-1} , 683 cm^{-1} and 1305 cm^{-1} . At p3 and p4, maghemite/ magnetite is identified with their peaks at 693 cm^{-1} , 551 cm^{-1} , 483 cm^{-1} , 1337 cm^{-1} and 1576 cm^{-1} , together with goethite by its specific peaks at 390 cm^{-1} and 300 cm^{-1} (Figure 4.142 d).

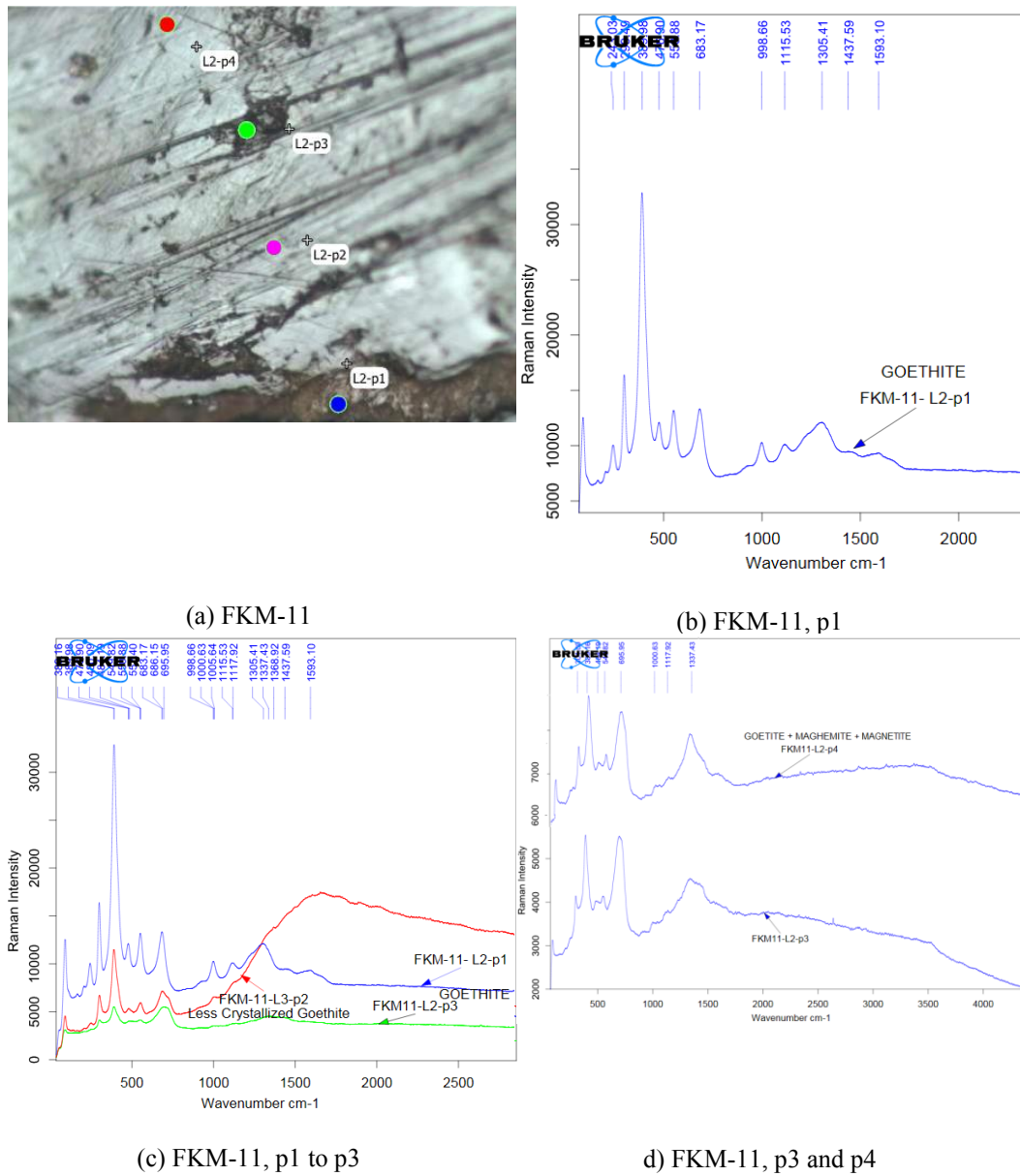


Figure 4. 142 μ -Raman spectra at the successive 4 points in the ICL next to RF: measurement points (a); goethite at p1 (b); goethite at p1 and p2, goethite with maghemite and magnetite at p3 (c); goethite with maghemite and magnetite at p3 and p4 (d).

The 3rd step consists of 4 points in ICL (Figure 4.143 a). A goethite phase is observed at p1 with its main peaks at 391 cm^{-1} , 299 cm^{-1} , 685 cm^{-1} and 1320 cm^{-1} (Figure 4.143 b). Maghemite / magnetite is identified together with a goethite phase having their peaks at 707 cm^{-1} , 552 cm^{-1} , 478 cm^{-1} , 391 cm^{-1} , 301 cm^{-1} , 1350 cm^{-1} and 1555

cm⁻¹ (Figure 4.143 c). At the 4th point, a well-crystallized goethite phase is observed with main peaks at 391 cm⁻¹, 299 cm⁻¹, 685 cm⁻¹ and 1330 cm⁻¹ (Figure 4.143 d).

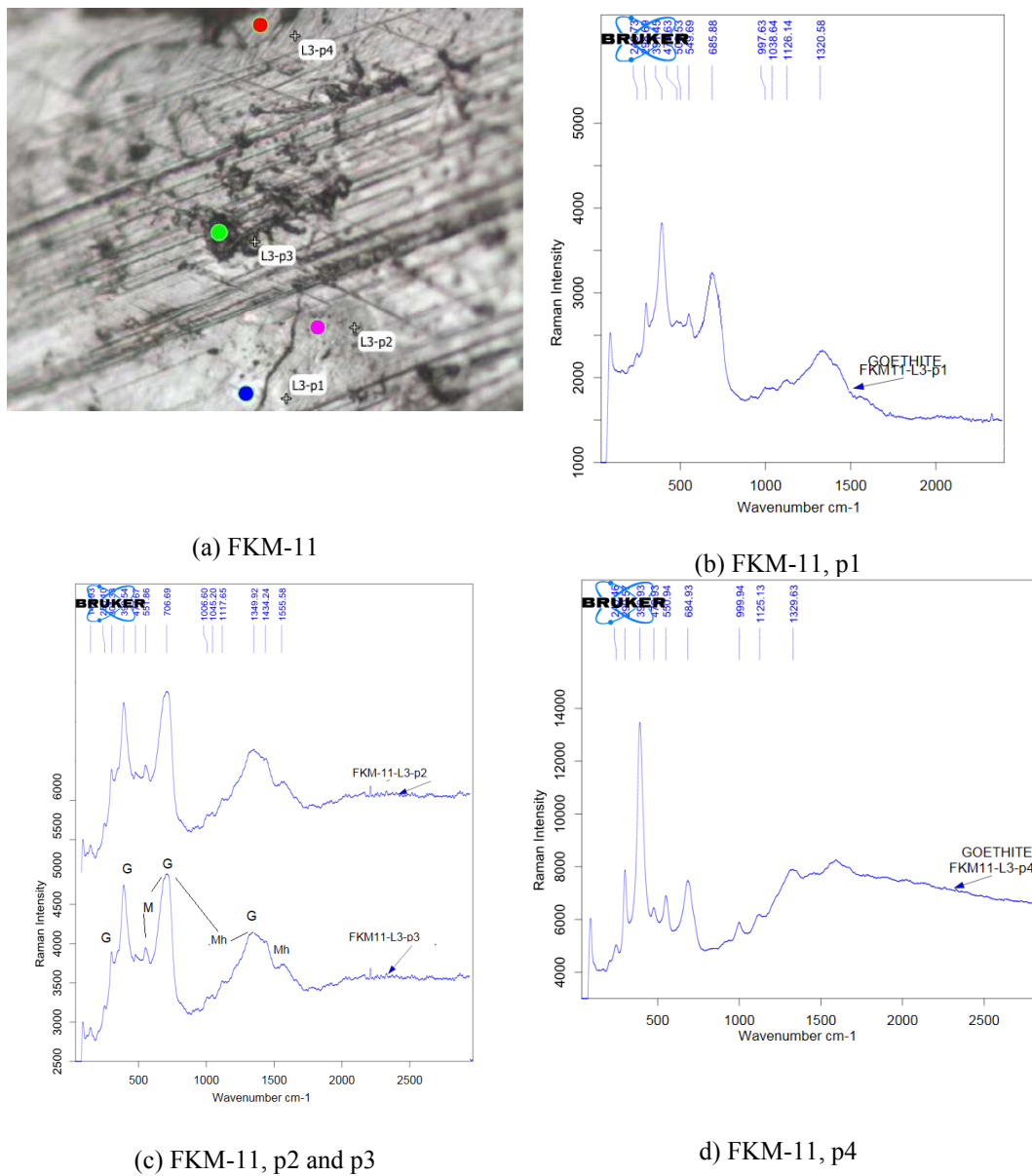
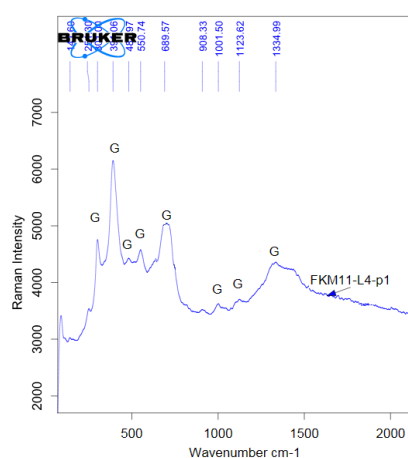
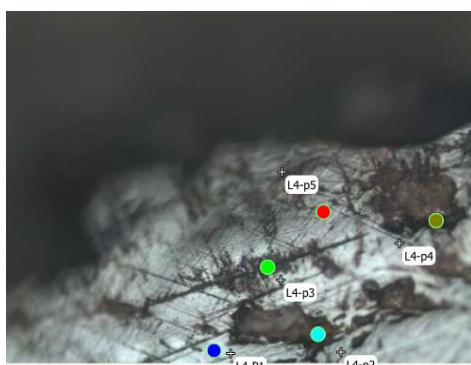
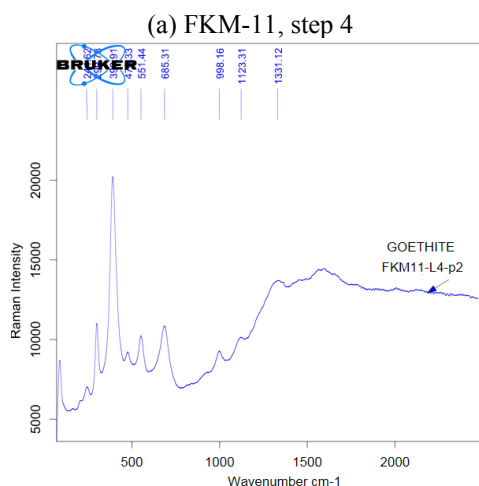


Figure 4. 143 μ -Raman spectra at the successive 4 points located in the ICL: measurement points (a); goethite at p1 (b); goethite, maghemite / magnetite at p2 and p3 (c); goethite at p4 (d).

The 4th step consisting of 5 points in ICL (Figure 4.144 a). A goethite phase is identified at all points with its main peaks at 391 cm⁻¹, 301 cm⁻¹, 689 cm⁻¹ and 1335 cm⁻¹ (Figures 4.144 b, c and d). At most points in this step the presence of sharp goethite peaks indicates its well crystallized state (Figure 4.144 d). Broader peaks of magnetite / maghemite and lepidocrocite observed in the previous steps are possibly due to their poor crystallization state.

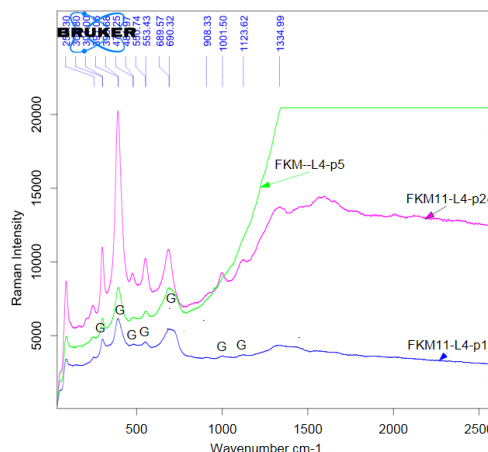


(b) FKM-11, step 4 - p1



(a) FKM-11, step 4

(c) FKM-11, step 4 - p2



(d) FKM-11, step 4 - p1 to p5

Figure 4. 144 μ -Raman spectra taken at the successive 5 points located in the ICL: measurement points (a); goethite at p1 to p5 (b, c, d).

The 5th step consisting of 5 points in ICL close to TM (Figure 4.145 a). A poorly crystallized goethite phase is observed at p1 with its main peaks at 391 cm⁻¹ and 300 cm⁻¹ (Figure 4.145 b). The 2 points (p4 and p5) before TM are characterized with a large band around ~710 cm⁻¹ and two broader bands at ~1428 cm⁻¹ and 1565 cm⁻¹. They are identified as hydrated iron (III) oxides or oxyhydroxides indicating several phases at a poor crystallization state (Figure 4.145 c and d).

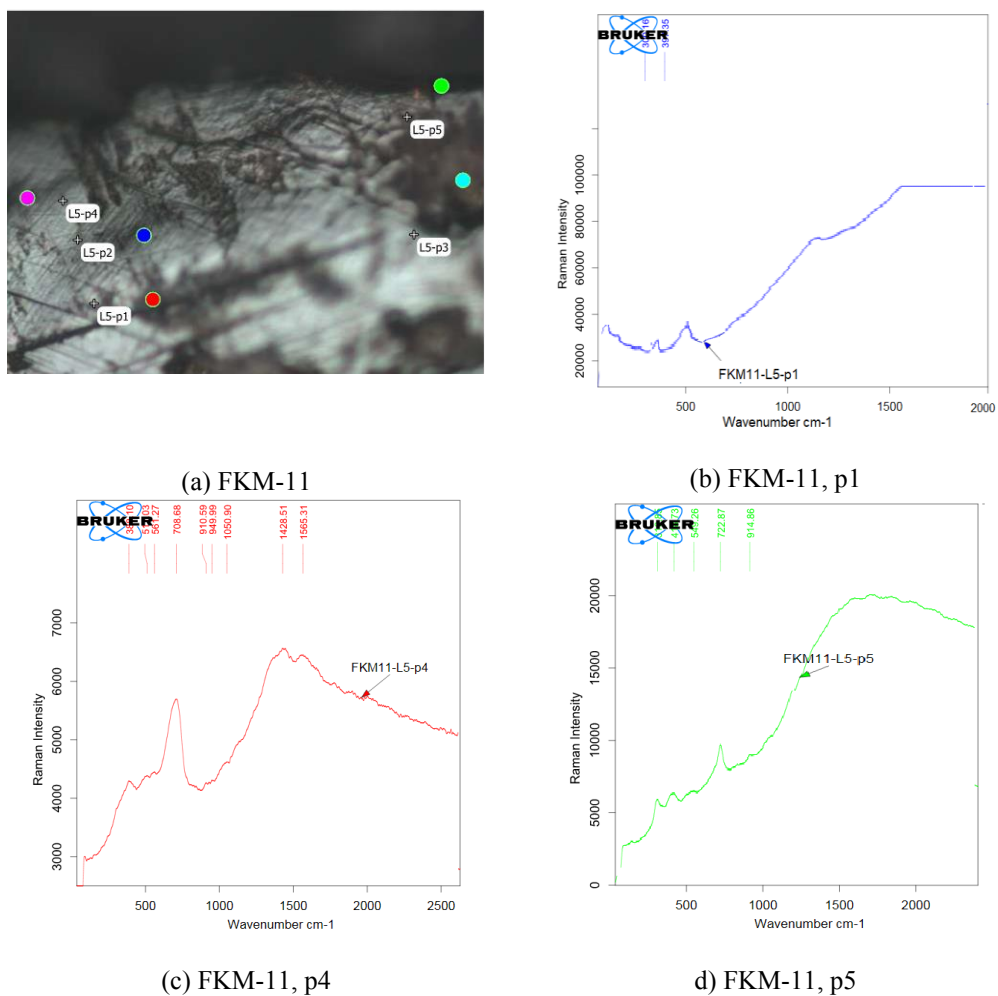
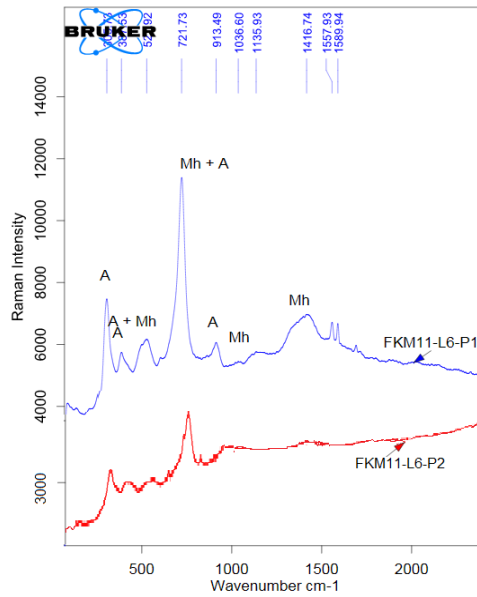


Figure 4. 145 μ -Raman spectra taken at successive 5 points located in the ICL near TM: measurement points (a); goethite at p1 (b); hydrated iron (III) oxides or oxyhydroxides at p2 to p5 (c, d).

The 6th step consists of 2 points in TM (Figure 4.146 a). At p1 and p2 together with maghemite and akageneite with main akageneite peaks at 306 cm⁻¹ and 387 cm⁻¹ are observed (Figure 4.146 b). Maghemite peaks are identified at 721 cm⁻¹ and 1416 cm⁻¹ (Figure 4.146 b). Sharpness of their major peaks indicate their well crystallization state.



(a) FKM-11

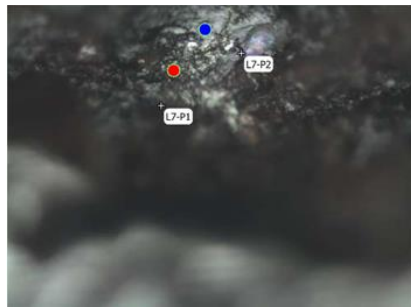


(b) FKM-11, p1 and p2

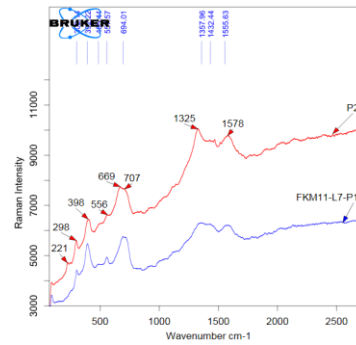
Figure 4. 146 μ -Raman spectra taken at successive 5 points located in TM: measurement points (a); maghemite and akageneite at p1 and p2 (b).

At the 7th step in TM, 2 points were analyzed. Goethite and maghemite / magnetite in low crystallization state are detected in those 2 points, p1 and p2 (Figure 4.147 a). Goethite is observed with its peaks at 398 cm⁻¹, 298 cm⁻¹ and 1325 cm⁻¹. Maghemite/magnetite is observed by their peaks at 556 cm⁻¹, 669 cm⁻¹, 707 cm⁻¹ and 1578 cm⁻¹ (Figure 4.147 b). Another location at the TM layer was analyzed in detail with 6 points (Figure 4.147 c). At all those points maghemite and akageneite are identified. Akageneite is characterized with its main peaks at 309 cm⁻¹ and 398 cm⁻¹; maghemite peaks are identified at 721 cm⁻¹ and 1418 cm⁻¹ (Figure 4.147 d and e). The comparison graph of the first point in RF and the last point in TM is shown in figure

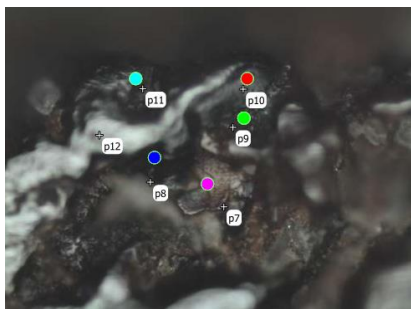
4.147 f. It is seen that in the reaction front maghemite and goethite are present in low crystallization state, while at the TM maghemite and akageneite are seen at a well crystallization state, as revealed by the sharpness of their peaks. Maghemite seems to be a transition phase towards or away from goethite.



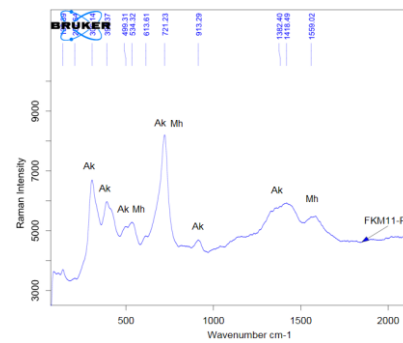
(a) FKM-11



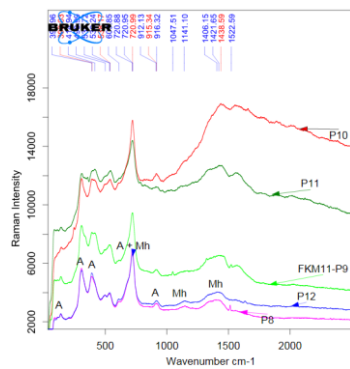
b) FKM-11, p1 and p2



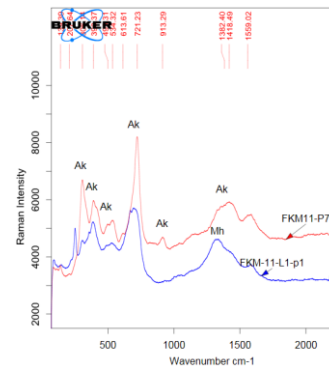
(c) FKM-11, at TM



(d) FKM-11, at TM - p7



(e) FKM-11, at TM - p8 to p12



(f) FKM-11, at TM - p7 and L1 - p1

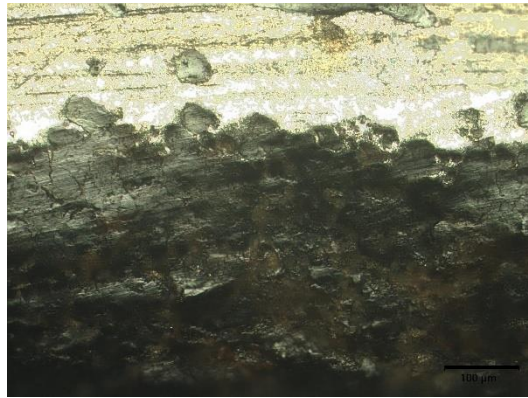
Figure 4. 147 Figure 4.147 μ -Raman spectra taken at successive 8 points located in TM of FKM-11: measurement points (a, c); akageneite and maghemite at p1 and 2 (b); akageneite and maghemite at p7 to p12 (d, e); comparison of the first point at RF and last point at TM.

Table 4. 43 Iron oxides followed by μ -Raman analyses in the corrosion layer of an iron nail (FKM-11) (19th cc).

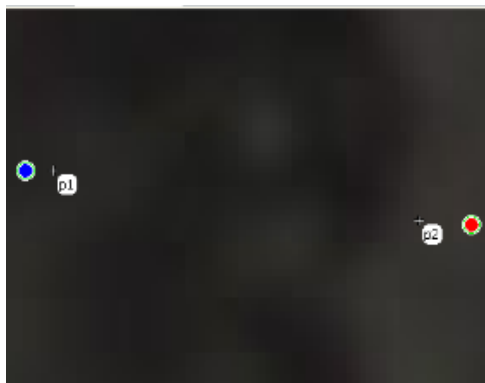
Location	Observed Corrosion Minerals						
	RF →	RF-ICL →	ICL →	ICL-TM →	TM (OSL)		
Partially open to atmospheric conditions - Embedded in building stone tuff, iron nail <i>FKM-11</i>	Maghemite Lepidocrocite Goethite	Goethite Maghemite/ Magnetite	Goethite Maghemite/ Magnetite	Goethite	Goethite Hydrated iron (III) oxides or oxyhydroxides	Maghemite Akageneite	Akageneite Maghemite

Another group of samples collected to investigate corrosion characteristics of the 19th century iron objects are from a dwelling of Tekkekoy, Samsun. A crossbar from the interior of the dwelling used for locking the main entrance door (T-D-01) and a nail (T-N-04) at the interior door frame were analyzed.

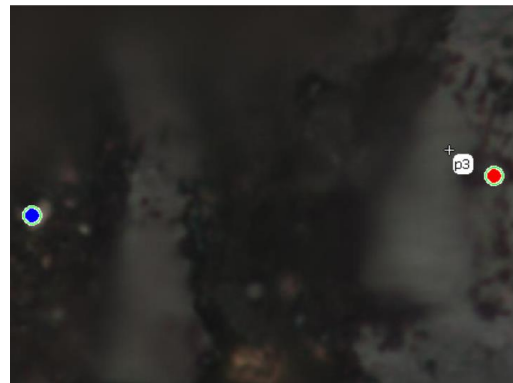
The digital microscopic image of the door lock piece (T-D-01) shows a compact corrosion layer having a uniform thickness of ICL around 350 μm (Figure 4.148 a). Examination from the metal body towards TM was done at 4 points in 2 steps (Figures 4.148 b and c). At points 1 and 2 mostly well crystalline magnetite with some maghemite in lower crystallization state is observed with their main peaks at 541 cm^{-1} , 668 cm^{-1} and 1324 cm^{-1} (Figure 4.148 d). At p3 and p4, hematite is the main phase with its characteristic peaks at 296 cm^{-1} , 413 cm^{-1} , 228 cm^{-1} and 1323 cm^{-1} together with some lepidocrocite, detected with its main peak at 248 cm^{-1} (Figure 4.148 d). The iron oxide layering of the door lock piece (T-D-01) is summarized in Table 4.44.



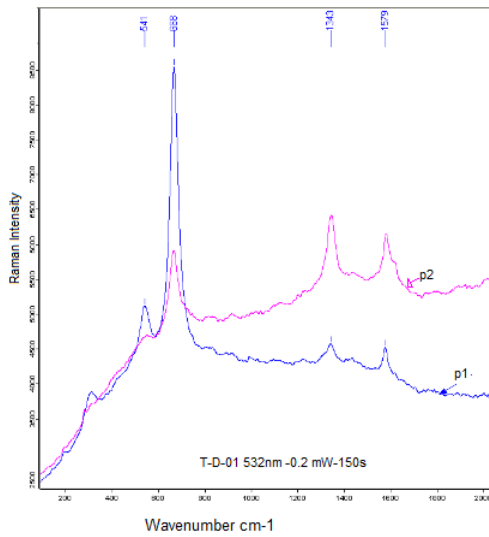
(a) T-D-01 (560X)



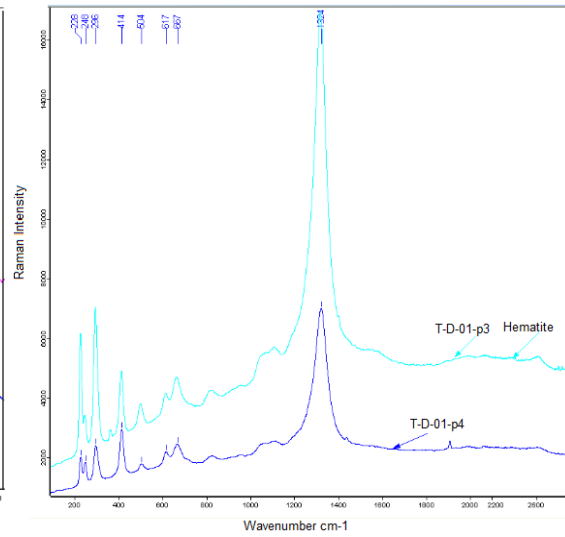
(b) T-D-01, p1 and p2



(c) T-D-01, p3 and p4



(d) T-D-01, second step - p1 and p2



(e) T-D-01, second step - p3 and p4

Figure 4. 148 The digital microscopic image (a) of the door lock piece (T-D-01) after etching with nitric acid in alcohol (19th cc). μ -Raman spectra taken at 4 points located in RF towards TM: measurement points (b, c); magnetite and maghemite at p1 and p2 (d); hematite at p3 and p4 (e).

Table 4. 44 Iron oxides followed by μ -Raman analyses in the corrosion layer of a door lock piece (T-D-01) (19th cc).

Location	Observed Corrosion Minerals			
	RF	→	ICL	→ TM
Interior – Door lock piece <i>T-D-01</i>	Magnetite	Magnetite	Hematite	Hematite
	Maghemite	Maghemite		

The digital microscopic image of the nail from the door frame (T-N-04) shows a variable thickness of $\sim 200 \mu\text{m}$ (Figure 4.149 a). The nail was analyzed at 14 points in 5 steps starting from RF towards TM. At p1 to p3 in RF a large band around 716 cm^{-1} and $\sim 1500 \text{ cm}^{-1}$ is observed and identified as hydrated iron (III) oxides or oxyhydroxides indicating several phases at a poor crystallization state (Figures 4.149 b and c). At p4 to p6 in the 2nd step towards ICL, a well crystallized goethite is detected at all 3 points with its sharp main peaks at 393 cm^{-1} , 300 cm^{-1} , 684 cm^{-1} and 1319 cm^{-1} (Figures 4.149 d and e). 2 points (p7 and p8) at the 3rd step in ICL are analyzed and a well crystallized goethite phase is continued to be seen at those 2 points with its sharp main peaks at 395 cm^{-1} , 301 cm^{-1} , 689 cm^{-1} and 1307 cm^{-1} (Figures 4.150 a and b). At the 4th step in ICL, at p9, a goethite phase with its sharp main peaks at 383 cm^{-1} , 301 cm^{-1} , 689 cm^{-1} and 1307 cm^{-1} is identified (Figures 4.150 c and d). Lepidocrocite having its peak at 249 cm^{-1} together with goethite is observed at p10 (Figures 4.150 c and d). 2 points (p11 and p12) towards TM are analyzed at the 5th step. P11 is a well crystallized lepidocrocite phase with its main peaks at 253 cm^{-1} , 389 cm^{-1} and 1303 cm^{-1} (Figures 4.151 a and b). Goethite is observed at p12 with its main peaks at 393 cm^{-1} , 310 cm^{-1} , 683 cm^{-1} and 1303 cm^{-1} (Figures 4.151 a and b). The last step is at the border of TM and consists of 2 points. Lepidocrocite with its main peak at 251 cm^{-1} together with some goethite having its main peak at 384 cm^{-1} are observed at p13 (Figures 4.151 c and d). This nail sample (T-N-04) shows that a reactive phase is composed of a phase with low crystallinity interpreted as hydrated iron (III) oxides or oxyhydroxides and followed by a compact goethite

phase at ICL with some well crystallized locations of lepidocrocite. The corrosion products of the steps from RF to TM are summarized in Table 4.45.

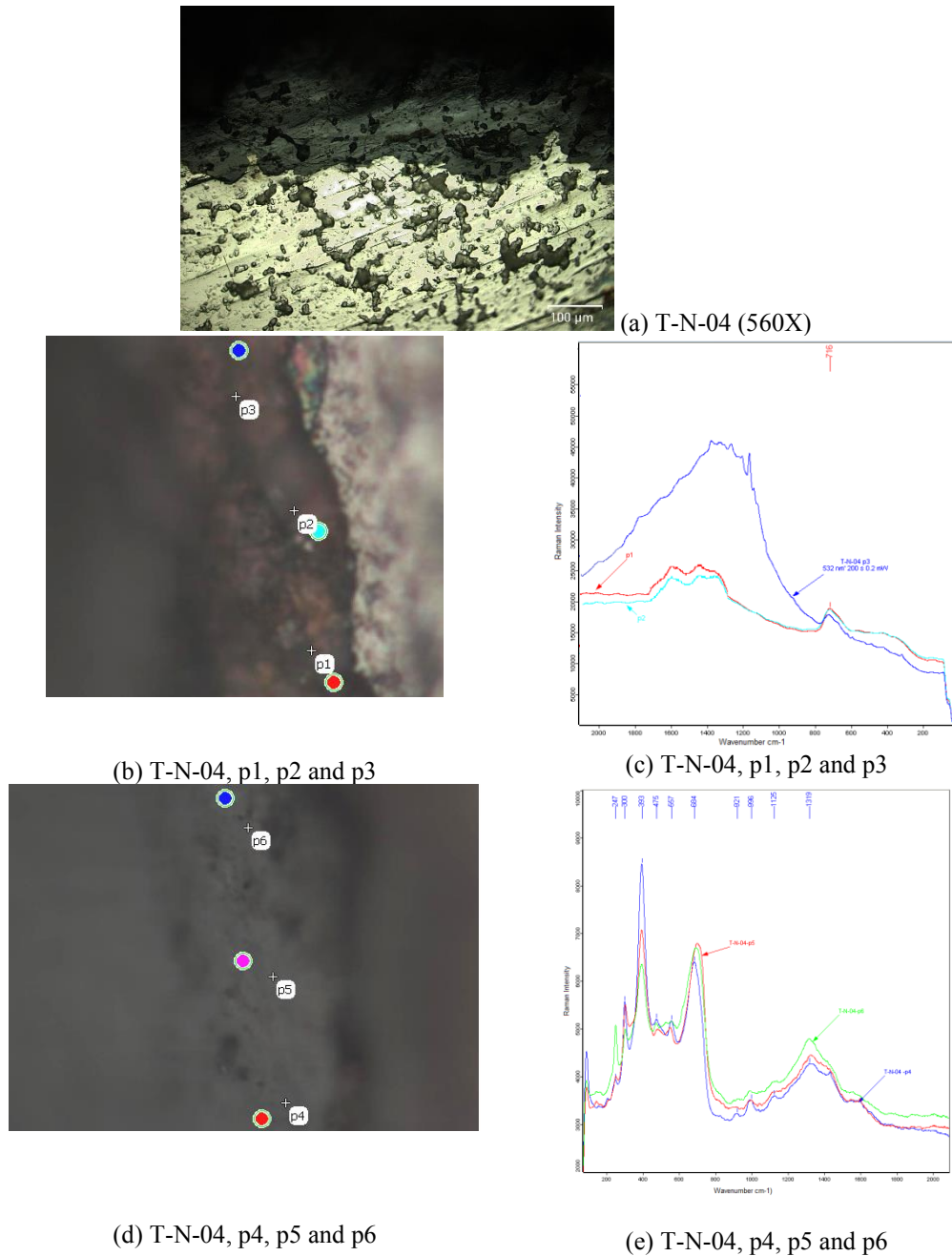
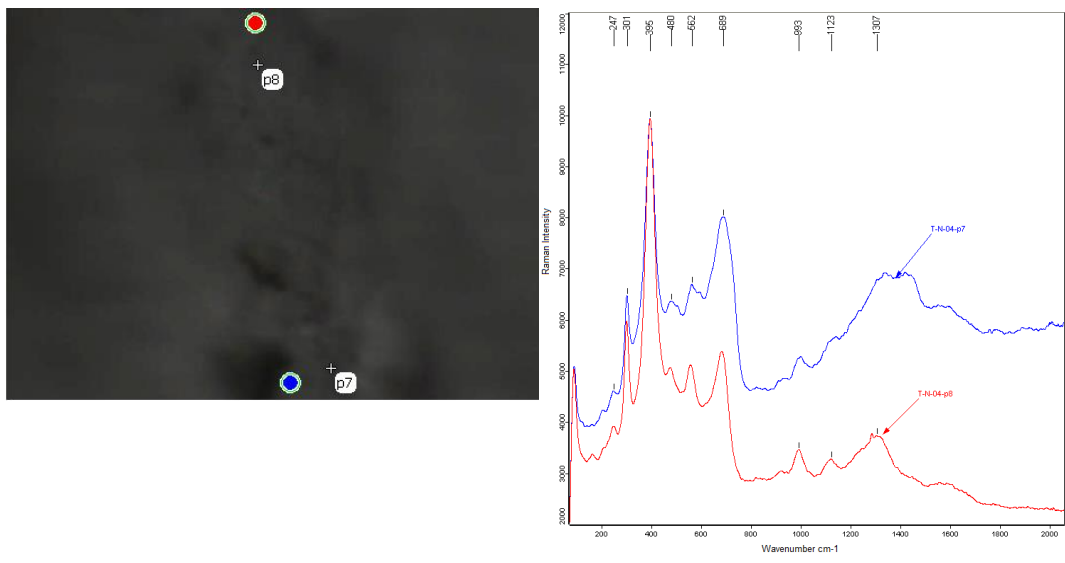


Figure 4. 149 Digital microscopic (a) image of the nail (T-N-04) from the door frame of a dwelling in Tekkekoy, Samsun after etching with nitric acid in alcohol (19th cc). μ -Raman spectra taken at 6 points located in RF towards ICL: measurement points (b, d); hydrated iron (III) oxides or oxyhydroxides at p1 to p3 in RF (c); goethite at p4 to p6 in RF - ICL border (e).

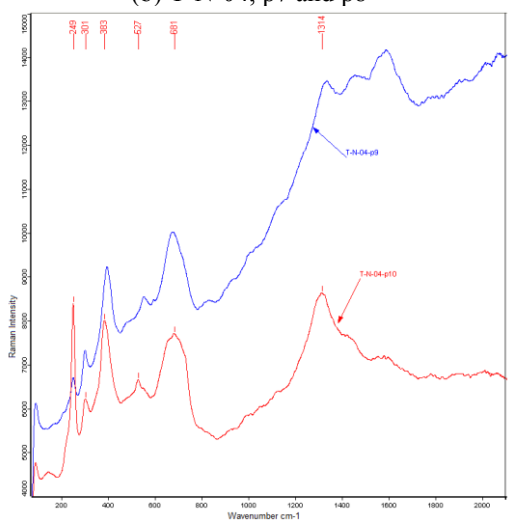


(a) T-N-04, p7 and p8

(b) T-N-04, p7 and p8



(c) T-N-04, p9 and p10

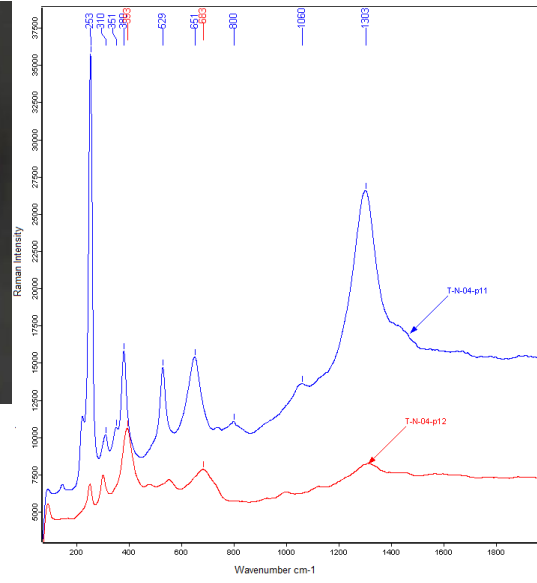


(d) T-N-04, p9 and p10

Figure 4. 150 μ -Raman spectra taken at the successive 4 points located in ICL: measurement points (a, c); goethite at p7 and p8 (b); goethite at p9 and lepidocrocite with goethite at p10 (d).



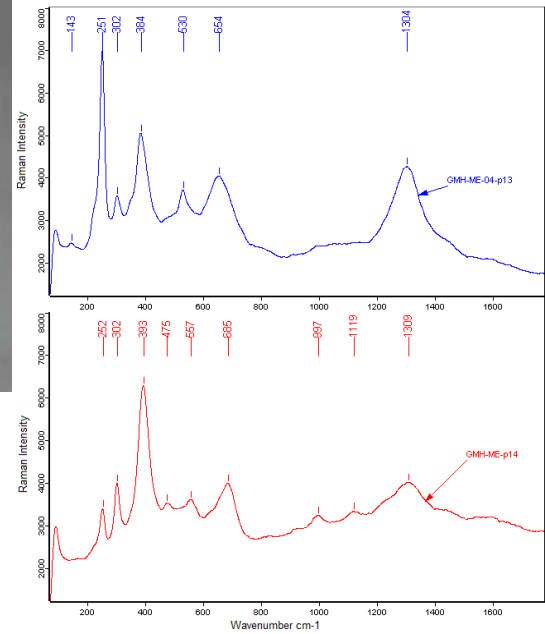
(a) T-N-04, p11 and p12



(b) T-N-04, p11 and p12



(c) T-N-04, p13 and p14



(d) T-N-04, p13 and p14

Figure 4. 151 μ -Raman spectra taken at the successive 4 points located in ICL towards TM: measurement points (a, c); lepidocrocite at p11 and goethite at p12 (b); lepidocrocite with goethite at p13 and goethite at p14 (d).

Table 4. 45 Iron oxides followed by μ -Raman analyses in the corrosion layer of a door lock piece (T-N-04) (19th cc).

Location	Observed Corrosion Minerals					
	RF →		ICL →		TM	
Interior – Nail from a door frame <i>T-N-04</i>	Hydrated iron (III) oxides or oxyhydroxides	Goethite	Goethite	Goethite Lepidocrocite	Goethite Lepidocrocite	Goethite Lepidocrocite

Iron oxides layering observed by μ -Raman Analysis in the corrosion of all samples collected from dwellings in Foça - İzmir and Tekkekoy - Samsun together with the results of the samples from Ottoman layer excavations in Foça - İzmir, all belonging to the 19th century are summarized in Table 4.46.

Table 4. 46 Iron oxides followed by μ -Raman analyses in the corrosion layers of the objects in dwellings of Foça – İzmir and Tekkekoy - Samsun together with the samples from Ottoman layer excavations in Foça - İzmir (19th cc).

Location	Observed Corrosion Minerals						
	RF	RF-ICL →		ICL	ICL-TM → (OSL)		TM
Interior of the dwelling –Embedded in timber <i>FKM-02</i>	Hematite	Hematite		Hematite	Hydrated iron (III) oxide or oxyhydroxide		-
Interior of the dwelling – Door lock piece <i>FKM-03</i>	Hydrated iron (III) oxide or oxyhydroxide	Goethite Hydrated iron (III) oxide or oxyhydroxide		Goethite Magnetite / Maghemite	Goethite		Hydrated iron (III) oxide or oxyhydroxide
Interior of the dwelling – Hinge from a main entrance door <i>FKM-04</i>	Goethite Hydrated iron (III) oxide or oxyhydroxide		Goethite Hydrated iron (III) oxide or oxyhydroxide	Hydrated iron (III) oxide or oxyhydroxide		Goethite Hydrated iron (III) oxide or oxyhydroxide	
Interior of the dwelling – Female Hinge from a main entrance door <i>FKM-05</i>	Goethite Hydrated iron (III) oxide or oxyhydroxide		Goethite Hydrated iron (III) oxide or oxyhydroxide			Goethite Hydrated iron (III) oxide or oxyhydroxide	
Ottoman layer excavation – Nail from burial condition <i>FKM-07</i>	Goethite						
Ottoman layer excavation – L-shaped iron object <i>FKM-08</i>	Goethite	Goethite Hydrated iron (III) oxide or oxyhydroxide	Goethite	Goethite Hematite Lepidocrocite Magnetite	Goethite Magnetite	Goethite	Goethite Magnetite / Maghemite Hydrated iron (III) oxide or oxyhydroxide
Ottoman layer excavation – Iron nail <i>FKM-10</i>	Goethite	Goethite Magnetite		Goethite Magnetite		Goethite Magnetite / Maghemite Lepidocrocite	Goethite Magnetite / Maghemite Lepidocrocite
Partially open to atmospheric conditions, embedded in building stone tuff - Iron nail <i>FKM-11</i>	Maghemite Lepidocrocite Goethite	Goethite Maghemite / Magnetite	Goethite Maghemite / Magnetite	Goethite	Goethite Hydrated iron (III) oxides or oxyhydroxide	Maghemite Akageneite	Akageneite Maghemite
Interior of a dwelling - Door lock piece <i>T-D-01</i>	Magnetite Maghemite		Magnetite Maghemite		Hematite		Hematite
Interior of a dwelling – Nail from a door frame - <i>T-N-04</i>	Hydrated iron (III) oxides or oxyhydroxides	Goethite	Goethite	Goethite Lepidocrocite	Goethite Lepidocrocite	Goethite Lepidocrocite	Goethite Lepidocrocite

4.5.4 Protective Ability Index (PAI) of the Corrosion Layer

In this study, the Protective Ability Index (PAI) of the corrosion layers were roughly estimated and expressed as the ratio of isotropic goethite band thickness to the total thickness of other oxides and oxyhydroxides being magnetite, maghemite, hematite, lepidocrocite, etc. in the corrosion layer, distinguished by micro-Raman (Aramendia *et al*, 2014, Kamimura *et al*, 2006). If PAI value of an object is equal or greater than 1 being the start value for protective condition, corrosion rate is less than 0.01 mm/y and if it is equal or greater than 2, corrosion stops and because a stable phase is reached (Kamimura *et al*, 2006).

A representative area is selected to quantify the corrosion products in ICL. PAI values were then calculated for the iron objects from the 15th, 16th and 19th centuries to compare their protective capability and their achievement of a stable rust layer.

PAI calculation of the 15th century iron objects were done on the selected two objects: a door lock piece (GMH-Me-02) and a plaster nail (GMH-Me-04) from an interior wall. The monument is in an urban environment and the PAI is calculated by equation for urban-industrial environment. The following data were used to calculate to find PAI value of each object (Table 4.47).

Table 4. 47 Corrosion layer thicknesses and PAI values of the 15th century objects.

Sample ID	Criteria	Result
A door lock piece (GMH-Me-02)	Total thickness of ICL including RF	~150 μm
	Total thickness of goethite layer (α)	50 μm
	Total thickness of other oxides (γ)	100 μm
	PAI Value calculated (α/γ)	0.5
A plaster nail (GMH-Me-04)	Total thickness of ICL including	75 μm
	Total thickness of goethite layer (α)	52.5 μm
	Total thickness of other oxides (γ)	22.5 μm
	PAI Value calculated (α/γ)	2.3

Consequently, the protective goethite band of the two objects sampled from a 15th century monument differ from each other. Even though they were exposed to the

same atmospheric conditions, they have quite different PAI values, being around 2.3 for the plaster nail (GMH-Me-04) and around 0.5 for the door lock piece (GMH-Me-02). The plaster nail has a stable protective corrosion layer composed of a uniform goethite band in ICL. On the other hand, the door lock piece, having a PAI value is smaller than 1, furthermore, it does not have a stable protective corrosion layer and has some active phases in ICL. It is possible that the door lock piece has been replaced by a more recently dated object which doesn't belong to the 15th century monument.

PAI calculation of the 16th century iron objects were done on the selected five objects: two nails from the dome (MSH-KAP-01 & -03), one iron object used for the jointing of other metals (e.g., chains) from the interior of the hammam building (MSH-KAP-02) and two nails of which one has been used for stone and one for the timber jointing of the interiors (MSH-KAP-09 & -12). The monument is in an urban environment and the PAI is calculated by equation for urban-industrial environment. The following data were used to calculate to find the PAI value of each object semi quantitatively (Table 4.48).

Table 4. 48 Corrosion layer thicknesses and PAI values of the 16th century objects.

Sample ID	Criteria	Result
Nail used for stone building, collected from dome (MSH-KAP-01)	Total thickness of ICL including RF	50 μm
	Total thickness of goethite layer (α)	40
	Total thickness of other oxides (γ)	10
	PAI Value calculated (α/γ)	4
Iron piece, used for jointing of other metals to the wall such as chains or hooks (MSH-KAP-02) Interior	Total thickness of ICL including RF	750
	Total thickness of goethite layer (α)	375
	Total thickness of other oxides (γ)	375
	PAI Value calculated (α/γ)	1
Nail used for stone building, collected from dome (MSH-KAP-03)	Total thickness of ICL including RF	100 μm
	Total thickness of goethite layer (α)	50
	Total thickness of other oxides (γ)	50
	PAI Value calculated (α/γ)	1
Nail used for stone building, square shape (MSH-KAP-09) Interior	Total thickness of ICL including RF	250
	Total thickness of goethite layer (α)	125
	Total thickness of other oxides (γ)	125
	PAI Value calculated (α/γ)	1
Nail used for timber jointing, square shape (MSH-KAP-12) Interior NO GOETHITE	Total thickness of ICL including RF	200 μm
	Total thickness of goethite layer (α)	0
	Total thickness of other oxides (γ)	200 μm
	PAI Value calculated (α/γ)	0

Consequently, the protective goethite band of the 16th century objects have been observed to be similar to each other. Both objects (MSH-KAP-01 and 03), exposed to outdoor atmospheric conditions have a stable goethite proactive layer, having a PAI around 2.5 for the nail (MSH-KAP-01) and around 1 for the second nail from the dome (MSH-KAP-03). The nail (MSH-KAP-01) having a higher stable protective corrosion layer than the other nail from the dome is composed of a uniform goethite band in ICL together with a well observed layering of RF, ICL, OSL and

TM. In the structure of the corrosion layer of the other iron object (MSH-KAP-02) from the interior, hydrated iron oxide and goethite are observed. For this reason, its PAI value was calculated as 1 and the goethite band has started to act as protective layer. The nail from the interior (MSH-KAP-09) has a PAI value of 2.1, being greater than 2 and the corrosion layer has a stable goethite proactive band. The timber jointing nail (MSH-KAP-12) does not show any goethite in its corrosion layer. The main phases in the ICL are magnetite, wustite and hematite which have been formed during a long period of time. In this study, the PAI equation for iron objects embedded in timber is defined as follows:

$$\alpha''/\gamma'' \text{ PAI} = \frac{\text{mass fraction (Fe}_3\text{O}_4 + \text{FeO)}}{\text{mass fraction } (\gamma - \text{FeOOH} + \beta - \text{FeOOH} + \gamma - \text{Fe}_2\text{O}_3)}$$

Nail used for timber jointing, square shape (MSH-KAP-12) Interior NO GOETHITE	Total thickness of ICL including RF	200 μm
	Total thickness of magnetite and wustite layer (α'')	100
	Total thickness of other oxides (γ'')	100 μm
	PAI Value calculated (α''/γ'')	1

Consequently, the PAI value of the nail (MSH-KAP-12) has been calculated as “1” with the new equation developed for the objects embedded in organic environments such as timber. Therefore, a wustite band formed of nanoscale particles has started to act as a protective band. The well preservation of the object also supports this opinion. Wustite remains stable for a prolonged periods due to a protective ligand; oleic acid reacts with the iron facilitating the nucleation of FeO nanocrystals. All objects from the 16th century have a PAI value greater than 1 and a stable protective corrosion band in ICL.

Ten iron objects from the 19th century were examined. Eight of them were from the dwellings and excavations in Foça, Izmir and two from the dwelling of Tekkekoy, Samsun. The selected samples analyzed from Foça were a nail for jointing main

timber beams (FKM-02), a door lock piece from the main entrance (FKM-03), a male hinge (FKM-04) and a female hinge (FKM-05) for the main entrance door, three nails (FKM-07, 10, 11) and an L-shaped iron object (FKM-08) from the Ottoman excavation layer representing the buried conditions.

The samples coming from the Tekkekoy dwelling were a nail at the interior door frame (T-N-04), and a crossbar from the interior of the dwelling used for locking the main entrance door (T-D-01). The objects from the dwellings in Foça and Tekkekoy are at the seaside, in a rural environment and their PAI is calculated by the equation regarding this environment. For the Ottoman layer excavation objects, the PAI is calculated by the equation for buried conditions. The following data were used to calculate to find the PAI value of each object from 19th century (Table 4.49).

The majority of the 19th century objects have a well-formed goethite band in ICL with variable PAI values in the range of 0.6 to >2. They are all in a good state of preservation. The timber jointing nail (FKM-02) embedded in timber but exposed to atmospheric conditions for a long period of time as a ruin does not show any goethite in its corrosion layer. The above-mentioned PAI equation proposed for the organic environment is used for the PAI value calculation. Its PAI value is 1 and the nail can be considered to be protected by a hematite band. The PAI values of the door lock piece (FKM-03) and the female hinge (FKM-05) both from the main entrance door were calculated as 1 and the goethite band has started to act as protective layer. The objects in buried condition (FKM-07, 08 and 10) have PAI values being >2, 2 and >1 respectively with a protective goethite band in their ICL observed by μ -Raman. The nail (FKM-11) being at partially open to atmosphere has PAI value of 2 indicates that the nail has reached a stable goethite proactive layer. Two objects from a dwelling in Tekkekoy also reveal different PAI values from each other. The nail (T-N-04) has a stable protective goethite band with a PAI value of 2. The PAI value of has found 1 meaning that start of a protective condition occurred in the corrosion layer. Although goethite is not detected in the ICL of the door lock piece (T-D-01)

by the restricted μ -Raman analysis carried out only at 4 points, FTIR results of the whole corrosion layer show the presence of both goethite and lepidocrocite almost with equal peak intensities. For this reason, the object is assumed to have a lower PAI value in comparison to the other 19th century object from Tekkekoy. Since the object is in good state of preservation, the estimated PAI value 1 may not reflect the protective properties of the goethite band in ICL. It is possible that lepidocrocite is largely located in the transformed media (TM).

Table 4. 49 Corrosion layer thicknesses and PAI values of the 19th century objects.

Sample ID	Criteria	Result
Nail for jointing main timber beams (FKM-02) NO GOETHITE	Total thickness of ICL including RF	150 μm
	Total thickness of hematite layer (α'')	75
	Total thickness of other oxides (γ'')	75
	PAI Value calculated (α''/γ'')	1
Door lock piece from the main entrance (FKM-03)	Total thickness of ICL including RF	200 μm
	Total thickness of goethite layer (α)	100
	Total thickness of other oxides (γ)	100
	PAI Value calculated (α/γ)	1
Male hinge from the main entrance door (FKM-04)	Total thickness of ICL including RF	80 μm
	Total thickness of goethite layer (α)	30
	Total thickness of other oxides (γ)	50
	PAI Value calculated (α/γ)	0.6
Female hinge from the main entrance door (FKM-05)	Total thickness of ICL including RF	112.5 μm
	Total thickness of goethite layer (α)	62.5
	Total thickness of other oxides (γ)	50
	PAI Value calculated (α/γ)	1.3

Table 4.49 Corrosion layer thicknesses and PAI values of the 19th century objects (continued).

Nail from the Ottoman layer (FKM-07) Buried	Total thickness of ICL including RF	475 μm
	Total thickness of goethite (α)	475
	Total thickness of other oxides (γ)	0 μm
	PAI Value calculated (α/γ)	>2
L-shaped iron piece from the Ottoman layer (FKM-08) Buried	Total thickness of ICL including RF	100 μm
	Total thickness of goethite and magnetite layer (α)	67
	Total thickness of other oxides (γ)	33
	PAI Value calculated (α/γ)	2
Nail from the Ottoman layer (FKM-10) Buried	Total thickness of ICL including RF	100 μm
	Total thickness of goethite and magnetite layer (α)	50
	Total thickness of other oxides (γ)	50
	PAI Value calculated (α/γ)	1
Nail from a dwelling embedded in building stone (FKM-11) Partially open to atmosphere	Total thickness of ICL including RF	1300 μm
	Total thickness of goethite layer (α)	850
	Total thickness of other oxides (γ)	450
	PAI Value calculated (α/γ)	2
Iron crossbar from the main entrance door locking (T-D-01) Partially open to atmosphere NO GOETHITE	Total thickness of ICL including RF	350 μm
	Total thickness of hematite layer (α'')	175
	Total thickness of other oxides (γ'')	175 μm
	PAI Value calculated (α/γ)	1
Iron nail from the door frame (T-N-04) Interior	Total thickness of ICL including RF	200 μm
	Total thickness of goethite layer (α)	135
	Total thickness of lepidocrocite, akaganeite, magnetite (γ)	65
	PAI Value calculated (α/γ)	2

4.6 Compositional characteristics of the corrosion layers in powder form by using X-ray powder diffraction (XRD) spectroscopy

The powdered corrosion products scraped from the surface of the samples and reduced to powder in agate mortar were directly measured by X-Ray Powder Diffraction (XRD) (Bruker, Model: D8 Advance Diffractometer with a SolX detector). XRD is a complimentary technique for both FTIR and Raman spectroscopic analyses. The analyses have been performed by XRD using $\text{CuK}\alpha$ radiation, adjusted to 40kV, 40mA. The XRD traces were recorded at 2Θ values from 2° - 70° and the instrument was set to scan speed of 2 seconds at 0.02° intervals. In general, the angular range of 10° - 60° at 2Θ is sufficient to identify the corrosion products formed with a particle size greater than 30 nm and are difficult to identify nanophase particles (Cook et al 1999). Due to broad and overlapping peaks of nanophase particles and being masked behind the high intensity peaks of large particles oxides, XRD is quite limited in corrosion product identification. It is not easy to distinguish between maghemite ($\gamma\text{-Fe}_2\text{O}_3$) and magnetite (Fe_3O_4) because of their similar crystal structure and lattice parameters while akaganeite is easily identified at $d= 1.6361 \text{ \AA}$ which is isolated from the diffraction peaks of all other iron oxides (Cook et al 1999).

Iron oxide minerals are represented by a variety of minerals that range from well to poor crystalline state. XRD allows the estimation of the particle size through the analysis of full width at the half maximum (FWHM) for the important peaks (Speakman, 2007). The relationship of the crystallite size with FWHM is indicated in Table 4.50.

Table 4. 50 The relationship with the crystallite size and the full width at half maximum derived from XRD analyses (Speakman, 2007).

Crystallite Size	FWHM (deg)
100 nm	0.099
50 nm	0.182
10 nm	0.871
5 nm	1.745

As an experimental work to study the long-term transformation characteristics of magnetite which is a well-crystallized iron oxide, it was expected to undergo some changes in aqueous media where the transformation products are closely related to the pH of the environment. The XRD peaks at 2θ data is documented for the most observed and important iron corrosion products in Table 4.51 (XRD Source: Mineral Powder Diffraction File Databook (Sets 1-42), 1993, JCPDS and www.mindat.org). The further analysis of the XRD data is made to better clarify the major and minor phases by using a full-profile search-match program by the Rietveld method (Luttorotti et al, 2019).

The typical samples of the iron objects from the 15th, 16th and 19th centuries are observed and compared for their corrosion minerals in the corrosion phase as a mixture of corroded layers on the metal bodies. The samples were prepared in the laboratory to verify the XRD spectrum. The results are summarized in Table 4.52.

Table 4. 51 XRD peaks at 2 θ data for most common iron oxides and common minerals observed (XRD Source: Mineral Powder Diffraction File Database (Sets 1-42), 1993, JCPDS and www.mindat.org).

Mineral Name	Chemical Formula	PDF No. ID No.	dÅ 1	dÅ 2	dÅ 3	dÅ 4	dÅ 5
Akaganéite-M (Iron oxide chloride Hydroxide)	$\beta\text{-FeO(OH.Cl)}$	-	7.468 (100)	2.551 (86)	3.345 (74)	3.334 (74)	
Akaganéite-M, syn (iron oxide hydroxide)	$\beta\text{-FeOOH}$	34-1266	3.333 (100)	2.5502 (55)	7.467 (40)	1.6434 (35)	2.2952 (35)
Bilinite	$\text{Fe}_3(\text{SO}_4)_2 \cdot 2\text{H}_2\text{O}$	mindat	4.31 (100)	3.51 (100)	4.84 (50)	4.10 (40)	4.96 (30)
Butlerite	$\text{FeSO}_4(\text{OH}) \cdot 2\text{H}_2\text{O}$	mindat	4.97 (100)	3.17 (50)	3.07 (20)	3.59	4.43
Calcite	CaCO_3	mindat	3.035 (100)	2.285 (18)	2.095 (18)	1.875 (17)	1.913 (17)
Chromite, syn Iron chromitum oxide	FeCr_2O_4	34-140 ICDD34-140	2.526 (100)	1.4812 (48)	1.6125 (39)	2.962 (33)	2.09 (20)
Fayalite, syn Iron silicate	Fe_2SiO_4	34-178	2.500 (100)	2.829 (86)	1.7781 (79)	1.7735 (65)	
Ferrihydrite, syn Iron oxide hydroxide hydrate	$\text{Fe}_3\text{O}_4(\text{OH}) \cdot 4\text{H}_2\text{O}$ $5\text{Fe}_2\text{O}_3 \cdot 9\text{H}_2\text{O}$	29-712	2.5 (100)	2.21 (80)	1.96 (80)	1.48 (80)	1.51 (70)
Ferrosulfate, syn (iron oxide hydroxide)	$\delta\text{-FeOOH}$	13-87	1.471 (100)	1.685 (100)	2.545 (100)	2.255 (100)	
Ferrous hydroxylchloride	$\beta\text{-Fe}_2(\text{OH})_3\text{Cl}$	34-0199					
Goethite (iron oxide hydroxide)	$\alpha\text{-FeOOH}$	29-713	4.183 (100)	2.450 (50)	2.693 (35)	1.7192 (20)	
Gypsum	CaSO_4	mindat	7.63 (100)	4.28 (100)	3.07 (80)	2.87 (50)	2.69 (40)
Hematite, syn	$\alpha\text{-Fe}_2\text{O}_3$	33-664	2.700 (100)	2.519 (70)	1.6941 (45)	1.8406 (40)	

Table 4. 51 XRD peaks at 2 θ data for most common iron oxides and common minerals observed (XRD Source: Mineral Powder Diffraction File Database (Sets 1-42), 1993, JCPDS and www.mindat.org). (continued).

Mineral Name	Chemical Formula	PDF No. ID No.	dÅ 1	dÅ 2	dÅ 3	dÅ 4	dÅ 5
Ilmenite, syn Iron titanium oxide	FeTiO ₃	29-733	2.754 (100)	2.544 (70)	1.7261 (55)	1.8683 (40)	
Lepidocrocite (iron oxide hydroxide)	γ -FeOOH	8-98	6.26 (100)	3.29 (90)	2.47 (80)	1.937 (70)	1.742 (40)
Maghemite-C, syn	γ -Fe ₂ O ₃	39-1346	2.5177 (100)	2.953 (35)	1.4758 (34)	1.6073 (24)	
Magnetite, syn	Fe ₃ O ₄	19-629	2.532 (100)	1.4845 (40)	1.6158 (30)	2.967 (30)	
Marcasite Iron sulfide	FeS ₂	37-475	2.693 (100)	1.757 (70)	3.439 (60)	2.413 (45)	
Magnesian Ferrite, high syn	MgFe ₂ O ₄	-	2.53x	1.494	2.974		
Melanterite, syn (Iron sulfate hydrate)	Fe ²⁺ SO ₄ •7H ₂ O	22-633	4.90 (100)	3.776 (60)	4.87 (50)	3.732 (20)	
Pyrite Iron sulfide	FeS ₂	42-1340	2.7055 (100)	1.6333 (69)	2.4209 (53)	2.2107 (40)	
Quartz	SiO ₂	mindat	3.342 (100)	4.257 (22)	1.8179 (14)	1.5418 (9)	2.457 (8)
Scorodite Iron Arsenate Hvadrates	FeAsO ₄ •2H ₂ O	37-468	4.472 (100)	3.178 (90)	5.609 (80)	3.060 (45)	
Siderite Iron carbonate	FeCO ₃	29-696	2.795 (100)	1.7315 (35)	1.7382 (30)	3.593 (25)	
Vivianite, syn Iron Phosphate Hydrate	Fe ₃ (PO ₄) ₂ •8H ₂ O	30-662	6.73 (100)	3.210 (16)	4.90 (12)	4.081 (12)	
Wustite, syn Iron Oxide	FeO	6-615	2.153 (100)	2.49 (80)	1.523 (60)	1.299 (25)	

Individual interpretation of XRD results will be given in the following paragraphs for groups of objects representing indoor and outdoor conditions, major corrosion products, indicating the relative intensities of XRD peaks and crystallinity. X-ray powder diffraction results of surface corrosion layers are summarized in Table 4.47 for the 15th, 16th century and the 19th century iron objects.

Corrosion characteristics of the 15th century iron objects were examined on one selected object: a plaster nail (GMH-Me-03) from the interior wall. The XRD traces were recorded at 2Θ values 2–70°. The instrument was set to a scan speed of 2 s at 0.02° intervals. Goethite (XRD pattern *d*: 4.148 (100), 2.445 (45), 2,705 (35), 1.717 (20)), lepidocrocite (XRD pattern *d*: 6.26 (100), 3.29 (90), 2.48 (80), 1.937 (70)), hematite (XRD pattern *d*: 2.706 (100), 2.532 (70), 1.691 (45), 1,829 (40)), magnetite (XRD pattern *d*: 2.532 (100), 1.484 (40), 1.620 (30), 2.941 (30)), maghemite (XRD pattern *d*: 2.5177 (100), 2.953 (35), 1.4758 (34), 1.6073 (24)) and ferrihydrite (XRD pattern *d*: 2.5 (100), 2.23 (80), 1.97 (80), 1.48 (80)) as iron oxides can be observed (Figure 4.152). The Rietveld search-match method with elements Fe, O, H and Si reveals the presence of nano crystallized iron oxides with the formula FeOOH and some silicates while the search with the elements Fe, O and H, gives the presence of nano crystallized iron oxides with the formulas FeOOH, Fe₂O₃ and Fe₃O₄. It is concluded that the XRD analysis shows that goethite is the major phase of surface corrosion layer with minor amounts of other phases such as lepidocrocite, magnetite, maghemite, ferrihydrite and hematite together with quartz. Goethite peaks are well formed and rather broad, the broadening at FWHL is about 0.5 deg. indicating that the crystallite size of goethite in indoor atmospheric condition may be in the range of 10 -50 nm.

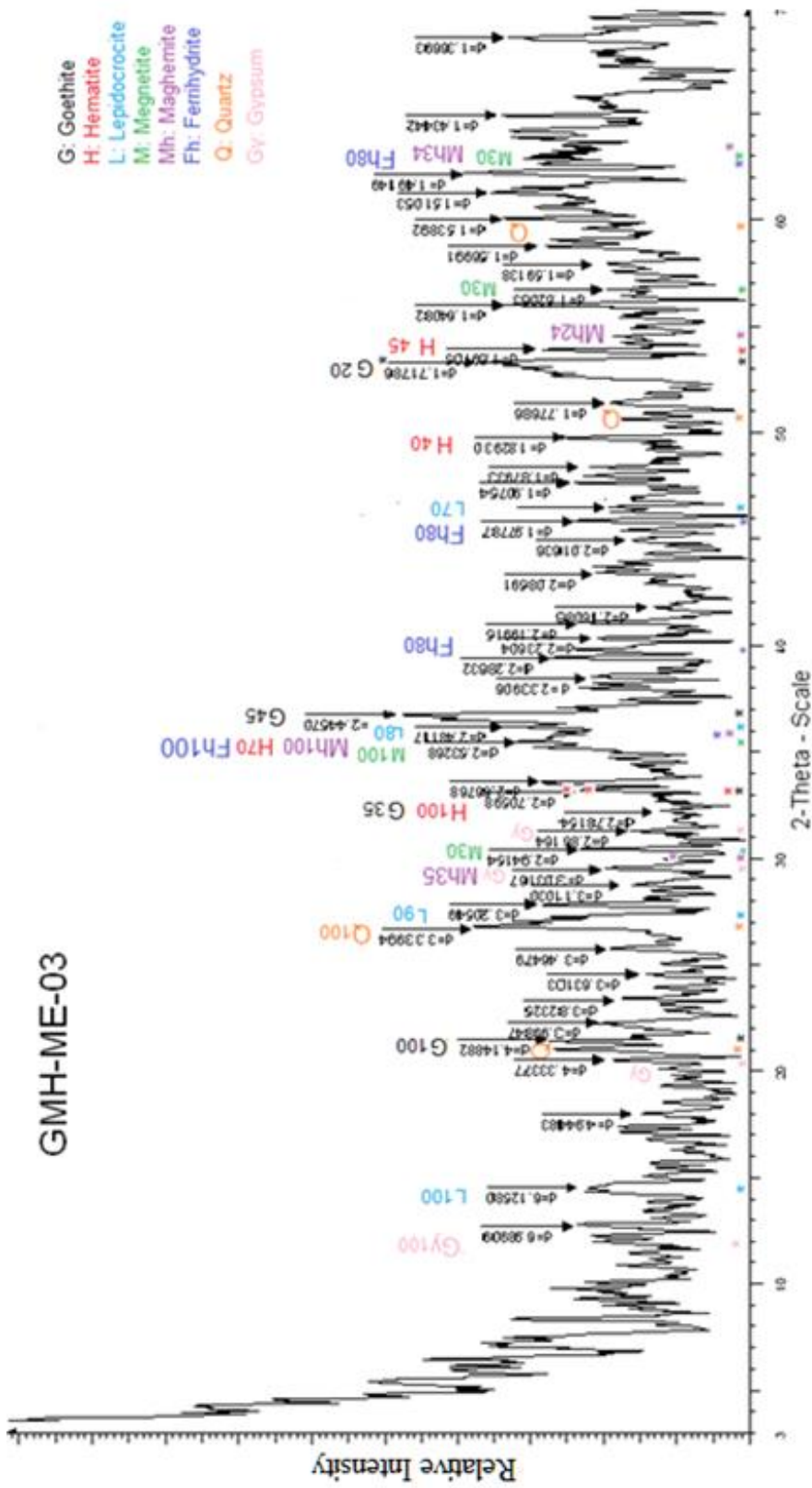


Figure 4. 152 XRD spectra of the corrosion layer powder including ICL and TM of the plaster nail (GMH-ME-03) (15th cc): maghemite (Mh), magnetite (M), hematite (H), goethite (G) and lepidocrocite (L) are identified.

Corrosion characteristics of the 16th century iron objects were examined on the three selected objects from Kılıç Ali Pasha Hammam, İstanbul: two nails from its dome (MSH-KAP-01 and 03) representing outdoor atmospheric conditions and a jointing iron piece (MSH-KAP-02) showing indoor conditions. The XRD traces were recorded at 2Θ values 2–70°. The instrument was set to a scan speed of 2 s at 0.02° intervals.

In the nail (MSH-KAP-01) from the dome, goethite (XRD pattern d : 4.138 (100), 2.442 (45), 2,676 (35), 1.714 (20)), lepidocrocite (XRD pattern d : 6.26 (100), 3.27 (90), 2,442 (80), 1.937 (70)), hematite (XRD pattern d : 2.676 (100), 2.519 (70), 1.694 (45), 1,840 (40)), magnetite (XRD pattern d : 2.51 (100), 1.484 (40), 1.615 (30), 2.926 (30)) and maghemite (XRD pattern d : 2.51 (100), 2.956 (35), 1.4758 (34), 1.6073 (24)) as iron oxides together with calcite impurities can be observed (Figure 4.153). The XRD analysis shows that goethite is the major phase of the surface corrosion layer with minor amounts of other phases such as lepidocrocite, magnetite, maghemite, hematite, together with abundant amount of calcite coming from transformed media. The Rietveld search-match method was applied to raw data of XRD pattern but probably due to decreased efficiency with nanocrystalline systems of greater complexity, no result was obtained. In addition, the method needs to be improved for the clay minerals inclusions in the system (Lutterotti *et al.*, 2019). Goethite peaks are well formed and rather broad. The broadening at FWHL is about 0.5 deg. indicating that the crystallite size of goethite in outdoor atmospheric condition may be in the range of 10 -50 nm showing a variable particle size of its nanocrystals.

In the nail (MSH-KAP-03) from the dome representing outdoor conditions, goethite (XRD pattern d : 4.138 (100), 2.437 (45), 2,693 (35), 1.709 (20)), lepidocrocite (XRD pattern d : 6.17 (100), 3.29 (90), 2.437 (80), 1.930 (70)), hematite (XRD pattern d : 2.70 (100), 2.510 (70), 1.694 (45), 1,840 (40)), magnetite (XRD pattern d : 2.53 (100), 1.471 (40), 1.615 (30), 2.926 (30)), maghemite (XRD pattern d : 2.51 (100), 2.956 (35), 1.471 (34), 1.609 (24)) wustite, ferrihydrite (XRD pattern d : 2.18 (100), 2.49 (80), 1.52 (60)) and ferrihydrite (XRD pattern d : 2.5 (100), 2.21 (80), 1.96 (80)),

1.471 (80)) as iron oxides together with quartz and calcite can be identified (Figure 4.154). The Rietveld search-match method with elements Ca, C, O and Si reveals the presence of some silicates and calcite while the search with the elements Fe, O and H, gives the presence of nano crystallized iron oxides with the formulas FeOOH, FeO, Fe₂O₃ and Fe₃O₄. It is concluded that the XRD analysis shows that goethite is the major phase of the surface corrosion layer with minor amounts of other phases such as lepidocrocite, magnetite, maghemite, wustite, ferrihydrite and hematite together with quartz and calcite impurities at TM. Goethite peaks are well formed and rather broad, the broadening at FWHL is about 0.8 deg. indicating that the crystallite size of goethite in indoor atmospheric condition may be 12 nm.

In the nail (MSH-KAP-02) from the interior wall jointing iron piece representing indoor conditions, goethite (XRD pattern *d*: 4.138 (100), 2.437 (45), 2.693 (35), 1.709 (20)), lepidocrocite (XRD pattern *d*: 6.17 (100), 3.29 (90), 2.437 (80), 1.930 (70)), hematite (XRD pattern *d*: 2.70 (100), 2.510 (70), 1.694 (45), 1.840 (40)), magnetite (XRD pattern *d*: 2.53 (100), 1.471 (40), 1.615 (30), 2.926 (30)), maghemite (XRD pattern *d*: 2.51 (100), 2.956 (35), 1.471 (34), 1.609 (24)), wustite (XRD pattern *d*: 2.18 (100), 2.49 (80), 1.52 (60)) and ferrihydrite (XRD pattern *d*: 2.5 (100), 2.21 (80), 1.96 (80), 1.471 (80)) as iron oxides together with some quartz and calcite are distinguished (Figure 4.155). The Rietveld search-match method with elements Ca, C, O and Si reveals the presence of some silicates and calcite while the search with the elements Fe, O and H, gives the presence of nano crystallized iron oxides with the formulas FeOOH, FeO, Fe₂O₃ and Fe₃O₄. It is concluded that the XRD analysis shows goethite and lepidocrocite as major phase of the surface corrosion layer with other phases such as magnetite, maghemite, wustite, ferrihydrite and hematite together with quartz and calcite impurities at TM. Goethite peaks are well formed and rather broad, the broadening at FWHL is about 0.4 deg. indicating that the crystallite size of goethite in indoor atmospheric condition may be in the range of 10 -50 nm.

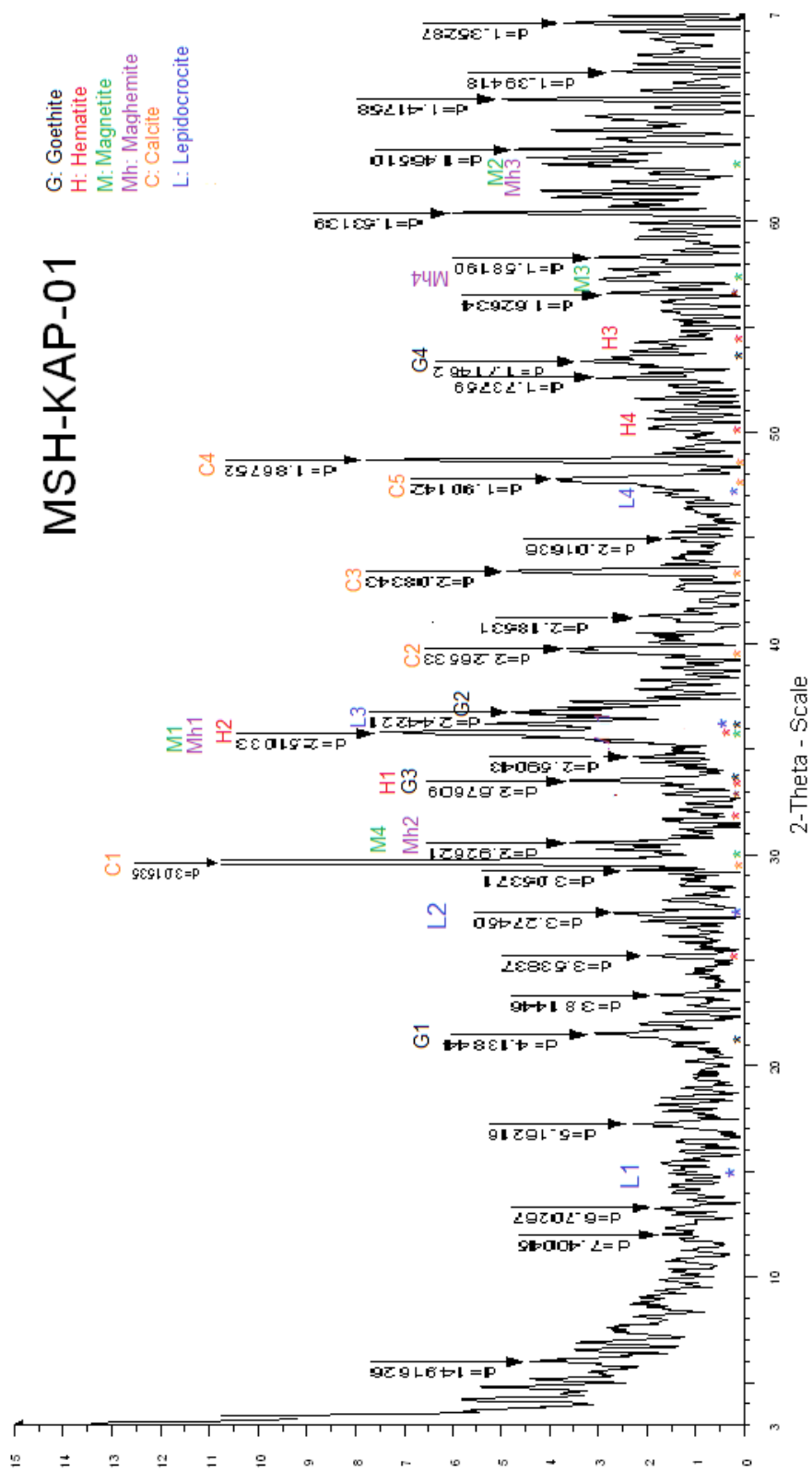


Figure 4. 153 XRD spectra of the corrosion layer powder including ICL and TM of the nail (MSH-KAP-01) (16th cc): goethite (G), maghemite (Mh), magnetite (M), hematite (H), lepidocrocite (L) and calcite (C).

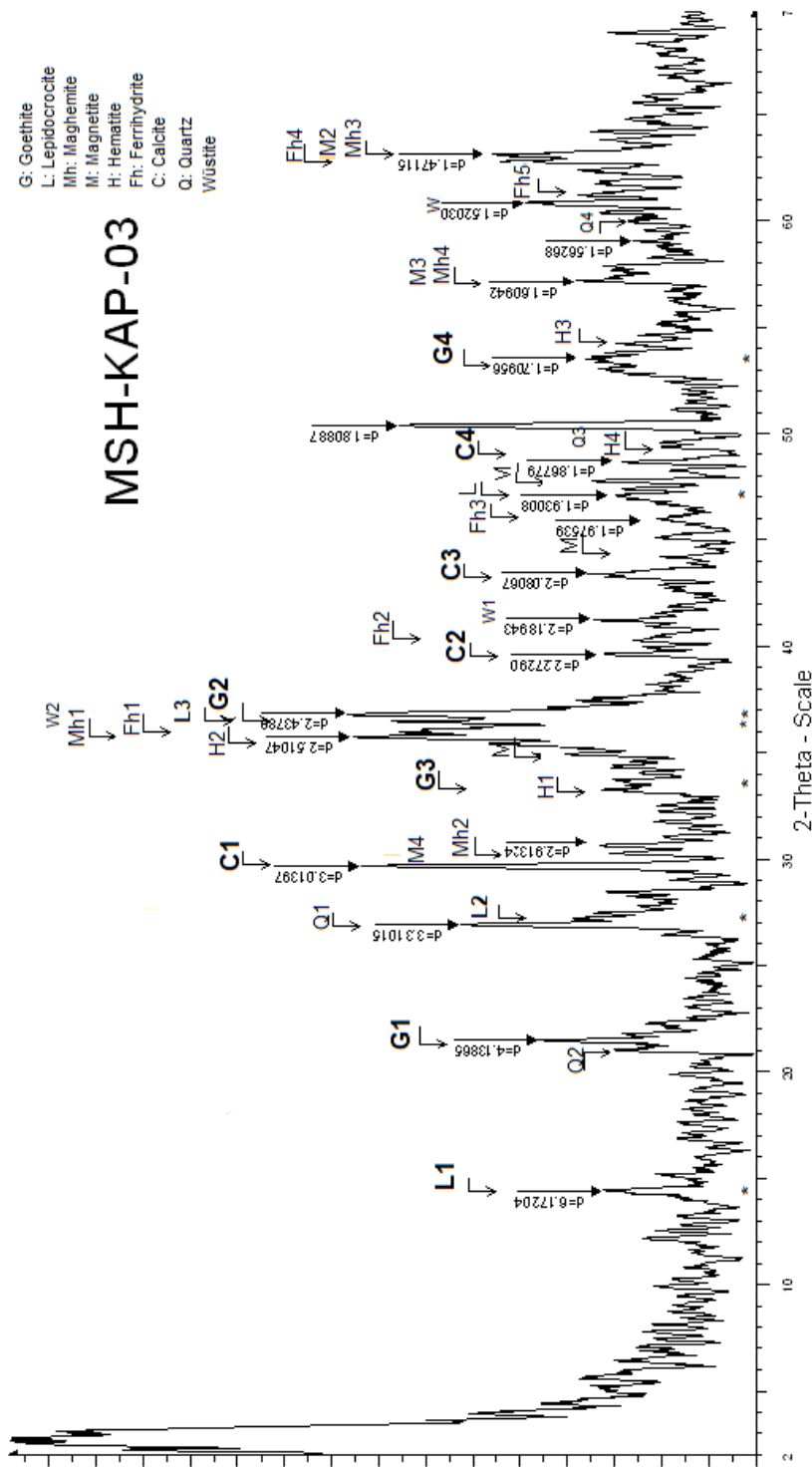


Figure 4. 154 XRD spectra of the corrosion layer powder including ICL and TM of the nail (MSH-KAP-03) (16th cc): maghemite (Mh), magnetite (M), hematite (H), goethite (G), lepidocrocite (L), ferrihydrate (Fh), wüstite (W), quartz (Q) and calcite (C) are identified.

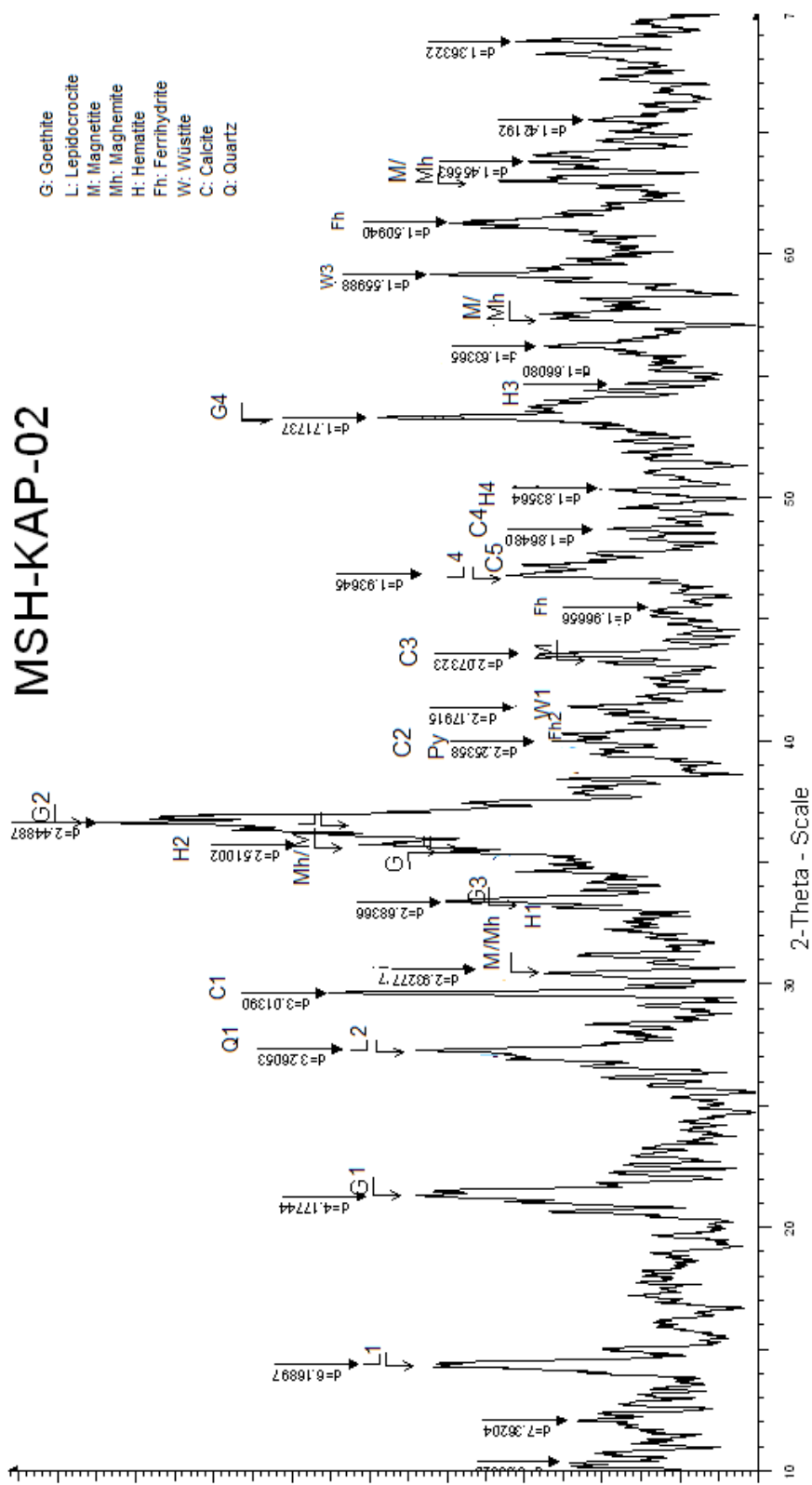


Figure 4. 155 XRD spectra of the corrosion layer powder including ICL and TM of the iron joining piece (MSH-KAP-02) (16th cc): maghemite (Mh), magnetite (M), hematite (H), goethite (G), lepidocrocite (L), ferrihydrate (Fh), wüstite (W), quartz (Q) and calcite (C)

Corrosion characteristics of the 19th century iron objects were examined on eight selected objects from Foça, Izmir. The objects represent different atmospheric conditions: a nail (FKM-02) used for jointing timber beams from the interior of a dwelling; both a main entrance door male hinge (FKM-04) and a nail (FKM-11) from building stone representing partially open to outdoor atmospheric conditions and iron pieces (FKM-06, FKM-08, FKM-09 and FKM-10) collected from the Ottoman layer excavations showing the buried conditions. The XRD traces were recorded at 2Θ values 2–70°. The instrument was set to a scan speed of 2 s at 0.02° intervals.

The nail (FKM-02) for jointing main timber beams reveals goethite (XRD pattern d : 4.109 (100), 2.439 (45), 2,688 (35), 1.723 (20)), hematite (XRD pattern d : 2.688 (100), 2.499 (70), 1.694 (45), 1,840 (40)), magnetite (XRD pattern d : 2.526 (100), 1.478 (40), 1.611 (30), 2.937 (30)), maghemite (XRD pattern d : 2.526 (100), 2.937 (35), 1.478 (34), 1.611 (24)), ferrihydrite (XRD pattern d : 2.492 (100), 2.205 (80), 1.960 (80), 1.478 (80)) and wustite (XRD pattern d : 2.150 (100), 2.492 (80), 1.523 (60)) as iron oxides together with siderite, calcite and quartz impurities (Figure 4.156). The Rietveld search-match method with elements Fe, O, H and Si reveals the presence of nano crystallized iron oxides with the formula FeOOH and some silicates, while the search with the elements Fe, O and H gives the presence of nano crystallized iron oxides with the formulas FeOOH, Fe₂O₃, Fe₃O₄ and FeO. The XRD analysis shows that goethite is the major phase of the surface corrosion layer with some amounts of other phases such as magnetite, maghemite, ferrihydrite, wustite and hematite together with minor amount of quartz and calcite. Goethite peaks are well formed and rather broad, the broadening at FWHL is about 0.6 deg. indicating that the crystallite size of goethite in outdoor atmospheric condition may be in the range of 10 - 50 nm indicating a variable particle size of its nanocrystals.

The main entrance door hinge (FKM-04) representing partially open to exterior atmospheric condition shows goethite (XRD pattern d : 4.169 (100), 2.445 (45), 2,690 (35), 1.719 (20)), lepidocrocite (XRD pattern d : 3.283 (90), 2,47 (80), 1.920 (70)), akageneite (XRD pattern d : 3.283 (100), 2.550 (55), 1.635 (35), 2.297 (30)),

hematite (XRD pattern *d*: 2.690 (100), 2.519 (70), 1.690 (45), 1,836 (40)), magnetite (XRD pattern *d*: 2.504 (100), 1.485 (40), 1.601 (30), 2.934 (30)), maghemite (XRD pattern *d*: 2.504 (100), 2.934 (35), 1.485 (34), 1.601 (24)), wustite (XRD pattern *d*: 2.173 (100), 2.504 (80), 1.528 (60)), ferrihydrite (XRD pattern *d*: 2.504 (100), 2.216 (80), 1.968 (80), 1.48 (70)) and feroxyhyte (XRD pattern *d*: 1.468 (100), 1.679 (100), 2.545 (100), 2.244 (100)) as iron oxides (Figure 4.157). The Rietveld search-match method with elements Fe, O and H, gives the presence of nano crystallized iron oxides with the formulas FeOOH, Fe₂O₃, Fe₃O₄ and FeO (Lutterotti *et al.*, 2019). The XRD analysis shows that goethite is the major phase of the surface corrosion layer with some amounts of other phases such as magnetite, maghemite, lepidocrocite, wustite, feroxyhyte, ferrihydrite and hematite. Goethite peaks are well formed and rather broad, the broadening at FWHL is about 0.33 deg. indicating that the crystallite size of goethite in partially open to exterior atmospheric condition may be in the range of 10 -50 nm.

The nail (FKM-11) embedded in building stone representing partially open to outdoor atmospheric condition reveals goethite (XRD pattern *d*: 4.1198 (100), 2.478 (45), 2,672 (35), 1.700 (20)), lepidocrocite (XRD pattern *d*: 6.17 (100), 3.32 (90), 2.478 (80), 1.935 (70)), akaganeite (XRD pattern *d*: 3.321 (100), 2.540 (55), 7.369 (40), 1.635 (35)), magnetite (XRD pattern *d*: 2.540 (100), 1.489 (40), 1.615 (30), 2.957 (30)), maghemite (XRD pattern *d*: 2.540 (100), 2.957 (35), 1.489 (34), 1.615 (24)) as iron oxides together with quartz impurities from TM (Figure 4.158). The Rietveld search-match method with elements Fe, H, O and Si reveals the presence of some silicates and FeOOH, while the search with the elements Fe, O and H, gives the presence of nano crystallized iron oxides with the formulas FeOOH, Fe₂O₃ and Fe₃O₄. The XRD analysis shows that goethite is the major phase of the surface corrosion layer with some akaganeite and minor amounts of magnetite / maghemite, lepidocrocite together with quartz impurities from TM. Goethite peaks are well formed and rather broad, the broadening at FWHL is about 0.33 deg. indicating that the crystallite size of goethite in partially open to exterior atmospheric condition may be in the range of 10 - 50 nm.

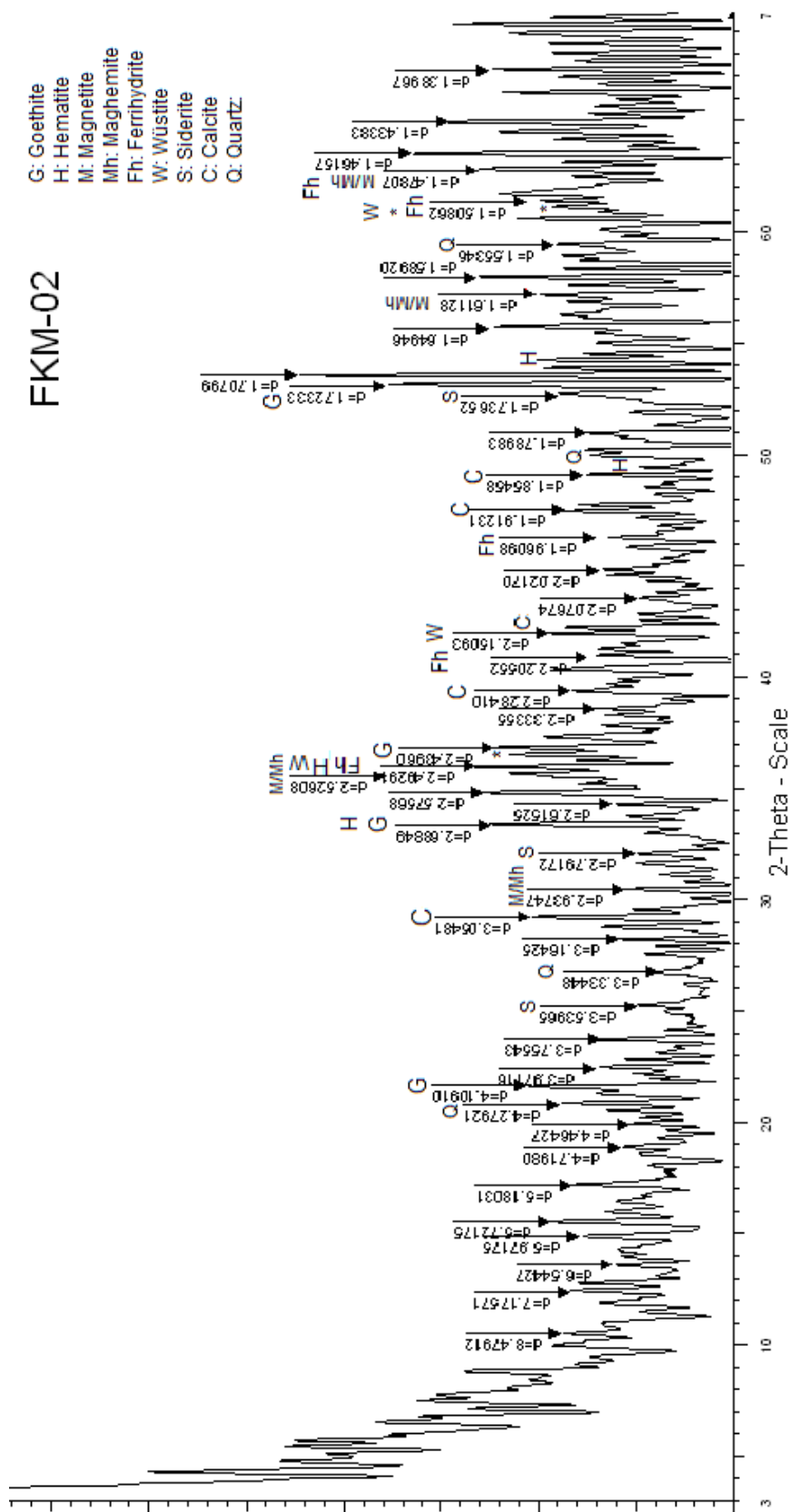


Figure 4. 156 XRD spectra of the corrosion layer powder including ICL and TM of the iron nail (FKM-02) (19th cc): goethite (G), maghemite (Mh), magnetite (M), hematite (H), ferrihydrite (Fh), wustite (W), siderite (S), quartz (Q) and calcite (C).

FKM04

- G: Goethite
- A: Akaganeite
- L: Lepidocrocite
- M: Magnetite
- Mh: Maghemite
- H: Hematite
- Fh: Ferrihydrite
- Fx: Ferroxyhyte

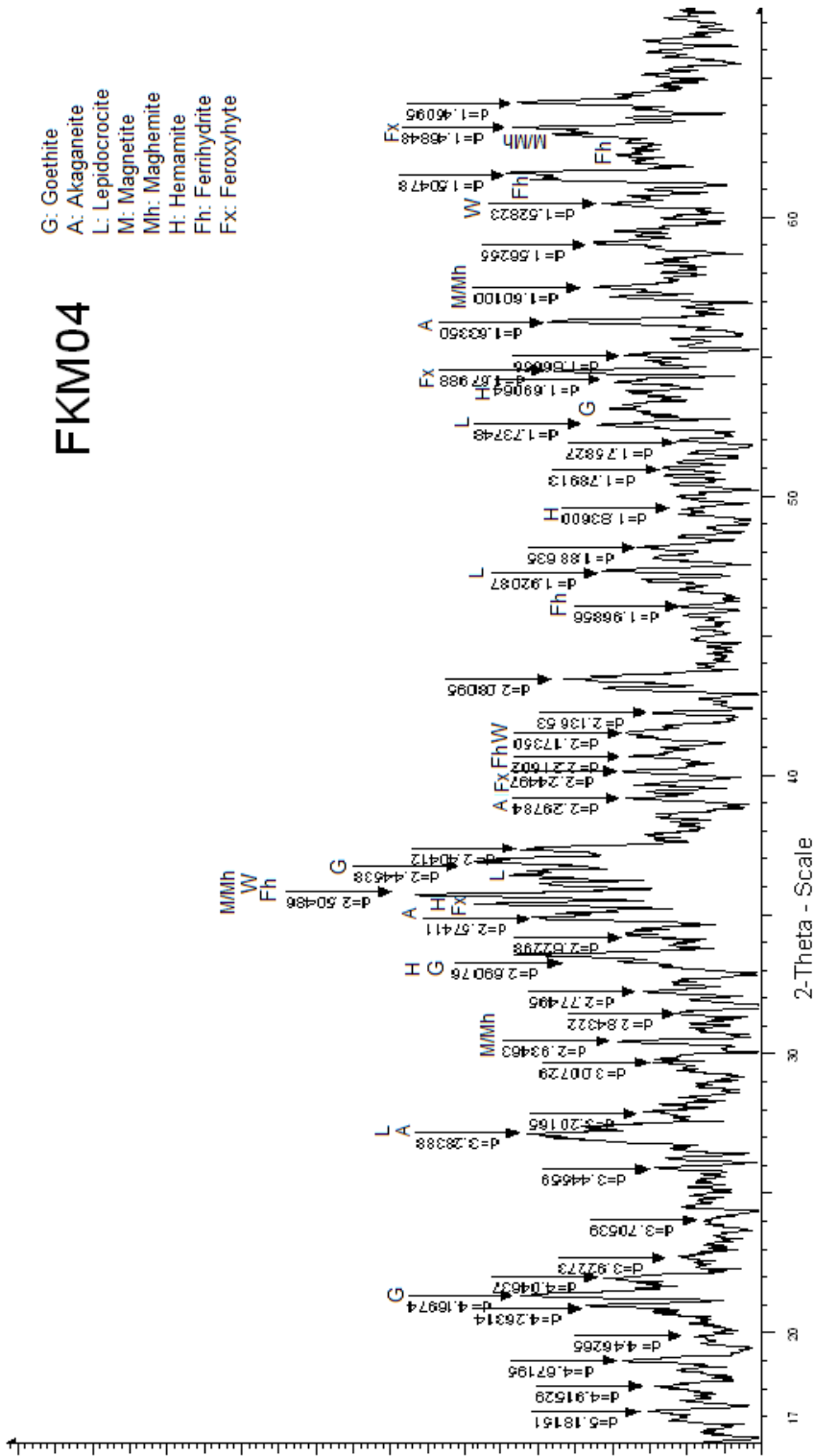


Figure 4. 157 XRD spectra of the corrosion layer powder including ICL and TM of the main entrance door hinge (FKM-04) (19th cc): goethite (G), akaganeite (A), maghemite (Mh), magnetite (M), hematite (H), lepidocrocite (L), ferrihydrite (Fh), ferroxyhyte (Fx).

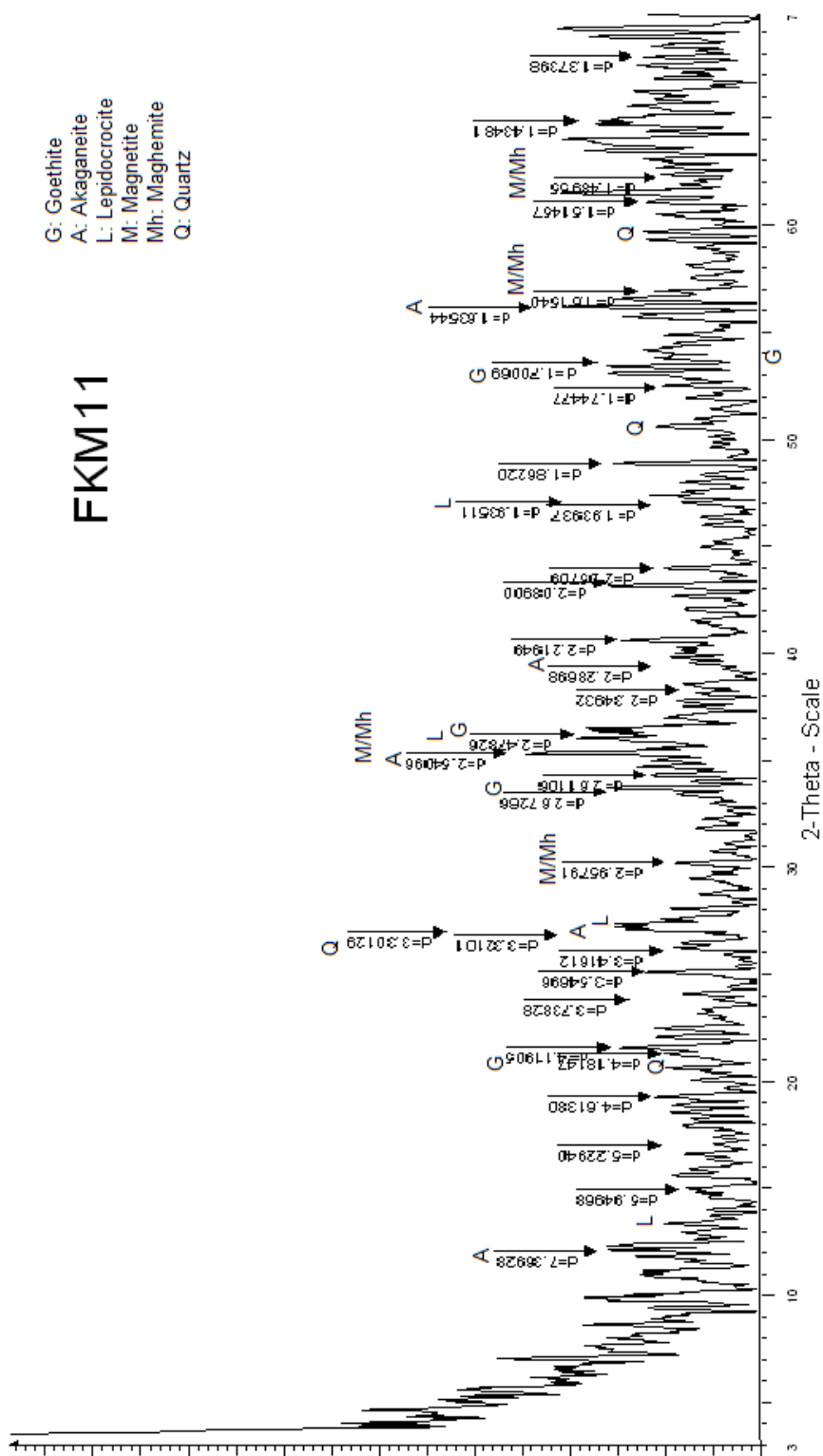


Figure 4. 158 XRD spectra of the corrosion layer powder including ICL and TM of the nail (FKM-11) (19th cc): goethite (G), akaganeite (A), maghemite (Mh), magnetite (M), lepidocrocite (L), quartz (Q).

The nail (FKM-06) from the Ottoman layer excavations representing buried condition shows goethite (XRD pattern d : 4.169 (100), 2.459 (45), 2,667 (35), 1.716 (20)), lepidocrocite (XRD pattern d : 3.306 (90), 2,459 (80), 1.942 (70)), akageneite (XRD pattern d : 3.306 (100), 2.574 (55), 7.36 (40), 1.652 (35), 2.272 (30)), hematite (XRD pattern d : 2,667 (100), 2.509 (70), 1.689 (45), 1,827 (40)), magnetite (XRD pattern d : 2.509 (100), 1.469 (40), 1.600 (30), 3.025 (30)), maghemite (XRD pattern d : 2.509 (100), 3.025 (35), 1.469 (34), 1.600 (24)), ferrihydrite (XRD pattern d : 2.509 (100), 2.205 (80), 1.942 (80), 1.469 (70)) and calcite (XRD pattern d : 3.025 (100), 2.272 (18), 2.078 (18), 1.892 (17)) as iron oxides (Figure 4.159). The Rietveld search-match method was applied to raw data of XRD pattern, but probably due to decreased efficiency with nanocrystalline systems of greater complexity, no result was obtained. Goethite peaks are well formed and rather broad, the broadening at FWHL is about 1.2 deg. indicating that the crystallite size of goethite in buried condition may be in the range of 5 -10 nm.

The iron piece (FKM-08) from the Ottoman layer excavations representing buried condition reveals goethite (XRD pattern d : 4.180 (100), 2.449 (45), 2.702 (35), 1.705 (20)), lepidocrocite (XRD pattern d : 6.26 (100), 3.205 (90), 2.445 (80), 1.937 (70)), hematite (XRD pattern d : 2.702 (100), 2.519 (70), 1.705 (45), 1.840 (40)), ferrihydrite (XRD pattern d : 2.521 (100), 2.218 (80), 1.993 (80), 1.477 (80)), magnetite (XRD pattern d : 2.521 (100), 1.477 (40), 1.610 (30), 2.911 (30)), and maghemite (XRD pattern d : 2.521 (100), 2.911 (35), 1.477 (34), 1.610 (24)) as iron oxides (Figure 4.160). The Rietveld search-match method with elements Fe, O and H gives the presence of nano crystallized iron oxides with the formulas FeOOH, Fe₂O₃ and Fe₃O₄. The XRD analysis shows that goethite is the major phase of the surface corrosion layer with minor amounts of other phases such as lepidocrocite, hematite, ferrihydrite, magnetite and maghemite. Goethite peaks are well formed and rather broad, the broadening at FWHL is about 0.62 deg. indicating that the crystallite size of goethite in buried condition may be in the range of 10 -50 nm.

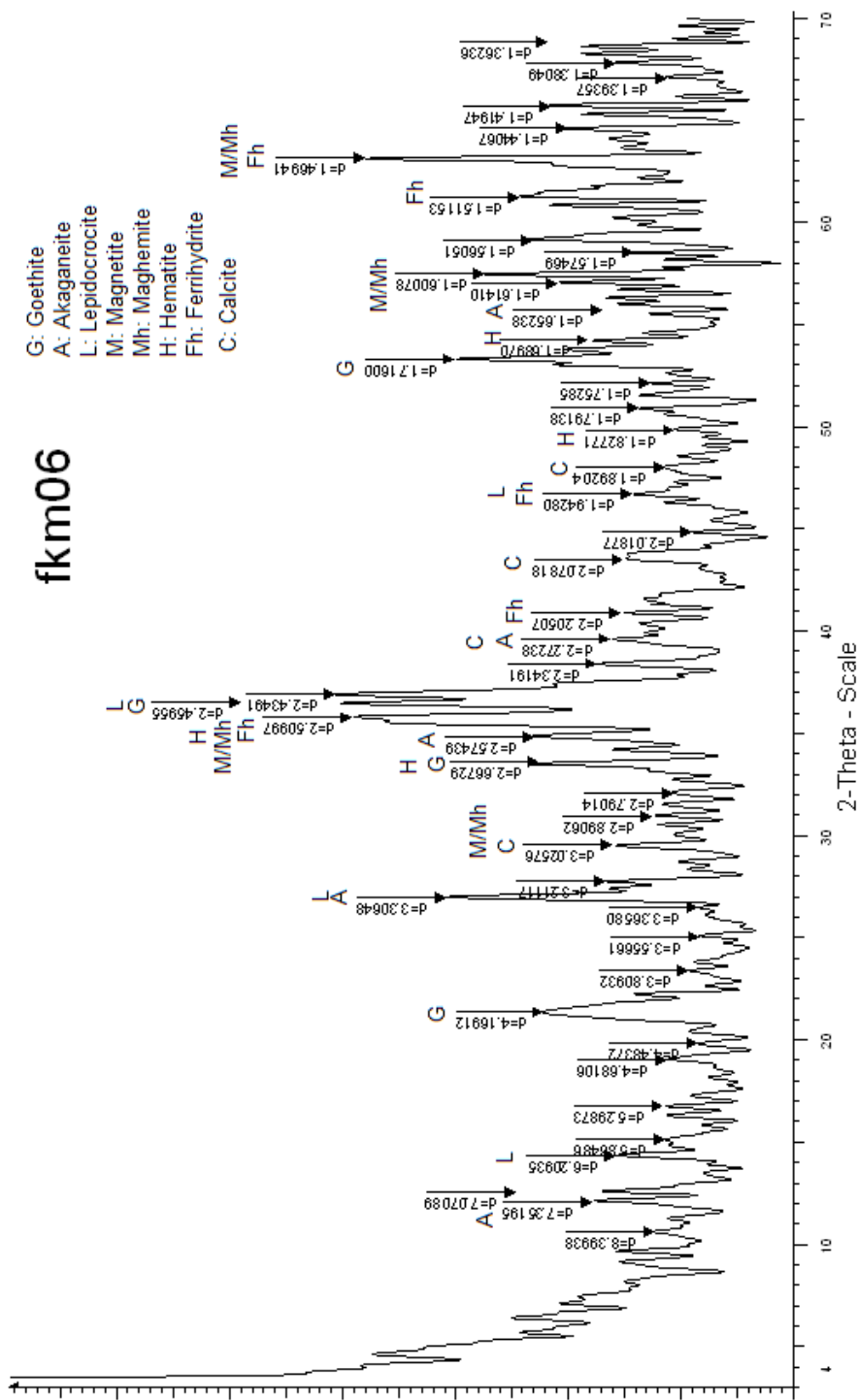


Figure 4. 159 XRD spectra of the corrosion layer powder including ICL and TM of the nail (FKM-06) (19th cc): goethite (G), akaganeite (A), maghemite (Mh), magnetite (M), hematite (H) lepidocrocite (L), ferrihydrate (Fh), calcite (C).

fk m08

- G: Goethite
- L: Lepidocrocite
- H: Hematite
- M: Magnetite
- Mh: Maghemite
- Fh: Ferrihydrite

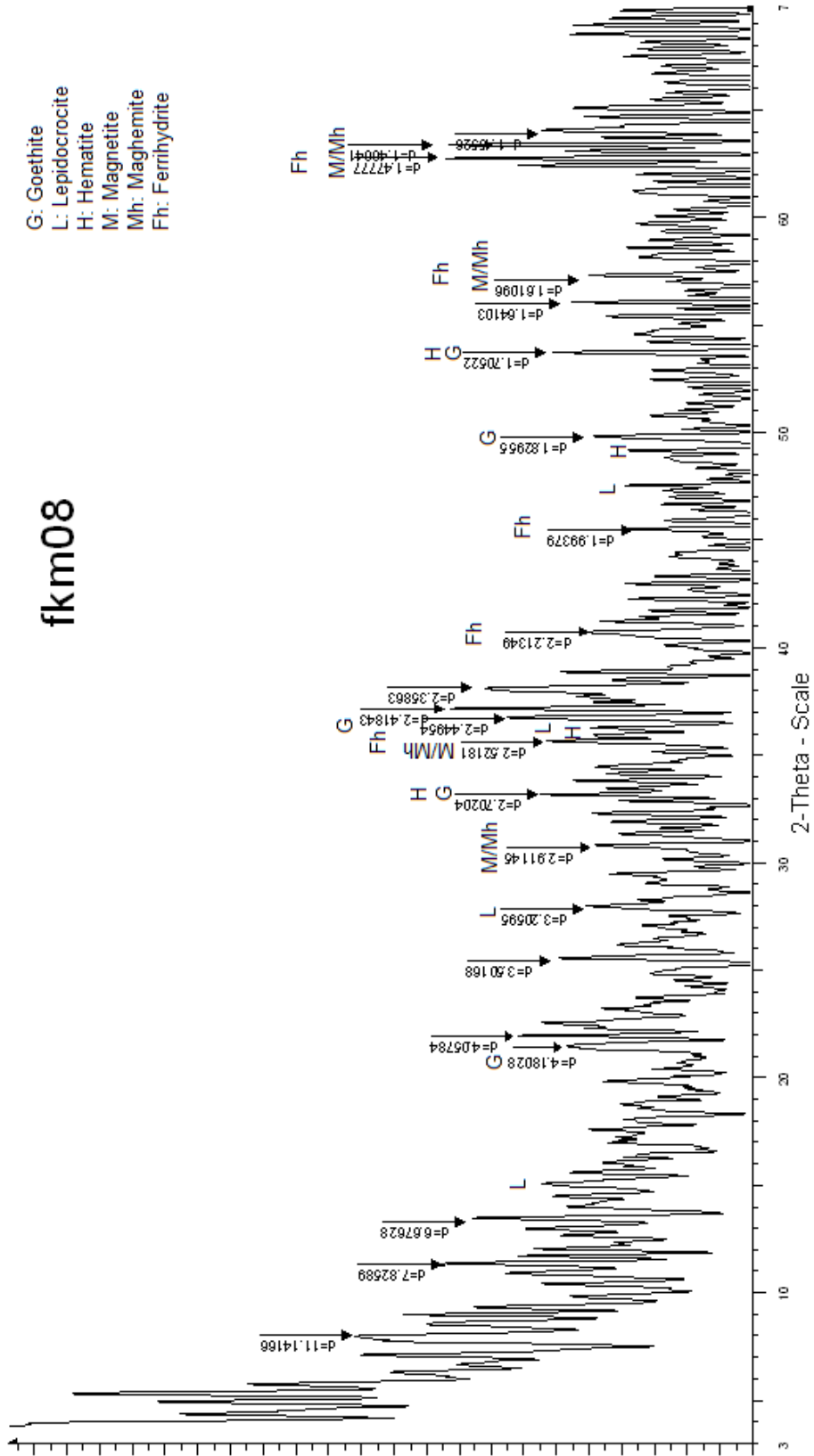


Figure 4. 160 XRD spectra of the corrosion layer powder including ICL and TM of the of the nail (FKM-11) (19th cc): goethite (G), hematite (H), maghemite (Mh), magnetite (M), lepidocrocite (L), ferrihydrite (Fh).

The nail (FKM-09) from the Ottoman layer excavations representing buried condition shows goethite (XRD pattern d : 4.192 (100), 2.442 (45), 2,664 (35), 1.719 (20)), lepidocrocite (XRD pattern d : 6.26 (100), 3.269 (90), 2,442 (80), 1.937 (70)), hematite (XRD pattern d : 2,664 (100), 2.503 (70), 1.692 (45), 1,856 (40)), magnetite (XRD pattern d : 2.503 (100), 1.481 (40), 1.615 (30), 2.967 (30)), maghemite (XRD pattern d : 2.509 (100), 2.967 (35), 1.481 (34), 1.607 (24)), wustite (XRD pattern d : 2.174 (100), 2.503 (80), 1.523 (60)) as iron oxides together with minor amount of quartz impurities from TM (Figure 4.161). The Rietveld search-match method with elements Fe, H, O and Si reveals the presence of some silicates and FeOOH while the search with the elements Fe, O and H, gives the presence of nano crystallized iron oxides with the formulas FeOOH, Fe₂O₃ and Fe₃O₄. Goethite peaks are well formed and rather broad; the broadening at FWHL is about 0.33 deg. indicating that the crystallite size of goethite in buried condition may be in the range of 10 -50 nm.

The nail (FKM-10) from the Ottoman layer excavations representing buried condition reveals goethite (XRD pattern d : 4.127 (100), 2.438 (45), 2.688 (35), 1.714 (20)), lepidocrocite (XRD pattern d : 6.147 (100), 3.286 (90), 2.438 (80), 1.921 (70)), hematite (XRD pattern d : 2.688 (100), 2.521 (70), 1.690 (45), 1.840 (40)), magnetite (XRD pattern d : 2.521 (100), 1.470 (40), 1.609 (30), 2.946 (30)), maghemite (XRD pattern d : 2.521 (100), 2.946 (35), 1.470 (34), 1.609 (24)) and ferrihydrite (XRD pattern d : 2.50 (100), 2.227 (80), 1.518 (60)) as iron oxides together with minor amount of quartz and calcite impurities from TM (Figure 4.162). The Rietveld search-match method was applied to raw data of XRD pattern, but probably due to decreased efficiency with nanocrystalline systems of greater complexity, no result was obtained. The XRD analysis shows that goethite, lepidocrocite, and magnetite / maghemite is the major phase of the surface corrosion layer with minor amounts of other phases such as hematite, ferrihydrite. Goethite peaks are well formed and rather broad; the broadening at FWHL is about 1 deg. indicating that the crystallite size of goethite in buried condition may be in the range of 5 - 10 nm.

fkmm09

- G: Goethite
- L: Lepidocrocite
- H: Hematite
- M: Magnetite
- Mh: Maghemite
- W: Wustite
- Q: Quartz

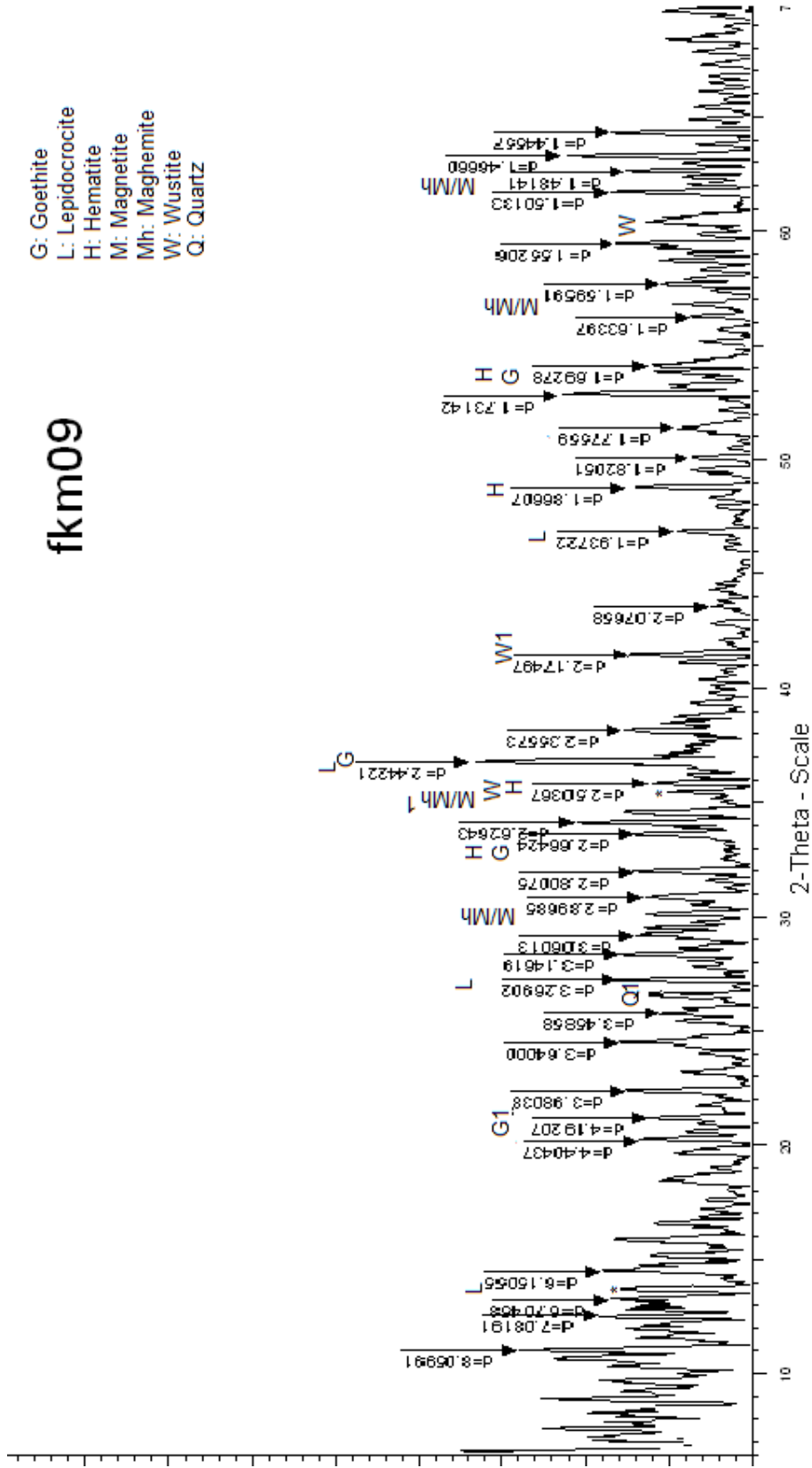


Figure 4. 161 XRD spectra of the corrosion layer powder including ICL and TM of the iron piece (FKM-09) (19th cc): goethite (G), hematite (H), maghemite (Mh), magnetite (M), lepidocrocite (L), wustite (W), quartz (Q).

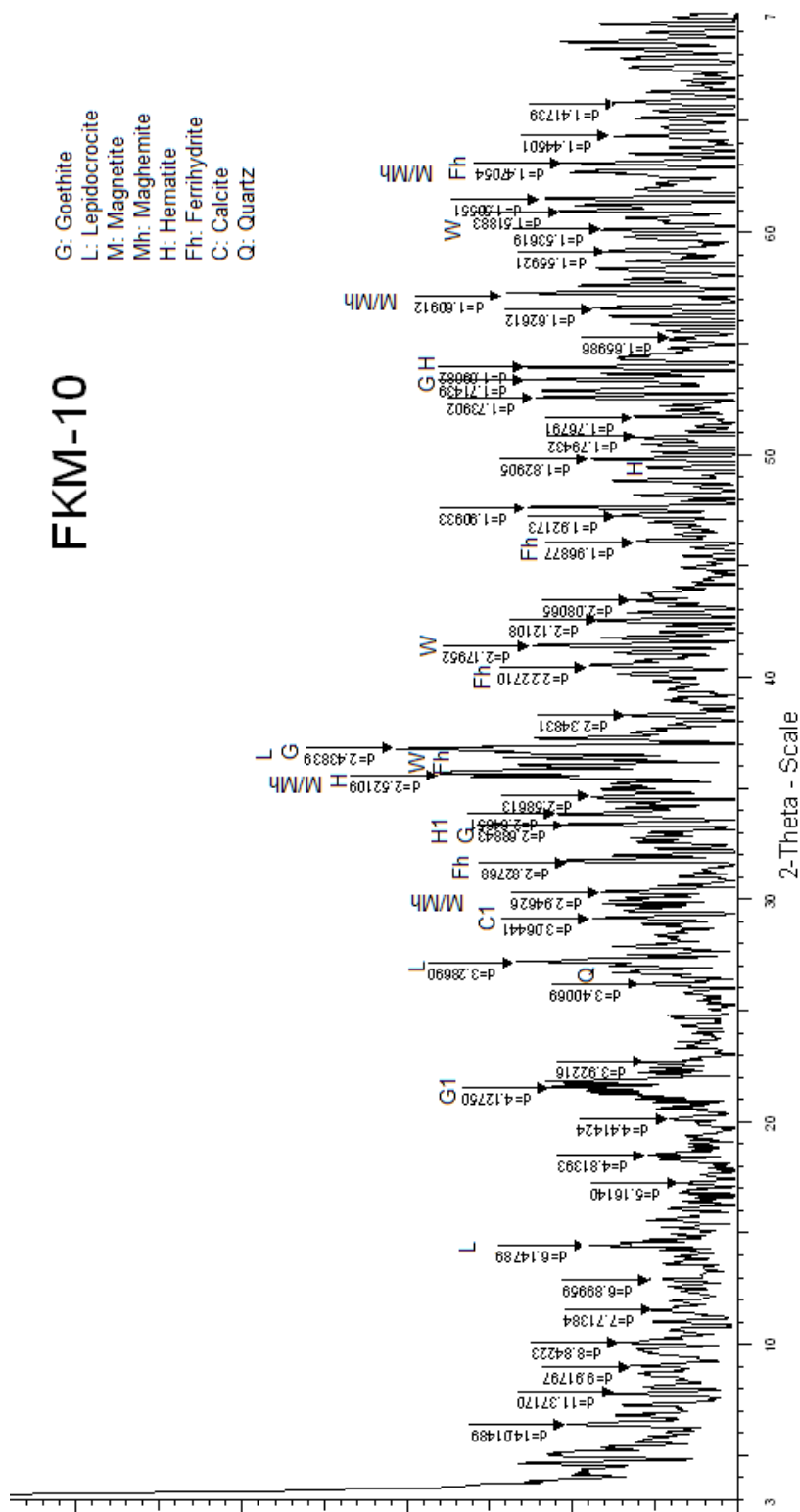


Figure 4. 162 XRD spectra of the corrosion layer powder including ICL and TM of the iron piece (FKM-10) (19th cc): goethite (G), hematite (H), maghemite (Mh), magnetite (M), lepidocrocite (L), ferrihydrite (fh), calcite (C), quartz (Q).

Table 4. 52 Iron oxides layering in the corrosion of the samples from the 15th, 16th and 19th centuries examined by XRD Analysis.

Sample ID and location	Minerals in the Powdered Mixture of the Corrosion Layer									
	Goethite (α -FeOOH)	Lepidocrocite (γ -FeOOH)	Hematite (α -Fe ₂ O ₃)	Magnetite (Fe ₃ O ₄) / Maghemite (γ -Fe ₂ O ₃)	Ferrihydrate (Fe ₂ O ₃ .H ₂ O)	Feroxyhyte (δ -FeOOH)	Akaganeite (β -FeOOH)	Wustite (FeO)	Impurities	
GMH-Me-03 - Plaster nail, <i>indoor</i>	goethite	lepidocrocite	hematite	M/Mh						
MSH-KAP-01 - Nail from dome, <i>outdoor</i>	goethite	lepidocrocite	hematite	M/Mh				calcite		
MSH-KAP-03 - Nail from dome, <i>outdoor</i>	goethite	lepidocrocite	hematite	M/Mh	ferrihydrate,		wustite	quartz and calcite		
MSH-KAP-02 - Iron piece from wall, <i>indoor</i>	goethite	lepidocrocite	hematite	M/Mh	ferrihydrate		wustite	quartz and calcite		
FKM-02 - Nail for jointing main timber beams, <i>indoor</i>	goethite	-	hematite	M/Mh	ferrihydrate		wustite	siderite, quartz and calcite		
FKM-04 - Male hinge from the main entrance door, <i>partially open to atmosphere</i>	goethite	lepidocrocite	hematite	M/Mh	ferrihydrate	feroxyhyte	akaganeite			
FKM-11 - Nail embedded in building stone, <i>partially open to atmosphere</i>	goethite	lepidocrocite	-	M/Mh	-	-	akaganeite	quartz		
FKM-06 - Nail from the Ottoman layer, <i>buried</i>	goethite	lepidocrocite	hematite	M/Mh	ferrihydrate	feroxyhyte	akaganeite			
FKM-08 - L-shaped iron piece from the Ottoman layer, <i>buried</i>	goethite	lepidocrocite	hematite	M/Mh	ferrihydrate					
FKM-09 - Iron piece from the Ottoman layer, <i>buried</i>	goethite	lepidocrocite	hematite	M/Mh	-	-	wustite	quartz		
FKM-10 - Nail from the Ottoman layer, <i>buried</i>	goethite	lepidocrocite	hematite	M/Mh	ferrihydrate	-	-	quartz and calcite		

CHAPTER 5

DISCUSSIONS

In this chapter, the combined results of the analyses performed on the historical iron constructional elements namely, several nails, a beam, anchoring elements, door and window hinges, two door locks from 15th, 16th and 19th century historical structures are discussed to describe their metallurgical properties and corrosion performance. Metallurgical properties are interrelated with production techniques and microstructure, hardness, workability and elemental composition.

Corrosion characteristics of individual objects are evaluated by detailed description of the corrosion layers and compared in terms of the thickness, sub-layering, compactness and corrosion products starting from main body towards exterior together with the related environmental conditions namely open air (urban, rural), interior and burial conditions.

Finally, properties of protective corrosion layers being mainly composed of goethite, factors effecting the formation of protective corrosion layer such as the metallurgical properties of the objects, environment, duration of the exposure and the possible mechanisms for the corrosion products are discussed.

5.1. Types and Properties of Protective Corrosion Layers on Historical Iron Objects

All iron objects examined have corrosion layers on their surface where the corrosion products are mainly goethite and rarely hematite. Here, the corrosion layers of individual objects are evaluated and compared in terms of their thickness, compactness and corrosion products starting from main body towards exterior in

relation to their environment namely open air (urban, rural), interior or burial conditions.

5.1.1 Classification of protective corrosion layers based on their thickness and morphological characteristics

In this study, protective corrosion layers of the iron objects were classified based on their thickness and the compactness indicating the absence of pores and cracks in the layer. The average corrosion thicknesses covering inner corrosion layer (ICL) including reaction front (RF) next to the metal of the objects fall into three groups being perfect (less than 200 μm), medium perfect (between 201-500 μm) and imperfect (above 500 μm) (Figure 5.1).

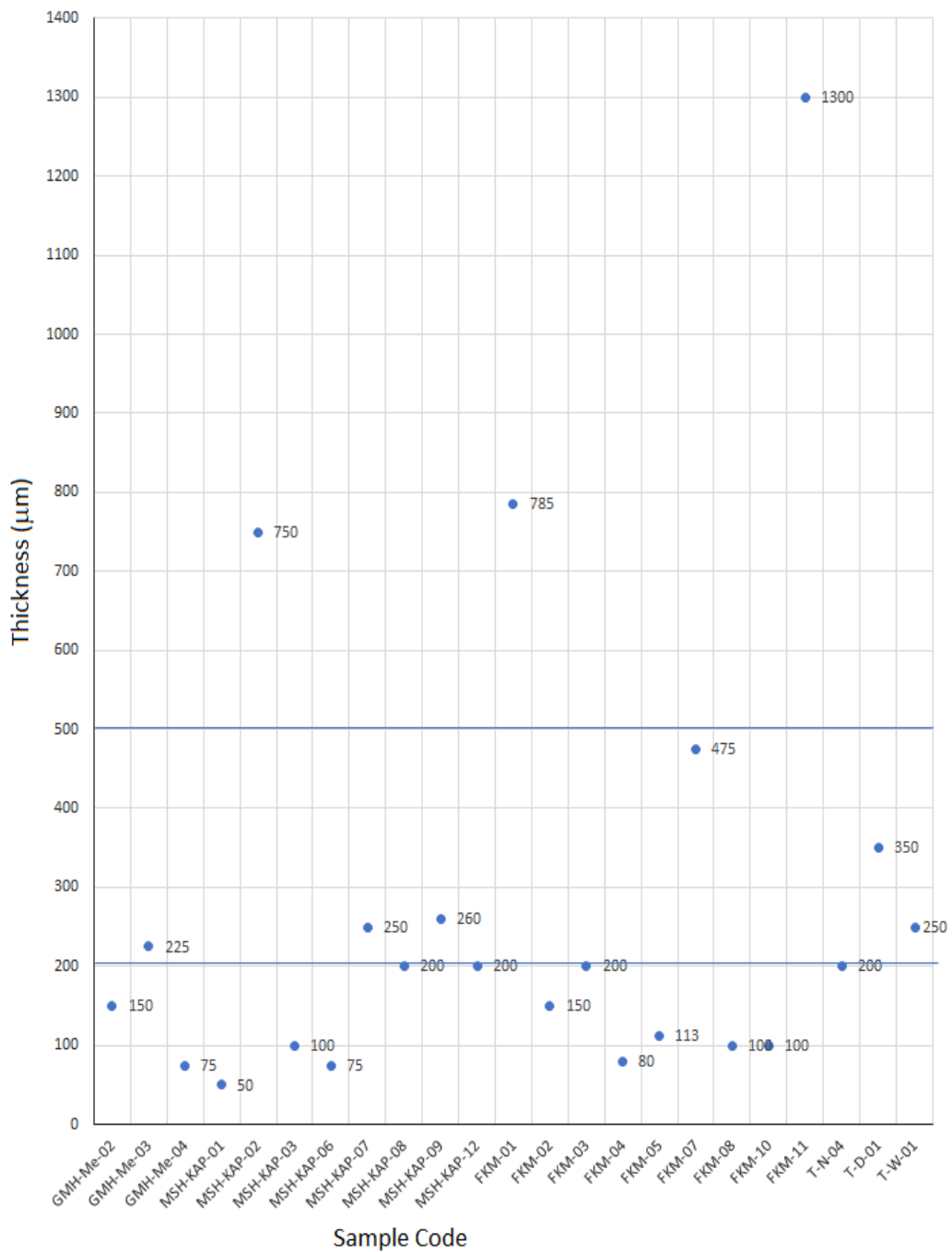


Figure 5. 1 Average thickness of corrosion layers on the 23 iron objects and their classification: as perfect ($\leq 200 \mu\text{m}$), medium perfect ($201-500 \mu\text{m}$ and imperfect ($>500 \mu\text{m}$).

The 14 objects out of the 23 have perfect corrosion layers within the thickness range of 50-200 μm . The perfect corrosion layers are compact and almost free of cracks and pores (GMH-Me-02 and -04, MSH-KAP-01, -03, -06, -08 and 12, FKM-02, -03, -04, -05, -08, -10 and T-N-04). Those samples except two (FKM-08 and -10) are from indoor and outdoor conditions, the other two are in the burial condition. The two objects out of 14 were the nails embedded in timber and the perfect corrosion layer is mainly composed of hematite while the others are composed of goethite.

The six objects out of the 23 have the medium perfect corrosion layers within the thickness range of 225-475 μm . The medium perfect corrosion layers being less compact than the perfect layer have fine cracks especially in the second halves of the ICL with some pores in them (GMH-Me-03, MSH-KAP-07 and -09, FKM-07, T-D-01 and T-W-01). Those samples are both from indoor, outdoor and one in burial conditions. The corrosion layers are mainly composed of goethite except door lock piece (T-D-01) from the 19th century having mainly hematite in the ICL.

The three objects out of the 23 have the imperfect corrosion layers within the thickness range of 750-1300 μm . The jointing element (MSH-KAP-02) from the interior of the hammam building has some fine cracks and pores in the compact body of ICL, a window guard iron piece (FKM-01) from a stone dwelling indicating outdoor atmosphere and the nail (FKM-11) embedded in lower parts of stone masonry wall has a less compact ICL with deep cracks in it. Therefore, those three objects (MSH-KAP-02, FKM-01 and FKM-11) represent both indoor and outdoor conditions. The corrosion layers are mainly composed of goethite at the inner part of ICL. The outer part of ICL of FKM-11 has akaganeite and maghemite in its composition.

A time dependent evaluation on the perfectness of the corrosion layers showed that seven samples out of 14 are from the 15th and 16th century buildings and the other seven of them are from the 19th century buildings. Three out of six objects have medium perfect corrosion layers where one from 15th and two from 16th century. The

other three objects have imperfect corrosion layers coming from the 16th and 19th century buildings.

Neither rural / urban atmosphere or outdoor / indoor conditions don't seem to play any important role in the formation of perfect corrosion layers for the iron objects which were around 600 years old and some around 150 years old. Since majority of those objects have perfect corrosion layers, those protective corrosion layers must have formed in the early life of the objects and started to play their protective role. Urban atmospheric conditions may not have yet been quite a serious problem in early life of the objects. It is possible that some indoor iron elements could have been replaced in the later periods or re-used. The indoor conditions of the monuments may not probably be continuous due to their lack of maintenance. That may be why we don't observe considerable difference between the corrosion layers formed at indoor and outdoor conditions. The outdoor objects which were mainly nails may reflect the history of corrosion in a more continuous way.

The perfect, medium and imperfect corrosion layers were also examined for their particle size and crystallinity characteristics of goethite in their composition (Table 5.1).

Particle size of the goethite was obtained from the full width of the half maximum (FWHM) measurement (Speakman, 2007). For all objects, goethite particles were nano sized in protective layers whether they were perfect, medium and imperfect corrosion layers. However, perfect goethite crystallites were in the finer range, the average being around 20 nm. The imperfect layers had the average particle size higher than the perfect layers being around 34 nm. The medium perfect layers had the average goethite particle size around 25 nm, in between the perfect and imperfect corrosion layers.

The crystallinity of the goethite corrosion layers was evaluated by the characteristics of their FTIR spectra. There are two important criteria: i) peak separation – higher the separation, higher the crystallinity and ii) sharpness of the two-major OH bending bands namely δ -OH at 890 cm^{-1} and γ -OH at 790 cm^{-1} . Sharpness of the δ -OH at 890

cm⁻¹ of goethite was correlated with the degree of crystallinity (Cornell and Schwertmann, 2003) as well as the particle size together with XRD FWHM. Not forgetting that the FTIR spectra represents the powdered samples including both ICL and TM. Most of the time interference of the impurities are unavoidable. A better spectrum obtained can give more information about the properties of the protective corrosion layer. In majority of perfect corrosion layers, FTIR reflects the presence of good crystallinity of goethite by the presence of sharp peaks at 890 cm⁻¹. It seems that it also an indication of finer particle size which is supported by XRD FWHM. Therefore, perfect corrosion layers have finer nano-sized particles and most likely with good crystallinity. The good crystallinity in nano size is thought to be indication of stability of goethite that has been experimentally supported by their higher band gap (Majzlan *et al*, 2008).

Table 5. 1 Summary of the analytical results on the properties of inner corrosion layers belonging to the iron objects from different historical periods (G: Goethite; L: Lepidocrocite; M-Mh: Magnetite-Maghemite; Hyd: Hydrated iron oxides or oxyhydroxides; W: Wustite; A: Akaganeite; POA: partially open to atmosphere)

Sample ID	Environment	Century	ICL Classification	Ave. Thickness of ICL (μm)	FWHM (deg)	Particle Size (nm)	Main Iron Oxide Phase				Crystallinity (Peak separation - boradening)	PAI Result
				SEM, Huvitz, Stereo*	XRD	XRD	Raman	XRD	FTIR	FTIR	Raman	
GMH-Me-02 - Door lock piece	Urban-industrial; PAO	15 th	Perfect	150			G/M/H / A/Hyd		G/L/ M	Variable	0,5	
GMH-Me-03 - plaster nail	Urban-industrial; indoor	15 th	Medium perfect	225	0,5	25		G/L/H/ M-Mh	G/L	Variable		
GMH-Me-04 - plaster nail	Urban-industrial; indoor	15 th	Perfect	75			G/L/H yd				3,5	
MSH-KAP-01 - nail from dome	Urban-industrial; outdoor	16 th	Perfect	50	0,5	25	G/M/H / M-Mh/L	G/L/H/ M-Mh	G/L/ H	Variable	4	
MSH-KAP-02 - iron piece for jointing the metals to the wall	Urban-industrial; indoor	16 th	Imperfect	750	0,4	32	G/Hyd	G/L/H/ W M-Mh	G/L	Variable	1	
MSH-KAP-03 - nail from dome	Urban-industrial; outdoor	16 th	Perfect	100	0,8	12	G/L/M / Mh/Hyd	G/L/H/ W M-Mh	G/L	Good	1	
MSH-KAP-06 - Iron element for towel hanging	Urban-industrial; indoor	16 th	Perfect	75								
MSH-KAP-07 - Nail used for stone building	Urban-industrial; indoor	16 th	Medium perfect	250								
MSH-KAP-08 - nail for lead covering from dome	Urban-industrial; outdoor	16 th	Perfect	200*								

Table 5.1 Summary of the analytical results on the properties of inner corrosion layers belonging to the iron objects from different historical periods (G: Goethite; L: Lepidocrocite; M-Mh: Magnetite-Maghemite; W: Wustite; Hyd: Hydrated iron oxides or oxyhydroxides; A: Akaganeite; POA: partially open to atmosphere) (continued).

Sample ID	Environment	Century	ICL Classification	Ave. Thickness of ICL (μm)	FWHM (deg)	Particle Size (nm)	Main Iron Oxide Phase			Crystallinity (Peak separation - broadening)	PAI Result
				SEM, Huvitz, Stereo*	XRD	XRD	Raman	XRD	FTIR	FTIR	Raman
MSH-KAP-09 - nail used for stone building	Urban-industrial	16 th	Medium perfect	260*			G with M/ Hyd/ L				
MSH-KAP-12 - nail used for timber jointing NO GOETHITE	Urban-industrial; indoor	16 th	Perfect	200			H with M/W				
FKM-01 - window guard iron piece from a stone dwelling	Rural, seaside; outdoor	19 th	Imperfect	785*					G/L	Good	
FKM-02 - nail for jointing main timber beams - NO GOETHITE	Rural, seaside; indoor	19 th	Perfect	150	0,6	20	H with Hyd	G/H/W M-Mh	G	Low	1
FKM-03 - door lock piece from the main entrance	Rural, seaside, PAO	19 th	Perfect	200*			G with Hyd/ M-Mh		G/L	Low	1
FKM-04 - male hinge from the main entrance door	Rural, seaside, PAO	19 th	Perfect	80*	0,33	35	G with Hyd	G/L/H/A M-Mh	G/L	Variable	0.6
FKM-05 - female hinge from the main entrance door	Rural, seaside, PAO	19 th	Perfect	112.5			G with Hyd		G/L	Low	1.3
FKM-06 - nail from the Ottoman layer excavation	Burial condition	19 th			1,2	5		G/L/H/A M-Mh/			
FKM-07 - nail from the Ottoman layer excavation	Burial condition	19 th	Medium perfect	475			G		L	-	>2

Table 5.1 Summary of the analytical results on the properties of inner corrosion layers belonging to the iron objects from different historical periods (G: Goethite; L: Lepidocrocite; M-Mh: Magnetite-Maghemite; W: Wustite; Hyd: Hydrated iron oxides or oxyhydroxides; A: Akaganeite; POA: partially open to atmosphere) (continued).

FKM-08 - L-shaped iron piece from the Ottoman layer excavation	Burial condition	19 th	Perfect	100	0,62	19	G with Hyd/ H/ L/ M/ M-Mh	G/L/H/ M-Mh	G/L	Variable	2
FKM-9 - iron piece from the Ottoman layer excavation	Burial condition	19 th			0,33	35		G/L/H/W M-Mh	G/L/H	Low	
FKM-10 - nail from the Ottoman layer excavation	Burial condition	19 th	Perfect	100	1	7	G with M/ M- M-Mh/ L	G/L/H/ M-Mh	G/L	Low	1
FKM-11 - nail from a dwelling embedded in building stone	Rural, seaside; PAO	19 th	Imperfect	1300	0,33	35	G with M/ L/ M-Mh/ Hyd/ A	G/L/A M-Mh	G	Low	2
T-D-01 - iron crossbar for the main entrance door locking NO GOETHITE	Rural, seaside; PAO	19 th	Medium perfect	350			H with M-Mh		G/L	Low	1
T-N-04 - iron nail from the door frame	Rural, seaside indoor	19 th	Perfect	200			G with Hyd/ L				2

5.1.2 Protective ability of corrosion layers for the 15th, 16th and 19th century objects in terms of their PAI Values, Rate of Corrosion, Average Particle Size of Goethite and Its Crystallinity

In this study, the protective “Protective Ability Index” (PAI) of the corrosion layers were roughly calculated as the ratio of isotropic goethite band thickness to the total thickness of other oxides and oxyhydroxides in the corrosion layer based on the presence of the products tracked along with a line crossing the corrosion layers observed by the μ -Raman (Aramendia *et al*, 2014, Kamimura *et al*, 2006). PAI values were calculated in a semi-quantitative way and documented in Table 5.2 and Table 4.1. Importance and indication of PAI value is described as follows: If PAI value is equal or greater than 1, protective condition starts, if it is equal or greater

than 2, corrosion stops and a stable phase is reached (Kamimura *et al*, 2006). PAI value is used as one of the variables to evaluate the protective function of the goethite layer formed on the iron objects (Table 5.2).

The protective goethite band of the two objects from a 15th century monument representing indoor conditions – a door lock piece (GMH-Me-02) and a plaster nail (GMH-Me-04) – both are classified as perfect corrosion layers with different PAI values. They are located in the urban environment. The door lock piece with a thickness of 150 μm has PAI value 0,5 indicated that the protective function of goethite phase is not yet completed. The plaster nail with a thickness of 75 μm has a PAI value of 3.5. So, the PAI values of the 15th century samples are quite different. The reason for that difference may be due to the installation of that door lock piece (GMH-Me-02) during the restoration of the hammam between 1961-1971 period. However, both objects have perfect corrosion layers with compact morphology. The dominance of hydrated iron (III) oxide or oxyhydroxide compounds observed in the door lock piece (GMH-Me-02) together with goethite phase that has variable crystallinity observed by FTIR analysis, and the marbling texture of the corrosion layer revealed by SEM, may be the indications of the electrochemically reactive environment with many wetting - drying cycles experienced by the object (Monnier, 2010).

The two 16th century nails in outdoor conditions of urban environment (MSH-KAP-01 and -03) have PAI values 4 and 1 belonging to perfect corrosion layers having thicknesses of 50 μm and 100 μm respectively. Three 16th century iron objects in indoor conditions of urban environment (MSH-KAP-02, -09 and -12) have PAI values 1 with imperfect, perfect and perfect corrosion layers morphology successively. Although the iron piece for jointing of other metals to the wall (MSH-KAP-02) has an imperfect corrosion layer morphology, it is fully composed of goethite. That object can be considered having a corrosion layer with full protective function. All objects from the 16th century have PAI values equal or greater than 1 indicating full protective property of corrosion layer has been reached. These

findings help to prove the authenticity of the above-mentioned 16th century objects. In addition, the presence of hydrated iron (III) oxide or oxyhydroxide compounds as marbling texture observed by SEM in their corrosion layers and the variable crystallinity of goethite detected by FTIR may be the indications of the electrochemically reactive environment with many wetting - drying cycles experienced by the object (Monnier *et al*, 2010). All objects from the 16th century have PAI values greater than 2 and a stable protective corrosion band in ICL. These findings help to prove the authenticity of the above-mentioned objects.

For the 19th century objects at the seaside open air rural environment (FKM-02, -03, -04, -05, -11, and T-D-01, T-N-04), the PAI values are 1, 1, 0.6, 1.3, 2, 1, 2 successively. They all have perfect corrosion layer morphology except the nail (FKM-11) with imperfect corrosion layer morphology and the door lock piece (T-D-01) with medium perfect corrosion layer morphology. In addition, all those samples have the variable / low crystallinity of goethite detected by FTIR. It seems that PAI numbers do not proportionally show the degree of protective ability. However, it exerts the importance of goethite layer for protection against further corrosion in a semi-quantitative way, e.g., the sample (FKM-04) having PAI less than 1 is with a perfect corrosion layer. One of the reasons for low PAI value in that sample may be due to difficulties in the quantitative detection of goethite and other iron oxides by μ -Raman. Typical intensity ratios of iron corrosion products in μ -Raman detection in comparable recording conditions were expressed as lepidocrocite (1) > wustite, hematite, goethite, hydroxy chloride, ferrihydrites, feroxyhyte ($\sim 1/3$) > akaganeite ($\sim 1/4$) >> magnetite and maghemite ($\sim 1/10$) (Colomban, 2011). While the presence of goethite was not well revealed by μ -Raman, FTIR and XRD both showed abundant presence of goethite in the sample (FKM-04). The objects in buried condition (FKM-07, 08 and 10) from 19th century have high PAI values being >2, 2 and 1 respectively with a protective goethite band in their ICL observed by μ -Raman. High protection of corrosion layer formed on the objects are observed for the buried condition. The surface soil in the archaeological site of Foça seems to be suitable for

formation of stable phases being well aerated and originated mostly from weathering of tuff.

The comparison of PAI values calculated by μ -Raman is not fully in line with FTIR and XRD results. It must be kept in mind that μ -Raman analysis describes the corrosion products on the examined points of the sample while FTIR and XRD reflect the corrosion products in the powdered sample giving an overall composition of ICL mixed with TM.

Although majority of protective corrosion layers are mainly composed of goethite, there are exceptions to that in some nails found embedded in timber. Their corrosion environment can be described as an environment with organic acids and natural resins. It was found that the protective corrosion layers in those nails were composed of wustite and hematite. Wustite together with magnetite and hematite is the densest phase because of its high Fe/O ratio indicating lack of oxygen (Colomban, 2011). Ahlström et al (2018) has studied the stability of wustite, magnetite and hematite coatings over steel in alkaline environment as well as chloride containing environment by electrochemical measurements. Hematite is the most stable phase over a wide pH range with a very low electric conductivity, roughly $10^{-9} \Omega^{-1} \cdot \text{cm}^{-1}$. Magnetite is stable in alkaline and reducing conditions and has high electrical conductivity, $100\text{-}1000 \Omega^{-1} \cdot \text{cm}^{-1}$. In alkaline environment steel and wustite are less noble in comparison to magnetite followed by hematite. In chloride containing environment steel and magnetite are less noble than wustite followed by hematite. Those comparisons lead us to the conclusion that the nail objects embedded in timber developing protective layers composed of wustite and hematite reflect a corrosion environment with organic acids and natural resins.

The stability of the protective layers is also evaluated in terms of average goethite particle size calculated from XRD peaks. An indoor plaster nail (GMH-Me-03) from the 15th century having medium perfect corrosion layer has the average goethite particle size around 25 nm. The average goethite particle size of two outdoor nails (MSH-KAP-01 and -02) with perfect corrosion layer morphology are around 25 nm

and 12 nm respectively. The iron piece from the same monument (MSH-KAP-02) has imperfect corrosion layer with the average goethite particle size of 32 nm. The objects from the 19th century have the average goethite particle sizes between 5 nm to 35 nm. While goethite was found to be more stable than hematite down to 150 nm and up to 40°C in natural atmospheric conditions (Cornell and Schwertmann, 2003), this study shows that goethite formation occurs down to much finer particle sizes on iron objects being in the range of 5 to 35 nm. The decrease in particle size of goethite relatively increases its stability that is related to band gap values (Zhang et al 2011). Goethite having particle size between 9-38 nm, similar to the range of particles in this study, appears to have band gap values in the range of 3.1-2.5 eV and it is relatively larger than band gap of hematite at around the same size range (Zhang *et al*, 2011). It seems that the protective ability of the corrosion layer is closely related with fine size of goethite particles and its compactness. The presence of relatively unstable oxides or oxyhydroxides in the layer do not have much influence on the protective ability of the corrosion layer. Those oxide or oxyhydroxides may lead to the further formation of fine nano particles as a compact layer under repeated wetting and drying conditions.

Crystallinity of goethite in the corrosion layers were examined by means of the two-major OH bending bands namely δ -OH at 890 cm^{-1} and γ -OH at 790 cm^{-1} of goethite taking into account their broadening and separation. Most objects have variable or low crystallinity. Varying crystallinity can be related to the average particle size (Cambier 1986). An outdoor nail (MSH-KAP-03) from the 16th century having the perfect corrosion layer morphology is the unique sample having good goethite crystallinity with very fine particle size, 12 nm. The assessment done on the results obtained from XRD and μ -Raman analysis together with FTIR analysis support that the δ -OH bending band's sharpness is a better indicator of good crystallinity than the higher separation of δ -OH and γ -OH bending bands to indicate good crystallinity. Therefore, the sharp goethite peaks in FTIR indicate higher crystallinity. The samples having perfect corrosion layer (MSH-KAP-01, -03 from the 16th century

and FKM-02, -04, from the 19th century) are found to have the good crystallinity of goethite along with the presence of minor lepidocrocite.

This study concludes that finer the particle size, sharper the FTIR peak intensities of goethite resulting higher crystallinity are the main qualifications of perfect corrosion layers composed of goethite.

In addition, it is significant that goethite is almost always accompanied with noticeable presence of lepidocrocite. Its presence is verified by combined results of the XRD, FTIR and μ -Raman analysis in 15th, 16th and 19th century objects. The protective corrosion layers including a reactive lepidocrocite phase towards TM may show the importance of wet-dry cycles helping the growth of a protective corrosion layer towards TM.

It is also possible to describe the goethite formation environment from the combined results of this study. There is always calcite available in the corrosion environment, the most pronounced one being the nail (MSH-KAP-01) having highest calcite peaks in its XRD traces. That sample has a perfect corrosion layer with a very thin and compact morphology. The pH of water or water film in equilibrium with air and in equilibrium with calcareous materials like mortars and plasters is most likely to be around 7.8 (Busenberg and Plummer, 1986). The historical iron objects in open atmospheric conditions having wetting-drying cycles may experience those conditions that lead to the goethite formation mechanisms.

Finally, this study attempts to comment on the rate of corrosion of the historical iron iron objects being considerably low in comparison to the today's weathering steel and other low carbon steel products. This rough evaluation is made by using the Kamimura's estimations on the rate of corrosion in a relatively short time scale based on the thickness measurements of corrosion layer and divided by the years of exposure to atmospheric conditions (Kamimura *et al*, 2006). They found that the object being in normal atmospheric conditions, if PAI value is less than 1, corrosion rate is less than 1 mm/y (1000 μ m/y). If PAI value is equal or greater than 1, being the starting value for protective ability, corrosion rate is less than 10 μ m/y and if it

is equal or greater than 2, corrosion stops and corrosion layer reaches a stable phase (Kamimura *et al*, 2006). Considering that information, corrosion layers of all iron objects in this study have reached their protective phase except the door lock piece (GMH-Me-02) from Gazi Mihal Hammam and a male hinge from the door (FKM-04) having PAI values less than 1. Both objects can be the replacement objects during a possible restoration. It is known that Gazi Mihal Hammam was restored during 1950-1960. If the door lock piece is assumed to be a replacement piece of the restoration as a new product, the rate of corrosion is approximately 2.5 $\mu\text{m}/\text{y}$. For the corrosion rates of the objects having the PAI value in the range of $1 < \text{PAI} < 2$, the average corrosion rate of the 16th century objects is approximately 0,76 $\mu\text{m}/\text{y}$, calculated through the ratio of the average corrosion layer thickness to the objects' age. The 19th century ones are around 1,33 $\mu\text{m}/\text{y}$. Those corrosion rates of the 15th, 16th and 19th century objects are much lower than the corrosion rates specified by Kamimura *et al* (2006). In addition, they are much lower than the corrosion rate of weathering steel which is about 6 $\mu\text{m}/\text{y}$ (Yamashita *et al*, 2004). Weathering steel is a kind of low-alloy steel characterized by a protective rust that is formed on its surfaces reducing the rate of corrosion (Kimura and Khira, 2005). The average corrosion rate of low alloy steel in urban atmospheric conditions is expected to be 2.29 $\mu\text{m}/\text{y}$ (Doruk, 2014). The historical low alloy steel objects mainly the nails from the Ottoman Periods have rather low rates of corrosion in coastal urban atmosphere. The door lock piece of 15th century hammam, which is assumed to be a replacement object during a relatively recent restoration, exhibits a similar corrosion rate (2.5 $\mu\text{m}/\text{y}$) expected from coastal urban atmospheric conditions (Doruk, 2014).

In conclusion, historical iron objects have considerably lower corrosion rates in comparison to today's weathering steel and other steel products. PAI values and corrosion rate calculations derived from the combined analysis of μ -Raman, FTIR, XRD together with SEM and several microscopical investigations are useful tools to investigate the authenticity of the iron objects through the examination of their corrosion layers.

5.2 Description of metallurgical properties of historical iron

The metal bodies of all historical iron objects from the 15th, 16th and 19th centuries were examined to investigate their metallurgical characteristics. In this section, the effect of the morphological characteristics and elemental composition of metal bodies are discussed to look for their contribution to the formation of perfect protective corrosion layers on the iron object.

5.2.1 Characteristics of Goethite Layer and Elemental Composition of Metal Body:

Steels are usually classified in terms of their level of carbon content and way of production. During production, some alloying elements may be added and / or some may come from iron ore itself such as silicon, phosphorous, nickel, chromium, sulfur, manganese, magnesium, copper and aluminum to impart the required properties. In this section, the elements in the composition of the iron objects and characteristics of the protective goethite layer are discussed to see whether some elements have importance in the control of corrosion.

Carbon content: Carbon content of most objects fall in the range of low carbon steel (up to 0.30%) (Figure 5.2). No direct relationship was found with the amount of carbon content and thickness of protective corrosion layer. However, the influence of other alloying elements in the composition of metal body has to be examined individually for their role in protective goethite layer formation. The objects having perfect corrosion layer is expected to indicate threshold values of individual elements for corrosion control.

Silicon content: Silicon content of the objects having perfect corrosion layer are as follows (Figure 5.2): 11 objects have silicon content being in the range of 0.003% - 0.226%. The object (FKM-02) with perfect corrosion layer having the highest silicon content has the one with lowest carbon content (0.002%). Three objects having medium perfect corrosion layer have considerable amounts of silicon in the range of

0.056% -0.571%. The object (MSH-KAP-07) having highest silicon content (0.571%) falls in the medium carbon steel range. However, the other three objects fall in low carbon steel range. Three objects having imperfect corrosion layer have silicon content in the range of 0.161% - 0.233%. Two of them (MSH-KAP-02 and FKM-11) has the lowest carbon content (0.002%) while one of them (FKM-01) has the highest carbon content (1.5%). It seems that the objects having perfect corrosion layer have rather low silicon content, the upper limit being 0.226%. 10 out of 11 objects having perfect corrosion layer have low carbon steel grade while one of them (FKM-04) within the high carbon steel grade.

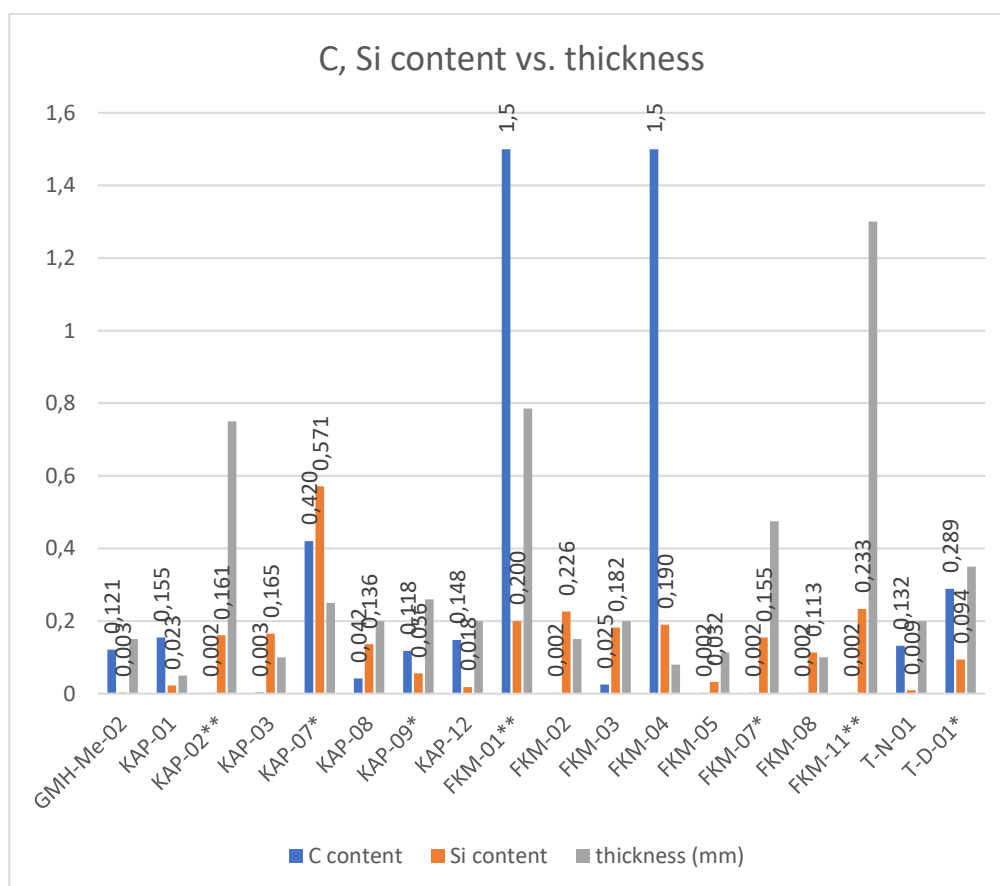


Figure 5. 2: Relationship between ICL thickness, silicon (Si) and carbon (C) contents of the objects from the 15th, 16th and 19th centuries. “*” indicates the objects with medium perfect corrosion layer. “**” indicates the objects with imperfect corrosion layer.

Phosphorous content: Objects having less than 0.05% phosphorous are known as good quality steels (Yıldız 2010). The presence of phosphorous over 0.04% reduces the steel’s ductility, resulting in cold shortness (Singh 2016). Higher phosphorous from 0.07% to 0.12% is included in steels that are specifically developed for machining to improve the cutting properties of steel (Singh 2016). Five objects (GMH-Me-02, MSH-KAP-01, -08, -012, T-N-01) having perfect corrosion layer fall in good quality steel category being in the range of 0.007 – 0.052% (Figure 5.3). The other six objects having perfect corrosion layer have phosphorous content higher than that value (0.126% - 0.262%). Seven objects with medium and thick corrosion layer have phosphorous content being in the range of 0.007% - 0.282%. Three objects having imperfect corrosion layer have phosphorous content being 0.243% and 0.282%.

When the perfect corrosion layer is considered, objects having phosphorous content below 0.05% falls in this category as well as the ones with higher than that value being up to 0.241%. The objects with the imperfect corrosion layer have high phosphorous content above 0.241% up to 0.282%.

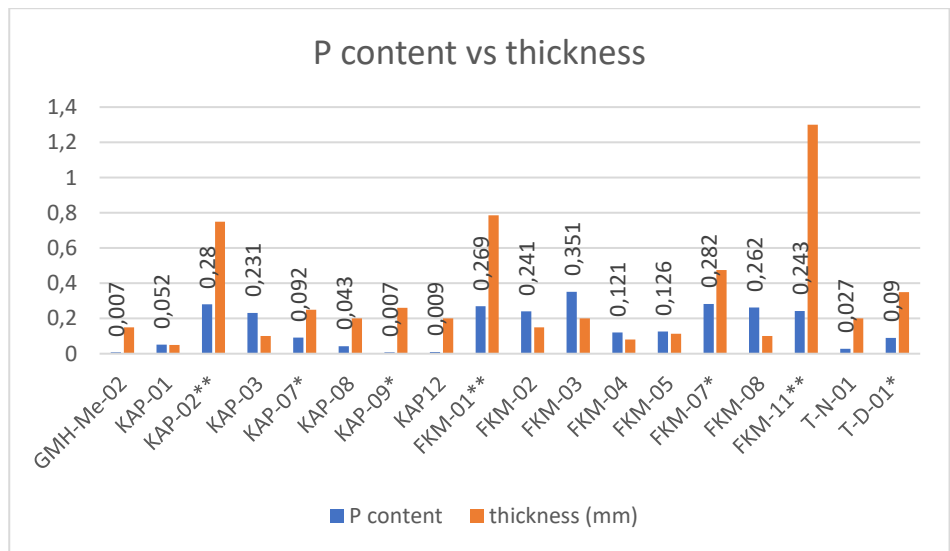


Figure 5. 3 Relationship between ICL thickness and phosphorous (P) content of the objects from the 15th, 16th and 19th centuries. “*” indicates the objects with medium perfect corrosion layer. “**” indicates the objects with imperfect corrosion layer.

Sulfur content: Amount of sulfur is an important parameter in relation to the weathering performance of the iron. High sulfur content causes brittleness in steel. Sulfur in good quality steel is generally kept below 0.05%, preferably, between 0.02% and 0.035 % (Yıldız, 2010). It combines with iron to form FeS which is a low-temperature melting alloy and tends to concentrate at grain boundaries (Singh 2016). Today, it is added to the steel composition up to 0.35% to improve its machinability but decreases the resistance against corrosion (Singh, 2016).

Sulfur content of nine objects (GMH-Me-02, MSH-KAP-01, -03, -08, -12, FKM-03, -04, -05, T-N-01) having perfect corrosion layer fall in the range of good quality steel being between 0.009 – 0.047% (Figure 5.4). The two objects (FKM-02 and FKM-08) having perfect corrosion layer has steel content higher than that value (0.077%-0.203%). In total, nine objects have sulfur content less than 0.05% which is a threshold value for good quality steel category, one object (T-D-01) has the lowest sulfur content (0.004%) but it falls in the medium perfect corrosion layer group. This sulfur value (0.004%) is below the minimum value of good quality steel range. Two objects (MSH-KAP-07 and FKM-07) with medium perfect corrosion layer have sulfur content above the threshold value being in the range of 0.052% - 0.06%. Both are above 0.05% which may be proposed as upper limit for a good quality steel. Three objects (MSH-KAP-02, FKM-01 and FKM-11) having imperfect corrosion layer have sulfur content higher than upper limit being 0.075%, 0.01% and 0.099% respectively. It is observed that the objects having sulfur content within good quality steel range (0.02%-0.05% S) have perfect goethite layer formation. Although FKM-02 and FKM-08 have high sulfur content (0.077% and 0.203%), they also have a perfect goethite layer formation.

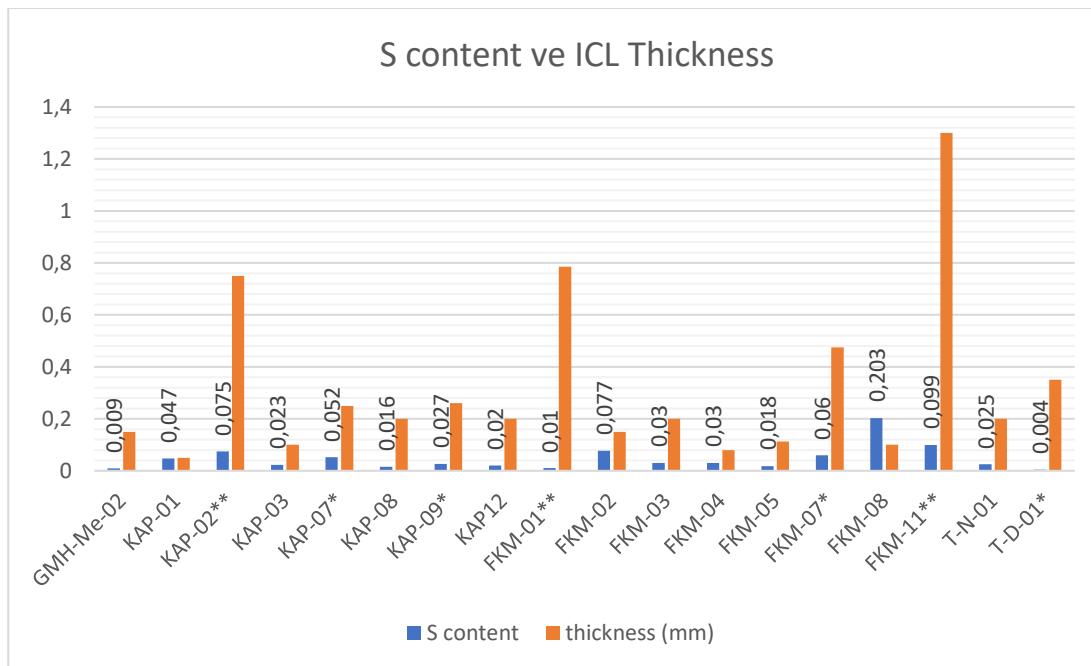


Figure 5. 4 Relationship between ICL thickness and sulfur content of the objects from the 15th, 16th and 19th centuries. “*” indicates the objects with medium perfect corrosion layer. “**” indicates the objects with imperfect corrosion layer.

Manganese content: Manganese is present in all commercial carbon steels in the range of 0.03% to 1.00% (Singh 2016). Manganese in the composition of steels above 1% makes the steel considerably harder (Yıldız 2010, Radovic et al 2010, Singh 2016). When the manganese content exceeds 0.80%, it acts as an alloying element to increase the strength and hardness in high carbon steels (Singh 2016). All 11 objects (GMH-Me-02, MSH-KAP-01, -03, -8, -12, FKM-02, -03, -04, -05, -08, T-N-01) having perfect corrosion layer are in low carbon steel category having manganese in the range of 0.001 – 0.511% (Figure 5.5). Four objects with medium corrosion layer have Mn content in the range of 0.019% - 0.916%. Three objects having imperfect corrosion layer have manganese content between 0.087% and 0.115%. The manganese content of the objects with perfect corrosion layer namely MSH-KAP-01 and T-N-01 is rather high but below the threshold value (0.80%) to affect hardness since they are in the soft hardness range. Therefore, it can be concluded that the manganese content above 0.80% have influence on hardness by

making the low carbon steel harder (Figure 5.6). On the other hand, no direct relationship between the manganese content and the formation of goethite layer was found.

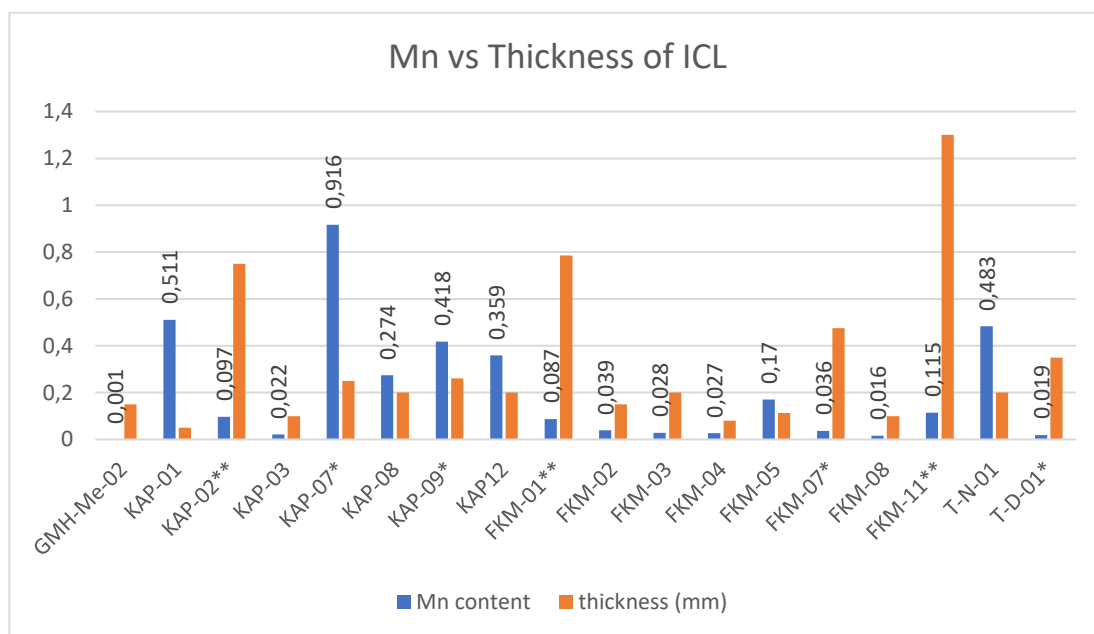


Figure 5. 5 Relationship between ICL thickness and manganese (Mn) content of the objects from the 15th, 16th and 19th centuries. “*” indicates the objects with medium perfect corrosion layer. “**” indicates the objects with imperfect corrosion layer.

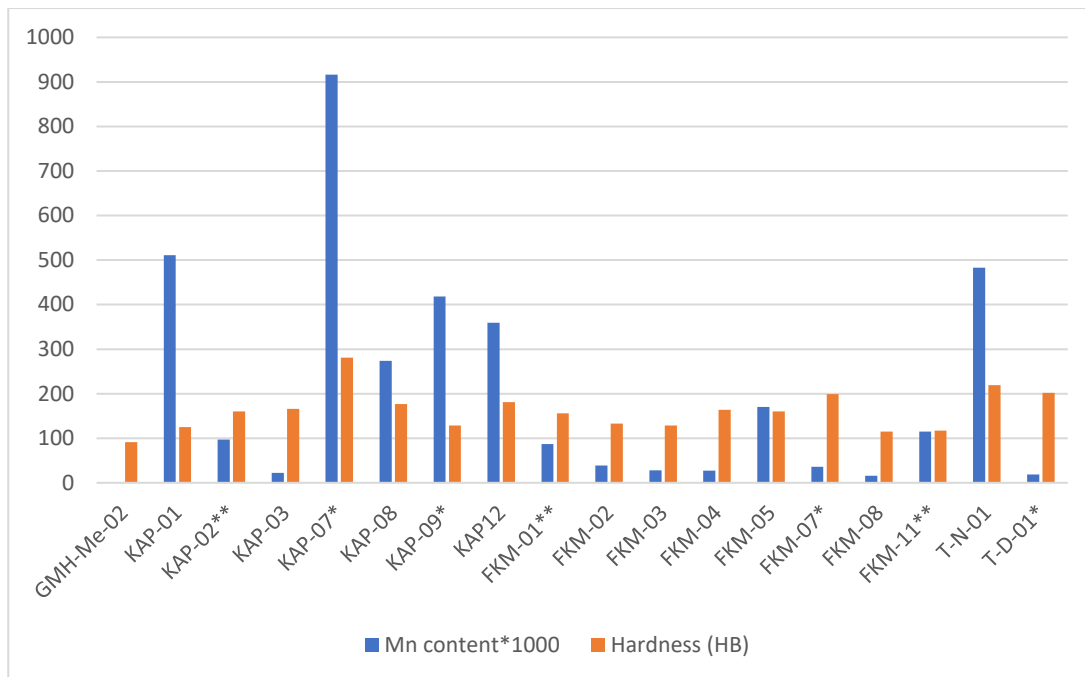


Figure 5. 6 Relationship between manganese (Mn) content and hardness of the objects from the 15th, 16th and 19th centuries. “*” indicates the objects with medium perfect corrosion layer. “**” indicates the objects with imperfect corrosion layer.

Magnesium content: Magnesium has an important effect on toughness and microstructure in low carbon steels (Li et al, 2019). Li et al (2019) has observed a significant increase in the proportion of ferrite for 0.0026% Mg-added steel. Chemical composition of spheroidal cast iron has 0.05% magnesium (Singh 2016). Today’s commercial carbon steels with low and medium carbon content contain magnesium below than 0.05% in their composition.

All 18 objects of this study have magnesium in the range of 0.000 – 0.0345% (Figure 5.7) similar to the today’s commercial carbon steels having low and medium carbon content. The 10 objects having thin and compact corrosion layer described as perfect protective corrosion layer in this study, have magnesium content lower than 0.0026% while only one object (FKM-02) having higher concentration than 0.0026% falls in this category. Seven objects having medium perfect and imperfect corrosion layer have magnesium higher than 0.0026% except one object (MSH-KAP-07) in medium carbon steel range has low magnesium content being 0.0007%. One object (FKM-

11) having the thickest imperfect corrosion layer has the highest magnesium content being 0.0345%. In this study, it is observed that when magnesium content of perfect, medium and imperfect protective corrosion layers is considered, the objects having low magnesium content have better formation of protective corrosion layer in low carbon steels.

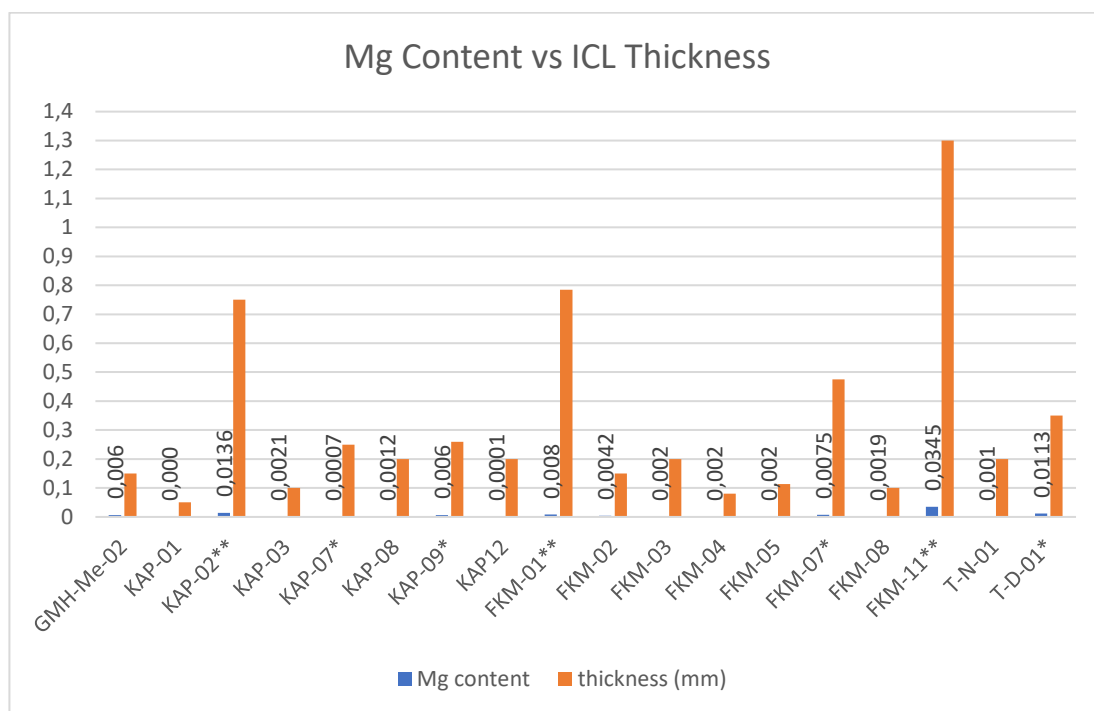


Figure 5. 7 Relationship between ICL thickness and magnesium (Mg) content of the objects from the 15th, 16th and 19th centuries. “*” indicates the objects with medium perfect corrosion layer. “**” indicates the objects with imperfect corrosion layer.

Aluminum content: Aluminum content in the composition of steels especially being 1% improves considerably the corrosion resistance of the steel and decreases the corrosion rate of the passivation film (Zhang et al, 2021). All 18 iron objects have low aluminum content in their composition ranging between 0.001 to 0.049% being less than 1% (Figure 5.8). The highest aluminum content is in the object (MSH-KAP-03) falls in the perfect ICL category. The very low aluminum content in the

compositions of the objects does not show its contribution to the corrosion resistance of the objects.

As a result, aluminum content of perfect, medium and imperfect corrosion layers is considered, there is seen that there is no direct relationship for the formation of protective corrosion layer for carbon steels with aluminum content being max. 0.049%.

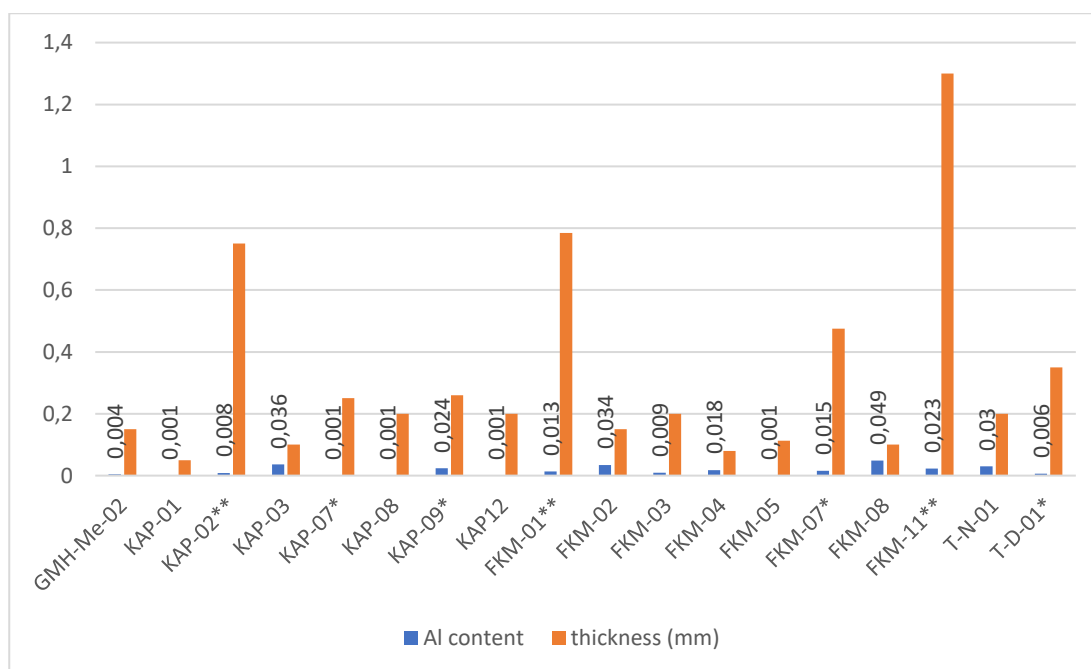


Figure 5. 8 Relationship between ICL thickness and aluminum (Al) content for objects from the 15th, 16th and 19th centuries. “*” indicates the objects with medium perfect corrosion layer. “**” indicates the objects with imperfect corrosion layer.

Chromium and Nickel Contents: 11 objects having perfect corrosion layer have low chromium content in their composition ranging between 0.001 to 0.135% (Figure 5.9). Objects having medium perfect and imperfect corrosion layers have chromium contents ranging between 0.001 to 0.38%.

Nickel content of the objects having perfect corrosion layer are as follows (Figure 5.9): Eighth objects out of eleven have considerable nickel content being in the range

of 0.010% - 0.150%. Two objects (FKM-02 and -08) with perfect corrosion layer having considerably high chromium content (0.129 and 0.104) have the lowest amount of nickel being 0.001% and 0.006% respectively. Four objects having medium perfect corrosion layer have considerable amounts of nickel in the range of 0.012% -0.129%. While one of them has lowest chromium being 0.001%, the other three have chromium in the range of 0.148% - 0.38%. Three objects having imperfect corrosion layer have the lowest amount of nickel being 0.001% for two of them and one having 0.013% whereas they have considerable amount of chromium. The positive effect of nickel content is observed at their low percentages being around 0,014% with no presence of chromium. On the other hand, the role of chromium content without the presence of nickel does not show important contribution on the perfect corrosion layer unless it is present at considerable amounts (0.104%) as in the object FKM-08. On the contrary, even if there is no nickel in the composition of the body, samples having lower and higher content of chromium that critical value have thick corrosion layer in the ICL (Figure 5.9).

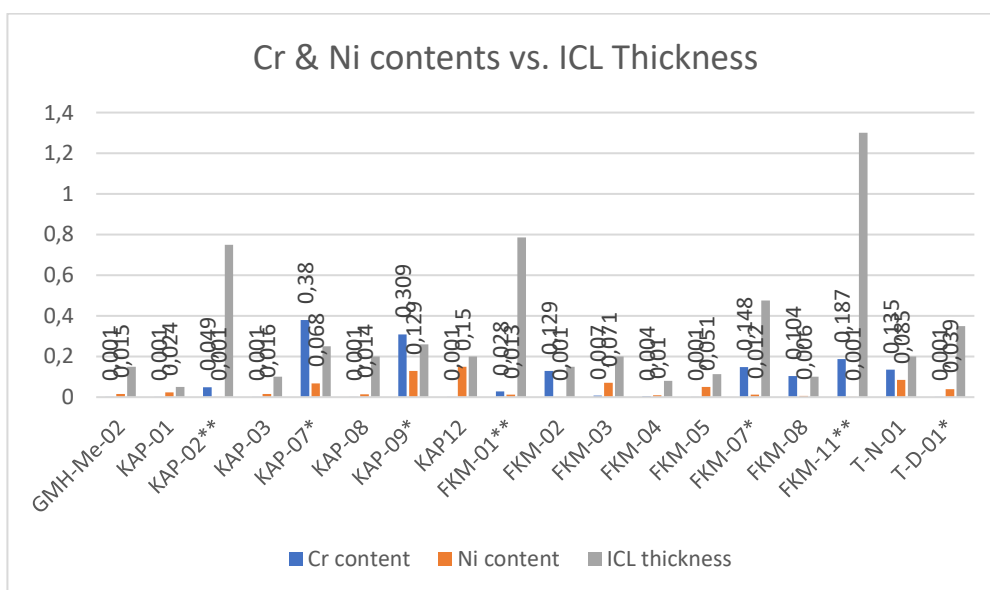


Figure 5. 9 Relationship between ICL, chromium (Cr) and nickel (Ni) contents of the objects from the 15th, 16th and 19th centuries. “*” indicates the objects with medium perfect corrosion layer. “**” indicates the objects with imperfect corrosion layer.

Mn and P contents: Considering the quality of the corrosion layer formation, samples having perfect corrosion layer have manganese concentration below 0.80% and phosphorous below 0,25% (Figure 5.10). Their hardness is in the soft range. The manganese is an element that is thought to increase hardness of the soft steels above 0.80% (Singh 2016) in agreement with this study. For the phosphorous, the although in the good quality steel the accepted value is below 0.05%, the objects with perfect corrosion layer have phosphorous content up to 0.24% which is a level that is thought to decrease ductility. In this study, it is seen that although the phosphorous content is above the threshold value (0.05%) for good quality steel, it doesn't seem to affect the ductility and the corrosion performance up to 0.24% which is the limit found for the objects with perfect corrosion layer.

When both phosphorous and manganese contents of perfect, medium and imperfect corrosion layers are considered, it is seen that there is a direct relationship between the formation of protective corrosion layer and these two elements in carbon steels with the newly found threshold values. They are successively below 0.80% for manganese and below 0.24% for phosphorous. Those two elements, do they complement each other that is when one of them is in low quantity the other one compensates it with its higher value?

Mn and S contents: SEM-EDX analyses of the metal bodies shows the existence of sword shaped manganese sulfide (MnS) locations. Their abundance depends on the amount of manganese and sulfur in the composition. Amount of sulfur is an important parameter in relation to the weathering performance of the iron and in good quality steel, it is generally kept below 0.05%. It is observed that the objects having sulfur content within good quality steel range (0.02%-0.05% S) have perfect corrosion layer formation except the nail (FKM-02) (Figure 5.11). Although FKM-02 has higher sulfur content (0.077%) than the limit, it also has a perfect corrosion layer formation which may be due to the very low manganese content and as a result few sword-shaped manganese sulfides (MnS) in the body of the object (FKM-02). High sulfur is expected to cause cracking and decrease corrosion resistance. How the prevention of that drawback by sulfur may happen will further be discussed in

relation to metallographic properties of the object and some probable inclusions that may exist in the metal body such as Ca and Al. If the Ca/S ratio is around the stoichiometric ratio, the formation of CaS inclusions with proper morphology that eliminate crack initiation is probable (Moon et al, 2013, Wang et al, 2019). The role of aluminum in that process may also be possible ($3\text{CaO}+2[\text{Al}]+3[\text{S}]=3\text{CaS}+\text{Al}_2\text{O}_3$) (Xu et al, 2016). Sulfur and aluminum contents may reveal the content of calcium that cannot be detected by the elemental analysis of this study.

The object (T-D-01) having medium corrosion layer has both very low Mn and S but it has higher P content than the accepted range in good quality steel composition.

Do manganese and sulfur have influence on the formation of perfect corrosion layer? Although all the objects having perfect corrosion layer, they have manganese and sulfur contents below the threshold value. Investigations of CaS and Al_2O_3 inclusions needs to be further studied.

Mg and Si contents: When **magnesium (Mg)** contents of the samples are compared, objects have magnesium content ranging from 0.000% to 0.0345% while silicon contents of the samples are ranging between 0.003% to 0.571% (Figure 5.12). The lowest amount of magnesium (0.000%) belongs to a nail from a dome (MSH-KAP-01) having the perfect corrosion layer and the highest amount of (0.0345%) belongs to a nail from 19th century (FKM-11) having the imperfect corrosion layer. The lowest amount of silicon (0.003%) belongs to an object from 15th century hammam building (GMH-Me-02) having the perfect corrosion layer and the highest amount of silicon (0.571%) belongs to a nail from 16th century (MSH-KAP-07) having the medium perfect corrosion layer. The results do not show any relationship with corrosion layer formation. However, the presence of those two elements may be related with the metallurgical process and/or raw materials' characteristics.

Al and Si contents: All iron objects have very low aluminum and silicon contents in their composition ranging between 0.001 to 0.034% being less than 1% for aluminum and 0.003% to 0.571% for silicon (Figure 5.13). Fe-Al-Si alloys are known to develop a protective aluminum oxide layer with a silicon oxide layer below

it with almost no iron oxide corrosion layer (Novak et al, 2019). In our case with low alloy carbon steels, presence of minor amounts of Al and Si may still play some role in inhibition of oxidation and/or formation of protective corrosion layer. When the possibility of their influence on inhibition of oxide layer formation is considered, following observation is made: The objects (MSH-KAP-03, FKM-02 and T-N-01) with perfect corrosion layer and having relatively considerable amounts of Al and Si in their composition may have benefited from their presence.

The objects (MSH-KAP-01 and MSH-KAP-12) from 16th century having perfect corrosion layer formation have similar silicon content with almost no magnesium and aluminum in their composition. Such a resemblance should also be further investigated in terms of their similar source together with other compositional properties as well as metallurgical properties.

The manganese content and fraction of pearlite do not seem to influence corrosion layer formation while they have some influence on hardness. On the other hand, phosphorous content has an influence on hardness after a certain threshold (0.25%). Although sulfur and manganese may be abundant in the composition and hardness is expected to be high, that may not be the case since some other formations such as CaS₂ and MnS spheres in the microstructure seen in SEM-EDX may prevent the increase on hardness.

5.2.2 Cross examination of Data Multiple Factors Effecting Formation of Goethite Layer

After assessment of minor elements contribution to the perfect protective layer, in this section, results of analyses on the metallurgical properties of iron objects in terms of microstructure, hardness and elemental composition are interpreted and discussed. In addition, compositional properties are compared with today's steel (e.g., weathering steel). The objects are classified in to three categories in terms of their hardness values as soft being up to 150 HB, medium hard between 150 to 250 HB and hard above 250 HB (Figure 5.16).

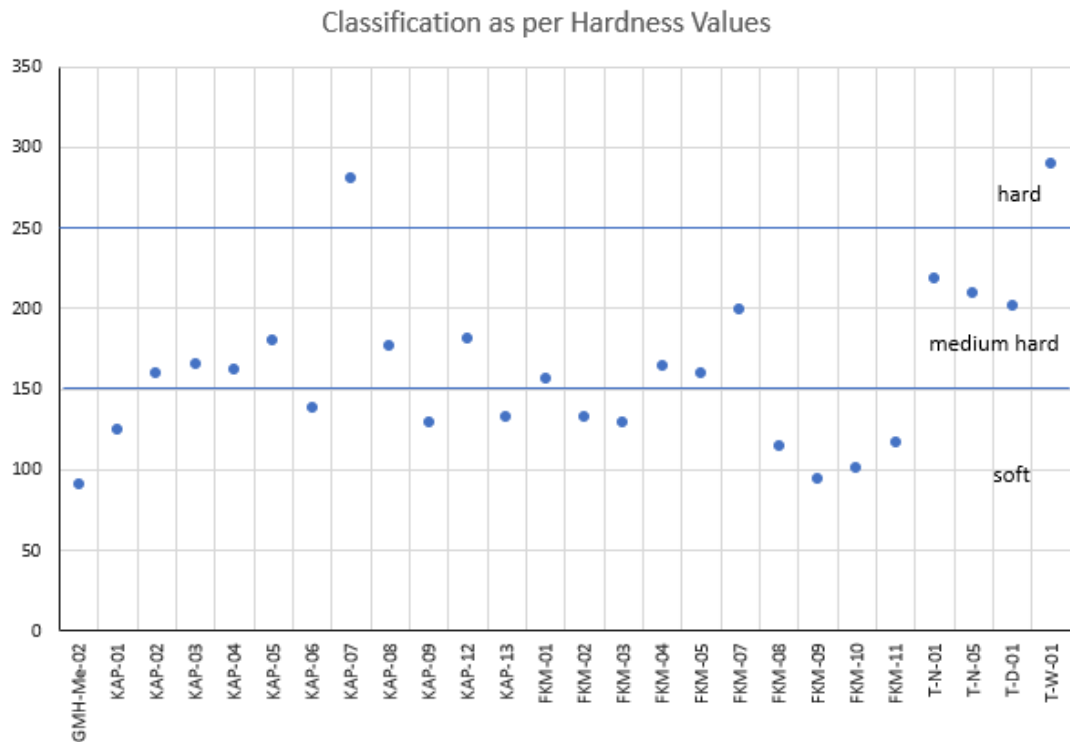


Figure 5. 10 The average hardness classification of the 26 objects from the 15th, 16th and 19th centuries: soft (up to 150 HB), medium hard (151-250 HB) and hard (>251 HB).

There is no direct relationship with corrosion layer formation and hardness of the objects as seen in the Figure 5.11. However, the results show that Brinell hardness values in the soft range are related with the ferritic structure. The objects with the perfect corrosion layer formation have hardness in the soft and medium range (91 HB to 219 HB) while the object having the thickest corrosion layer formation (FKM-11) has the hardness in the soft range (117 HB). The hardest object (MSH-KAP-07) with the hardness value 281 HB has the medium perfect corrosion layer formation.

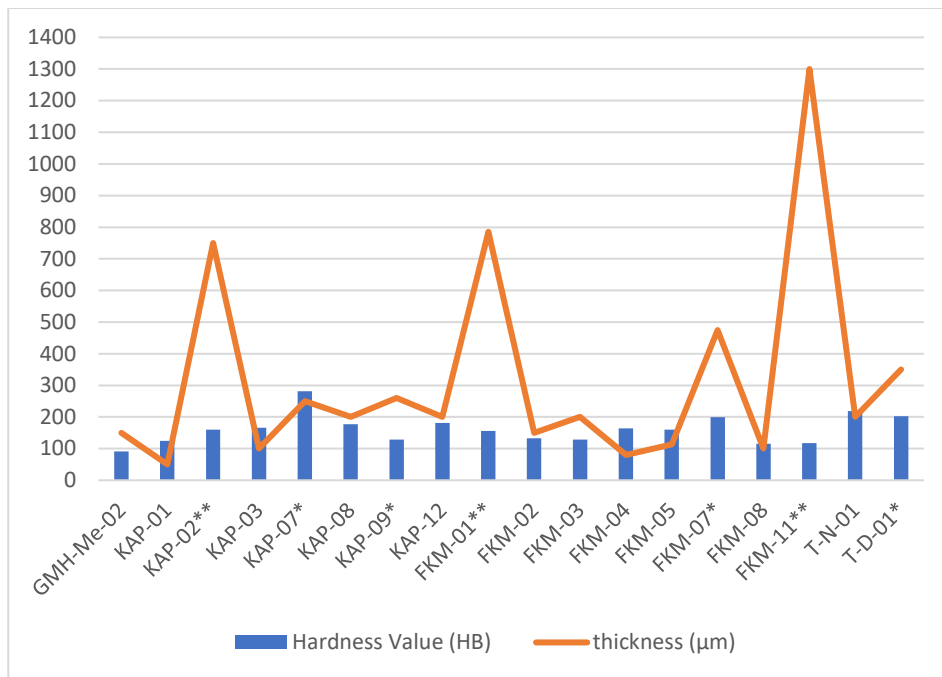


Figure 5. 11 Comparison of hardness and corrosion layer thickness of the objects.

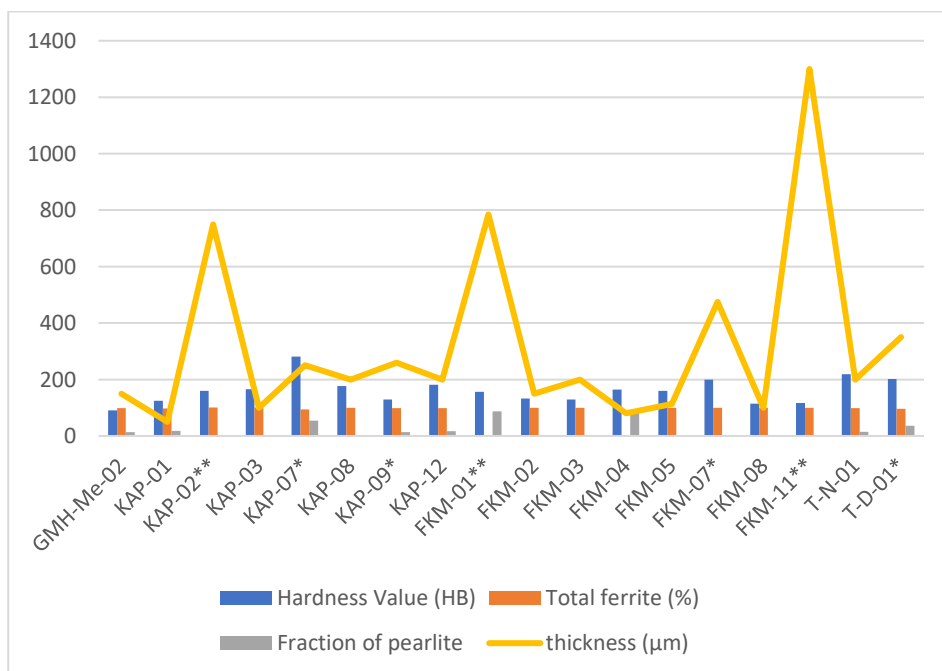


Figure 5. 12 Comparison between hardness and microstructure (in terms of total ferrite and fraction of pearlite contents) of the objects from the 15th, 16th and 19th centuries to investigate the effect on the formation of perfect corrosion layer.

Observations of the corrosion layers show that the iron samples from the exterior of the hammam exposed to atmospheric conditions have a compact corrosion layer where inner corrosion layer (ICL) and transported media (TM) are well observed. The corrosion layers of iron samples from interiors, despite being compact, include some areas with cracks and pores. The effect of microstructure and hardness values of the objects on the formation of perfect corrosion layers are evaluated in figure 5.12. Eleven objects (GMH-Me-02, MSH-KAP-01, 02, -03, -08 and -12, FKM-02, -03, -04, -08, T-N-01) with perfect corrosion layer formation have mainly ferritic structure ranging between 98% to 100% with visible ferrite grain boundaries having ferrite grain size between 25-60 μm . Their hardness value ranging from the 91-219 HB. Four objects having medium perfect corrosion layer have ferritic structure ranging between 94% to 100% with visible ferrite grain boundaries having ferrite grain size between 10-120 μm . Their hardness value ranging from 129 HB to 281 HB. MSH-KAP-07 is in the hard category being 281 HB. MSH-KAP-07 has the highest amount of pearlite within the 16th century samples. Possibly, repair material dating from recent times. Three objects having imperfect corrosion layer have ferritic structure ranging between 0% to 100% with visible ferrite grain boundaries having ferrite grain size between 100-155 μm . Their hardness value ranging from 117 HB to 160 HB.

A nail and a door lock piece (T-N-01 and T-D-01 respectively) from the dwelling in Tekkeköy, Samsun, have 98.4% - 96% total ferrite and 14.9% - 36% pearlite respectively. The hardness values of Tekkekoy iron samples are in medium hard and very hard range (from 202 HB to 290 HB). Possibly repair material dating from recent time.

The objects having perfect corrosion layer has fine grains with maximum 60 μm while the imperfect ones have the grain size above 100 μm . The pearlitic structure may be related to the heat and the way of processing (production technology).

When compared to two nails having perfect corrosion layer collected from the same location, there are some differences observed in terms of ferrite grain size, hardness

and compositional properties. The nail (MSH-KAP-01) with lower ICL thickness (50 μm) has lower hardness with smaller ferrite grains having manganese (Mn) and carbon (C) being higher than the nail (MSH-KAP-03). The nail (MSH-KAP-03) with respectively higher ICL thickness (100 μm) has hardness value within medium hardness range with coarse ferrite grain size having silicon (Si) and phosphorous (P) being more than the other nail (MSH-KAP-01).

CHAPTER 6

CONCLUSION

The study on the historical iron objects gives the opportunity to discover the reasons of the long-term durability related to the technological properties of those materials. The long-term corrosion characteristics of the Ottoman period low alloy steels, mainly as low carbon steels, were not well-known. In this thesis, corrosion layers of the 15th, 16th and 19th century low alloy steel objects were studied mainly by μ -Raman analysis and supported by stereo and digital microscopes, SEM-EDX, XRD and FTIR analysis.

All iron objects examined have corrosion layers on their surface where the corrosion products are mainly goethite and rarely hematite formed in open air environments namely urban, rural (interior, exterior) and burial environment. Neither rural / urban atmosphere nor outdoor / indoor conditions don't seem to play any important role in the formation of perfect corrosion layers on the iron objects which were around 600 years old and some around 150 years old. Majority of those objects have perfect corrosion layers that must have formed in the relatively early life of the objects and played their protective role since then. The outdoor objects which were mainly nails reflect the history of corrosion in more continuous way.

The objects which had perfect, medium and imperfect protective layers, had nano-sized goethite particles and were free of impurities. In the perfect protective layers, goethite crystallites were in the finer range, the average size being around 20 nm whereas the imperfect layers had the average particle size higher than the perfect ones being around 34 nm. The medium perfect layers had the average goethite particle size around 25 nm, in between the perfect and imperfect corrosion layers as estimated by the XRD FWHM measurements. The perfect corrosion layers have

finer nano-sized particles and appear to have good crystallinity revealed by their FTIR peaks. The good crystallinity in nano size particles is thought to be an indication of good stability for goethite in comparison to its amorphous state.

Protective ability of corrosion layers can be expressed with their PAI values. If PAI value is equal or greater than 1, protective function starts, if it is equal or greater than 2, protective function is more efficient and the corrosion layer becomes a stable phase (Kamimura et al, 2006). The PAI values being lower than 1 calculated for a 15th century sample and a 19th century sample are quite different than their contemporary objects. The reason for those differences may be due to their installation as new objects at later periods. All other objects have the PAI values equal or greater than 1 indicating full protective function of corrosion layers and the layers formed stable phase. The PAI value calculations can also help to prove the authenticity of the objects together with the morphology of the corrosion layers. The objects in buried condition from the 19th century have high PAI values indicating the high protective ability of corrosion layer formed on the objects in burial condition. The surface soil in the archaeological site of Foça seems to be suitable for formation of stable phase with its well aerated and compositional properties formed mainly from weathering of ignimbrite (tuff) formations in the area.

The dominance of hydrated iron (III) oxide or oxyhydroxide compounds together with goethite phase with variable crystallinity observed from FTIR analysis, and the marbling texture of the corrosion layers revealed by SEM may be the indication of electrochemically reactive environment with many wet - dry cycles experienced by the object. The protective goethite phases including a reactive lepidocrocite phase towards TM indicate the importance of wet - dry cycles helping the growth of a protective corrosion layer towards TM.

The objects embedded in timber have developed protective layers composed of wustite and hematite reflecting an environment with organic acids and natural resins.

In this study, the goethite formation occurs down to much finer particle sizes on the examined historical iron objects being in the range of 5 to 35 nm. Nano-sized goethite appears to have band gap values in the range of 3.1-2.5 eV and that values are relatively larger than the band gap of hematite at around the same size range (Zhang *et al*, 2011). It seems that the protective ability of the corrosion layer is closely related with fine size of goethite particles and its compactness. Iron is a well-known ferromagnetic metal and the iron objects can be considered as permanent magnets that have influence on the super-paramagnetic nano-sized goethite particles. The iron object itself may help to the compactness of nano-sized goethite particles formed on its surface.

The presence of relatively unstable oxides or oxyhydroxides in the layer do not have much influence on the protective ability of the corrosion layer. However, those oxide or oxyhydroxides may lead to the further formation of fine nano particles and incorporate in the compact layer during repeated wet – dry cycles.

This study concludes that finer the particle size, sharper the FTIR peak intensities showing higher crystallinity of goethite and its compactness are the main qualifications of perfect protective corrosion layers.

It is also possible to describe the goethite formation environment from the combined results of this study. There is always calcite available in the corrosion environment. Therefore, the pH of water in equilibrium with air and in equilibrium with calcareous materials like mortars and plasters is most likely to be around 7.8 (Busenberg and Plummer, 1986). The historical iron objects in open atmospheric conditions having wet-dry cycles most likely experience those conditions that lead to the goethite formation mechanisms.

The corrosion rates of the 15th, 16th and 19th century objects are much lower than the corrosion rates of today's low alloy steel (Kamimura *et al* 2006). The 16th century objects have the average corrosion rate of 0,76 $\mu\text{m}/\text{y}$ while the 19th century ones being around 1,33 $\mu\text{m}/\text{y}$. The corrosion rate of weathering steel is about 6 $\mu\text{m}/\text{y}$ (Yamashita *et al*, 2004). The average corrosion rate of low alloy steel in urban

atmospheric conditions is expected to be 2.29 $\mu\text{m}/\text{y}$ (Doruk, 2014). The door lock piece of 15th century hammam, which is assumed to be a replacement object during a relatively recent restoration, exhibits a similar corrosion rate (2.5 $\mu\text{m}/\text{y}$) expected from low alloy steel in coastal urban atmosphere.

Contribution of the minor elements in the composition and the microstructure of low alloy steel is of importance in the formation of perfect corrosion layer. It seems that the objects having perfect corrosion layer have rather low silicon content, the upper limit being 0.226% being as in low carbon steel grade. Objects with perfect corrosion layer have phosphorous content below 0.05% as well as the ones with higher than that value being up to 0.241%. The objects with the imperfect corrosion layer have high phosphorous content above 0.241% up to 0.282%. It is seen that although the phosphorous content of historical objects is above the threshold value (0.05%) of today's good quality steel, it doesn't seem to affect the ductility and the corrosion performance of the historical object up to 0.24% which is the limit found for the objects with perfect corrosion layer. The manganese content above 0.80% is known to have influence on hardness by making the low carbon steel harder. In this study, that threshold exist and it has influence on hardness but there is no direct relationship between the manganese content and the formation of corrosion layer. All samples have low magnesium content ranging from 0.000% to 0.0345%. The objects having relatively lower magnesium content have better formation of protective corrosion layer observed in the historical low carbon steels. There is no direct relationship with the aluminum content and the formation of protective corrosion layer for the samples studied. The role of chromium content without the presence of nickel does not show important contribution on the perfect corrosion layer unless it is present at considerable amounts (0.104%).

The objects with perfect corrosion layer and having relatively considerable amounts of Al and Si in their composition may have benefited from their presence.

Some minor elements are found to have influence on hardness. However, there is no direct relationship with corrosion layer formation and hardness of the objects.

Manganese content and fraction of pearlite have some influence on hardness. Phosphorous content has an influence on hardness after a certain threshold (0.25%). Although sulfur and manganese are abundant in the composition of some objects, their hardness is not high, that may be due to formation of CaS_2 and MnS particles in the microstructure observed by SEM-EDX and those formations may prevent the increase on hardness.

The microstructural properties of the historical objects seem to have some influence on perfect corrosion layer formation. The objects having perfect corrosion layer has fine grains maximum size being $60\ \mu\text{m}$ while the imperfect ones have the grains above $100\ \mu\text{m}$ size. The pearlitic structure may be related to the heat and the way of processing (production technology).

The comparison of two nails from the same location, both having perfect corrosion layer, show some differences in their microstructure with ferrite grains, hardness and compositional properties. The object with lower corrosion layer thickness ($50\ \mu\text{m}$) has lower hardness and it has smaller ferrite grains with manganese (Mn) and carbon (C) being higher than the other object with higher corrosion layer thickness ($100\ \mu\text{m}$). The object having corrosion layer thickness ($100\ \mu\text{m}$) has silicon (Si) and phosphorous (P) contents higher than the nail with lower thickness ($50\ \mu\text{m}$).

The presence of goethite as the main protective corrosion layer on the historical iron object was investigated in terms of its formation and morphology in detail. The importance of nano-sized goethite acting as a protective corrosion layer needs to be further studied.

6.1 Future Studies

In this study, specifications of perfect corrosion layer composed of mainly goethite is rather well described in terms of its compact morphology, good crystallinity and finer nano particle size. Further study is needed on the protective goethite layers to

investigate in more detail their morphology and particle size by SEM-EDX. The possibilities for the artificial formation of such a layer can be further investigated.

Fine ferritic structure seems to support perfect corrosion layer formation. The importance of elemental composition that lead to fine ferritic structure will be further investigated on the historical samples by detailed elemental analysis of their metal body in relation to the microstructure.

The current production of ductile iron pipes used for potable water transmission lines are lined with cement mortar internally to prevent their corrosion. This study inspires that the formation of protective goethite layer for the contemporary ductile iron surfaces can be a better choice and environmentally friendly. In potable water transmission lines, pH is around 7-8 which is a good initial condition for goethite formation.

REFERENCES

- Ahlström J, Tidblad J., Tang L., Sederholm B., and Leijonmarck S. 2018. Electrochemical Properties of Oxide Scale on Steel Exposed in Saturated Calcium Hydroxide Solutions with or without Chlorides. *International Journal of Corrosion*, 2018, doi.org/10.1155/2018/5623504.
- Albani, O.A., Gassa, L.M., Zerbino, J.O., Vilche, J.R., and Arvia, A.J. 1990. Comparative study of the passivity and the breakdown of passivity of polycrystalline iron in different alkaline solutions. *Electrochimica Acta*, 35, 1437-1444.
- Aktakka, G. 2006. Analysis of warm forging process. M.Sc. Thesis, The Graduate School of Natural and Applied Sciences of METU, 1-22 p.
- Antelo, J., Avena, M., Fiol, S., Lopez, R., and Arce, F. 2005. Effects of pH and ionic strength on the adsorption of phosphate and arsenate at the goethite-water interface. *Journal of Colloid Interface Science*, 285, 476-486.
- Antunes, R. A., Costa, I., and Araujo de Faria, D. L. 2003. Characterization of corrosion products formed on steels in the first months of atmospheric exposure. *Materials Research*. 6 (3), 403–408. doi: 10.1590/S1516-14392003000300015
- Aramendia, J., Gomez-Nubla, L., Castro, K., Martinez-Arkarazo, I., Vega, D., Sanz López de Heredia, A., García Ibáñez de Opakua, A., and Madariaga, J.M. 2012. Portable Raman study on the conservation state of four CorTen steel-based sculptures by Eduardo Chillida impacted by urban atmospheres. *J. Raman Spectroscopy*, 43, 1111-1117. doi:10.1002/jrs.3158
- Aramendia, J., Gomez-Nubla, L., Arrizabalaga, I., Prieto-Taboada, N., Castro, K., and Madariaga, J. M. 2013. Multi-analytical approach to study the dissolution process of weathering steel: The role of urban pollution. *Corrosion Science*, 76, 154-162. doi: 10.1016/j.corsci.2013.06.038

- Aramendia J. Gomez-Nubla L., Bellot-Gurlet L., Castro K., Paris C., Colomban P. and Madariaga J. 2014. Protective ability index measurement through Raman quantification imaging to diagnose the conservation state of weathering steel structures. *Journal of Raman Spectroscopy*, 45, 1076–1084, doi: 10.1002/jrs.4549.
- Arıkan, Y. 1969. Örendüzü pizolitik sedimenter demir yatakları (İçel, Gülnar, Gilindire) (Pizolithic sedimentary iron ore deposits in Örendüzü (İçel, Gülnar, Gilindire)). *Madencilik Dergisi*, 1-3.
- Asami, K., and Kikuchi, M. 2003. In-depth distribution of rusts on a plain carbon steel and weathering steels exposed to coastal-industrial atmosphere for 17 Years. *Corrosion Science*, 45, 2671-2688.
- Aşut, F. 2012. Mevcut Edirne hamamları ve zen İbrahim paşa hamamı restorasyonu üzerine bir araştırma (A research on the existing Edirne Turkish baths and the restoration of zen İbrahim paşa bath), MSc. Thesis, Trakya Üniversitesi, Fen Bilimleri Enstitüsü, Mimarlık Ana Bilim Dalı, Edirne.
- Ayduz S. 2006. *Artillery Trade of the Ottoman Empire*, Foundation of Science Technology and Civilization Limited, Manchester.
- Bagin, V.I. 1967. The chemical remanent magnetization at temperature transitions of lepidocrocite and goethite (in Russian), *Izv. Akad. Nauk USSR, Fiz. Zem.*, 2, 104–108.
- Balasubramaniam, R. 2000. On the corrosion resistance of the Delphi iron pillar. *Corrosion Science*, 42, 2103-2129.
- Balasubramaniam, R., 2004. Delphi iron pillar (Part 1). *IIM Metal News*, 7, 11-17.
- Balasubramaniam, R., 2004. Delphi iron pillar (Part 2). *IIM Metal News*, 7, 5-13.

- Balasubramaniam, R., and Kumar, A.V.R. 2000. Characterization of Delhi iron pillar rust by X-ray diffraction, Fourier transform infrared spectroscopy and Mossbauer spectroscopy. *Corrosion Science*, 42, 2085-2101.
- Balasubramaniam, R. 2002. *Delhi Iron Pillar: New Insights*. Indian Institute of Advanced Study, Shimla and Aryan Books International, New Delhi.
- Baş, Y. 2011. Kiğı demir madeni ve humbarahanesi (Kiğı iron mines and humbara workshops). *Turkish Studies - International Periodical for The Languages, Literature and History of Turkish or Turkic*, 6/4, 409-430 p.
- Barkan Ö. L. 1972-1979. Süleymaniye Cami ve İmaretinin inşaatı (1550-1557) (Construction of Süleymaniye Mosque and Imaret (1550-1557)). vol. 1 and 2, Türk Tarih Kurumu, Ankara.
- Batur, A. 2009. Geç Osmanlı mimarlığında betonarme yapım tekniği (Building technique of reinforced concrete in late Ottoman architecture). *Mimarlıkta Malzeme*, 4, 39-44.
- Berner, R. A. 1969. Goethite stability and the origin of the red beds. *Geochim. Cosmochim. Acta*, 33, 267-273.
- Bellot-Gurlet, L., Neff D., Reguer S., Monnier, Saheb M., and Dillmann P. 2009. Raman studies of corrosion layers performed on archeological irons in various media. *Journal of Nano Research*, 8, 147-156.
- Biber, H., Sevin, V., and Yalçın, Ü. 2008. Technological and Archeometallurgical studies on the Urartian swords and daggers. *Ancient Mining in Turkey and The Eastern Anatolia*, Ankara, Turkey, 15 - 22 June 2008, vol.1, 149-173 p.
- Bilgi Ö., 2004. In *Anatolia Cradle of Castings*. ed. Bilgi Ö., Döktaş, İstanbul, XI p.
- Busenberg E., and Plummer, L. N. 1986. A comparative study of the dissolution and crystal growth kinetics of calcite and aragonite. *Studies in Diagenesis*, 1578, 139-168.

- Callister, Jr., W. D., and Rethwisch, D. G. 2017. *Materials Science and Engineering: An Introduction*. 10th ed. Wiley, USA, 270-279 p.
- Cambier, P. 1986. Infrared study of goethites of varying crystallinity and particle size: I. Interpretation of OH and lattice vibration frequencies. *Clay Minerals*, 21 (2), 191-200. doi:10.1180/claymin.1986.021.2.08
- Cambier, P. 1986. Infrared study of goethites of varying crystallinity and particle size: II. Crystallographic and morphological changes in series of synthetic goethites. *Clay Minerals*, 21 (2), 201-210.
doi: 10.1180/claymin.1986.021.2.09
- Cengiz, A. 2018. Kalkan (Simav-Kütahya) demir yatağının oluşumunun incelenmesi (Investigation of formation of Kalkan (Simav-Kütahya) Iron deposit). Unpublished M.Sc. Thesis, Ankara Üniversitesi Fen Bilimleri Enstitüsü, Ankara, ii p.
- Cheng, X. Q., Tian, Y. W., Li, X. G., and Zhou, C. 2014. Corrosion behavior of nickel-containing weathering steel in simulated marine atmospheric environment. *Materials and Corrosion*, 65 (10), 1033-1037.
- Cheng, X., Jin, Z., Liu, M., and Li, X. 2017. Optimizing the nickel content in weathering steels to enhance their corrosion resistance in acidic atmospheres. *Corrosion Science*, 115, 135-142, doi.org/10.1016/j.corsci.2016.11.016.
- Chernyshova, I. V., Ponnurangama, S., and Somasundarana, P. 2010. On the origin of an unusual dependence of (bio)chemical reactivity of ferric hydroxides on nanoparticle size. *PCCP*, 12, 14045-14056, doi.org/10.1039/C0CP00168F.
- Coey, J.M.D., 1988. Magnetic properties of iron in soil oxides and clay minerals. In: *Iron in soils and clays Minerals*, Eds: Stucki, J. W., Goodman, B. A., and Schwertmann, U., Reidel Publishing Company, 397-466 p.

- Coey, J.M.D., and Readman, P. W. 1988. Characterisation and magnetic properties of natural ferric gel. *Earth and Planetary Science Letters*, 21, 45-51.
- Colomban, Ph. 2011. In *New Trends and Developments in Automotive System Engineering*. M. Chiaberge (ed.), InTech., 28, 567.
- Colpas-Ruiz, M.A., Gnecco-Molina, C., Pérez-Mendoza, J., Higuera-Cobos, O., and Jiménez-Rodríguez, G. 2020. Obtaining a hematite pigment by thermal transformation of the surface oxide of reinforcing steel bars. *Rev. UIS Ing.*, 19 (3), 143-152, doi: <https://doi.org/10.18273/revuin.v19n3-2020014>.
- Cook, D. C., Oh, S. J., Balasubramanian, R., and Yamashita, M. 1999. The role of goethite in the formation of the protective corrosion layer on steels. *Hyperfine Interactions*, 122, 59.
- Cornell R.M., and Giovanoli R. 1990. Transformation of akaganeite into goethite and hematite in alkaline media. *Clays and Clay Minerals*, 38, 469-476.
- Cornell, R. M., and Schwertmann, U. 2003. *The Iron Oxides: Structures, Properties, Reactions, Occurrences and Uses* (2nd ed.). Wiley-VCH GmbH and Co. KGaA, Weinheim, 115-117 p.
- Cudennec, Y., and Lecerf, A. 2006. The transformation of ferrihydrite into goethite or hematite. *Journal of Solid-State Chemistry*, 179, 716-722.
- Çağlan, D., Tosun, L., Avcı, S. O., Turuç, O., and Kanaat, G. 2016. Şamlı (Balıkesir) Demir madeni doğu ocağı batı şevlerini oluşturan kaya kütlelerinin duraylılık değerlendirmesi (Slope stability assessment of rock masses in western sector of Balıkesir Şamlı eastern open pit iron mine). *Jeoloji Mühendisliği Dergisi*, 40, 1-26.
- Çelik S., 2009. Sülemaniye Külliyesi Malzeme, Teknik ve Süreç (Materials, Techniques and Process in Süleymaniye Complex). Atatürk Kültür ve Dil Tarih Yüksek Kurumu, Ankara.

- Danişman G. 2007. Ottoman mining, metal working and fire-arms technology in south east Europe (15th-17th centuries). Foundation of Science Technology and Civilization Limited, Manchester.
- Danişman H. H. G., Özbal H., Tanyeli G., and Yalcin Ü. 2006. Kırklareli-Demirköy endüstri arkeolojisi çalışmaları: 2005 Sezonu İlk Çalışmaları (Kırklareli-Demirköy industrial archeology studies: First studies of the 2005 season). 22. Arkeometri Sonuclari Toplantisi (22nd Archaeometry Results Meeting), T.C. Kultur Bakanligi, Ankara, 1-22.
- Danişman H. H. G., Gerritsen F., Kaçar M., Özbal H., Özbal R., Tanyeli G., Yalçın Ü., Yazıcı N., and Yılmaz Z. 2012, Kırklareli, Demirköy’de Osmanlı dönemi demir dökümhanesinde çok disiplinli endüstri arkeolojisi projesi (Multidisciplinary industrial archeology project in the Ottoman era iron foundry in Demirköy, Kırklareli). International Iron & Steel Symposium, Karabük, Türkiye, 320-327.
- Danişman, H. H. G., Gerritsen, F., Kaçar, M., Özbal, H., Özbal, R., Tanyeli, G., Yalçın, Ü., and Yılmaz, Z. 2007. Demirköy - Samakocuk Demir Dökümhanesi: Trakya’da Osmanlı Demir İşlik Bölgesindeki Endüstriyel Arkeoloji Projesi (Demirköy-Samakocuk Iron Foundry: An Industrial Archaeology Project at an Ottoman Metal Work-Shop Complex in Thrace). TÜBA-AR dergisi, X, 91-109.
- Danişman, G., and Özbal, H. 2010. Kırklareli, Demirköy Fatih dökümhanesi 2008 yılı kazıları (Kırklareli, Demirköy Fatih foundry excavations in 2008). 31. Kazı Sonuclari Toplantisi (31st Excavation Results Meeting), 3, T.C. Kultur Bakanligi, Ankara, 1-20.
- Das, S., and Hendry, M.J. 2011. Application of Raman Spectroscopy to Identify Iron Minerals Commonly Found in Mine Wastes. Chemical Geology, 290, 101-108. doi:10.1016/j.chemgeo.2011.09.001
- De la Fuente, D., Díaz, I., Simancas, J., Chico, B., and Morcillo, M. 2011. Long-term atmospheric corrosion of mild steel. Corrosion Science, 53, 604-617.

- De Bakker, P.M.A., De Grave, E., Vandenberghe, R.E., Bowen, L.H., Pollard, R.J., and Persoons, R.M. 1991. Mossbauer study of the thermal decomposition of lepidocrocite and characterization of the decomposition products. *Phys. Chem. Miner.*, 18, 131–143.
- Dekkers, M. J., Hanckmann, W. J. F., Spassov, S., and Behrends, T. 2017. Mineral magnetic properties of partially oxidized siderite. *American Geophysical Union, Fall Meeting 2017*, abstract #GP23A-0914.
- Diakonov I., Khodakovsky, I., Schott, J., and Sergeeva, E. 1994. Thermodynamic properties of iron oxides and hydroxides. I. Surface and bulk thermodynamic properties of goethite (α -FeOOH) up to 500 K. *Eur. J. Mineral.*, 6, 967-983. doi:10.1127/ejm/6/6/0967
- Dillmann, P., Béranger, G., Piccardo, P., and Mathiesen, H. 2007. Corrosion of metallic heritage artefacts: Investigation, conservation and prediction of long-term behaviour (EFC 48). EFC, Woodhead Publishing, Cambridge.
- Dillmann, Ph., Mazaudier, F., and Hoerl S. 2004. Advances in understanding atmospheric corrosion of iron. I. Rust characterization of ancient ferrous artefacts exposed to indoor atmospheric corrosion. *Corrosion Science*, 46, 1401 – 1429 p.
- Doruk, M. 2014. *Metallik malzemeler ve korozyon (Metallic materials and corrosion)*, Korozyon Derneği (The Corrosion Association), Ankara.
- DPT, 2001. *Sekizinci Beş Yıllık Kalkınma Planı Madencilik Özel İhtisas Komisyonu Raporu Metal Madenler Alt Komisyonu Demir Çalışma Grubu Raporu*. Ankara, 34-35 p.
- Erdoğan, M. 1953. Osmanlı mimarı tarihinin arşiv kaynakları (Archival sources of the history of Ottoman architecture). *Tarih Dergisi*, 3, 95-122.
- Erdoğan M. 1955. *Mimar Davud Ağa'nın hayatı ve eserleri (Life and works of Architect Davud Ağa)*. *Türkiyat Mecmuası*, 12, 179-204.

- Ertin G. 2001. Biga yarımadasında madencilik (Mining in the Biga peninsula). *Coğrafya Dergisi*, 9, 81-108.
- Eruz, F. 2004. In *Anatolia Cradle of Castings*. ed. Bilgi Ö., Döktaş, İstanbul, 249 p.
- Evans, U. R. 1965. Electrochemical mechanism of atmospheric rusting. *Nature*, 206 (4988), 980-982.
- Evans, U. R., and Taylor, C. A. J. 1972. Mechanism of atmospheric rusting. *Corrosion Science*, 12 (3), 227-246. doi:10.1016/S0010-938X(72)90671-3.
- Fendorf, S., Eick, M.J., Grossl, P., and Sparks, D.L. 1997. Arsenate and chromate retention mechanisms on goethite. 1: Surface structure. *Environmental Science & Technology*, 31, 315-320.
- Feron, D., Crusset, D., Gras, J.M., and Macdonald D. D. 2004. Prediction of long-term corrosion behavior in nuclear waste systems. *Science and Technology Series*, ed. ANDRA, Chatenay-Malabry, 201.
- Ferrier, A. 1966. Influence de l'état de division de la goethite et de l'oxyde ferrique sur leurs chaleurs de réaction. *Rev. Chim. minérale*, 3, 587-615.
- Fischer, W. R., and Schwertmann, U. 1975. The formation of hematite from amorphous iron (III) hydroxide. *Clays & Clay Minerals*, 23, 33-37.
- Gadsden, J.A. 1975. *Infrared Spectra of Minerals and Related Inorganic Compounds*. Butterworths, London.
- Gehring, A.U. and Hofmeister, A.M. 1994. The transformation of lepidocrocite heating: a magnetic and spectroscopic study. *Clays & Clay Minerals*, 42, 409-415.

- Gencer, C. İ., and Çokuğraş, I. 2018. Çok yönlü bir cumhuriyet mimarı: Mualla Eyüboğlu Anhegger (A versatile republican architect: Mualla Eyüboğlu Anhegger). *Mimarlık Dergisi*, 55-59.
- Gendler, T. S., Bagin, V. I., Butuzova, G. Y., and Haliulina, E. A. 1999. The peculiarities of formation of Fe-Mn minerals from Tetis deep: data of magnetic mineralogy and Mossbauer spectroscopy (in Russian), in *Paleomagnetism and Rock Magnetism*. ed. Scsherbakov V.P., UIPE RAS, Moscow, 18–19 p.
- Gendler, T. S., Shcherbakov, V. P., Dekkers, M. J., Gapeev, A. K., Gribov, S. K., and McClelland E. 2005. The lepidocrocite–maghemite–haematite reaction chain - I. Acquisition of chemical remanent magnetization by maghemite, its magnetic properties and thermal stability. *Geophys. J. Int.*, 160, 815–832. doi: 10.1111/j.1365-246X.2005.02550.x.
- Gotic, M., and Music, S. 2007. Mossbauer, FT-IR and FE SEM investigation of iron oxides precipitated from FeSO₄ solutions. *Journal of Molecular Structure*, 834–836, 445–453. <https://doi.org/10.1016/j.molstruc.2006.10.059>.
- Granados-Correa, F., Corral-Capulin, N. G., Olguin, M. T., and Acosta-Leon, C. E. 2011. Comparison of the Cd(II) adsorption processes between boehmite (gamma-AlOOH) and goethite (alpha-FeOOH). *Chemical Engineering Journal*, 171, 1027-1034.
- Grau-Crespo, R., Al-Baitai, A.Y., Saadoun, I., and De Leeuw, N.H. 2010. Low-temperature magnetic properties of lepidocrocite, Vacancy ordering and electronic structure of γ -Fe₂O₃ (maghemite): a theoretical investigation. *Journal of Phys.: Condens. Matter*, 22, 255401.
- Guyodo, Y., Mostrom, A., Penn, R. L., and Banerjee, S. K. 2003. From Nanodots to Nanorods: Oriented aggregation and magnetic evolution of nanocrystalline goethite. *Geophysical Research Letters*, 30, 191-194.
- Hedley, I. G. 1968. Chemical remanent magnetization of the FeOOH, Fe₂O₃ system. *Phys. Earth planet. Inter.*, 1, 103–121.

- Hanesch, M. 2009. Raman spectroscopy of iron oxides and (oxy)hydroxides at low laser power and possible applications in environmental magnetic studies. *Geophysical Journal International.*, 177, 941.
- He, Y. T., and TRAINA, S. J. 2007. Transformation of magnetite to goethite under alkaline pH conditions. *Clay Minerals*, 42 (1), 13–19. doi: 10.1180/claymin.2007.042.1.02.
- Hiemstra, T. 2013. Surface and mineral structure of ferrihydrite. *Geochimica et Cosmochimica Acta*, 105, 316-325. doi: 10.1016/j.gca.2012.12.002.
- Hirt, A. B., and Lanci, L. 2002. Low-temperature magnetic properties of lepidocrocite. *Journal of Geophysical Research*, 107 (B1), 2011. doi: 10.1029/2001JB000242
- Hodges, H. 1964, *Artifacts: An introduction to early materials and technology.* Michigan University, Michigan, 217-218 p.
- Inalcık, H. 1957. Osmanlılarda ateşli silahlar (Firearms in the Ottomans). *Belleten*, 83, 509.
- Jaiswal, A., Banerjee, S., Mani, R., and Chattopadhyaya, M. C. 2013. Synthesis, characterization and application of goethite mineral as an adsorbent. *Journal of Environmental Chemical Engineering*, 1, 281-289.
- Jang, J., Dempsey, B. A., Catchen, G. L., and Burgos, W. D. 2003. Effects of Zn(II), Cu(II), Mn(II), Fe(II), NO₃⁻, or SO₄²⁻ at pH 6.5 and 8.5 on transformations of hydrous ferric oxide (HFO) as evidenced by Mossbauer spectroscopy. *Colloids and Surfaces A: Physicochemical and Engineering Aspects*, 221, 55–68.
- Janot, C., Gibert, H., and Tobias, C. 1973. Characterisation de kaolinites ferrifere par spectrometrie Mössbauer. *Bull. Soc. Fr. Mineral. Cristallog.* 96, 281-291.

- Jin J., Zhu X., Li, P., Li, Y., and Han, Y. 2022. Clean utilization of limonite ore by suspension magnetization roasting technology. *Journal of Minerals*, 12 (260), 1-13. doi: 10.3390/min12020260.
- Jolivet, J., Belleville, P., Tronc, E., and Livage, J. 1992. Influence of Fe(II) on the formation of the spinel iron oxide in alkaline medium. *Clays and Clay Minerals*, 40, 531–539.
- Kamimura, T., Hara, S., Miyuki, H., Yamashita, M., and Uchida, H. 2006. Composition and protective ability of rust layer formed on weathering steel exposed to various environments. *Corrosion Science*, 48, 2799.
- Kimura, M., and Kihira, H. 2005. Nanoscopic mechanism of protective rust formation on weathering steel surfaces. *Nippon Steel Tech. Rep.*, 91, 86.
- Kaneko, K., and Inouye, K. 1974. Electrical properties of ferric oxyhydroxides. *Bull. Chem. Soc.*, 47, 1139-1142.
- Koç, Ş., and Değer, M. A. 1991. Payas (Hatay) bölgesi boksitli demir cevherleşmesinin oluşumu (Formation of iron ore with bauxite in Payas (Hatay) Region), *MTA Dergisi*, 113, 113-126.
- Koç, Ş., Kaya Özer, C., and Öksüz, N. 2008. Karacaali (Kırıkkale) Demir cevherlerinin minerolojik özellikleri (Mineralogic properties of iron deposit in Karacaali (Kırıkkale) region. *S.Ü. Müh.-Mim. Fak. Derg.*, 23, 49-60.
- Kurt Y. 2014. Giresun Bulancak Kirazören bölgesi skarn tipi demir yataklarının jeolojik ve jeokimyasal incelenmesi (Geological and geochemical investigation of the skarn-type Iron ore deposits of the Kirazören Region, Bulancak, Giresun), Unpublished M.Sc. Thesis, İstanbul Üniversitesi Fen Bilimleri Enstitüsü, İstanbul, xiii p.
- Li, X., Zhang, T., Min, Y., Liu C., and Jiang, M. 2019. Effect of magnesium addition in low-carbon steel part 1: behavior of austenite grain growth. *Ironmaking & Steelmaking*, 46:3, 292-300. doi: 10.1080/03019233.2017.1368953

- Li, Z., Zhang, T., and Li, K. 2011. One- step synthesis of mesoporous two-line ferrihydrite for effective elimination of arsenic contaminants from natural water. *Dalton Transactions*, 40, 2062-2066.
- Lide, D. R. 2004. *Handbook of Chemistry and Physics*, 85th ed. Boca Raton, FL: CRC Press.
- Luttoretti, L., Pillière, H., Fontugne, C., Boullay, P., and Chateigner, D. 2019. Full-profile search–match by the Rietveld method. *J. Appl. Cryst.* 52, 587-598. doi: 10.1107/S160057671900342X
- Mazeina, L., and Navrotsky, A. 2007. Enthalpy of water adsorption and surface enthalpy of goethite (α -FeOOH) and hematite (α -Fe₂O₃). *Chemistry of Materials*, 19, 825-833.
- Majzlan, J., Lang, B. E., Stevens, R., Navrotsky, A., Woodfield, B. F., and Boerio-Goates, J. 2003. Thermodynamics of iron oxides: Part I. Standard entropy and heat capacity of goethite (α -FeOOH), lepidocrocite (γ -FeOOH), and maghemite (γ -Fe₂O₃). *American Mineralogist*, 88, 846-854.
- Majzlan J., Grevel K. D., and Navrotsky A. 2003. Thermodynamics of Fe oxides: Part II. Enthalpies of formation and relative stability of goethite (α -FeOOH), lepidocrocite (γ -FeOOH), and maghemite (γ -Fe₂O₃), *American Mineralogist*, 88, 855–859.
- Majzlan J., Navrotsky A. and Schwertmann, U. 2004. Thermodynamics of iron oxides: Part III. Enthalpies of formation and stability of ferrihydrite (\sim Fe(OH)₃), schwertmannite (\sim FeO(OH)_{3/4}(SO₄)_{1/8}), and ϵ -Fe₂O₃. *Geochimica et Cosmochimica Acta*, 68 (5), 1049–1059.
- Majzlan J., Koch C. B., and Navrotsky A. 2008. Thermodynamic properties of feroxhyte (δ -FeOOH). *Clays and Clay Minerals*, 56 (5), 526–553, doi: 10.1346/CCMN.2008.0560506.
- Mann, S., Sparks, N. H. C., Couling, S. B., Larcombe, M. C., and Frankel, R. B. 1989. Crystallochemical characterization of magnetic spinels prepared from

aqueous solution. *Journal of the Chemical Society Faraday Transactions I*, 85, 3033–3044.

McClelland, E. and Goss, C. 1993. Self-reversal of chemical magnetization on the transformation of maghemite to haematite. *Geophys. J. Int.*, 112, 517–532.

McHale, J. M., Auroux, A., Perrotta, A. J., and Navrotsky, A. 1997. Surface energies and thermodynamic phase stability in nanocrystalline aluminas. *Science*, 277, 788-791.

Misawa, T., Kyuno, T., Suetaka, W., and Shimodaira, S. 1971. The mechanism of atmospheric rusting and the effect of Cu and P on the rust formation of low alloy steels. *Corrosion Science*, 11 (1), 35-48.

Misawa, T., Asami, K., Hashimoto, K., and Shimodaira, S. 1974. The mechanism of atmospheric rusting and the protective amorphous rust on low alloy steel. *Corrosion Science*, 14 (4), 279-289.

Monnier J., Bellot-Gurlet L., Baron D., Neff D., Guillot I., and Dillmann P. 2011. A methodology for Raman structural quantification imaging and its application to iron indoor atmospheric corrosion products. *Journal of Raman Spectroscopy*, 42, 773–781, doi: 10.1002/jrs.2765.

Monnier, J., Réguer, S., Vantelon, D., Dillmann, P., Neff, D., and Guillot, I. 2010. X-rays absorption study on medieval corrosion layers for the understanding of very long-term indoor atmospheric iron corrosion. *Appl. Phys. A* 99, 399–406. doi: 10.1007/s00339-010-5638-8

Montes-Hernandez, G., Beck, P., Renard, F., Quirico, E., Lanson, B., Chiriac, R., and Findling, N. 2011. Fast precipitation of acicular goethite from ferric hydroxide gel under moderate temperature (30 and 70 degrees C). *Crystal Growth & Design*, 11, 2264-2272.

Moon, J., Kim, S. J., and Lee, C. 2013. Role of Ca treatment in hydrogen induced cracking of hot rolled API pipeline steel in acid sour media. *Met. Mater. Int.* 19, 45–48.

- Morcillo, M., Chico, B., Díaz, I., Cano, H., and de la Fuente, D. 2013. Atmospheric corrosion data of weathering steels: A review. *Corrosion Science*, 77, 6–24. doi: 10.1016/j.corsci.2013.08.021
- Morcillo, M., Díaz I, Chico B., Cano H., and de la Fuente D. 2014. Weathering steels: From empirical development to scientific design: A review, *Corrosion Science*, 83, 6–31. doi: 10.1016/j.corsci.2014.03.006.
- Murad, E., and Schwertmann, U. 1993. Temporal stability of a fine-grained magnetite. *Clays Clay Min.*, 41, 111-113.
- Múzquiz-Ramos, E. M., Guerrero-Chávez, V., Macías-Martínez, B. I., López-Badillo C. M., and García-Cerda, L. A. 2015. Synthesis and characterization of maghemite nanoparticles for hyperthermia applications. *Ceramics International*, 41 (1A), 397-402.
- Nagata, R., Tachibana, S., and Aso T. 2016. The influence of temperature and humidity on rust growth on weathering steel. *The Third Australasia and South-East Asia Structural Engineering and Construction*, Malaysia, Integrated Solutions for Infrastructure Development, Edited by Lau, H. H., Tang, F. E., Ng, C. K., and Singh, A. ISEC Press, ISBN: 978-0-9960437-3-1
- Nakamoto, K. 1997. Infrared and Raman spectra of inorganic and coordination compounds (Part A: Theory and applications in inorganic chemistry). John Wiley & Sons, Inc., Hoboken.
- Nasrazadani, S. 1990. Formation and Transformation Characteristics of Magnetite (Fe₃O₄) Under Different Laboratory and Field Conditions. PhD Dissertation, The Louisiana State University and Agricultural and Mechanical Col.
- Nasrazadani, S. 1997. The application of infrared spectroscopy to a study of phosphoric and tannic acids interactions with magnetite (Fe₃O₄), goethite (α -FeOOH) and lepidocrocite (γ -FeOOH). *Corrosion Science*, 39, 1845-1859.

- Navrotsky, A., Mazeina, L., and Majzlan, J. 2008. Size-driven structural and thermodynamic complexity in iron oxides. *Science*, 319, 1635–1638.
- Neff, D., Reguer, S., Bellot-Gurlet, L., Dillmann, Ph., and Bertholon, R. 2004. Structural characterization of corrosion products on archaeological iron: an integrated analytical approach to establish corrosion forms. *Journal of Raman Spectroscopy*, 35, 739-745. doi: 10.1002/jrs.1130
- Neff, D., Bellot-Gurlet, L., Dillmann, Ph., Reguer, S., and Legrand, L. 2006. Raman imaging of ancient rust scales on archaeological iron artefacts for long-term atmospheric corrosion mechanisms study. *Journal of Raman Spectroscopy*, 37, 1228-1237. doi: 10.1002/jrs.1581
- Nieuwmeijer G. G. 2005. The maintenance of historic iron and steel structures: coping with corrosion: In *structural Studies, Repairs and Maintenance of Heritage Architecture IX*, ed. C. A. Brebbia and A. Torpiano, 545-54. WIT Transactions on The Built Environment, Vol 83.
- Novák P., and Nová K. 2019. Oxidation behavior of Fe-Al, Fe-Si and Fe-Al-Si intermetallics. *Materials (Basel)*. 12(11):1748. doi: 10.3390/ma12111748. PMID: 31146415; PMCID: PMC6600787.
- Ocepek, D. 1989. Bogatenje mineralnih in energetskih surovin (Enrichment of mineral and energy raw materials), Edvard Kardel University, FNT VTOZD Montanistika, Ljubljana, 350 p.
- Oh S. J., Cook D. C., and Townsend H. E. 1999. Atmospheric corrosion of different steels in marine, rural and industrial environments. *Corrosion Science*, 41, 1687-1402.
- Özbal, H. 2010. Demirköy Demirci İşliği (Demirköy Blacksmith Workshop). 25. Arkeometri Sonuçları Toplantısı (25th Archaeometry Results Meeting), T.C. Kültür Bakanlığı, Ankara, 237-262 p.
- Özbal, H., Yalçın, Ü., and Dervişoğlu, R. 2008. Geç Osmanlı döneminde demir üretim teknolojileri: Demirköy 2006 sezonu buluntularının analiz sonuçları

(Iron production technologies in the Late Ottoman period: Analysis results of Demirköy 2006 season finds). 23. Arkeometri Sonuclari Toplantisi (23th Archaeometry Results Meeting), T.C. Kultur Bakanligi, Ankara, 27-40 p.

Özdemir, Ö. & Dunlop, D.J. 1993. Chemical remanent magnetization during γ - FeOOH phase transformation. *J. Geophys. Res.*, 98 (3), 4191–4198.

Öztunalı, Ö. 1965. Demirtepe-Çavdar, Osmankuyu-Kisir (Çine Maisifi) uranyum zuhurlarının petrografileri ve oluşumları (Petrographs and occurrences of uranium in Demirtepe-Çavdar, Osmankuyu-Kisir (Çine Massif)). *MTA Derg.*, 65, 109-121.

Pani, S., Singh, S. K., and Mohapatra, B. K. 2016. Vibrational Spectroscopic Study for Qualitative Assessment of Mn-oxide Ore. *Resour Geol*, 66, 12– 23. doi: 10.1111/rge.12083.

Parry V. J. 1970. *Materials of war in the Ottoman Empire, studies in the economic history of the Middle East from the rise of Islam to the present day.* ed. Cook M. A., Oxford University Press, London, 220-227.

Pedersen, H.D. 2006. The transformation of Fe(III) oxides catalyzed by Fe²⁺ and the fate of arsenate during transformation and reduction of Fe(III) oxides. *DTU Environment*.

Pedersen, H. D., Postma, D., Jakobsen, R., and Larsen, O. 2005. Fast transformation of iron oxyhydroxides by the catalytic action of aqueous Fe(II). *Geochimica et Cosmochimica Acta*, 69, 3967–3977.

Perelomov, L.V., Pinskiy, D.L., Violante, A. 2011, Effect of organic acids on the adsorption of copper, lead, and zinc by goethite: *Eurasian Soil Science*, 44, 22-28.

Pitcher, M.W., Ushakov, S.V., Navrotsky, A., Woodfield, B.F., Li, G., Boerio-Goates, J., and Tissue, B.M. 2005. Energy crossovers in nanocrystalline zirconia. *Journal of the American Ceramic Society*, 88, 160-167.

- Prasad, P. S. R., Shiva Prasad, K., Krishna Chaitanya, V., Babu, E. V. S. S. K., Sreedhar, B., and Ramana Murthy, S. 2006. In situ FTIR study on the dehydration of natural goethite. *Journal of Asian Earth Sciences*, 27, 503-511.
- Quinn, R. K., Nasby, R. D., and Baughman, R. J. 1976. Photo assisted electrolysis of water using single crystal α -Fe₂O₃ anodes. *Mat. Res. Bull.* 11, 1011-1018.
- Radović, N., Koprivica, A., Glišić, D., Fadel A., and Drobñjak, D. 2010. Influence of Cr, Mn and Mo on structure and properties of V micro alloyed medium carbon forging steels. *MJoM*, 16 (1), 1-9.
- Robbie, R. A., Cabell, B. F., and Hemingway, B. S., 1982. Heat capacity and entropy of fayalite (Fe₂SiO₄) between 5.1 and 383 K: comparison-of calorimetric and equilibrium values for the QFM buffer reaction. *American Mineralogist*, 67, 463-469.
- Ruan, H.D., Frost, R.L., and Klopogge, J.T. 2001. The behavior of hydroxyl units of synthetic goethite and its dehydroxylated product hematite. *Spectrochimica Acta Part a-Molecular and Biomolecular Spectroscopy*, 57, 2575-2586.
- Sakash, G.S., and Solntseva, L.S. 1971. Mechanism of thermal decomposition of synthesized γ -Fe-oxyhydroxide (in Russian). *J. Appl. Spectrosc.*, 16, 741.
- Salama, W., El Aref, M., and Gaupp, R. 2015. Spectroscopic characterization of iron ores formed in different geological environments using FTIR, XPS, Mössbauer spectroscopy and thermos analyses. *Spectrochim Acta A Mol Biomol Spectrosc.* 136 Pt C:1816-26. doi: 10.1016/j.saa.2014.10.090.
- Salopek, B., Krasi, D., and Filipovi, S. 1992. Measurement and application of zeta-potential. *Rudarsko-geoloiko-naftni zbornik*, 4, 147-151.
- Sato K., Sudo T., Kurosawa F. and Kammori O., 1969. The influence of crystallization on the infrared spectra of α - and γ -ferric oxyhydroxides. *Nippon Kinzoku Gakkaishi (J. Japan Inst. of Metals)*, 33, 1371-1376.

- Schmolt, B. 2016. Evolution of the Hopewell furnace blast machinery. *The Journal of the Society for Industrial Archeology*, 42 (2), 5–22.
- Schwertmann, U. 1959. Die fraktionierte Extraktion der freien Eisenoxide in Böden, ihre mineralogischen Formen und ihre Entstehungsweisen: *Z. Pflanzenernähr. Diingung Bodenkunde* 84, 194-204
- Schwertmann, U., and Fischer, W. R. 1966. Zur Bildung von α -FeOOH und α -Fe₂O₃ aus amorphem Eisen(III)-hydroxid. III: *Z. Anorg. Allg. Chem.* 346, 137-142.
- Schwertmann, U., and Murad., E. 1983. Effect of pH on the formation of goethite and hematite from ferrihydrite. *Clays and Clay Minerals*, 31 (4), 277-284.
- Schwertmann, U., Cambier, P., and Murad, E. 1985. Properties of goethites of varying crystallinity. *Clays Clay Minerals.*, 33, 369-378.
- Schwertmann, U., and Taylor, R. M. 1989. Iron Oxides, Mineral in Soil Environments, ed. Dixon, B., and Weed, S.B., Soil Science Society of America, 379-427 p. doi: 10.2136/sssabookser1.2ed.c8.
- Schwertmann, U., and Cornell, R.M. 1991. Iron oxides in the laboratory. VCH, Weinheim, 137 p.
- Schwertmann, U., Stanjek, H., and Becher, H. H. 2004. Long-term in vitro transformation of 2-line ferrihydrite to goethite/hematite at 4, 10, 15 and 25 °C. *Clay Minerals*, 39, 433-438.
- Schwertmann, U., and Cornell, R. M. 2007. Iron oxides in the laboratory: Preparation and characterization. Weinheim, Wiley-VCH Verlag, GmbH., X p.
- Seyitdanlıoğlu, M. 2006. Tanzimat dönemi Osmanlı sanayi (1839-1876) (Ottoman industry in the Tanzimat period (1839-1876)). *Türk Modernleşme Tarihi*

Araştırmaları Sempozyumu, 14 Mayıs 2005, Bildiri-Makaleler, Ercüment Kuran'a Saygı, Ankara, 263-278 p.

Seeba, M. 2022. Technical White Paper: Analysis of microplastics using FTIR and Raman microscopy. Published in Bruker's website.

Shao, Y., Veasey, T. J., and Rowson, N. A. 1996. Wet high intensity magnetic separation of iron minerals. *Magnetic and Electrical Separation*, 8, 41–51.

Shokrollahi, H. 2017. A review of the magnetic properties, synthesis methods and applications of maghemite. *Journal of Magnetism and Magnetic Materials*, 426, 74–81. doi: 10.1016/j.jmmm.2016.11.033.

Singh, A. K., Ericsson, T., and Haggstrom, L. 1985. Mössbauer and x-ray diffraction phase analysis of rusts from atmospheric test sites with different environments in Sweden. *Corrosion Science*, 25 (10), 931-945.

Singh, R. 2016. *Applied Welding Engineering: Processes, Codes and Standards*. 2nd Ed. Elsevier Inc., Butterworth - Heinemann, 7-86 p. doi: 10.1016/C2015-0-00784-5.

Sklute, E. C., Kashyap, S., Dyar, M. D., Holden, J. F., Tague, T., Wang, P., and Steven, J. J. 2018. Spectral and morphological characteristics of synthetic nanophase iron (oxyhydr)oxides. *Phys Chem Minerals* 45, 1–26. doi: 10.1007/s00269-017-0897-y

Snow, C. L., Smith, S. J., Lang, B. E., Shi, Q., Boerio-Goates, J., Woodfield, B. F., and Navrotsky, A. 2011. Heat capacity studies of the iron hydroxides akaganéite (β -FeOOH) and lepidocrocite (γ -FeOOH), *J. Chem. Thermodyn.*, 43, 190-199.

Snow, C. L., Lilova, K. I., Radha, A. V., Shi, Q., Smith, S., Lang, B. E., Navrotsky, A., Boerio-Goates, J., and Woodfield, B. F. 2013. Heat capacity and thermodynamics of a synthetic two-line ferrihydrite, FeOOH.0.027H₂O. *Science Direct*, 58, 307-314. doi: 10.1016/j.jct.2012.11.012.

- Speakman, S. A., Estimating Crystallite Size Using XRD. Lecture Notes. MIT Center for Materials Science and Engineering. <http://prism.mit.edu/xray>.
- Stoianovich T. 1994. *Balkan Worlds: The First and The Last Europe*. New York, M. E. Sharpe.
- Tanyeli G. 1990. Osmanlı Mimarlığında Demirin Strüktürel Kullanımı, 15.-18. Yüzyıl (Structural Use of Iron in Ottoman Architecture during 15th-18th Centuries). Unpublished Ph.D. Thesis, ITU Fen Bilimleri Enstitüsü, İstanbul.
- Tanyeli G., Geçkinli E., and Ata A. 1990. Osmanlı mimarisinde kullanılan demir elemanların üretim teknolojisi (Production technology of iron elements used in Ottoman architecture). In 6. Arkeometri Sonuçları Toplantısı (6th Archaeometry Results Meetings), T.C. Kültür Bakanlığı, Ankara, 109 p.
- Tanyeli G., and Tanyeli U. 1993. 16. Yüzyıl Osmanlı Mimarlık Teknolojisi (16th century Ottoman period architectural technology). 21. Yüzyıl Eğitim ve Kültür Vakfı, İstanbul, 125 p.
- Tanyeli G., Geçkinli E., and Ata A. 1990. VI. Arkeometri Sonuçları Toplantısı (6th Archaeometry Results Meetings). T.C. Kültür Bakanlığı, Ankara, 109 – 126.
- Tiringa, D., Ünlü, T., and Sayılı, İ. S. 2009. Kayseri-Yahyalı-Karaköy, Karaçat Demir Yatağının Maden Jeolojisi (Mining Geology of Karaçat Iron Deposit, Karaköy, Yahyalı, Kayseri). *Jeoloji Mühendisliği Dergisi*, 33, 1-44.
- Tiringa, D., Çelik, Y., and Demirkıran, G. 2019. Balaban Demir Cevherleşmesinin (Kırklareli-Demirköy) Kökeni ve Ekonomik Potansiyelinin Değerlendirilmesi (Evaluation of the Origin and Economic Potential of the Balaban Iron Mineralization (Kırklareli-Demirköy)). Presentation in MTA Scientific Events Week 2019.
- Tronc, E., Belleville, P., Jolivet, J., and Livage, J. 1992. Transformation of ferric hydroxide into spinel by FeII adsorption. *Langmuir*, 8, 313–319.

- Tylecote, R. F. 1976. A history of metallurgy. The Metals Society, London.
- Uluengin B. 2005. Mimari metallar özellikleri, bozulma nedenleri, koruma ve restorasyon teknikleri (Architectural metals, deterioration reasons, conservation and restoration techniques). Birsen Yayınevi, İstanbul.
- Veneranda, M., Aramendia, J., Bellot-Gurlet, L., Colomban, Ph., Castro, K., and Madariaga, J. M. 2018. FTIR spectroscopic semi-quantification of iron phases: A new method to evaluate the protection ability index (PAI) of archaeological artefacts corrosion systems. *Corrosion Science*, Elsevier, 133, 68 – 77 p. – doi: 10.1016/j.corsci.2018.01.016.hal-01734761
- Villacís-García, M., Ugalde-Arzate, M., Vaca-Escobar, K., Villalobos, M., Zanella, R., and Martínez-Villegas, N. 2015. Laboratory synthesis of goethite and ferrihydrite of controlled particle sizes. *Boletín de La Sociedad Geológica Mexicana*, 67 (3), 433–446.
- Villalobos, M., Leckie, J. O. 2001. Surface complexation modeling and FTIR study of carbonate adsorption to goethite. *Journal of Colloid and Interface Science*, 235, 15-32.
- Wang, Z., Liu, J., Wu, L., Han, R., and Sun, Y. 2013. Study of the corrosion behavior of weathering steels in atmospheric environments, *Corrosion Science*, 67, 1–10. doi: 10.1016/j.corsci.2012.09.020.
- Wang, F., Guo, H., Liu, W., Yang, S., Zhang, S., and Li, J. 2019. Control of MnS Inclusions in High- and Low-Sulfur Steel by Tellurium Treatment. *Materials (Basel)*; 12 (7), 1034. doi: 10.3390/ma12071034.
- Waseda, Y., and Suzuki, S., 2005. Characterization of corrosion products on steel surfaces. Springer Berlin, Heidelberg, VII p., doi.org/10.1007/978-3-540-35178-8.

- Waters, K. E., Rowson, N. A., Greenwood, R. W., and Willams, A. J. 2008. The effect of heat treatment on the magnetic properties of pyrite. *Minerals Engineering*, 21, 679–682, doi:10.1016/j.mineng.2008.01.008.
- Wefers, K. 1966a. Zum System $\text{Fe}_2\text{O}_3\text{-H}_2\text{O}$. 1. Teil. *Ber. Dtsch. Keram. Ges.*, 43, 677-702.
- Xu, G., Jiang, Z., and Li, Y. 2016. Formation Mechanism of CaS-Bearing Inclusions and the Rolling Deformation in Al-Killed, Low-Alloy Steel with Ca Treatment. *Metall Mater Trans B* 47, 2411–2420. doi: 10.1007/s11663-016-0695-9.
- Xu, X., Zhang, T., Wua, W., Jiang, S., Yang, J., and Liu, Z. 2021. Optimizing the resistance of Ni-advanced weathering steel to marine atmospheric corrosion with the addition of Al or Mo. *Construction and Building Materials*, 279, 122341. doi: 10.1016/j.conbuildmat.2021.122341.
- Yalçın, Ü. 2012. *Metallhandwerk in Anatolien (Metal Crafts in Anatolia)*. Lecture presentation in Hambourg.
- Yalçın, Ü. 2008, Ancient metallurgy in Anatolia, ancient mining in Turkey and the Eastern Mediterranean. ed. Yalçın, Ü., Özbal, H., and Paşamehmetoğlu, A. G., Atılım University, Ankara, 15-40 p.
- Yamashita, M., Miyuki, H., Matsuda, Y., Nagano H., and Misawa, T. 1994. The long-term growth of the protective rust layer formed on weathering steel by atmospheric corrosion during a quarter of a century. *Corrosion Science*, 36, 283-299. doi: 10.1016/0010-938X(94)90158-9.
- Yamashita, M., Nagano, H., Misawa, T., and Townsend, H. E. 1998. Structure of protective rust layers formed on weathering steel in the industrial atmospheres of Japan and Nort America. *ISIJ International*, 38 (3), 285-290.
- Yamashita M., Konishi H., Mizuki J., and Uchida H. 2004. Nanostructure of protective rust layer on weathering steel examined using synchrotron

radiation X-rays. *Materials Transactions*, 45, 1920–1924. doi: 10.2320/matertrans.45.1920.

Yıldız, N. 2010, *Demir Cevheri (Iron Ore)*, Ertem Basım Yayın Ltd. Şti., Ankara, 19-20 p.

Yin, M., Chen, Z., Deegan, B., and O'Brien, S. 2007. Wüstite nanocrystals: Synthesis, structure and superlattice formation. *Journal of Materials Research*, 1987-1995. doi: 10.1557/jmr.2007.0247.

Zachara, J. M., Kukkadapu, R. K., Fredrickson, J. K., Gorby, Y. A., and Smith, S. 2002. Biomineralization of poorly crystalline Fe(III) oxides by dissimilatory metal reducing bacteria (DMRB). *Geomicrobiology Journal*, 19, 179–207.

Zamiri, R., Ahangar, H.A., Zakaria, A., Zamiri, G., Bahari, H.R., and Drummen, G.P.C. 2014. Hydrothermal synthesis of goethite (α -FeOOH) nanorods in the presence of ethylenediamine: thiourea. *Journal of Nanoparticle Research*, 16, 2332-2342.

Zhang, L., Boxall, C., and Kelsall, G. H. 1993. Photo electrophoresis of colloidal iron oxides. I. Hematite (α -Fe₂O₃). *Colloids and Surfaces. A Physics Chemical and Engineering Aspects*, 73, 145-163.

Zhang, J., Tan, P., Zhao, W., Jun, L., and Zhao, J., 2011. Raman study of ultrathin Fe₃O₄ films on GaAs (001) substrate: stoichiometry, epitaxial orientation and strain, *J. Raman Spectroscopy*, 42, 1388–1391, doi: 10.1002/jrs.2863.

Zhang, L., Niu, D., Wen, B., Fu, Q., Peng, G., Su, L., and Blackwood, D. J., 2021. Initial-corrosion condition behavior of the Cr and Al alloy steel bars in coral concrete for marine construction, *Cement and Concrete Composites*, 120, 1-14. doi: 10.1016/j.cemconcomp.2021.104051.

CURRICULUM VITAE

Surname, Name: Yücel, Nurdan

EDUCATION

Degree	Institution	Year of Graduation
MS	University of Nottingham Human Factors in Manufacturing Systems	1996
BS	METU Mechanical Engineering	1995
High School	Bahçelievler Deneme Lisesi, Ankara	1988

FOREIGN LANGUAGES

Advanced English, Intermediate Italian

PUBLICATIONS

1. Yücel N., Kalkanlı A. and Caner Saltık E. N. " Investigation of atmospheric corrosion layers on historic iron nails by micro-Ramanspectroscopy ", Journal of Raman Spectroscopy, (2016), DOI 10.1002/jrs.5014
2. Yücel N. and Caner Saltık E. N. " Structural and compositional Characteristics of Komana Bracelets ” in Komana Small Finds Ed. By D. Burcu Erciyas-Meryem Acara Eser, 1st Ed., 339-345 (2019)
3. Bakırer Ö., Erciyas B., Caner Saltık E. N and Yücel N. " Tokat-Komana Kazısı Buluntularından Cam Boncukların Biçimsel ve Yapısal Özellikleri ", V. ODTÜ Arkeometri Çalıştayını Bildiriler Kitabı, 153-164 (2019)
4. Yücel N., Caner Saltık E. N. and Demirci Ş. " Divriği Ulu Camii ve Darüşşifası'nın Yapı Taşı Olan Dolomitin Bileşimindeki Demir Minerallerinin Anıttaki Taş Bozulmalarına Etkisi ", IV. ODTÜ Arkeometri Çalıştayını Bildiriler Kitabı, (2016)
5. Yücel N., Kalkanlı A. and Caner Saltık E. N. " İstanbul Kılıç Ali Paşa Hamamı Yapımında Kullanılan Bazı Demir Elemanların Alaşım ve Korozyon Karakteristikleri ", IV. ODTÜ Arkeometri Çalıştayını Bildiriler Kitabı, (2013)